

DTIC FILE COPY

AD-A223 124

AIR FORCE OFFICE OF
SCIENTIFIC RESEARCH
UNITED STATES AIR FORCE
RESEARCH INITIATION
PROGRAM

CONDUCTED BY
UNIVERSAL ENERGY SYSTEMS
U.E.S.

1988

TECHNICAL REPORT

VOLUME 2 OF 4

RODNEY C. DARRAH
PROGRAM DIRECTOR, UES

SUSAN K. ESPY
PROGRAM ADMINISTRATOR, UES

LT. COL. CLAUDE CAVENDER
PROGRAM MANAGER, AFOSR

DISTRIBUTION STATEMENT A

Approved for public release
Distribution Unlimited

REPORT DOCUMENTATION PAGE

Form Approved
OMB No. 0704-0188

Please regarding copies of this document to the Director is enclosed in envelope 1. Also see reference, including the use of reporting instructions, regarding security clearances, personnel and management and other requests, and regarding the reporting of information. Also regarding reporting the various phases of any other aspect of the conduct of operations, including suggestions for reducing the burden, to the following reporting services, including the information concerning the report, 1215 Jefferson Davis Highway, Suite 1204, Arlington, VA 22202-4302, and to the Office of Management and Budget, Paperwork Reduction Project (0704-0188), Washington, DC 20503.

1. AGENCY USE ONLY (Leave blank)		2. REPORT DATE		3. REPORT TYPE AND DATES COVERED	
		1988 Vol. 2 of 4		Technical Report	
4. TITLE AND SUBTITLE				5. FUNDING NUMBERS	
United States Air Force Research Initiation Program				61102F 3484/D5	
6. AUTHOR(S)					
Rodney C. Darrah Lt Col Claude Cavender					
7. PERFORMING ORGANIZATION NAME(S) AND ADDRESS(ES)				8. PERFORMING ORGANIZATION REPORT NUMBER	
Universal Energy Systems				AFOSR-TR-00000000 0708	
9. SPONSORING / MONITORING AGENCY NAME(S) AND ADDRESS(ES)				10. SPONSORING / MONITORING AGENCY REPORT NUMBER	
AFOSR/XOT Bld 410 Bolling AFB DC 20332-6448				F49620-88-C-0053	
11. SUPPLEMENTARY NOTES					
12a. DISTRIBUTION / AVAILABILITY STATEMENT				12b. DISTRIBUTION CODE	
Unlimited					
13. ABSTRACT (Maximum 400 words)					
See Attached					
14. SUBJECT TERMS				15. NUMBER OF PAGES	
				16. PRICE CODE	
17. SECURITY CLASSIFICATION OF REPORT		18. SECURITY CLASSIFICATION OF THIS PAGE		19. SECURITY CLASSIFICATION OF ABSTRACT	
Unclassified		Unclassified		Unclassified	
				20. LIMITATION OF ABSTRACT	
				N/A	

NSN 7540-01-280-5500

STANDARD FORM 298 (870104 Draft)
PREPARED BY GPO 195 220-10
220-01

UNITED STATES AIR FORCE
1988 RESEARCH INITIATION PROGRAM

Conducted by
UNIVERSAL ENERGY SYSTEMS, INC.

under
USAF Contract Number F49620-88-C-0053

RESEARCH REPORTS
VOLUME II OF IV

Submitted to
Air Force Office of Scientific Research
Bolling Air Force Base
Washington, DC

By
Universal Energy Systems, Inc.
April 1990



Accession For	
NTIS CRA&I	<input checked="checked" type="checkbox"/>
DTIC TAB	<input type="checkbox"/>
Unannounced	<input type="checkbox"/>
Justification	
By _____	
Distribution /	
Availability Codes	
Dist	
A-1	

TABLE OF CONTENTS

<u>SECTION</u>	<u>PAGE</u>
INTRODUCTION	i
STATISTICS	ii
PARTICIPANT LABORATORY ASSIGNMENT	vii
RESEARCH REPORTS	xvii

INTRODUCTION

Research Initiation Program - 1988

AFOSR has provided funding for follow-on research efforts for the participants in the Summer Faculty Research Program. Initially this program was conducted by AFOSR and popularly known as the Mini-Grant Program. Since 1983 the program has been conducted by the Summer Faculty Research Program (SFRP) contractor and is now called the Research Initiation Program (RIP). Funding is provided to establish RIP awards to about half the number of participants in the SFRP.

Participants in the 1988 SFRP competed for funding under the 1988 RIP. Participants submitted cost and technical proposals to the contractor by 1 November 1988, following their participation in the 1988 SFRP.

Evaluation of these proposals was made by the contractor. Evaluation criteria consisted of:

1. Technical Excellence of the proposal
2. Continuation of the SFRP effort
3. Cost sharing by the University

The list of proposals selected for award was forwarded to AFOSR for approval of funding. Those approved by AFOSR were funded for research efforts to be completed by 31 December 1989.

The following summarizes the events for the evaluation of proposals and award of funding under the RIP.

- A. Rip proposals were submitted to the contractor by 1 November 1988. The proposals were limited to \$20,000 plus cost sharing by the universities. The universities were encouraged to cost share since this is an effort to establish a long term effort between the Air Force and the university.
- B. Proposals were evaluated on the criteria listed above and the final award approval was given by AFOSR after consultation with the Air Force Laboratories.
- C. Subcontracts were negotiated with the universities. The period of performance of the subcontract was between October 1988 and December 1989.

Copies of the Final Reports are presented in Volumes I through IV of the 1988 Research Initiation Program Report. There were a total of 92 RIP awards made under the 1988 program.

STATISTICS

PROGRAM STATISTICS

Total SFRP Participants	153
Total RIP Proposals submitted by SFRP	121
Total RIP Proposals submitted by GSRP	5
Total RIP Proposals submitted	126
Total RIP's funded to SFRP	85
Total RIP's funded to GSRP	3
Total RIP's funded	88
Total RIP's Proposals submitted by HBCU's	8
Total RIP's Proposals funded to HBCU's	4

LABORATORY PARTICIPATION

<u>Laboratory</u>	<u>SFRP Participants</u>	<u>RIP's Submitted</u>	<u>RIP's Funded</u>
AAMRL	10	8 (1 GSRP)	5
AFWAL/APL	8	8	4
ATL	8	9 (1 GSRP)	8 (1 GSRP)
AEDC	5	5 (1 GSRP)	4 (1 GSRP)
AFWAL/AL	8	8	4
ESMC	1	0	0
ESD	2	2	2
ESC	8	7	5
AFWAL/FDL	10	9 (1 GSRP)	6 (1 GSRP)
FJSRL	7	5	4
AFGL	12	7	5
HRL	14	13	9
AFWAL/ML	12	9	6
OEHL	4	3	3
AL	8	7	6
RADC	12	8	8
SAM	16	9	8
WL	6	7 (1 GSRP)	4
WHMC	2	2	1
Total	153	126	88

LIST OF UNIVERSITIES THAT PARTICIPATED

Akron, University of	- 1	Louisiana Tech. University	- 1
Alabama, University of	- 1	Lowell, University of	- 2
Albany College	- 1	Maine, University of	- 1
Arizona State University	- 1	Meharry Medical College	- 1
Arizona, University of	- 1	Miami University	- 1
Arkansas State University	- 1	Miami, University of	- 1
Arkansas, University of	- 2	Michigan State University	- 1
Auburn University	- 1	Michigan Tech. University	- 1
Austin Peay State Univ.	- 1	Michigan, University of	- 2
Ball State University	- 1	Minnesota, University of	- 1
Boston College	- 1	Missouri Western State Coll.	- 1
California State Univ.	- 2	Missouri, University of	- 2
California, Univ. of	- 1	Montana, University of	- 1
Calvin College	- 1	Montclair State College	- 1
Carnegie Mellon University	- 1	Morehouse College	- 1
Central State University	- 3	Muhlenberg College	- 1
Central Wesleyan College	- 1	Murray State University	- 1
Cincinnati, University of	- 3	Nebraska, University of	- 1
Clarkson University	- 2	New Hampshire, Univ. of	- 3
Clemson University	- 1	New Mexico, University of	- 1
Colorado State University	- 2	New York State University	- 2
Columbia Basin College	- 1	New York, City College of	- 1
Dayton, University of	- 5	North Carolina State Univ.	- 1
Delta State University	- 1	North Carolina, Univ. of	- 2
East Texas State University	- 1	Northern Illinois Univ.	- 1
Eastern New Mexico Univ.	- 1	Ohio State University	- 2
Fairleigh Dickinson Univ.	- 1	Oklahoma State University	- 1
Fayetteville State Univ.	- 1	Oral Roberts University	- 1
Florida Inst. of Technology	- 1	Oregon Inst. of Technology	- 2
Florida, University of	- 1	Oregon State University	- 1
Francis Marion University	- 1	Pennsylvania State Univ.	- 1
George Mason University	- 1	Polytechnic University	- 1
Georgia Inst. of Technology	- 2	Prairie View A&M Univ.	- 2
Georgia, University of	- 1	Presbyterian College	- 1
Gonzaga University	- 1	Purdue University	- 1
Hampton University	- 1	Redlands, University of	- 1
Illinois Inst. of Technology	- 1	Rennselaer Polytechnic Inst	- 1
Indiana University	- 1	Rice University	- 1
Iowa State University	- 1	Rochester Inst. of Tech.	- 1
Jackson State University	- 3	Rose-Hulman Inst. of Tech.	- 1
Jacksonville State Univ.	- 1	Saint Paul's College	- 1
Jarvis Christian College	- 1	San Francisco State Univ.	- 1
Kentucky, University of	- 1	Santa Clara University	- 1
LaVerne, University of	- 1	Southeast Oklahoma State U.	- 1
Louisiana State University	- 2	Southern Mississippi, Univ.	- 1

LIST OF UNIVERSITIES THAT PARTICIPATED
Continued

Southern University	- 2	Tuskegee University	- 1
Southwest Missouri State U.	- 1	Virginia Polytechnic Inst.	- 1
St. Norbert College	- 1	Warren Wilson College	- 1
Staten Island, College of	- 1	Wayne State University	- 1
Syracuse University	- 1	Wesleyan College	- 1
Taylor University	- 1	West Florida, University of	- 1
Tennessee Space Inst., Univ.	- 1	West Texas State Univ.	- 1
Tennessee Tech. University	- 2	West Virginia Tech.	- 1
Tennessee, University of	- 1	Western Illinois University	- 1
Texas A&I University	- 1	Western Michigan University	- 1
Texas Lutheran College	- 1	Widener University	- 1
Texas, University of	- 4	Wilberforce University	- 1
Towson State University	- 1	Wisconsin-Madison, Univ. of	- 1
Trinity University	- 1	Wright State University	- 5
Total			153

PARTICIPANTS LABORATORY ASSIGNMENT

PARTICIPANT LABORATORY ASSIGNMENT

AERO PROPULSION LABORATORY

(Wright-Patterson Air Force Base)

Dr. Suresh K. Aggarwal (1987)
University of Illinois at Chicago
Specialty: Aerospace Engineering

Dr. Mingking K. Chyu
Carnegie Mellon University
Specialty: Heat Transfer

Dr. Derek Dunn-Rankin
University of California
Specialty: Laser Diagnostics (combustion)

Dr. Wayne A. Eckerle
Clarkson University
Specialty: Experimental Fluid Mechanics

Dr. Arthur A. Mason (1986)
University of Tennessee Space Institute
Specialty: Physics

Dr. Douglas G. Talley
University of Michigan
Specialty: Combustion

Dr. Richard Tankin (1987)
Northwestern University
Specialty: Mechanical Engineering

Dr. Cheng-Hsiao Wu (1987)
University of Missouri
Specialty: Solid State Physics

ARMAMENT LABORATORY

(Eglin Air Force Base)

Dr. Ibrahim A. Ahmad
Northern Illinois University
Specialty: Statistics and Operations

Dr. Charles Bell (1987)
Arkansas State University
Specialty: Mechanical Engineering

Dr. Stephen J. Dow
Univ. of Alabama in Huntsville
Specialty: Discrete Mathematics

Dr. Joseph J. Feeley (1987)
University of Idaho
Specialty: Electrical Engineering

Dr. Manuel A. Huerta
University of Miami
Specialty: Plasma Physics

Prof. Anastas Lazaridis
Widener University
Specialty: Ablation, Solar Energy

Dr. Kwang S. Min
East Texas State University
Specialty: Signal Processing

Dr. Joseph J. Molitoris
Muhlenberg College
Specialty: Nuclear Physics

Prof. Wafa E. Yazigi
Columbia Basin College
Specialty: Solid Mechanics

Harry G. Armstrong Aerospace Medical Research Laboratory
(Wright-Patterson Air Force Base)

Dr. Charles D. Covington
University of Arkansas
Specialty: Digital Signal Processing

Dr. Barry P. Goettl
Clemson University
Specialty: Engineering Psychology

Dr. David G. Payne
SUNY Binghamton
Specialty: Human Memory

Dr. Donald Robertson (1987)
Indiana University of PA
Specialty: Psychology

Dr. Joseph E. Saliba
University of Dayton
Specialty: Engineering Mechanics

Dr. Sanford S. Singer
University of Dayton
Specialty: Enzymology

ARNOLD ENGINEERING DEVELOPMENT CENTER
(Arnold Air Force Base)

Mr. Ben A. Abbott (GSRP)
Vanderbilt University
Specialty: Electrical Engineering

Dr. Eustace L. Dereniak
University of Arizona
Specialty: Infrared Physics

Prof. William M. Grissom
Morehouse College
Specialty: Combustion Diagnostics

Dr. William Sutton (1985)
University of Oklahoma
Specialty: Heat Transfer

Dr. Ahmad D. Vakili
Univ. of Tennessee Space Inst.
Specialty: Unsteady Flows

ASTRONAUTICS LABORATORY
(Edwards Air Force Base)

Dr. Gurbux S. Alag (1987)
Western Michigan University
Specialty: Systems Engineering

Dr. Clarence Calder
Oregon State University
Specialty: Stress Wave Propagation

Mr. David B. Chenault (GSRP)
University of Alabama
Specialty: Physics

Dr. David W. Jensen
Pennsylvania State University
Specialty: Advanced Composite Materials

Dr. John Kenney (1987)
Eastern New Mexico University
Specialty: Physical Chemistry

Dr. Mark A. Norris
Virginia Polytechnic Inst. & State Univ.
Specialty: Structural Dynamics &
Controls

ASTRONAUTICS LABORATORY

(Edwards Air Force Base)

(continued)

Dr. Phillip A. Christiansen
Clarkson University
Specialty: Physical Chemistry

Dr. Susan T. Collins
California State University
Specialty: Matrix Isolation Spectroscopy

Dr. Rameshwar P. Sharma
Western Michigan University
Specialty: Fluid Mechanics

Dr. Siavash H. Sohrab (1986)
Northwestern University
Specialty: Engineering Physics

AVIONICS LABORATORY

(Wright-Patterson Air Force Base)

Prof. William K. Curry (1987)
Rose-Hulman Inst. of Technology
Specialty: Computer Science

Dr. Gerald W. Grams
Georgia Tech.
Specialty: Atmospheric Physics

Dr. David Hemmendinger
Wright State University
Specialty: Logic Programming

Dr. Periasamy K. Rajan
Tennessee Tech. University
Specialty: Digital Signal Processing

Dr. Mateen M. Rizki
Wright State University
Specialty: Modeling and Simulation

ENGINEERING AND SERVICES CENTER

(Tyndall Air Force Base)

Dr. Wayne A. Charlie
Colorado State University
Specialty: Geotechnical Engineering

Dr. David H. DeHeer
Calvin College
Specialty: Molecular Biology

Dr. Deanna S. Durnford
Colorado State University
Specialty: Groundwater

Dr. Neil J. Hutzler
Michigan Tech. University
Specialty: Environmental Engineering

Dr. Peter Jeffers (1987)
S.U.N.Y.
Specialty: Chemistry

Dr. Richard S. Myers
Delta State University
Specialty: Experimental Physical Chem.

Dr. William Schulz (1987)
Eastern Kentucky University
Specialty: Chemistry

Dr. Dennis Truax (1987)
Mississippi State University
Specialty: Civil Engineering

ELECTRONIC SYSTEMS DIVISION

(Hanscom Air Force Base)

Mr. George N. Bratton
Austin State Peay State Univ.
Specialty: Statistics

Dr. John F. Dalphin
Towson State University
Specialty: Computer Science

Dr. Stephan Kolitz (1986)
University of Massachusetts
Specialty: Operations Reserach

FLIGHT DYNAMICS LABORATORY

(Wright-Patterson Air Force Base)

Dr. Peter J. Disimile (1986)
University of Cincinnati
Specialty: Fluid Mechanics

Dr. James A. Sherwood
University of New Hampshire
Specialty: Solid Mechanics

Mr. Thomas Enneking (GSRP), (1987)
University of Notre Dame
Specialty: Civil Engineering

Dr. Gary Slater (1987)
University of Cincinnati
Specialty: Aerospace Engineering

Dr. Awatef Hamed
University of Cincinnati
Specialty: Engineering

Dr. Kenneth M. Sobel
The City College of New York
Specialty: Eigenstructure

Dr. Yulian B. Kin
Purdue University Calumet
Specialty: Stress Analysis

Dr. Forrest Thomas (1987)
University of Montana
Specialty: Chemistry

Dr. Oliver McGee (1987)
Ohio State University
Specialty: Engineering Mechanics

Mr. David F. Thompson (GSRP)
Purdue University
Specialty: Computer Information

Dr. William E. Wolfe
Ohio State University
Specialty: Geotechnical Engineering

FRANK J. SEILER RESERACH LABORATORY

(United States Air Froce Academy)

Dr. Richard Bertrand (1985)
University of Colorado
Specialty: NMR Spectroscopy, Atomic Spectroscopy

Dr. Tammy J. Melton
St. Norbert College
Specialty: Inorganic Synthesis

FRANK J. SEILER RESEARCH LABORATORY

(United States Air Force Academy)
(continued)

Dr. Dan R. Bruss
Albany College of Pharmacy
Specialty: Physical Organic Chemistry

Dr. Charles M. Bump (1987)
Hampton University
Specialty: Organic Chemistry

Dr. Michael L. McKee
Auburn University
Specialty: Molecular Orbital Theory

Dr. Patricia L. Plummer
Columbia Univ. of Missouri
Specialty: Quantum Chemistry

Dr. Howard Thompson (1987)
Purdue University
Specialty: Mechanical Engineering

Dr. Melvin Zandler (1987)
Wichita State University
Specialty: Physical Chemistry

GEOPHYSICS LABORATORY

(Hanscom Air Force Base)

Dr. Lucia M. Babcock
Louisiana State University
Specialty: Gas Phase Ion-Molecule Chem.

Dr. Pradip M. Bakshi
Boston College
Specialty: Quantum Theory

Dr. Donald F. Collins
Warren Wilson College
Specialty: Optics, Image Processing

Dr. Lee Flippin (1987)
San Francisco State University
Specialty: Organic Chemistry

Dr. Janet U. Kozyra
University of Michigan
Specialty: Space Physics

Dr. Steven Leon (1987)
Southeastern Massachusetts
Specialty: Mathematics

Dr. John P. McHugh
University of New Hampshire
Specialty: Fluid Mechanics

Dr. Timothy Su (1987)
Southeastern Massachusetts Univ.
Specialty: Physical Chemistry

HUMAN RESOURCES LABORATORY

(Brooks, Williams and Wright-Patterson Air Force Base)

Dr. Ronna Dillion (1987)
Southern Illinois University
Specialty: Educational Psychology

Dr. J. Kevin Ford
Michigan State University
Specialty: Industrial/Organ. Psychology

Dr. Jorge L. Mendoza (1986)
Texas A&M University
Specialty: Psychology

Dr. Philip D. Olivier (1986)
University of Texas
Specialty: Electrical Engineering

HUMAN RESOURCES LABORATORY

(Brooks, Williams and Wright-Patterson Air Force Base)

(continued)

Dr. Hugh. P. Garraway, III
Univ. of Southern Mississippi
Specialty: Computer Based Learning

Dr. Douglas E. Jackson
Eastern New Mexico University
Specialty: Math/Statistical Information

Dr. Charles E. Lance
University of Georgia
Specialty: Industrial/Organizational Psy.

Dr. Thomas L. Landers
University of Arkansas
Specialty: Reliability & Maintainability

Dr. Mufit H. Ozden
Miami University
Specialty: Operations Research

Dr. Dharam S. Rana
Jackson State University
Specialty: Quantitative Techniques

Dr. Jonathan M. Spector
Jacksonville State University
Specialty: Logic

Dr. Charles Wells (1987)
University of Dayton
Specialty: Management Science

Dr. Robert K. Young
University of Texas
Specialty: Experimental Psychology

LOGISTICS COMMAND

(Wright-Patterson Air Force Base)

Dr. Ming-Shing Hung (1986)
Kent State University
Specialty: Business Administration & Management Science

MATERIALS LABORATORY

(Wright-Patterson Air Force Base)

Dr. Bruce Craver (1987)
University of Dayton
Specialty: Physics

Dr. Parvis Dadras
Wright State University
Specialty: Mechanics of Materials

Dr. David A. Grossie
Wright State University
Specialty: X-ray Crystallography

Dr. Gordon Johnson (1987)
Walla Walla College
Specialty: Electrical Engineering

Dr. L. James Lee
The Ohio State University
Specialty: Polymer & Composite
Processing

MATERIALS LABORATORY

(Wright-Patterson Air Force Base)
(continued)

Dr. Barry K. Fussell
University of New Hampshire
Specialty: Systems Modeling & Controls

Dr. Michael Sydor
University of Minnesota
Specialty: Optics, Material Science

Dr. John W. Gilmer (1987)
Penn State University
Specialty: Physical Chemistry

Dr. Richard S. Valpey
Wilberforce University
Specialty: Organic Synthesis

OCCUPATIONAL AND ENVIRONMENT HEALTH LABORATORY

(Brooks Air Force Base)

Dr. Steven C. Chiesa
Santa Clara University
Specialty: Biological Waste Treatment

Dr. Gary R. Stevens
Oklahoma State University
Specialty: Stochastic Processes

Dr. Larry R. Sherman
University of Akron
Specialty: Organotin Chemistry

Dr. Shirley A. Williams (1986)
Jackson State University
Specialty: Physiology

ROME AIR DEVELOPMENT CENTER

(Griffiss Air Force Base)

Dr. Keith A. Christianson
University of Maine
Specialty: Electronic Materials

Dr. David Sumberg (1987)
Rochester Institute of Tech.
Specialty: Physics

Dr. Hugh K. Donaghy
Rochester Inst. of Technology
Specialty: Natural Language Processing

Dr. Donald R. Ucci
Illinois Inst. of Technology
Specialty: Adaptive Arrays

Dr. Oleg G. Jakubowicz
State University of New York
Specialty: Neural Nets

Dr. Peter J. Walsh
Fairleigh Dickinson University
Specialty: Superconductivity

Dr. Louis Johnson (1987)
Oklahoma State University
Specialty: Electrical Engineering

Dr. Kenneth L. Walter
Prairie View A&M University
Specialty: Chemical Engineering Process

Dr. Samuel P. Kozaitis
Florida Institute of Tech.
Specialty: Optics, Computer Architecture

Dr. Gwo-Ching Wang
Rensselaer Polytechnic Inst.
Specialty: Surface Sciences

SCHOOL OF AEROSPACE MEDICINE

(Brooks Air Force Base)

Dr. Ronald Bulbulian
University of Kentucky
Specialty: Exercise Physiology

Dr. John A. Burke, Jr.
Trinity University
Specialty: Inorganic Compounds

Dr. Hoffman H. Chen (1986)
Grambling State University
Specialty: Mechanical Engineering

Dr. Frank O. Hadlock (1986)
Florida Atlantic University
Specialty: Mathematics

Dr. Eric R. Johnson
Ball State University
Specialty: Protein Biochemistry

Dr. Harold G. Longbotham
Univ. of Texas - San Antonio
Specialty: Nonlinear Digital Filtering

Dr. Mohammed Maleque (1987)
Meharry Medical College
Specialty: Pharmacology

WILFORD HALL MEDICAL CENTER (Lackland Air Force Base)

Dr. David R. Cecil
Texas A&I University
Specialty: Algebra (Finite Fields)

WEAPONS LABORATORY (Kirtland Air Force Base)

Dr. Albert W. Biggs (1986)
University of Alabama
Specialty: Electrical Engineering

Dr. Parsottam J. Patel (1986)
Meharry Medical College
Specialty: Microbiology

Dr. William Z. Plachy
San Francisco State University
Specialty: Physical Chemistry

Dr. Ralph Peters (1987)
Wichita State University
Specialty: Zoology

Dr. Thomas R. Rogge
Iowa State University
Specialty: Finite Element Analysis

Prof. Sonia H. Sawtelle-Hart
Univ. of Texas - San Antonio
Specialty: Exercise Physiology

Dr. Wesley Tanaka (1987)
University of Wisconsin
Specialty: Biochemistry

Dr. John R. Wright
Southeast Oklahoma State Univ.
Specialty: Biochemistry

Dr. Donald Welch (1986)
Texas A&M University
Specialty: Microbiology

Dr. William M. Jordan
Louisiana Tech. University
Specialty: Composite Materials

WEAPONS LABORATORY

(Kirtland Air Force Base)

(continued)

Dr. Lane Clark
University of New Mexico
Specialty: Graph Theory

Dr. David A. Dolson
Murray State University
Specialty: Laser Spectroscopy

Dr. Arkady Kheyfets
North Carolina State Univ.
Specialty: Mathematical Physics

Dr. Barry McConnell (1987)
Florida A&M University
Specialty: Computer Science

Dr. William Wheless (1987)
New Mexico State University
Specialty: Electrical Engineering

RESEARCH REPORTS

MINI-GRANT RESEARCH REPORTS
1988 RESEARCH INITIATION PROGRAM

<u>Technical Report Number</u>	<u>Title and Mini-Grant No.</u>	<u>Professor</u>
Volume I		
Armament Laboratory		
1	Statistical Analysis of Residual Target Performance and for Measures of Target Partial Availability Pending Approval 210-9MG-010	Dr. Ibrahim A. Ahmad
2	Synergistic Effects of Bomb Cratering, Phase II 760-7MG-025	Dr. Charles Bell (1987)
3	Automated Motion Parameter Determi- nation from an Image Sequence 210-9MG-025	Dr. Stephen J. Dow
4	Modeling and Simulation on Micro- computers, 1989 760-7MG-070	Dr. Joseph J. Feeley (1987)
5	Two Dimensional MHD Simulation of Accelerating Arc Plasmas 210-9MG-090	Dr. Manuel A. Huerta
6	Modeling Reactive Fragments 210-9MG-011	Prof. Anastas Lazaridis
7	Target-Aerosol Discrimination for Active Optical Proximity Sensors 210-9MG-016	Dr. Kwang S. Min
8	The Dynamics of Impact 210-9MG-008	Dr. Joseph J. Molitoris
9	Report Not Acceptable at this Time 210-9MG-015	Prof. Wafa E. Yazigi

Arnold Engineering Development Center

- | | | |
|----|--|---------------------------|
| 10 | Multigraph Kernel for Transputer Based Systems
21-9MG-087 | Mr. Ben A. Abbott (GSRP) |
| 11 | MTF Studies of IR Focal Plane Arrays at Low Flux Levels
210-9MG-020 | Dr. Eustace L. Dereniak |
| 12 | Droplet Size Distributions and Combustion Modeling in a Pintle Injector Spray
210-9MG-069 | Prof. William M. Grissom |
| 13 | Multiple Scattering in Solid Fuel Rocket Plumes
760-0MG-091 | Dr. William Sutton (1985) |
| 14 | Influence of Forced Disturbances on the Vortex Core and the Vortex Burst
210-9MG-056 | Dr. Ahmad D. Vakili |

Astronautics Laboratory

- | | | |
|----|--|------------------------------|
| 15 | Large Space Structure Parameter Estimation
760-7MG-042 | Dr. Gurbux S. Alag (1987) |
| 16 | Integrated Strain Measurement in Composite Members Using Embedded Constantan Wire
Pending Approval
210-9MG-076 | Dr. Clarence Calder |
| 17 | Calibration of the Infrared Spectropolarimeter
210-9MG-026 | Mr. David B. Chenault (GSRP) |
| 18 | Computer Code to Include Core Polarization in Effective Potential Basis Set Expansion Studies
210-9MG-092 | Dr. Phillip A. Christiansen |
| 19 | Fluorescence Spectra of Matrix-isolated Lithium
210-9MG-115 | Dr. Susan T. Collins |

20	Calibration of Composite-Embedded Fiber-Optic Strain Sensors Pending Approval 210-9MG-052	Dr. David W. Jensen
21	Energy-And Time-Resolved Photophysics and Photochemistry of High Energy Cryogenic Metal-Containing Rocket Fuels 760-7MG-019	Dr. John Kenney (1987)
22	Experimental Verification and Develop- ment of Structural Identification Techniques on a Grid 210-9MG-045	Dr. Mark A. Norris
23	Report Not Available at this Time 210-9MG-103	Dr. Rameshwar P. Sharma
24	Experimental Investigation of the Stability of Jets Near the Critical Point 760-6MG-110	Dr. Siavash H. Sohrab (1986)
Electronics Systems Division		
25	HF Network Evaluation 210-9MG-012	Mr. George N. Bratton
26	Report Not Available at this Time 210-9MG-023	Dr. John F. Dalphin
27	Reliability in Satellite Communication Networks Pending Approval 760-6MG-094	Dr. Stephan Kolitz (1986)
Engineering and Services Center		
28	High Intensity Compressive Stress Wave Propagation Through Unsaturated Sands 210-9MG-075	Dr. Wayne A. Charlie
29	Decontamination and Elisa Analysis of Blood Group Substances from Human Tissue Pending Approval 210-9MG-112	Dr. David H. DeHeer

- | | | |
|----|---|---------------------------|
| 30 | Estimation of Jet Fuel Contamination
in Soils
210-9MG-074 | Dr. Deanna S. Durnford |
| 31 | Extraction of Volatile Organic Chemicals
from Unsaturated Soil: Experimental
Results and Model Predictions
210-9MG-059 | Dr. Neil J. Hutzler |
| 32 | Homogeneous Hydrolysis Rate Constants
for Selected Chlorinated Methanes,
Ethanes, Ethenes, and Propanes
760-7MG-038 | Dr. Peter Jeffers (1987) |
| 33 | Sorption Kinetics of Volatile Organic
Compounds on Aquifer Materials
210-9MG-047 | Dr. Richard S. Myers |
| 34 | Report will be Submitted Under
Mini-Grant 210-10MG-095 | Dr. William Schulz (1987) |
| 35 | Report Not Available at this Time
760-7MG-105 | Dr. Dennis Truax (1987) |

Volume II

Frank J. Seiler Research Laboratory

- | | | |
|----|---|-----------------------------|
| 36 | NMR Studies of Alkylammonium-Chloro-
oaluminate Room-Temperature Electrolytes
760-0MG-095 | Dr. Richard Bertrand (1985) |
| 37 | Mechanistic Studies on the Thermal
Decomposition of NTO by High
Performance Liquid Chromatography
210-9MG-111 | Dr. Dan R. Bruss |
| 38 | Aromatic Nitrations in Chloroaluminate
Melts
760-7MG-076 | Dr. Charles M. Bump (1987) |
| 39 | Calculated C-NO ₂ Bond Dissociation
Energies (Part I) and A MCSCF Study of
the Rearrangement of Nitromethane to
Methyl Nitrite (Part II)
210-9MG-054 | Dr. Michael L. McKee |
| 40 | Sodium as an Electrode for Chloroaluminate
Melts
210-9MG-098 | Dr. Tammy J. Melton |

41	Report Not Available at this Time 210-9MG-097	Dr. Patricia L. Plummer
42	Transient Shock Waves in a Mach 3 Flow 760-7MG-071	Dr. Howard Thompson (1987)
43	Ab-initio and Semi-Empirical Molecular Orbital Studies of Energetic Materials (Nitrogen Heterocyclics) and Polymers 760-7MG-092	Dr. Melvin Zandler (1987)
Geophysics Laboratory		
44	Radiative Association in Ion-Molecule Reactions: Reactions of Some Carbon Cations 210-9MG-086	Dr. Lucia M. Babcock
45	Impulse Approximation Formalism for Atom Molecule Collisions 210-9MG-109	Dr. Pradip M. Bakshi
46	Stellar Photometry, Vehicle Glow, and Advanced Image Analysis 210-9MG-100	Dr. Donald F. Collins
47	Synthesis of Organometallic Reagents for SIFT Studies of Electron Attachment Reactions 760-7MG-056	Dr. Lee Flippin (1987)
48	Theoretical and Observational Studies of Geomagnetic Storm-Related Ion and Electron Heating in the Subauroral Region 210-9MG-084	Dr. Janet U. Kozyra
49	Algorithms for Generalized Exponential Inversion 760-7MG-036	Dr. Steven Leon (1987)
50	Report Not Available at this Time 210-9MG-125	Dr. John P. McHugh
51	Trajectory Calculations of High Tempera- ture and Kinetic Energy Dependent Ion- Polar Molecule Collision Rate Constants 760-7MG-040	Dr. Timothy Su (1987)

Rome Air Development Center

- | | | |
|----|---|---------------------------|
| 52 | Aging Studies of GaAs Schottky Barriers
210-9MG-073 | Dr. Keith A. Christianson |
| 53 | Report Not Available at this Time
210-9MG-094 | Dr. Hugh K. Donaghy |
| 54 | Neural Network for Aiding Intelligent
Analysis
Pending Approval
210-9MG-124 | Dr. Oleg G. Jakubowicz |
| 55 | Supply Line Testing in CMOS Digital
Circuits
760-7MG-050 | Dr. Louis Johnson (1987) |
| 56 | Characterization of Detectors for
Optical Pattern Recognition
210-9MG-018 | Dr. Samuel P. Kozaitis |
| 57 | Fiber Optic Distribution for Phased
Array Antennas
Pending Approval
760-7MG-113 | Dr. David Sumberg (1987) |
| 58 | Continuation Study of the Effect of
Nonlinearities of High Speed Analog-
to-Digital Converters on Digital
Beamforming Arrays
210-9MG-040 | Dr. Donald R. Ucci |
| 59 | Analysis of Microwave Surface Impedance
of High Temperature Superconductors
210-9MG-072 | Dr. Peter J. Walsh |
| 60 | Report Not Available at this Time
210-9MG-113 | Dr. Kenneth L. Walter |
| 61 | X-Ray Pole-Figure Analysis of $\text{YBa}_2\text{Cu}_3\text{O}_{7-x}$
Thin Film on $\text{SrTiO}_3(100)$ Prepared by RF
Diode Sputtering
210-9MG-077 | Dr. Gwo-Ching Wang |

Weapons Laboratory

- | | | |
|----|--|----------------------------|
| 62 | Slow Wave Transmission Line Transformers | Dr. Albert W. Biggs (1986) |
| | 760-6MG-072 | |

- | | | |
|----|--|----------------------------|
| 63 | Report Not Available at this Time
210-9MG-119 | Dr. Lane Clark |
| 64 | Vibrational Energy Transfer in Sulfur
Monoxide
210-9MG-101 | Dr. David A. Dolson |
| 65 | Development of an Experimental Program
to Evaluate Laser Composite Material
Damage Models
210-9MG-034 | Dr. William M. Jordan |
| 66 | Report Not Available at this Time
210-9MG-114 | Dr. Arkady Kheyfets |
| 67 | Report Not Available at this Time
760-7MG-047 | Dr. Barry McConnell (1987) |
| 68 | Slow to Fast Wave Transition Analysis
760-7MG-068 | Dr. William Wheless (1987) |

Volume III

Air Force Wright Aeronautical Laboratories

Aero Propulsion Laboratory

- | | | |
|----|--|-------------------------------|
| 69 | Vaporization Behavior of Pure and
Multicomponent Fuel Droplets in a
Hot Air Stream
760-7MG-061 | Dr. Suresh K. Aggarwal (1987) |
| 70 | Effects of Injection-To-Mainstream
Density Ratios on Film Cooling Heat
Transfer
Pending Approval
210-9MG-096 | Dr. Mingking K. Chyu |
| 71 | Accurate Temperatures Using Cars in
Droplet Laden Flows
Pending Approval
210-9MG-055 | Dr. Derek Dunn-Rankin |
| 72 | Report Not Available at this Time
210-9MG-019 | Dr. Wayne A. Eckerle |
| 73 | Report Not Available at this Time
760-6MG-099 | Dr. Arthur A. Mason (1986) |
| 74 | Report Not Available at this Time
210-9MG-022 | Dr. Douglas G. Talley |

- | | | |
|----|--|---------------------------|
| 75 | Vortical Structures in 2-D Slot
Burner-Cold Flow
760-7MG-051 | Dr. Richard Tankin (1987) |
| 76 | Calculations of Interface-State Occupation
Function and GaAs/Ge Heterostructure Solar
Cell Efficiency
760-7MG-093 | Dr. Cheng-Hsiao Wu (1987) |

Avionics Laboratory

- | | | |
|----|---|-------------------------------|
| 77 | Computer Simulation of Adaptive Resource
Management in Real-Time
760-7MG-081 | Prof. William K. Curry (1987) |
| 78 | Study of Sky Backgrounds and Subvisual
Cirrus
Pending Approval
210-9MG-120 | Dr. Gerald W. Grams |
| 79 | Proving Equivalence of High-and Low-Level
Architectural Descriptions in VHDL
210-9MG-108 | Dr. David Hemmendinger |
| 80 | Report Not Available at this Time
210-9MG-051 | Dr. Periasamy K. Rajan |
| 81 | Applications of Evolutionary Learning
Strategies to Pattern Recognition Tasks
210-9MG-058 | Dr. Mateen M. Rizki |

Flight Dynamics Laboratory

- | | | |
|----|---|--------------------------------------|
| 82 | The Effect of a Roughened Surface on
Turbulent Boundary Layer Separation
at Mach 6.0
760-6MG-075 | Dr. Peter J. Disimile (1986) |
| 83 | A Stochastic Model of Fatigue Crack
Growth Due to Random Loading for
Application to Aircraft Wheels
760-7MG-124 | Mr. Thomas Enneking (GSRP)
(1987) |
| 84 | An Investigation of the Flow Field in
Shock Wave/Boundary Layer/Bleed
Interactions
Pending Approval
210-9MG-061 | Dr. Awatef Hamed |

85	Fatigue Characteristics of F-16 Composite Transparency Material Determined by Long-Term and Accelerated Methods 210-9MG-038	Dr. Yulian B. Kin
86	Convergence of Upper-Bound Optimum Design of Large-Scale Structures with Specified Frequency Bands 760-7MG-115	Dr. Oliver McGee (1987)
87	Report Not Available at this Time 210-9MG-088	Dr. James A. Sherwood
88	Robustness with Positive Real Controllers for Large Space Structures 760-7MG-088	Dr. Gary Slater (1987)
89	Robust Eigenstructure Assignment for Flight Control Design 210-9MG-035	Dr. Kenneth M. Sobel
90	Comparative Burning Rates and Duplex Loads of Solid Propellants 760-7MG-080	Dr. Forrest Thomas (1987)
91	Optimal and Sub-Optimal Loop Shaping in Quantitative Feedback Theory Pending Approval 210-9MG-106	Mr. David F. Thompson (GSRP)
92	Low Velocity Impact of Composite Materials 760-7MG-102 and 210-9MG-082	Dr. William E. Wolfe
Logistics Command		
93	Aircraft Availability Model: Feasibility Study for POM Forecasting 760-6MG-105	Dr. Ming S. Hung (1986)
Materials Laboratory		
94	Tunable Absorption in Doping Superlattices 760-7MG-097	Dr. Bruce Craver (1987)
95	Joining of Carbon-Carbon Composites 210-9MG-004	Dr. Parviz Dadras
96	Report Not Available at this Time 210-9MG-064	Dr. Barry K. Fussell

- | | | |
|--|---|-----------------------------|
| 97 | Characterization of the Phase Separation Behavior of Poly(p-phenylene benzobisthiazole)/Amorphous Nylon Molecular Composites by Small Angle Light Scattering
760-7MG-013 | Dr. John W. Gilmer |
| 98 | Structural Analysis of Model Compounds with Potential Second and Third Order Nonlinear Optical Properties
210-9MG-080 | Dr. David A. Grossie |
| 99 | Liquid Crystal Biomolecules for use as Optical Filters
760-7MG-075 | Dr. Gordon Johnson (1987) |
| 100 | Knowledge Development for the Rule Based Process Automation of Resin Transfer Molding
210-9MG-063 | Dr. L. Jmaes Lee |
| 101 | Photorefectance Measurements of the Quality of Undoped GaAs
210-9MG-031 | Dr. Michael Sydor |
| 102 | Synthesis of 2, 6-Diformyl Pyridobisimidazoles
210-9MG-029 | Dr. Richard S. Valpey |
|
Volume IV | | |
| Human Systems Division Laboratories | | |
| Harry G. Armstrong Aerospace Medical Research Laboratory | | |
| 103 | Auditory Modeling
210-9MG-060 | Dr. Charles D. Covington |
| 104 | Assessing the Cognitive Demands of Tracking Strategies
210-9MG-078 | Dr. Barry P. Goettl |
| 105 | Report Not Available at this Time
210-9MG-121 | Dr. David G. Payne |
| 106 | Effect of System Reliability on Probabilistic Inference
Pending Approval
760-7MG-094 | Dr. Donald Robertson (1987) |

107	Optimization of the Nonlinear Discrete Parameter Model of the Seated Human Spine 210-9MG-071	Dr. Joseph E. Saliba
108	In Vitro Modeling of Perfluoro-N-Decanoate Effects on Enzymes of Fatty Acid Metabolism 210-9MG-002	Dr. Sanford S. Singer
Human Resources Laboratory		
109	Report Not Acceptable at this Time 760-7MG-100	Dr. Ronna Dillion (1987)
110	An Investigation of Training Content Validity and Training Efficiency in the Air Force Airmen Basic-In-Residence Training Course 210-9MG-066	Dr. J. Kevin Ford
111	An Intelligent Tool to Facilitate the Development of Qualitative Process Models in Novice Programmers 210-9MG-007	Dr. Hugh P. Garraway, III
112	On the Effect of Range Restriction on Correlation Coefficient Estimation 210-9MG-027	Dr. Douglas E. Jackson
113	Validation of an Enlisted Air Force Specialty Task Taxonomy and Cross-AFS Ease-of-Movement Predictions 210-9MG-017	Dr. Charles E. Lance
114	Proportional Intensity Reliability Analysis for Repairable Items 210-9MG-104	Dr. Thomas L. Landers
115	A Monte Carlo Comparison of Validity Generalization Procedures 760-6MG-136	Dr. Jorge L. Mendoza (1986)
116	A Network Tutor Based on the Heuristic of Polya 760-6MG-032	Dr. Philip D. Olivier (1986)
117	Graphical Programming of Simulation Models in an Object-Oriented Environment 210-9MG-028	Dr. Mufit H. Ozden

118	Report Not Available at this Time 210-9MG-043	Dr. Dharam S. Rana
119	Refinement Considerations for an Advanced Instructional Design Advisor 210-9MG-021	Dr. Jonathan M. Spector
120	Engineering Design with Decision Support: An Application of Goal Decomposition 760-7MG-046	Dr. Charles Wells (1987)
121	Report Not Available at this Time 210-9MG-099	Dr. Robert K. Young
Occupational and Environment Health Laboratory		
122	Solvent Extraction of Boron from Industrial Wastewaters 210-9MG-102	Dr. Steven C. Chiesa
123	Comparison of Asbestos Analysis by SEM-EDXA and TEM-SAED 210-9MG-122	Dr. Larry R. Sherman
124	An Examination of Kriging Techniques for Ground Water Monitoring 210-9MG-070	Dr. Gary R. Stevens
125	Cortisol Prevention of Chronic Beryllium Disease in Postpartum Rats: A Pilot Study 760-6MG-078	Dr. Shirley A. Williams (1986)
School of Aerospace Medicine		
126	Blood Flow Distribution in the Non- Working Forearm During Exercise 210-9MG-057	Dr. Ronald Bulbulian
127	Photophysics and Photochemistry of Transition Metal Complexes 210-9MG-091	Dr. John A. Burke, Jr.
128	Serum Squalene and Cholesterol Ratio as Risk Predictor for Coronary Artery Disease 760-6MG-118	Dr. Hoffman H. Chen (1986)
129	A Feasibility Study for a Computerized ECG Database 760-6MG-073	Dr. Frank O. Hadlock (1986)

130	Development of a New Ultrasensitive Cholesterol Assay System for the Determination of Free Cholesterol in Biological Fluids 210-9MG-105	Dr. Eric R. Johnson
131	Application of Nonlinear Filters to VEP Data 210-9MG-033	Dr. Harold G. Longbotham
132	Effects of Low Dose Soman on CNS Neurotransmitters 760-7MG-078	Dr. Dr. Mohammed Maleque (1987)
133	Cleansing of Bone-Marrow by Lymphokine Activated Killer Cells (LAK-Cells) 760-6MG-131	Dr. Parsottam J. Patel (1986)
134	Transcutaneous Oxygen Delivery 210-9MG-042	Dr. William Z. Plachy
135	Report Not Acceptable at this Time 760-7MG-091	Dr. Ralph Peters (1987)
136	A Computer Model of the Human Systemic Arterial Tree 210-9MG-003	Dr. Thomas R. Rogge
137	The Effect of Age, Family Status, and Physical Activity on Select Dietary Components of TAC Pilots 210-9MG-095	Prof. Sonia H. Sawtell-Hart
138	Comprehensive Lipoprotein Analysis by High-Performance Molecular Exclusion Chromatography 760-7MG-043	Dr. Wesley Tanaka (1987)
139	Nmr and Temperature-Dependence Studies of the Metal-Ion Catalyzed Chemiluminescence of Luminol 210-9MG-037	Dr. John R. Wright
Wilford Hall Medical Center		
140	Enhancements to PC-Mainframe Interface for Data Entry 210-9MG-048	Dr. David R. Cecil

141

Effect of Hyperoxia on the Permeability
of the Blood-Brain Barrier in Several
Laboratory Species and on Organotypic
Explant Tissue Cultures of Hamster Brain
760-6MG-091

Dr. Donald Welch (1986)

1985 USAF Mini-grant Program
Sponsored by the
AIR FORCE OFFICE OF SCIENTIFIC RESEARCH
Conducted by the
UNIVERSAL ENERGY SYSTEMS, INC.
FINAL REPORT

NMR Studies of Alkylammonium-Chloroaluminate
Room-Temperature Electrolytes

Prepared by:	Richard D. Bertrand
Academic Rank:	Professor of Chemistry
University:	University of Colorado at Colorado Springs
Date:	March 28, 1986
Contract No.:	F49620-85-C-0013/SB5851-0360
Subcontract No.:	S-760-OMG-095

NMR Studies of Alkylammonium-Chloroaluminate

Room-Temperature Electrolytes

by

Richard D. Bertrand

ABSTRACT

Confirmation of the NMR relaxation results determined earlier by the author is reported for more carefully prepared samples of the title materials. Chemical shift studies of the NMR of lead, tin and chlorides and preliminary studies of gallium chloride dissolved in the title compounds as solvents are also discussed. While studies of lead chloride proved difficult, that of tin revealed the formation of a complex of tin with chloride having a stoichiometric ratio of three chlorides per tin.

I. INTRODUCTION: The author's professional background includes 20 years experience in the applications of Nuclear Magnetic Resonance (NMR) spectroscopy to problems in chemistry. This experience has included the measurement of the values and signs of spin-spin coupling constants in transition metal complexes of phosphorus donors, study of aromatic-solvent induced chemical shifts, study of ^{13}C - ^{13}C spin-spin coupling in small ring molecules, and examination of the mechanisms of ^{13}C spin lattice relaxation. This background proved valuable to the people of the Frank J. Seiler Research Laboratory for in discussions with Dr. Wilkes at the Seiler Laboratory it was noted that Seiler personnel could not reproduce the work of Matsumoto and Ichikawa¹ which involved measurement of ^{27}Al spin lattice relaxation times in room temperature molten salts. Indeed, it appeared they were unable to measure this parameter for the aluminum chloride system of interest. Since the author is quite experienced at NMR spectroscopy, and spin lattice relaxation time measurements in particular, it was decided to propose examination of this problem. In addition, study of the nature of materials dissolved in the molten salts was proposed. It was suggested that examination of compounds known to form complexes with chloride might prove to be instructive.

II. OBJECTIVES OF THE RESEARCH EFFORT: Recent work of the author has focused on the measurement of ^{27}Al NMR spin lattice relaxation times for the 1-methyl-3-ethylimidazolium chloride/aluminum chloride room-temperature electrolyte system.² This work was unable to reproduce that of Matsumoto and Ichikawa in which non-linear logarithmic longi-

tudinal magnetization recovery curves were obtained for ^{27}Al at some compositions in the n-butylpyridinium chloride/aluminum chloride system. These authors explain their results as non-single exponential magnetization decay due to a combination of slow aluminum exchange between the species present and more rapid relaxation by the higher order chloroaluminate species. It was suggested that perhaps the source of the discrepancy in results is due to a high sensitivity of aluminum exchange rate to chloroaluminate composition. It was therefore proposed that the longitudinal magnetization decay curves as a function of chloroaluminate composition be studied. At higher magnetic field strengths it is possible to separate the ^{27}Al resonances due to AlCl_4^- and Al_2Cl_7^- . It was also proposed that some of the ^{27}Al relaxation measurements be made at higher magnetic field strength.

A second project was originally proposed for the SFRP program but, because of limited time, little was attempted. The proposal involved examination of the NMR spectra of metal ions dissolved in the room temperature molten salts such as the 1-methyl-3-ethylimidazolium chloride/aluminum chloride system. Metal nuclei of interest include ^{119}Sn , ^{195}Pt and ^{207}Pb because their spectra are relatively easily observed, these metals have a well understood chemistry in other solvent systems, and their chemistry in room temperature molten salt solvent systems is of interest. The Seiler Laboratory is interested in the use of these room temperature salts as battery electrolytes, thus the chemistry of possible metallic battery electrode and case materials is of interest. The chemistry that might be uncovered in such an investigation involves

the nature of any metal complexes formed from components of the melt. These are likely to be halide complexes. The nature of possible interaction between the metal ions or their complexes with solvent cations might also be uncovered.

Since the NMR chemical shift of the metal ions is very sensitive to the nature and number of attached ligands, the procedure proposed in this study involves examination of the NMR chemical shift of the metal ion as a function of metal ion concentration in melts of fixed composition as well as determination of the metal ion chemical shift as a function of electrolyte composition for fixed metal ion concentration.

III. RESULTS AND DISCUSSION:

A. ^{27}Al RELAXATION STUDIES Examination of the ^{27}Al NMR spin-relaxation phenomena in the title materials was continued. It appears that we have come to closure on this aspect of the proposed research. As shown earlier by this author², examination of ^{27}Al spin-lattice relaxation in the title compounds showed linear logarithmic magnetization recovery curves for a 1-methyl-3-ethylimidazolium chloride melt consisting of 0.60 mole fraction aluminum chloride (AlCl_3) under a wide range of sample and spectrometer conditions. The reason for further study of these observations is that these results disagreed with the work of Matsumoto and Ichikawa who observed non-linear logarithmic magnetization recovery curves for ^{27}Al at non-stoichiometric AlCl_3 compositions for similar melts. Their results were explained by postulating a non-single exponential relaxation due to a combination of relaxa-

tion rates from at least two slowly exchanging aluminum species. Additional work was proposed to try to discover the reason for the discrepancy between the two studies.

Careful examination of the details of the experiment and sample preparation lead to the conclusion that Matsumoto and Ichikawa's results are in error. These studies included examination of sample composition including the presence of possible impurities such as iron(III) and aluminum oxides, with no change in the linearity of the logarithmic magnetization recovery curves. Changing the mole fraction of added aluminum chloride (as AlCl_3) also has no effect on the linearity of these plots.

The conclusions reached earlier thus seem valid. The work of Wilkes, Frye and Reynolds³ indicate a relatively slow aluminum exchange between AlCl_4^- and Al_2Cl_7^- for melts of 1-methyl-3-ethylimidazolium chloride. At the temperatures involved in these studies (20 - 50 °C), the exchange lifetime is 2 - 3 ms. The T_1 for $^{27}\text{AlCl}_4^-$ in 0.50 mole fraction melt is in the neighborhood of 50 ms, whereas the T_1 for ^{27}Al in the 0.60 mole fraction AlCl_3 is around 0.2 ms. Since the relaxation of AlCl_4^- is larger than its exchange lifetime, the contribution of $^{27}\text{AlCl}_4^-$ to the overall ^{27}Al relaxation time cannot be any less than the exchange lifetime and no contribution to ^{27}Al relaxation due to slow aluminum exchange can be found. It should be emphasized that in this study, linear logarithmic magnetization recovery curves were obtained over a time span covering nearly complete magnetization recovery.

3. NMR OF METALS IN ROOM TEMPERATURE MELTS The work described in part III. A. above ended about the first of June, 1986, and it was decided to attack the problem associated with the study of the nature of NMR receptive metals dissolved in the AlCl_3 /1-methyl-3-ethylimidazolium chloride room temperature melts. Initial candidate metals were lead and tin, both with isotopes having magnetic spin quantum numbers of $1/2$, high natural abundances and thus good NMR sensitivities. Work with platinum would be delayed until results were in hand for the less expensive lead and tin studies. Based on aqueous chemistry, it was expected that these metals would both form chloro complexes in solutions with excess chloride.

At the time this project began it was quite apparent the electromagnet of the JEOL spectrometer was in disrepair and its performance was becoming progressively worse. The result was the spectrometer needed resolution tuning at shorter and shorter intervals. Since the NMR sensitivities of the metals proposed for study was high, it was expected that the time required to obtain satisfactory spectra for chemical shift determinations of the metals of interest would be short.

Considerable effort was expended in establishing NMR reference standards for lead and tin. The literature indicates the use of tetramethyl lead and tetramethyl tin as the materials of choice. Since these compounds are extremely poisonous and difficult to handle, secondary standards were established. For lead, a saturated D_2O solution of lead(II) nitrate in a melting point capillary was used; for tin, a saturated solution of tin(II) chloride in 50% D_2O : 50% aqueous hydro-

chloric acid proved useful.

The strategy used in these studies was to attempt to dissolve the metal(II) halide in the room temperature molten salts of varying AlCl_3 composition in order to vary the chloride to metal stoichiometric ratio. Examination of chemical shift changes of the metal would be indicative of the presence of any complexes formed between metal and chloride and possibly their stoichiometry.

Study of the lead system was somewhat disappointing. It was found that lead(II) chloride was not very soluble in room temperature molten salts with a moderate excess chloride (for example, molten salts with mole fraction AlCl_3 equal 0.49 and sufficient PbCl_2 for a $\text{Cl}^-/\text{Pb}^{++}$ ratio of 4 or 6). When solution was successful the lead chloride often soon precipitated, making NMR analysis difficult. At lower mole fraction AlCl_3 molten salts (for example, 0.35 mole fraction AlCl_3) and high ratios of Cl^- to Pb^{++} , the concentration of lead was sufficient to observe NMR signals. Changes in the Cl^- to Pb^{++} mole ratios produced little if any chemical shift change. The conclusion is that either (1) the lead complexes which formed with chloride in these melts have low formation constants or (2) the chemical shifts of any complexes formed with chloride in these melts have very similar chemical shifts. Results of studies with tin (vide infra) suggest that the second conclusion is not likely. One implication of the first possibility is that various other species in the molten salts compete for chloride more successfully than lead.

Results of similar studies with Sn(II) were quite successful and a

substantial conclusion can be made. In this case, solutions of tin(II) chloride in melts of varying composition in aluminum chloride and 1-methyl-3-ethylimidazolium chloride were prepared. The chemical shift of ^{119}Sn was measured as a function of the mole fraction of aluminum chloride. Representative results are presented in the Table.

Table. ^{119}Sn NMR chemical shifts of solutions of SnCl_2 in aluminum chloride/1-methyl-3-ethylimidazolium chloride solvent. Shifts are in Hz relative to an external capillary of tin(II) chloride in 50% D_2O : 50% aqueous hydrochloric acid. The magnetic field strength was 2.1 Tesla.

Mole Fraction AlCl_3	$\text{Cl}^-:\text{Sn}$ Mole Ratio	Chemical Shift (Hz)
0.355	14.0	6 074.3
0.375	19.9	6 802.1
0.450	9.7	8 220.6
0.475	8.8	8 979.6
0.495	3.1	10 632.3
0.53	2.0	20 117.2
0.55	2.0	18 859.9
0.575	2.0	18 261.7
0.60	2.0	19 018.5
0.625	2.0	17 529.3
0.65	2.0	19 427.0

Two plots of these data are shown in Figures 1 and 2. It is clear from these results that a complex between tin and chloride forms with a stoichiometry $3 \text{Cl}^- : 1 \text{Sn}^{++}$. No evidence for higher order complexes are indicated from these results. In aqueous media, it is commonly understood that tin(II) forms a tetrachloro complex. The nature of the liquid electrolyte melts as solvents is obviously quite different.

The work on the tin solutions ended about the first of September, 1986. At this time the NMR electromagnet had become all but unusable. The Seiler Research Laboratory had decided to order a replacement magnet. A nine month delay was anticipated before the order could be filled due to the long procurement process of the Air Force and the manufacturing time of the vendor.

IV. Suggestions for Further Work Some preliminary studies were carried out at the end of these projects which bear further study. It was learned that gallium chloride also forms room temperature liquids when mixed with 1-methyl-3-ethyl imidizolium chloride. Mixtures of gallium chloride in aluminum chloride/1-methyl-3-ethyl imidizolium chloride melts were prepared, and gallium NMR signals were observed. Difficulty was encountered developing a suitable external standard. The nature of these solutions of gallium chloride needs investigation. Using gallium and aluminum NMR spectroscopy, it may be possible to examine the nature of any gallium-aluminum exchange associated with the various metalloid chloro species. To this end, numerous solutions of gallium chloride in aluminum chloride/1-methyl-3-ethyl imidizolium chloride melts were prepared in sealed NMR tubes for eventual analysis when a replacement

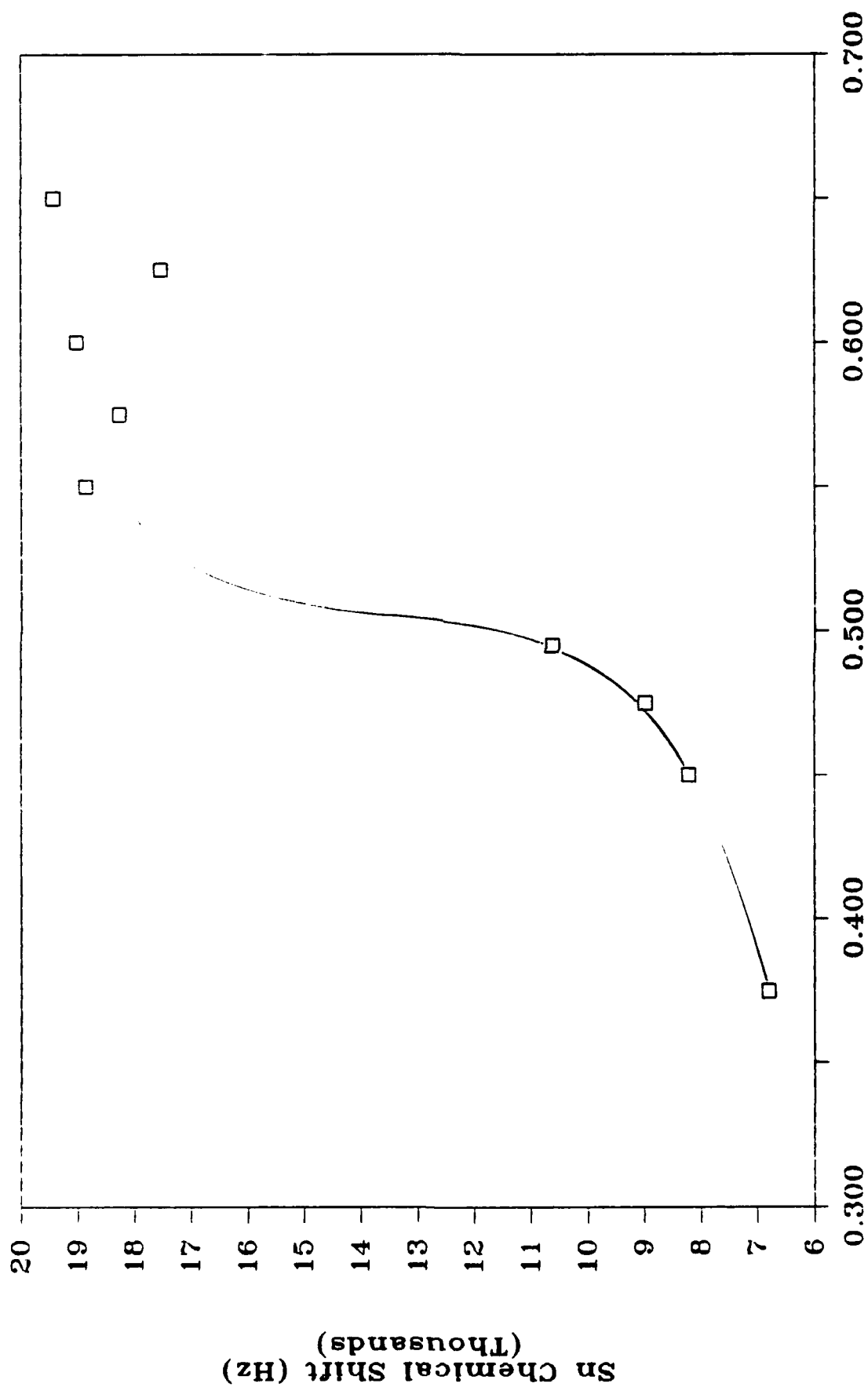


Figure 1. A plot of tin chemical shift vs. aluminum chloride mole fraction for solutions of tin(II) chloride in aluminum chloride/1-methyl-3-ethylimidazolium chloride solvent.

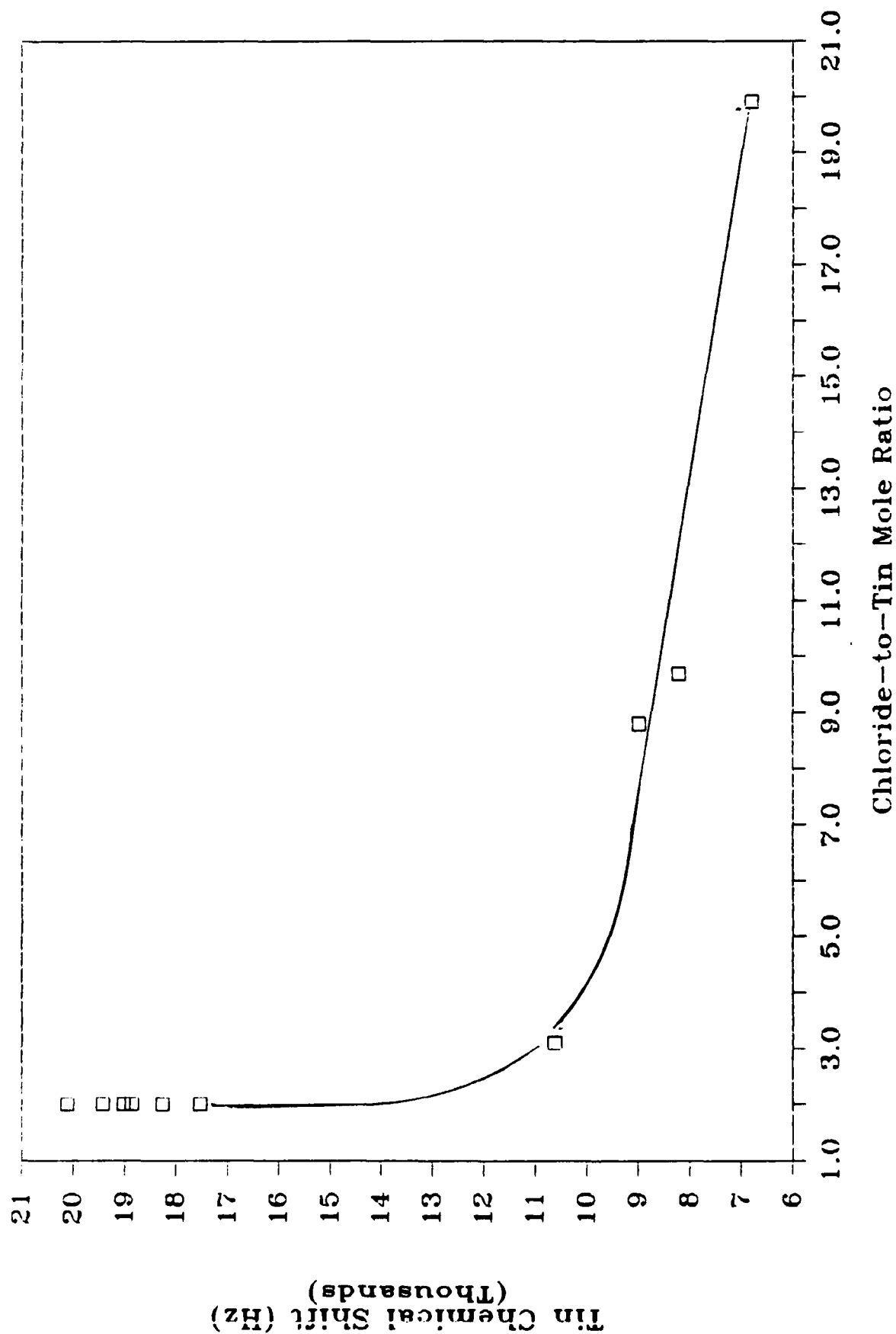


Figure 2. A plot of tin chemical shift vs. chloride-to-tin mole ratio for solutions of tin(II) chloride in aluminum chloride/1-methyl-3-ethylimidazolium chloride solvent.

electromagnet is obtained. This work carried through to early February, 1987. These solutions have been left with the workers at the Seiler Research Laboratory for future examination.

ACKNOWLEDGMENTS

I would like to thank a number of people at the Frank J. Seiler Research Laboratory for their assistance in helping me carry out this work. The encouragement of John Wilkes is greatly appreciated. His assistance in introducing me to the details of laboratory procedures and his helpful comments on the nature of the experimental results are greatly appreciated. Towner Scheffler and Lloyd Pflug were very helpful in teaching me the operation of the NMR spectrometer. Jack Fannin's help was invaluable in debugging the least-squares routine used in the data reduction for this project. His comments about the meaning of the measurements are much appreciated. Jeff Boon's help by preparing the compounds used in these studies saved me much time and is greatly appreciated. Helpful discussions with Chet Dymek are also appreciated. Sponsorship of this work by the Air Force Systems Command, Air Force Office of Scientific Research, is gratefully acknowledged.

LITERATURE CITED

1. Matsumoto, T., Ichikawa, K., "Determination of Aluminum-27 Spin Lattice Relaxation time and Relative Number of Each Chloroaluminate Species in the Molten 1-n-Butylpyridinium Chloride/ AlCl_3 System," J. Am. Chem. Soc., **1984**, vol. 106, pp 4316-4320.
2. Bertrand, R. D., " ^{27}Al Spin Lattice Relaxation Measurements in Alkylammonium-Chloroaluminate Room-temperature Electrolytes," Final

Report Submitted to Universal Energy Systems, Sept. 3, 1985.

3. Wilkes, J. S., Frye, J. S., and Reynolds, G. F., Inorg. Chem., **1984**,
vol 22, pp 3870-3872.

1989 AFOSR-UES Research Initiation Program

Final Report

Mechanistic Studies on the Thermal Decomposition of NTO by
High Performance Liquid Chromatography

Dan R. Bruss, Ph.D.
Albany College of Pharmacy
Albany, NY.

December 31, 1989

Contract No:
F49620-88-C-0053/SB5881-0378

Mechanistic Studies on the Thermal Decomposition of NTO by
High Performance Liquid Chromatography

by

Dan R. Bruss

Abstract

The thermochemical condensed phase decomposition of 3-nitro-1,2,4-triazol-5-one, NTO, was examined over the temperature interval of 508-518 K. Temporal profiles of loss of NTO as measured by high performance liquid chromatography suggested an autocatalytic decomposition process. Empirical rate constants obtained for the global decomposition process exhibited Arrhenius behavior, yielding an activation energy of 92.32 kcal/mol.

Decomposition of the perdeuteriated NTO analog demonstrated a primary kinetic deuterium isotope effect, exhibiting a $k_H/k_D = 2.44$ when recalculated to 298 K. Preliminary studies indicate self-coupling of NTO or solvolysis with DMSO at 393 K.

I. Introduction

The nitrated heterocycle 3-nitro-1,2,4,-triazol-5-one, NTO, depicted in Figure 1, is of considerable interest as a new generation insensitive high explosive.¹ An understanding of the decomposition of NTO would provide insight into the structural features that trigger its decomposition, and should spark potential avenues to more efficient energetic materials. In addition, a better understanding of such parameters as storage, preparation, and use of the material, would be possible. With the groundwork laid by the preliminary kinetic studies carried out during the 1988 Summer Faculty Research Program, the stage was set for a more in-depth study.

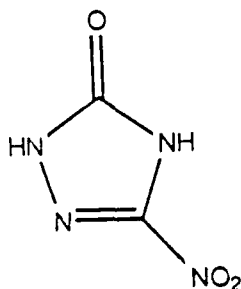


Figure 1. 3-Nitro-1,2,4-Triazol-5-one (NTO)

The work conducted during this project focused on the kinetics exhibited in the temperature interval of 508 K - 518 K. The choice of the temperature interval examined for this study was driven by practical considerations. A

time frame was needed that was long enough to observe the kinetic profile with confidence, and yet not so long that reactions needed to be carried out over many hours. From a processing standpoint, it is advantageous to obtain kinetic information near the melting point of NTO. However, at temperatures above 518 K, NTO exhibits a tendency to undergo adiabatic processes that yield higher order decomposition reactions such as deflagration or thermal explosion. In addition, reaction times increase very rapidly as the temperature is decreased, changing from a few minutes above 518 K, to several hours, within a few degrees below this threshold.

High performance liquid chromatography continued to be the analytical method utilized to provide direct measurement of unreacted NTO. A typical temporal decomposition profile of NTO is illustrated in Figure 2. As discussed earlier,² this pattern is characteristic of a process that exhibits autocatalytic kinetics. As the temperature is increased for a decomposition reaction, the induction time is shortened and the loss curve is steeper. The temporal data for loss of NTO was then fitted to an empirical autocatalytic rate expression, utilizing a nonlinear least squares fitting routine developed at the Frank J. Seiler Laboratory.

While decomposition experiments with NTO had been carried out by the principal investigator during the

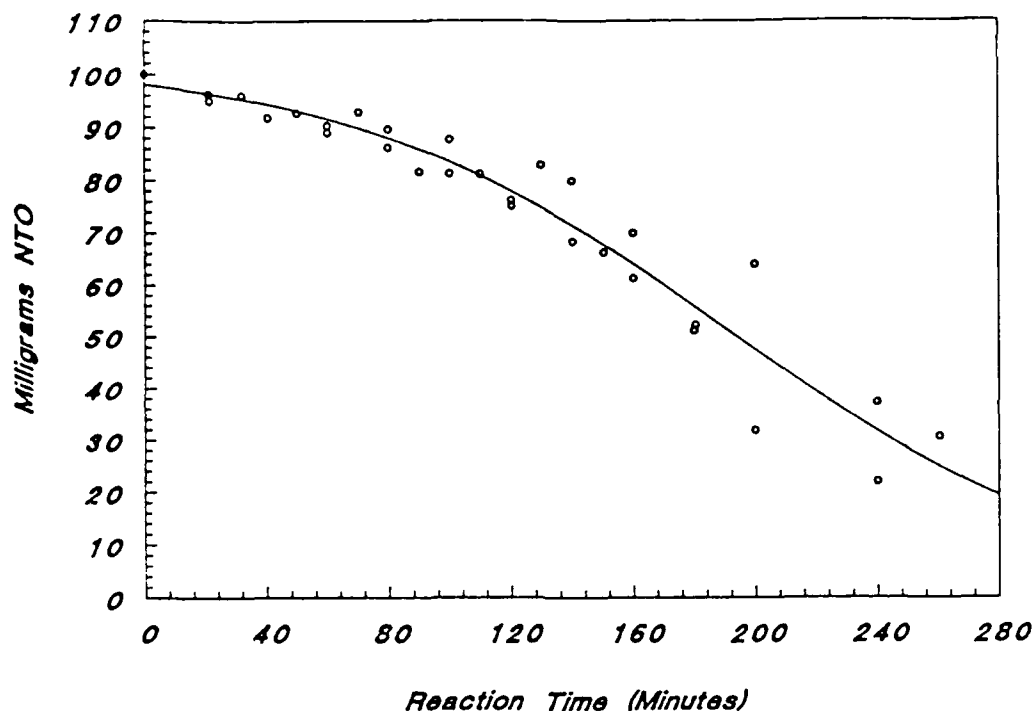


Figure 2. NTO decomposition profile at 513 K.

previous SFRP period, several reactions were repeated in an effort to assure statistical reliability. In addition, reactions were carried out with 50 mg samples to give a more complete kinetic picture.

To provide a glimpse of the decomposition mechanism, kinetic studies were carried out on the perdeuteriated NTO analog. The kinetic deuterium isotope effect is an established mechanistic probe used to provide specific information on the rupture of covalent bonds involved in the rate determining components of multi-step processes. Although this method has been employed to explore solution and gas phase reactions, the isotope effect has also been

successfully utilized in neat, condensed phase studies.³ Kinetic data obtained from NTO-d² would provide direct, nonintrusive identification of the role of N-H bond rupture in the rate controlling step.

The HPLC assay we developed for the kinetic studies did not provide any information concerning intermediate formation during decomposition. Since such intermediates would more than likely be present in only low levels and be quite reactive, it was felt that the use of radical trapping agents might provide a reasonable route to isolation and characterization. Nitrosobenzene, a stable yet potent trapping agent, was employed as a possible mechanistic tool in this regard. Reactions involving nitrosobenzene as a reaction adjunct were carried out at several temperatures, both as a neat mixture and as solutions with NTO and moderately high boiling solvents such as DMSO or DMF. In addition, reactions of NTO dissolved in DMSO or DMF in the absence of trapping agents were also carried out to see if, for example, solvolysis or perhaps some other solvent effects might be occurring. Any information obtained from decomposition behavior would be useful, since applications involving mixed melts are a reasonable possibility.

During the 1988 SFRP project, the principal investigator reported preliminary results involving the pH dependent ultraviolet absorption shift of NTO². At the

time, it appeared that the shift had its origin in different tautomeric forms of NTO. In an effort to understand the nature of this more fully, the ultraviolet spectrum of NTO was closely monitored within the pH range of 3.0-7.0. Since isolation of pure tautomers is not practical, attempts were made to synthesize N- and O-methyl NTO derivatives in an effort to mimic the UV spectra of the unsubstituted tautomers.

II. Objectives

As discussed in the Research Initiation Program proposal, the thrust of the current work was to further examine the thermochemical condensed phase decomposition of NTO by firmly establishing the global kinetic order for the process, examining the extent of kinetic deuterium isotope effect, and attempting to isolate and characterize reaction intermediates.

III. Results and Discussion

The kinetic information obtained from the 1988 SFRP work provided rate constants that gave a first approximation for the activation energy of the thermal decomposition process of NTO. The fitting procedure employed a logarithmic expression to plot the amount of NTO remaining as a function of time. This plot was not as sensitive to changes in k as it should have been. In addition, when the initial weight of NTO was cut in half, the rate constants that resulted for these reactions were

four times greater than those obtained at 100 mg levels. While at first glance this behavior may seem unusual, this type of behavior is not uncommon in complex multipath processes.

Since the rate constants should be the same even though the observed rate is different, modification had to be made to the empirical rate expression to incorporate this behavior. An empirical autocatalytic rate expression, Equation 1, was derived at Seiler to take into account the "amount dependence".⁴ Linearization was abandoned in an effort to avoid loss in data precision. Instead, a nonlinear least squares fitting routine was employed to fit the data. Rate constants obtained from this process is presented in Table 1.

$$A = \frac{A_0(k_1+k_2A_0)}{k_2A_0+k_1e^{((k_1+k_2)A_0)t/A_0^2}}$$

Equation 1. Empirical rate expression for the condensed phase thermochemical decomposition of NTO
(A = amount of NTO at time = t and A₀ = initial amount of NTO).

Decomposition reactions employing perdeuteriated NTO were then carried out to determine if N-H bond rupture is intimately involved in the global rate determining step. The deuterium isotope effect has proven to be of great utility in ascertaining the mechanism of condensed phase

thermal decomposition of the nitro-aromatics. Shackelford, et al.⁵ employed this to demonstrate that benzylic carbon-hydrogen bond rupture was critical in the rate determining step of the decomposition of TNT. The global rate constants calculated for NTO-d₂ at temperatures in the 505-515 K temperature interval is presented in Table 2.

NTO rate constants

<u>Temp.</u>	<u>100mg</u>	<u>50mg</u>
508	$6.825 \times 10^{-1} \pm 3.89 \times 10^{-2}$	$6.202 \times 10^{-1} \pm 6.726 \times 10^{-3}$
511	$9.138 \times 10^{-1} \pm 2.66 \times 10^{-2}$	$9.2589 \times 10^{-1} \pm 3.266 \times 10^{-2}$
513	$1.529 \pm 3.431 \times 10^{-2}$	$1.513 \pm 5.031 \times 10^{-2}$
518	$3.6798 \pm 5.609 \times 10^{-2}$	--

Table 1. Empirical global rate constants for the condensed phase thermochemical decomposition of NTO.

NTO-d₂ rate constants

508	$3.839 \times 10^{-1} \pm 4.685 \times 10^{-2}$	$3.9997 \times 10^{-1} \pm 7.2988 \times 10^{-2}$
513	$9.695 \times 10^{-1} \pm 3.111 \times 10^{-2}$	$9.445 \times 10^{-1} \pm 4.8783 \times 10^{-2}$
518	$2.13899 \pm 6.548 \times 10^{-2}$	$2.0953 \pm 5.9846 \times 10^{-2}$

Table 2. Empirical global rate constants for perdeuteriated NTO.

The maximum for the isotope effect k_H/k_D involving C-H bond rupture approaches 7 at room temperature, and decreases with higher temperatures.⁶ This value is achieved when the bond-breaking and bond-making of the

hydrogen in question is equal in the transition state of the rate determining step. A ratio near or above 2 is considered to be a substantial deuterium isotope effect, and is good evidence that the hydrogen being studied is intimately involved in the chemistry of the rate determining transition state. Generally, ratio values near 2 indicate the transition state resembles either product or reactant, while values that approach the maximum argue for pronounced influence of both product and reactant.⁶ Table 3 shows the observed deuterium isotope effect at the temperatures studied.

<u>Temp.</u>	<u>100mg</u>	<u>50mg</u>
508	1.778	1.551
511	--	--
513	1.482	1.602 & 1.697
518	1.720	--

$$\text{Mean } kH/kd = 1.638 \pm 0.112$$

Table 3. Observed kinetic isotope effect for decomposition of NTO using 50 and 100 mg samples.

Isotope effect calculations are generally measured at 298 K. If one assumes a mean temperature of 513 K, the observed kH/kD of 1.638 provides a calculated kH/kd of 2.44 at 298 K, which is clearly a primary isotope effect.

The rate constants derived from the temporal rate loss data for both NTO and NTO- d_2 were then utilized in an Arrhenius equation plot of the $\ln K$ versus $-1/RT$, as

Once the kinetic data was in hand, work was carried out to isolate reaction intermediates. Since there was no evidence from HPLC analysis that stable intermediates were being formed in measurable quantities, reactions were carried out in the presence of nitrosobenzene in an effort to trap transient radical species. When one or two percent nitrosobenzene was mixed with NTO, only starting material and the self-coupling product of nitrosobenzene were detected. The same HPLC profiles were seen, whether the reactions were carried out at 393 K or 423 K. Increasing the reaction time only showed an increased concentration of the self-coupling product. The same reaction was then carried out at 393 K with DMSO as a solvent. HPLC analysis of this reaction mixture showed several other components, whose concentrations increased with longer reaction times. To determine if these products were radicals trapped by nitrosobenzene or solvolysis products with DMSO, reactions were performed with various combinations of the reagents. From this it was found that the new peaks were formed only when NTO was in the presence of DMSO. While these components have been collected from the HPLC, their identity is still unknown at this time.

Additional work was carried out to study the structure of the tautomers of NTO. Ultraviolet spectra of NTO were carried out at various pH. The lambda max increased from 319 nm at pH = 3.0 to 340 at pH = 4.4. This is a lower pH

illustrated in Figure 3. The activation energies and pre-exponential factors derived from this plot are summarized in Table 4.

	<u>E_a (kcal/mol)</u>	<u>$\ln A$</u>
NTO	92.31628 ± 5.70934	90.93194 ± 5.61193
NTO-d ²	88.36041 ± 1.58186	86.58058 ± 1.551421

Table 4. Activation energies and pre-exponential values for NTO and NTO-d².

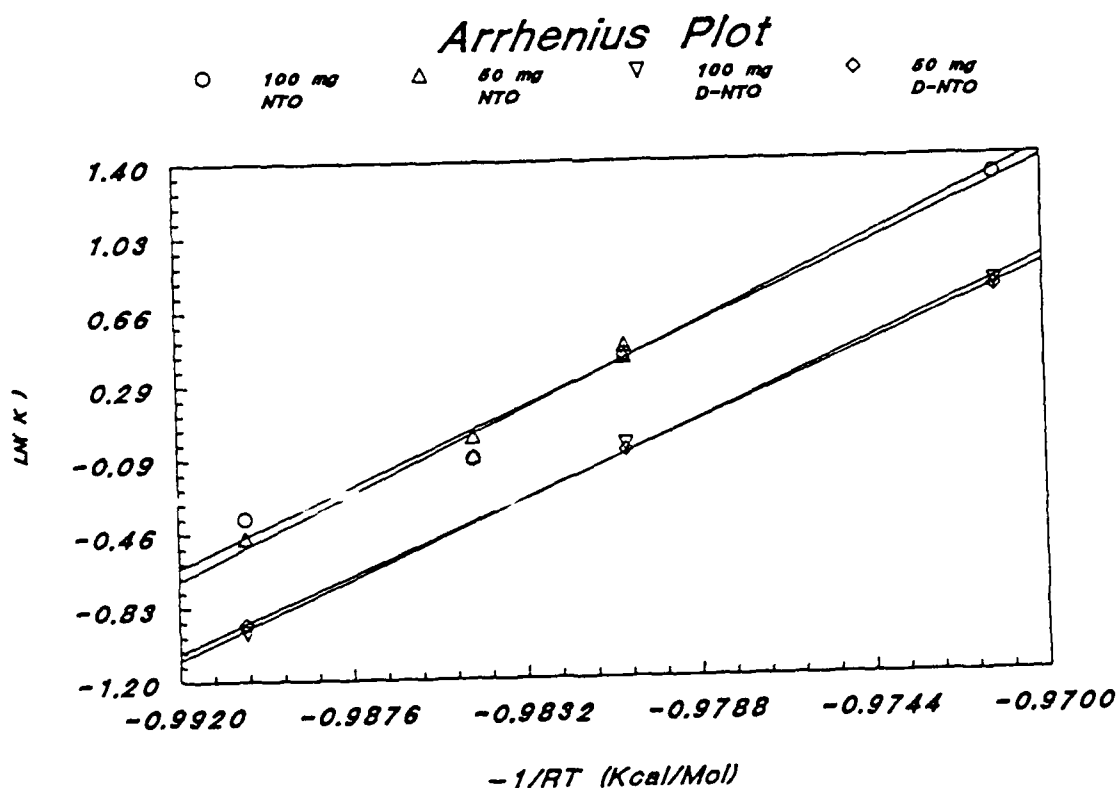


Figure 3. Arrhenius plot of NTO and NTO-d².

range than was preliminarily reported in the 1988 SFRP.² Since this is the region surrounding the pKa of NTO, it seemed reasonable that N- or O-alkylation of NTO might provide an ultraviolet spectrum to mimic the keto or "enol" species. Ritchie⁸ showed that there is a theoretical preference for the proton nearer the nitro group to be the more acidic, and that the keto tautomeric conjugate base is the more stable. To verify this experimentally, N-methylation via abstraction of the more acidic hydrogen by diazomethane was chosen as a chemical probe. While diazomethane has successfully been used to generate methyl esters, it is also capable of abstracting other acidic protons. Depending on whether diazomethane reacts with the N-H or the tautomeric O-H, there are four possible methyl derivatives. These are illustrated in Figure 4.

The reaction mixture was analyzed by HPLC and found to exhibit three peaks in addition to unreacted NTO. Mass spectral analysis of the reaction mixture revealed there were three components with parent ion masses of 142, 156, and 185. The mass spectrum of the minor (4%) component showed a parent ion of 185, and its spectrum matched that of N,4-dimethylbenzenesulfonamide, a by-product from Diazald. The other two components, 142 (80%) and 156 (15%), are consistent with methyl and dimethyl substituted NTO, respectively. Separation by thin layer chromatography (chloroform/acetone, 85%:15%) also showed two spots other

than NTO. Scale-up to flash chromatography scale, unfortunately, did not provide clean separation. Use of dynamic radial chromatography afforded a few milligrams which, when analyzed by carbon NMR, yielded a spectrum with three carbons exhibiting resonances at 163, 107, and 59 ppm. NTO gives two carbon resonances: 154 and 148 ppm. The carbon at 59 ppm is most likely N- or O-substituted, but the pronounced shift of one of the ring carbons indicates that something other than substitution at nitrogen had occurred.

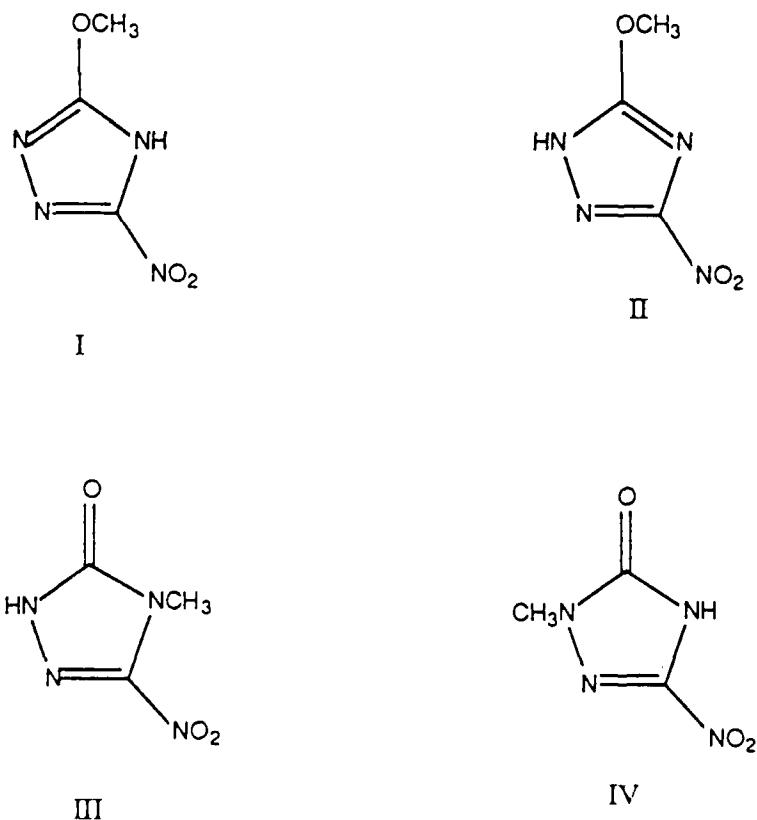


Figure 4. Possible N- and O-substituted products from the reaction of NTO with diazomethane.

One possible explanation is that increased electron density, due to extended conjugation, causes a dramatic shielding of one of the carbons.⁹ Tautomer "I" in Figure 4 provides support for the experimental results. It should be stressed, however, that this is only a preliminary hypothesis, and further work must be done to provide a definitive answer.

III. Experimental

Preparation of 1,2,4-triazol-3-one

Semicarbazide hydrochloride, 46.03 g (0.39 mol), was slowly added with stirring to 45 mL of 85% formic acid solution. After the addition was complete, the mixture was refluxed for five hours, followed by concentration of the reaction mixture by distilling off half of the volume. The concentrate was then diluted with 50 mL of water, and the solution again concentrated by collecting 70 mL of distillate. The residual solution was then chilled, and the resulting precipitate filtered and dried overnight in an oven maintained at 95°C. The crude product was recrystallized from ethanol, yielding 24.4 g of product (70%). The recrystallized product melted at 234-236°C (Lit.¹ 234-235°C).

Preparation of 5-nitro-1,2,4-triazol-3-one.

To a stirred solution of 4.0mL of H₂ and 8.5 mL of 90% HNO₃ at 50°C was added slowly 3.91 g (0.0045 mol) of 1,2,4-triazol-3-one. The temperature was carefully maintained at

50°C by heating on a hot plate. After the addition was complete, the mixture was heated to 80°C, at which time brown fumes began to evolve. The mixture continued to boil and evolve fumes even after the reaction was removed from the hot plate. After several minutes a heavy white precipitate formed and the fumes subsided. The reaction was then quenched with 5 mL of ice water. The precipitate was then filtered and washed with two additional 5 mL portions of ice water. The remaining precipitate was recrystallized from water to yield 3.68 g of product which melted at 268-270°C. (Lit.₁ 265-268°C.) Observed ¹H NMR (DMSO-d₆) 12.76 ppm and 10.92 ppm. (Lit.₁ 12.8)

Preparation of perdeuteriated NTO.

Perdeuteriated NTO was prepared by refluxing an NTO/D₂O solution for one hour, after which time the solution was cooled to 0°C and the recrystallized NTO-d₂ vacuum filtered. Mass spectral analysis indicated 95% conversion to the perdeuteriated species and 5% monodeuteriated.

Thermochemical Decomposition of NTO.

Isothermal decomposition experiments of NTO and NTO-d₂ were carried out at 508, 511, 513, and 518 K as follows. Reaction tubes measuring 20cm x 8mm were first made from standard Pyrex stock. The tubes were then cleaned in a KOH/methanol bath, washed with distilled-deionized water and dried overnight in an oven. Into each of thirteen

tubes was placed 100mg of NTO or NTO-d₂. The tubes were then loosely fitted with corks and twelve were placed in a Tecam fluidized bath preheated to the specified temperature which was temperature controlled to within ± 0.5 K. The remaining tube was maintained at ambient temperature and used as a control. Individual tubes were subsequently removed at regular 20 minute intervals and immediately quenched in an ice bath. All of the solid material from each tube was taken up in DMSO and transferred to individual 5mL volumetric flasks. To assure quantitative transfer of reaction material, each tube was washed with several aliquots of DMSO, and the washings were added to the volumetric. After additional DMSO was added to provide precisely 5 mL, 100 microliters of each solution was then transferred to individual 4 mL vials. Each vial was tared and the sample diluted with 2.500 mL of water. Duplicate decomposition reactions were similarly carried out at each of the temperatures using 50mg of NTO or NTO-d₂ material.

All NTO and NTO-d₂ concentration measurements were obtained by high performance liquid chromatography on a Hewlett-Packard 1090 or Beckman 110B/166 liquid chromatograph. Elution was carried out with an isocratic 90:10 water/1% acetic acid:methanol solvent system on a 15 cm C-18 reverse phase column. NTO and NTO-d₂ were detected at 254 nm and the measured areas were converted to milligrams of NTO. The resulting weights were then

normalized to 100 mg or 50 mg, depending on sample size used, to correct for small variations in weighing. In addition, a minimum of three repetitive assays were carried out on each sample to insure precision in sample weight determination.

The temporal data for loss of NTO was then fitted to an empirical autocatalytic rate expression, Equation 1, utilizing a nonlinear least square fitting routine which was developed at the Frank J. Seiler Research Laboratory. Linearization of the equation was not used in an effort to avoid loss in data precision. The empirical rate constants derived from this fitting routine were then utilized in an Arrhenius equation plot of $\ln k$ versus $1/RT$. Figure 3 graphically illustrates the plot.

Reaction of NTO with diazomethane

To a solution of 1.2 g KOH in 1.9 mL water, was added 2.4 mL of 95% ethanol. This mixture was placed into a 100 mL distilling flask which was connected to a condenser delivering into two receiving flasks both cooled in ice. The first receiving flask contained a solution of 500 mg of NTO in 20 mL of methanol cooled to 0°C. The second receiver contained 25 mL of diethyl ether and the inlet tube dipped below the surface of the ether. The distilling flask was heated in a water bath at 65°C and a solution of 1.2 g Diazald in 30 mL ether was added from a dropping funnel to the distilling flask in about 10 minutes. When

the dropping funnel was empty, 20 mL of ether was slowly added and the distillation continued until the distillate was colorless. The distillate was evaporated to dryness, yielding 472 mg of crude product.

Radical trapping experiments with nitrosobenzene

Solutions containing 50 mg NTO and 1 mL DMSO were prepared in 5 mL volumetric flasks. The mouths of the flasks were covered with aluminum foil and the flasks were then suspended in a Tecam fluidized bath which was previously stabilized at 393 K. Flasks were removed at 2, 4, 8, and 12 hour intervals. The reaction mixtures were analyzed by injecting 20 uL samples of the undiluted solutions onto a Beckman 110B/166 HPLC. Elution was accomplished with a water/1% acetic acid:methanol solvent system employing a gradient from 0-30% methanol. Components were detected at 254 nm. Similar reactions were carried out with mixtures of NTO, nitrosobenzene and DMSO or nitrosobenzene and DMSO.

IV. Recommendations

The thermochemical condensed phase decomposition of NTO is autocatalytic as measured by empirical techniques. The high energy of activation for the overall decomposition indicates complex global reaction kinetics that probably involve initiation, a number of propagation steps and termination. In addition, the kinetic deuterium isotope effect studies indicate a primary N-H isotope effect.

With this kinetic data in hand, the next logical step would be to probe specific mechanistic routes. Future mechanistic work should be done in concert with the ESR studies currently under way at Seiler.

The preliminary work involving DMSO solvolysis should be followed up, both for its possible mechanistic implications, and also from a processing standpoint. If NTO forms adducts at 393 K in the presence of DMSO, what, for example, happens when it is formed as a mixed melt with TNT? In addition, the study involving the experimental determination of the tautomeric structures of N- and O-substituted NTO needs to be completed to corroborate the theoretical studies by Ritchie.

V. Acknowledgments

The author would like to thank the Air Force Office of Scientific Research and the Albany College of Pharmacy for sponsoring this project. I would also like to thank Maj. Scott Shackelford and Lt. Col. Steve Lander for their technical discussions, Lloyd Pflug for providing mass spectral analyses, and, in particular, Capt. Joe Menapace for his invaluable technical contributions and encouragement throughout the project.

Vi. References

1. K.Y. Lee, L.B. Chapman, M.D. Coburn, J. Energ. Mater., 5, 27 (1987).
2. D.R. Bruss, Final Report, UES-AFOSR, (1988).
3. S.A. Shackelford, Chemistry and Physics of the Molecular Processes of Energetic Materials, NATO Advanced Study Institute, Altavilla Micilia, Italy, 3-15 September 1989.
4. J.A. Menapace, personal communication.
5. S.A. Shackelford, J.W. Beckmann, J.S. Wilkes, J. Org. Chem., 42, 4201 (1977).
6. T.H. Lowry, K.S. Richardson, Mechanism and Theory in Organic Chemistry, Harper and Row, New York, NY, 1981, pp. 205-212.
7. F.A. Carey, R.J. Sundberg, Advanced Organic Chemistry Part A: Structure and Mechanism. Plenum Press, New York, NY, 1977, pp. 149-150.
8. J.P. Ritchie, J. Org. Chem., 54, 3553 (1989).
9. G.C. Levy, R.L. Lichter, G.L. Nelson, Carbon-13 Nuclear Magnetic Resonance Spectroscopy, New York, NY, 1980, pp 117-119.

FINAL REPORT

AROMATIC NITRATIONS IN CHLOROALUMINATE MELTS

**Dr. Charles M. Bump
Hampton University
Hampton, VA 23666**

May 8, 1989

INTRODUCTION

The objective of this project was to assess the effectiveness of various nitrating agents in an ionic liquid composed of aluminum chloride and 1-Methyl-3-Ethyl Imidazolium Chloride (MEIC). The ionic liquid employed had an apparent mole fraction of aluminum chloride of 0.667. Nitrating agents to be studied were nitryl chloride, nitrosyl chloride, and acetyl nitrate. The work was important for two reasons: first, it involved the use of the ionic liquid as a reaction solvent/catalyst, and second, it addressed the development of methods for the synthesis of energetic materials.

Preliminary results were obtained at the end of the principal investigator's 1987 summer research period at the Frank J. Seiler Research Lab concerning nitrations in the molten salt medium. Four specific goals were given: 1) determining the optimum ratio of aromatic substrate:melt:nitrating agent, 2) determining the relative rate of nitration of toluene and benzene using nitryl chloride, 3) determining the chemical identity and reactivity of the product obtained from nitryl chloride and aluminum chloride, and 4) determining the effectiveness of nitrosyl chloride and acetyl nitrate as nitrating agents in the chloroaluminate melts. Aromatic substrates to be used for this study were benzene, toluene, chlorobenzene, acetophenone, and nitrobenzene. Toluene represents a typical aromatic activated toward electrophilic aromatic substitution by the inductive influence of the methyl group. Chlorobenzene deactivates aromatics by virtue of its inductive electron withdrawing power while directing further substitution to the ortho and para positions by resonance. Acetophenone is a mildly deactivated compound by resonance while nitrobenzene is a strongly deactivated compound by resonance.

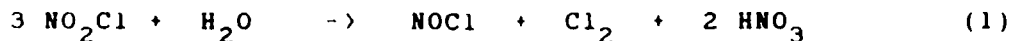
RESULTS

Most of the goals of this investigation were not fully realized. The principal investigator had set up a laboratory with the necessary glovebox apparatus to carry out the planned research and ordered the required chemicals by May of 1988. A graduate student was supported at Hampton during the summer of 1988. He was a citizen of Grenada and therefore ineligible to accompany the principal investigator to the Frank J. Seiler Research Lab during that time period. The principal investigator left a detailed list of work to be done by the grad

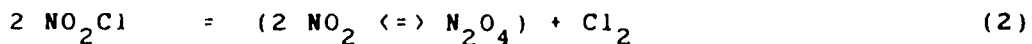
student and instructions to make weekly calls to the Seiler Lab for the principal investigator's information and guidance. A copy of these instructions is appended. Arrangements were made for other faculty members to assist the student should any difficulties arise. The graduate student accomplished virtually nothing and left before the end of the summer. In September of 1988 a new graduate assistant was selected to carry on with the project. This individual accomplished more in one week than the previous student had done during the entire summer. Many experiments were carried out both in preparing the molten salt and in nitrating benzene. He learned the techniques of preparing nitryl chloride and using it in reactions. The gas chromatographic conditions for the separation, identification, and quantification of reaction products were determined. During the Spring semester, graduate support for this work had expired so the student was required to spend considerable time preparing materials for the teaching labs.

No progress was made concerning the establishment of the optimum ratio of aromatic:melt:nitrating agent, on the relative rate of nitration of toluene and benzene using nitryl chloride, and in assessing the effectiveness of nitrosyl chloride and acetyl nitrate as nitrating agents in the molten salt medium.

In the nitration of benzene with nitryl chloride, the technique in handling the nitryl chloride plays a major role in determining the yield of the reaction. The ratio of aromatic:melt:nitrating agent was held at 1:1.5:1.5. The principal investigator stored nitryl chloride overnight in a freezer for use the following day. The use of that nitryl chloride on the following day becomes a matter of some importance. If the nitryl chloride is permitted to remain in the freezer a great length of time, the nitrating agent decomposes and gives a higher yield of chlorinated rather than nitrated products. One week of storage lowered the nitration and raised the chlorination yield to the point where they were nearly identical. Nitryl chloride stored overnight and used the following day produced at least a two fold excess of nitrated products over chlorinated products. The equation for the decomposition of nitryl chloride with moisture (for example from the freezer) is shown below²:



Nitryl chloride will also decompose in the absence of moisture according to the reaction below².



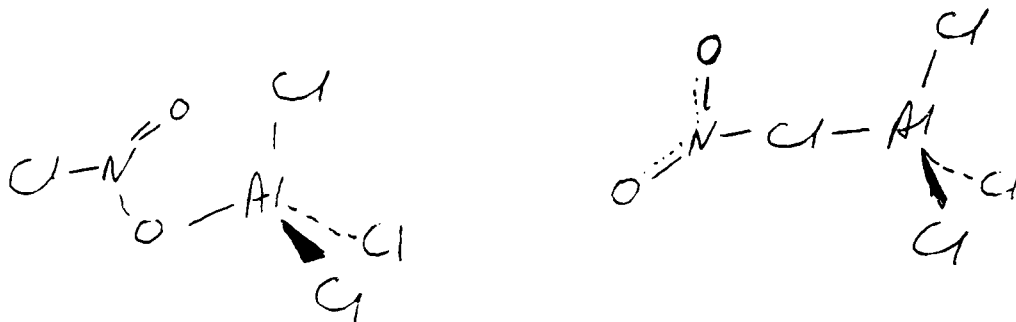
The generation of elemental chlorine no doubt is responsible for the increase in chlorinated products. It is also imperative that the nitryl chloride be cooled to a liquid before introduction of the melt containing the aromatic substrate. Several experiments have verified that the yield of nitrobenzene is effectively cut in half if the nitryl chloride is cooled only to an ice-water bath temperature rather than a dry-ice acetone bath temperature. Presumably some of the nitryl chloride escaped into the atmosphere before it could be dissolved in the chloroaluminate melt to carry out a nitration. In reactions that were carried out on freshly prepared nitryl chloride cooled to a liquid state before adding the melt and aromatic the more unreacted benzene that was recovered at the end of the reaction, the more chlorobenzene could be expected as product, and the less nitrobenzene could be expected to be produced.

The principal investigator's results at the Frank J. Seiler Research Laboratory indicated that approximately 44% of the nitrobenzene theoretically possible is obtained. The current results show a much lower yield (20%) of nitrobenzene due to the handling of nitryl chloride.

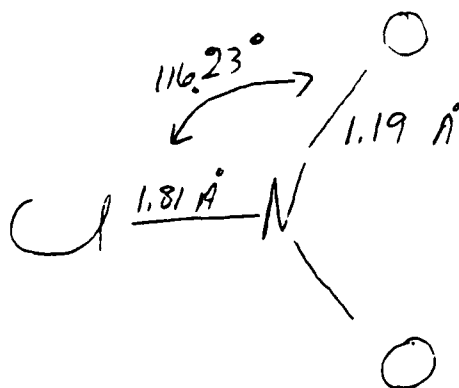
The nitration of chlorobenzene was also carried out maintaining the 1:1.5:1.5 ratio of aromatic:melt:nitrating agent. The separation of the ortho and para isomers of chloronitrobenzene was not possible using the gas chromatographic column employed (OV-101). Pure authentic samples of each isomer gave peaks of differing retention times. However, the peaks obtained from reaction mixtures were not adequately resolved to permit determination of the isomers present. Results were obtained and calculated as if the nitrated product was exclusively the para isomer. Results during this research period were comparable to those obtained by the principal investigator at the Seiler Lab: namely that about forty percent (40%) of the chlorobenzene was nitrated and that about twenty percent (20%) was chlorinated. Although the chloronitrobenzenes could not be separated, the dichlorobenzenes could be separated. The reaction of nitryl chloride gave a twofold excess of para dichlorobenzene over the ortho isomer. No such distinction was made concerning the isomer distribution at the Seiler Lab.

The adduct formed between nitryl chloride and aluminum chloride was investigated during the principal investigator's Summer 1988 research at the Seiler Lab. Those results indicated that the adduct itself would readily form a pi complex with an aromatic but would not continue to form a sigma complex and carry out the nitration in synthetically reasonable yield. The structure of the adduct remains a mystery as the spectral evidence may be interpreted in more than one way. The material is isolated as a yellow solid. The color rules out free nitronium ion as stable nitronium ions are colorless. On addition of anhydrous acetonitrile the yellow color disappears and the adduct gives a single UV-visible absorbance at 232 nm.

Authentic nitronium tetrafluoroborate gave a single peak in the same solvent at 235 nm. Whatever the nature of the adduct, a nucleophilic solvent releases nitronium ion. The obvious reaction of benzene with the nitryl chloride-aluminum chloride adduct in acetonitrile has not been carried out. Aluminum-27 magnetic resonance spectroscopy of the adduct shows a signal at 101 PPM versus $\text{Al}(\text{H}_2\text{O})_6^{3+}$. That chemical shift is characteristic of the tetrachloroaluminate ion⁴. It is also possible that the shift is due to aluminum with four electronegative atoms around it. Two possible structures for this adduct are shown below:



The structure featuring coordination of nitryl chloride to the aluminum chloride through the oxygen is chemically more reasonable from the standpoint of the greater electronic charge on oxygen than chlorine. The Pauling electronegativity value of oxygen is given as 3.5 while chlorine's is 3.0. The greater electron density on oxygen is also supported in a MOPAC⁵ calculation of nitryl chloride. The optimized geometry of the molecule is shown below:



The cartesian coordinates and charge are tabulated below:

ATOM	X	Y	Z	CHARGE
Cl	0.0000	0.0000	0.0000	-0.0978
N	1.8097	0.0000	0.0000	0.5407
O	2.3361	1.0683	0.0000	-0.2215
O	2.3361	-1.0683	0.0000	-0.2215

SUMMARY

Many of the specific objectives of the proposed research were not realized. Equipment obtained through this mini-grant has made it possible to carry out research on organic reactions in chloroaluminate molten salts. Research addressing the original objectives cited continues at Hampton University and forms the basis for an M. S. candidate's thesis research. When sufficient results have been obtained to warrant publication, the Seiler Lab will be advised.

REFERENCES

1. Charles M. Bump, Reactions of Nitryl Chloride with Aromatic Substrates in Chloroaluminate Melts, Final Report, 1987 USAF-UES Summer Faculty Research Program, 27 August 1987.
2. M. J. Collins, F. P. Gintz, D. R. Goddard, E. A. Hebdon, and G. J. Minkoff, "Nitryl Chloride. Part I Its Preparation and the Properties of its Solutions in Some Organic Solvents", J. Chem. Soc., (1958), 438.
3. Charles M. Bump, Preparation and Properties of Nitronium Tetrachloroaluminate, Final Report, 1988 USAF-UES Summer Faculty Research Program, 12 August 1988.
4. J. J. Delpuech in NMR of Newly Accessible Nuclei, Vol. 2, Chemically and Biochemically Important Elements, ed. Pierre Laszlo, Academic Press, New York, 1983, pp.153-195.
5. James J. P. Stewart, MOPAC Manual, 4th Edition, A General Molecular Orbital Package, USAF Systems Command, FJSRL-TR-87-0006, October 1987, ADA 188623.

1988
SUMMER RESEARCH OBJECTIVES
LISTON CYRUS

*call
M. Let thing*

I Sensitivity Factors (solutions about 0.1 M in CH₂Cl₂)
(solids may be less concentrated)

A Benzene series

benzene
chlorobenzene
m-xylene
bromobenzene
nitrobenzene
o-dichlorobenzene
m
p
o-chloronitrobenzene
m
p
o-dinitrobenzene

$$F_x = \frac{A_{\text{sample}}/W_{\text{sample}}}{A_{\text{std}}/W_{\text{std}}}$$

use { m-xylene as the standard
bromobenzene as a standard

B Toluene series

toluene
m-xylene
o-chlorotoluene
m
p
o-nitrotoluene
m
p

at least 6 six replicates

calculate standard and relative deviation

make up "unknowns" and analyze them

C Chlorobenzene series

chlorobenzene
m-xylene
bromobenzene
o-dichlorobenzene
m
p
o-chloronitrobenzene
m
p

all compds F_x already determined

~~scribble~~

D Acetophenone series

m-xylene
bromobenzene
acetophenone
o-nitroacetophenone
m
p

E Nitrobenzene series

m-xylene
bromobenzene
nitrobenzene *
o-chloronitrobenzene *
m
p
m-dinitrobenzene *

all cups for already determined

II Reaction Chemistry

A nitrations with acetyl nitrate (in acetic anhydride)

ref. M.A.Paul, J. Amer. Chem. Soc., (1958), 80, 5329
5332

-repeat on scale in literature

-use smaller scale and extract nitrated product with CH_2Cl_2
and analyze by gc

B nitration with acetyl nitrate (in acidic melt)

- ratio melt; nitrating agent:substrate

- competitive nitration benzene and toluene

1989 USAF-UES RESEARCH INITIATION PROGRAM

Sponsored by the

AIR FORCE OFFICE OF SCIENTIFIC RESEARCH

Conducted by the

Universal Energy Systems, Inc.

FINAL REPORT

CALCULATED C-NO₂ BOND DISSOCIATION ENERGIES (PART I)

and

**A MCSCE STUDY OF THE REARRANGEMENT OF
NITROMETHANE TO METHYL NITRITE (PART II)**

Prepared by:	Michael L. McKee
Academic Rank:	Associate Professor
Department and University:	Department of Chemistry Auburn University
Research Location:	Auburn University Auburn, Alabama 36849-5312
Date:	December 31, 1989
Contract No:	F49620-88-C-0053/SB5881-0378

Calculated C-NO₂ Bond Dissociation Energies Part I

Michael L. McKee, Ph.D.

ABSTRACT

The effect of substituents on C-NO₂ bond energies was explored with high level calculations. Geometries for the compounds NO₂-CXH₂; X=H, F, OH, NH₂, CH₃ and NO₂-CH=Y; Y=O, CH₂ were optimized with the 3-21G basis set. Bond energies, calculated with full MP4/6-31G* energies, were corrected to 298K by including scaled zero-point corrections and heat capacity corrections. In the series where X was varied, the bond dissociation energy (BDE) remained nearly constant (59.0-62.3 kcal/mol). In contrast, the NO₂-CH=O bond is much weaker (52.0 kcal/mol) and the NO₂-CH=CH₂ bond is much stronger (71.0 kcal/mol) compared to the C-NO₂ bond in the NO₂-CXH₂ series. Bond strengths were compared when H replaces NO₂. It was found that the constant C-NO₂ bond energy in the NO₂-CXH₂ series is due to two offsetting effects. Namely, substituents which increase the intrinsic bond energy (IBE) also increase the stability of the radical.

A MCSCF Study of the Rearrangement of Nitromethane to Methyl Nitrite Part II

Michael L. McKee, Ph.D.

ABSTRACT

An ab initio study has been made of the unimolecular rearrangement of nitromethane to methyl nitrite. Geometry optimizations employing the 6-31G* basis have been carried out for nitromethane and methyl nitrite with a two configuration wavefunction and for the unimolecular transition state with a 20-configuration wavefunction. Energies were determined by using a multiconfigurational expansion including all configurations generated by excitation from the two highest occupied orbitals into the two lowest empty orbitals (4-electrons in 4-orbitals). The transition state indicates a weak interaction between a methyl radical and nitro radical. In the transition state the breaking CN bond and the forming CO bond are 3.617 and 3.700Å respectively and there is a significant difference predicted in the NO bond lengths in the transition state (1.37/1.155Å). At the highest level of calculation used in this work (truncated Multireference CI) the unimolecular barrier is predicted to be 10.0 kcal/mol above the sum of CH₃ and NO₂ radical energies which is in conflict with experiment since the unimolecular rearrangement is observed to occur.

Acknowledgments

The Air Force Systems Command is acknowledged for sponsorship of this research and the Air Force of Scientific Research for the opportunity to carry out some of the research at their facilities. Financial support for the Summer Faculty Research Program Fellowship was administered through Universal Energy Systems.

The MCSCF program GAMESS was provided by Mark Gordon at North Dakota State University. Acknowledgment is also made to Dr. Mike Schmidt who provided assistance in running GAMESS. Calculations were carried out on the VAX cluster at the Frank J. Seiler Research Laboratory, on the CRAY2 at Kirkland Air Force Base, and on the CRAY XMP/24 at the Alabama supercomputer Center. I would also like to thank the donors of the Petroleum Research Fund, administered by the American Chemical Society, for financial support. Drs. R. P. Saxon and M. Yoshimine are thanked for providing a preprint of their work.

CALCULATED C-NO₂ BOND DISSOCIATION ENERGIES (PART I)

I. Introduction and Objectives

Bond dissociation energies (BDE) are useful quantities in interpreting chemical phenomena.[1,2] In many reactions the rate determining step is bond cleavage and in these reactions the bond dissociation energy is also the activation barrier. Pyrolysis of nitro-containing compounds often fall into this category where breaking a C-NO₂ or N-NO₂ bond is the initial step in thermal decomposition.[3] Recently, however, work has been reported which supports a concerted nitro-to-nitrite rearrangement in nitromethane[4] and nitrobenzenes[5-7] which is competitive with bond rupture. The purpose of the present work is to predict bond dissociation energies in a series of related nitro compounds. It is hoped that a comparison of these values with experimental activation barriers for thermal decomposition may indicate whether or not the rearrangement barrier is lower than the BDE. If the experimental activation energy is lower than the BDE, then it is clear that the reaction must be concerted.

The BDE is determined by the sum of two contributions; the intrinsic bond energy (IBE) and the electronic stabilization of the product radicals, E_S(I) and E_S(II) (eq 1).

$$\text{BDE} = \text{IBE} + \text{E}_S(\text{I}) + \text{E}_S(\text{II}) \quad (\text{eq 1})$$

When a bond breaks the radical fragments undergo geometric and electronic relaxations in such a way that the remaining bonds in the fragment become stronger or weaker. This reorganization, while difficult to precisely define, makes the breaking bond appear to be weaker or stronger.[1] The intrinsic bond energy (IBE) is defined as the bond energy in the absence of this effect. While there is no straightforward way to separate the two contributions in eq 1, a table of stabilization energies of free radicals has been developed.[1] In a series of related compounds substituents which strengthen a bond

(increase IBE) will often also stabilize the resulting radicals ($E_S(I) + E_S(II)$ become more negative). The two effects are often similar in magnitude and opposite in sign which means the BDE may remain nearly constant.

II. Method

All calculations have been calculated at the HF/3-21G level (Figure 1) and single-point calculations have been carried out at the full PMP4/6-31G* level where 'P' indicates that the larger spin contamination has been projected out[9] of the UMP correlation energies. Vibrational frequencies were calculated at the HF/3-21G level in order to determine the zero-point energies (frequencies scaled by 0.9) and heat capacities C_v (frequencies unscaled).[10] Bond dissociation energies were corrected to 298K by including a zero-point correction and heat capacity correction.[11]

A final correction requires some explanation. It is known that nitro-containing compounds have a multiconfigurational ground state where the second largest coefficient is about 0.2.[12-16] Since the Møller-Plesset correlation treatment requires a dominant configuration, it might be expected that the series would be slow to converge for nitro-containing molecules. A method which estimates the residual error at the MP4/6-31G** level due to incomplete convergence has been developed[17] and incorporated into the BACMP4 method.[18-26] The method is based on the fact that wavefunctions which need more than one configuration are usually unstable with respect to symmetry breaking (allowing different spatial orbitals for the a and b electrons).[27] Empirically, it is found[17] that an accurate coorection can be made by lowering the energy by 10 kcal/mol times the spin-squared value of the broken-symmetry solution. Since the correction is empirical, in the present work the 10 kcal/mol will be changed to 11.5 kcal/mol, which is the value which brings theory and experiment into agreement for the BDE in nitromethane.

III. Results and Discussion

Total energies are listed in Table I as well as scaled zero-point energies and heat capacities. Spin-squared values for the broken-symmetry solution and for radicals are also given in Table I as well as the energy lowering (kcal/mol) obtained from the unrestricted broken-symmetry solution. Calculated bond dissociation energies are given in Table II. Two values are given under each method. The first value refers to the electronic contribution while the second value includes zero-point and heat capacity corrections. The final estimate of the BDE refers to the corrected PMP4/6-31G* BDE's to which an empirical correction has been added for the incomplete convergence of the MP perturbation series. It is clear from Table II that electron correlation is necessary to obtain reliable results as shown by the nearly 20 kcal/mol increase in the BDE found when electron correlation is introduced at the PMP2 or PMP4 level.[28] The zero-point and heat capacity corrections reduce the BDE by about 4-5 kcal/mol while the S^2/BS (Spin-squared/Broken-Symmetry) correction increases the BDE by about 4-7 kcal/mol.

Of the calculated bond dissociation energies, only two are known experimentally; NO_2CH_3 (60.1 kcal/mol) and $\text{NO}_2\text{CH}_2\text{CH}_3$ (60.5 kcal/mol, Table II). While agreement with the BDE of NO_2CH_3 is exact since the S^2/BS correction was chosen to reproduce this value, theory and experiment both predict that the BDE of NO_2CH_3 is smaller than that of $\text{NO}_2\text{CH}_2\text{CH}_3$. A further comparison can be made with BDE's predicted from estimated heats of formation (last column, Table II). Leroy et al.[29] have used HF/6-31G energies to calculate reaction energies of carefully chosen isodesmic reactions and find a standard deviation of 3.6 kcal/mol between predicted and experimental heats of formation. While agreement with NO_2CH_3 , $\text{NO}_2\text{CH}_2\text{CH}_3$ and $\text{NO}_2\text{CH}_2\text{CH}_2\text{F}$ is quite good, deviations of 6.1 and 7.9 kcal/mol are found for $\text{NO}_2\text{CH}_2\text{OH}$ and $\text{NO}_2\text{CH}_2\text{NH}_2$, respectively.

Table III collects relevant experimental heats of formation for various compounds and

related radicals and the derived BDE values. By comparing the BDE for C-H and C-NO₂ it should be possible to partially isolate the intrinsic bond energy (IBE). If eq 1 is used to compare the differences in bond dissociation energies indicated in eq 2 as the definition of the stabilization energy of a substituent attached to a radical center. This requires that $\Delta\text{IBE}(\text{XH} - \text{CH}_4) = 0$ in eq 3 and leads to eq 4.



$$\Delta\text{BDE}(\text{XH} - \text{CH}_4) = \Delta\text{IBE}(\text{XH} - \text{CH}_4) + \Delta\text{E}_\text{S}(\text{X} - \text{CH}_3) \quad (\text{eq 3})$$

$$\Delta\text{BDE}(\text{XH} - \text{CH}_4) = \Delta\text{E}_\text{S}(\text{X} - \text{CH}_3) \quad (\text{eq 4})$$

Analogously, eq 5 and eq 6 will yield the BDE of C-NO₂ relative to CH₃NO₂ which will have a contribution from the relative stabilization of the radical ($\Delta\text{E}_\text{S}(\text{X} - \text{CH}_3)$) and from the intrinsic bond energy ($\Delta\text{IBE}(\text{XNO}_2 - \text{CH}_3\text{NO}_2)$).



$$\Delta\text{BDE}(\text{XNO}_2 - \text{CH}_3\text{NO}_2) = \Delta\text{IBE}(\text{XNO}_2 - \text{CH}_3\text{NO}_2) + \Delta\text{E}_\text{S}(\text{X} - \text{CH}_3) \quad (\text{eq 6})$$

Relative BDE's from eq 3 and eq 6 are presented in Table IV. Also included are recent high- level theoretical values for the relative C-H BDE's. The best calculations are single-point full MP4/6-31G* calculations at 6-31G* optimized geometries[32] which compare well with experimental relative C-H BDE's. It is apparent that the BDE is nearly constant in

NO₂-CXH₂; X=H, F, OH, NH₂, and CH₃ while the bond energy is substantially higher for Y equals CH₂ and lower for Y equals O in NO₂-CH=Y. A glance at the relative C-H BDE's (Table IV) reveals that the C-NO₂ BDE trend is not paralleled by the C-H BDE trend. This indicates that there must be a variation in the intrinsic bond energy contribution to the C-NO₂ BDE's. The last column in Table IV gives the results from eq 7 which is the difference in the C-NO₂ and C-H relative

$$\Delta BDE(XNO_2 - CH_3NO_2) - \Delta BDE(XH - CH_4) = \Delta IBE(XNO_2 - CH_3NO_2) \quad (\text{eq 7})$$

BDE's and is an estimate of the stabilizing effect (relative to CH₃NO₂) of the NO₂ group on the intrinsic bond energies. Since the calculated C-H relative BDE's have not been corrected to 298K and are not available for H-CH=O and H-CH=CH₂, the experimental values will be used in eq 7. Either choice of values led to the same relative ordering from eq 7 which represents an approximate partitioning of the BDE into an intrinsic bond energy part (IBE) and a radical stabilization part.

The stabilization is positive for all substituents which indicates that the substituents in Table IV have a stabilizing effect on the C-NO₂ IBE relative to CH₃. A tabulation of the absolute BDE and relative IBE is given in Table V in order of decreasing group electronegativity. While no general trend is apparent, there is a notable increase in the IBE as the electronegativity decreases in the order CH₂F, CH₂OH, and CH₂NH₂. It is known that the nitro group is particularly efficient in stabilizing negative charge. Since the group CH₂F would be expected to have the least negative (most positive) charge on carbon, that group would have a smallest stabilizing effect on the C-NO₂ bond energy which is what is observed.

The BDE for the C-NO₂ bond in NO₂-CH=O is predicted to be 19.0 kcal/mol smaller than the BDE for the same bond in NO₂-CH=CH₂ (52.0 and 71.0 kcal/mol, respectively). This is entirely due to a larger radical stabilization energy in HC=O as compared to H₂C=CH since the intrinsic bond energy of the C-NO₂ bond in NO₂CH=O is actually 3.0 kcal/mol larger than the C-NO₂ bond in NO₂-CH=CH₂ (Table IV).[33]

The fact that the radical stabilization in H₂C=CH₂ is 22.6 kcal/mol less than the radical stabilization in H₂C=O (Table IV) indicates that there is a significant mode of stabilization for the HC=O sigma radical compared to the H₂C=CH sigma radical. A simple explanation for the difference would be that the unpaired electron in the HC=O sigma radical can readily delocalize into the oxygen in-plane lone pair orbital while a similar delocalization is not possible in H₂C=CH.

IV. Conclusion

The BDE (bond dissociation energy) in nitro-containing compounds can be analyzed in terms of IBE (intrinsic bond energies) and radical stabilization energies by comparing the BDE of C-H and C-NO₂ in a series of related compounds. In the series NO₂-CXH₂; X=H, F, OH, NH₂ and CH₃ the bond dissociation is nearly constant (59-62 kcal/mol) due to a near cancellation of the increase of IBE (more positive) due to the substituent and an increase in the radical stabilization energy (more negative). The smaller BDE of NO₂-CH=O and the larger BDE of NO₂-CH=CH₂ can be traced to differences in radical stabilization.

V. References

- 1) R. T. Sanderson, Polar Covalence, Academic, New York 1983.
- 2) D. Griller and J. M. Kanabus-Kaminska, THEOCHEM **163** (1988) 125.
- 3) R. Guirguis, D. Hsu, D. Bogan and E. Oran, Combustion and Flame **61** (1985) 51.
- 4) A. M. Wodtke, E. J. Hintsa and Y. T. Lee, J. Phys. Chem. **90** (1986) 3549.5) A. C.

- Gonzalez, C. W. Larson, D. F. McMillen and D. M. Golden, J. Phys. Chem. **89** (1985) 4809.
- 6) W. Tsang, D. Robaugh and W. G. Mallard, J. Phys. Chem. **90** (1986) 5968.
 - 7) R. P. Saxon, J. Phys. Chem. **93** (1989) 3130.
 - 8) GAUSSIAN 86, M. J. Frisch, J. S. Binkley, H. B. Schlegel, K. Raghavachari, C. F. Melius, R. L. Martin, J. J. P. Stewart, F. M. Bobrowicz, C. M. Rohlfing, L. R. Kahn, D. J. Defrees, R. Seeger, R. A. Whiteside, D. J. Fox, E. M. Fleuder, and J. A. Pople, Carnegie-Mellon Quantum Chemistry Publishing Unit, Pittsburgh, PA 1984.
 - 9) C. Sosa and H. B. Schlegel, Int. J. Quantum Chem. **29** (1986) 1001. H. B. Schlegel, J. Chem. Phys. **84** (1986) 4530.
 - 10) For a description of basis sets and use of the 0.9 weighting factor for vibrational frequencies see: W. J. Hehre, L. Radom, P. v. R. Schleyer and J. A. Pople, Ab Initio Molecular Orbital Theory, Wiley, New York 1986.
 - 11) See: M. L. McKee, P. B. Shevlin and H. S. Rzepa, J. Am. Chem. Soc. **108** (1986) 5793.
 - 12) D. A. Kleier and M. A. Lipton, THEOCHEM **109** (1984) 39.
 - 13) D. S. Marynick, A. K. Ray, J. L. Fry and D. A. Kleier, THEOCHEM **108** (1984) 45.
 - 14) D. S. Marynick, A. K. Ray and J. L. Fry, Chem. Phys. Lett. **116** (1985) 429.
 - 15) C. Chabalowski, P. C. Hariharan and J. J. Kaufman, Int. J. Quantum Chem. **17** (1983) 643.
 - 16) M. L. McKee, J. Phys. Chem., **93** (1989) 7365.
 - 17) If PMP4/6-31G*/6-31G* energies and a set of corrections based on bond type are used, heats of formation for most organic compounds can be predicted to within an accuracy of 2-3 kcal/mol. Compounds which have a multiconfigurational ground state, such as singlet biradicals, are an exception. However, if an additional factor is included equal to a constant times the spin squared value of the broken-symmetry solution, similar accuracy for these compounds can also be achieved. A constant of 10 kcal/mol

was chosen in the BACMP4 method because this value gives a reasonable prediction of the heats of formation of ozone and singlet methylene. C. F. Melius Thermochemistry of Hydrocarbon Intermediates in Combustion: Application of the BACMP4 Method Ed. T. Just, Springer Verlag, DFVLR, Lecture Notes, in press.

- 18) C. F. Melius and J. S. Binkley, Symp. (Int.) Combust. [Proc.] 20th (1984) 575.
- 19) R. A. Perry and C. F. Melius, Symp. (Int.) Combust., [Proc.] 20th (1984) 639.
- 20) C. F. Melius and J. S. Binkley, ACS Symp. Ser. 249 (1984) 103.
- 21) C. F. Melius and J. S. Binkley, J. S. Symp. (Int.) Combust., [Proc.] 21st (1986) 1953.
- 22) P. Ho, M. E. Coltrin, J. S. Binkley and C. F. Melius, J. Phys. Chem. 89 (1985) 4647.
- 23) J. A. Miller, C. Parish and N. J. Brown, J. Phys. Chem. 90 (1986) 3339.
- 24) P. Ho, M. E. Coltrin, J. S. Binkley and C. F. Melius, J. Phys. Chem. 90 (1986) 3399.
- 25) F. P. Tully, A. T. Droege, M. L. Koszykowski and C. F. Melius, J. Phys. Chem. 90 (1986) 691.
- 26) P. Marshall, A. Fontijn and C. F. Melius, J. Chem. Phys. 86 (1987) 5540.
- 27) For a discussion and leading references, see: G. Chambaud, B. Levy and P. Millie, Theor. Chim. Acta 48 (1987) 103.
- 28) For a discussion of correlation effects on calculated BDE of hydrocarbons see: V. Kellö, M. Urban, J. Noga and G. H. F. Dierksen, J. Am. Chem. Soc. 106 (1984) 5864.
- 29) M. Sana, G. Leroy, D. Peeters and C. Wilante, THEOCHEM 164 (1988) 249. G. Leroy, M. Sana, C. Wilante and D. Peeters, THEOCHEM 187 (1989) 251.
- 30) M. J. S. Dewar, M. A. Fox and D. J. Nelson, J. Organomet. Chem. 185 (1980) 157.
- 31) D. J. Pasto, P. Kransnansky and C. Zercher, J. Org. Chem. 52 (1987) 3062.
- 32) M. B. Coolidge and W. T. Borden, J. Am. Chem. Soc. 110 (1988) 2298.
- 33) Determining the cause for a trend in bond dissociation energies is not always easy. Because the C-X BDE decreases in the order Me-X, Et-X, i-Pr-X, it was once felt that increasing alkylation stabilized the radical.[2] However, Rüchardt showed[34] that the

trend can rather be attributed to a decrease in the intrinsic bond energy due to increased steric repulsion as the alkyl group becomes larger.

34) C. Rüchardt, Angew. Chem. Int. Ed. Engl. **9** (1970) 830.

Table I. Absolute Energies (hartrees), Zero-Point Energies (kcal/mol); and Heat Capacities (cal/mol-K) for Various Species

	3-21G	6-31G*	PMP2/6-31G*	PMP4/6-31G*	ZPE(NIF) ^a	C _v	HF->UHF ^b	<S ² > ^c
NO ₂ CH ₃	-242.25586	-243.65377	-244.33159	-244.37381	32.58(0)	12.4	6.1	0.52
NO ₂ CH ₂ F	-340.56248	-342.49454	-343.34058	-343.38612	28.19(0)	14.0	6.1	0.38
NO ₂ CH ₂ OH	-316.69123	-318.50293	-319.35803	-319.40648	35.60(1)	13.9	4.7	0.48
NO ₂ CH ₂ NH ₂	-296.98190	-298.68211	-299.52143	-299.57485	44.51(0)	16.9	4.4	0.47
NO ₂ CH ₂ CH ₃	-281.08165	-282.69265	-283.50159	-283.55989	52.02(0)	16.8	5.4	0.50
NO ₂ CH=O	-315.50623	-317.32592	-318.17741	-318.22191	20.00(0)	13.5	12.0	0.65
NO ₂ CH=CH ₂	-279.88906	-281.49563	-282.29176	-282.34599	36.36(0)	14.6	6.8	0.59
NO ₂	-202.84346	-204.02539	-204.56317	-204.58862	4.69(0)	7.0		0.77
CH ₃	-39.34261	-39.55899	-39.67060	-39.69032	19.47(0)	7.5		0.76
CH ₂ F	-137.65264	-138.40063	-138.68051	-138.70312	16.52(0)	7.2		0.76
CH ₂ OH	-113.77257	-114.40513	-114.69596	-114.72142	23.40(0)	8.2		0.76
CH ₂ NH ₂	-94.06305	-94.58469	-94.86048	-94.89077	33.02(0)	10.0		0.76
CH ₂ CH ₃	-78.16365	-78.59706	-78.83728	-78.87312	39.66(0)	10.7		0.76
CH=O	-122.60380	-113.24645	-113.53421	-113.55569	8.79(0)	6.2		0.76
CH=CH ₂	-76.96280	-77.39028	-77.61458	-77.64704	24.30(0)	7.8		1.02

a) Scaled zero-point energy and number of imaginary frequencies in parentheses.

b) Energy-lowering (kcal/mol) from broken-symmetry solution.

c) Spin-squared value of radical or broken-symmetry solution at the UHF/6-31G* level.

Table II. Bond Dissociation Energies (at 298K) of NO₂-CXH₂; X=H, F, OH, NH₂, CH₃, and NO₂-CH=Y; Y=O, CH₂

	6-31G*		PMP2/6-31G*		PMP4/6-31G*		S ² /BSC ^a	est BDE	exptl ^c	estim ^d
	elect	corr	elect	corr	elect	corr				
NO ₂ CH ₃	43.5	38.1	61.4	56.0	59.5	54.1	6.0	60.1	60.1	59.5
NO ₂ CH ₂ F	43.0	38.4	60.7	56.1	59.2	54.6	4.4	59.0		59.9
NO ₂ CH ₂ OH	45.4	40.7	62.0	57.3	60.5	55.8	5.5	61.3		55.2
NO ₂ CH ₂ NH ₂	45.2	40.8	61.4	57.0	59.9	55.5	5.4	60.9		53.0
NO ₂ CH ₂ CH ₃	44.0	38.9	63.5	58.4	61.6	56.5	5.8	62.3	60.5	62.6
NO ₂ CH=O	33.9	29.7	50.2	46.0	48.7	44.5	7.5	52.0		
NO ₂ CH=CH ₂	50.2	45.2	71.5	66.5	69.2	64.2	6.8	71.0		

a) Correction based on the spin-squared value of the broken-symmetry solution (factor = 11.5 X <S²>).

b) Corrected PMP4/6-31G* bond dissociation energies plus a correction (S²/BS) based on the spin-squared value of the broken symmetry solution of a nitro-containing compound.

c) See Table III.

d) The BDE is based on a theoretical estimate of the heat of formation of the nitro-containing compound. Reference 29.

Table III. Experimental Heats of Formation (kcal/mol) and C-H and C-NO₂ Bond Energies (kcal/mol)

X	$\Delta H_f^{a,b}$	H-X	ΔH_f^c	NO ₂ -X	ΔH_f^c	C-H BDE	C-NO ₂ BDE
CH ₃	34.4 ^d	CH ₄	-17.8	NO ₂ CH ₃	-17.8	104.3	60.1
CH ₂ F	-7.6	CH ₃ F	-56.0 ^e	NO ₂ CH ₂ F	[-59.6]	100.5	[59.9] ^f
CH ₂ OH	-6.2	CH ₃ CH	-48.2	NO ₂ CH ₂ O	[-53.5] ^f	94.1	[55.2] ^f
CH ₂ NH ₂	27.8 ^d	CH ₃ NH ₂	-5.5	NO ₂ CH ₂ NH ₂	[-17.3] ^f	85.4	[53.0] ^f
CH ₂ CH ₃	28.2	CH ₃ CH ₃	-20.0	NO ₂ CH ₂ CH ₃	-24.4	100.3	60.5
H=CO	8.9	H ₂ C=O	-26.0 ^e	NO ₂ CH=O		87.0	
HC=CH ₂	70.0	H ₂ C=CH ₂	12.5 ^e	NO ₂ CH=CH		109.6	

a) Unless otherwise indicated experimental values are from A. J. Colussi, Chemical Kinetics of Small Organic Radicals, ed.

Z. B. Alfassi, CRC Boca Raton, Florida 1988, p. 25.

b) ΔH_f of H and NO₂ are 52.1 and 7.9 kcal/mol, respectively.

c) Unless otherwise indicated experimental values are from J. B. Pedley, R. D. Naylor and S. P. Kirby, Thermochemical Data of Organic Compounds, 2nd Ed., Chapman, New York 1986.

d) J. L. Holmes, F. P. Lossing and A. Maccoll, J. Am. Chem. Soc. **110** (1988) 7339.

e) S. W. Benson, Thermochemical Kinetics, 2nd Ed. Wiley, New York 1976.

f) Estimated from ab initio energies; reference 29.

Table IV. Tabulated C-H and C-NC₂ BDE (kcal/mol) Derived from eq 2 and 5

	Relative C-H BDE from eq 2				Relative C-NO ₂ BDE from eq 5 ^a			
	ROHF/ 6-31G ^b	MP2/ 6-31G ^{*c}	MP4/ 6-31G ^{*d}	HF/ 6-31G ^{*e}	PMP2/ 6-31G ^{*f}	PMP4/ 6-31G ^{*f}	estim ^f	Δ IBE ^g (eq 7)
CH ₃	0.0	0.0	0.0	0.0	0.0	0.0	0.0	0.0
CH ₂ F	-1.8	-4.7	-4.4	-3.8	0.1	0.5	-1.1	2.7
CH ₂ OH	-5.8	-8.9	-8.6	-10.2	1.3	1.7	1.2	11.4
CH ₂ NH ₂	-10.3	-11.4	-12.2	-18.9	1.0	1.4	0.8	19.7
CH ₂ CH ₃	-2.5	-3.3	-4.0	0.8	2.4	2.4	2.2	6.2
CH=O	-17.3		-17.3	-8.4	-10.2	-9.6	-8.7	8.6
C ⁺ =CH ₂	5.3		5.3	7.1	10.5	10.1	10.9	5.6

^a) Relative BDE's are obtained from energies at the indicated level and include zero-point and heat capacity (298K) corrections.

Geometries are optimized at the HF/3-21G level.

b) D. J. Pasto, *J. Am. Chem. Soc.* **110** (1988) 8164.

c) See: P. v. R. Schleyer, *Pure Appl. Chem.* **59** (1987) 1647.

d) Reference 32.

e) From Table III.

f) Includes S²/BS correction, see text.

g) The relative intrinsic bond energy is determined by subtracting the radical stabilization energy (value under column marked 'exptl') from the relative BDE (value under column marked 'estim').

Table V. Comparison of Group Electronegativities and Experimental and Theoretical C-NO₂ BDE (kcal/mol)

X (X-NO ₂)	Group Electronegativity ^a		BDE		ΔBDE
	χ	exptl	theory		
CH=O	2.87		52.0		8.6
CH=CH ₂	2.78		71.0		5.6
CH ₂ F	2.64		59.9		2.7
CH ₂ OH	2.59		61.3		11.4
CH ₂ NH ₂	2.54		60.9		19.7
CH ₂ CH ₃	2.48	60.5	62.3		6.2
CH ₃	2.18	60.1	60.1		0.0

a) N. Inamoto and S. Masuda, *Chemistry Letters* (1982) 1003.

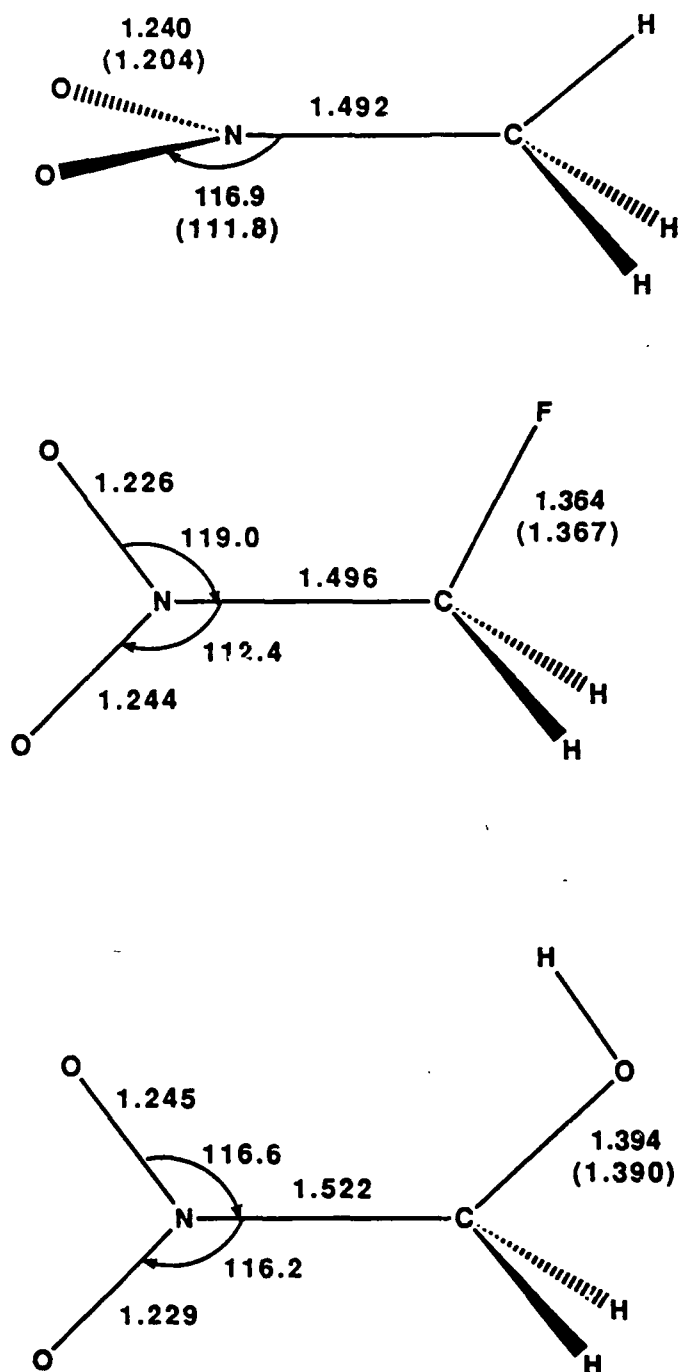


Figure 1. Selected geometric parameters for nitro-containing compounds optimized at the HF/3-21G level of theory. Values in parentheses are the corresponding calculated values in the free radical.

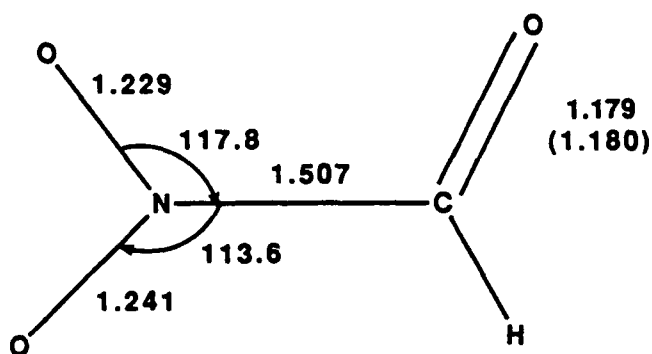
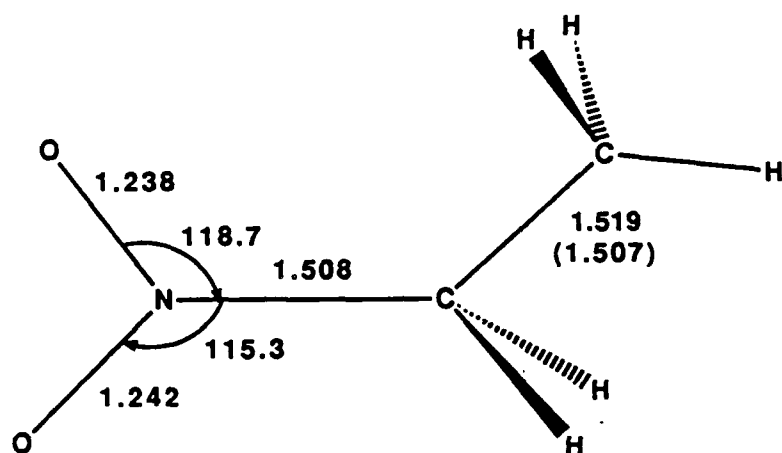
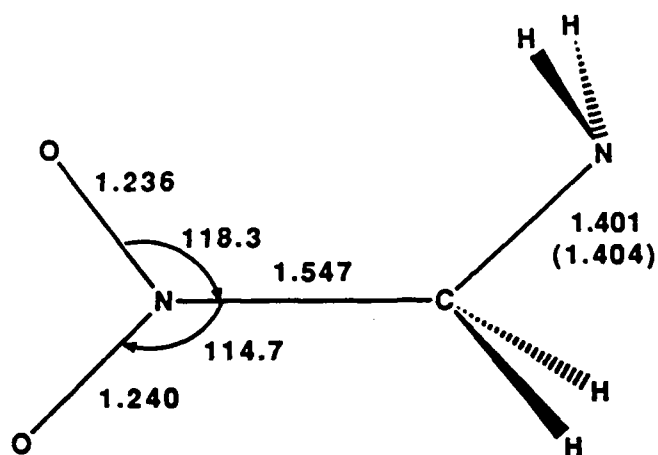


Figure 1. Continued.

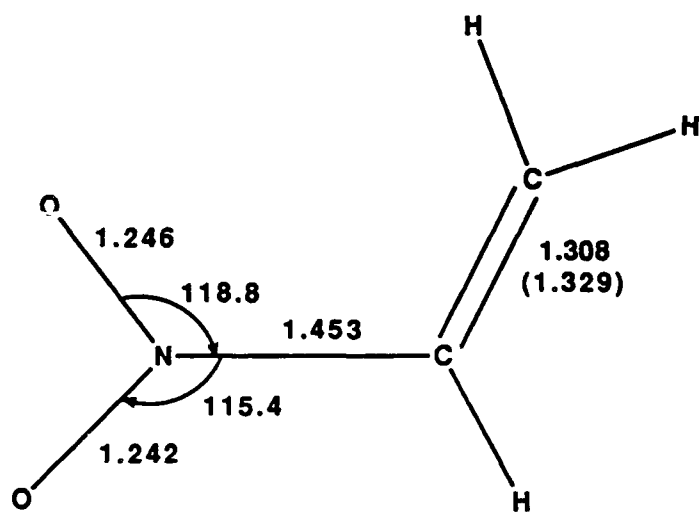


Figure 1. Continued.

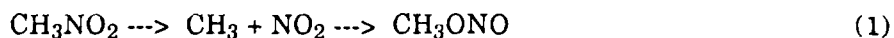
A MCSCF STUDY OF THE REARRANGEMENT OF NITROMETHANE TO METHYL NITRITE (PART II)

VI. Introduction

It has recently been predicted[1] and verified[2,3] that the unimolecular rearrangement of nitromethane to methyl nitrite might be competitive with simple C-N bond rupture. The predictions were based on MINDO/3 calculations performed by Dewar and coworkers,[1] who found the concerted transition state to have an energy 14.6 kcal/mol lower than the energy of radicals. When a less favorable entropy for the rearrangement is taken into account, Dewar concluded that the two pathways would be competitive. Recent experimental work[3] has led to a confirmation of these predictions. Employing infrared multiple-photon dissociation (IRMPD), Lee and coworkers[3] have been able to determine the barrier to be between 51.5 to 57.0 kcal/mol with 55.5 kcal/mol as the most probable value. For comparison the C-N bond energy in nitromethane is determined to be 59.4 kcal/mol.[4]

The experimental results above contrast sharply with previous ab initio results[5] where the unimolecular rearrangement barrier to CH_3ONO was found to be 16.1 kcal/mol higher than the C-N bond energy in CH_3NO_2 (75 and 57.4 kcal/mol, respectively). The calculations were performed using the 6-31G* basis[6] to determine geometries and zero-point corrections and the MP2/6-31G* electron correlation treatment[6] on 6-31G* optimized geometries to determine relative energies. It was anticipated that the method would poorly describe the unimolecular transition state since it was based on a single-determinant wavefunction while the transition state is expected to have considerable open shell character. In order to avoid an unfavorable 4-electron 2-orbital interaction, the C-N bond would be expected to be nearly completely broken before the C-O bond begins to form. If the C-N bond is completely broken before the C-O bond begins to form, the pathway is best

described as eq 1. If the bond rupture is not complete, eq 2 better describes the process.



A careful determination of the transition state is essential for a discrimination of the two possible pathways. The wavefunctions used to determine the geometry must be able to adequately describe the $^2\text{A}_1$ states of CH_3 (C_{3v} Symmetry) and NO_2 , respectively and to describe the bond being broken in CH_3NO_2 and being formed in CH_3ONO .

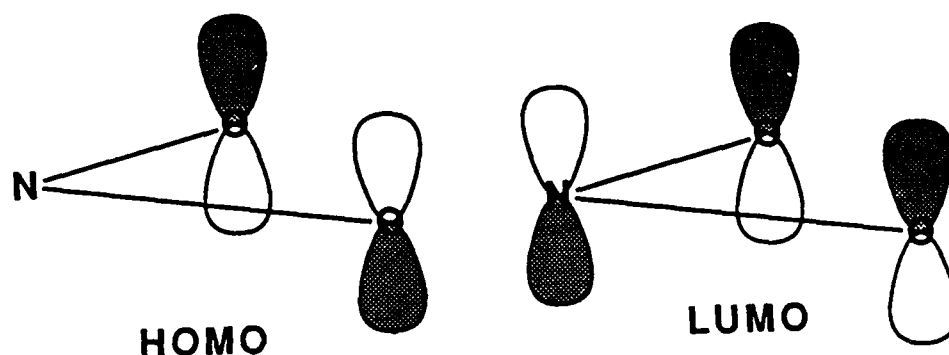
In a recent MCSCF study on the nitro-nitrite rearrangement of the isoelectronic NH_2NO_2 , Saxon and Yoshimine[7] have found that the transition state is best described as an interaction of an NO_2 and an NH_2 radical. Geometries were optimized with the 4-31G basis and a CAS (Complete Active Space) MCSCF with 10-electrons in 7-orbitals. The breaking NN bond and forming NO bond in the transition state were 2.84 and 3.21Å, respectively, and the energy (MRCI/6-31G*) was 0.9 kcal/mol lower than radicals.

The calculations used in the present study are based on a multiconfiguration treatments[8] which allows the optimal linear combination of different configurations where the term configuration refers to a particular occupation of molecular orbitals. In contrast to a single-configuration method, the multiconfiguration method can correctly describe forbidden reactions where an orbital crossing occurs, as well as homolytic bond cleavages where the wavefunction must describe the radical products.

VII. Approach

The simplest example of a nitro-nitrite rearrangement is the $\text{HNO}_2 \rightarrow \text{HONO}$ rearrangement; however, a system more relevant to the study of combustion is the nitro to nitrite rearrangement in nitromethane. It has been found[9] that an accurate description of the wavefunction of a molecule containing a nitro group requires at least two configurations. In a single-configuration calculation the orbital on the left (see below) is

the highest occupied orbital (HOMO) and the orbital on the right (LUMO) is unoccupied. In a two-configuration calculation the "LUMO" has significant occupation.



In the region of the transition state the wavefunction can be described as two interacting radicals. The important orbitals to correlate are the bonding and antibonding combination of the CN sigma bond and the two combinations of the oxygen lone pair (see above). As the transition state for rearrangement is approached and the CN bond elongates, the CN bonding and antibonding orbitals can each accommodate one of the unpaired electrons of CH_3 and NO_2 . The two combinations of the oxygen lone pair are included to correctly describe the nitro portion of the transition state. If all excitations are allowed from the two highest occupied orbitals into the two lowest unoccupied orbitals, the resulting multiconfigurational wavefunction is referred to as a 4x4CAS-MCSCF (4-electrons in 4-orbitals Complete Active Space-MCSCF). For the transition state which has C_1 symmetry the 4x4CAS wavefunction consists of 20 configurations.

Exploratory calculations were carried out at the MCSCF/STO2G level in order to determine reasonable starting geometries for higher levels of theory. Geometries and energies are compared in Figure 1 and Tables I and II where the conformation chosen for geometry optimization was the lowest energy conformation at the MP2/6-31G*//6-31G* level.[5] A 2x2CAS was used to determine the geometry and energy of NO₂, CH₃NO₂, and CH₃ONO, while a 4x4CAS was used for the transition state. The CN bond energy of CH₃NO₂ is overestimated by 19 kcal/mol at the 2x2CAS/STO2G level (exptl.[10] 59.4 kcal/mol; 2x2CAS/STO2G, 78.2 kcal/mol) which indicates that the calculations at this level of theory are not reliable. It should be expected that the restricted active space and modest basis set cannot provide accurate energies, however, it is interesting that the transition state for the nitro-nitrite rearrangement is predicted to be 9.6 kcal/mol lower than the energy of NO₂ and CH₃ radicals (Table II). This result is in agreement with MINDO/3 results where a difference of 14.6 kcal/mol is obtained. The transition state is characterized by a long CO and CN bond and a significant NO bond alternation in the NO₂ fragment.

The next step was full optimization at the 4x4CAS/6-31G* level for the transition state and at the 2x2CAS/6-31G* level for NO₂, CH₃NO₂ and CH₃ONO. The results of these calculations are given in Figure 2. Total energies are given in Table I and relative energies are given in Table II. Single point calculations at the 4x4CAS/6-31G* level were made on the 2x2CAS/6-31G* optimized geometries for CH₃NO₂ and CH₃ONO. Optimization at the 4x4CAS/6-31G* level was not necessary because the CN or CO bonds are well described by a doubly occupied orbital in the reactant or product, and correlating this orbital with the antibonding orbital would have little effect on the geometry.

All optimizations were straightforward except the location of the transition state. Due to the very loose nature of the transition state, a precise stationary point could not be located in

50 cycles of optimization. The stopping criterion requires that the largest component of the gradient be less than 5×10^{-4} hartrees/bohr (or hartrees/radian) and the root mean square (rms) gradient be less than 1.7×10^{-4} . After about 20 cycles of optimization there was little change in geometry or energy. Since the optimization seemed to be "stalled" around the transition state, the point with the lowest rms gradient was used as the converged structure. This geometry was characterized by a rms gradient about four times larger than the normal stopping criterion.

A comparison of optimized geometries at the HF/6-31G* and MCSCF/6-31G* levels indicated that the additional configuration(s) resulted in only small geometry changes for all structures except the transition state. The largest change in the CH_3NO_2 geometry when comparing the HF/6-31G* (1 configuration) and the 2x2CAS/6-31G* geometries (2 configurations) is a lengthening of the NO bond by 0.013Å. This is to be expected since the additional configuration contains two electrons in a NO antibonding orbital which is unoccupied in the SCF wavefunction. The ONO bond angle decreases by 0.9° due to the bonding interaction between oxygens in the additional configuration (see "LUMO" of NO_2 above). The coefficient of the second configuration has a value of 0.25 indicating a significant contribution. The MCSCF/6-31G* wavefunction of methyl nitrite was also characterized by a significant second coefficient (0.21) and the geometry changes between the HF/6-31G* and MCSCF/6-31G* levels are comparable to those for CH_3NO_2 (Figure 2). Inclusion of an additional configuration in the optimization of the NO_2 radical had a smaller effect. Compared to the HF/6-31G* optimized geometry a 2x2CAS/6-31G* wavefunction leads to an increase of the NO bond length by only 0.005Å and no change in the ONO bond angle.

A comparison of geometric parameters calculated for the transition state at different levels of theory is given in Table III. At the 4x4CAS/STO2G and 4x4CAS/6-31G* levels the

transition state[11] is characterized by extremely long CO and CN bond distances, in contrast to single-configuration methods (MINDO/3, 6-31G*) where the transition state is much tighter. This distinction becomes important in the context of the experimental activation barrier determined by Lee and coworkers.[3] In this work the A factor calculated by Dewar et al.[1] for the tight transition state ($10^{13.3}$) was used in fitting the data to determine an activation barrier. The transition state calculated by MCSCF methods is much looser and the associated A factor probably would be closer to the experimental A factor for simple CN bond rupture ($10^{15.6}$).[3] If the assumed A factor is too small, then the calculated activation barrier would be underestimated.

If the CN is decreased, or if the CO distance is decreased in the transition state, CH_3NO_2 or CH_3ONO should be formed, respectively. However, if both distances are decreased, the energy should increase due to increased repulsion from the 4-electron 2-orbital interaction. In order to see how sensitive the energy was to this geometry change, one calculation at the 4x4CAS/6-31G* level was made after moving the CH_3 group 1A closer to the NO midpoint. This geometry led to an energy increase of 7.8 kcal/mol relative to the transition state.

VIII. Results and Discussion

There are several qualitative interpretations of the rearrangement mechanism. In an approximate sense the reaction is orbitally forbidden as shown in Figure 3. The sigma CN bonding orbital correlates with a sigma CO antibonding orbital while the sigma CN antibonding orbital correlates with a sigma CO bonding orbital (Figure 3). However, since both orbitals have the same symmetry in the transition state (C_1) the crossing will be avoided. Nevertheless, the barrier would be expected to be high. As the transition state is approached the energy difference between the bonding and antibonding CN orbitals becomes smaller. At the transition state three configurations become important in the

MCSCF expansion. The configuration with one electron in the σ_{CN}^* orbital and one electron in the σ_{CN} orbital (the labels are not an accurate description in the transition state, however, they are convenient labels in the present context) makes the largest contribution to the wavefunction (61%) which suggests that the transition state is best described as interacting radical fragments. Two other configurations, one with the σ_{CN}^* orbital doubly occupied, contribute a total of 29% while the remaining 17 configurations contribute 10%.

The radicals NO_2 and CH_3 have very similar ionization potentials (9.6eV and 9.8eV, respectively[12]) which perhaps explains why these three configurations contribute strongly in the transition state since the orbital energies would be nearly the same.

A more intuitive interpretation can be obtained by a simple consideration of resonance structures (Figure 4). As the transition state is approached and the fragments become "radical-like", the first and third resonance structures of NO_2 become more important than the second and fourth due to the fact that the latter two resonance structures indicate an alternation of single and double NO bonds opposite to that found in the product. Further, the first resonance structure will be more important at the transition state than the third due to the greater unpaired electron density on oxygen which ultimately becomes the C-O bond in methyl nitrite. Evidence for this interpretation comes from the transition state geometry. First, there is a large alternation of NO bonds (1.371/1.155Å, 4x4CAS/6-31G*) clearly indicating a localized single and double bond. Secondly, the ONO angle is reduced from 124.9° in CH_3NO_2 to 113.0° in the transition state which is due to the increased steric repulsion of the nitrogen lone pair.

The methyl ($^2\text{A}''$ state) and the nitro radical ($^2\text{A}_1$ state) are ideally suited for combining to form a CN sigma bond in CH_3NO_2 since the unpaired electrons are directed along the

bond axis. This is not the case for formation of CH_3ONO where the NO_2 radical requires promotion to a more suitable electronic distribution (i.e. $\cdot\text{NO}_2 \rightarrow \cdot\text{ONO}$). A promoted NO_2 radical will have more unpaired electron density on one oxygen in an orbital perpendicular to the NO_2 plane. This effect can be seen easily in the contributing configuration of the promoted NO_2 fragment depicted in Figure 5 which has three unpaired electrons and a coefficient of 0.59 (35% contribution to the wavefunction). One electron is in the nitrogen lone pair orbital while the two combinations of the oxygen lone pair orbitals have one electron each. To form a sigma CO bond the CH_3 radical would then approach the prepared NO_2 radical form above which is exactly what is observed in the transition state geometry.

The rearrangement barrier can be related to two factors. First, the energy required to promote the NO_2 fragment and second, the interaction energy of the two radicals. If the interaction energy is greater than the promotion energy, then the rearrangement barrier will be less than the CN bond energy. On the other hand, if the promotion energy is greater, the barrier will be greater than the CN bond energy. The promotion energy was determined as the energy difference between the optimized NO_2 radical and the NO_2 fragment in the transition state (Table IV). At the 3x4CAS/6-31G* level this value is 25.4 kcal/mol and increases to 46.4 kcal/mol at the PMP4/6-31G* level. For the CH_3 fragment the promotion energy is very small at both the CAS/6-31G* and PMP4/6-31G* levels (0.02 and 0.1 kcal/mol, respectively). The second factor, the interaction energy, was determined as the energy difference between the isolated frozen fragments, CH_3 and NO_2 , and the transition state. This value is -17.7 kcal/mol at the 4x4CAS/6-31G* level, which leads to an activation barrier 7.7 (25.4-17.7) kcal/mol higher than radicals.

Activation barriers calculated at the MP4/6-31G* level generally yield accurate results when the transition state is characterized by a single configuration.[6] This is definitely

not the case for the nitro to nitrite transition state. While the PMP4/6-31G* relative energies are in good agreement with experiment (Table II), the activation barrier is calculated to be 51.9 kcal/mol higher than the CH₃ and NO₂ radicals! A similar discrepancy is found in the promotion energy of NO₂ where the PMP4/6-31G* method predicts the promotion energy to be 21.0 kcal/mol greater than the 3x4CAS/6-31G* method.

To explore the effects of additional electron correlation, truncated multireference second order CI calculations (with the 6-31G* basis) were carried out on the CAS/6-31G* geometries for fragments and the transition state. Orbitals were divided into four spaces: frozen occupied (11 orbitals), active (5 doubly occupied and 2 unoccupied), external (10 orbitals), and frozen virtual (38 orbitals). The configuration list was generated by including all excitations within the active space and single and double excitations into the external space. The virtual space of the starting wavefunction was first compacted by calculating a second order CI with a smaller active space but including all virtual orbitals in the external space (14 frozen, 4 active, and 48 external orbitals). The CH₃ and NO₂ radicals were calculated together (C_s symmetry separated by 20.0Å) since the multireference CI is not size consistent. The CI expansion for the combined fragments contained approximately 29,300 configurations while the CI expansion for the transition state (C₁ symmetry) contained 58,500 configurations.

At the 4x4CAS/6-31G* level the stability of CH₃ONO is overestimated with respect to CH₃NO₂. While the difference is reduced at the MRCI/6-31G* level, methyl nitrite is still predicted to be too stable. One possible source of this discrepancy is the limited number of orbitals included in the CAS. The 4-electrons in 4-orbitals CAS used in the optimization of the transition state correlates the σ_{CN} and σ_{CN^*} orbitals as well as the two combinations of the oxygen lone pairs orbitals. In the reactant and product some care must be exercised to insure that the corresponding orbitals are chosen for the CAS since the bonding and

antibonding combinations will be greatly stabilized and destabilized, respectively. This can only partially be done since the mixing of orbitals in the CAS will be much different in the reactant, transition state, and product. While a larger CAS insures that more orbitals will be treated uniformly, computational costs increase substantially.

IX. Conclusion

It should be pointed out that the relative energy for fragments and transition state at the MRCI/6-31G* level of theory is very similar to the 4x4CAS/6-31G* results (7.7 kcal/mol 4x4CAS/6-31G*; 10.0 kcal/mol MRCI/6-31G*; Table II). The ab initio methods used in this work predict an activation barrier for rearrangement which is higher than the energy of CH₃ and NO₂ radicals while the experimental work of Lee and coworkers[2,3] suggest that it is lower. A lower computed rearrangement barrier would result if the promotion energy were overestimated or if the interaction energy were underestimated. On the other hand, a higher experimental barrier would result if a more reasonable A factor for the transition state were used (see above). It is probable that this level of theory correctly describes the qualitative features of the rearrangement mechanism; however, quantitative determination of the barrier will require more accurate computational methods (i. e. larger active space, bigger basis sets and more CI).

X. References

1. M. J. S. Dewar, J. P. Ritchie and J. Alster J. Org. Chem. 1985, **50**, 1031.
2. A. M. Wodtke, E. J. Hintsa and Y. T. Lee J. Chem. Phys. 1986, **84**, 1044.
3. A. M. Wodtke and Y. T. Lee J. Phys. Chem. 1986, **90**, 3549.
4. S. W. Benson and H. E. O'Neal Kinetic Data on Gas Phase Unimolecular Reactions; Natl. Stand. Ref. Data Ser., National Bureau of Standards: Washington, DC, 1970.
5. M. L. McKee J. Am. Chem. Soc. **108** (1986) 5784.

6. W. J. Hehre, L. Radom, P. v. R. Schleyer and J. A. Pople Ab Initio Molecular Orbital Theory, Wiley, New York: 1986.
7. R. P. Saxon and M. Yoshimine J. Phys. Chem. **93** (1989) 3130.
8. The GAMESS program has been used for all calculations. M. Dupuis, D. Sprangler, J. J. Wendolski GAMESS, QGO1, Program Library of Institute for Molecular Science. The version we used had been heavily modified by M. Schmidt at North Dakota State and S. T. Elbert at Iowa State. We thank Dr. M. Schmidt and Prof. M. Gordon for providing us with this program.
9. D. S. Marynick, A. K. Ray, J. L. Fry and D. A. Kleier J. Mol. Struct. **108** (1984) 45.
10. S. W. Benson and H. E. O'Neal Kinetic Data on Gas Phase Unimolecular Reactions; Natl. Stand. Ref. Data Ser., National Bureau of Standards, Washington, DC, 1970.
11. The vibrational frequencies of the transition state were calculated at the 4x4CAS/STO2G level by using finite differences of analytical first derivatives. Besides the expected transition vector, a second eigenvector with a negative eigenvalue was obtained which corresponded to a CH₃ tilt with respect to NO₂. Despite repeated attempts a lower energy stationary point could not be found.
12. R. D. Levin and S. G. Lias Ionization Potentials and Appearance Potential Measurements, 1971-1981, NSRDS-NBS 71, issued October 1982.

Table I. Total Energies (hartrees) and Zero-Point Energies (kcal/mol) at Various Levels of Theory^a

Method	CH ₃ NO ₂	CH ₃ ONO	CH ₃	NO ₂	TS
6-31G**/6-31G*	-243.66199	-243.66864	-39.55899	-204.03149	-243.53194
MP2/6-31G**/6-31G* ^b	-244.33794	-244.33148	-39.67296	-204.55965	-244.21624
CAS/STO2G//CAS/STO2G	-233.39136	-233.38223	-37.93407	-195.33278	-233.28209
PMP4/6-31G**//CAS/6-31G* ^c	-244.36869	-244.36447	-39.69002	-204.57924	-244.18662
CAS/6-31G**//CAS/6-31G*	-243.71525	-243.75134	-39.55476	-204.05339	-243.59673 ^d
MRCI/6-31G**//CAS/6-31G*	-243.76834	-243.78775	-243.65320	-243.63729	
ZPE/6-31G* ^e	30.82	30.32	17.49	5.56	25.05
exptl. ZPE	30.23 ^f		16.17 ^g	5.40 ^g	

- a) Level of CAS optimization is 2x2CAS except for the transition state which was optimized at the 4x4CAS level.
- b) All orbitals are correlated and spin contaminations not projected out. Reference 5.
- c) The frozen core approximation is used and the energy lowering due to projecting out spin contamination at the MP3 level is used to correct the MP4 energies.
- d) If the CH₃ group is moved 1A closer to the NO midpoint, the energy increases 7.8 kcal/mol.
- e) The calculated zero point energy is multiplied by a factor of 0.9.
- f) See M. L. McKee, *J. Am. Chem. Soc.* **107** (1985) 1900.
- g) M. W. Chase, Jr., C. A. Davies, J. R. Downey, Jr., D. J. Frurip, R. A. McDonald and A. N. Syverud *J. Phys. Chem. Ref. Data*, 1985, Vol. 14, Supplement 1 JANAF Thermochemical Tables, 3rd Ed.

Table II. Relative Energies (kcal/mol) of Species on the CH_3NO_2 Potential Energy Surface

Method	CH_3NO_2	CH_3ONO	$\text{CH}_3 + \text{NO}_2$	TS
MINDO/3 ^a	0.0	4.1	76.7(59.5) ^b	44.9
6-31G**/6-31G*	0.0	-3.4	44.9	81.6
MP2/6-31G**/6-31G*	0.0	4.0	66.1	76.4
CAS/STO2G//CAS/STO2G	0.0	5.7	78.2	68.6
PMP4/6-31G**//CAS/6-31G*	0.0	2.6	62.4	114.3
PMP4/6-31G**//CAS/6-31G*+ZPC ^c	0.0	2.1	54.6	106.5
CAS/6-31G**//CAS/6-31G*	0.0	-22.6	67.2	74.4
CAS/6-31G**//CAS/6-31G*+ZPC ^c	0.0	-23.1	61.4	68.6
MRCI/6-31G**//CAS/6-31G*	0.0	-12.7	72.3	82.3
exptl ^d	0.0	2.3	59.4 ^{e5}	55.5 ^{f,g}

a) Reference 1.

b) The value in parentheses refers to the relative energy when the experimental heat of formation is used for NO_2 rather than the MINDO/3 calculated value.

c) A zero point correction is included. The zero point correction for the transition state is assumed to be the sum of the zero point corrections for CH_3 and NO_2 .

d) See reference 5.

e) Reference 4.

f) Reference 3.

g) This value may be too low due to an underestimation of the A factor for the nitro to nitrite rearrangement (see text).

Table III. Comparison of Geometric Parameters (Angstroms, Degrees) for the Nitro to Nitrite Transition State

Parameter ^a	MINDO/3 ^b	6-31G*	CAS/STO2G	CAS/6-31G*
CN	1.516	1.928	3.625	3.616
CO	1.584	2.01	3.538	3.700
NO ₁	1.299	1.251	1.471	1.371
NO ₂	1.438	1.181	1.222	1.155
ONO			110.0	113.0

a) In the transition state the CH₃ group is migrating to O₁.

b) Reference 1.

Table IV. Calculated Promotion Energy (kcal/mol) and Interaction Energy

Method	NO ₂ Promotion	CH ₃ Promotion	NO ₂ /CH ₃ Interaction
CAS/6-31G**a	25.4	0.02	-17.7
PMP4/6-31G*	46.4	0.1	

a) The dominant configuration in the MCSCF expansion contributes only 64% to the wavefunction for the frozen NO₂ fragment.

In contrast the dominant configuration contributes 95% for the optimized NO₂ radical. The second configuration for the frozen NO₂ fragment (34%) is characterized by three unpaired electrons coupled as a doublet (²A' state) where an electron from the oxygen lone pair (a" symmetry) has been promoted into a higher oxygen lone pair orbital (a" symmetry).

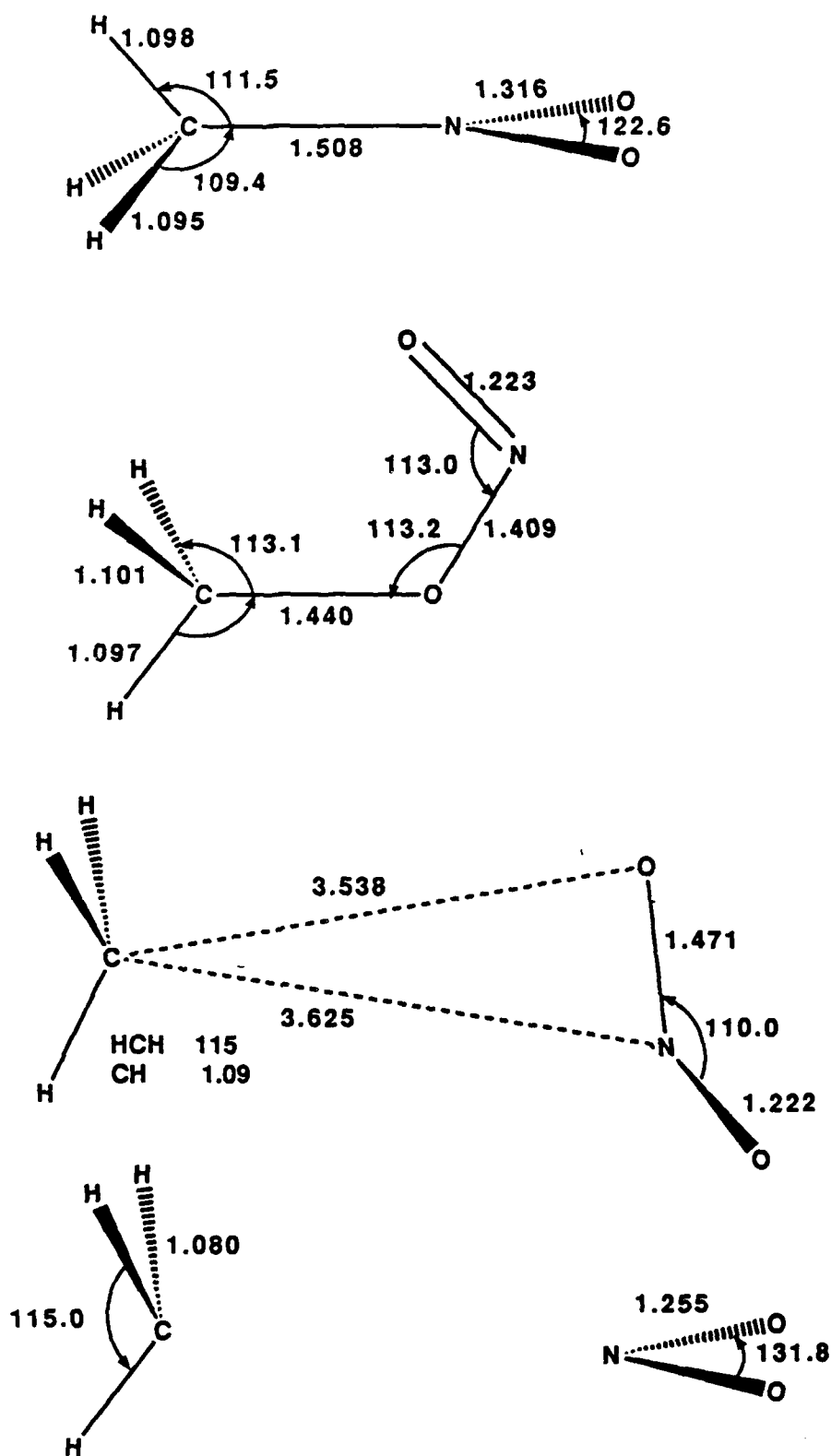


Figure 1. Geometric parameters at the CAS/STO2G level.

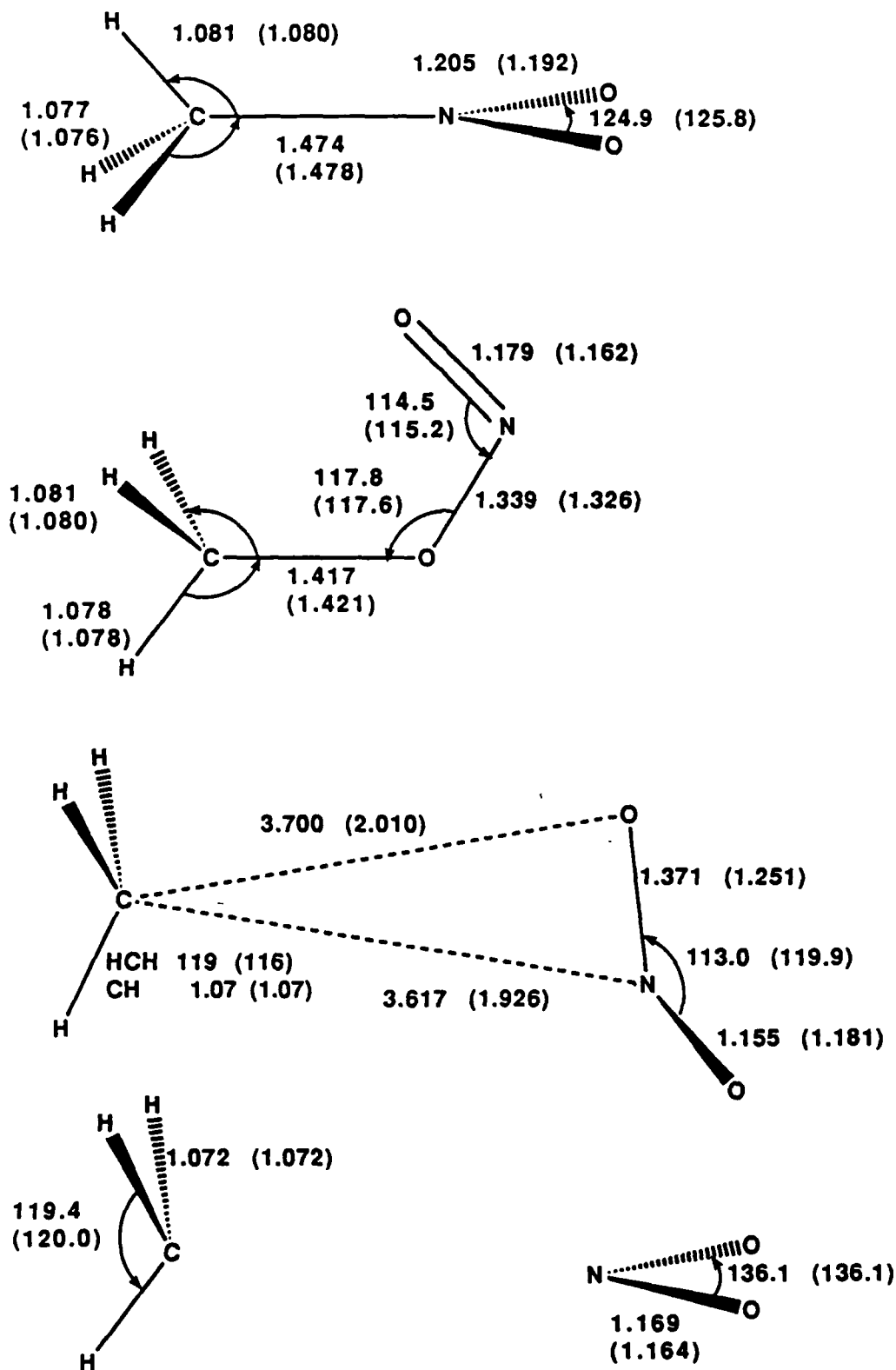


Figure 2. Geometric parameters at the CAS/6-31G* level. In parentheses are the values at the HF/6-31G*.

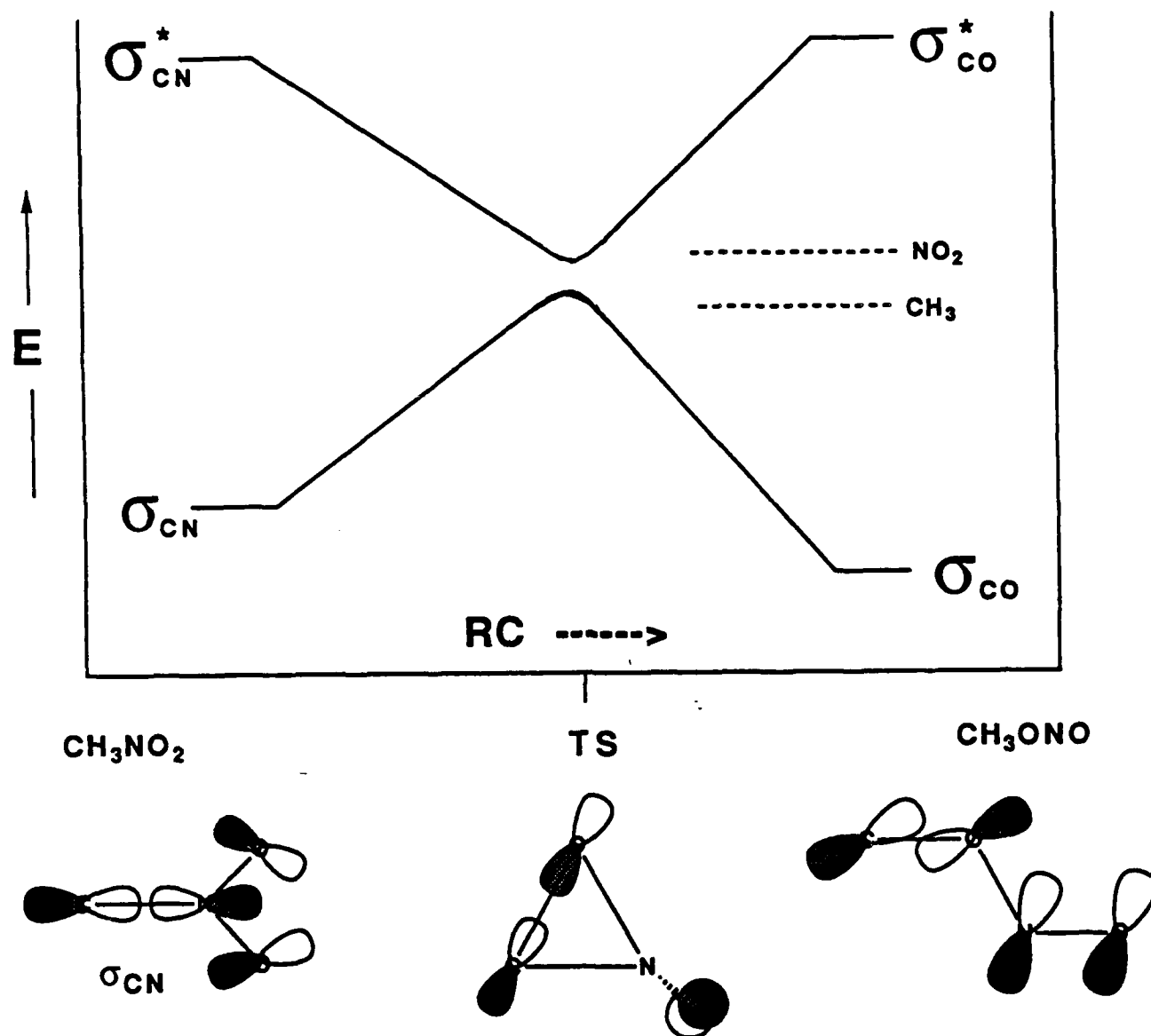


Figure 3. Correlation diagram indicating an avoided crossing of the sigma CN bonding and antibonding orbitals. In the transition state the two orbitals will have energies similar to the orbitals containing the unpaired electrons in the CH_3 and NO_2 radicals.

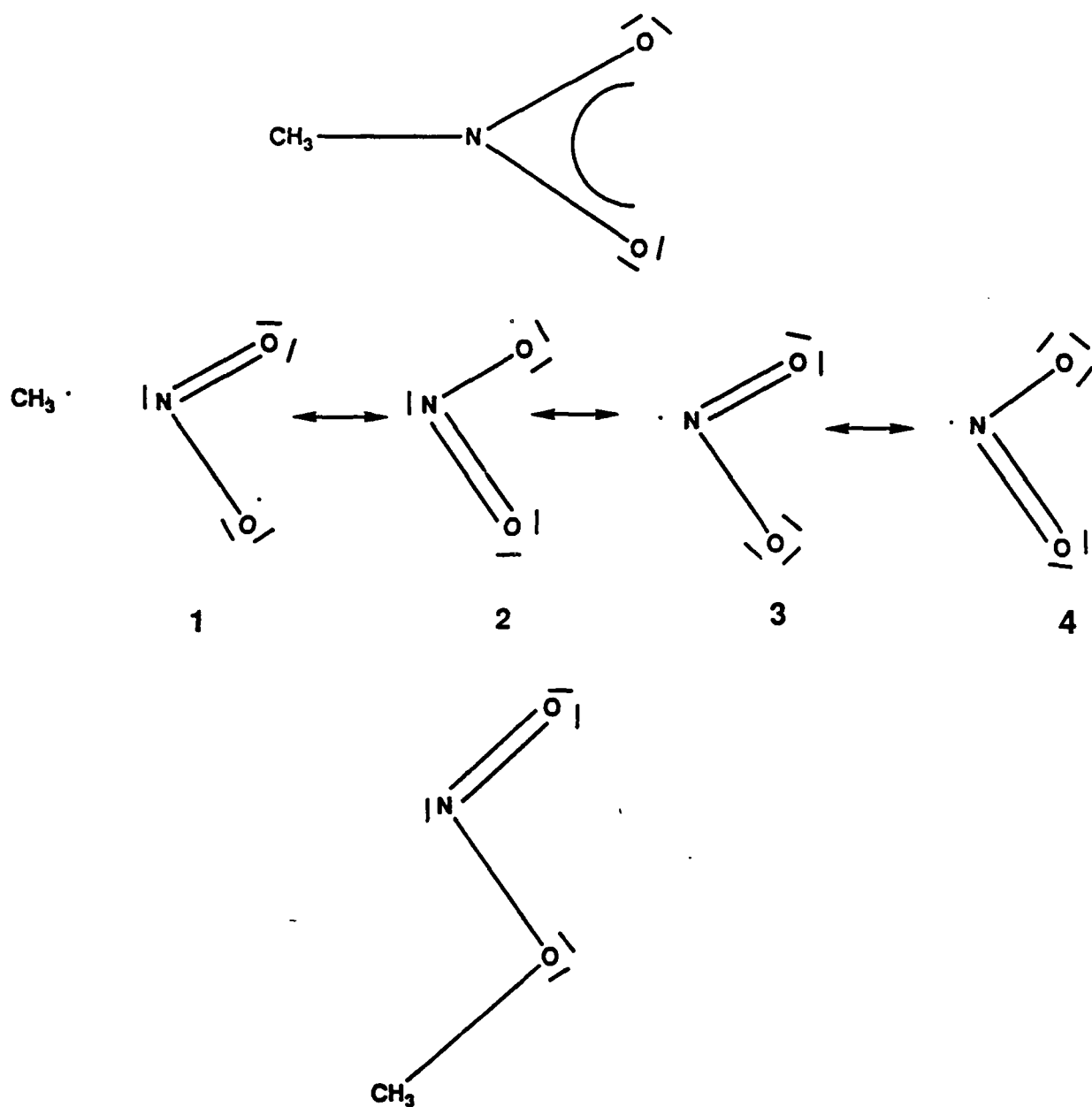


Figure 4. Resonance structures of species on the CH_3NO_2 potential energy surface. As the CN bond breaks, resonance structure 1 will become increasingly important. The CH_3 group will migrate above the NO_2 plane and form a sigma bond with the unpaired electron in an orbital perpendicular to the NO_2 plane.

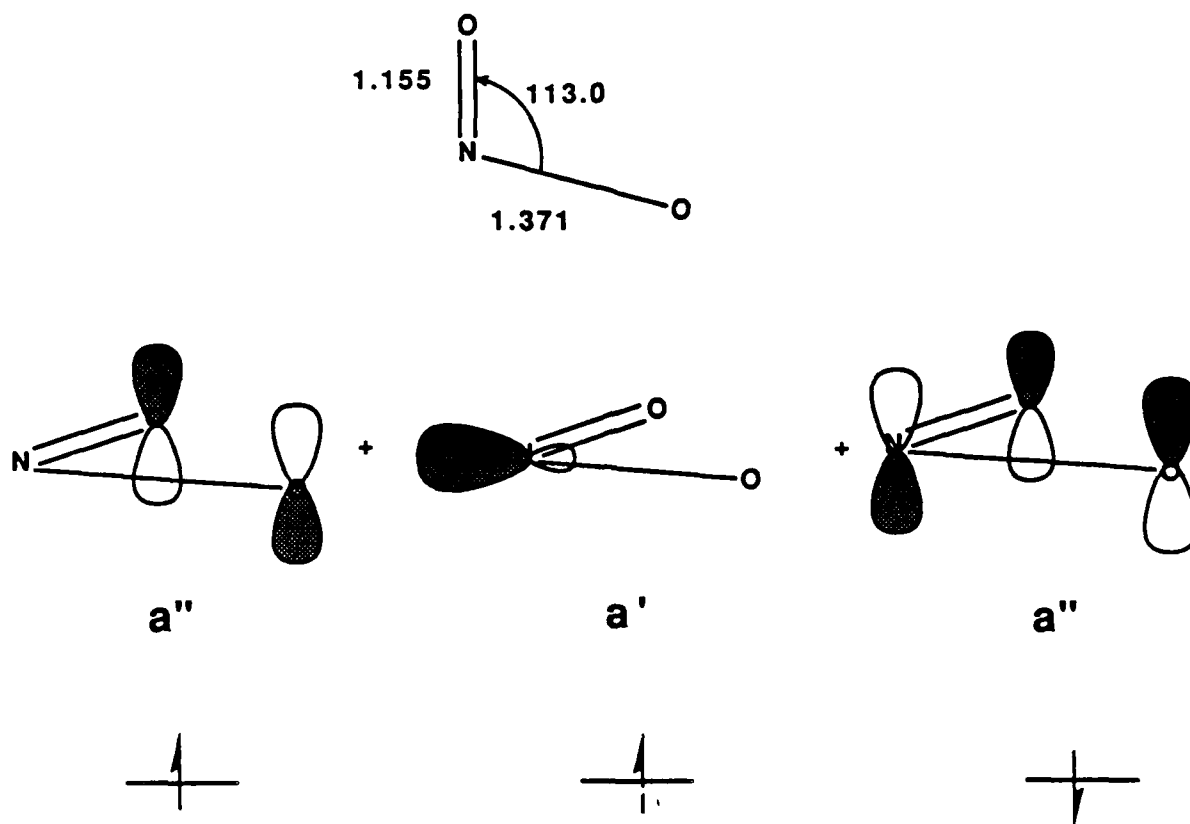


Figure 5. An important contributing configuration in the NO_2 fragment (frozen in the transition state geometry). The three unpaired electrons are distributed in the nitrogen lone pair orbital and the two π combinations of the oxygen lone pair orbitals.

XL. Recommendation:

On the basis of the above studies the following recommendations can be made:

Part I

- (1) That accurate bond dissociation energies can be calculated with present computational programs.
- (2) That changes in the intrinsic bond energy are mirrored by changes in the radical stabilization energy.
- (3) That incomplete convergence of the perturbative series for calculating electron correlation can lead to an underestimation of the BDE by up to 6 kcal/mol.

Part II

- (1) That geometry optimizations of nitro containing compounds using a multiconfigurational wavefunction is probably unnecessary as the small changes in geometry do not justify the additional expense.
- (2) That transition states be located with an MCSCF procedure as it is shown that the geometry of the transition state depends very strongly on the level of calculation.
- (3) That energies be determined with additional electron correlation, preferably multireference CI (MRCI) which will recover important dynamic electron correlation.

FINAL REPORT

1988 Research Initiation Program

Sponsored by the
AIR FORCE OFFICE OF SCIENTIFIC RESEARCH

Conducted by the
Universal Energy Systems, Inc.

Sodium As An Electrode for Chloroaluminate Melts

Prepared by:	Tammy J. Melton. Ph.D.
Academic Rank:	Assistant Professor
Research Location:	Department of Chemistry St. Norbert College De Pere, WI 54115
Duration:	1 Jan 1989 to 31 Dec 1989
Contract No:	F49620-88-C-0053/SB5881-0378

ABSTRACT

Sodium As An Electrode For Chloroaluminate Melts

The effects of adding sodium chloride to room temperature molten salts containing 1-methyl-3-ethylimidazolium chloride and aluminum chloride was studied by this investigator during the summer of 1988. Sodium chloride will dissolve in basic or neutral melts, but only in small quantities. The solubility in acidic melts is much greater. The limit to the solubility was found to be that quantity which would reduce the mole fraction of aluminum chloride to 0.5. This renders the melt neutral, and provides a wide electrochemical window for potential battery applications. The purpose of this research was to investigate the use of elemental sodium as an electrode in sodium chloride-buffered chloroaluminate melts.

ACKNOWLEDGEMENTS

This research was generously sponsored by the AIR FORCE OFFICE OF SCIENTIFIC RESEARCH, BOLLING AFB, DC. I am grateful for their support.

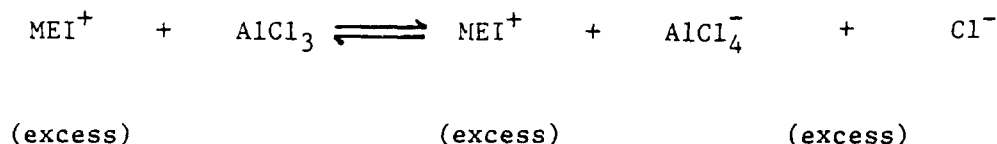
I would also like to thank Universal Energy Systems for the administrative and directional assistance in this research effort.

It is a pleasure to acknowledge Dr. John Wilkes for his expert guidance and advice, his patience, and his willingness to give assistance in preparing the starting materials. I am deeply indebted to him for his concern. I would also like to thank Dr. Joseph Maloy, who kindly offered his expertise in electrochemistry in the early stages of this work.

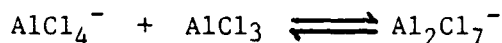
Finally, I am pleased to acknowledge the work of Mr. Francis Brennan, who is currently a graduate student at Michigan Technical University.

I. INTRODUCTION

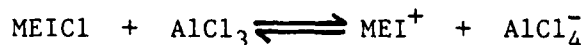
Mixtures of aluminum chloride and 1-methyl-3-ethylimidazolium chloride (MEICl) are ionic liquids (melts) at room temperature when the mole fraction of aluminum chloride (N_{AlCl_3}) is between approximately 0.33 and 0.66, inclusive.¹ These ionic liquids are potentially useful as electrolytes in batteries. The Lewis acid-base characteristics of these melts vary depending on the composition. Binary mixtures with mole fraction of AlCl_3 less than 0.5 ($N_{\text{AlCl}_3} < 0.5$) are basic due to the presence of excess Cl^- , a Lewis base.



Acidic melts are formed when mole fractions of AlCl_3 are greater than 0.5. The presence of excess AlCl_3 drives the tetrachloroaluminate ion to heptachloroaluminate ion, a Lewis acid.



When AlCl_3 and MEICl are present in equimolar quantities ($N = 0.5$) negligible concentrations of Cl^- and Al_2Cl_7^- exist, and the molten salt is considered neutral.



The specific conductivity of these melts is relatively low, but reaches a maximum for the neutral melt.^{2,3} This unexpectedly low conductivity has been attributed to the relatively strong association of the Cl^- to the hydrogen atoms at the 2, 4, and 5 positions of the MEI^+ (with the strongest of these at the 2 position). This interaction is believed to render the Cl^- less mobile. The conductivities of various melts and the sodium chloride-buffered melts have been measured and are reported here.

II. OBJECTIVES

The overall goal of the work was to determine the feasibility of using sodium in an aluminum chloride/1-methyl-3-ethylimidazolium chloride battery. The objectives were proposed in four phases: (1) determining the maximum sodium ion content which is possible for these systems, (2) optimizing the characteristics of a sodium electrode, (3) determining the potential for the Na/Na^+ couple, and (4) investigating the feasibility of using potassium in an analogous electrochemical role. Later the objective of specifically determining the conductivities of the buffered melts was added.

III. RESEARCH

Melts composed of aluminum chloride and sodium chloride have been studied extensively⁴ as well as melts of aluminum chloride and lithium chloride.⁵ Moreover, ternary mixtures of aluminum chloride, lithium chloride and sodium chloride have been studied.⁶

In this research, I continued the investigations begun in the summer of 1988 in the area of ternary mixtures of aluminum chloride, 1-methyl-3-ethyl-imidazolium chloride, and sodium chloride.

It has been shown that sodium chloride dissolves in acidic mixtures of $\text{AlCl}_3/\text{MEICl}$ to an extent controlled by the mole fraction of AlCl_3 . Addition of sodium chloride can continue as long as the resulting mole fraction of aluminum chloride is greater than 0.5. When this limiting value is reached, sodium chloride ceases to dissolve appreciably in the melts. Therefore, beginning with very acidic melts increases the total amount of sodium ion which could be present in the melt. The theoretical solubility of NaCl can then be expressed as $S = A - M$, where S = moles of sodium chloride, A = moles of aluminum chloride, and M = moles of 1-methyl-3-ethyl-imidazolium chloride.

Interestingly, it was found that the most acidic melt, $N \approx 0.667$, was susceptible to total solidification when the amount of sodium chloride added was slightly greater than the theoretical amount. The solidification of these melts was observed on several occasions. Efforts to return the samples to the molten state by addition of AlCl_3 and/or MEICl were unsuccessful.

It is clear that a very useful way has been discovered to prepare $\text{AlCl}_3/\text{MEICl}$ melts which are neutral in the Lewis sense.

Neutral melts have the enormous advantage of a large electrochemical window, that is, the oxidation-reduction limits are the oxidation of AlCl_4^- and the reduction of the MEI^+ . The potential difference between these two events is greater than 4.0 V.

Conductivities of these room temperature molten salts have been

measured and reported.^{2,3} The addition of sodium chloride to these melts to produce buffered melts would be expected to change the conductivity. Moreover, since the solubility of sodium chloride has been shown to be a function of the initial mole fraction aluminum⁷

$$S = A - M \quad (1)$$

S = moles of sodium chloride

A = moles of aluminum chloride

M = moles of MEICl

there was expected to be a marked change in conductivity with increasing solubility of sodium chloride. However, as discussed below, no significant change in conductivity was observed.

Relative conductivities were measured on 10 g samples of melts of various compositions and on several different sodium chloride saturated melts with a platinum electrode attached to a Micronta conductivity meter. The specific conductivity for all sodium chloride melts averaged $0.019 \text{ mhos}\cdot\text{cm}^{-1}$ at 22°C .

We can compare this to specific conductivities obtained on non-buffered chloroaluminate melts : $0.0117 \text{ mhos}\cdot\text{cm}^{-1}$ for $N = 0.44$, $0.0227 \text{ mhos}\cdot\text{cm}^{-1}$ for $N = 0.50$, and $0.0154 \text{ mhos}\cdot\text{cm}^{-1}$ for $N = 0.67$ at 29.7 , 29.7 , 30.9 , and 32.2°C , respectively.

Since all of the sodium chloride-containing melts are buffered to $N = 0.50$, it is reasonable to compare this to a non-buffered neutral melt. The value obtained in this lab, $0.019 \text{ mhos}\cdot\text{cm}^{-1}$, is slightly less than the $0.0227 \text{ mhos}\cdot\text{cm}^{-1}$ measurement. This difference may well be attributable to the difference in temperature at which the two

measurements were made.

This brings into question the role of Na^+ in the actual conductivity. In neutral melts the amount of free Cl^- is extremely low, so any change in conductivity would have to be a direct result of the presence of free Na^+ . Moreover, since initially unbuffered melts can dissolve sodium chloride based on the value of N in the binary mixture, melts originally with $N_{\text{AlCl}_3} = 0.67$ dissolve the greatest amount of salt (Eq 1) and therefore contain the greatest amount of Na^+ . It is puzzling then to observe no difference in conductivity between buffered melts containing large amounts of sodium and those containing small amounts. Further, there appears to be no significant difference in conductivity between any buffered melt and a simple binary neutral melt.

The most obvious conclusion is that the Na^+ is tied up in the extensive chloroaluminate liquid ionic lattice and is not therefore mobile enough to effect change in the conductivity.

Although extensive effort was put forth to quantitatively determine the exact sodium ion concentrations in the various melts, these efforts were frustrated by the difficulty of determining extremely low sodium ion levels in the presence of aluminum ion. It is reasonable that the sodium ion concentrations in the buffered melts are as indicated in Equation 1, as the behavior of exactly neutral melts is well documented and the electrochemical behavior of the buffered melts precisely duplicates that observed for binary neutral melts.

In preliminary work carried out during the summer, a sodium electrode was constructed in the following manner. Elemental sodium

was warmed on a hot plate, the oxide coating was discarded, and the molten or softened metal was drawn into a glass tube 5 mm in diameter with an interior diameter of 3 mm. A copper wire was inserted into the cooled metal to serve as a contact for the cell. As the electrode surface corroded, a fresh sodium surface could be extruded by pushing on the copper wire, and drawing the tip of a spatula across the fresh surface.

Use of this electrode presented a number of problems. First, under the conditions mentioned, the electrode surface needed renewing after every two or three scans (by cyclic voltammetry) because of the rapid decomposition of the surface. Second, replication of experiments proved difficult due to variations in the surface of the new sodium layer. Sodium metal is quite soft and somewhat "sticky". Rather than being planar, many times the surface would be jagged, uneven, and of different sizes (surface area). Third, and most important, the rapid decomposition of the surface results in a concomitant decrease in current. A satisfactory improvement in this electrode has not been achieved. A more facile method of surface preparation should be pursued to achieve better precision in surface characteristics when the surface must be renewed. The nature of the decomposition at the electrode surface is not well understood. If it becomes clear that this layer is a real detriment to the ability of the sodium electrode to carry current (and preliminary work indicates that this is probably the case), a method should be sought that would separate the electrode from direct contact with the melt, but would still allow for the electrochemical circuit to be completed. Such a construction might involve the sodium electrode being placed in a

separate compartment which is then in contact with the rest of the cell.

An attempt was made to use a sodium electrode in a neutralized melt with an appreciable sodium ion content. The resting potential of the cell was consistently approximately -2.05 V. After a few sweeps in the positive direction, a grey-black deposit was observable on the sodium surface and the rest potential became more positive (to about -1.8 V.) It was observed that the current rapidly decreased with each scan, presumably as the black layer being deposited on the electrode became thicker.

A corrosion study confirmed these findings and indicated that although the rest potential was about -2.0 V., the maximum current flow was at about -0.85 V, considerably less.

IV. RECOMMENDATIONS

There has been considerable interest in observing the reduction of Na^+ to Na in room temperature chloroaluminate melts. An effort was made using cyclic voltammetry to locate the potential of the Na^+/Na reduction of the sodium electrode described above. The Li^+/Li reduction has been reported to occur in this system at -2.0 V. It is possible that the sodium reduction is beyond the cathodic limit, or that it overlaps somewhat with MEI^+ reduction. The reduction may have been observed as the shoulder on another (stripping) peak at approximately -3.0 V. It is hoped that optimization of the sodium electrode will facilitate the location of the Na^+/Na reduction potential.

The similarities between Na and K are very well established, and especially so for Na^+ and K^+ . However, work with lithium chloride has been carried out and it is clear that the behavior of lithium is markedly dissimilar. For example, it is believed that LiCl forms complexes such as LiCl_2^- in $\text{AlCl}_3/\text{MEICl}$ melts.

Once a successful model has been established for sodium and sodium ion, it is certainly prudent to also investigate the possibility of potassium functioning in an analogous manner. The solubility of potassium chloride in acidic $\text{AlCl}_3/\text{MEICl}$ melts should be determined first. Should these tests indicate solubility behavior similar to sodium chloride (and preliminary tests indicate that this is so¹⁰), an attempt should be made to construct a potassium electrode. However, the difficulties in working with metallic potassium are fully appreciated; the construction of this electrode may present new problems not encountered with sodium.

REFERENCES

1. Wilkes, J. S., Levisky, J. A., Wilson, R. A., and Hussey, C. L.
Inorg. Chem., 21, 1263 (1982).
2. Floreani, D. A., Stech, D. J., Wilkes, J. S., Williams, J. L.,
Peirsma, B. J., King, L. A., and Vaughn, R. L. Proc. 30th Power
Sources Symp., The Electrochemical Society, Princeton, N. J., p. 84,
June 1982.
3. Fannin, A. A., Floreani, D. A., King, L. A., Landers, J. S., and
Williams, J. L. J. Phys. Chem., 88, 2614, (1984).
4. Fannin, A. A., King, L. A., Seegmiller, D. W., Oye, H.A. J. Chem.
Eng. Data, 27, 114, (1982) and references therein.
5. Carpio, R. A., King, L. A., Kibler, F. C., and Fannin, A. A. J.
Electrochem. Soc., 126, 1650, (1979).
6. Carpio, R. A., Kibler, F. C., King, L. A., Brokner, K. T., Oye, H.
A. Ber. Bunsenges. Phys. Chem., 85, 31, (1981).
7. Melton, T. J. "The Effects of Sodium Chloride on Room Temperature
Molten Salts", Report of AFOSR/UES Summer Faculty Research Program,
Summer 1988.

8. Lipsztajn, M. and Osteryoung, R. A. Inorg. Chem., 24, 716 (1985).
9. Dr. Joseph Malor, private communication.
10. Dr. John Wilkes, private communication.

FINAL REPORT NUMBER 41
REPORT NOT AVAILABLE AT THIS TIME
Dr. Patricia L. Plummer
210-9MG-097

TSPC Report Number 89-12

TRANSIENT SHOCK WAVES
IN A MACH 3 FLOW

Final Report

Prepared by

H. Doyle Thompson

Thermal Sciences and Propulsion Center

School of Mechanical Engineering

Purdue University

West Lafayette, IN 47907

Sponsored by

AIR FORCE OFFICE OF SCIENTIFIC RESEARCH

Bolling Air Force Base, DC

April 1989

ABSTRACT

A computer program has been developed to compute the time accurate unsteady start-up flow in a supersonic wind tunnel. The program is based on the unsteady Euler equations for one-dimensional flow with area change. Six numerical algorithms were programmed and numerical results compared with each other and with experimental measurements taken in the U.S. Air Force Academy's trisonic wind tunnel. The numerical algorithms include two versions each of the Lax's method, MacCormack's method, and the method of characteristics. The difference in the two versions involved the manner that the non-homogeneous terms in the conservation form of the governing equations were differenced. The method of characteristics formulation was derived for conservation variables. This is the first known method of characteristics formulation for unsteady, one dimensional flow with area change using conservation variables.

LIST OF FIGURES

- Figure 1. Experimental test section pressures.
- Figure 2. Schlieren pictures at 0.5 millisecond intervals of the transient start-up shocks in a Mach 3 tunnel.
- Figure 3. Grid point numbering scheme for the invese marching method of characteristics.
- Figure 4. Driving pressure downstream of the control valve.
- Figure 5. Nondimensional flow area.
- Figure 6. Calculated static pressures vs x at select times for the LAX1 method.
- Figure 7. Calculated static pressures vs x at select times for the LAX2 method.
- Figure 8. Calculated static pressures vs x at select times for the FB1 method.
- Figure 9. Calculated static pressures vs x at select times for the FB2 method.
- Figure 10. Calculated static pressures vs x at select times for the MOC1 method.
- Figure 11. Calculated static pressures vs x at select times for the MOC2 method.
- Figure 12. Calculated stagnation pressures for the LAX1 method.
- Figure 13. Calculated stagnation pressures for the LAX2 method.
- Figure 14. Calculated stagnation pressures for the FB1 method.
- Figure 15. Calculated stagnation pressures for the FB2 method.
- Figure 16. Calculated stagnation pressures for the MOC1 method.
- Figure 17. Calculated stagnation pressures for the MOC2 method.
- Figure 18. Calculated test section pressure for the LAX1 method.
- Figure 19. Calculated test section pressure for the LAX2 method.
- Figure 20. Calculated test section pressure for the FB1 method.
- Figure 21. Calculated test section pressure for the MOC1 method.
- Figure 22. Calculated test section pressure for the MOC2 method.

LIST OF TABLES

- Table 1. Finite Difference Algorithms

I. INTRODUCTION

Most of the design, testing, and operation of the high performance aircraft, missiles, and space craft of today is based on an assumed steady flow. Unsteady flows, on the other hand, are generally viewed unfavorably. They are associated with boundary layer separations, with stall on control and lifting surfaces with large transient forces that are not predicted in steady flow calculations, and with instabilities.

The requirements for more advanced design have greatly increased the interest in understanding transient phenomena so that their effects can be used to enhance performance.

One area of recent research toward that end has resulted from the observation that the lift coefficient on a rapidly pitching airfoil is many times the steady-state value just before it stalls. Several attempts to understand that phenomena have been made, including some very interesting and productive experimental research at the Frank J. Seiler Research Laboratory at the U.S. Air Force Academy in Colorado Springs, CO (see Refs. 1-4). That research uses a rapidly pitched airfoil in a low speed wind tunnel with flow visualizations (smoke wire) and static pressure measurements made on the airfoil surface. The practical applications for this research are many and varied.

Reference 5 reports the results of an experimental study using the trisomic wind tunnel facilities at the U.S. Air Force Academy to study unsteady transients in supersonic flows. A 20 degree symmetric wedge, six inches wide, was mounted in the one foot square test section of the Mach 3 tunnel. High response pressure transducers were mounted on the upper and lower wedge surfaces and on the tunnel sidewall upstream of the test section. The transient shock waves, generated during tunnel start-up and shut-down, were recorded using a Schlieren optical system focussed directly on the front lens of a 16 mm high speed camera. Pressure measurements and

Schlieren pictures were recorded at half millisecond intervals over an eight second run time.

Figure 1 is representative of the pressure measurements made on the wedge, and shows unexpectedly large pressure spikes just before steady-state operation is reached. The pressure traces are from transducers 1 and 2 which were located respectively on the top and on the bottom of the wedge at one inch from the leading edge. The difference between the pressures indicates that there was a strong upward pitching moment associated with the tunnel start-up. Data from other runs show a similar situation, but with a downward pitching moment. Large pitching moments have been measured by the force and moment balance during start-up with other models. It is clear that steady flow calculations do not predict the very large, short duration forces that can arise in transient supersonic flows.

Figure 2 is a sequence of eight Schlieren pictures, taken at one half millisecond intervals, that show the passage of the primary shock over the wedge. The shock angle on the wedge in the eighth frame confirms a steady state Mach 3 flow. The shock speed as determined from the sequence of pictures is of the order of 125 feet per second (38 m/s) relative to the model. The air speed at Mach 3 is about 2000 feet per second (610 m/s).

As an extension to the experimental research reported in Ref. 5, a program was undertaken to numerically model the unsteady start-up transient in a supersonic wind tunnel. That work is the subject of this report. The flow was modeled as a one-dimensional, unsteady flow with area change. The governing equations are hyperbolic. Six time accurate numerical algorithms were developed and tested to evaluate their shock capturing capabilities and overall accuracy. The initial conditions are a no-flow condition. The boundary conditions are the time dependent flow conditions downstream of the control valve, and an exit flow to ambient pressure. The time dependent pressure and temperature downstream of the control

valve were analytically modeled to approximate the measured valves reported in References 6 and 7.

The six numerical algorithms tested were all finite difference algorithms for the solution to the Euler equations. All were formulated using conservation variables. Two of the algorithms used the Lax method, two used the MacCormack (forward-backward) method, and two used a newly formulated method of characteristics for conservation variables. The variable area requirement introduces non-homogeneous terms. The difference between the two algorithms for each method is the method for grouping and computing the non-homogeneous terms. The method of characteristics algorithms are new. Their development in this study has merit in its own right.

In Chapter II the analysis for the numerical algorithms are developed. Chapter III is the results section, and Chapter IV is the summary and recommendations.

II. ANALYSIS

In this section the governing equations for a one-dimensional, unsteady, inviscid flow with area change are summarized. The equations are cast in conservation variables. Two sets of conservation variables are used. The first is the usual conservation variables for a one-dimensional unsteady flow. That is,

$$\mathbf{W}_1 = (\rho, \rho u, E)^T \quad (1)$$

where

$$E = P/(\gamma-1) + \rho u^2/2 \quad (2)$$

for a perfect gas.

The second set of conservation variables is the flow area times the variables in Eq. (1). That is,

$$W_2 = (\rho A, \rho A u, EA)^T \quad (3)$$

The numerical algorithms for the Lax method, for MacCormack's (forward-backward) method, and for the method of characteristics are derived. The method of characteristics algorithm is derived for both sets of conservation variables.

The boundary conditions are derived for the wind tunnel start-up. The area variation as a function of position for the U.S. Air Force Academy Trisonic Wind Tunnel is described.

A. Governing Equations

The governing equations are the continuity, momentum and energy equations. A perfect gas is assumed. Those equations in conservation law form for a one-dimensional, inviscid, unsteady flow, without area change are

$$W_{1t} + F_{1x} = 0 \quad (4)$$

where W_1 is given by Eq. (1) and

$$F_1 = \left[\rho u, P + \rho u^2, u(E + P) \right]^T \quad (5)$$

In so-called primitive variables the governing equations with area change are

$$\rho_t + \rho u_x + u \rho_x + \rho u A_x / A = 0 \quad (6)$$

$$\rho u_t + \rho u u_x + P_x = 0 \quad (7)$$

$$P_t + u P_x - a^2 (\rho_t + u \rho_x) = 0 \quad (8)$$

where a is the local sound speed. For an ideal gas

$$a^2 = \gamma P / \rho \quad (9)$$

With some manipulation Eqs. (6), (7) and (8) can be written

$$W_{1t} + F_{1x} = G_1 \quad (10)$$

where W_1 and F_1 are given by Eqs. (1) and (5), and

$$G_1 = \left[-\rho u A_x/A, -\rho u^2 A_x/A, -u(E + P) A_x/A \right]^T \quad (11)$$

With some further manipulation, and noting that the area is not time dependent (i.e., $A_t = 0$), a second form of the governing equations, as given below, can be obtained. They are,

$$W_{2t} + F_{2x} = G_2 \quad (12)$$

where W_2 is given by Eq. (3) and,

$$F_2 = \left[\rho A u, P A + \rho A u^2, u(E A + P A) \right]^T \quad (13)$$

and

$$G_2 = \left[0, P A_x, 0 \right] \quad (14)$$

Notice that the form of Eqs. (4) for flow without area change and Eqs. (12) for flow with area change are very much alike when the conservation variables in Eq. (1) are replaced by those in Eq. (3). The difference is the single non-homogeneous term in Eq. (14).

B. The Lax Finite Difference Algorithm

The Lax finite difference algorithm for equally space nodes in the x-direction is:

$$w_i^{n+1} = \frac{1}{2} (w_{i+1}^n + w_{i-1}^n) - \frac{\Delta t}{2\Delta x} (f_{i+1}^n - f_{i-1}^n) + \frac{1}{2} (g_{i+1}^n + g_{i-1}^n) \Delta t \quad (15)$$

where superscripts (n, n+1) denote the time level and subscripts (i-1, i, i+1) denote the space index. The variables w, f and g indicate the components of the vectors W, F and G in Eqs. (10) or (12). The time step, Δt , is calculated to satisfy the CFL

stability criteria for the most restrictive case at each time level.

The Lax algorithm is first order. In addition, it numerically generates artificial flow velocities when applied to Eq. (12). This can be seen by examining the no-flow case, i.e., the case for $u = 0$, where P , ρ and E are uniform, and the boundary conditions do not introduce any flow velocities. Notice that even though P , ρ and E are uniform, the variables PA , ρA , and EA are not uniform. Thus for the no flow case the first of Eqs. (12) reduces to

$$(\rho A)_i^{n+1} = \frac{1}{2} \left[(\rho A)_{i+1}^n + (\rho A)_{i-1}^n \right] \quad (16)$$

so that the new value of $(\rho A)_i^{n+1}$ is not $(\rho A)_i^n$, as it should be when $u = 0$, but is rather the average of the unequal values on either side. The same is true for the third of Eqs. (12). The result is that the no flow case generates flow velocities that continue to increase.

The Lax algorithm applied to Eqs. (10) does not generate artificial flow velocities.

C. The MacCormack Finite Difference Algorithm

The MacCormack finite difference algorithm is one of the most popular numerical methods in use today. That method employs a two-step algorithm to produce second order accuracy. There are two versions of the algorithm for a one-dimensional unsteady flow. The forward-backward (F-B) version uses forward differences on the one-sided predictor step, and backward differences on the corrector step. This is the version for which the algorithm is given below. The backward-forward (B-F) version is similar except that the directions of the one-sided differences are reversed. It has been found in this and other shock tube studies that for a right traveling shock wave the B-F version often predicts negative values of absolute pressure across a shock of sufficient strength, thus causing the computer program to fail. The F-B version undershoots the pressure, also, but is more robust than the B-F version.

For equally spaced nodes in the x-direction the finite difference numerical algorithm for the F-B MacCormack method is

$$w_i^{n+1} = w_i^n - \frac{\Delta t}{\Delta x} \left(f_{i+1}^n - f_i^n \right) + g_i^n \Delta t \quad (17)$$

$$w_i^{n+1} = \frac{1}{2} \left\{ \left(w_i^n + \overline{w_i^{n+1}} \right) - \frac{\Delta t}{\Delta x} \left(\overline{f_i^{n+1}} - f_{i-1}^{n+1} \right) + \overline{g_i^{n+1}} \Delta t \right\} \quad (18)$$

where the bar over the n+1 superscript indicates the predictor value. To ensure that the no flow conditions do not generate a false numerical velocity for Eq. (12), the nonhomogeneous terms in Eqs. (17) and (18) are

$$g_i^n = \left(P A_x \right)_i^n = \left(P_{i+1}^n + P_i^n \right) \left(A_{i+1} - A_i \right) / (2\Delta x) \quad (19)$$

$$g_i^{\overline{n+1}} = \left(P A_x \right)_i^{\overline{n+1}} = \left(\overline{P_i^{n+1}} + P_{i-1}^{\overline{n+1}} \right) (A_i - A_{i-1}) / (2\Delta x) \quad (20)$$

In Eqs. (19) and (20) the pressure terms are averaged. When the algorithm was run without averaging the pressure the program calculated negative pressures and densities when the shock strength was sufficiently large.

D. The Method of Characteristics in Conservation Variables

Of all the numerical algorithms, the direct marching method of characteristics is the most accurate. The inverse marching method of characteristics where the characteristic rays are projected backward onto an initial value surface from a prescribed node point is probably the second most accurate method. The problems are the following:

- 1.) The direct method generates a non-uniform grid, it is more difficult to program, and the extension to more than two dimensions is extremely complex. Also, shock waves need to be tracked explicitly, which can be very

difficult in a complex flow.

2.) The inverse method takes more effort to program than most finite difference methods, has here-to-fore been limited to primitive variables, and will handle only weak shocks. Explicit shock tracking is required to handle strong shocks.

3.) Method of characteristic algorithms take more CPU time per grid point calculation. This inefficiency is partially compensated for by the increased accuracy.

One of the methods tested for the computation of the start-up flow in the trisonic tunnel is the method of characteristics in conservation variables. This is the first time that conservation variables have been used for characteristic calculations in an unsteady flow with area change. The idea of characteristics is to make a linear combination of the governing equations such that the partial derivatives combine to form total derivatives in the characteristic directions. For example, Eq. (10) or (12) could be written

$$W_t + A W_x = G \quad (21)$$

where A is a coefficient matrix

$$A = \left[a_{ij} \right] = \left[\frac{\partial f_i}{\partial w_j} \right] \quad (22)$$

Applying characteristic theory to Eq. (21), one obtains the characteristic equations

$$\left| A^T - \lambda I \right| = 0 \quad (23)$$

which expands to the cubic equation in λ ,

$$\lambda^3 - B_1 \lambda^2 + B_2 \lambda - B_3 = 0 \quad (24)$$

If the roots of Eq. (24) are real and distinct, the original equation set is hyperbolic and the equations $dx/dt = \lambda$ are the equations for the characteristic curves in the (x,t) plane. With considerable tedious algebra it can be shown that the characteristic curves for Eqs. (10) and Eqs. (12) are

$$\lambda_1 = dx/dt = u + a \quad (25)$$

$$\lambda_2 = dx/dt = u - a \quad (26)$$

and

$$\lambda_3 = dx/dt = u \quad (27)$$

where a is the local sound speed given by Eq. (9). The characteristic curves, that is, the directions along which information is propagated, are identical to the characteristic directions for primitive variables. This, of course, is the expected result.

The compatibility equations are derived by eliminating σ_1 , σ_2 and σ_3 from the equation

$$\sigma_1 dw_1 + \sigma_2 dw_2 + \sigma_3 dw_3 = \sigma_2 g_2 \quad (28)$$

where

$$\begin{aligned} \lambda &= \frac{\sigma_1 a_{11} + \sigma_2 a_{21} + \sigma_3 a_{31}}{\sigma_1} = \frac{\sigma_1 a_{12} + \sigma_2 a_{22} + \sigma_3 a_{32}}{\sigma_2} \\ &= \frac{\sigma_1 a_{13} + \sigma_2 a_{23} + \sigma_3 a_{33}}{\sigma_3} \end{aligned} \quad (29)$$

The compatibility equations are different for Eqs. (10) and Eqs. (12). Again after considerable algebra the following results are obtained. First, from Eqs. (10) with the dependent variables given by Eq. (1),

$$\left(\frac{u^2}{2} - \frac{a^2}{\gamma-1} \right) d\rho - u d(\rho u) + dE = 0 \quad (\text{on } \lambda_3 = u) \quad (30)$$

$$\left(\frac{u^2}{2} - \frac{ua}{\gamma-1} \right) d\rho - \left(u - \frac{a}{\gamma-1} \right) d(\rho u) + dE = \frac{-\rho u a^2}{\gamma-1} \frac{A_x dt}{A} \quad (\text{on } \lambda_1 = u+a) \quad (31)$$

$$\left(\frac{u^2}{2} + \frac{ua}{\gamma-1} \right) d\rho - \left(u + \frac{a}{\gamma-1} \right) d(\rho u) + dE = \frac{-\rho u a^2}{\gamma-1} \frac{A_x dt}{A} \quad (\text{on } \lambda_2 = u-a) \quad (32)$$

The compatibility equations corresponding to Eqs. (12) with the dependent variables given by Eq. (3) are

$$\left(\frac{u^2}{2} - \frac{a^2}{\gamma-1} \right) d(\rho A) - u d(\rho A u) + d(EA) = -u P A_x dt \quad (\text{on } \lambda_3 = u) \quad (33)$$

$$\begin{aligned} & \left(\frac{u^2}{2} - \frac{ua}{\gamma-1} \right) d(\rho A) - \left(u - \frac{a}{\gamma-1} \right) d(\rho A u) + d(EA) \\ & = - \left(u - \frac{a}{\gamma-1} \right) P A_x dt \quad (\text{on } \lambda_1 = u+a) \end{aligned} \quad (34)$$

$$\begin{aligned} & \left(\frac{u^2}{2} + \frac{ua}{\gamma-1} \right) d(\rho A) - \left(u + \frac{a}{\gamma-1} \right) d(\rho A u) + d(EA) \\ & = - \left(u + \frac{a}{\gamma-1} \right) P A_x dt \quad (\text{on } \lambda_2 = u-a) \end{aligned} \quad (35)$$

The point numbering scheme for a single grid point calculation using the inverse marching scheme is illustrated in Fig. 3. The unknown point, point 4, is at a specified x -location and at a specified Δt from the initial value surface. Δt is chosen such that the CFL stability criteria is satisfied everywhere. The determination of the variables w_i at point 4 is accomplished by following the predictor-corrector-iteration procedure as described below.

Predictor step 1: Locate the initial value points 1, 2 and 3 by projecting the characteristics as straight lines through point 4. The values of u_0 and a_0 are used to

determine the characteristic slopes.

Predictor step 2: Interpolate between the known points 5, 6 and 7 for the flow variables at the base points, that is points 1, 2 and 3. Determine u and a at points 1, 2 and 3. The interpolation can be linear or quadratic.

Predictor step 3: Repeat step 1 using the values of u and a at the base points, as determined in step 2, to calculate the characteristic slopes through point 4. Reinterpolate for the flow variables at points 1, 2 and 3.

Predictor step 4: Calculate the flow variables at point 4 by simultaneously solving the finite difference form of the compatibility equations. The coefficients are evaluated at their respective base points. The variables $(w_i)_4$ are determined by using Gauss reduction to solve the matrix equation

$$RX = T \quad (36)$$

For Eqs. (30)-(32)

$$R = [r_{ij}] ; X = \left(\rho_4, (\rho u)_4, E_4 \right)^T ; T = [t_i] \quad (37)$$

and

$$r_{11} = \left[\frac{u^2}{2} - \frac{a^2}{\gamma-1} \right]_3 ; r_{12} = -u_3 ; r_{13} = 1 \quad (38-a)$$

$$r_{21} = \left[\frac{u^2}{2} - \frac{ua}{\gamma-1} \right]_1 ; r_{22} = - \left[u - \frac{a}{\gamma-1} \right]_1 ; r_{23} = 1 \quad (38-b)$$

$$r_{31} = \left[\frac{u^2}{2} + \frac{ua}{\gamma-1} \right]_2 ; r_{32} = - \left[u + \frac{a}{\gamma-1} \right]_2 ; r_{33} = 1 \quad (38-c)$$

$$t_1 = r_{11}\rho_3 + r_{12}(\rho u)_3 + r_{13}E_3 \quad (39-a)$$

$$t_2 = r_{21}\rho_1 + r_{22}(\rho u)_1 + r_{23}E_1 - \frac{\rho_1 u_1 a_1^2}{(\gamma - 1)} \frac{(A_x)_1}{A_1} \Delta t \quad (39-b)$$

$$t_3 = r_{31}\rho_2 + r_{32}(\rho u)_2 + r_{33}E_2 - \frac{\rho_2 u_2 a_2^2}{(\gamma - 1)} \frac{(A_x)_2}{A_2} \Delta t \quad (39-c)$$

For Eqs. (33)-(35) the values of R , X , and T are

$$R = [r_{ij}] ; X = [(\rho A)_4, (\rho A u)_4, (EA)_4]^T ; T = [t_i] \quad (40)$$

where the r_{ij} are given by Eqs. (38), and the t_i terms are

$$t_1 = r_{11}(\rho A)_3 + r_{12}(\rho A u)_3 + r_{13}(EA)_3 + b_1 \quad (41-a)$$

$$t_2 = r_{21}(\rho A)_1 + r_{22}(\rho A u)_1 + r_{23}(EA)_1 + b_2 \quad (41-b)$$

$$t_3 = r_{31}(\rho A)_2 + r_{32}(\rho A u)_2 + r_{33}(EA)_2 + b_3 \quad (41-c)$$

where

$$b_1 = r_{12}P_3(A_x)_3 \Delta t \quad (42-a)$$

$$b_2 = r_{22}P_1(A_x)_1 \Delta t \quad (42-b)$$

$$b_3 = r_{32}P_2(A_x)_2 \Delta t \quad (42-c)$$

Caution must be taken in evaluating the non-homogeneous terms b_1 , b_2 and b_3 to ensure that they do not give rise to a numerically generated artificial flow when $u = 0$ and P , ρ and E are constant. To prevent artificial numerical flow generation the A_x terms must be differenced. The following differences are used.

$$b_1 = -P_3(A_4 - A_3) \quad (43-a)$$

$$b_2 = - \left(u - \frac{a}{\gamma-1} \right)_1 P_1 (A_4 - A_1) / (u + a)_1 \quad (43-b)$$

$$b_3 = - \left(u + \frac{a}{\gamma-1} \right)_2 P_2 (A_4 - A_2) / (u - a)_2 \quad (43-c)$$

Corrector step 1: Relocate the initial value points 1, 2 and 3 by projecting the characteristic lines through point 4, determined from the average slope between the base point and point 4. The values from the predictor step 4 are used to determine the properties at point 4. For example the characteristic slope connecting points 1 and 4 is

$$\lambda_1 = (1/2) \left[(u_1 + a_1) + (u_4 + a_4) \right] \quad (44)$$

Corrector step 2: Interpolate for the flow variables at points 1, 2 and 3.

Corrector step 3: Calculate the flow variables at point 4. Equation (36) can be used where the R matrix is the average of the values along the appropriate characteristic. That is

$$r_{11} = (1/2) \left\{ \left[\frac{u^2}{2} - \frac{a^2}{\gamma-1} \right]_3 + \left[\frac{u^2}{2} - \frac{a^2}{\gamma-1} \right]_4 \right\} \quad (45)$$

etc.

The nonhomogeneous terms in Eqs. (39), (41) and (43) are averaged appropriately. The corresponding corrector values for Eqs. (43) are

$$(b_1)_c = - (P_3 + P_4) (A_4 - A_3) / 2 \quad (46-a)$$

$$(b_2)_c = (r_{22})_c (P_1 + P_4) (A_4 - A_1) / \left[(u + a)_1 + (u + a)_4 \right] \quad (46-b)$$

$$(b_3)_c = (r_{32})_c (P_2 + P_4) (A_4 - A_2) / [(u - a)_2 + (u - a)_4] \quad (46-c)$$

E. Boundary and Initial Conditions

The numerical algorithms are time marching algorithms for which initial and boundary conditions must be specified. The initial conditions at $t = 0$ are $u = 0$, $P = 82.45$ kPa, $E = P/(\gamma-1)$, and $T = 295^\circ\text{K}$. The left-hand boundary condition is a specified static temperature and pressure at $x = 0$ as a function of time. The right-hand boundary condition is a specified static pressure as a function of time.

The right-hand boundary condition that was used is $P_R = 82.45$ kPa (ambient pressure) for all time. The remaining flow variables (i.e., u , ρ , E) are computed using an inverse method of characteristics computation. Primitive variables are used, and the area is assumed constant at the right-hand boundary.

The left-hand boundary conditions are that the static temperature remains constant ($T_L = T_{\text{amb}} = 295^\circ\text{K}$), and the static pressure is a specified function of time. In the throttling process for an ideal gas it is the stagnation temperature that remains constant. But in this flow the velocities in the plenum chamber are so low that the static and stagnation temperatures are nearly equal, and the assumption that the static temperatures is constant introduces very little error. That assumption is also very convenient for applying the boundary condition.

The start-up of the supersonic blowdown wind tunnel is accomplished by the rapid opening of the control regulator valve. The prescribed pressure in the plenum chamber is reached in about one second. References 6 and 7 contain measured pressure-time plots for the static pressure just downstream of the control valve. The pressure-time plot shown in Fig. 4 is similar to the measured plots except that the time axis has been compressed. The compression of the time axis was done to reduce the computation time to reach steady-state operation. Check computations indicated that compressing the pressure rise time did not effect the general character of the

computed results.

The pressure-time curve in Fig. 4 is a combination of an exponential pressure rise from P_{amb} to P_1 , a quadratic curve from P_1 to P_2 , and an error function decay to the steady state pressure P_3 . The equations are

$$P = P_{amb} c_1^t, \quad 0 \leq t \leq t_1 \quad (47)$$

$$P = P_2 - C_2(t - t_2)^2, \quad t_1 \leq t \leq t_2 \quad (48)$$

$$P = P_3 + (P_2 - P_3) \exp(-(t - t_2)^2), \quad t > t_2 \quad (49)$$

when P is in Pascals and t is in milliseconds. The values of C_1 , C_2 and t_1 are chosen such that the slopes of the curve segments match at the nodal points P_1 and P_2 .

To obtain the pressure-time curve in Fig. 4 the values of $P_{amb} = 82.45$ kPa, $P_1 = 250$ kPa, $P_2 = 400$ kPa, $P_3 = 380$ kPa, and $t_2 = 200$ ms were used.

The method of characteristics is used with the known pressure and temperature at the left-hand boundary to compute the velocity at the boundary points.

F. Area Variation

The area variation of the Mach 3 trisonic wind tunnel was modeled as shown in Fig. 5. The figure is for a nondimensional area vs a nondimensional length. The reference area is the plenum area of 1.0723 m^2 . The reference length is 6.35 m . The figure represents a series of curves fit together to approximate the actual area variation of the trisonic tunnel at the U.S. Air Force Academy with the Mach 3 nozzle blocks. The nozzle throat area is $A/A_{ref} = 0.01918$ ($A = 0.02056 \text{ m}^2$). The throat is at $x/x_{ref} = 0.348$ ($x = 2.21 \text{ m}$). The test section area is $A/A_{ref} = 0.08664$ ($A = 0.0929 \text{ m}^2$). Both the area reduction due to the test article (wedge) in the test section and the area reduction due to the second throat (downstream of the test section) are modeled.

III. RESULTS

There are six different finite difference numerical algorithms that were tested for this problem. They are listed in Table 1. For each calculation 501 data points were used along the tunnel. The overall tunnel length was 6.35 m so that the points were spaced about 12.7 mm (1/2 inch.) apart. The driving pressure for each case was that shown in Fig. 4. The rise time for the pressure, after the control valve was opened, was modeled at 200 ms even though the measured values in References 6 and 7 are closer to one second. The shorter rise time was used to reduce the overall computer run time. Comparison with calculations using an 800 ms rise time indicated that the shorter rise time had very little effect on the character of the computed results.

For each run three different plots were generated. The first is a plot of the calculated static pressure in the tunnel at various times in the transient start-up. The static pressure is normalized by the driving pressure shown in Fig. 4. The position along the tunnel is normalized by the overall length of 6.35 m. Figures 6 thru 11 are the static pressures calculated by the six different numerical methods listed in Table 1.

The second type of plot is the calculated stagnation pressure in the tunnel at various times in the transient start-up. The stagnation pressures are dimensional (kPa). Figures 12 thru 17 are the stagnation pressure plots for the six different numerical methods listed in Table 1.

The third type of plot shows the computed absolute static pressure (kPa) in the test section as a function to time (ms). This type of plot is characteristic of the pressures that would be measured by a pressure transducer in the test section, and is the numerical analog of the measurements in Fig. 1. Figures 18 thru 22 are the test section pressure plots for five of the six numerical algorithms. There is no plot for the FB2 method. That method failed numerically and a test section plot was not

generated.

One objective of this report is to evaluate the six numerical algorithms. That evaluation consists of (a) comparison with each other, (b) comparison with the expected results, and (c) comparison with experimental data. Those comparisons are made in the following.

A. The LAX1 Method

Figure 6 shows the calculated static pressure (divided by the driving pressure) along the length of the wind tunnel at 58, 98, 138 and 253 ms after the control valve is opened. The rise time for the driving pressure is shown in Fig. 4. Five hundred points were used for the spatial grid.

Qualitatively the results are what is expected. The flow quickly chokes at the first throat ($x/x_{\max} = 0.348$) and a normal shock forms in the diverging portion of the Mach 3 nozzle blocks. The shock moves downstream, passes through the test section, through the second throat, and becomes established in the diverging portion of the wind tunnel exit. The pressure profile at 253 ms represents steady state operation.

Figure 12 shows the stagnation pressure along the tunnel at select times. The stagnation pressure was back calculated from the values of P , and ρu , and E . That is, P_o is calculated from the equations

$$P = (\gamma - 1)[E - (\rho u)^2 / (2\rho)] \quad (50)$$

$$M^2 = (\rho u)^2 / (\gamma \rho P) \quad (51)$$

$$P_o = P / \left(1 + \frac{\gamma - 1}{2} M^2 \right)^{\frac{\gamma}{\gamma - 1}} \quad (52)$$

From a philosophical viewpoint changes in the stagnation pressure curve at any time are the result of one of three different effects, namely (a) shock waves, (b) unsteady flow effects, or (c) numerically generated inconsistencies. The curves in Fig.

12 show all three effects. The variation from a constant value over the first 30% of the tunnel is primarily due to unsteady flow effects. The drop in the curves between $0.3 \leq x/x_{\max} \leq 0.4$ is due to the inability of the numerical algorithm to properly calculate flows with large area variations when the flow is choked. The stagnation pressure drops across the shock wave are obvious.

Figure 18 shows the calculated test section pressure as a function of time. The result appears to be qualitatively correct, based on the measured results shown in Fig. 1. Notice that the measured pressure spike (Fig. 1) that passed through the test section just before steady state operation was reached is not present in the numerical calculations. In fact, that measured pressure transient was not produced by any of the numerical algorithms.

With regard to the LAX1 calculation the following observations are made:

1. The pressure profile thru the nozzle blocks up to the shock location is essentially identical to the theoretical one-dimensional steady state profile for a choked flow. The theoretical curve is not shown on the figure.
2. The moving shock wave is "captured" by the method, but is "smeared" over several grid points. There is no ringing associated with the shock capturing.
3. The shock speed through the test section is about 30 m/s. This compares favorably with the measured shock speed of about 38 m/s from the Schlieren photographs in Fig. 2.
4. The method is robust, first order, and computationally efficient.
5. The calculated stagnation pressure losses near the nozzle throat are an indication of numerical inaccuracies. Quantative results should be viewed as containing considerable error.
6. The method generates artificial flow.

B. The LAX2 Method

The LAX2 results are shown in Figs. 7, 13, and 19. The computed results appear to be qualitatively correct, and are similar to the LAX1 results. The major differences are a somewhat slower shock speed through the test section (about 22 m/s) and a different stagnation pressure variation in the nozzle throat section.

C. The FB1 Method

The FB1 results are shown in Figs. 8, 14, and 20. The results are qualitatively similar to those obtained from the LAX1 and LAX2 methods. The results are an improvement over the LAX methods in that the shock is captured in fewer grid points (about 2 or 3), and the stagnation pressures remain constant through the rapid area change region of the nozzle throat. The method does show some "ringing" across the shock, a feature that experience has shown can be corrected by introducing some artificial damping into the numerical algorithm. The features of the FB1 algorithm are summarized below.

1. The static pressure profile thru the nozzle blocks up to the shock location is essentially identical to the theoretical profile for a steady, one-dimensional choked flow through the area variation shown in Fig. 5.
2. The moving shock wave is captured by the method in two or three grid points.
3. There is some "ringing" (pressure overshoot) both ahead of and behind the shock. Experience with MacCormack's method for unsteady one-dimensional flows indicates that the pressure overshoot can be almost eliminated by introducing some artificial (numerical) damping.
4. The magnitude of the calculated static pressure ratio and stagnation pressure ratio across the shock are close to the values for a stationary normal shock in steady flow where the shock strength is determined from the area ratio.

5. The calculated shock speed thru the test section is about 40 m/s which compares very favorably with the measured shock speed of about 38 m/s from the Schlieren photographs in Fig. 2.

6. The method is second order, does not artificially generate flow velocities for the no flow initial conditions, and is computationally efficient.

7. Overall the FB1 method is the preferred method of the six algorithms that were tested. The method is believed to be quantitatively accurate within the limits of the one-dimensional flow approximation.

8. The FB1 method did not reproduce the short duration pressure spikes associated with the shock passage, as shown in Fig. 1.

D. The FB2 Method

The FB2 results are shown in Figs. 9 and 15. The results at 50 ms, 84 ms and 118 ms are very similar to those for the FB1 method. However the ringing associated with the shock capturing resulted in a negative absolute pressure and density so that the computer calculations "crashed". As a consequence there is no test section pressure plot for this method. It is probable that the introduction of numerical damping across the shock would correct the pressure overshoot so that results comparable to the FB1 results could be obtained.

E. The MOC1 Method

The results for the MOC1 method are shown in Figs. 10, 16, and 21. From Fig. 10 it appears that the MOC1 method correctly computes, at least qualitatively, the shock formation and the initial shock motion through the diverging portion of the nozzle blocks. However the method calculates a "blocked" flow passage where the flow chokes at the second throat and traps the initial shock wave in the divergent section behind the first throat. Increasing the area of the second throat did not

produce an unblocked flow. This is disturbing since conservative calculations for the minimum area of the second throat indicate that the flow should not be blocked.

The method appears to capture shocks in a single grid point without ringing. It is computationally inefficient with regard to computer time. The method also generates bumps in the stagnation pressure profiles near the first throat, as can be seen in Fig. 16.

F. The MOC2 Method

The results for the MOC2 method are shown in Figs. 11, 17 and 22. They are similar to those for the MOC1 method. The calculated stagnation pressure variation near the throat of the nozzle blocks is a slightly different shape, but both represent a deficiency in the algorithms. The calculations indicate that the flow will block, which is contrary to the experimental result.

IV. SUMMARY AND RECOMMENDATIONS

One of the objectives of the work was to determine whether the method of characteristics in the newly formulated conservation variable form could be used effectively for shock capturing in a one dimensional, unsteady, supersonic flow with area change. The results for both the MOC1 and MOC2 methods indicate good shock capturing ability with no ringing. However, the stagnation pressure variation due to area change indicates a problem with the algorithm when strong area gradients are present. Further work needs to be done to resolve that discrepancy. Also, further investigation into the reasons the MOC methods predict a blocked flow is needed.

The FB1 method using MacCormack's algorithm appeared to give the best overall numerical results. However, even that method gave no indication of the source of the pressure spikes observed in the experimental data. It is clear that the computational methods are deficient, but the source of that deficiency is not clear. Certainly the

flow is not one dimensional as can be seen by the oblique shock pattern in Fig. 2. Also, the effects of viscosity on the transient flow have been neglected.

Since the source of the transient pressure spikes is of considerable interest, some further investigation into their source, and how to model them numerically, is undoubtedly justified.

V. ACKNOWLEDGEMENTS

Funding for this work was provided by the U.S. Air Force, Office of Scientific Research, Bolling AFB, DC, as part of their Research Initiation Program. That program is administered by Universal Energy Systems, Inc., 4401 Dayton-Xenia Road, Dayton, OH 45432, under contract #F49620-85-C-0013/SB5851-0360. The work was performed under UES Project 760, Purchase Order S-760-7MG-071 to Purdue University, Division of Sponsored Programs, PRF #530-1288-0803. The author acknowledges with appreciation the financial support of AFOSR and the support and encouragement received from the personnel at the Frank J. Seiler Research Laboratory and the Aero Department of the U.S. Air Force Academy. Major John Walker and Lt. Col. Randy Stiles deserve special mention.

VI. NOMENCLATURE

a	acoustic speed (see Eq. (9))
A	area
\mathbf{A}	transformation matrix defined by Eq. (22)
b_1, b_2, b_3	constants
B_1, B_2, B_3	coefficients (see Eq. (24))
C_1, C_2	constants (see Eqs. (47) and (48))
E	energy dependent variable (see Eq. (21))
\mathbf{F}_1	vector of dependent variables defined by Eq. (5)
\mathbf{F}_2	vector of dependent variables defined by Eq. (13)
g_i	components of \mathbf{G} vector
\mathbf{G}_1	vector of nonhomogeneous terms defined by Eq. (11)
\mathbf{G}_2	vector of nonhomogeneous terms defined by Eq. (14)
\mathbf{I}	the identity matrix
M	Mach number
P	static pressure
P_o	stagnation pressure
r_{ij}	elements of \mathbf{R} matrix
\mathbf{R}	coefficient matrix
t	time (independent variable)
t_1	constant
t_2	constant (200 ms)
t_i	components of \mathbf{T} vector
T	static temperature
T_o	stagnation temperature
\mathbf{T}	vector of right-hand-side terms (see Eq. (36))
u	gas velocity
w_i	components of \mathbf{W} vector
\mathbf{W}_1	vector of dependent variables (see Eq. (1))
\mathbf{W}_2	vector of dependent variables (see Eq. (3))
x	independent space variable
x_{\max}	the length of the wind tunnel (6.35 m)
\mathbf{X}	solution vector (see Eq. (36))
γ	specific heat ratio
∂	partial derivative operator
λ	eigenvalue
$\lambda_1, \lambda_2, \lambda_3$	slope of characteristic curve in the (x, t) -plane
ρ	density (dependent variable)
$\sigma_1, \sigma_2, \sigma_3$	multipliers

Subscripts

amb	ambient value
C	corrector value
i	evaluated at space node i
i+1	evaluated at space node i+1
i-1	evaluated at space node i-1
L	evaluated at left-hand boundary
ref	reference value
R	evaluated at right-hand boundary
t	partial derivative with respect to time

x partial derivative with respect to space

Superscripts

n evaluated at time level n
 $\underline{n+1}$ evaluated at time level $n+1$
 $\overline{n+1}$ predictor value
 T transpose of a vector

VII. REFERENCES

1. Walker, J.M. and Chou, D.C., "Forced Unsteady Vortex Flows Driven by Pitching Airfoils," AIAA Paper 87-1331.
2. Helin, H.E. and Walter, J.M. "Interrelated Effects of Pitch Rate and Pivot Point on Airfoil Dynamic Stall," AIAA Paper 85-0130.
3. Walker, J.M., Helin, H.E., and Chou, D.C., "Unsteady Surface Pressure Measurements on a Pitching Airfoil," AIAA Paper 85-0532.
4. Walker, J.M., Helin, H.E., and Strickland, J.H., "An Experimental Investigation on an Airfoil Undergoing Large Amplitude Pitching Motions," AIAA J., Vol. 23, No. 8, Aug. 1985, pp 1141-1142.
5. Thompson, H.D., "The Effect of Transient Shock Waves in a Mach 3 Flow," 1987 USAF-UES Summer Faculty Research Report, 8 September 1987.
6. Causey, W., Hinkle, S., and Hamner, B., "USAF Academy Trisomic Wind Tunnel Starting Load Investigation," USAFA Department of Aeronautics Report, 3 May 1988.
7. Laughauser, D.B. and Montoya, J.C., "USAF Academy Trisomic Wind Tunnel Starting Loads," USAFA AERO 450 Report, 23 November 1987.

Table 1: Finite Difference Algorithms

Designation	Description	Figure
LAX1	The Lax algorithm with the dependent variables ρA , ρAu , and EA .	6,12,18
LAX2	The Lax algorithm with the dependent variables ρ , ρu and E .	7,13,19
FB1	The MacCormack (forward-backward) algorithm with dependent variables ρA , ρAu and EA .	8,14,20
FB2	The MacCormack (F-B) algorithm with dependent variables ρ , ρu and E .	9,15
MOC1	The method of characteristics algorithm with dependent variables ρA , ρAu and EA .	10,16,21
MOC2	The method of characteristics algorithm with dependent variables ρ , ρu and E .	11,17,22

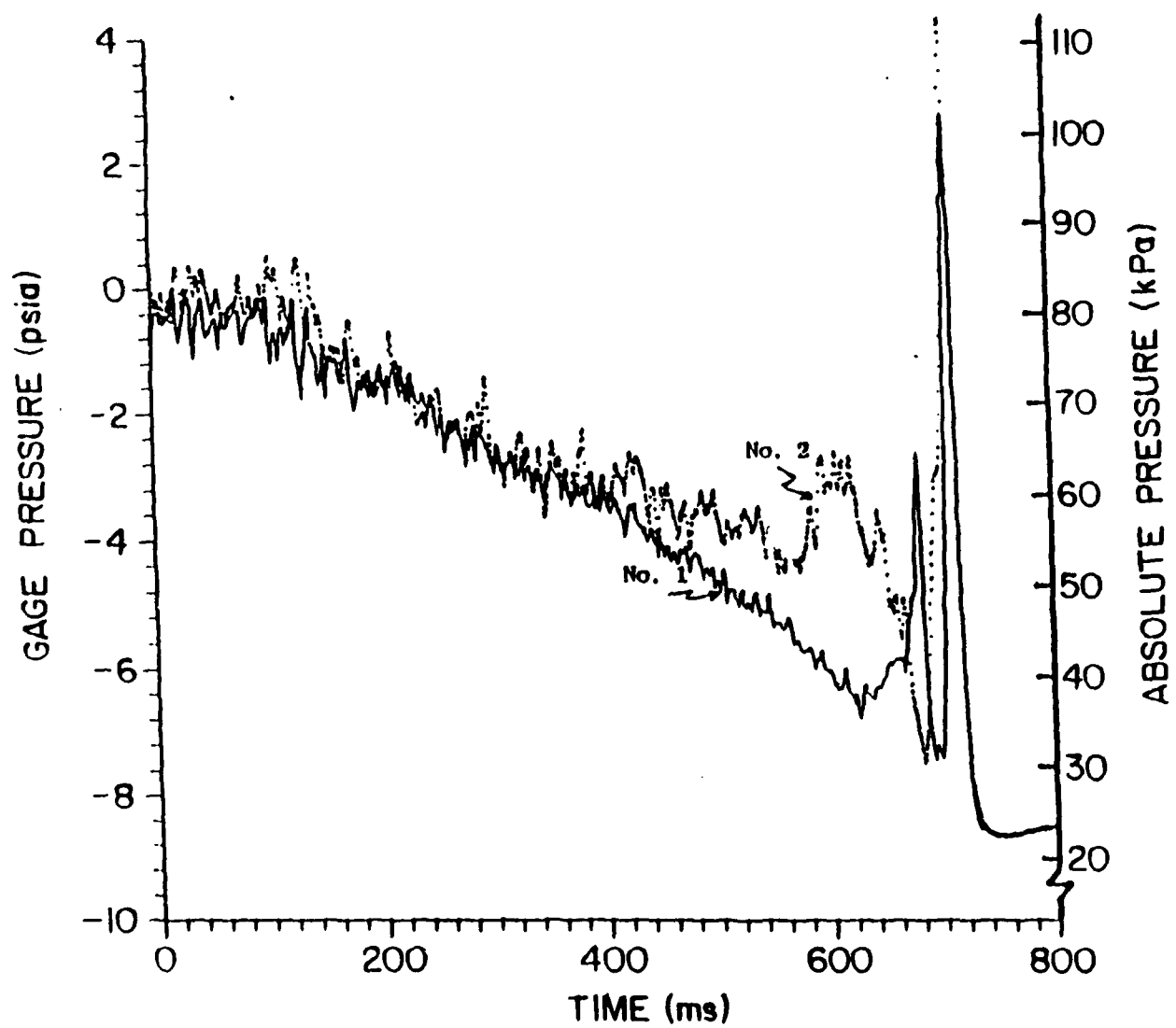


Figure 1: Experimental test section pressures.

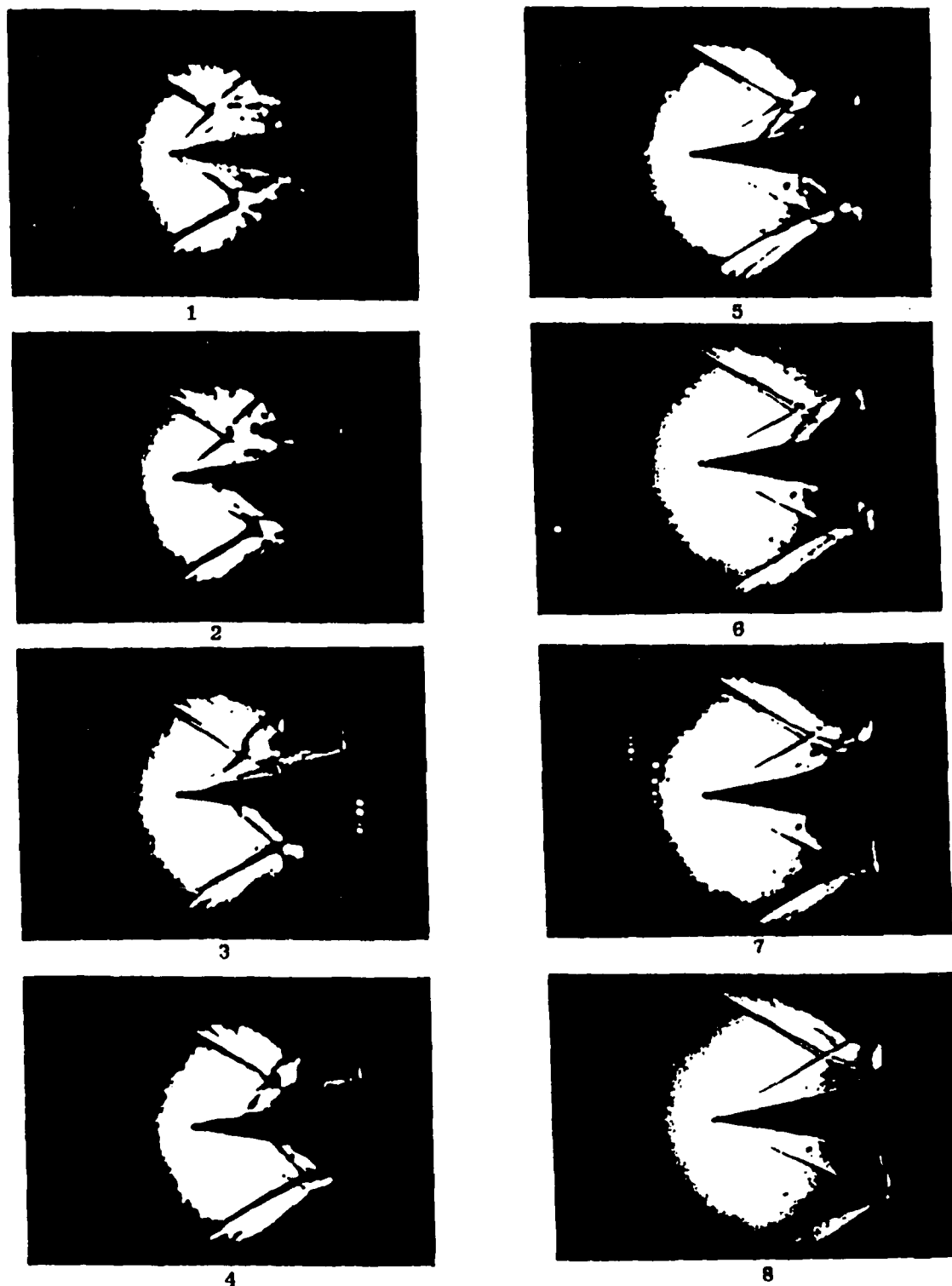


Figure 2: Schlieren pictures at 0.5 millisecond intervals of the transient start-up shocks in a Mach 3 wind tunnel.

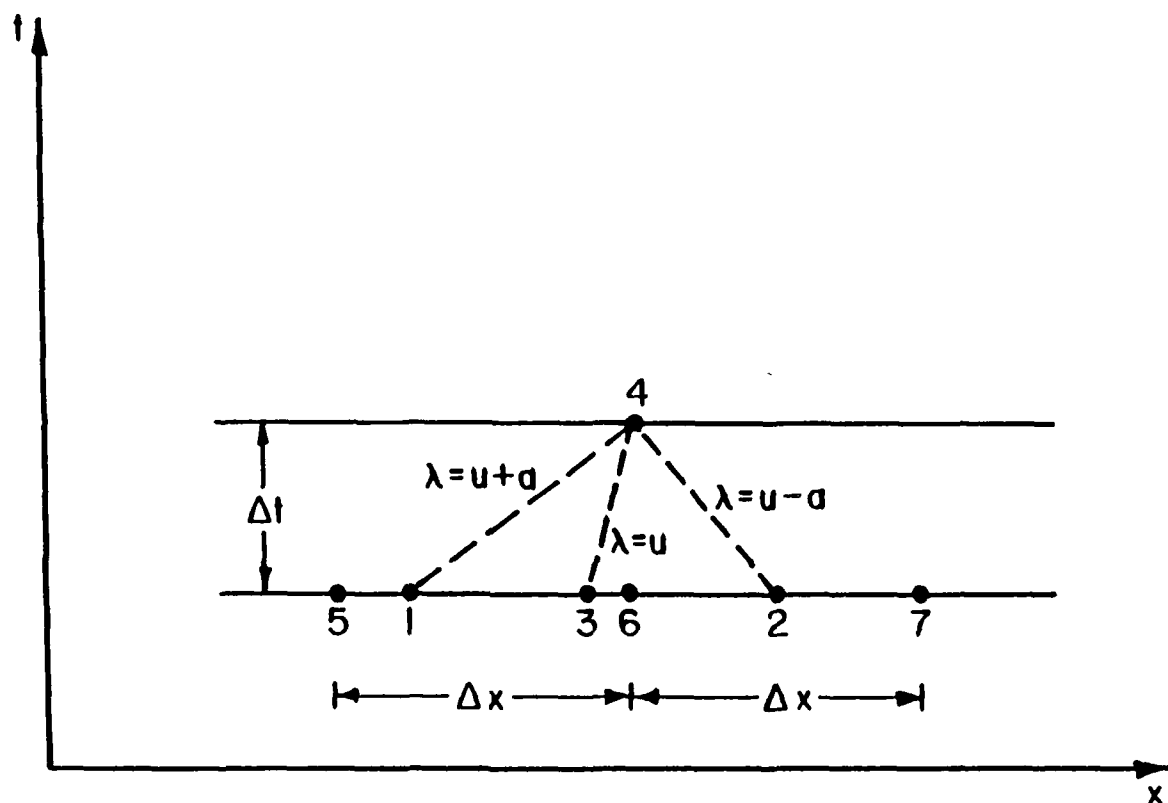


Figure 3: Grid point numbering scheme for the inverse marching method of characteristics.

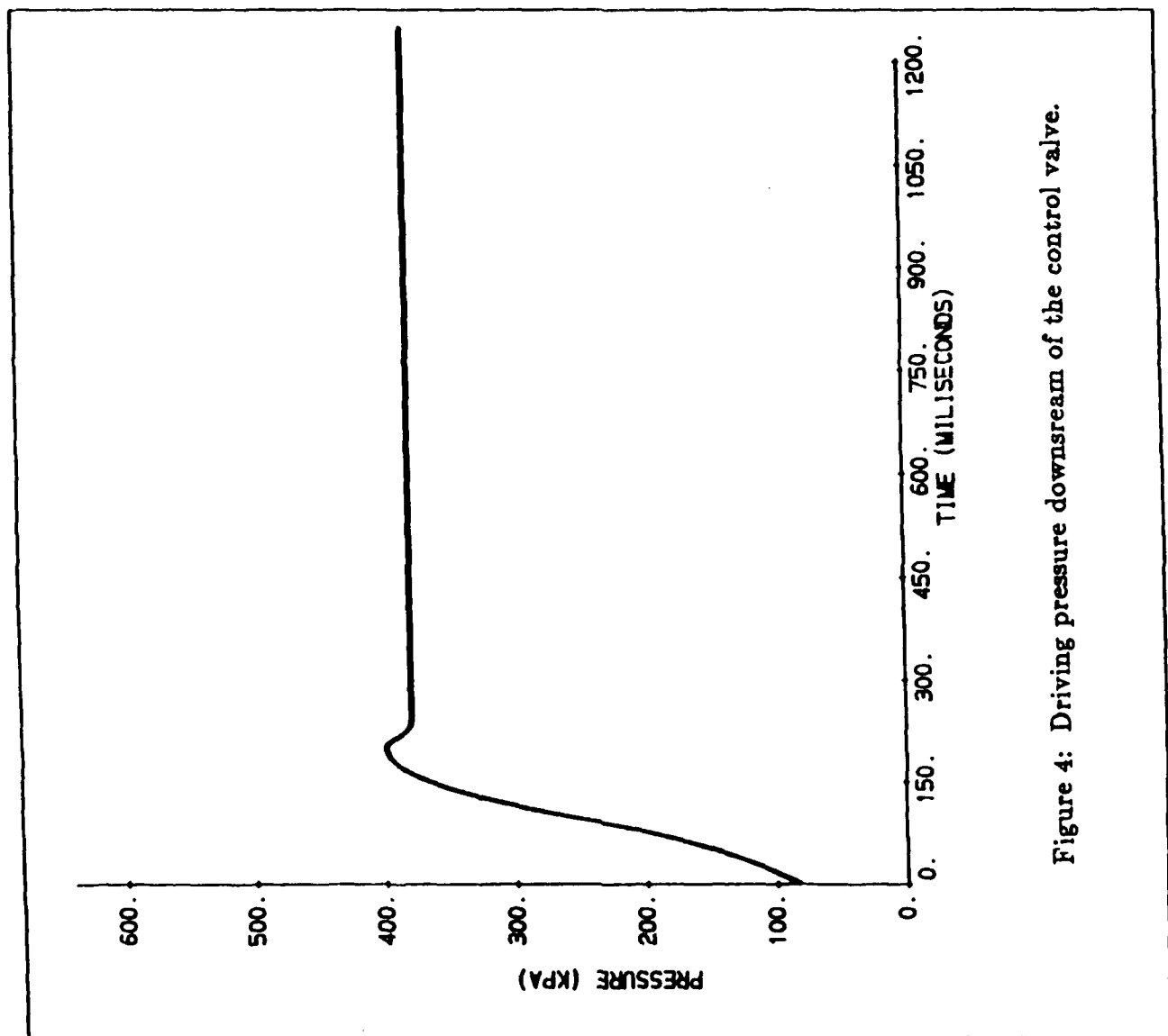


Figure 4: Driving pressure downstream of the control valve.

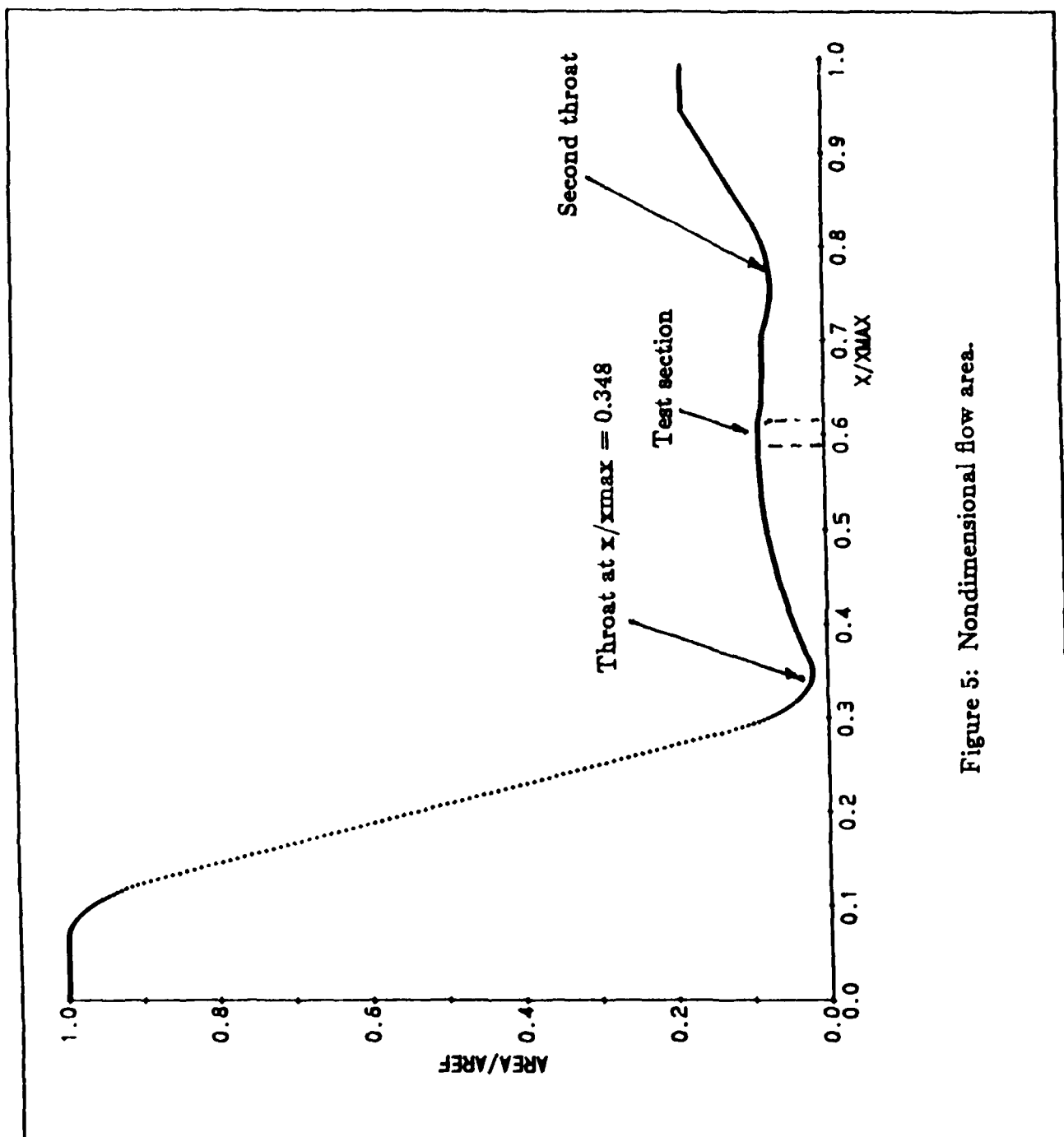


Figure 5: Nondimensional flow area.

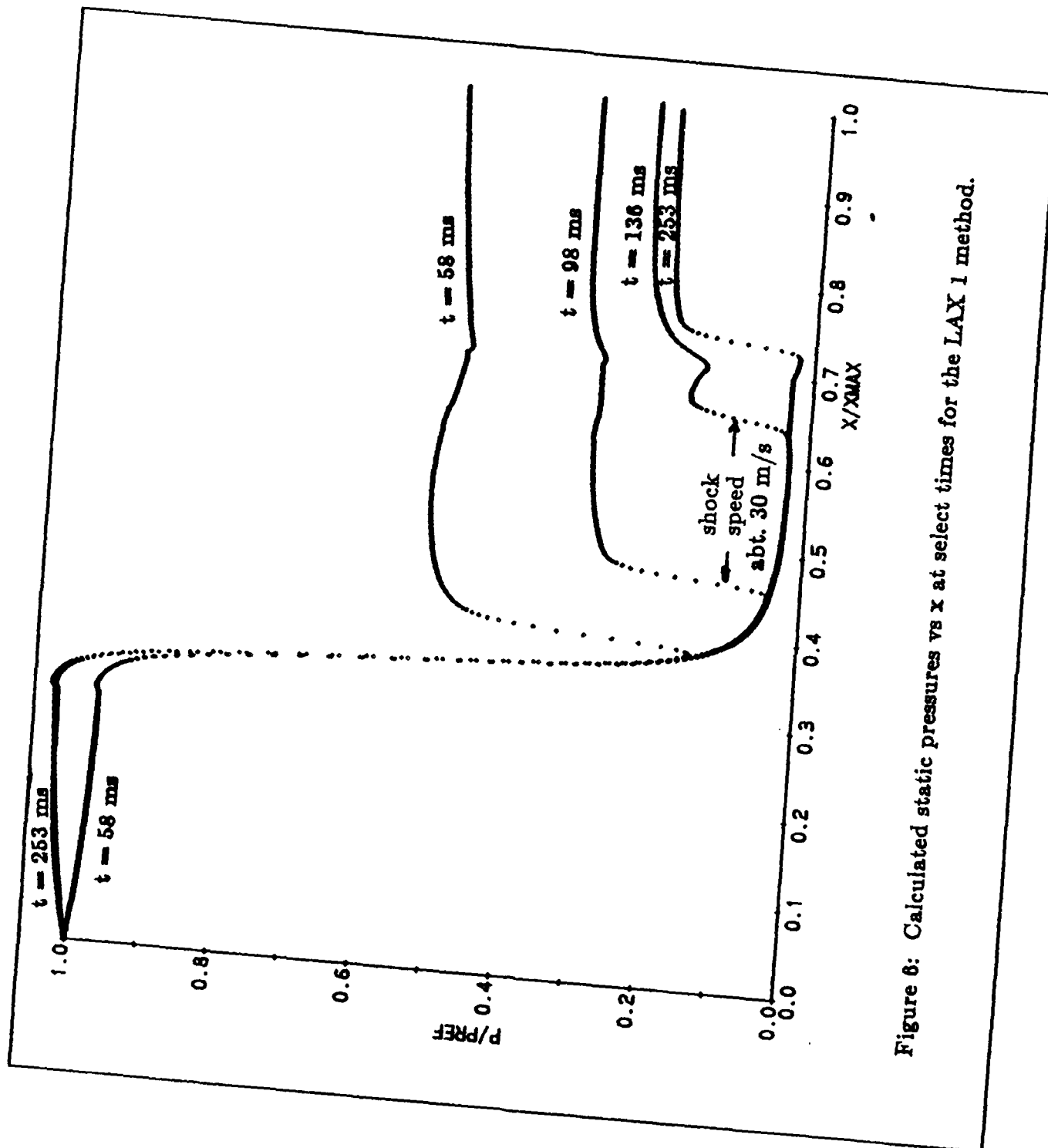


Figure 6: Calculated static pressures vs x at select times for the LAX 1 method.

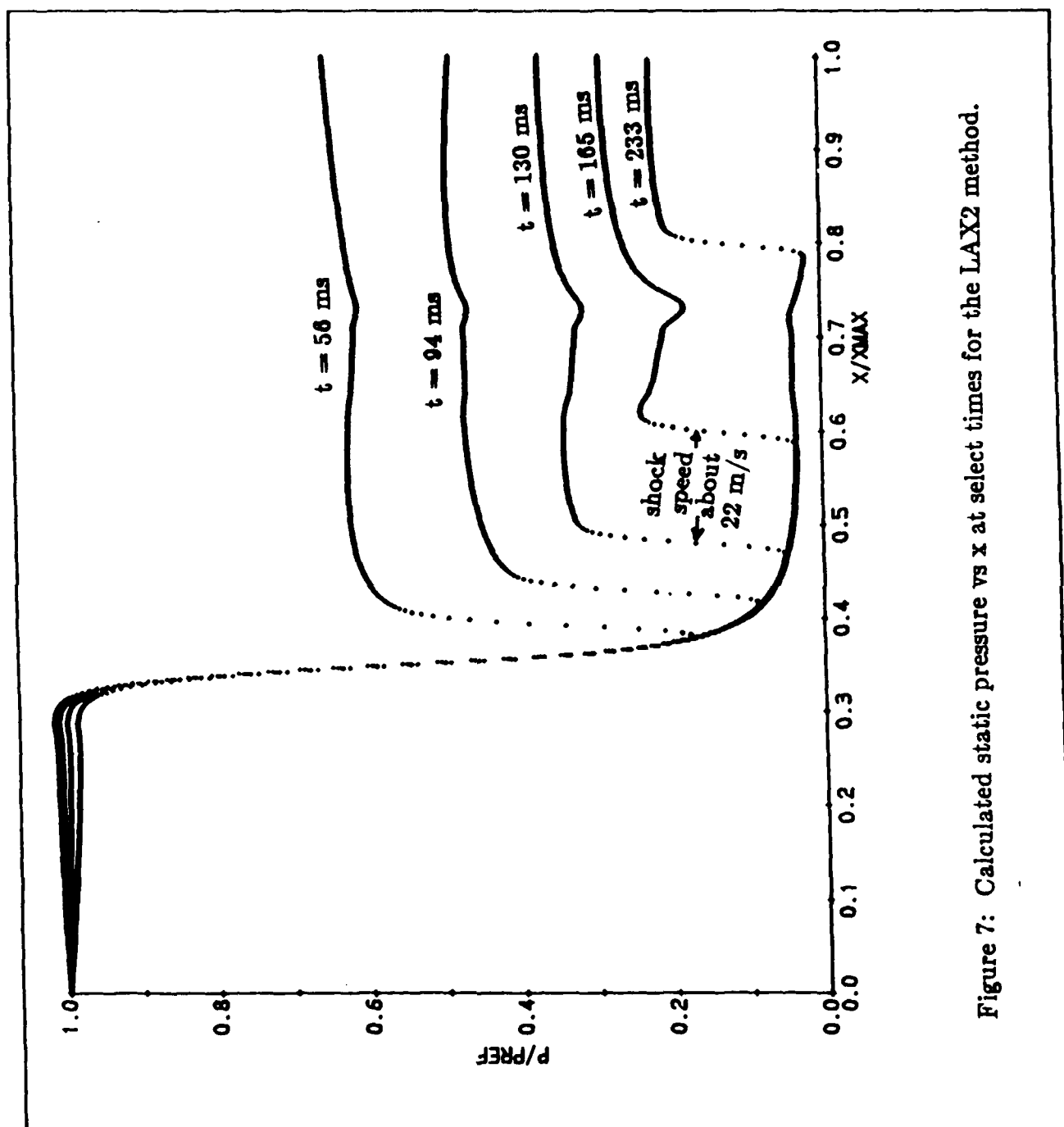


Figure 7: Calculated static pressure vs x at select times for the LAX2 method.

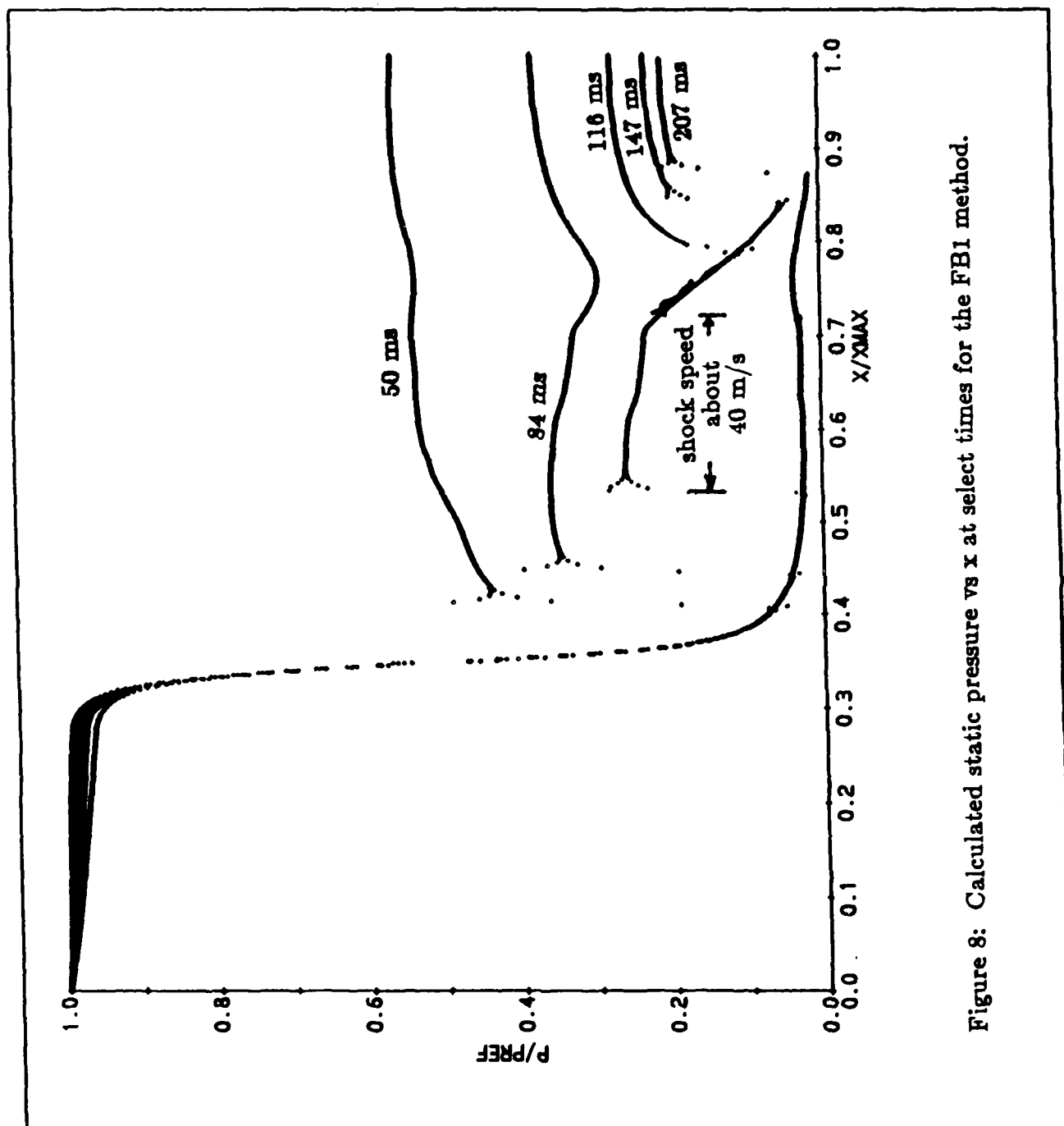


Figure 8: Calculated static pressure vs x at select times for the FBI method.

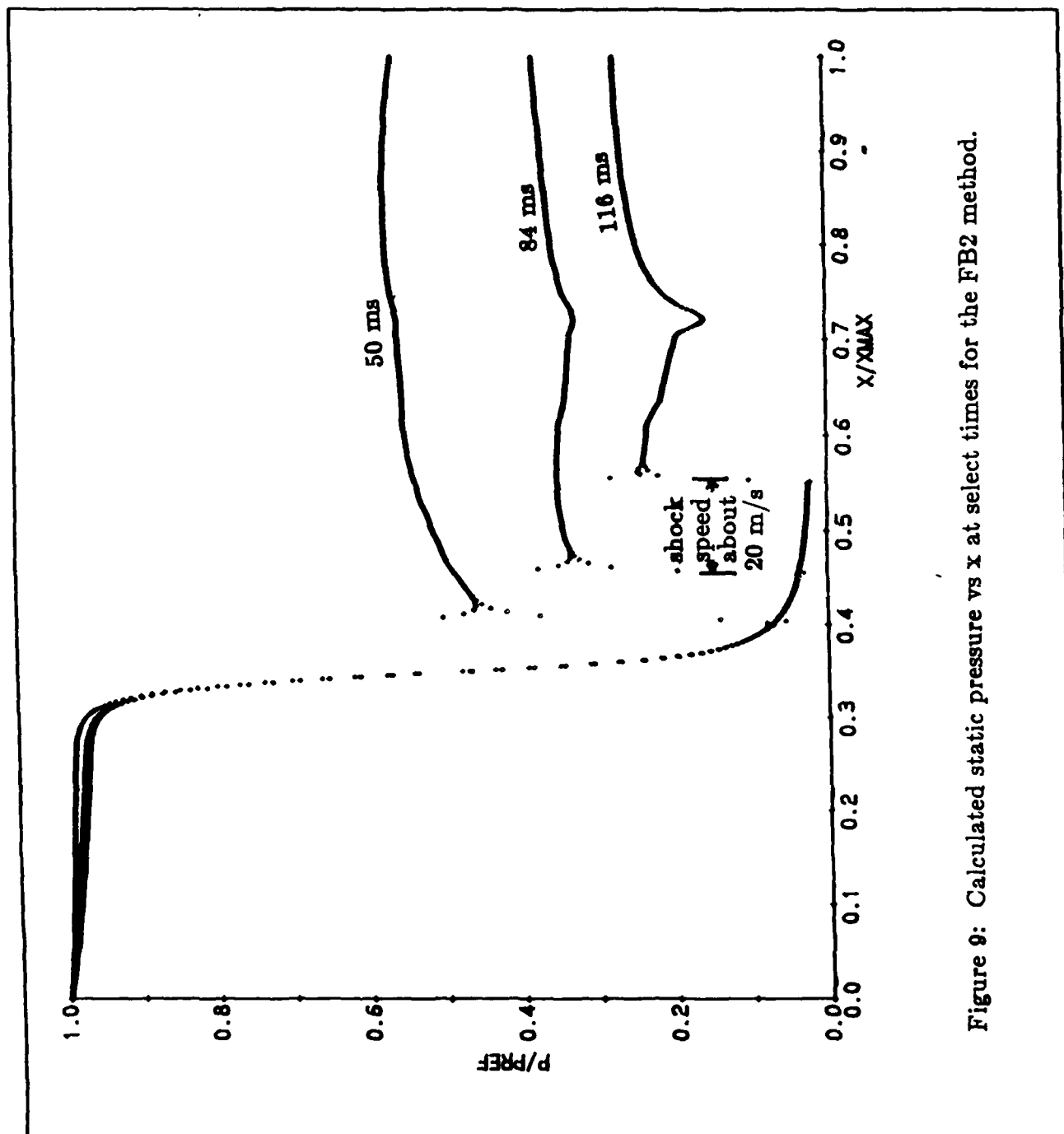


Figure 9: Calculated static pressure vs x at select times for the FB2 method.

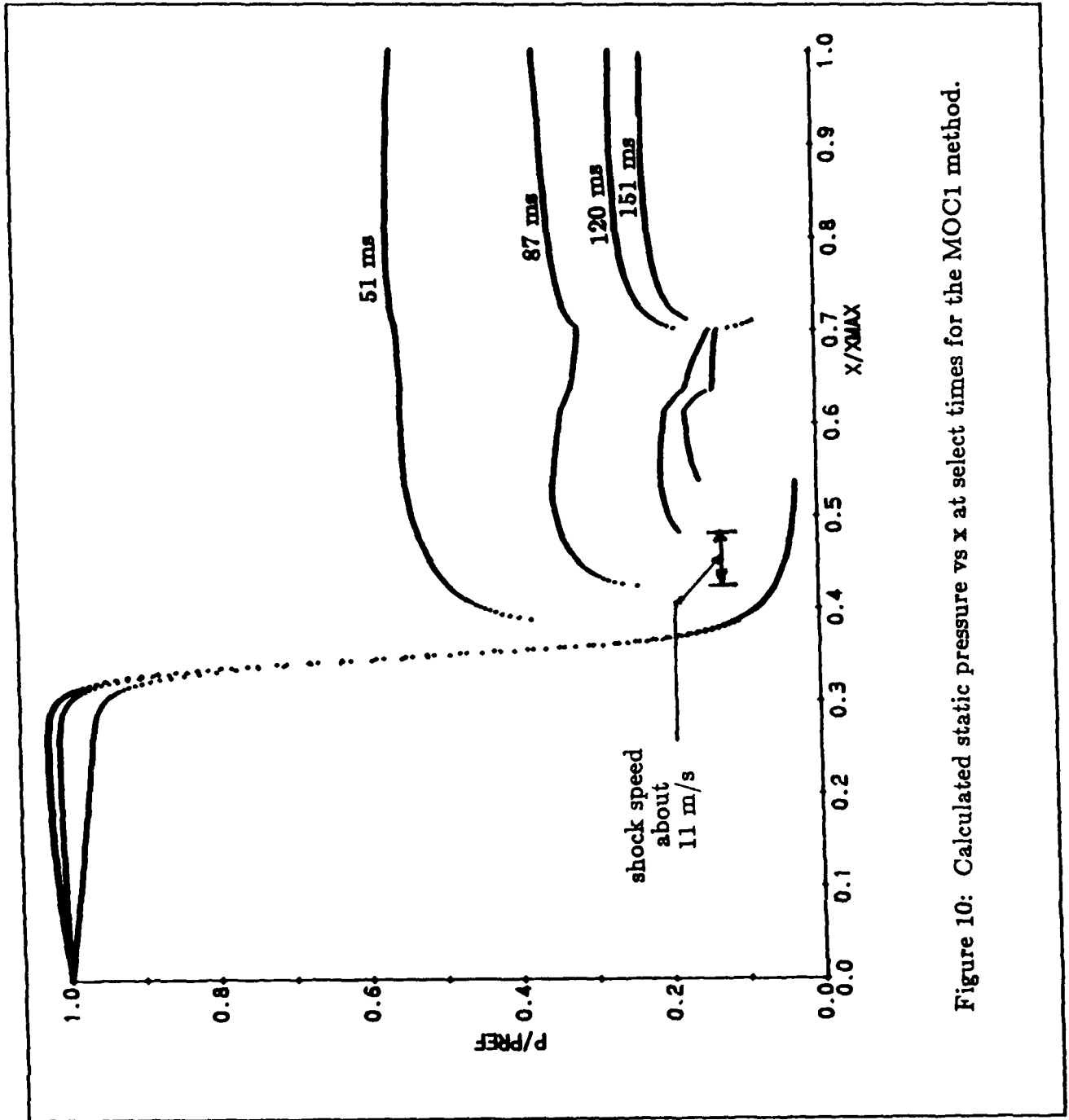


Figure 10: Calculated static pressure vs x at select times for the MOC1 method.

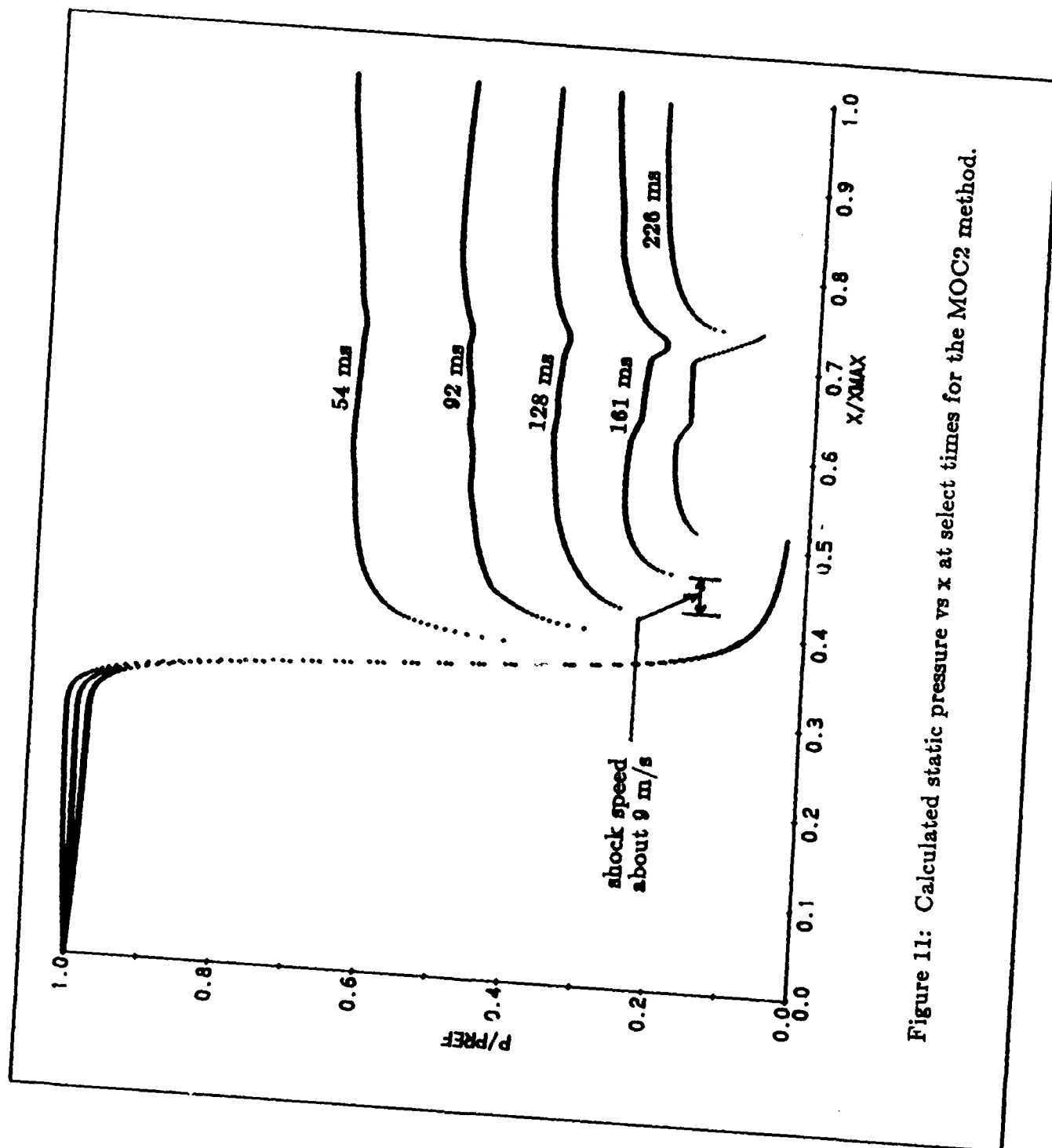


Figure 11: Calculated static pressure vs x at select times for the MOC2 method.

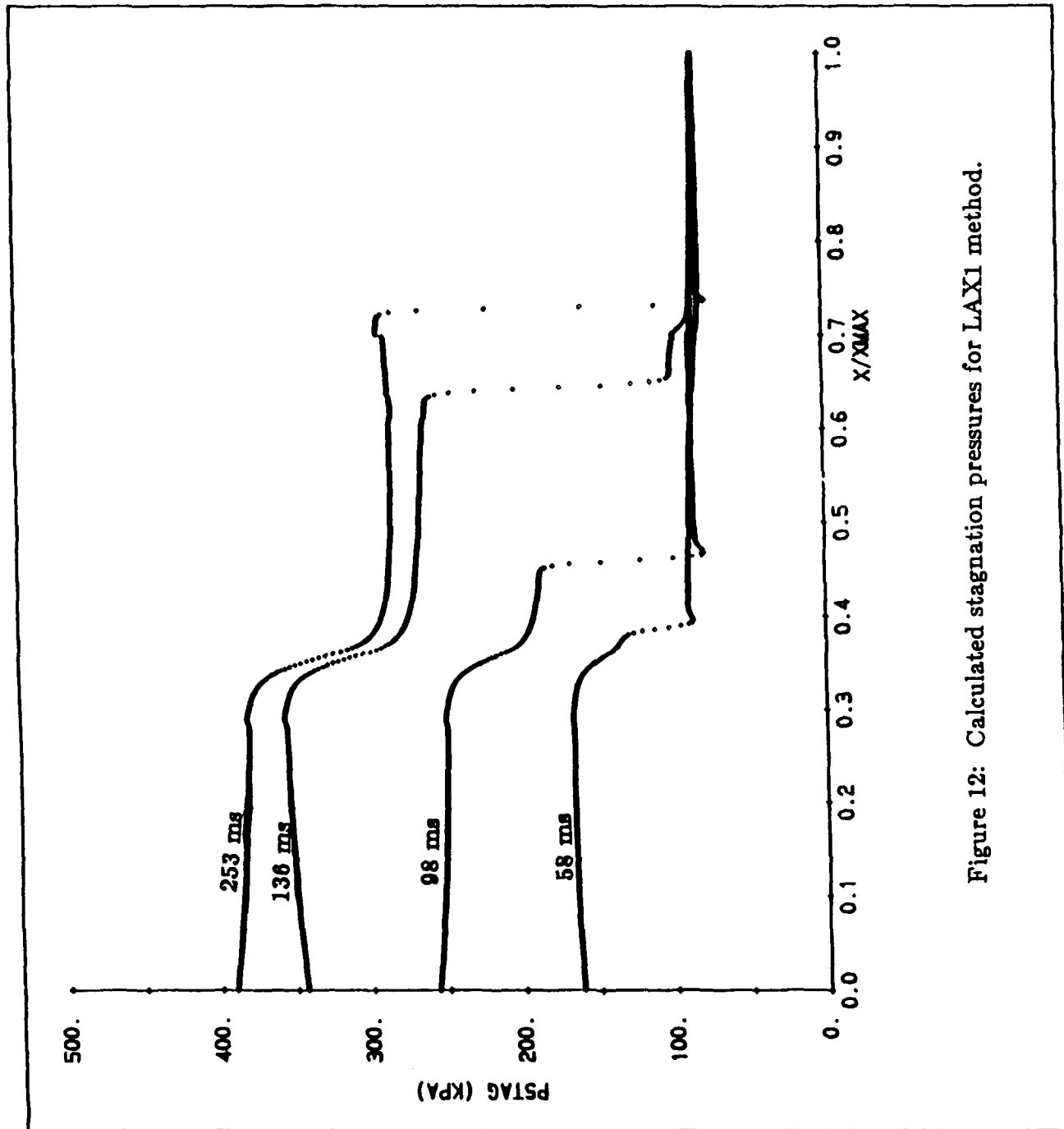


Figure 12: Calculated stagnation pressures for LAX1 method.

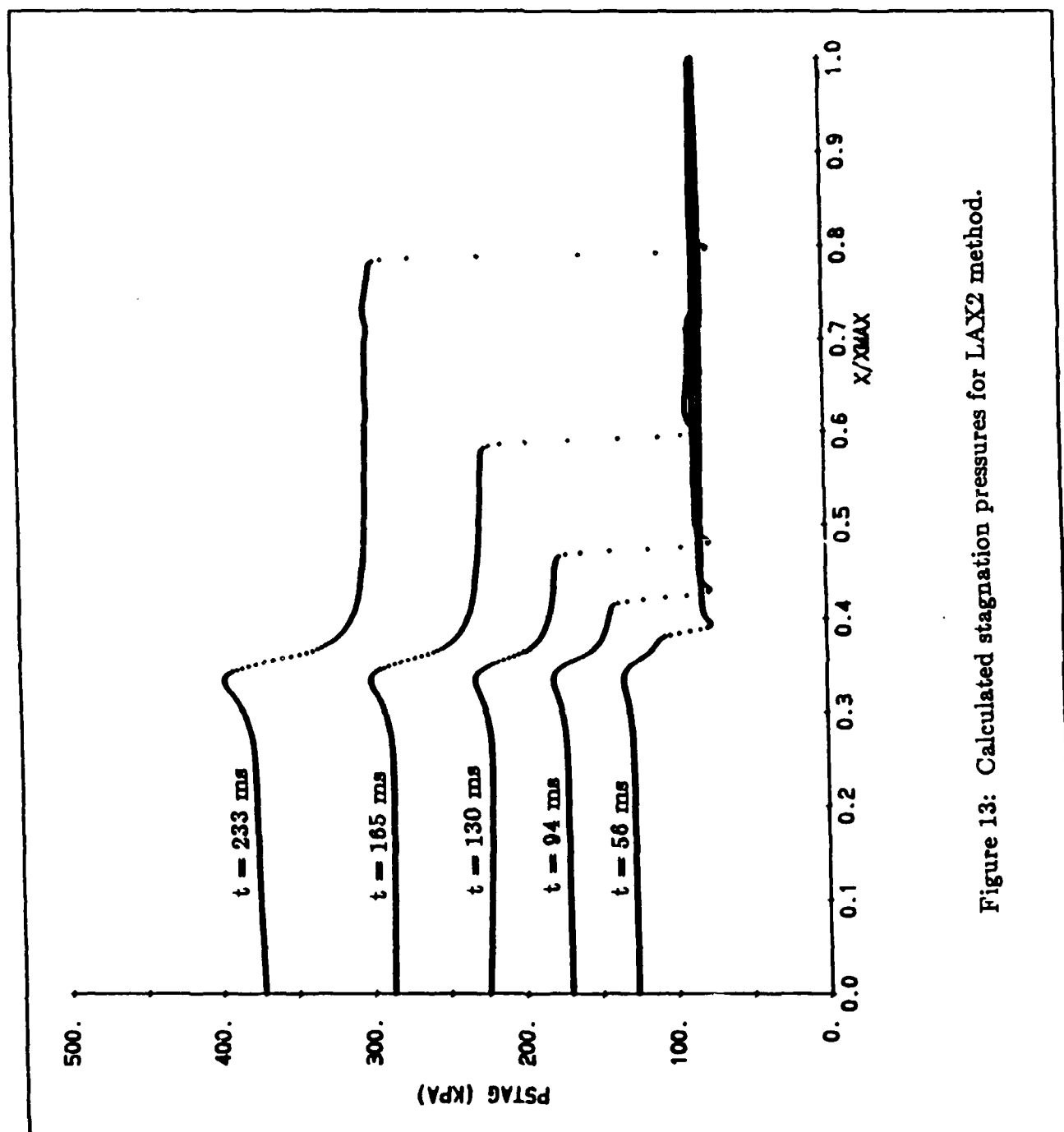


Figure 13: Calculated stagnation pressures for LAX2 method.

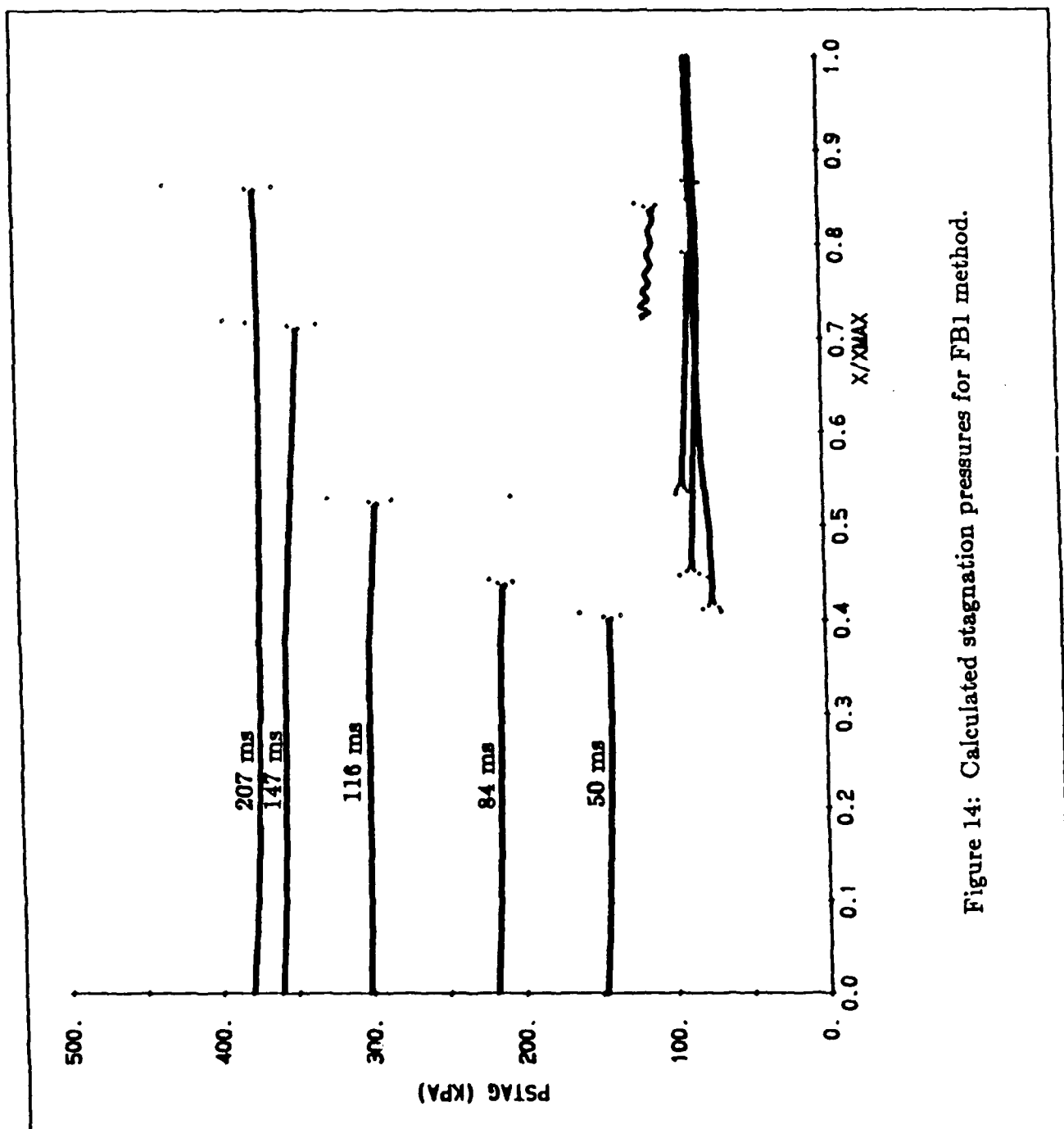


Figure 14: Calculated stagnation pressures for FB1 method.

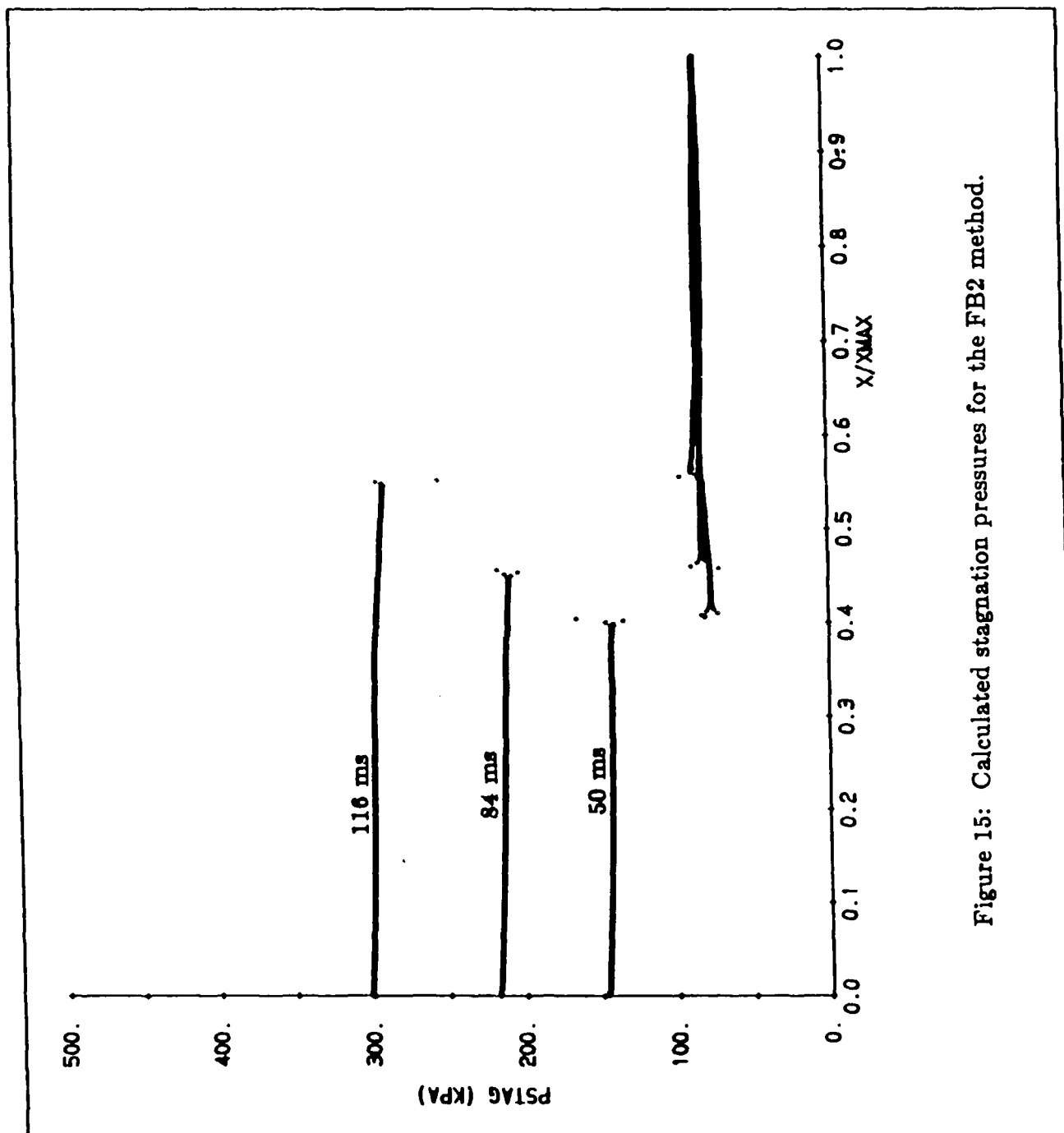


Figure 15: Calculated stagnation pressures for the FB2 method.

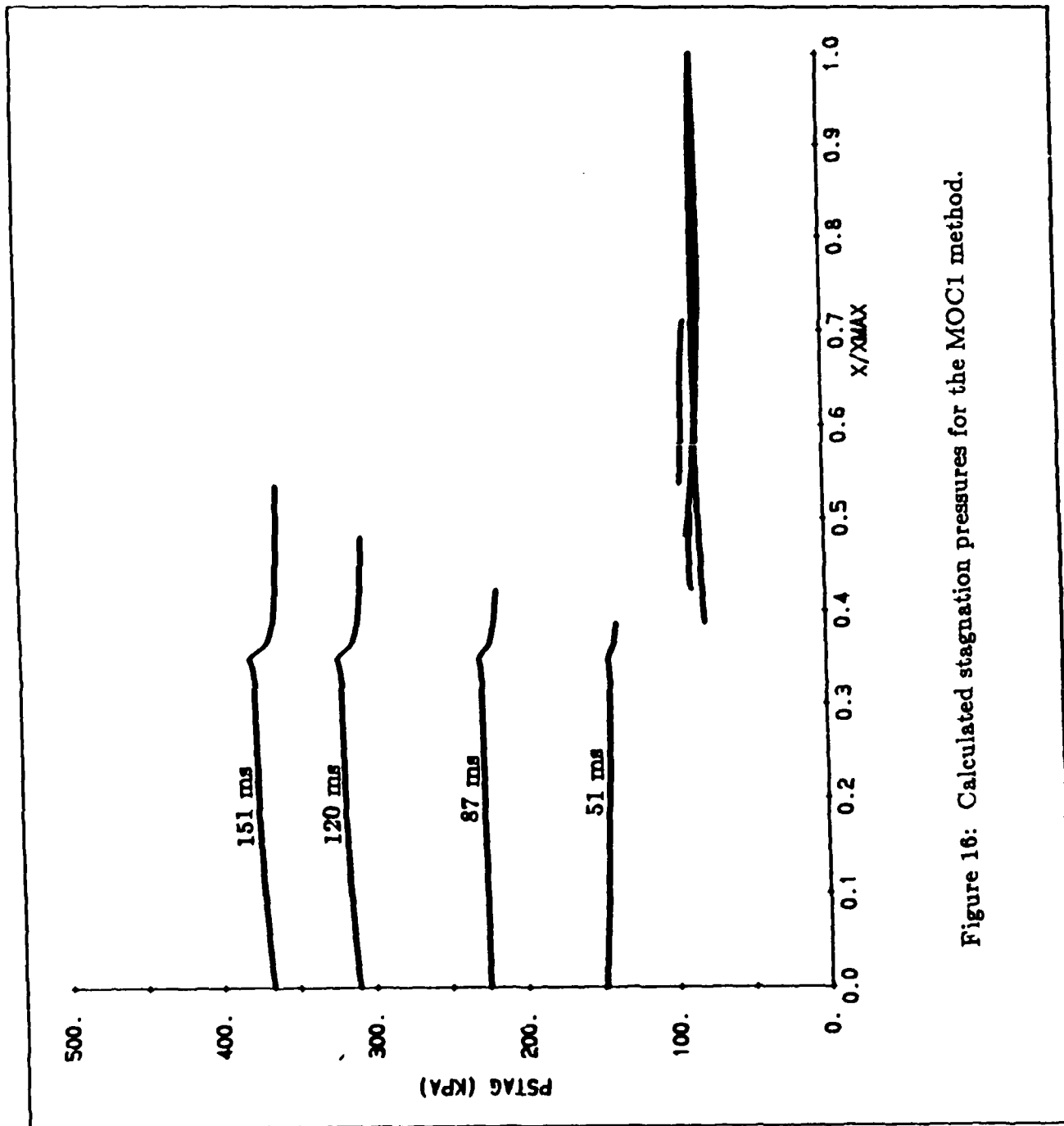


Figure 16: Calculated stagnation pressures for the MOC1 method.

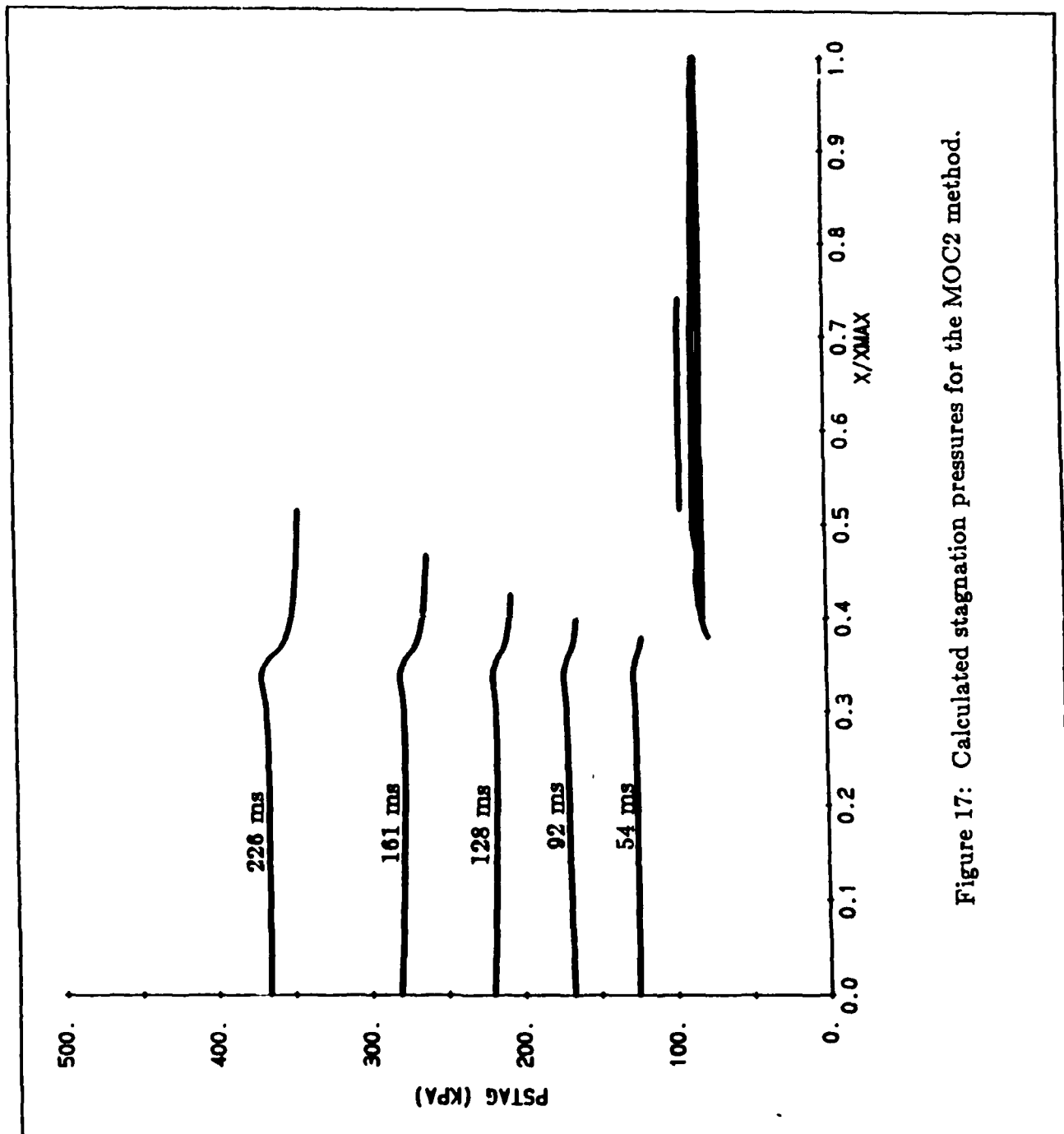


Figure 17: Calculated stagnation pressures for the MOC2 method.

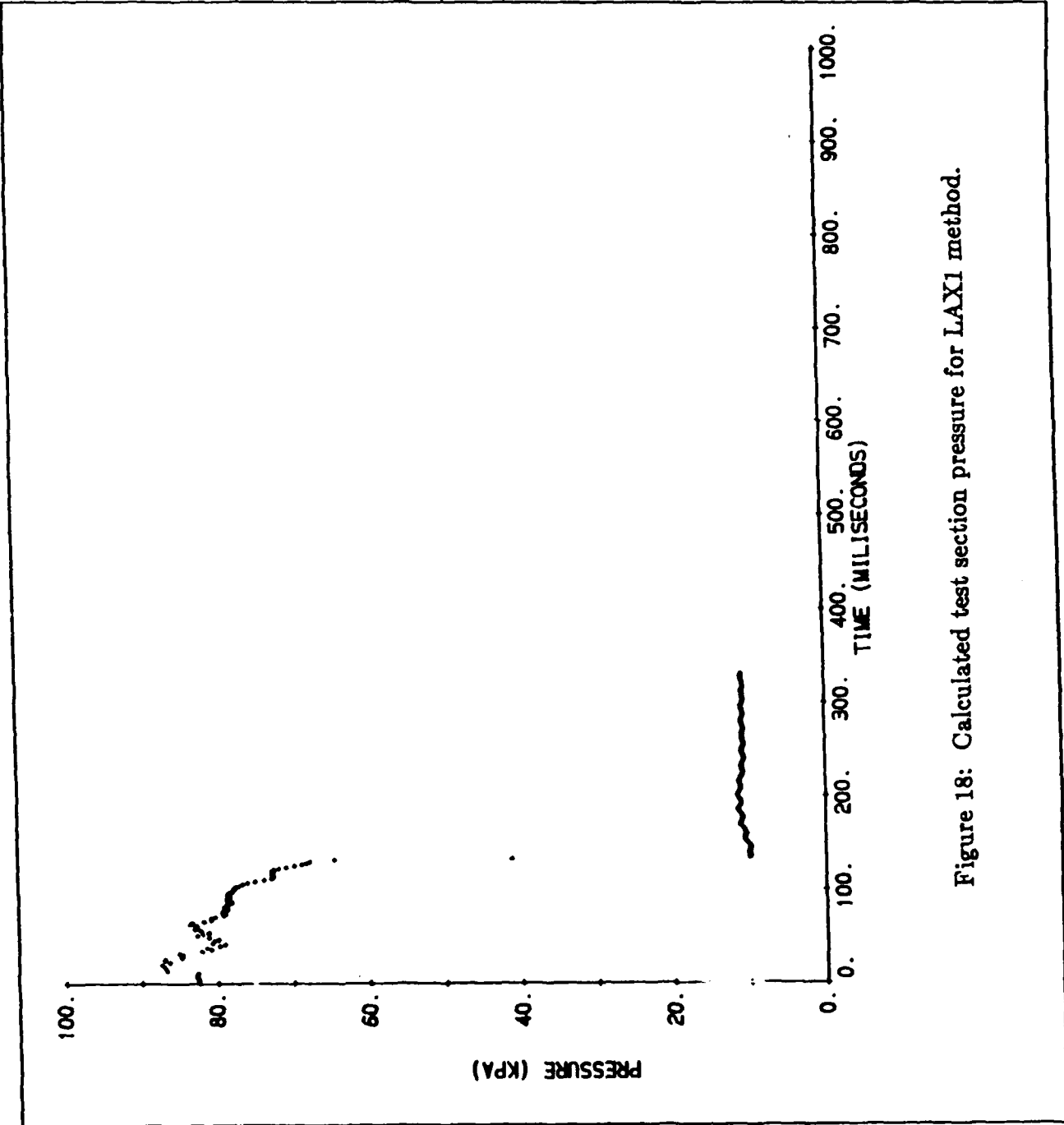


Figure 18: Calculated test section pressure for LAX1 method.

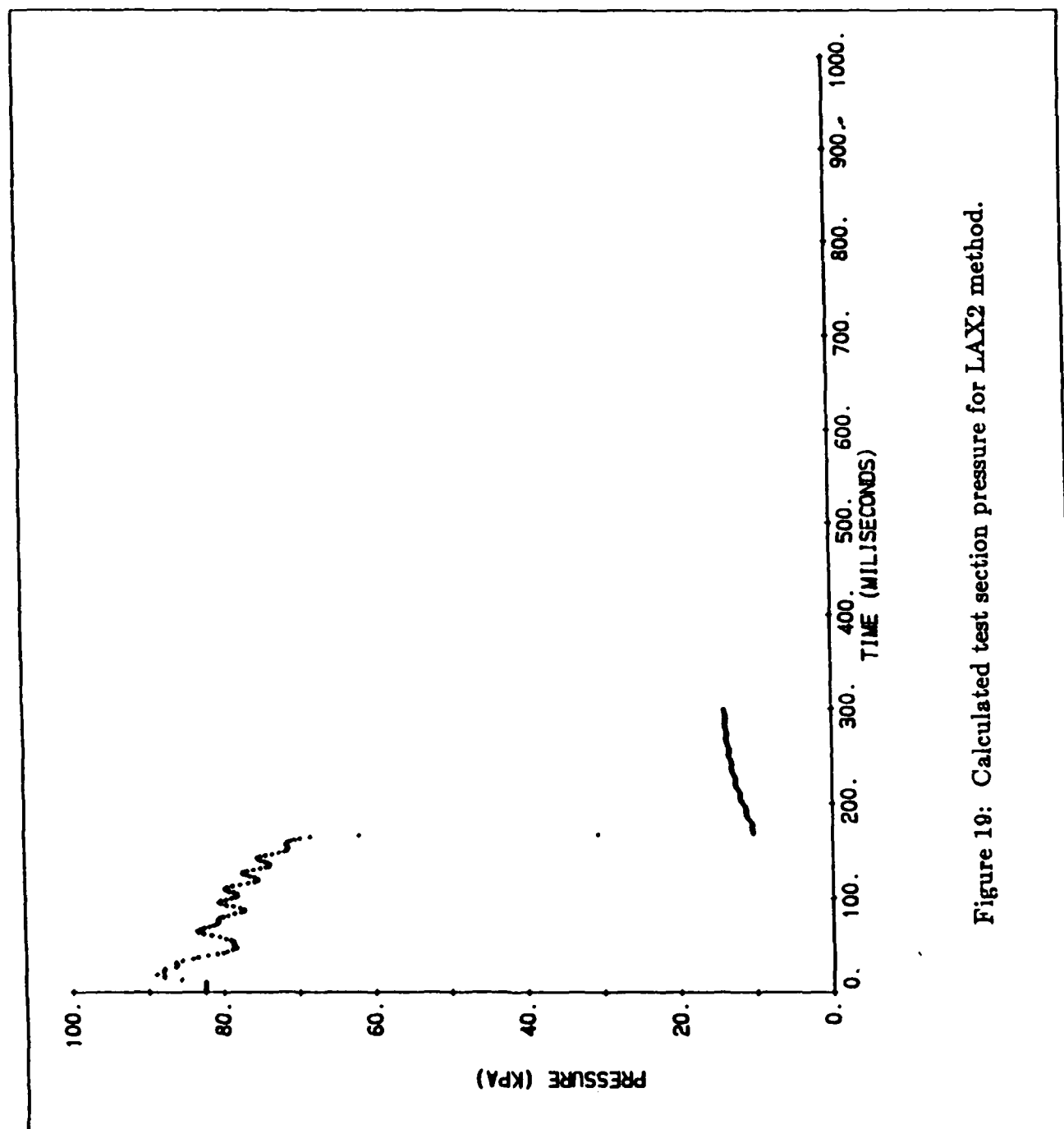


Figure 19: Calculated test section pressure for LAX2 method.

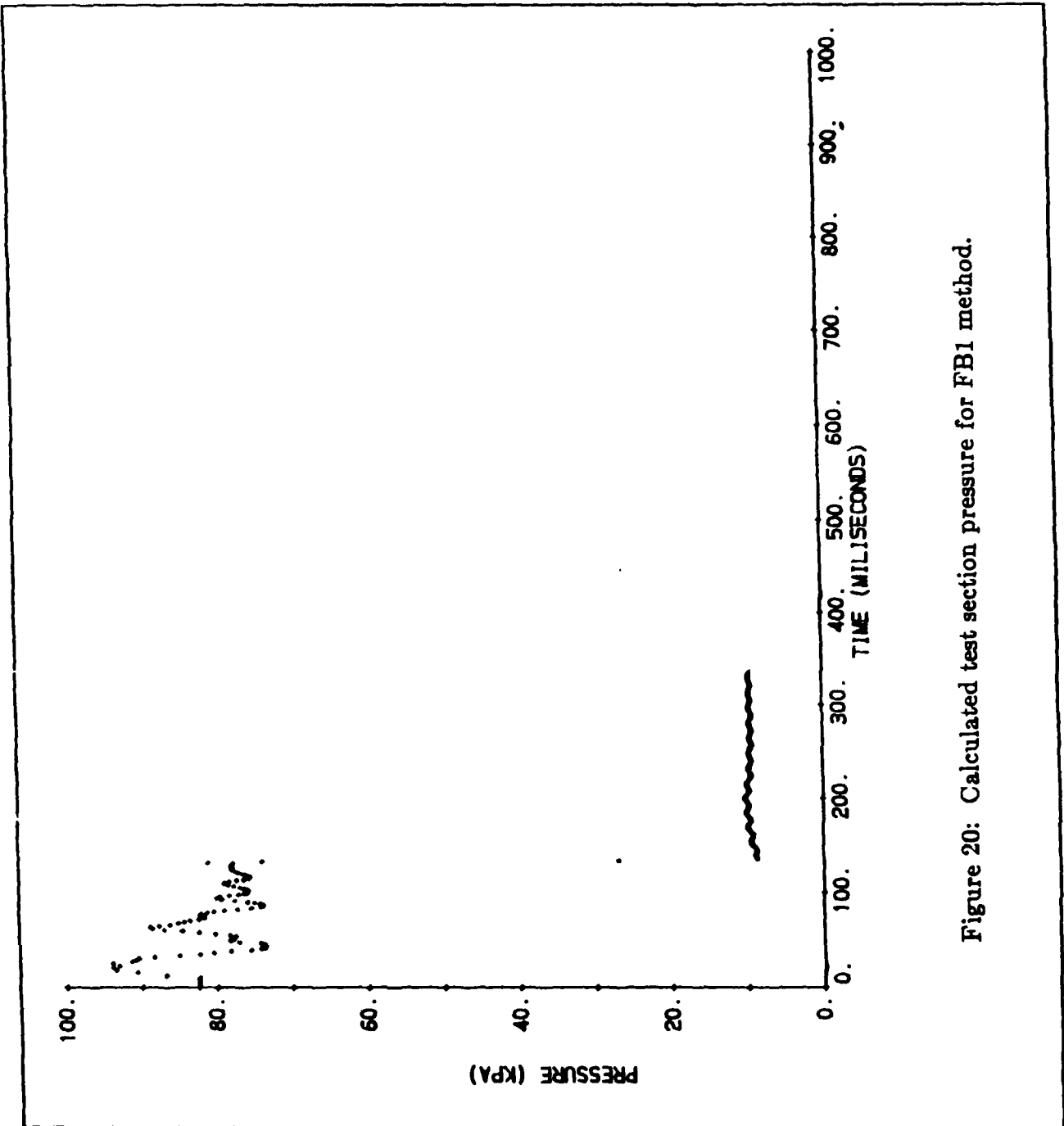


Figure 20: Calculated test section pressure for FB1 method.

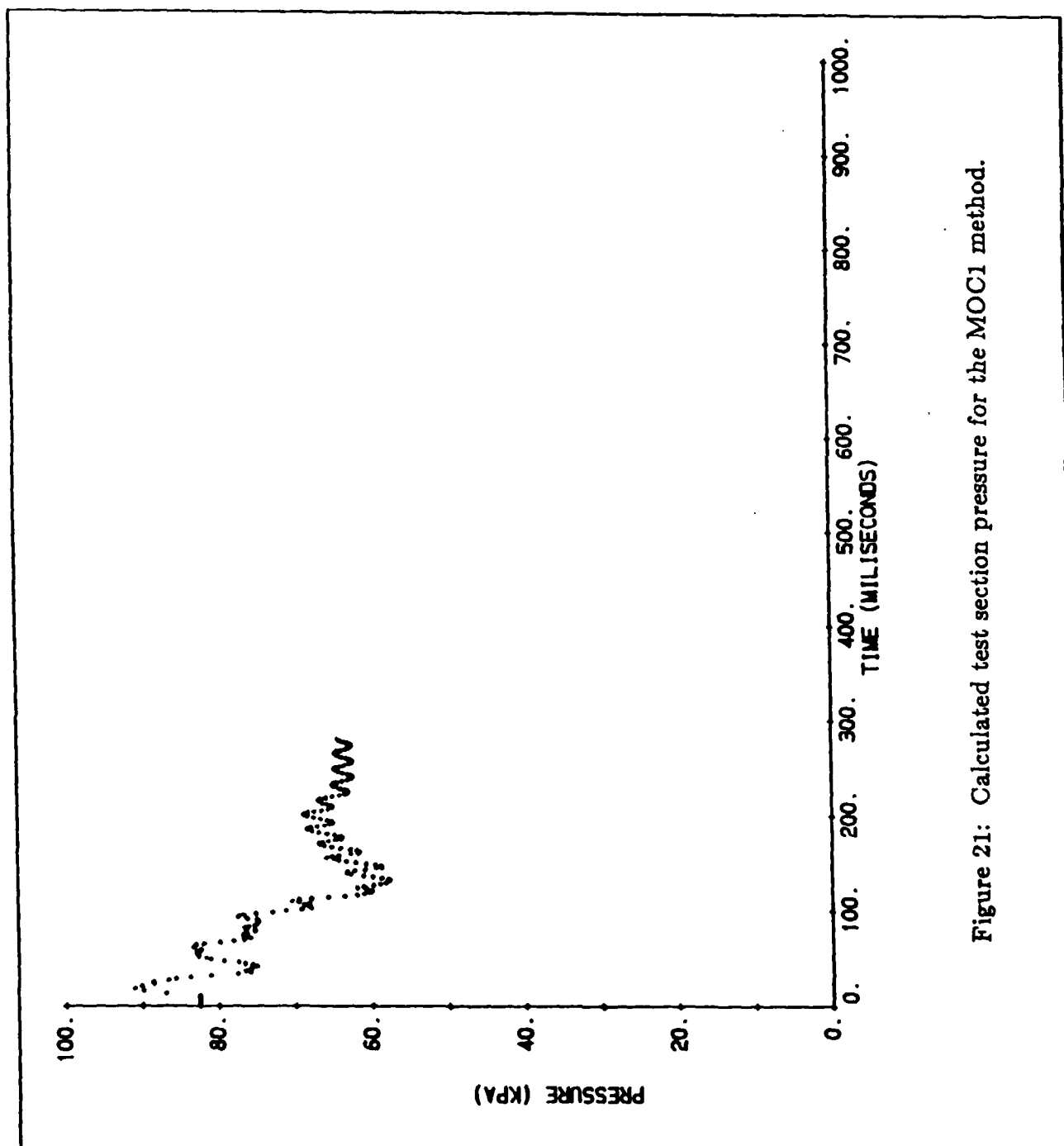


Figure 21: Calculated test section pressure for the MOC1 method.

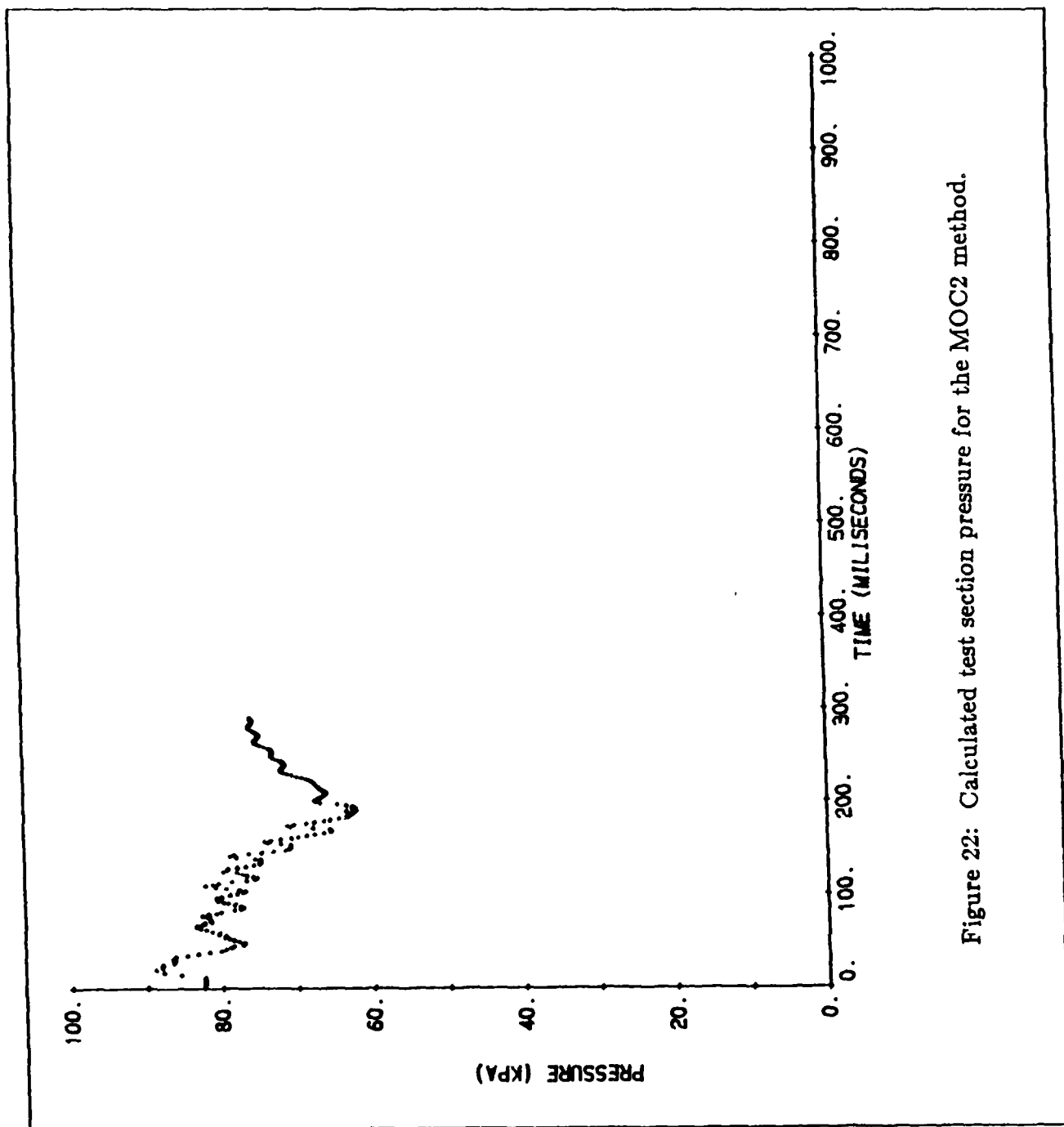


Figure 22: Calculated test section pressure for the MOC2 method.

1987-88 USAF-UES RESEARCH INITIATION PROGRAM

Sponsored by the

AIR FORCE OFFICE OF SCIENTIFIC RESEARCH

Conducted by the

Universal Energy Systems, Inc.

FINAL REPORT

Ab-initio and Semi-Empirical Molecular
Orbital Studies of Energetic
Materials (Nitrogen Heterocyclics)
and Polymers

Prepared by:	Melvin E. Zandler, Ph.D.
Academic Rank:	Associate Professor
Department:	Chemistry Department
University:	Wichita State University
Research Location:	Wichita State University
USAF Researchers:	Captain Jon Swanson (Early 1988) Dr. James J. P. Stewart (Mid 1988) Major Kenneth Dieter (Late 1988)
USAF Location:	Frank J. Seiler Research Lab USAF Academy Colorado Springs, CO 80918
Date:	May 25, 1989
Contract No.:	#F49620-85-C-0013/SB5851-0360
Purchase Order:	S-760-7MG-092

Ab-initio and Semi-Empirical Molecular Orbital Studies
of Energetic Materials (Nitrogen Heterocyclics) and Polymers

Melvin E. Zandler

ABSTRACT

The research started in connection with the Summer 1987 Faculty Research Program at the USAF Academy was continued, the properties of several different molecules were calculated, and a new idea concerning a surprisingly accurate but simple conversion of *ab-initio* energies to standard heats of formation using only information contained in the formula was pursued. Specifically, the following results were obtained.

(1) Semi-empirical (MOPAC) calculations of the properties of a wide range of nitrogen containing compounds and their isomers, were performed. Compounds studied include triazolinone and nitrotriazolinone, 1-nitro-2-propanol, aziridinone and cyclopropanone, the drug molecules haliperidol and spiperone (containing a piperidine ring), a human leukocyte elastase inhibitor (containing a succinimide ring), cyclophosphamides, and several polycyclic hydrocarbons. *Ab-initio* (GAUSSIAN-86) calculations were performed on 1-nitro-propanol, the triazolinones and NTO, the aziridinones and cyclopropanones, and several 10-valence-electron HAB type molecules and ions (i.e., HCS⁺ - HSC⁺, HBO - HOB, HALO - HOAl, HBS - HSB, HCP - HPC, HBF⁺ - HFB⁺, etc.).

(2) The well known problem of the tendency for gradient energy optimization routines to converge to stationary points that are not local minima, was explored. Definitive documentation was obtained showing that MOPAC and GAUSSIAN-86 converge to various eclipsed and staggered forms of propane, depending on starting geometry. A proposed remedy for these false predictions would utilize the internally generated Hessian to define new directions for exploration for true energy minima.

(3) A wide range of *ab-initio* energies and experimental heats of formation were collected from the literature to allow determination, by linear regression, of a set of empirical parameters (atom equivalents) for converting *ab-initio* energies of organic compounds to heat of formation values. The standard error by this method of the 6-31G* calculated heats of formation of some 75 compounds was 2.57 kcal/mol. A major conclusion of this research is that correlation between 6-31G* energies and experimental enthalpies of formation, is much better for hydrocarbons and organic compounds containing oxygen, nitrogen, and/or fluorine than for small inorganic compounds, cations, and radicals.

(4) The Dynamic Reaction Coordinate feature of MOPAC was used to follow several of the lower anharmonic vibrational modes of butane and pentane for 300 to 1000 femtoseconds. The aim was

to investigate the possibility of calculating the thermal expansion properties of polymers by computing the time averaged length of a short section of polymer over a complete cycle of anharmonic vibration for various quanta of energy injected into each important vibrational (internal rotational) mode, then calculating a Boltzman temperature weighted average length over these modes.

The results are interesting in that plots of end-carbon end-carbon distance vs. time shows considerable transfer of energy from the excited low frequency mode to high frequency C-H stretching modes on this classical energy surface. Due to this unforeseen complexity and extensive computational time required, estimation of the thermal expansion of polyethylene was abandoned. However, using insights gained here, work is in progress to use the MOPAC DRC program to verify studies of energy transfer in molecules, such as the CH_3CN study made by Donald Thompson using an empirical force field.

Acknowledgments

I wish to thank the Air Force Systems Command and the Air Force Office of Scientific Research for Sponsorship of this research, and Universal Energy Systems for their excellent administration of the Research Initiation Program.

Last year, 1988, was an especially rewarding time in regard to acquiring the two computers (PC with AEON 32032 coprocessor and UNIX, and the VAXstation 2000), installing MOPAC and GAUSSIAN 86, engaging in research last summer with graduate student Paul Karr (who now is a Ph.D. student under my direction), cooperating with Prof. Erach Talaty on HAB molecules, aziridinones, and cyclophosamides and performing calculations hopefully useful in research programs directed by Prof. William Groutas and William Carper - all faculty at Wichita State University. Also rewarding was the opportunity to present a paper at the International Symposium on Physical-Organic/ Theoretical Chemistry in honor of Michael J. S. Dewar at The University of Texas at Austin, and to attend the Twelfth Austin Symposium on Molecular Structure also at The University of Texas both held in February, 1988.

I am especially indebted to Dr. James J. P. Stewart, at the Frank J. Seiler Research Laboratory at the Air Force Academy for his tremendous knowledge of computational chemistry and programming, and his willingness to share his knowledge with me and to answer my numerous questions.

I. INTRODUCTION

The research reported here covers several topics in computational chemistry. All results were generated on two computers purchased with funds from this grant and/or with time obtained on the VAX-8650 computer residing in the Institute of Aviation Research at Wichita State University. The MOPAC calculations were performed on an 10 MHz IBM-PC clone fitted with a 14" white monochrome monitor, a 40 MB hard drive and AEON 32032 coprocessor board containing 2 MB memory. The operating system is UNIX V.3, complete with FORTRAN and C compilers and linkers and a TEKTRONIX 4107 graphics emulator is included. An Epson LQ-850 is used for output. The computer has been running MOPAC and DRAW, 24 hours a day since May 22, 1988, at 1/3 VAX-780 speed. The complete unit with printer was purchased for \$3900.00.

The second computer, a VAXstation 2000 complete with 6 MB memory, 159 MB hard disk, 19" white monochrome high resolution windowing monitor, mouse, VMS-5.0 operating system running FORTRAN and BASIC, and ethernet and RS-232 connections, was purchased for \$8030.00. The system has been running GAUSSIAN-86 at 1/3 VAX-8650 speed 24 hours a day since November 20, 1988, with only 2 hours total downtime due to power outage. An RS-232 connection to a Zenith PC allows transfer of ASCII files to floppy disk, to a printer, and to the VAX-8650.

During summer 1988, grant funds were used for part time support of this investigator and Mr. Paul Karr, a potential graduate student in theoretical chemistry. He is now in the Ph.D. program under my direction at Wichita State University.

II. SEMI-EMPIRICAL (MOPAC) AND *AB-INITIO* (GAUSSIAN-86) CALCULATIONS ON NITROGEN CONTAINING COMPOUNDS AND ISOMERS

The properties of several compounds, their isomeric forms, and, in some cases, the barriers for isomerization were computed by means of the energy gradient optimization routines in MOPAC and GAUSSIAN-86. Appendices A and B contain submitted papers concerning 1-nitro-2-propanol and haliperidol that recognize AFOSR support. Appendices C and D contain papers presented at poster sessions of national meetings. Summaries of results for these and other molecules follow:

Triazolinone (TO) and Nitrotriazolinone (NTO). When I began the Summer Faculty Research Program in summer 1987, NTO (3-nitro-1,2,4-triazolin-5-one) was a compound of only theoretical interest as a potentially useful energetic material. It has now become one of the most promising of a new class of powerful but stable and insensitive explosives - currently being prepared in large quantities for testing and evaluation. As part of the research accomplished during summer 1987 at the USAF Academy, AM1 calculations were performed on NTO, TO, and radicals formed by addition, abstraction, and intramolecular transfer of a hydrogen atom (Figure 1). These results should be useful toward understanding aspects of various possible decomposition mechanisms and for estimation of the various measures of performance of NTO and similar compounds as an explosive or propellant.

We report here preliminary *ab-initio* calculations on TO and

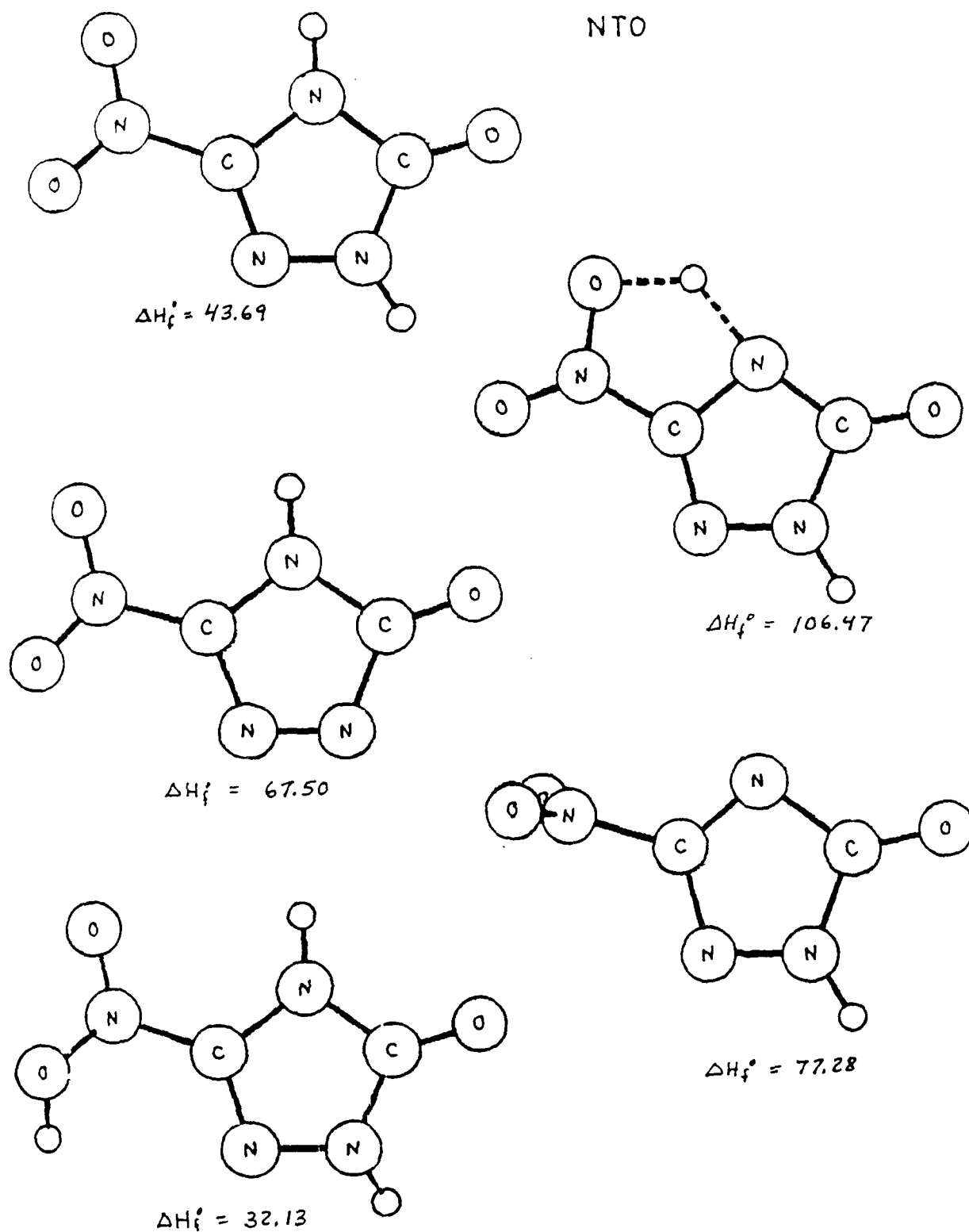


Figure 1. Geometrical structure and heat of formation of NTO and species resulting from addition or abstraction of hydrogen atoms, using the AM1-UHF model.

Input Geometry (AM1) to GAUSSIAN-86 (3-21G) for " TO "

Z-MATRIX (ANGSTROMS AND DEGREES)							
CD	CENT	ATOM	N1	LENGTH	N2	ALPHA	BETA
1	1	N	1	1.357760(1)			
2	2	N	2	1.449700(2)	1	109.997(9)	
3	3	C	3	1.427800(3)	2	104.215(10)	1 9.359(16)
4	4	N	4	1.411755(4)	3	105.877(11)	2 -6.562(17)
5	5	C	5	0.999490(5)	4	119.703(12)	3 147.149(18)
6	6	H	6	0.984570(6)	5	126.273(13)	4 164.019(19)
7	7	H	7	1.096200(7)	4	122.931(14)	3 -179.442(20)
8	8	O	8	1.238010(8)	4	127.437(15)	5 179.272(21)

Optimized Geometry for " TO " from 3-21G

Z-MATRIX (ANGSTROMS AND DEGREES)							
CD	CENT	ATOM	N1	LENGTH	N2	ALPHA	BETA
1	1	N	1	1.421322(1)			
2	2	N	2	1.367928(2)	1	112.913(9)	
3	3	C	3	1.391680(3)	2	101.884(10)	1 0.249(16)
4	4	N	4	1.379269(4)	3	109.051(11)	2 -0.248(17)
5	5	C	5	0.991587(5)	4	127.027(12)	3 180.289(18)
6	6	H	6	0.993952(6)	5	127.448(13)	4 179.535(19)
7	7	H	7	1.062262(7)	4	123.244(14)	3 -179.700(20)
8	8	H	8	1.062262(7)	4	123.244(14)	3 -179.700(20)
9	9	O	9	1.212317(8)	4	120.334(15)	5 173.243(21)

For " TO " HF/3-21G Energy = -313.90744 au.

Optimized Geometry for " TO " from 6-31G

Z-MATRIX (ANGSTROMS AND DEGREES)							
CD	CENT	ATOM	N1	LENGTH	N2	ALPHA	BETA
1	1	N	1	1.389047(1)			
2	2	N	2	1.361049(2)	1	112.978(9)	
3	3	C	3	1.382773(3)	2	102.146(10)	1 -0.007(16)
4	4	N	4	1.378444(4)	3	108.854(11)	2 0.007(17)
5	5	C	5	0.987290(5)	4	126.398(12)	3 179.944(18)
6	6	H	6	0.989446(6)	5	127.555(13)	4 180.029(19)
7	7	H	7	1.062631(7)	4	124.119(14)	3 179.963(20)
8	8	H	8	1.062631(7)	4	124.119(14)	3 179.963(20)
9	9	O	9	1.224590(8)	4	120.314(15)	5 179.999(21)

For " TO " HF/6-31G Energy = -315.52431 au.

Optimized Geometry for " NTO " from 3-21G

Z-MATRIX (ANGSTROMS AND DEGREES)							
CD	CENT	ATOM	N1	LENGTH	N2	ALPHA	BETA
1	1	N	1	1.400117(1)			
2	2	N	2	1.384510(2)	1	112.940(11)	
3	3	C	3	1.391708(3)	2	101.571(12)	1 0.067(20)
4	4	N	4	1.363719(4)	3	107.962(13)	2 -0.092(21)
5	5	C	5	0.993385(5)	4	127.262(14)	3 180.021(22)
6	6	H	6	0.996050(6)	5	125.494(15)	4 179.904(23)
7	7	H	7	1.203880(7)	4	129.348(16)	3 179.939(24)
8	8	O	8	1.418303(8)	4	120.753(17)	5 180.229(25)
9	9	N	9	1.250368(9)	5	114.475(18)	4 -0.061(26)
10	10	O	10	1.229632(10)	5	118.111(19)	4 179.946(27)

For " NTO " HF/3-21G Energy = -516.17789 au.

NTO. We expected to be able to verify most of the AM1 results but rapidly understood that larger and more powerful computers would be required than the VAXstation 2000, or that shortcuts would be necessary (perhaps GAUSSIAN-88 will solve virtual disk problems). The VAX-8650 might be adequate, but insufficient time was available to complete this part of the project. The following tables show the input geometry (from AM1 optimization) and the final optimized results for 3-21G on TO and NTO, and for 6-31G on NTO. A substantial different geometry is predicted by the *ab-initio* models in that the AM1 geometry is quite non-planar with a short N-N bond and long N-C bond compared to *ab-initio*. Further work is in progress to untangle these confusing results (we are beginning a study using the PM3 parameter set of MOPAC 5.0). An X-ray structure of NTO, and 6-31G* calculations have been reported by J. P. Ritchie at the American Chemical Society meeting in Dallas.

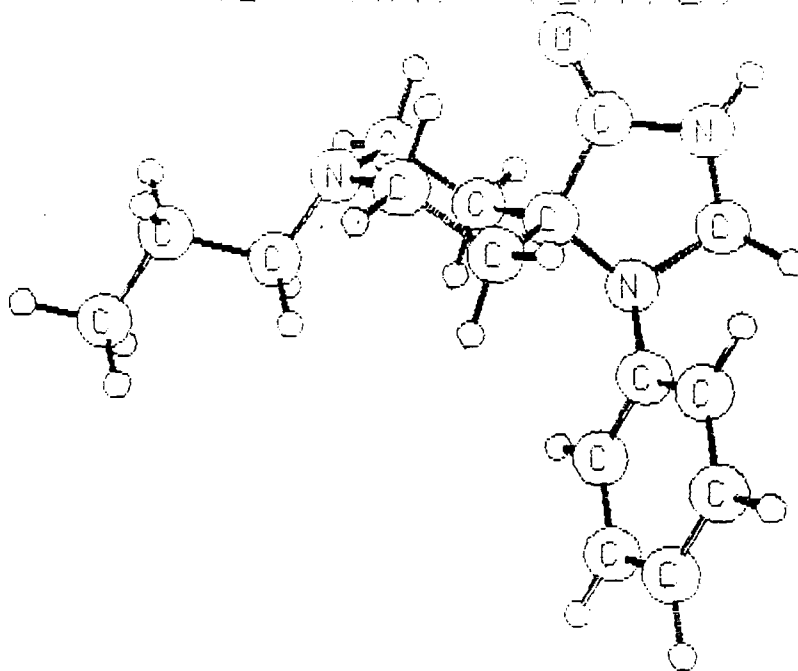
1-nitro-2-propanol. The AM1 geometry and energy of the three conformers (rotamers) of 1-nitro-2-propanol were obtained along with computed vibrational frequencies. The results are summarized in Figure 2. The AM1 geometry for the most stable conformer (1) was used as the starting geometry for a 3-21G calculation. The major difference between the semi-empirical and *ab-initio* results was a substantial shortening of the OH--NO₂ hydrogen bond distance from 2.22 (AM1) to 2.04 (3-21G) angstroms. For more details see Appendix A.

Haliperidol and Spiperone. These materials are widely prescribed central nervous-system depressants. The molecular conformation of these molecules is of particular interest toward understanding their mode of action. Of particular interest is the conformation of the piperidine ring present in both molecules, and the extent to which the various ring or nitrogen inversions occur in solution.

Optimization of the rather large molecule, haliperidol, $C_{21}H_{23}ClFNO_2$, yielded extremely good agreement with the crystal structure and NMR observations. For more details on haloperidol, see Appendix B. One interesting result was the increase in stability of the equatorial vs. axial positions of the alkyl group on the nitrogen of the piperidine ring as the chain length increases from H to propyl. Although calculations on spiperone are not yet finished, it appears that equally good results are forthcoming. Optimized AM1 structures for two isomers of the molecule terminated at a propyl group attached to the piperidine nitrogen are shown in Figure 3.

3-benzyl-N-((trans-styrylsulfonyl)oxy)succinimide. The title compound is an effective inhibitor⁽¹⁾ of human leukocyte elastase (HLE), presumably a chief agent in the progression of emphysema. This large molecule, $C_{19}H_{17}NO_5S$, was completely optimized with AM1 (MNDO parameters for sulfur), and barriers evaluated for rotation of the benzyl and styryl groups, and rotation around the SO and NO bonds. All rotations were nearly free (2-5 kcal/mol) except rotation of the sulfur around the NO

SPIPERONE (PROP-AX) (CRYST)



SPIPERONE (PROP-EQ) (CRYST)

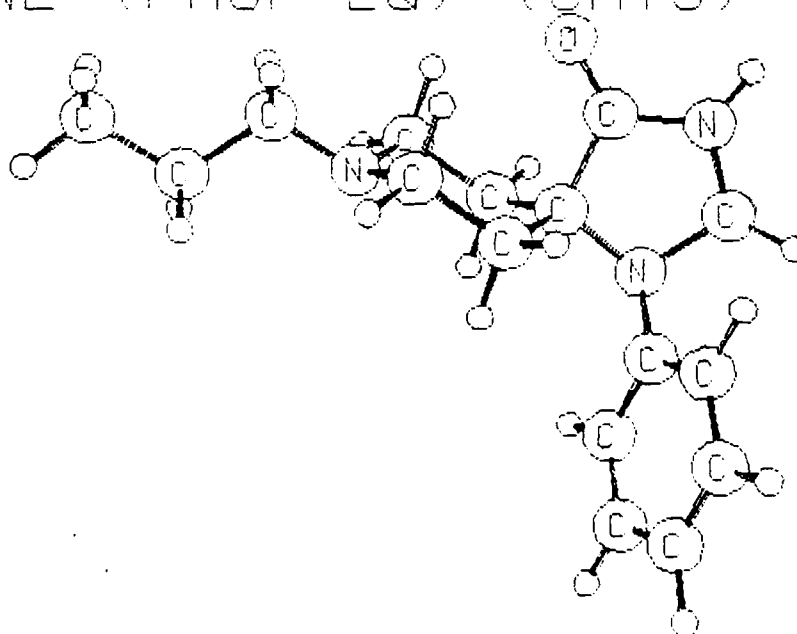


Figure 3. Two isomers of spiperone truncated at a propyl group attached to the piperidine ring from AM1 optimization.

3-benzyl-N-((*trans*-styrylsulfonyl)oxy)succinimide

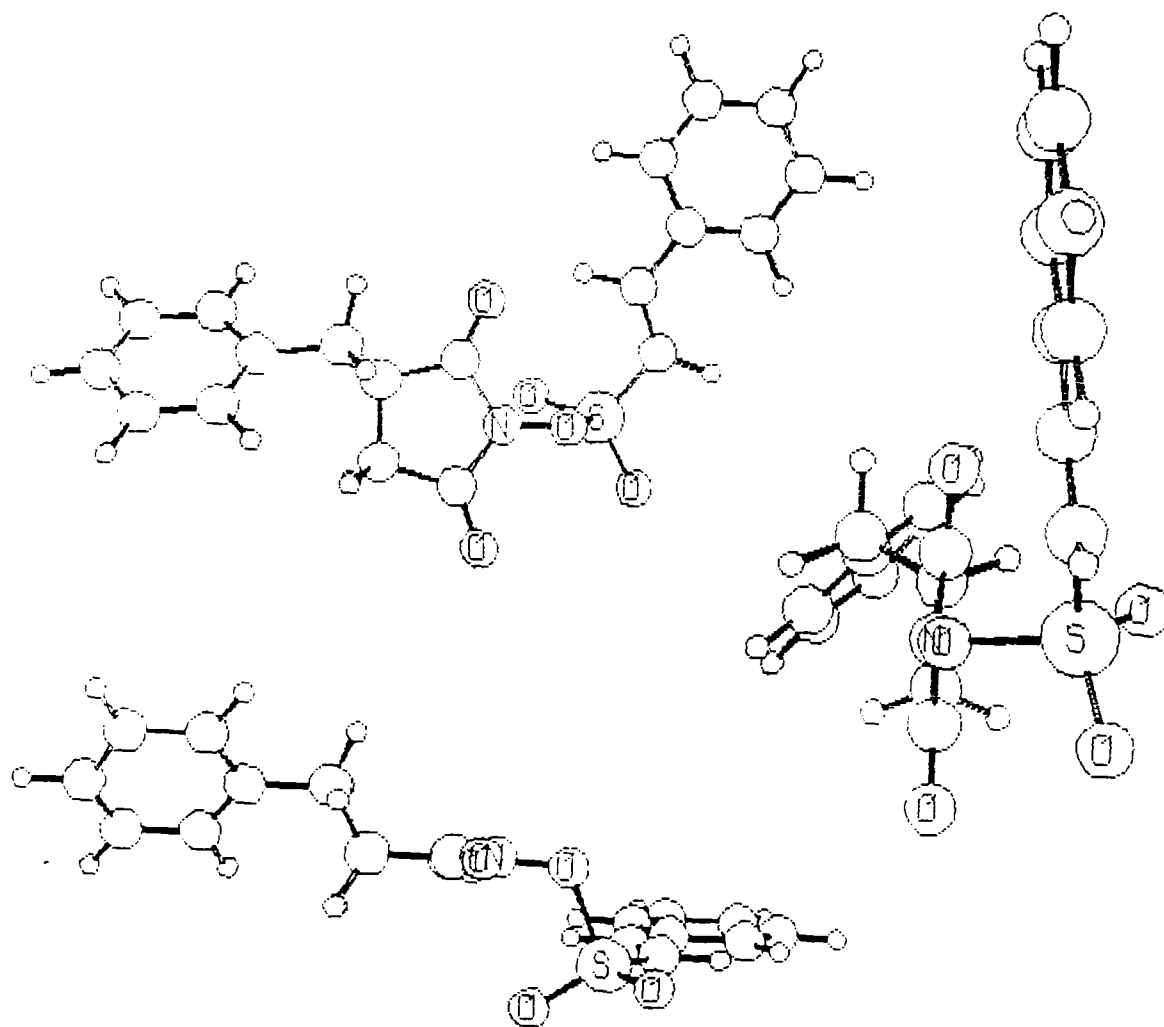


Figure 4. Three orthogonal views of an HLE inhibitor optimized with AM1 (MNDO for sulfur).

bond, for which the barrier was about 18 kcal/mol. Three orthogonal views of the molecule are shown in Figure 1. It is hoped that these results will aid in the design of even better inhibitors for HLE by docking experiments using molecular modeling programs such as SYBYL. We have the crystal structure coordinates for HLE but force fields are not yet readily available for the succinimide ring and SO_3 components.

Aziridinone and Cyclopropanone. A search for isomers and transition states on the aziridinone, $\text{C}_2\text{H}_3\text{NO}$, and cyclopropanone, $\text{C}_3\text{H}_4\text{O}$, AM1 energy surfaces yielded several predicted isomers and new forms with unusual square arrangements⁽²⁾ of the heavy atoms. These forms, which might be interpreted as resulting from intramolecular nucleophilic attack of the exocyclic atom on one of the ring atoms, may lie on a low energy isomerization pathway. *Ab-initio* (3-21G) results are in substantial agreement with the AM1 results. For more information, see Appendix C, which contains a poster paper presented at the National American Chemical Society Meeting at Los Angeles in September, 1988.

Ten Valence Electron HAB Molecules. Several years ago, we reported⁽³⁾ STO-3G calculations that showed that several HAB molecules and ions containing 10 valence electrons were bent - contrary to predictions of Walsh's rules. The potential energy surface was scanned for some 42 HAB-ABH isomer pairs, where A and B were selected from Be, B, C, N, O, F, Mg, Al, P, S, and Cl, and resulting charges of -2, -1, 0, +1, and +2 were used. We

suggested the following rules for isomeric structure: The isomer with the atomic number in location B larger than in location A, generally corresponds to the most stable linear isomer. If the order is reversed, a less stable isomer corresponding to a local minimum is obtained that may be bent if the center atom is from the second row of the periodic table and/or if the electronegativity of A is sufficiently larger than that of B.

Considerable time was spent checking our discovery in 1982⁽¹⁾ that HSC^+ was substantially bent at the 3-21G* level, with bond angle near 90 degrees, an energy 80 kcal/mol higher than HCS^+ , and isomerization barrier of 22 kcal/mol. This result differed from the calculated results of Bruna, Peyerimhoff, and Buenker (Chem. Phys. 27, 33, 1978), wherein they characterized the HSC^+ species to be linear at 110 kcal/mol - corresponding to a saddle point on the potential energy surface instead of a minimum. At higher *ab-initio* HF levels the molecule remained bent but the barrier became smaller (11.1 kcal/mol for HF/6-31G**) and almost disappeared when electron correlation was used (i.e., 0.3 kcal/mol for full-core MP2/6-31G**, 2.9 kcal/mol for frozen-core MP3/6-31G**, and 2.2 kcal/mol for FC MP4/6-31G**). Just after near completion of this work, Radom reported virtually identical results⁽⁵⁾.

The following four tables report on recently completed equally high level calculations on HBO-BOH, HALO-ALOH, HBS-BSH, and HALS-ALSH. Tabulated are the bond lengths (R-AB, R-HA, and R-HB), the bond angles ($\angle\text{HAB}$ and $\angle\text{HBA}$), the AB bond midpoint (HALF), the H distance from the AB midpoint (R-MH), the angle

10 valence electron HAB species

A/B	Be	B	C	N	O	F
Be				HBeL ⁺ L G	HBeO ⁻ L G	HBeF L G
B			HBC ²⁻ L G	HBN L G	HBO L G	HBF ⁺ L G
C		HCB ²⁻ L L	HCC ⁻ L G	HCN L G	HCO ⁺ L G	HCF ²⁺ L G
N	HNB ²⁻ L L	HNB ⁻ L L	HNC L L	HNN ⁺ L G	HNO ²⁺ L G	
O	HOBe ⁻ B L	HOB B L	HOC ⁺ L L	HON ²⁺ L L		
F	HFB ²⁻ B L	HFB ⁺ B L	HFC ²⁺ B L			

10 valence electron HAB species

A/B	Mg	Al	Si	P	S	Cl
Be				HBeF ⁺ L G	HBeS L G	HBeCl L G
B			HBS ⁻ L G	HBP ⁻ L G	HBS L G	HBCl ⁺ L G
C		HCAI ²⁻ L G	HCS ⁻ L G	HCP ⁻ L G	HCS ⁺ L G	HCCl ²⁺ L G
N	HNMg ²⁺ B G	HNAI ⁻ L G	HNS ⁻ L G	HNP ⁺ L G	HNS ²⁺ L G	
O	HOmg ⁻ B L	HOAI B G	HOSi ⁺ L G	HOP ²⁺ L G		
F	HFMg B G	HFAI ⁺ B G	HFSi ²⁺ B G			

10 valence electron HAB species

A/B	Be	B	C	N	O	F
Mg				HmgN ²⁻ B L	HmgO ⁻ L G	HmgF L L
Al			HAlC ¹⁺ B L	HAlN ⁻ B L	HAlO L L	HAlF ⁺ L L
Si		HSiB ²⁻ B L	HSiC ⁻ B L	HSiN B L	HSiO ⁺ L L	HSiF ²⁺ L L
P	HPBe ²⁻ B L	HPB ⁻ B L	HPC B L	HPN ⁺ B L	HPO ²⁺ L L	
S	HSBe ⁻ B L	HSB B L	HSC ⁺ B L	HSN ²⁺ L L		
Cl	HClBe B L	HClB ⁺ B L	HClC ²⁺ B L			

10 valence electron HAB species

A/B	Mg	Al	Si	P	S	Cl
Mg				HmgL ⁺ L G	HmgS ⁻ L G	HmgCl L G
Al			HAlSi ⁻ L L	HAlP ⁻ L L	HAlS L L	HAlCl ⁺ L G
Si		HSiAl ²⁺ B G	HSiSi ⁻ B G	HSiP ⁻ L L	HSiS ⁺ L L	HSiCl ²⁺ L G
P	HPmg ²⁻ B L	HPAI ⁻ B G	HPSi ⁻ B G	HP ⁺ B G	HPS ²⁺ L L	
S	HSmg ⁻ B L	HSAl B G	HSSi ⁻ B G	HSP ²⁺ L L		
Cl	HClmg B L	HClAI ⁺ B G	HClSi ²⁺ B G			

STRUCTURE AND MINIMA OF 10 VALENCE ELECTRON HAB MOLECULES AND IONS

STO-36

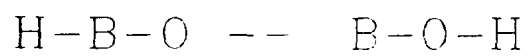
		M-B-O <---> B-O-H										
		H-B-O										
		H-B-E	HALF	R-HB	<HBA	E (Hartree)	E (Kcal)	R-AB	R-HA	<HAB	R-HB	<HBA
HF 3-31G	HBO1631	0.6090	1.7543	0.00	-99.605948	0.00	1.2105	1.1590	180.00	2.3695	0.00	
	HBO3631	0.6284	1.2240	83.00	-99.452722	96.16	1.2508	1.3063	68.46	1.4425	57.39	
	HBO2631	0.6564	1.5540	163.13	-99.545004	38.04	1.3129	2.2004	11.90	0.9550	151.63	
	HBO4631	0.6513	1.6007	180.00	-99.545098	38.19	1.3037	2.2545	0.00	0.9508	180.00	
HF 6-31G	HBO1631	0.6000	1.7553	0.00	-100.118584	0.00	1.2004	1.1551	180.00	2.3550	0.00	
	HBO3631	0.6235	1.2155	85.67	-99.960944	98.92	1.2472	1.3236	66.31	1.4074	59.45	
	HBO2631	0.6517	1.5684	168.68	-100.054986	39.91	1.3033	2.2111	8.01	0.9382	160.84	
	HBO4631	0.6435	1.5861	180.00	-100.054914	39.95	1.2991	2.2356	0.00	0.9365	180.00	
HF 6-31G*	HBO163D	0.5927	1.7594	0.00	-100.166146	0.00	1.1853	1.1667	180.00	2.3520	0.00	
	HBO363D	0.6090	1.1968	83.43	-100.019158	92.24	1.2184	1.2793	68.33	1.4036	57.89	
	HBO263D	0.6499	1.4039	144.70	-100.090775	47.30	1.2997	1.9704	24.31	0.9508	121.44	
	HBO463D	0.6364	1.5741	180.00	-100.084531	51.21	1.2727	2.2104	0.00	0.9377	180.00	
HF 6-31G**	HBO163P	0.5927	1.7577	0.00	-100.167173	0.00	1.1855	1.1649	180.00	2.3504	0.00	
	HBO363P	0.6085	1.1976	82.68	-100.022477	90.80	1.2173	1.2724	69.00	1.4109	57.35	
	HBO263P	0.6488	1.4036	145.21	-100.098414	43.15	1.2977	1.9715	23.97	0.9462	122.17	
	HBO463P	0.6357	1.5702	180.00	-100.092011	47.16	1.2734	2.2069	0.00	0.9335	180.00	
HF 6-31G**	HBO163M	0.6086	1.7717	0.00	-100.436923	0.00	1.2171	1.1632	180.00	2.3803	0.00	
	HBO363M	0.6290	1.1477	89.42	-100.307285	82.60	1.2581	1.3003	61.72	1.3144	60.82	
	HBO263M	0.6550	1.4190	144.33	-100.349289	56.25	1.3126	1.9893	24.58	0.9649	120.97	
	HBO463M	0.6440	1.5958	180.00	-100.344326	59.35	1.2882	2.2400	0.00	0.9517	180.00	
HF 6-31G**	HBO163M2	0.6008	1.7639	0.00	-100.436343	0.00	1.2015	1.1631	180.00	2.3640	0.00	
	HBO363M2	0.6217	1.1668	86.76	-100.308495	80.23	1.2434	1.2906	64.50	1.3527	59.44	
	HBO263M2	0.6545	1.4113	144.15	-100.359631	48.14	1.3089	1.9792	24.68	0.9606	120.63	
	HBO463M2	0.6418	1.5886	180.00	-100.354056	51.63	1.2836	2.2304	0.00	0.9468	180.00	
HF 6-31G**	HBO163M4	0.6117	1.7761	0.00	-100.458456	0.00	1.2233	1.1644	180.00	2.3877	0.00	
	HBO363M4	0.6322	1.1511	89.17	-100.330057	80.57	1.2644	1.3053	61.85	1.3213	60.59	
	HBO263M4	0.6587	1.4170	144.08	-100.373319	53.42	1.3173	1.9883	24.71	0.9644	120.46	
	HBO463M4	0.6455	1.5975	180.00	-100.387934	56.80	1.2930	2.2440	0.00	0.9510	180.00	
HF 6-311G**	HBO1632	0.5898	1.7530	0.00	-100.194230	0.00	1.1795	1.1632	180.00	2.3428	0.00	
	HBO3632	0.6052	1.2050	82.60	-100.051241	89.73	1.2102	1.2769	69.36	1.4163	57.53	
	HBO2632	0.6444	1.3969	144.87	-100.128357	41.34	1.2888	1.9592	24.22	0.9457	121.78	
	HBO4632	0.6327	1.5689	180.00	-100.121487	45.65	1.2653	2.2995	0.00	0.9342	180.00	
HF 6-311G**	HBO162	0.6081	1.7775	0.00	-100.537997	0.00	1.2162	1.1694	180.00	2.3856	0.00	
	HBO32	0.6297	1.1623	88.93	-100.413311	78.24	1.2594	1.3116	62.38	1.3322	60.73	
	HBO22	0.6546	1.3849	141.28	-100.457815	50.31	1.3092	1.9394	26.54	0.9654	120.18	
	HBO42	0.6422	1.5943	180.00	-100.450823	54.70	1.2844	2.2365	0.00	0.9521	180.00	
HF 6-311G	HBO16321	0.5897	1.7529	0.00	-100.199337	0.00	1.1794	1.1632	180.00	2.3426	0.00	
	(2d,2p)	HBO36321	0.6048	1.2039	82.51	-100.058080	88.64	1.2096	1.2749	69.43	1.4160	57.46
	FL	HBO26321	0.6433	1.3959	145.03	-100.135016	40.36	1.2866	1.9581	24.11	0.9437	122.03
		HBO46321	0.6300	1.5616	180.00	-100.127545	45.05	1.2599	2.1915	0.00	0.9316	180.00
HF 6-311G	HBO121	0.6046	1.7663	0.00	-100.541027	0.00	1.2092	1.1617	180.00	2.3709	0.00	
	(2d,2p)	HBO321	0.6243	1.1588	89.17	-100.414561	79.36	1.2486	1.3083	62.33	1.3242	61.05
	FL	HBO221	0.6501	1.4135	144.54	-100.459036	51.45	1.3002	1.9793	24.48	0.9611	121.44
		HBO421	0.6374	1.5865	180.00	-100.453231	55.09	1.2748	2.2239	0.00	0.9491	180.00

H-B-S (H-B-S) B-S-H											
H-B-S											
H-A-B	HALF	R-MH	<HMA	E(Hartree)	E(kcal)	R-AB	R-HA	<HAB	R-HE	<HBA	
HF/3-21G	HBS1321	0.9089	1.9679	0.00	-420.697645	0.00	1.6177	1.1390	180.00	2.7767	0.00
	HBS3321	0.8628	1.3166	78.02	-420.532855	103.41	1.7256	1.4180	65.45	1.7191	48.62
	HBS2321	0.9461	1.7868	131.75	-420.595170	70.58	1.8923	2.5179	31.96	1.3549	100.37
	HBS4321	0.9227	2.2624	180.00	-420.557417	87.99	1.8454	3.1851	0.00	1.3357	180.00
HF/6-31G	HBS1631	0.8154	1.9767	0.00	-422.750093	0.00	1.6309	1.1612	180.00	2.7821	0.00
	HBS3631	0.8670	1.3049	77.70	-422.585650	103.19	1.7339	1.4043	65.21	1.7135	48.07
	HBS2631	0.9481	1.7916	131.83	-422.637642	70.56	1.8963	2.5247	31.92	1.3577	100.47
	HBS4631	0.9291	2.2736	180.00	-422.508863	88.62	1.8582	3.2027	0.00	1.3445	180.00
HF/6-31G*	HBS163D	0.7984	1.9654	0.00	-422.792078	0.00	1.5969	1.1670	180.00	2.7638	0.00
	HBS363D	0.8345	1.2750	75.76	-422.638389	96.44	1.6689	1.3412	67.14	1.6868	47.11
	HBS263D	0.9155	1.6602	126.73	-422.684015	67.81	1.8309	2.3264	34.89	1.3329	93.33
	HBS463D	0.9029	2.2343	180.00	-422.634480	98.89	1.8059	3.1372	0.00	1.3313	180.00
HF/6-31G**	HBS163P	0.7986	1.9647	0.00	-422.793247	0.00	1.5972	1.1661	180.00	2.7633	0.00
	HBS363P	0.8331	1.2761	75.00	-422.643330	94.07	1.6661	1.3312	67.81	1.6949	46.66
	HBS263P	0.9150	1.6536	126.34	-422.688158	65.94	1.8299	2.3162	35.10	1.3335	92.79
	HBS463P	0.9030	2.2322	180.00	-422.638964	96.81	1.8060	3.1352	0.00	1.3292	180.00
HF/6-31G**	HBS163H	0.9017	1.9689	0.00	-423.011225	0.00	1.6035	1.1671	180.00	2.7706	0.00
	HBS363H	0.8470	1.2075	81.23	-422.871129	87.91	1.694	1.3651	60.95	1.5772	49.17
	HBS263H	0.9043	1.5616	121.25	-422.890073	76.02	1.8085	2.1728	37.91	1.3393	85.97
	HBS463H	0.8868	2.2349	180.00	-422.954242	98.51	1.7736	3.1217	0.00	1.3491	180.00
HF/6-31G**	HBS163M3	0.7994	1.9662	0.00	-423.011037	0.00	1.5989	1.1667	180.00	2.7656	0.00
	HBS363M3	0.8447	1.2266	78.93	-422.876722	84.28	1.6895	1.3491	63.16	1.6175	48.09
	HBS263M3	0.9080	1.5855	122.39	-422.900715	69.23	1.8161	2.2092	37.30	1.3402	87.49
	HBS463M3	0.8886	2.2332	180.00	-422.861620	93.75	1.7773	3.1219	0.00	1.3446	180.00
HF/6-31G**	HBS163M4	0.8081	1.9778	0.00	-423.026692	0.00	1.6163	1.1696	180.00	2.7859	0.00
	HBS363M4	0.8559	1.2101	80.99	-422.892241	84.37	1.7118	1.3684	60.85	1.5878	48.83
	HBS263M4	0.9116	1.5791	121.90	-422.912673	71.55	1.8232	2.2014	37.52	1.3429	86.71
	HBS463M4	0.8954	2.2513	180.00	-422.878820	92.79	1.7907	3.1466	0.00	1.3559	180.00
HF/6-311G	HBO121	0.7961	1.9606	0.00	-422.826093	0.00	1.5922	1.1645	180.00	2.7569	0.00
	HBO221	0.8292	1.2923	74.62	-422.683272	89.62	1.6582	1.3376	58.67	1.7105	46.76
	HBO221	0.9094	1.6291	125.07	-422.726120	62.73	1.8188	2.2767	35.85	1.3337	91.14
	HBO421	0.8896	2.2288	180.00	-422.671769	96.84	1.7993	3.1285	0.00	1.3292	180.00

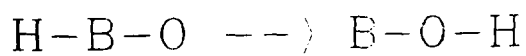
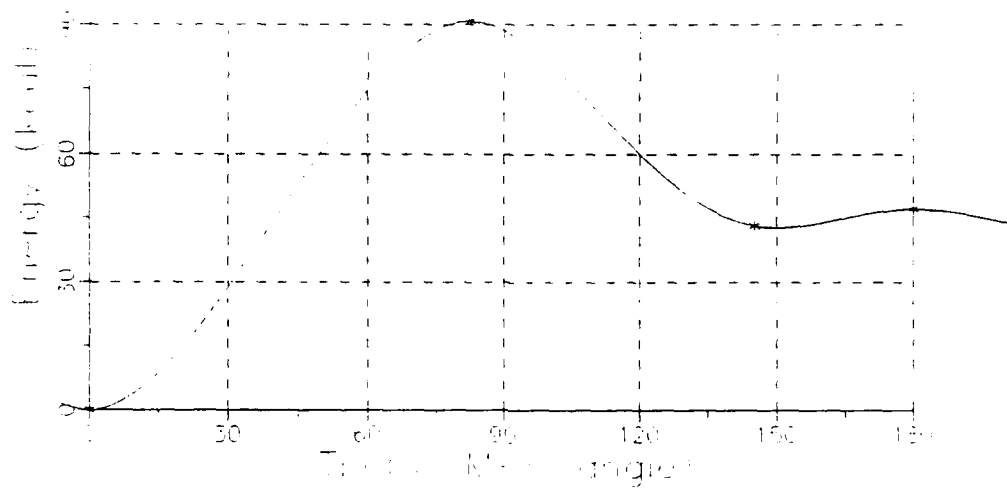
H-A1-S (----) A1-S-H

	H-A1-S											
	H-A-S	HALF	R-HH	<HHA	E(Hartree)	E(kcal)	R-AB	R-HA	<HAS	R-HB	<HBA	
HF 3-210	HA1S1321	1.0320	2.6025	0.00	-636.750772	0.00	2.0656	1.5697	180.00	3.6353	0.00	
	HA1S3321	1.0880	1.6824	71.34	-636.557371	52.61	2.1761	1.6861	70.97	2.2772	44.42	
	HA1S2321	1.1820	2.0153	139.50	-636.761332	-6.53	2.3643	3.0138	25.72	1.3546	105.00	
	HA1S4321	1.1260	2.4750	180.00	-636.748355	1.52	2.2751	3.6120	0.00	1.3269	180.00	
HF 6-310	HA1S1631	1.0324	2.6035	0.00	-639.967380	0.00	2.0667	1.5701	180.00	3.6368	0.00	
	HA1S3631	1.0896	1.6876	71.59	-639.874735	58.14	2.1792	1.6952	70.83	2.2795	44.62	
	HA1S2631	1.1863	2.0422	140.50	-639.980680	-8.35	2.3725	3.0523	25.19	1.3562	106.69	
	HA1S4631	1.1439	2.4842	180.00	-639.967441	-0.04	2.2877	3.6281	0.00	1.3403	180.00	
HF 6-310*	HA1S1630	0.9960	2.5576	0.00	-640.014151	0.00	1.9920	1.5616	180.00	3.5536	0.00	
	HA1S3630	1.0375	1.6497	71.94	-639.916607	61.21	2.0750	1.6543	71.46	2.2043	45.36	
	HA1S2630	1.1340	1.8434	134.04	-640.020505	-3.99	2.2680	2.7550	28.75	1.3334	96.35	
	HA1S4630	1.1048	2.4295	180.00	-639.993873	12.72	2.2096	3.5343	0.00	1.3247	180.00	
HF 6-310**	HA1S163P	0.9951	2.5559	0.00	-640.015128	0.00	1.9921	1.5598	180.00	3.5519	0.00	
	HA1S363P	1.0364	1.6514	71.61	-639.918111	60.88	2.0728	1.6497	71.79	2.2093	45.18	
	HA1S263P	1.1331	1.8344	133.70	-640.024692	-6.00	2.2663	2.7424	28.92	1.3330	95.78	
	HA1S463P	1.1044	2.4271	180.00	-639.998207	10.52	2.2088	3.5315	0.00	1.3227	180.00	
HF 2/6-310**	HA1S163H	1.0021	2.5622	0.00	-640.210958	0.00	2.0042	1.5601	180.00	3.5643	0.00	
	HA1S363H	1.0376	1.6719	75.09	-640.135327	47.46	2.0753	1.6457	67.37	2.0945	46.49	
	HA1S263H	1.1172	1.7352	129.60	-640.214450	-2.19	2.2344	2.5944	31.02	1.3370	89.53	
	HA1S463H	1.0874	2.4169	180.00	-640.191146	12.43	2.1747	3.5043	0.00	1.3296	180.00	
HF 2/6-310**	HA1S1H3	0.9950	2.5596	0.00	-640.207220	0.00	1.9990	1.5601	180.00	3.5591	0.00	
	HA1S3H3	1.0412	1.6028	73.93	-640.136634	44.29	2.0827	1.6520	68.79	2.1395	46.04	
	HA1S2H3	1.1189	1.7469	129.98	-640.217854	-6.67	2.2378	2.6106	30.85	1.3385	90.15	
	HA1S4H3	1.0879	2.4176	180.00	-640.193073	8.88	2.1758	3.5055	0.00	1.3297	180.00	
HF 4/6-310**	HA1S1H4	0.0000	0.0000	0.00	-640.219500	0.00	2.0170	0.0000	180.00	0.0000	0.00	
	HA1S3H4	1.0480	1.5900	74.90	-640.131700	42.55	0.0000	0.0000	0.00	0.0000	0.00	
	HA1S2H4	0.0000	0.0000	0.00	-640.226800	-4.58	2.2400	0.0000	0.00	0.0000	90.00	
	HA1S4H4	0.0000	0.0000	180.00	-640.202800	10.48	2.1800	0.0000	0.00	0.0000	180.00	

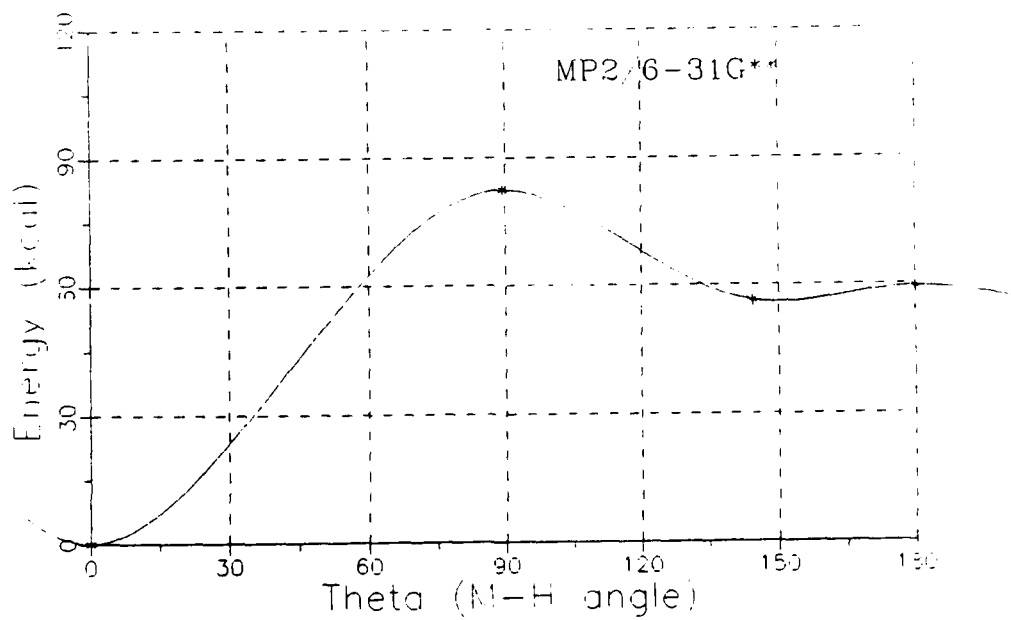
H-A1-C (----) A1-O-H											
H-A1-O	H-A-B	HALF	R-NH	<HMA	E(Hartree)	E(kcal)	R-AB	R-HA	<HAB	R-HE	<HBA
HF/3-21G	HA10132*	0.0000	0.0000	0.00	-315.560732	0.00	1.6045	1.5685	180.00	0.0000	0.00
	HA10332*	0.9359	1.6289	75.08	-315.482235	49.26	1.6715	1.6422	0.00	2.0017	57.39
	HA10232*	0.3095	0.0000	0.00	-315.688450	-57.59	1.5563	0.0000	0.00	0.9493	179.98
	HA10432*	0.8095	0.0000	180.00	-315.688450	-57.59	1.5563	0.0000	0.00	0.9494	180.00
HF/6-31G	HA10163	0.0000	0.0000	0.00	-317.247062	0.00	1.5244	1.5657	180.00	0.0000	0.00
	HA10363	0.8456	1.6218	77.02	-317.163125	52.67	1.6911	1.6521	0.00	1.9902	59.45
	HA10263	0.0000	0.0000	0.00	-317.360850	-71.40	1.6930	0.0000	0.00	0.9370	179.97
	HA10463	0.0000	0.0000	180.00	-317.360850	-71.40	1.6928	0.0000	0.00	0.9371	180.00
HF/6-31G*	HA10163D	0.0000	0.0000	0.00	-317.300569	0.00	1.5722	1.5592	180.00	0.0000	0.00
	HA10363D	0.8101	1.5846	77.41	-317.209310	57.27	1.6201	1.6148	0.00	1.9305	0.00
	HA10263D	0.0000	0.0000	0.00	-317.381951	-51.07	1.6818	0.0000	0.00	0.9398	154.99
	HA10463D	0.0000	0.0000	180.00	-317.381890	-51.03	1.6718	0.0000	0.00	0.9375	180.00
HF/6-31G**	HA10163P	0.0000	0.0000	0.00	-317.301504	0.00	1.5724	1.5572	180.00	0.0000	0.00
	HA10363P	0.8099	1.5846	77.28	-317.210477	57.12	1.6198	1.6129	0.00	1.9319	0.00
	HA10263P	0.0000	0.0000	0.00	-317.389744	-55.37	1.6695	0.0000	0.00	0.9329	179.00
	HA10463P	0.0000	0.0000	180.00	-317.389744	-55.37	1.6693	0.0000	0.00	0.9331	180.00
HF2/6-31G**	HA10163H	0.0000	0.0000	0.00	-317.574905	0.00	1.5254	1.5609	180.00	0.0000	0.00
	HA10363H	0.9219	1.4980	82.61	-317.502900	45.25	1.6437	0.0000	0.00	0.0000	0.00
	HA10263H	0.0000	0.0000	0.00	-317.634594	-37.46	1.6878	0.0000	0.00	0.9511	179.98
	HA10463H	0.0000	0.0000	180.00	-317.634594	-37.46	1.6879	0.0000	0.00	0.9510	180.00
HF2/6-31G**	HA101H3	0.0000	0.0000	0.00	-317.549200	0.00	1.5900	1.5500	180.00	0.0000	0.00
	HA103H3	0.8240	1.5700	78.00	-317.485800	39.78	1.6400	0.0000	0.00	0.0000	0.00
	HA102H3	0.0000	0.0000	0.00	-317.630038	-50.73	1.6815	0.0000	0.00	0.9464	179.86
	HA104H3	0.0000	0.0000	180.00	-317.630000	-50.63	1.3037	0.0000	0.00	0.0000	180.00

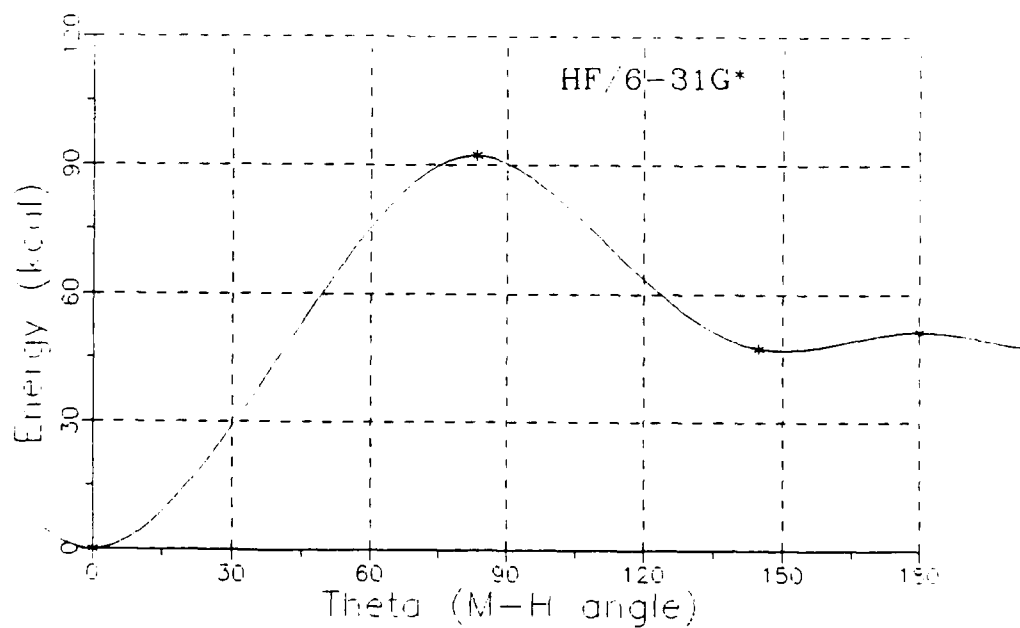
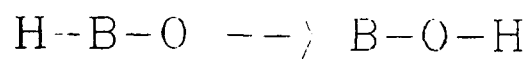
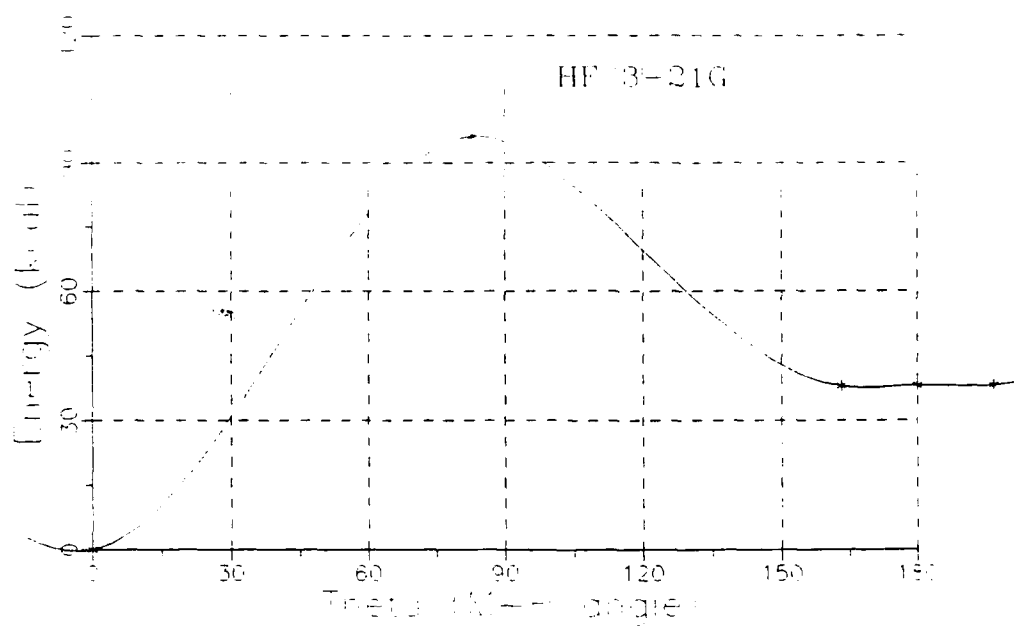


HF/6-31G**



MP2/6-31G**





from the midpoint (CHMA), and the absolute and relative energies. HOB , HSB , and HSAI are bent at the highest levels calculated, whereas HCAI appeared to be bent at the HF/6-31G^* level but became linear at higher levels. A paper incorporating these results will be submitted soon for publication. Similar calculations on $\text{HBF}^+-\text{BFH}^+$, HCP-CPH , HBeF-BeFH , HSiP-SiPH , $\text{HSiS}^+-\text{SiSH}^+$, and $\text{HPN}^+-\text{PNH}^+$ are in various stages of progress.

Other Molecules. Many calculations have been performed on other molecules not reported here. For example, complete MNDO optimizations have been carried out on various derivatives of cyclophosphamide, which might serve as potential anti-cancer drugs. Pictured in Figure 5 are three orthogonal views of an adamantyl derivative synthesized by Talaty. AM1 calculations have been carried out on several of the polycyclic hydrocarbons up to triphenylene and tetracene, both of formula, $\text{C}_{18}\text{H}_{12}$ (see Figure 6).

Considerable work has been done to study the rotational or inversional barrier to isomerization around the $\text{N}=\text{N}$ bond in diimide, diazodiethene, and azobenzene and around the $\text{C}=\text{C}$ bond in butadiene, hexatriene, and stilbene (see Figure 7). One conclusion of this work is that the rotation of the benzene rings in stilbene and azobenzene is surprisingly free, suggesting much less 'conjugation' through the central bond than commonly believed (the MOPAC, π bond order between a central $\text{C}=\text{C}$ carbon and the ring carbon is less than 0.1).

ADAMANTYL CPA MUSTARD (AE)

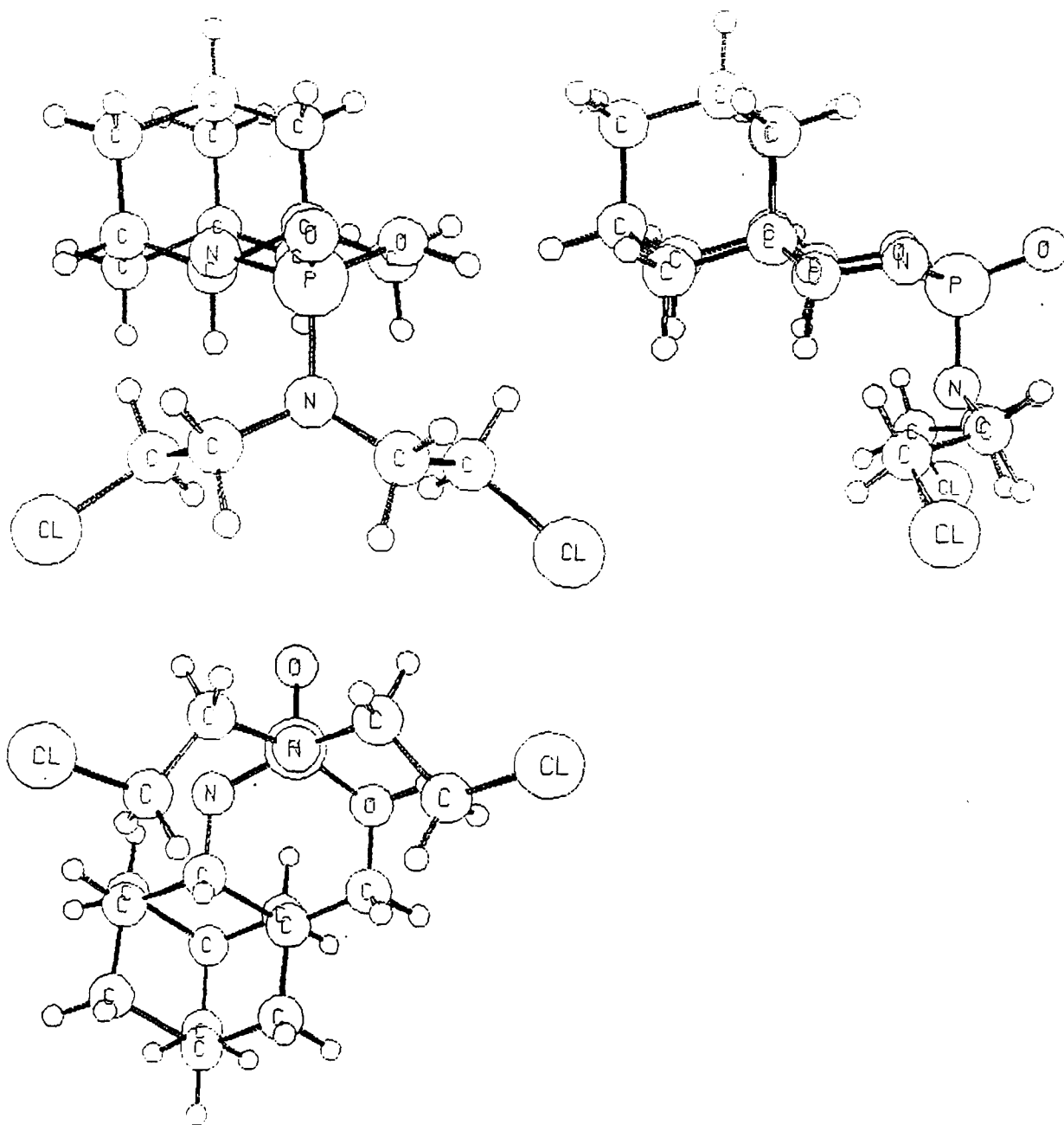
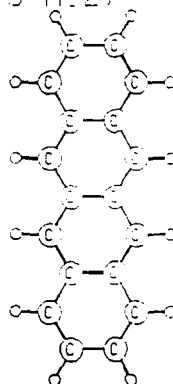


Figure 5. Three orthogonal views of an adamantyl derivative of (2-[bis(2-chloroethyl)amino]-2H-1,3,2-oxazaphosphorinane 2-oxide optimized with MNDO.

TETRACENE (C18 H12)

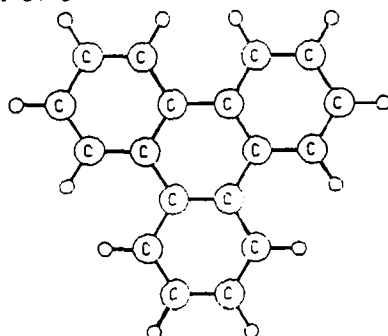


c18h12tet.arc

NO	ATOM	X	Y	Z
1	C	+0.000	+0.000	+0.000
2	C	+1.430	+0.000	+0.000
3	C	+2.170	+1.233	+0.000
4	C	+1.434	+2.459	+0.000
5	C	-0.000	+1.233	+0.000
6	C	-0.003	+2.459	+0.000
7	C	-2.120	-1.233	+0.000
8	C	-1.434	-2.459	+0.000
9	C	-1.439	-1.233	+0.000
10	C	-2.121	-2.457	+0.000
11	C	-0.002	-1.233	+0.000
12	C	+1.431	+4.874	+0.000
13	C	-0.000	+3.702	+0.000
14	C	+0.000	+4.874	+0.000
15	C	+2.121	-3.702	+0.000
16	C	+1.431	-4.874	+0.000
17	C	-0.000	-3.702	+0.000
18	C	-0.000	-4.874	+0.000
19	H	+3.001	+1.237	+0.000
20	H	-1.790	+1.227	+0.000
21	H	-3.221	-1.227	+0.000
22	H	-1.780	-1.227	+0.000
23	H	+3.222	+3.687	+0.000
24	H	+1.453	+3.842	+0.000
25	H	-1.791	+3.687	+0.000
26	H	-3.222	+3.842	+0.000
27	H	+3.222	-3.687	+0.000
28	H	+1.453	-3.842	+0.000
29	H	-1.791	-3.687	+0.000
30	H	-3.222	-3.842	+0.000

HEAT OF FORMATION = +86.9420 KCAL/MOL
 IONIZATION POTENTIAL = +7.7473 EV
 MOLECULAR DIPOLE = +0.0001 DEBYE
 GRADIENT NORM = +0.0000

c18h12tp.arc



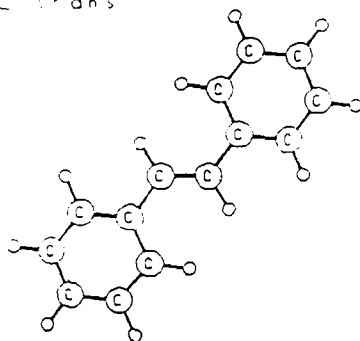
c18h12tp.arc

NO	ATOM	X	Y	Z
1	C	+0.000	+0.000	+0.000
2	C	+1.415	+0.000	+0.000
3	C	+2.145	+1.237	+0.000
4	C	+1.426	+2.483	+0.000
5	C	-0.000	+1.280	+0.000
6	C	-0.016	+2.484	+0.000
7	C	-2.094	-1.237	+0.000
8	C	-1.405	-2.457	+0.000
9	C	-0.006	-1.233	+0.000
10	C	+1.133	+1.280	+0.000
11	C	-2.879	+2.487	+0.000
12	C	-2.145	+3.692	+0.000
13	C	-0.000	+2.488	+0.000
14	C	+3.353	+1.284	+0.000
15	C	+2.126	+2.481	+0.000
16	C	+2.167	+3.687	+0.000
17	C	+3.353	+1.693	+0.000
18	C	+1.953	+1.270	+0.000
19	C	+1.781	-3.190	+0.000
20	C	-1.781	-3.186	+0.000
21	C	-3.344	-3.389	+0.000
22	C	-2.121	-2.454	+0.000
23	C	-3.371	+2.488	+0.000
24	C	-2.121	+3.687	+0.000
25	C	-0.000	+4.850	+0.000
26	C	+2.120	+4.850	+0.000
27	C	+3.350	+2.480	+0.000
28	C	+1.447	+4.838	+0.000
29	C	+4.104	+4.644	+0.000

HEAT OF FORMATION = +73.4964 KCAL/MOL
 IONIZATION POTENTIAL = +8.6374 EV
 MOLECULAR DIPOLE = +0.0016 DEBYE
 GRADIENT NORM = +0.0000

Figure 6. Optimized stuctures of two isomers of C₁₈H₁₂with AM1. Top - Tetracene. Bottom - Triphenylene

STILBENE trans

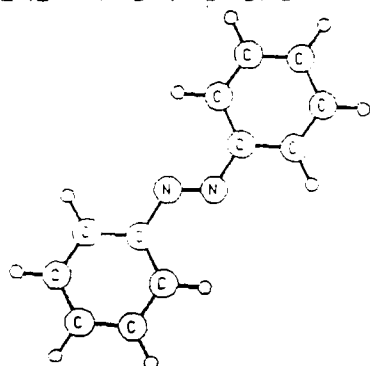


HEAT OF FORMATION
IONIZATION POTENTIAL
MOLECULAR DIPOLE
GRADIENT NORM

+40.8627 KCAL/MOL
+8.4899 EV
+.0000 DEBYE
+.0000

NO	ATOM	X	Y	Z
1	C	0.000	0.000	0.000
2	C	1.344	0.000	0.000
3	C	2.184	1.185	0.000
4	C	2.184	-1.185	0.000
5	C	1.344	0.000	0.000
6	C	0.000	0.000	0.000
7	C	-1.344	0.000	0.000
8	C	-2.184	1.185	0.000
9	C	-2.184	-1.185	0.000
10	C	-1.344	0.000	0.000
11	C	0.000	0.000	0.000
12	C	1.344	0.000	0.000
13	C	2.184	1.185	0.000
14	C	2.184	-1.185	0.000
15	C	1.344	0.000	0.000
16	C	0.000	0.000	0.000
17	C	-1.344	0.000	0.000
18	C	-2.184	1.185	0.000
19	C	-2.184	-1.185	0.000
20	C	-1.344	0.000	0.000
21	C	0.000	0.000	0.000
22	C	1.344	0.000	0.000
23	C	2.184	1.185	0.000
24	C	2.184	-1.185	0.000
25	C	1.344	0.000	0.000
26	C	0.000	0.000	0.000
27	C	-1.344	0.000	0.000
28	C	-2.184	1.185	0.000
29	C	-2.184	-1.185	0.000
30	C	-1.344	0.000	0.000
31	C	0.000	0.000	0.000
32	C	1.344	0.000	0.000
33	C	2.184	1.185	0.000
34	C	2.184	-1.185	0.000
35	C	1.344	0.000	0.000
36	C	0.000	0.000	0.000
37	C	-1.344	0.000	0.000
38	C	-2.184	1.185	0.000
39	C	-2.184	-1.185	0.000
40	C	-1.344	0.000	0.000
41	C	0.000	0.000	0.000
42	C	1.344	0.000	0.000
43	C	2.184	1.185	0.000
44	C	2.184	-1.185	0.000
45	C	1.344	0.000	0.000
46	C	0.000	0.000	0.000
47	C	-1.344	0.000	0.000
48	C	-2.184	1.185	0.000
49	C	-2.184	-1.185	0.000
50	C	-1.344	0.000	0.000
51	C	0.000	0.000	0.000
52	C	1.344	0.000	0.000
53	C	2.184	1.185	0.000
54	C	2.184	-1.185	0.000
55	C	1.344	0.000	0.000
56	C	0.000	0.000	0.000
57	C	-1.344	0.000	0.000
58	C	-2.184	1.185	0.000
59	C	-2.184	-1.185	0.000
60	C	-1.344	0.000	0.000
61	C	0.000	0.000	0.000
62	C	1.344	0.000	0.000
63	C	2.184	1.185	0.000
64	C	2.184	-1.185	0.000
65	C	1.344	0.000	0.000
66	C	0.000	0.000	0.000
67	C	-1.344	0.000	0.000
68	C	-2.184	1.185	0.000
69	C	-2.184	-1.185	0.000
70	C	-1.344	0.000	0.000
71	C	0.000	0.000	0.000
72	C	1.344	0.000	0.000
73	C	2.184	1.185	0.000
74	C	2.184	-1.185	0.000
75	C	1.344	0.000	0.000
76	C	0.000	0.000	0.000
77	C	-1.344	0.000	0.000
78	C	-2.184	1.185	0.000
79	C	-2.184	-1.185	0.000
80	C	-1.344	0.000	0.000
81	C	0.000	0.000	0.000
82	C	1.344	0.000	0.000
83	C	2.184	1.185	0.000
84	C	2.184	-1.185	0.000
85	C	1.344	0.000	0.000
86	C	0.000	0.000	0.000
87	C	-1.344	0.000	0.000
88	C	-2.184	1.185	0.000
89	C	-2.184	-1.185	0.000
90	C	-1.344	0.000	0.000
91	C	0.000	0.000	0.000
92	C	1.344	0.000	0.000
93	C	2.184	1.185	0.000
94	C	2.184	-1.185	0.000
95	C	1.344	0.000	0.000
96	C	0.000	0.000	0.000
97	C	-1.344	0.000	0.000
98	C	-2.184	1.185	0.000
99	C	-2.184	-1.185	0.000
100	C	-1.344	0.000	0.000
101	C	0.000	0.000	0.000
102	C	1.344	0.000	0.000
103	C	2.184	1.185	0.000
104	C	2.184	-1.185	0.000
105	C	1.344	0.000	0.000
106	C	0.000	0.000	0.000
107	C	-1.344	0.000	0.000
108	C	-2.184	1.185	0.000
109	C	-2.184	-1.185	0.000
110	C	-1.344	0.000	0.000
111	C	0.000	0.000	0.000
112	C	1.344	0.000	0.000
113	C	2.184	1.185	0.000
114	C	2.184	-1.185	0.000
115	C	1.344	0.000	0.000
116	C	0.000	0.000	0.000
117	C	-1.344	0.000	0.000
118	C	-2.184	1.185	0.000
119	C	-2.184	-1.185	0.000
120	C	-1.344	0.000	0.000
121	C	0.000	0.000	0.000
122	C	1.344	0.000	0.000
123	C	2.184	1.185	0.000
124	C	2.184	-1.185	0.000
125	C	1.344	0.000	0.000
126	C	0.000	0.000	0.000
127	C	-1.344	0.000	0.000
128	C	-2.184	1.185	0.000
129	C	-2.184	-1.185	0.000
130	C	-1.344	0.000	0.000
131	C	0.000	0.000	0.000
132	C	1.344	0.000	0.000
133	C	2.184	1.185	0.000
134	C	2.184	-1.185	0.000
135	C	1.344	0.000	0.000
136	C	0.000	0.000	0.000
137	C	-1.344	0.000	0.000
138	C	-2.184	1.185	0.000
139	C	-2.184	-1.185	0.000
140	C	-1.344	0.000	0.000
141	C	0.000	0.000	0.000
142	C	1.344	0.000	0.000
143	C	2.184	1.185	0.000
144	C	2.184	-1.185	0.000
145	C	1.344	0.000	0.000
146	C	0.000	0.000	0.000
147	C	-1.344	0.000	0.000
148	C	-2.184	1.185	0.000
149	C	-2.184	-1.185	0.000
150	C	-1.344	0.000	0.000
151	C	0.000	0.000	0.000
152	C	1.344	0.000	0.000
153	C	2.184	1.185	0.000
154	C	2.184	-1.185	0.000
155	C	1.344	0.000	0.000
156	C	0.000	0.000	0.000
157	C	-1.344	0.000	0.000
158	C	-2.184	1.185	0.000
159	C	-2.184	-1.185	0.000
160	C	-1.344	0.000	0.000
161	C	0.000	0.000	0.000
162	C	1.344	0.000	0.000
163	C	2.184	1.185	0.000
164	C	2.184	-1.185	0.000
165	C	1.344	0.000	0.000
166	C	0.000	0.000	0.000
167	C	-1.344	0.000	0.000
168	C	-2.184	1.185	0.000
169	C	-2.184	-1.185	0.000
170	C	-1.344	0.000	0.000
171	C	0.000	0.000	0.000
172	C	1.344	0.000	0.000
173	C	2.184	1.185	0.000
174	C	2.184	-1.185	0.000
175	C	1.344	0.000	0.000
176	C	0.000	0.000	0.000
177	C	-1.344	0.000	0.000
178	C	-2.184	1.185	0.000
179	C	-2.184	-1.185	0.000
180	C	-1.344	0.000	0.000
181	C	0.000	0.000	0.000
182	C	1.344	0.000	0.000
183	C	2.184	1.185	0.000
184	C	2.184	-1.185	0.000
185	C	1.344	0.000	0.000
186	C	0.000	0.000	0.000
187	C	-1.344	0.000	0.000
188	C	-2.184	1.185	0.000
189	C	-2.184	-1.185	0.000
190	C	-1.344	0.000	0.000
191	C	0.000	0.000	0.000
192	C	1.344	0.000	0.000
193	C	2.184	1.185	0.000
194	C	2.184	-1.185	0.000
195	C	1.344	0.000	0.000
196	C	0.000	0.000	0.000
197	C	-1.344	0.000	0.000
198	C	-2.184	1.185	0.000
199	C	-2.184	-1.185	0.000
200	C	-1.344	0.000	0.000
201	C	0.000	0.000	0.000
202	C	1.344	0.000	0.000
203	C	2.184	1.185	0.000
204	C	2.184	-1.185	0.000
205	C	1.344	0.000	0.000
206	C	0.000	0.000	0.000
207	C	-1.344	0.000	0.000
208	C	-2.184	1.185	0.000
209	C	-2.184	-1.185	0.000
210	C	-1.344	0.000	0.000
211	C	0.000	0.000	0.000
212	C	1.344	0.000	0.000
213	C	2.184	1.185	0.000
214	C	2.184	-1.185	0.000
215	C	1.344	0.000	0.000
216	C	0.000	0.000	0.000
217	C	-1.344	0.000	0.000
218	C	-2.184	1.185	0.000
219	C	-2.184	-1.185	0.000
220	C	-1.344	0.000	0.000
221	C	0.000	0.000	0.000
222	C	1.344	0.000	0.000
223	C	2.184	1.185	0.000
224	C	2.184	-1.185	0.000
225	C	1.344	0.000	0.000
226	C	0.000	0.000	0.000
227	C	-1.344	0.000	0.000
228	C	-2.184	1.185	0.000
229	C	-2.184	-1.185	0.000
230	C	-1.344	0.000	0.000
231	C	0.000	0.000	0.000
232	C	1.344	0.000	0.000
233	C	2.184	1.185	0.000
234	C	2.184	-1.185	0.000
235	C	1.344	0.000	0.000
236	C	0.000	0.000	0.000
237	C	-1.344	0.000	0.000
238	C	-2.184	1.185	0.000
239	C	-2.184	-1.185	0.000
240	C	-1.344	0.000	0.000
241	C	0.000	0.000	0.000
242	C	1.344	0.000	0.000
243	C	2.184	1.185	0.000
244	C	2.184	-1.185	0.000
245	C	1.344	0.000	0.000
246	C	0.000	0.000	0.000
247	C	-1.344	0.000	0.000
248	C	-2.184	1.185	0.000
249	C	-2.184	-1.185	0.000
250	C	-1.344	0.000	0.000
251	C	0.000	0.000	0.000
252	C	1.344	0.000	0.000
253	C	2.184	1.185	0.000
254	C	2.184	-1.185	0.000
2				

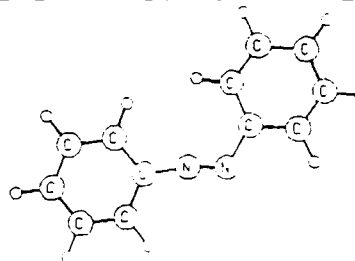
AZOBENZENE (trans-planar)



HEAT OF FORMATION = +100.0551 KCAL/MOL
 IONIZATION POTENTIAL = +9.1086 EV
 MOLECULAR DIPOLE = +.0000 DEBYE
 GRADIENT NORM = +.0000

asibenz.arc			
NO	ATOM	X	Y
1	N	+0.000	+0.000
2	N	+0.000	+0.000
3	C	+1.231	+0.000
4	C	+1.231	+1.747
5	C	+3.353	+1.149
6	C	+1.432	+1.247
7	C	-1.232	+1.149
8	C	-1.432	+1.247
9	C	-3.353	+1.149
10	C	-1.231	+0.000
11	C	+1.349	+3.322
12	C	+3.322	+1.349
13	C	+1.349	+3.322
14	C	+3.322	+1.349
15	C	+1.349	+3.322
16	C	+3.322	+1.349
17	C	+1.349	+3.322
18	C	+3.322	+1.349
19	C	+1.349	+3.322
20	C	+3.322	+1.349
21	C	+1.349	+3.322
22	C	+3.322	+1.349
23	C	+1.349	+3.322
24	C	+3.322	+1.349

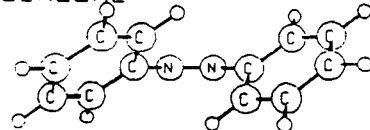
AZOBENZENE TRANSITION STATE



HEAT OF FORMATION = +128.2831 KCAL/MOL
 IONIZATION POTENTIAL = +9.3428 EV
 MOLECULAR DIPOLE = +2.1033 DEBYE
 GRADIENT NORM = +.0000

asibenz.arc			
NO	ATOM	X	Y
1	N	+0.000	+0.000
2	N	+1.191	+0.000
3	C	+1.440	+1.267
4	C	+3.346	+1.148
5	C	-1.351	+1.202
6	C	-1.882	+1.514
7	C	+1.433	+2.288
8	C	+3.345	+3.357
9	C	-1.348	+3.354
10	C	-1.798	+2.288
11	C	-3.814	+1.153
12	C	-1.338	+2.184
13	C	-4.202	+4.433
14	C	-1.719	+2.881
15	C	-3.814	+1.153
16	C	-1.798	+2.288
17	C	-4.157	+1.014
18	C	-2.244	+3.891
19	C	-1.820	+2.895
20	C	-3.814	+1.153
21	C	-1.719	+2.737
22	C	-3.814	+1.153
23	C	-1.884	+1.925
24	C	-4.305	+1.535

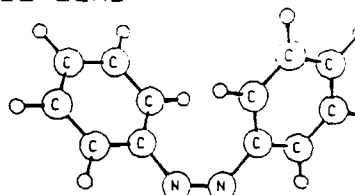
CIS AZOBENZENE



HEAT OF FORMATION = +94.0390 KCAL/MOL
 IONIZATION POTENTIAL = +9.2495 EV
 MOLECULAR DIPOLE = +3.2298 DEBYE
 GRADIENT NORM = +.0000

asibenz2.arc			
NO	ATOM	X	Y
1	N	+0.000	+0.000
2	N	+1.204	+0.000
3	C	+2.128	+0.000
4	C	+1.952	+1.107
5	C	+1.952	+1.107
6	C	+2.128	+0.000
7	C	-1.952	+1.104
8	C	-1.952	+1.104
9	C	-2.128	+0.000
10	C	-1.952	+1.104
11	C	-1.952	+1.104
12	C	-2.128	+0.000
13	C	-1.952	+1.104
14	C	-1.952	+1.104
15	C	-2.128	+0.000
16	C	-1.952	+1.104
17	C	-1.952	+1.104
18	C	-2.128	+0.000
19	C	-1.952	+1.104
20	C	-1.952	+1.104
21	C	-2.128	+0.000
22	C	-1.952	+1.104
23	C	-1.952	+1.104
24	C	-2.128	+0.000

CIS AZOBENZENE

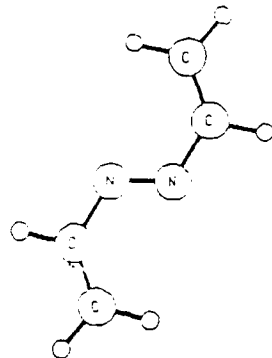


HEAT OF FORMATION = +94.0390 KCAL/MOL
 IONIZATION POTENTIAL = +9.2495 EV
 MOLECULAR DIPOLE = +3.2298 DEBYE
 GRADIENT NORM = +.0000

asibenz2.arc			
NO	ATOM	X	Y
1	N	+0.000	+0.000
2	N	+1.204	+0.000
3	C	+2.128	+0.000
4	C	+1.952	+1.107
5	C	+1.952	+1.107
6	C	+2.128	+0.000
7	C	-1.952	+1.104
8	C	-1.952	+1.104
9	C	-2.128	+0.000
10	C	-1.952	+1.104
11	C	-1.952	+1.104
12	C	-2.128	+0.000
13	C	-1.952	+1.104
14	C	-1.952	+1.104
15	C	-2.128	+0.000
16	C	-1.952	+1.104
17	C	-1.952	+1.104
18	C	-2.128	+0.000
19	C	-1.952	+1.104
20	C	-1.952	+1.104
21	C	-2.128	+0.000
22	C	-1.952	+1.104
23	C	-1.952	+1.104
24	C	-2.128	+0.000

Figure 7. (continued)

DIAZOETHENE (cis trans cis)

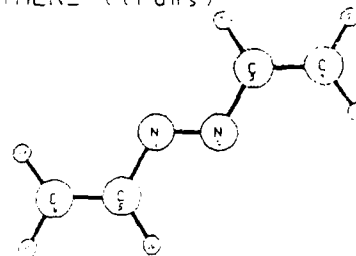


azethct.arc

NO	ATOM	X	Y	Z
1	N	+0.000	+0.000	+0.000
2	N	+1.231	+0.000	+0.000
3	C	+1.431	+1.228	+0.000
4	C	+1.493	+1.488	+0.001
5	H	-0.718	+1.228	+0.000
6	H	-0.762	+1.488	+0.002
7	H	+0.429	+0.731	+0.002
8	H	+0.489	+0.939	+0.001
9	H	+0.034	+1.004	+0.001
10	H	-0.804	+0.732	+0.003
11	H	-0.754	+0.939	+0.002
12	H	-1.803	+1.004	+0.001

HEAT OF FORMATION = +80.0809 KCAL/MOL
 IONIZATION POTENTIAL = +9.7041 EV
 MOLECULAR DIPOLE = +0.014 DEBYE
 GRADIENT NORM = +0.0000

DIAZOETHENE (trans)

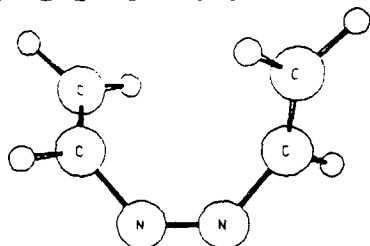


azethn.arc

NO	ATOM	X	Y	Z
1	N	+0.000	+0.000	+0.000
2	N	+1.232	+0.000	+0.000
3	C	+1.909	+1.242	+0.000
4	C	+3.250	+1.312	+0.000
5	H	-1.877	+1.242	+0.000
6	H	-2.012	+1.312	+0.001
7	H	+0.897	+0.426	+0.001
8	H	+3.770	+2.280	+0.000
9	H	+1.310	+2.194	+0.000
10	H	-2.843	+1.426	+0.004
11	H	-2.538	+2.280	+0.002
12	H	-0.078	+2.194	+0.002

HEAT OF FORMATION = +84.2030 KCAL/MOL
 IONIZATION POTENTIAL = +9.4689 EV
 MOLECULAR DIPOLE = +0.0006 DEBYE
 GRADIENT NORM = +0.0000

DIAZOETHENE (all cis)

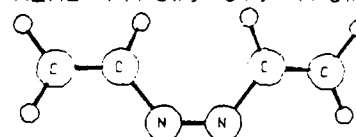


azethcsf.arc

NO	ATOM	X	Y	Z
1	N	+0.000	+0.000	+0.000
2	N	+1.207	+0.000	+0.000
3	C	+2.119	+1.098	+0.000
4	C	+2.132	+0.127	+0.000
5	H	-0.912	+1.098	+0.000
6	H	-0.944	+0.125	+0.000
7	H	+1.397	+2.201	+1.828
8	H	+1.778	+2.823	+0.824
9	H	+2.911	+0.940	+0.739
10	H	-1.281	+2.297	+1.634
11	H	-1.704	+2.832	+0.922
12	H	-1.708	+0.942	+0.744

HEAT OF FORMATION = +76.5884 KCAL/MOL
 IONIZATION POTENTIAL = +9.8134 EV
 MOLECULAR DIPOLE = +2.9311 DEBYE
 GRADIENT NORM = +0.0000

DIAZOETHENE (trans cis trans)



azethcsr.arc

NO	ATOM	X	Y	Z
1	N	+0.000	+0.000	+0.000
2	N	+1.209	+0.000	+0.000
3	C	+2.073	+1.144	+0.000
4	C	+3.354	+1.077	+0.000
5	H	-1.843	+1.143	+0.000
6	H	-2.133	+1.082	+0.000
7	H	+0.997	+1.120	+0.000
8	H	+3.773	+1.120	+0.000
9	H	+1.688	+2.085	+0.442
10	H	+2.585	+1.190	+0.824
11	H	-2.797	+1.957	+1.207
12	H	-2.441	+2.073	+1.201

HEAT OF FORMATION = +78.3914 KCAL/MOL
 IONIZATION POTENTIAL = +9.7785 EV
 MOLECULAR DIPOLE = +2.8403 DEBYE
 GRADIENT NORM = +0.0000

Figure 7. (continued)

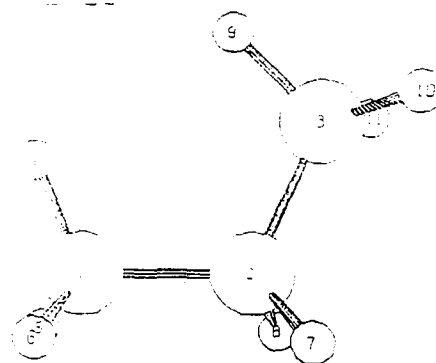
III. CONVERGENCE OF GRADIENT ENERGY OPTIMIZATION ROUTINES TO STATIONARY POINTS THAT ARE NOT LOCAL MINIMA

It is rather well known that gradient minimization routines sometimes "stick" at stationary points that are not minima. In order to investigate this phenomena more closely, we made several energy optimization calculations on propane with various starting geometries. Shown in Figure 8 are three structures that are stationary points on the AM1 and 3-21G energy surfaces. Starting with atoms 1, 1, 2, 3, and 9 in planar arrangement, and approximate bond lengths, the eclipsed-eclipsed (EE) form is reached by both AM1 and 3-21G. Starting with atoms 4, 1, 2, 3, and 10 in a plane, the eclipsed-staggered (ES) form results. Finally, with almost any geometry not close to EE or ES, the global minimum, staggered-staggered (SS) form results.

The EE form has AM1 energy (standard enthalpy of formation) of -21.293 kcal/mol with two negative eigenvalues of the Hessian matrix yielding imaginary frequencies of 179 and 171 cm^{-1} . The ES form has AM1 energy of -22.939 kcal/mol with one negative eigenvalue yielding imaginary frequency of 158 cm^{-1} . The SS form has AM1 energy of -24.263 kcal/mol. The 3-21G energies are EE = -117.60211 au. (7.0 kcal/mol), ES = -117.60810 au. (3.3 kcal/mol), and SS = -117.61330 au. (0.0 kcal/mol).

The interesting effect is that starting with a geometry corresponding to rotation of one methyl group by 10 degrees from the C_{2v} EE form, AM1 optimizes to the ES form, while rotation of one methyl group by 5 degrees yields the SS form! For 3-21G, 10 degrees yields SS while 20 degrees yields ES! Rotating the methylene group 10 degrees out of the plane of the carbons

PROPANE SS



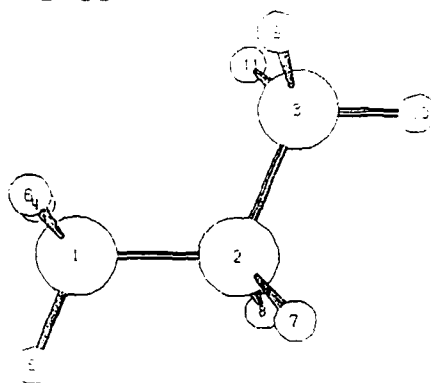
propEE0.arc
 HEAT OF FORMATION * -21.2922 KCAL/MOL
 IONIZATION POTENTIAL * +11.3462 EV
 MOLECULAR DIPOLE * +0.0111 DEBYE
 GRADIENT NORM * +0.0000

NO	ATOM	X	Y	Z
1	C	+0.000	+0.000	+0.000
2	C	+1.311	+0.000	+0.000
3	C	+2.155	+1.307	+0.000
4	H	-0.410	+1.026	+0.001
5	H	-0.395	-0.708	+0.002
6	H	-0.394	-0.225	+0.905
7	H	+1.879	-0.265	+0.890
8	H	+1.879	-0.265	-0.898
9	H	+1.344	+2.183	+0.001
10	H	+2.764	+1.529	+0.902
11	H	+2.762	+1.529	-0.903

propEE0.arc
 HEAT OF FORMATION * -21.2922 KCAL/MOL
 IONIZATION POTENTIAL * +11.3462 EV
 MOLECULAR DIPOLE * +0.0111 DEBYE
 GRADIENT NORM * +0.0000

NO	ATOM	X	Y	Z
1	C	+0.000	+0.000	+0.000
2	C	+1.311	+0.000	+0.000
3	C	+2.155	+1.307	+0.000
4	H	-0.410	+1.026	+0.001
5	H	-0.395	-0.708	+0.002
6	H	-0.394	-0.225	+0.905
7	H	+1.879	-0.265	+0.890
8	H	+1.879	-0.265	-0.898
9	H	+1.344	+2.183	+0.001
10	H	+2.764	+1.529	+0.902
11	H	+2.762	+1.529	-0.903

PROPANE SS



propSS.arc
 HEAT OF FORMATION * -24.2622 KCAL/MOL
 IONIZATION POTENTIAL * +11.3244 EV
 MOLECULAR DIPOLE * +0.0043 DEBYE
 GRADIENT NORM * +0.0000

NO	ATOM	X	Y	Z
1	C	+0.000	+0.000	+0.000
2	C	+1.307	+0.000	+0.000
3	C	+2.067	+0.999	+0.000
4	H	-0.394	-0.225	+0.905
5	H	-0.390	-0.240	+0.000
6	H	-0.394	-0.240	+0.905
7	H	+1.881	-0.253	+0.902
8	H	+1.881	-0.253	-0.902
9	H	+1.727	+0.949	+0.005
10	H	+3.183	+0.959	+0.000
11	H	+1.727	+0.959	-0.905

Figure 8. Three stationary state structures of propane.

yielded the ES form in both AM1 and 3-21G. Ethane converges to a staggered form, S, regardless of input geometry (even an eclipsed starting geometry, E).

It is interesting that results seem to show that with starting geometries close to a stationary point but having a few coordinates far from optimum, the gradient routines will move the offending components toward minimizing the gradient even though one or more eigenvalues are negative. If the geometry is such that most components are close to a stationary point, the routines may find a direction such that the line minimization will distort the molecule so severely that the global minimum results. Clearly, this situation destroys confidence in the existing gradient routines to find a true minimum. For larger molecules it is very inconvenient and time consuming to evaluate the normal mode frequencies (FORCE keyword in MOPAC, FREQ keyword in GAUSSIAN-86) to insure that there are no negative eigenvalues of the Hessian matrix.

We are currently evaluating a possible fix for this problem. In the process of gradient optimization, both the MOPAC and GAUSSIAN-86 routines update the inverse Hessian matrix. If any negative eigenvalues appear, both routines arbitrarily change the sign of the offending eigenvalue and continue the search. We propose instead to make use of the admittedly approximate and incomplete information implicit in the Hessian to search along the eigenvector corresponding to the negative eigenvalue. Since MOPAC does not take the time to diagonalize the inverse Hessian at each step, this search could be optionally performed after

apparent convergence to a minimum. Due to the much longer computation time in GAUSSIAN-86 and since diagonalization is already performed at each step, little extra time would be consumed by this search. Preliminary results to this point have been disappointing.

IV. ATOM EQUIVALENTS FOR CONVERTING *AB-INITIO* ENERGIES TO STANDARD ENTHALPIES OF FORMATION

A simple procedure is described for relating *ab-initio* 6-31G* calculated energies to enthalpies of formation for compounds containing C, H, N, O, and F atoms. The model, first suggested by Dewar and Storch⁽⁶⁾ assumes that the heats of formation can be estimated from the difference between the calculated *ab-initio* energy and the sum of atom contributions (atom equivalents).

$$\Delta H_f^\circ = E_{6-31G^*} - \sum_{i=1}^5 a_i n_i \quad \begin{array}{l} n_i = \text{number of atoms} \\ a_i = \text{atom equivalent} \end{array}$$

A linear regression fit, using QUATTRO, for some 75 compounds yielded the following atom contributions and standard errors (in au.) with an overall standard error of estimation of the heats of formation of gaseous species of 2.57 kcal/mol. Atom equivalents for C, H, N, O, and F are -37.88298 (0.000387), -0.57156 (0.000228), -51.46298 (0.000747), -71.79780 (0.000709), and -99.35000 (0.000660), respectively.

Causes of inaccurate prediction include: inability of HF/SCF calculations to properly represent observed properties, no explicit incorporation of kinetic (thermal + zero-point)

energies, experimental errors in gaseous heats of formation, etc.

The aim of this research is not to obtain the best possible estimate of heats of formation from *ab-initio* energies, but to provide a general systematic framework for evaluating the predictions of various computational schemes and basis sets. Wiberg⁽⁷⁾ and Ibrahim and von R. Schleyer⁽⁸⁾ have suggested schemes (where the atom contributions depend on bonding patterns) that are somewhat more accurate, but involve many more parameters and cannot easily be applied to non-standard bonding patterns such as appear in transition states, delocalized bonds, "non-classical" structures, etc.

A major conclusion of this research is that the correlation between 6-31G* energies and experimental standard enthalpies of formation is much better for hydrocarbons and organic compounds containing oxygen, nitrogen and/or fluorine atoms, than for small inorganic compounds, cations, or radicals.

Either the HF/SCF calculations at the 6-31G* level are more appropriate (or at least more consistent) for these organic systems, or the model assumptions (i.e., that correlation effects, thermal and zero-point effects, unusual bonding effects, etc., can be partitioned into atom equivalents) are better satisfied for organic systems than for smaller inorganic systems.

It will be interesting to see if the correlation for 3-21G energies and experimental standard enthalpies of formation will be poorer (as was found by previous studies) and/or if the correlation will be substantially better for MP2 correlation energies. Work is in progress toward these aims. Dewar⁽⁹⁾ and

others⁽¹⁰⁾ have used effectively atom equivalents but their aim seems to be to credential AM1 rather than to find the best values of atom equivalents for general use.

V. AVERAGE LENGTH OF BUTANE FOR THE LOWER VIBRATIONAL MODES WITH VARIOUS QUANTA OF ENERGY USING THE DRC FEATURE OF MOPAC

The Dynamic Reaction Coordinate feature of MOPAC was used to follow several of the lower anharmonic vibrational modes of butane, pentane, and hexane, for 300 to 900 femtoseconds. The aim was to investigate the possibility of calculating the thermal expansion properties of polymers by computing the time averages length of a short section of polymer over a complete cycle of anharmonic vibration for various quanta of energy injected into each important vibrational (internal rotational) mode, then calculating a Boltzman temperature weighted average length over these modes as a function of temperature.

In Figure 9 is shown preliminary results for the C=O bond length and O-O distance followed for 100 and 600 femtoseconds, respectively. There appears to be some irregularity in the amplitudes of these waves, but would seem to be easily explained through the different frequencies of the stretch and bending modes, both of which contribute to the O-O distance.

More interesting is the plots of Figure 10, where the C1-C4 distance is being monitored for the zero point energy, $v=0$ (i.e., 1/2 quanta of kinetic energy injected along the eigenvector) of butane in normal modes 1, 3, 4, and 5. Note that in modes 1, and

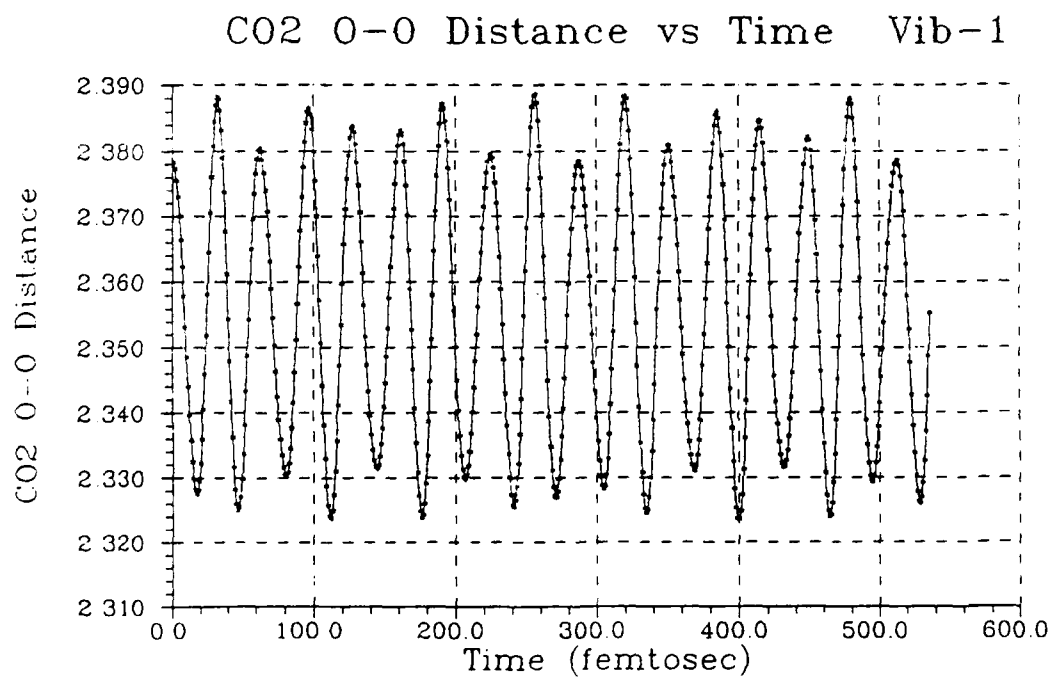
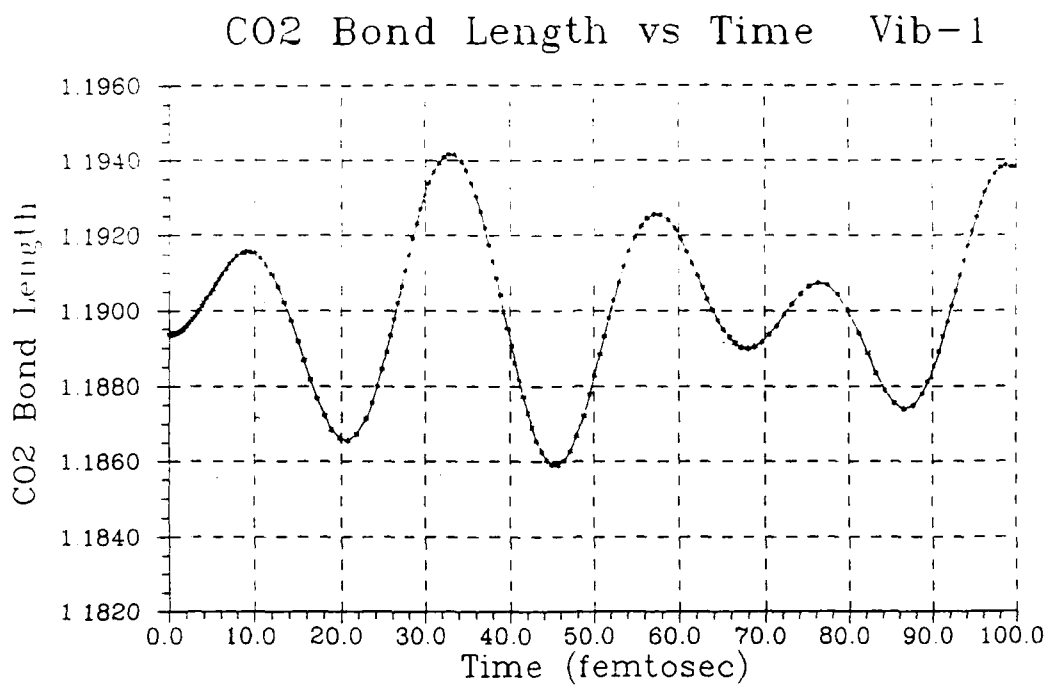


Figure 9. Preliminary AM1 DRC results for carbon dioxide.

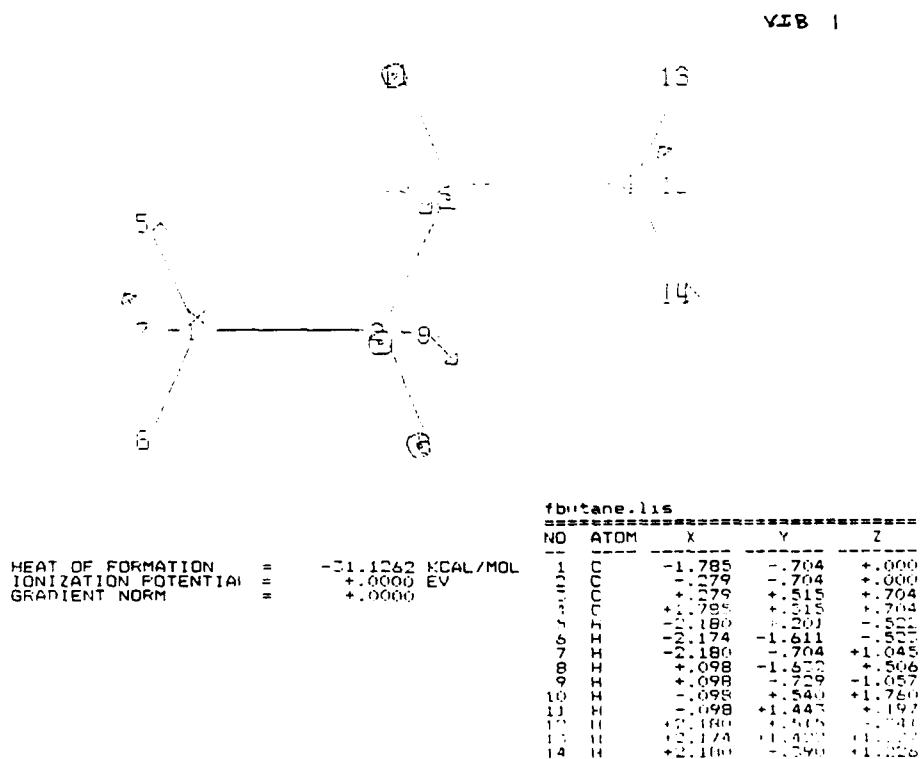
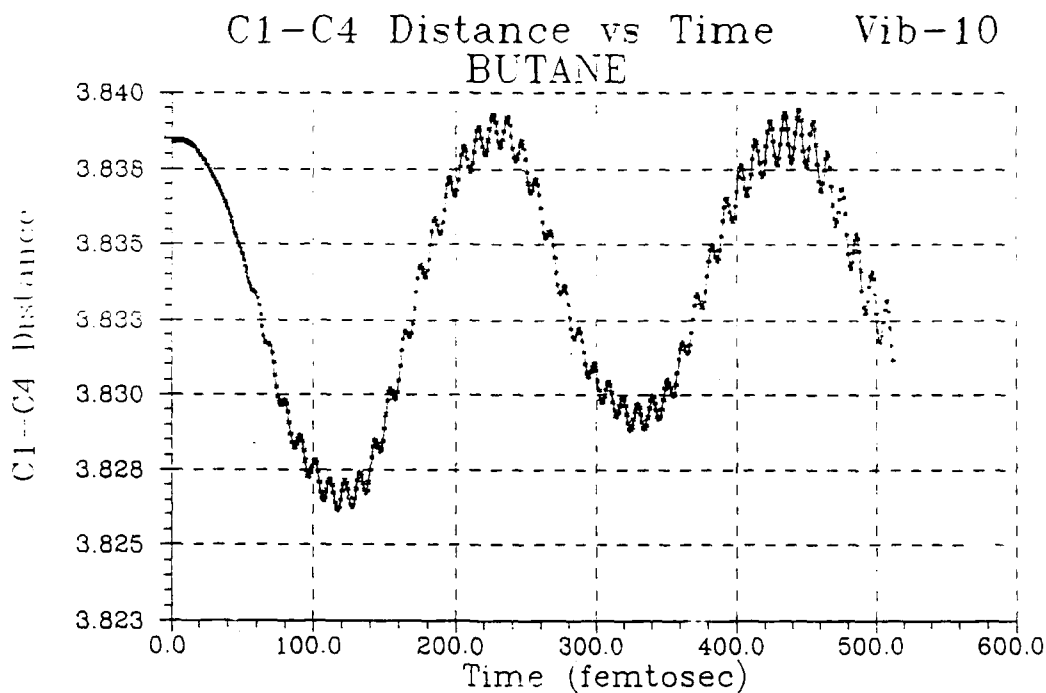
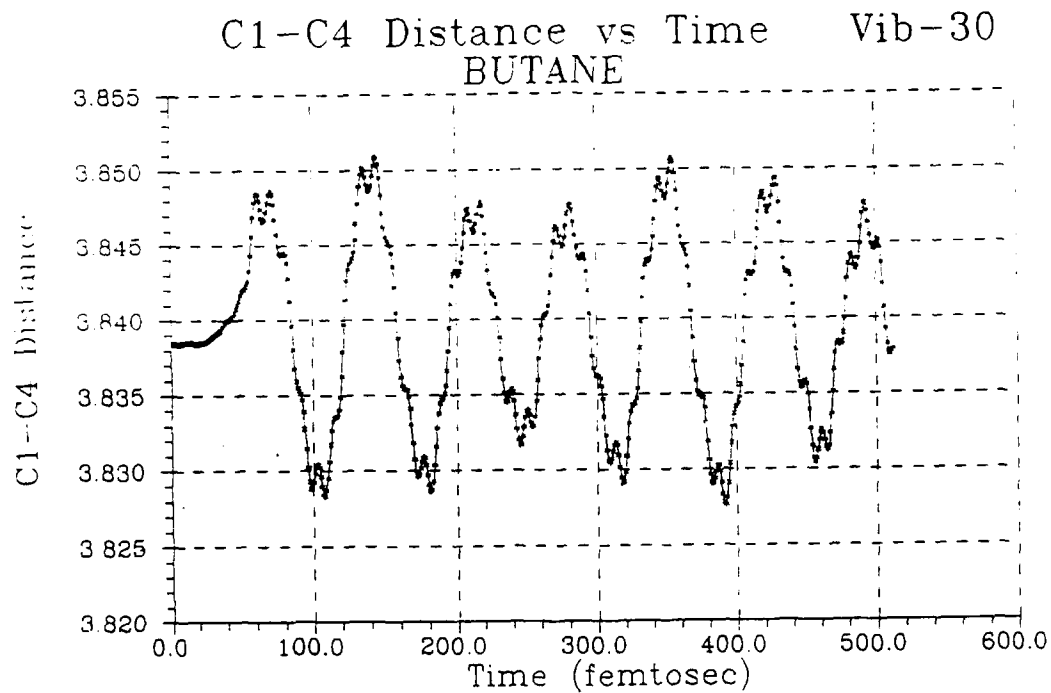


Figure 10. C1-C4 distance for v=0 states of modes 1, 3, 4, and 5 for butane.



VIB 3

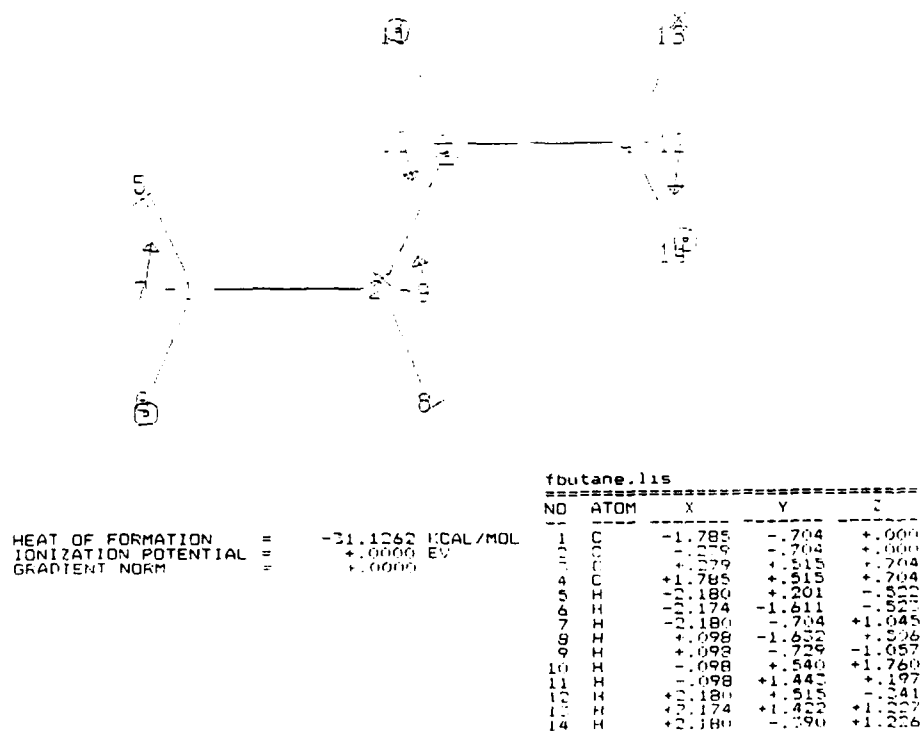
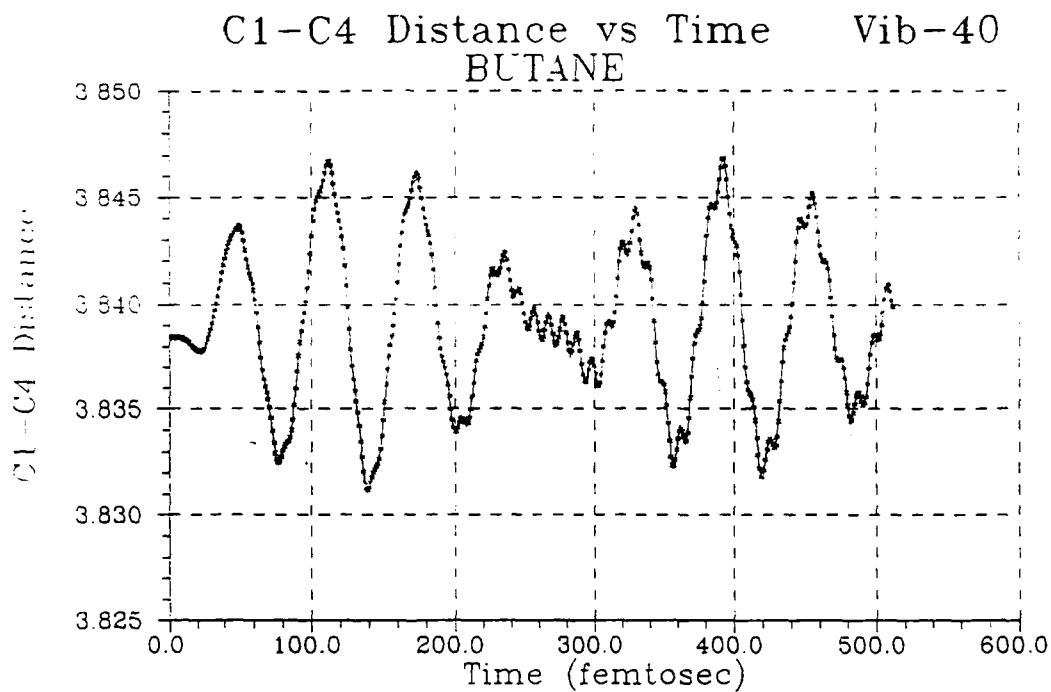
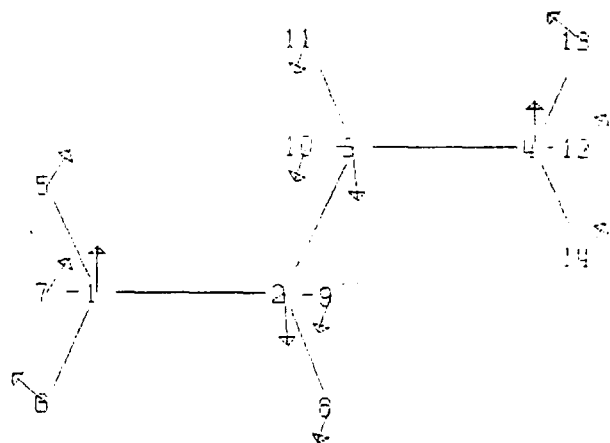


Figure 10. Continued



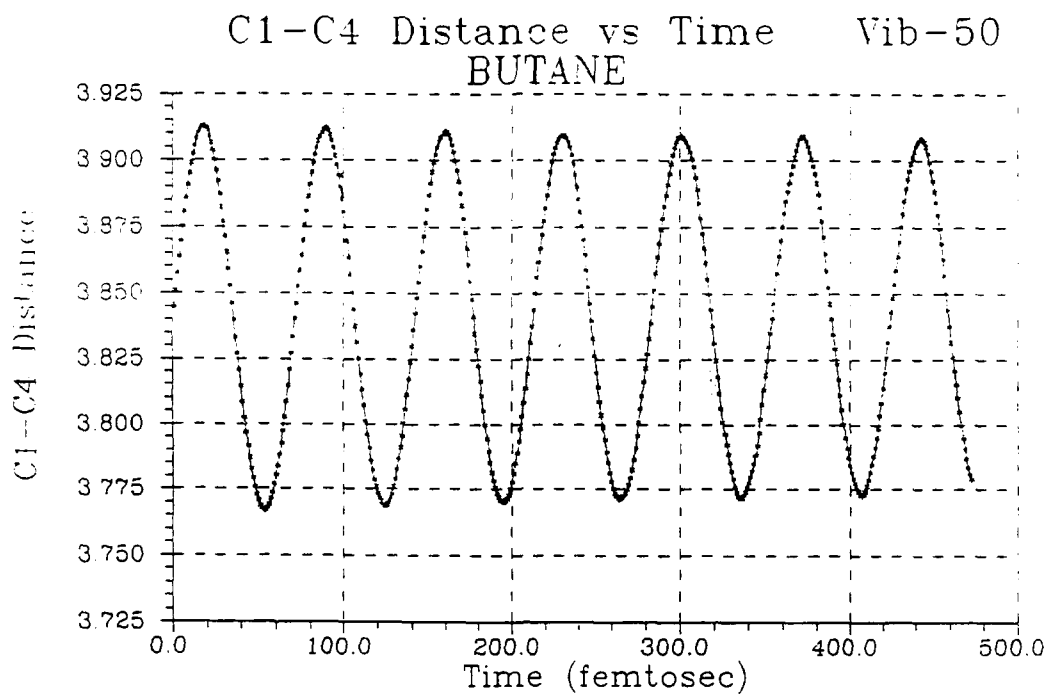
VIB 4



fbutane.lis				
NO	ATOM	X	Y	Z
1	C	-1.785	-1.704	+1.000
2	C	-1.279	-1.704	+1.000
3	C	+1.279	+1.515	+1.704
4	C	+1.785	+1.515	+1.704
5	H	+2.180	+1.201	-1.522
6	H	+2.174	-1.611	-1.522
7	H	+1.180	-1.704	+1.045
8	H	+1.098	-1.637	+1.506
9	H	+1.098	-1.729	-1.057
10	H	+1.098	+1.540	+1.760
11	H	+1.098	+1.440	+1.197
12	H	+2.180	+1.515	-1.141
13	H	+2.174	+1.422	+1.127
14	H	+2.180	-1.590	+1.226

HEAT OF FORMATION	=	-31.1262 KCAL/MOL
IONIZATION POTENTIAL	=	+1.0000 EV
GRADIENT NORM	=	+1.0000

Figure 10. Continued



VIB 5

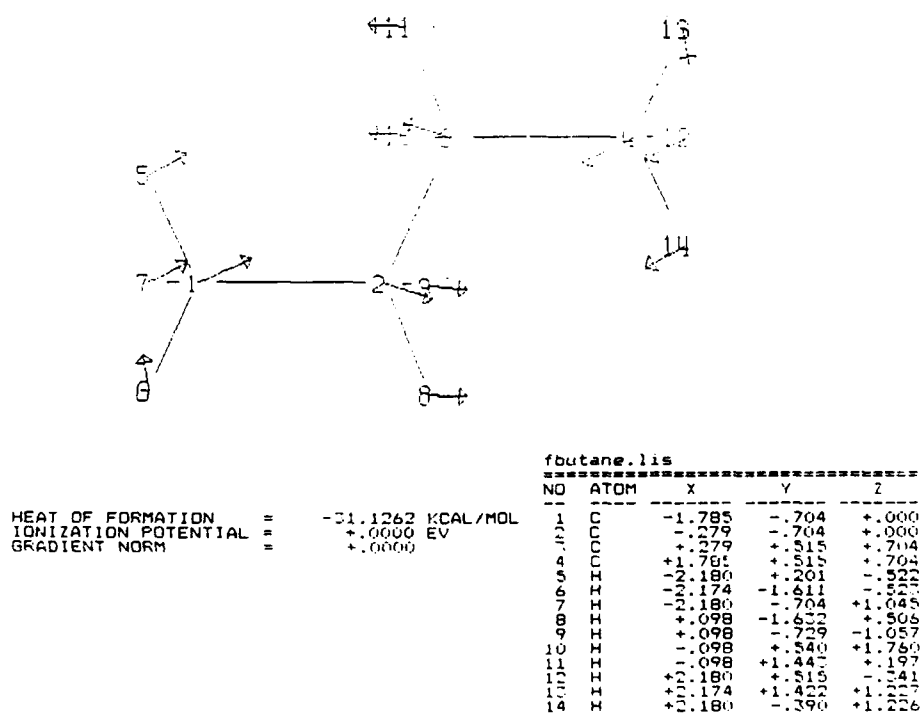


Figure 10. Continued

3 and to a lesser extent mode 4, there is considerable transfer of low frequency energy to very high frequency modes (essentially C-H stretch modes). At this low energy of excitation, quantum mechanics would not allow this transfer, so this must be interpreted as an artifact of the effectively classical surface being monitored by the DRC. A possible, but experimentally questionable, rational for transfer of energy to high frequency modes might be that of a thousand molecules, a certain number are excited at the expense of others losing energy.

In Figure 11, one and one half quanta of kinetic energy was injected (i.e., $v=1$) in mode 1, while Figure 12 show 2.5 quanta (i.e., $v=2$) in mode 1.

Although the average C1-C4 distance is considerably shorter in the more excited vibrational modes, the problem with interpretation and the extremely lengthy computational time suggested that this approach to computation of the coefficient of thermal expansion of polyethylene be abandoned. However, this attempt yielded considerable experience with the DRC routine from which much insight into following anharmonic vibrational motions was gained. Work is in progress to use the MOPAC DRC to verify studies of energy transfer in molecules, such as the CH_3CN , HONO, and nitro-N,N-dimethylamine studies performed by Donald Thompson⁽¹¹⁾ using classical empirical force field trajectories.

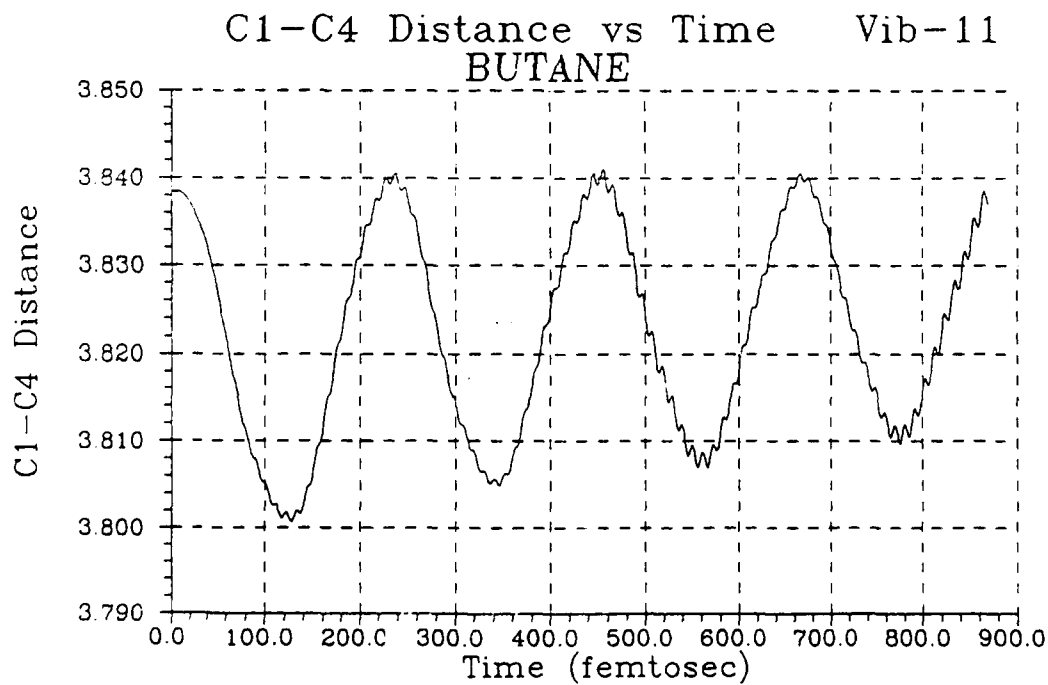
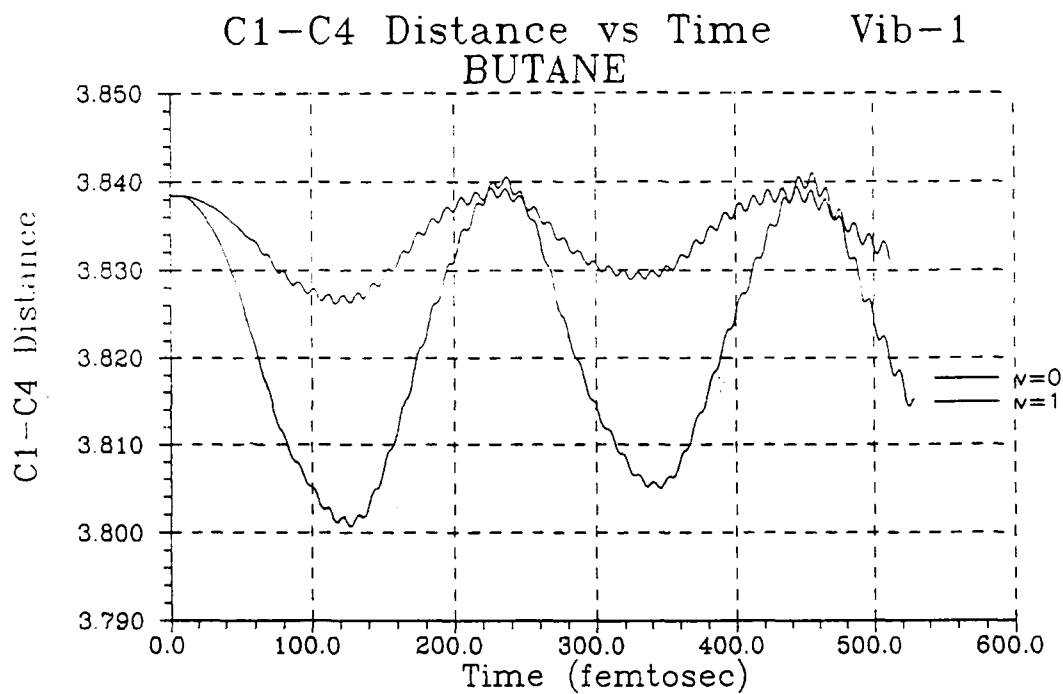


Figure 11. AM1 C1-C4, C1-C3, and C2-C3, distances for $v=1$ states of mode 1 for butane.

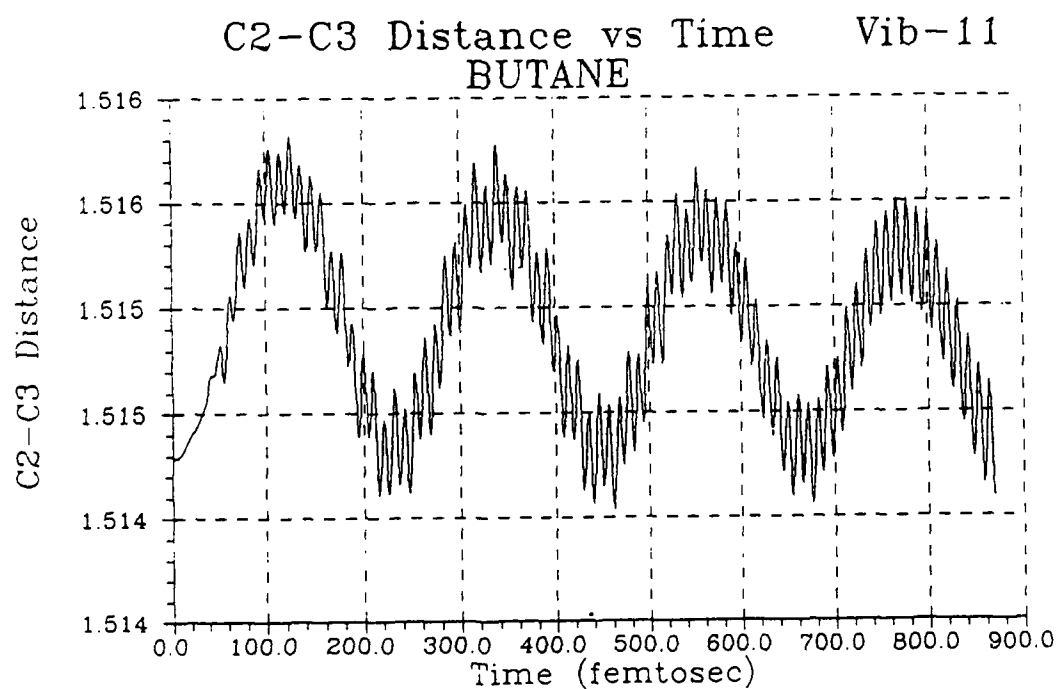
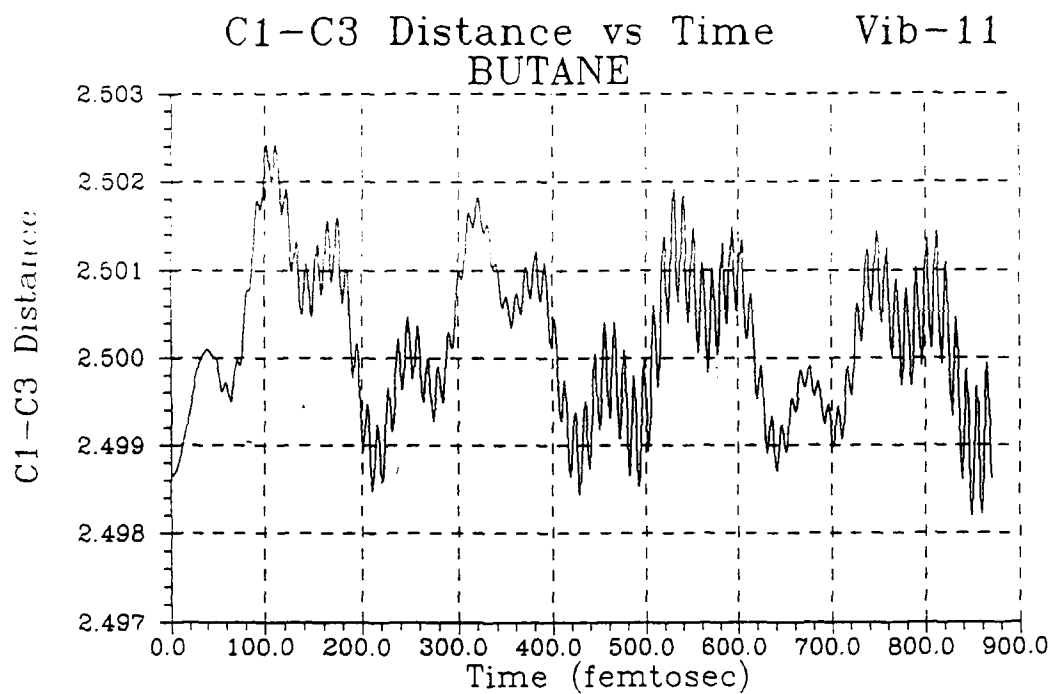


Figure 11. Continued

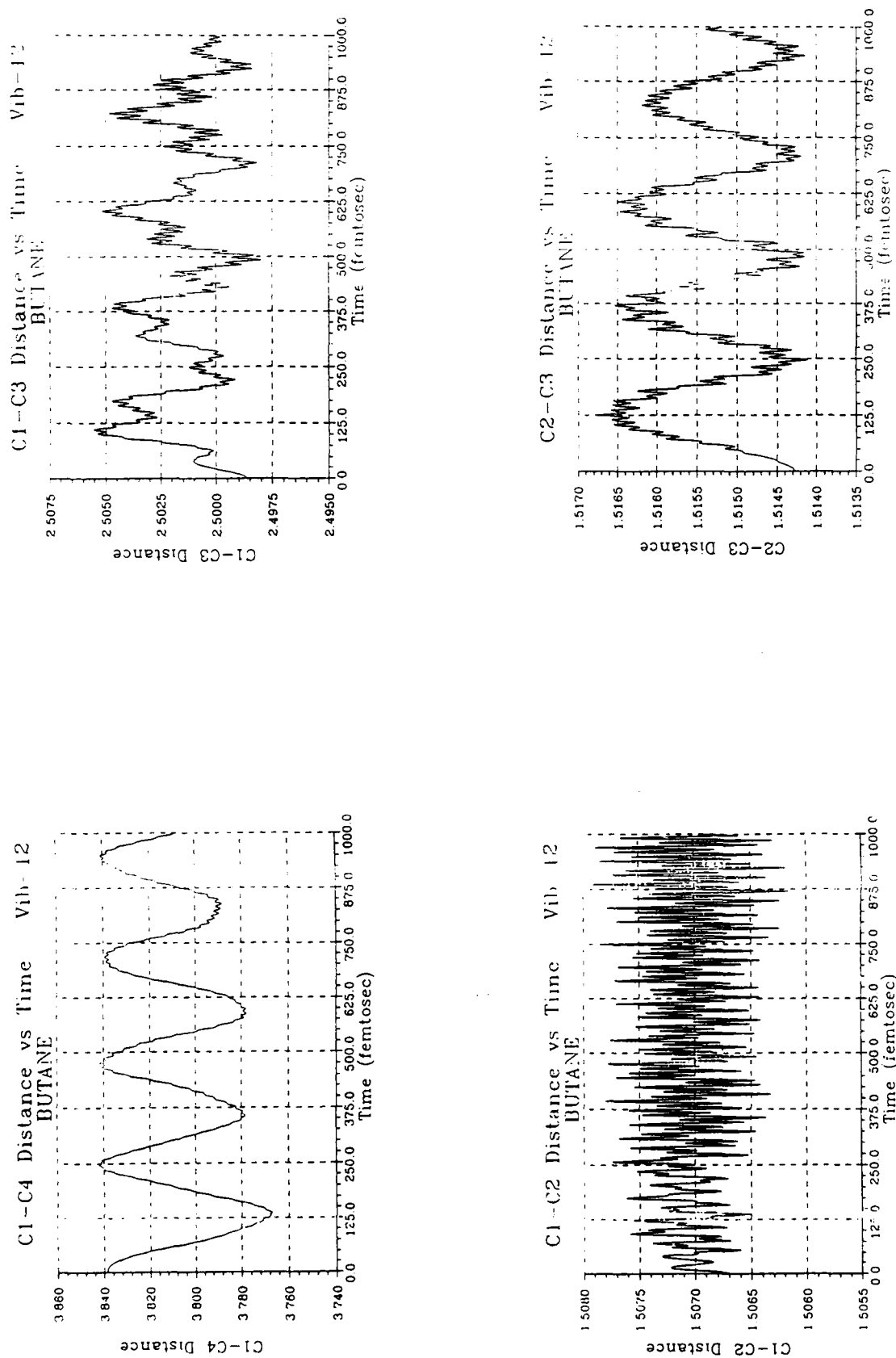


Figure 12. AM1 C1-C4, C1-C3, and C2-C3 distances for $v=2$ states of mode 1 for butane.

VI. CONCLUSION

Although, this report covers a very large number of projects, I believe that this is a very appropriate activity for research initiation. Perhaps the greatest achievement of this project is the accumulation of working equipment (computers), working software, and considerable experience with semi-empirical and *ab-initio* routines on fairly large molecules, such that project selection and accomplishment should come easier in the future.

REFERENCES

1. W. C. Groutas, M. J. Brubaker, M. E. Zandler, M. A. Stanga, T. L. Huang, J. C. Castrisos, and J. P. Crowley, "Sulfonate Salts of Amino Acids: Novel Inhibitors of the Serine Proteinases", Biochem and Biophys. Research Commun., **128**, 90 (1985).
W. C. Groutas, M. J. Brubaker, M. E. Zandler, V. Maze-Gray, S. A. Rude, J. R. Crowley, J. C. Castrisos, D. A. Dunshee, and P. K. Giri, "Inactivation of Luekocyte Elastase by Aryl Azolides and Sulfonate Salts. Structure-Activity Relationship Studies", J. Med. Chem., **29**, 1302 (1986).
2. M. E. Zandler, C. E. Choc, and C. K. Johnson, "Alene Oxide - Cyclopropanone Isomerization: A Low Barrier Pathway on the CNDO/2 Energy Surface", J. Amer. Chem. Soc., **96**, 3317 (1975).
E. R. Talaty and M. E. Zandler, "An INDO Study of the Isomerization of Aziridinone", J. Heterocyclic Chem., **12**, 151 (1975).
3. M. E. Zandler, Y. Huang, and E. R. Talaty, "Novel, Non-Linear Ten-Valence-Electron HAB Isomers on the *Ab-initio* SCF Potential Energy Surface". Paper presented at the Amer. Chem. Soc. Meeting at St. Louis, April 1984.
M. E. Zandler, and E. R. Talaty, "*Ab-initio* SCF Potential Energy Surfaces and Shapes of Isomers of HAB and HABH Type Molecules or Ions Containing Ten Valance Electrons". Paper presented at the Eleventh Austin Symposium on Molecular Structure, The University of Texas, Austin, Texas March 1986.
4. Yanchu Huang, "Studies of 10 Valence Electron HAB Type Isomers Using *ab-initio* SCF Potential Energy Surfaces", M.S. Thesis, Wichita State University, 1983.
5. M. W. Wong, R. H. Nobes, and L. Radom, "The $[HCS]^+$ and $[H_2CS]^+$ Potential Energy Surfaces: Predictions of Bridged Equilibrium Structures", J. Molec. Struct. (Theochem), **163**, 51 (1988).
6. M. J. S. Dewar and D. M. Storch, "Comparative Tests of Theoretical Procedures for Studying Chemical Reactions", J. Amer. Chem. Soc., **107**, 3898 (1985).
M. J. S. Dewar, "Quantum Mechanical Molecular Models", J. Phys. Chem., **89**, 2145 (1985).
7. K. B. Wiberg, "Group Equivalents for Converting *Ab-initio* Energies to Enthalpies of Formation", J. Comp. Chem., **5**, 197 (1984).
8. M. R. Ibrahim, and P. von R. Schleyer, "Atom Equivalents for Relating *Ab-initio* Energies to Enthalpies of Formation", J. Comp. Chem., **6**, 157 (1985).

9. M. J. S. Dewar, and E. M. O'Connor, "Testing *Ab-initio* Procedures: The 6-31G* Model", Chem. Phys. Letters, 138, 141 (1987).
10. N. C. Baird and G. C. Hadley, "An Analysis of Predictions by the Semi-Empirical MNDO Molecular Orbital Method for Some Aspects of Molecular Energetics", Chem. Phys. Letters, 128, 31 (1986).
11. B. G. Sumpter and D. L. Thompson, "Intramolecular Dynamics of the Overtone-Induced Isomerization of Methyl Isocyanide", J. Chem. Phys., 87, 5609 (1987).
Y. Guan, G. C. Lynch, and D. L. Thompson, "Intramolecular Energy Transfer and *cis-trans* Isomerization in HONO", J. Chem. Phys., 87, 6957 (1987).

Appendices can be obtained from
Universal Energy Systems, Inc.

1988 USAF-UES RESEARCH INITIATION PROGRAM

Sponsored by the
AIR FORCE OFFICE OF SCIENTIFIC RESEARCH

Conducted by the
UNIVERSAL ENERGY SYSTEMS, INC.

FINAL REPORT

RADIATIVE ASSOCIATION IN ION-MOLECULE REACTIONS:
REACTIONS OF SOME CARBON CATIONS

Submitted by: Lucia M. Babcock
Associate Professor of Chemistry
Department of Chemistry
Louisiana State University, Baton Rouge, LA

USAF Researcher: John F. Paulson

Date: 1 January 1989 - 31 December 1989

Contract No: F49620-88-C-0053/SB5881-0378

RADIATIVE ASSOCIATION IN ION-MOLECULE REACTIONS:
REACTIONS OF SOME CARBON CATIONS

by

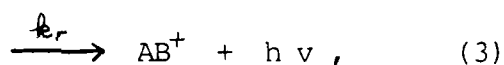
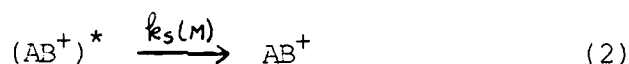
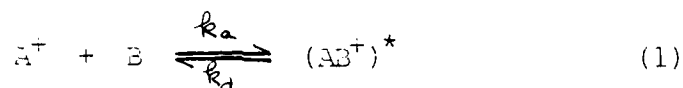
Lucia A. Babcock

ABSTRACT

In this final report, we describe our continued examination of gas phase ion-molecule association reactions, paying particular attention to the phenomenon of radiative association. In previous studies we identified the addition of halide ions to the boron trihalides as a class of reaction which undergoes radiative as well as collisional stabilization in ion-molecule association reactions. Because CX_3^+ ions are isoelectronic with BX_3 , they are likely candidates for radiative association also. In addition, these reactions are of particular interest because of the relevance of carbocations to interstellar ion-molecule chemistry where radiative association is presumed to be of key importance in synthesizing larger ions. Our work on the carbocation reactions was begun under the SFRP program in Dr. John F. Paulson's laboratory at Geophysics Laboratory (AFSC), and continued in our own laboratory as part of the AFCSR Research Initiation Program. We targeted three areas for emphasis: (1) analysis of data already gathered, (2) complementary flowing afterglow (FA) studies, and (3) continuation of the search for new systems and modification to our instrument to enhance these studies. In this final report, we present the results of data analysis for reactions of CH_3^+ , CD_3^+ , and CF_3^+ with SO_2 over the pressure range 0.25-1.00 Torr as a function of temperature over the range 190 - 470K. Complementary studies involving the FA apparatus are reported for the reaction of CF_3^+ with SO_2 . A thorough characterization of the properties of He, Ar, and N_2 as buffer gases has been carried since examination of these reactions in different third-bodies is very important in assessing the radiative component. Finally, we have modified our flowing afterglow substantially to enhance our experimental capabilities.

I. INTRODUCTION:

Radiative association in ion-molecule reactions is of fundamental mechanistic interest and is also of paramount importance in the interstellar medium where number densities are so low that synthesis of larger ions by a three-body process is negligible. As a result of this interest, both theoretical and experimental descriptions of radiative association are most desirable. However, few experimental characterizations of radiative ion-molecule association exist, due generally to the fact that under most experimentally accessible temperature and pressure conditions, collisional stabilization dominates. A general mechanism for ion-molecule association reactions is given below:



where k_a , k_d , $k_s(M)$, and k_r are rate coefficients characteristic of association to form excited $(AB^+)^*$, unimolecular decomposition of $(AB^+)^*$ back to reactants, collisional stabilization of $(AB^+)^*$ by collision with M , and radiative stabilization of $(AB^+)^*$. Of course bimolecular channels for $A^+ + B$ may exist, and this would complicate analysis of the reaction rate data. For this reason, we have carefully chosen systems where no bimolecular product channel is available under our experimental conditions. Clearly, from the mechanism shown above, radiative stabilization is favored by low pressure conditions while collisional stabilization is favored by high pressure conditions; low temperatures facilitate both processes because the lifetime of $(AB^+)^*$ increases as temperature decreases.

The importance of radiative stabilization in interstellar processes was recognized¹ and incorporated into models² as early as 1973 despite the lack of corroborating experimental evidence

at that time. To date there are still relatively few studies which report evidence for radiative association. The low pressure association of Li^+ ions with carbonyl compounds is postulated to proceed via a radiative association mechanism³ as is the low pressure, non-dissociative electron attachment to several fluorinated molecules.⁴ An ion cyclotron study of CH_3HCN^+ formation from CH_3^+ and HCN was originally thought to involve radiative association,⁵⁻⁷ but in a recent re-examination, at least some of the workers conclude that radiative stabilization is not significant in this system.⁸ In 1984 Barlow, Dunn, and Schauer⁹ reported the first low temperature, low pressure kinetic evidence for radiative association in the reaction of CH_3^+ with H_2 to produce CH_5^+ , a key interstellar reaction. In none of the experimental work has a photon emitted in the process of radiative association been observed; for all systems where radiative association is involved, it has been inferred on the basis of kinetic information. This is due, at least in part, to the difficulty of performing experiments in the low pressure, low temperature regime which favors radiative over collisional stabilization. For example, using the accepted upper limit of 10^{-3} s^{-1} for emission of an IR photon from a vibrationally excited ion^{10,11} along with a value of $5 \times 10^{-10} \text{ cm}^3 \text{ molec}^{-1} \text{ s}^{-1}$ for k_5 (a typical value for an inert third-body such as He), one finds that the collisional stabilization and radiative stabilization channels are of equal probability at about 10^{-5} Torr at 300K. For radiative association to predominate would require pressures several orders of magnitude lower. Furthermore, pressure requirements become even more severe if collisional stabilization is particularly efficient or if radiative stabilization does not occur at its upper limit. In addition to experimental work, theoretical contributions to the study of radiative association have also been invaluable. Bass et al.⁶ have used the phase space approach while Herbst and Bates have done extensive theory using a statistical approach.¹⁰⁻¹²

Recently we have identified some addition reactions of the boron trihalides as reactions in which radiative stabilization is

occurs, and, most importantly, it occurs on a time scale which is competitive with collisional stabilization under typical flow afterglow experimental conditions.¹³⁻¹⁵ The radiative stabilization rate coefficients which we estimate from our kinetic data are on the order of 10^5 to 10^6 s⁻¹. While these rate coefficients are larger than the 10^3 s⁻¹ associated with emission of an IR photon,¹⁶ we have suggested that a low lying electronic state may be participating.^{14,15} Indeed, in 1988, Herbst and Bates^{10,11} incorporated electronic states into their theoretical model and obtained enhancements in the radiative rate coefficient of factors of 10 to 100 over the case where vibrational relaxation alone is considered. This enhancement brings rate coefficients for radiative association into the precise range which we observe for the BX₃ systems. The agreement is quite exciting since it suggests that, if participation of low-lying states is a general phenomenon, then relatively "high pressure" techniques such as FA can be used to probe this process. If low-lying electronic states are important, and since the BX₃ systems have proven so fruitful, it is reasonable to assume that isoelectronic and/or isovalent systems are excellent candidates for extending the investigation of radiative association in ion-molecule reactions. The work detailed in this final report represents just this effort. An examination of reactions of carbon cations (isoelectronic and/or isovalent with neutral trigonal boron complexes) began under the sponsorship of the Summer Faculty Research Program (SFRP) and was continued as Contract Number F49620-88-C-0053/SB5881-0378.

II. OBJECTIVES OF THE RESEARCH EFFORT:

With extension of our work in radiative association, we hope to begin to understand why some systems undergo efficient radiative association while others do not. Our previous work has shown that, although F^- , Cl^- , and Br^- additions to BF_3 and BCl_3 have large radiative association components,¹³⁻¹⁵ the analogous reactions of SiF_4 proceed via collisional stabilization alone.^{17,18} If, in fact, excited electronic states play a significant role, then it is reasonable to look for systems, such as the carbon cations, which are similar to the boron halides. It is also quite striking that in the interstellar medium where radiative association is of key importance, carbon cations are among the most prevalent species. Our initial work on carbon cation association reactions indicates that there is a strong possibility of radiative association. Further elucidation of these systems was a main objective of the proposed research effort. In previous BX_3 studies, we had discovered that NO_2^- adds to BX_3 with what appears to be a significant radiative component. Since SO_2 is isovalent with NO_2^- , it was our first choice of neutral partner in the study of CX_3^+ cation reactions. Furthermore, as shown in Table I below, energetic considerations preclude any charge transfer between SO_2 and the CH_3^+ , CD_3^+ , CF_3^+ , and CCl_3^+ cations. Indeed, no competing bimolecular channel was observed for any of the reactions.

Table I. Energetics (eV) for Charge Transfer Reactions^a



CH_3^+	CD_3^+	CF_3^+	CCl_3^+
+2.48	+2.49	+2.61	+3.54

^a Energetics are calculated from ionization potentials given in reference 16.

Our work carried out under the SFRP included an examination of apparent bimolecular rate coefficients for these reactions over

the temperature range 190 - 470K for pressures of 0.3 - 1.0 Torr in helium using the variable temperature selected-ion flow tube (SIFT) in Dr. John F. Paulson's laboratory at Geophysics Laboratory. The research effort described in this final report includes a detailed analysis of these results. Furthermore, it represents an extension of the work carried out on our FA apparatus.

A second important goal of the research effort was the examination of these addition reactions in a variety of third-bodies. As we have shown in our boron trihalide work, a systematic examination of the addition reaction in a series of third-bodies provides perhaps the most conclusive indication of whether radiative association is occurring in a given system. For all the reactions of SC_2 with CX_3^+ where association occurred, intercepts in plots of the observed bimolecular rate coefficients as a function of helium buffer gas (third-body) concentration were non-zero. For association reactions where radiative stabilization is important, the intercept of the plot described above must be non-zero; however, since a non-zero intercept can arise for other reasons, it, in itself, is not sufficient evidence for a significant radiative channel. If, on the other hand, the same reaction is examined in several different buffer gases, and the non-zero intercept is the same for a series of third-bodies at a given temperature, this provides strong evidence for the presence of radiative association.

Our final goal included continued modification and updating of our flowing afterglow instrument to expand the range of our experiments as well as our overall capabilities. While kinetic information is most important in elucidating radiative association in ion-molecule reactions, the most conclusive result will be the observation of the emitted radiation. It is toward this end that many of our modifications are directed. This effort includes addition of a monochromator and suitable photon detection system to our flowing afterglow as well as optimization of the entire system to maximize the possibility of observing

photons from such a diffuse source over a wide range of possible energies. As stated above, part of our goal was also to broaden the range of experimental data which can be gathered. Modifications along this avenue are directed, in part, toward the measurement of a wider range of rate coefficients in order to characterize as fully as possible the behavior of bimolecular rate coefficients as a function of temperature and pressure for very slow as well as very fast association reactions. Finally, FA and SIFT instruments are different and both are uniquely valuable in studies such as these. While SIFT instruments allow for injection of only a single reactant ion and, therefore, provide a much less complex environment in which reaction occurs, they pay a price in limited pressure range and are restricted to helium almost exclusively as the buffer gas. In FA instruments, ions are produced in the flow tube itself, and the chemistry of reacting systems can become more complex, but the experimental range of accessible pressures is much broader and a variety of buffer gases can be used provided that they have been characterized. Furthermore, number densities are much higher in the FA, a factor which will be crucial in spectroscopic studies. For association reactions, it is necessary to have well defined chemistry and also to obtain data over as wide a range of pressures and third-bodies as possible. Therefore, an instrument with both FA and SIFT capabilities is desirable, and some of our effort is directed toward this goal as well.

III. RESULTS:

Results are divided into three main categories: a) reduction and analysis of $\text{CH}_3^+ + \text{SO}_2$ data, b) flowing afterglow studies of the reactions of CH_3^+ as well as flowing afterglow characterizations of He, Ar, and N_2 buffer gases, and c) modifications which have been made to the flowing afterglow apparatus.

A. Data Analysis

During the SFRP appointment, reactions of CH_3^+ , CD_3^+ , CF_3^+ , and CCl_3^+ with SO_2 were examined a function of pressure at four different temperatures. This represents measurement of over 200 rate coefficients. We have analyzed these results using the general method developed in our study of halide ion additions to BF_3 and BCl_3 .^{13-15,18} The overall rate coefficient for the mechanism shown in equations (1) - (3) is given by the following:

$$k_{\text{obs}} = \frac{k_a[k_s(M) + k_r]}{k_d + k_s(M) + k_r} \quad , \quad (4)$$

where k_{obs} is the apparent bimolecular rate coefficient at constant pressure (that is, at constant (M)), and the other rate coefficients are as defined previously. In the limit of high pressure, $k_s(M) \gg k_d + k_r$, k_{obs} is equal to the collision rate coefficient k_a , while in the low pressure limit, $k_s(M) \ll k_d + k_r$, expression (4) reduces to the following:

$$k_{\text{obs}} = \frac{k_a k_s(M)}{k_d + k_r} + \frac{k_a k_r}{k_d + k_r} \quad , \quad (5)$$

which further reduces to

$$k_{\text{obs}} = \frac{k_a k_s(M)}{k_d} \quad , \quad (6)$$

where radiative stabilization is not significant. The

intermediate regime of pressures is known as the fall-off region, and the full expression, equation (4), must be used. This equation assumes that k_d is independent of pressure, an approximation which is only valid over a relatively narrow pressure range. For the range of pressures accessible in our experiments, the dependence of k_d upon (M) should be negligible. For each k_{obs} at a given temperature and three-body concentration, we have calculated a value of the ratio k_d/k_r . These values are independent of (M) as discussed, and since k_r is not expected to be a function of temperature, the temperature dependence of k_d has been deduced. We have had considerable success in applying this method to the boron trihalide systems, and have been able to compare the magnitude of the temperature dependence obtained to that predicted using a modified thermal theory.²⁰ Comparisons of the experimentally determined and theoretically calculated magnitudes of the temperature dependence of k_d yield information about the number of vibrational modes active in the association process. This has been done for addition of SO_2 to CH_3^+ to form $CH_3SO_2^+$.

One final point must be noted before results of the individual reactions are discussed. The term $k_s(M)$ in the overall rate coefficient represents collisional stabilization. Therefore the specific rate coefficient k_s must reflect not only the rate of collision, but also the probability that collision will lead to stabilization. It can be represented as the following:

$$k_s = \beta k_{ADO} \quad , \quad (7)$$

where k_{ADO} is the collision rate coefficient calculated using the average dipole orientation (ADO) theory,²¹ and β is the fraction of collisions resulting in stabilization. In our BX_3 work, we have found that the collisional efficiency for helium is 0.3. This number can only be determined by examination of relative efficiencies of a wide range of third-bodies, a study which cannot be carried out on a SIFT where these data were obtained.

One of the objectives of our characterization of other third-bodies (see a subsequent section) is to obtain values for β for these reactions. In the interim, we have elected to use 0.3 for helium, which is most likely close to the actual value.

1. $\text{CH}_3^+ + \text{SO}_2$

The only product observed in this reaction is CH_3SO_2^+ . Apparent bimolecular rate coefficients were measured over a range of He third-body concentrations from 1×10^{16} to 4×10^{16} molec cm^{-3} at 468K, 371K, 297K, and 200K. All of the temperatures show pressure dependence curves which have non-zero intercepts, indicative of the possibility of radiative association. Using the method stated above, we determined the ratio of k_d/k_r at each temperature for a collision efficiency of 0.3. These values are given in Table II below.

Table II. $k_d(T)/k_r$ for CH_3^+ in He

T(K)	468	371	297	196
$k_d(T)/k_r$	524	257	145	5.50

A value for k_r can be calculated from the data at a single temperature knowing the ratios of $k_d(T)/\beta$ and $k_d(T)/k_r$ which have been determined. At the highest temperature, 468K, the data are subject to the least curvature and we have chosen to calculate k_r from these points; we have also done a similar calculation for the 298K data for comparison. Using the 468K data, we obtain the value $k_r = 1.28 \times 10^5 \text{ s}^{-1}$; k_d at each temperature can be calculated and $k_d(T)$ determined. Table III presents values of k_d obtained at each temperature for $k_r = 1.28 \times 10^5 \text{ s}^{-1}$ (the 468K value), for $k_r = 1.99 \times 10^6 \text{ s}^{-1}$ (the 298K value), and $k_r = 0$ (that is, no radiative component) in k_d columns 1, 2, and 3 respectively.

Table III. $k_d(T)$ for $\text{CH}_3^+ + \text{SO}_2$ in He

T, K	1. k_1, s^{-1}	2. k_2, s^{-1}	3. k_3, s^{-1}
468	5.42×10^7	1.22×10^8	5.05×10^7
371	3.06×10^7	5.07×10^7	2.92×10^7
297	1.79×10^7	2.85×10^7	1.71×10^7
200	9.84×10^6	1.42×10^7	9.66×10^6

When a temperature dependence of the general form $k_d = AT^n$ is used, values of n obtained from $\log k_d$ as a function of $\log T$ for columns 1, 2, and 3 above are: 2.47, 2.17, and 2.12 respectively. Correlation coefficients are all 0.98 which indicates that the fits are not truly linear. The temperature dependence is fairly insensitive to the choice of k_r , as can be seen above. An examination of the raw data shows that for the low temperature points (obtained using pulsed liquid nitrogen cooling) there is quite a variation in temperature over the course of the data collection. If this temperature point is omitted, values of n obtained are: 3.20 (0.994), 2.81 (0.997), and 2.78 (0.997) for columns 1, 2, and 3 respectively, where correlation coefficients are given in parentheses. The fits are much better, but this analysis does not aid in determining the correct value for k_r . Clearly, work in other third-bodies is necessary to answer this question. Finally, temperature dependencies were calculated using the modified thermal theory²⁰ for various numbers of vibrational modes participating; there is very little difference observed in n for 1, 2, or 3 frequencies of SO_2 used. With these analyses of data, we conclude from our work thus far that it is likely that this addition reaction has a significant radiative component, but further work in different third-bodies is mandatory to make a definite statement. We believe that the value of the unimolecular rate coefficient, $k_d(T)$, varies as $T^{2.81}$ where we have chosen as best values $k_r = 1.28 \times 10^5 \text{ s}^{-1}$ (that is, the 468K value) and a collisional stabilization efficiency of 0.3.

2. $CD_3^+ + SO_2$

As in the case of the CD_3^+ reaction, the association product, $CD_3SO_2^+$, is the only product observed. The data are obtained for k_r concentrations in the range 1.1×10^{-12} to 3.0×10^{-13} molec cm^{-3} for temperatures of 468K, 373K, 297K, and 191K. Once again we employed a collisional stabilization efficiency factor of 0.3 for helium. The ratio k_d/k_r has been calculated for each temperature and is given in Table IV below.

Table IV. $k_d(T)/k_r$ for $CD_3^+ + SO_2$ in He

T (K)	468	373	297	191
$k_d(T)/k_r$	55.5	11.2	6.6	1.9

The value of k_r calculated from the 468K data is $6.10 \times 10^5 s^{-1}$ while that calculated from the 297K data is $2.41 \times 10^6 s^{-1}$. As discussed in the section above, we feel that the 468K value is the best choice, but others are given for the sake of comparison. Table V presents values of k_d at each temperature for the two different k_r values; no $k_r = 0$ set has yet been calculated. Column 1 gives values calculated using $k_r = 6.10 \times 10^5 s^{-1}$ and column 2 those calculated using $k_r = 2.41 \times 10^6 s^{-1}$.

Table V. $k_d(T)$ for $CD_3^+ + SO_2$ in He

T (K)	1. k_d, s^{-1}	2. k_d, s^{-1}
468	4.49×10^7	6.94×10^7
373	2.17×10^7	3.16×10^7
297	1.14×10^7	1.58×10^7
191	4.17×10^6	5.75×10^6

For the general temperature dependence $k_d = AT^n$, fits of $\log k_d(T)$ as a function of T yield the following values of n: $n = 2.63$ (0.997) and $n = 2.75$ (0.995) for the 468K and 297K values of k_r respectively; the correlation coefficients for the linear fits

are given in parentheses. The low temperature data for this set of reactions is much more reliable, and this is reflected in the above values. It is once again quite clear that temperature dependence data alone will not distinguish between various values of k_p . Our choice of best value for k_p is the 463K value of $3.10 \times 10^5 \text{ s}^{-1}$. This results in $k_d(T)$ varying as $T^{2.63}$.

3. $\text{CF}_3^+ + \text{SO}_2$

For the reaction of SO_2 with CF_3^+ ions, the addition product, CF_3SO_2^+ , alone is observed at all temperatures and pressures examined. The apparent rate coefficients for these reactions were approximately fifty times smaller than those for CH_3^+ and CD_3^+ reactions with SO_2 . Addition reactions were studied as a function of pressure at 213K, 243K, 296K, and 372K, and graphs of the log of the ion signal as a function of reaction progress (that is, of added neutral reactant) showed significant curvature. There are several possible reasons for this curvature. First, there could be some reverse process which causes production of reactant ion at large extents of reaction - this is the behavior one observes in a system where equilibrium is being established. It is possible that collisional break-up of the CF_3SO_2^+ complex is important. If this is the case, rate information obtained from initial stages of the reaction where the equilibrium is far from established should represent the forward process. A second possible source of curvature arises from the slowness of the reaction. For the SIFT instrument used to obtain the data, the available reaction distance required addition of very large amounts of neutral SO_2 in order to observe any decrease in reactant ion signal. These large amounts can perturb the flow and diffusion properties, introducing errors into measured rate coefficients. Third, it must be considered that the curvature is instrumental in origin.

We carried out analysis of the data using the initial portions of our data where curvature was not yet significant (by visual inspection). Unfortunately, this also means that very small changes in CF_3^+ concentration were observed and that rate

coefficients were obtained from slopes of very shallow lines, often defined by only a few points. While linear plots of k_{obs} as a function of $P(\text{SO}_2)$ can be obtained in this way, we are not at all confident of the accuracy of these data points. This is especially true since the results differ quite dramatically from data taken on our FA instrument at LSU which is better designed to examine slow reactions; these results are described in a subsequent section. As a result, we can only make qualitative conclusions based upon our SFRP data for this reaction, and will carry out further studies. The qualitative conclusions are: (1) there appears to be only addition occurring, and it occurs much more slowly than do the corresponding reactions of CH_3^+ and CD_3^+ , (2) the rate coefficients increase as temperature decreases as expected for association reactions, (3) it appears that k_{obs} does depend linearly on pressure, (4) an equilibrium-type analysis of the data indicates that collisional break-up is not responsible for the curvature observed, (5) curvature is probably due to the large amounts of SO_2 added to observe reaction or is due to some instrumental characteristic; indeed, this is supported by the absence of curvature in the data obtained on our FA which is described in the following section, and (6) there appears to be a common non-zero intercept of $3 \times 10^{-12} \text{ cm}^3 \text{ molec}^{-1} \text{ s}^{-1}$ for all temperatures; this is unusual and could actually represent a "zero" value for the SIFT instrument. In any event, it is impossible to say whether or not radiative association plays a role in this reaction on the basis of the SIFT data.

B. Flowing Afterglow Studies

1. $\text{CF}_3^+ + \text{SO}_2$

This reaction was repeated on our ambient temperature flowing afterglow instrument which has considerably longer reaction distances than are available on the GL SIFT. We examined the reaction at 297K over the pressure range 0.25 - 1.31 Torr in helium. The only product observed was CF_3SO_2^+ as in the previous studies. With reaction distances of 60 and 84 cm, we are able to study slower reactions without addition of so much

neutral reactant. Under no conditions was curvature observed, and linearity of k_{obs} with helium concentration was good for the entire range. It must be concluded that curvature observed in the SIFT data was an artifact of the necessary operating conditions or of the instrument. Rate coefficients obtained from the FA data are a factor of approximately five smaller than those obtained from initial slopes of the SIFT data, but are much more reliable. The intercept is very small but non-zero at approximately $1 \times 10^{-12} \text{ cm}^3 \text{ molec}^{-1} \text{ s}^{-1}$. Clearly more work on this reaction must be carried out using our FA instrument to characterize the rates of reaction and to determine whether or not radiative association is occurring.

2. Time of Flight Determinations of v_i/v_0

A series of studies involving the use of different third-bodies will help us to determine whether or not the non-zero intercepts observed in some ion-molecule association reaction rate data are due to radiative association. Furthermore, these studies will permit us to obtain values of the radiative association rate coefficients, or at least to place upper limits on them. Toward this end, we have made a thorough characterization of flow properties of He, Ar, and N_2 in our flowing afterglow apparatus.

In FA and SIFT techniques, experiments are carried out under continuous flow conditions. That is, the reaction time is constant, and is defined by the reaction distance and the velocity with which the reactant mixture flows down the tube. Under typical experimental conditions, the flow profile in the reactor is that of laminar, parabolic flow.^{17,22} The ions travelling at the point of the parabola reach the detector with a velocity greater than the bulk flow velocity, and the ratio of the ion velocity to the bulk flow velocity is given by v_i/v_0 . While it is ion velocity which is needed in order to obtain rate information from data, the bulk flow velocity is more easily measured and is then adjusted by the factor v_i/v_0 . If this method is to be used, it is most important to have established

that the ratio v_i/v_o is constant over the experimental range used, or to obtain a table of appropriate values.

We have measured v_i/v_o for He, Ar, and N_2 as a function of pressure, buffer gas flow, nature of plasma (that is, ion-electron or ion-ion plasma), electron emission current, positive or negative ion regime, perturbing pulse amplitude, perturbing pulse width, and mass of signal monitored. This represents the collection of well over 500 pairs of data points. We have found v_i/v_o not to vary significantly with any of these parameters over a wide range studied, with perhaps one exception. The ratio v_i/v_o for Ar appears to increase as emission current is increased, and although the increase is slight and within reproducibility limits, the trend is there. For example, a value of $v_i/v_o = 1.53 \pm 0.07$ is obtained at 150 μA of current while $v_i/v_o = 1.50 \pm 0.05$ is obtained at 75 μA of emission current. Average values for v_i/v_o for each of the three buffer gases are given in Table VI below. The Ar number has been calculated from the average of all data points, regardless of emission current.

Table VI. Average Values of v_i/v_o for He, Ar, and N_2

	He	Ar	N_2
v_i/v_o	1.58	1.54	1.54

C. Instrument Modification

During the granting period we have begun or completed several modifications to the flowing afterglow instrument to enable us to obtain data under as wide a range of conditions as possible, as well as to provide capabilities for undertaking new types of experiments. A capillary inlet system has been built and is currently being calibrated. This will permit controlling of flows down to much smaller values than is currently possible with the linear mass flow controllers. A third neutral reactant inlet port has been added at a reaction distance of about 28 cm. This enables us to examine rapid reactions over a wider range of

reactant ion concentration than our other ports corresponding to 50 and 64 cm reaction distances. Once again, this broadens the range over which we can obtain data. With broad neutral flow range capabilities and three different reaction distances from which to choose, we have a dynamic range of at least four orders of magnitude in rate coefficient which we can span. We have also begun design of a SIFT limb to be attached to our FA. This will provide the opportunity to operate either in the flowing afterglow mode or in the selected ion mode. The quadrupole rods and associated electronics have been purchased. Finally, we are in the process of setting up the instrument to look for radiation emitted in the radiative association process. For this purpose, a monochromator has been purchased, and design modifications and purchase of further equipment is currently in progress.

IV. EXPERIMENTAL TECHNIQUE: FLOWING AFTERGLOW:

The LSU flowing afterglow apparatus has been described in detail in the literature,¹⁷ and we have recently begun modifications to include temperature variability, SIFT capabilities, and spectroscopic detection. Kinetic studies of the $\text{CF}_3^+ + \text{SO}_2$ reaction were carried out at ambient temperature in helium buffer gas. Ions are produced by electron impact on the He buffer gas; electrons are produced by heating a thoriated iridium filament inside the flow tube. The reactant ion, CF_3^+ , was made from CF_4 dissociative charge exchange with He^+ initially formed in the plasma. Neutral SO_2 was added incrementally through a linear mass flow controller at a downstream inlet. Reactant and product ions were monitored by an Extrel quadrupole mass filter, and rate coefficients obtained from slopes of the lines of log ion concentration versus concentration of added neutral reactant gas.

Time of flight data were obtained using the same apparatus, but replacing the neutral inlet ports at 60 and 84 cm with electrodes. A square pulse was applied to one electrode and then to the other, and the time taken for the resulting perturbation in the ion signal to reach the detector was recorded. The difference between the two times represents the time taken for the ions to travel the 24 cm between the two electrodes. This difference measurement removes uncertainties attached with the "dead time" of ions in the detection portion of the apparatus. From the distance travelled and the time required to travel that distance, the ion velocity, v_i , is measured. Bulk flow velocity, v_0 , is obtained from measurements of pressure and buffer gas flow rate. The ratio v_i/v_0 is then calculated easily from these two.

V. SUMMARY AND RECOMMENDATIONS:

Radiative stabilization in ion-molecule reactions is an important and interesting area of study. The systems identified which can radiate on a time scale comparable to collisional stabilization provide the unique opportunity to examine this phenomenon in FA and SIFT studies. Indeed, this phenomenon may not be limited to only the BX_3/X^+ systems we have studied previously, but may also include the reactions of CX_3^+ as shown in our current work. Our data and data analysis have pointed to these carbon cation systems as good candidates for further studies. We have carried out the buffer gas characterizations necessary to do studies of these reactions in Ar and N_2 . This will be most important since it provides the strongest kinetic evidence either supporting or discounting radiative association. The search for other association reactions with significant radiative components should be continued in order to obtain as complete a picture as possible about the phenomenon itself. The overall goals of such an extended program are as follows: (1) assessment of the importance of electronic states in the radiative process, (2) investigation of the temperature dependence of the overall association process, (3) evaluation of rate coefficients for the elementary processes involved, (4) identification and comparison of ion-molecule association reactions showing both radiative and collisional stabilization, and (5) development and implementation of spectroscopic methods for examining the radiative association process directly.

ACKNOWLEDGMENTS

We would like to thank Dr. John F. Paulson and his research group at Geophysics Laboratory (AFSC) where initial work was carried out under an SFRP award. We are especially indebted to Fred Dale for continued instrumentation advice. The support of the Air Force Systems Command and the Air Force Office of Scientific Research for Contract No. F49620-88-C-0053/SB5881-0378 is gratefully acknowledged.

REFERENCES

1. Black, J.M.; Dalgarno, A. *Astrophys. Lett.* **1973**, 15, 79.
2. Herbst, E.; Klempner, R. *Astrophys. J.* **1973**, 185, 505.
3. Hoodin, R.L.; Beauchamp, J.L. *Chem. Phys.* **1979**, 41, 1.
4. Hoodin, R.L.; Foster, H.S.; Beauchamp, J.L. *J. Chem. Phys.* **1980**, 72, 4223.
5. McEwan, M.J.; Anicich, V.G.; Huntress, W.T.; Kemper, P.R.; Bowers, M.T. *Chem. Phys. Lett.* **1980**, 75, 278.
6. Bass, L.M.; Kemper, P.M.; Anicich, V.G.; Bowers, M.T. *J. Am. Chem. Soc.* **1981**, 103, 5283.
7. Gilbert, R.J.; McEwan, M.J. *Aust. J. Chem.* **1985**, 38, 231.
8. Kemper, P.R.; Bass, L.M.; Bowers, M.T. *J. Phys. Chem.* **1985**, 89, 1105.
9. Barlow, S.E.; Dunn, G.H.; Schauer, M. *Phys. Rev. Lett.* **1984**, 54, 902.
10. Herbst, E.; Bates, D. *Astrophys. J.* **1988**, 329, 410.
11. Bates, D.R.; Herbst, E. in Rate Coefficients in Astrochemistry, eds. Millar, T.J.; Williams, D.A., Kluwer Academic Publishers, **1988**, 17.
12. Herbst, E. in Interstellar Molecules, ed. Andrew, B.H., D. Reidel Publishing Co., **1980**, 317.
13. Babcock, L.M.; Streit, G.E. *J. Phys. Chem.* **1984**, 88, 5025.
14. Herd, C.R.; Babcock, L.M. *J. Phys. Chem.* **1987**, 91, 2372.
15. Herd, C.R.; Babcock, L.M. *J. Phys. Chem.* **1989**, 93, 245.
16. Herbst, E. *Astrophys. J.* **1985**, 291, 225.
17. Babcock, L.M.; Taylor, W.S.; Herd, C.R. *Int. J. Mass. Spectrom. Ion Processes* **1987**, 81, 259.
18. Herd, C.R. in A Study of the Temperature Dependence of Ion-Molecule Association Reactions: Halide Ion Addition to a Selected Group of Lewis Acids, Ph.D. Dissertation, Louisiana State University, May 1987.
19. Rosenstock, H.M.; Draxl, K.; Steiner, B.W.; Herron, J.T. *J. Phys. Chem. Ref. Data* **1977**, 6.
20. Viggiano, A.A. *J. Chem. Phys.* **1986**, 84, 244.
21. see: Su, T.; Bowers, M.T. in Gas Phase Ion Chemistry, Volume 1 ed. Bowers, M.T., Academic Press, **1979**, 84; and references

therein.

22. Ferguson, E.L.; Fehsenfeld, F.C.; Schmeltekopf, A.L. Adv. Atomic Molec. Phys. 1969, 5, 1.

IMPULSE APPROXIMATION FORMALISM
FOR ATOM MOLECULE COLLISIONS

FINAL REPORT

Research Initiation Program

Universal Energy Systems, Inc.
4401 Dayton-Xenia Road
Dayton, Ohio, 45432

Pradip Bakshi

Physics Department, Boston College
Chestnut Hill, MA 02167

December 1989

I. INTRODUCTION

Impulse Approximation (IA) was originally introduced in 1950 by Chew¹ in the context of neutron-deuteron collisions. The central idea of IA is to treat the three body process as a pair of two-body collisions, with the third atom remaining a spectator. Considerable formal theoretical work was done soon thereafter²⁻⁴. Applications to the atom-molecule collisions were developed in the nineteen seventies⁵⁻⁸, and more recently⁹, in 1981. These applications dealt with hyperthermal collisions, where the incident particle energy was the dominant factor in providing the relative velocity of the two body process.

In the past work⁵⁻⁹, the IA has been employed by making a further approximation called the Peaking Approximation (PA) to simplify evaluation of the scattering amplitudes. While IA can be applied to many physical situations, PA is rather restrictive, and applicable mainly for high projectile energy collisions.

The main goals of the Research Initiation Program (RIP) were:

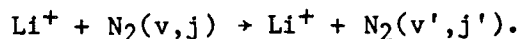
- (1) Development of the IA formalism beyond the PA for collisions with arbitrary ratios of internal molecular and external kinetic energies and
- (2) Assessing the errors involved in the use of PA in the past calculations in the literature.

These goals were met during the RIP, resulting in a paper, already published¹⁰, and another paper, submitted for publication¹¹. The main accomplishments are described in the Section II, general references appear in Section III, the details of the publications related to the RIP are listed in Section IV, the reprint of Ref.10 and preprint of Ref.11 are attached as the final Section V of this Report.

II. ACCOMPLISHMENTS

The general theory of IA as applied to atom-molecule collisions is given by Eckelt et al⁶⁻⁸, and Beard and Micha⁹. The Impulse Amplitude, expressed as an integral of the two-body t-matrix weighted by the product of final and initial wave functions, was not evaluated exactly in these works. Instead, they resorted to the Peaking Approximation (PA) which simplified the calculations. The validity and accuracy of using PA, however, had not been assessed.

By developing a technique for the exact evaluation of the Impulse Amplitude, we were able to go beyond PA and assess its validity and accuracy. The formalism for the evaluation of the exact amplitude is described by Eqs.(3) to (12) of our Ref.10. This formalism was then applied to study the process:



The exact differential cross sections were found to be smaller than the PA results (Figs.1 and 2, Ref.10). For small angles, this disparity was substantial reaching almost two orders of magnitude for near forward scattering. The total cross section ratio of the exact and PA calculations (displayed in Fig.3., Ref. 10) diminished from one to almost one-half for the vibrationally elastic process ($v=v'=0$) as the rotational inelasticity was increased (larger j'). For vibrationally inelastic processes ($v'=1$, $v'=2$), the greatest disparity occurred for the small angular momentum transfers (small Δj). We concluded that PA overestimates the true IA results for energy loss processes (where the projectile gives up energy to the molecule). In subsequent work¹² we extended these comparisons to energy gain processes (where the projectile gains energy from the internal energy

of the molecule). For such processes, IA generally underestimates the true IA results.

Another major study carried out during the RIP period was the investigation of the internal consistency of IA¹¹. This was beyond the originally proposed scope of the RIP, but it was feasible since the techniques and computational codes for this study were essentially the same. We applied the time reversal and space inversion symmetries to test the internal consistency of the IA formalism. These symmetries require the forward and reverse cross sections to be related by the semi detailed balance (sdb) condition. It was shown that this condition was well satisfied for backwards scattering and for moderately large scattering angles. A progressive breakdown occurred for smaller angles (Figs.1 and 2, Ref.11). The ratio of forward and reverse differential cross sections was studied as a function of angle (or momentum transfer) for different relative translational energies and incident particle masses (Figs.3 and 4, Ref.11). Higher energies and smaller masses enlarged the domain of compliance of the sdb condition (Fig.5, Ref. 11).

We concluded that IA is not applicable in its present form for small scattering angles. For large scattering angles, where sdb is satisfied, it appears reasonable to regard IA to be a good representation of the collision process. Also, the post-prior discrepancy⁶ appears to be a consequence of the failure of IA to be invariant under time reversal¹¹.

Much was accomplished during the RIP period. Yet, several other aspects of the IA formalism are worth pursuing further, both for their intrinsic interest, and from the point of view of applications to understand various experimental results. The scope and celerity of future

work will depend on the availability of subsequent research support.

III. REFERENCES

1. G.F. Chew, Phys. Rev. 80, 196-202 (1950).
2. G.F. Chew and G.C. Wick, Phys. Rev. 85, 636-642 (1952).
3. J. Ashkin and G.C. Wick, Phys. Rev. 85, 686 (1952).
4. G.F. Chew and M.L. Goldberger, Phys. Rev. 87, 778 (1952).
5. A. Bogan, Phys. Rev. A, 9, 1230 (1974).
6. P. Eckelt, H.J. Korsch and V. Philipp, J. Phys. B, 7, 1649 (1974).
7. H.J. Korsch and V. Philipp, Phys. Rev. A, 13, 497 (1976).
8. V. Philipp, H.J. Korsch and P. Eckelt, J. Phys. B, 9, 2345 (1976) and 10, 117 (1977).
9. L.H. Beard and D.A. Micha, J. Chem. Phys. 74, 6700 (1981).
10. R.D. Sharma, P.M. Bakshi and J.M. Sindoni, Phys. Rev. A 40, 1692 (1989).
11. R.D. Sharma, P.M. Bakshi and J.M. Sindoni "On the Internal Consistency of the Impulse Approach to Collisions", submitted to Phys. Rev. A.
12. R.D. Sharma, P.M. Bakshi and J.M. Sindoni, paper under preparation.

IV. PUBLICATIONS

1. R.D. Sharma, P.M. Bakshi and J.M. Sindoni, "Impulse Formalism for Atom-Molecule Collisions: Inadequacy of the Peaking Approximation", published as a Rapid Communication in Physical Review A, Vol.40, pp.1692-1695, (1989).

2. R.D. Sharma, P.M. Bakshi and J.M. Snidoni, "On the Internal Consistency of the Impulse Approach to Collisions", submitted as a Rapid Communication in Physical Review A. Editorial Comments should be available in about a month.
3. R.D. Sharma, P.M. bakshi and J.M. Sindoni, "Impulse Approach to Collisions", a much longer paper with considerable background and detail has been under preparation for some time. It will be submitted to Physical Review A after some additional work.

V. ATTACHMENTS

Publication 1: (Reference 10)

Publication 2: (Reference 11)

STELLAR PHOTOMETRY, VEHICLE GLOW,
AND
ADVANCED IMAGE ANALYSIS

Final Report

Contract No. F49620-88-C-0053/SB5881-0378
Purchase Order No. S-210-9MG-100
Universal Energy Systems, Inc.

Donald F. Collins
Principal Investigator
Warren Wilson College
Swannanoa, NC 28778

ABSTRACT

Digital imaging photometry of point-like images has been developed which effectively extracts the photometry information from noisy background. The images are digitized from RS170 video, including a solid state camera which allows time integration for low light levels. The photometry algorithm sums the total brightness signal over the area of the image. A threshold is determined based on background signal statistics to separate signal from a noisy background. The techniques is used extensively to develop a variable star photometry program. Success in photometry of several variable stars (Beta Lyrae, R Lyrae, and Beta Persei or Algol) is presented. Other applications of digital image photometry in introductory physics are briefly discussed.

ACKNOWLEDGEMENTS

In addition to the U. S. Air Force Office of Scientific Research and Universal Energy Systems, Inc. for funding this research project, the author wishes to thank Chris Stergis and Vic Baisley of AFGL/LIU for their support and endorsement of this project, Warren Wilson College for providing facilities and assistance personnel, and to those individuals who helped in the data acquisition: Ray Stock, Dean Kahl, Luis DeLucia, and Robert Reed. Student contributions to the work came from Seth Russell (Kármán vortices), Alok Aurovillian (variable star project - Beta Lyrae, R Lyrae, and Algol), and Jeff Faust (program development for photometric data acquisition and reduction). The author also wishes to thank the North Carolina Academy of Sciences for providing partial support to Alok Aurovillian for the student project in variable stars.

I. INTRODUCTION

Point-source digital imaging photometry techniques have been needed by AFGL to calibrate imaging systems in the AFGL Calibration Facility (Collins, 1989; Huffman et. al., 1980) and to measure the brightness of space-craft vehicle glow detected by ground based telescopes. These techniques have led to the development of an extensive variable star photometry program at Warren Wilson College using and integrating CCD video camera, and 8-inch telescope, and video digitization equipment.

Image analysis of airglow and auroral images had been proposed for part of this study, but has been deferred do to time constraints.

II. POINT-SOURCE DIGITAL PHOTOMETRY ALGORITHM

A.Video Equipment

The analysis apparatus consists of a video digitizer (Image Technology Inc. Model FG100-AT) mounted in an MS-DOS computer. This equipment digitizes RS170 video in 1/30 sec to a precision of 8-bits. This 8-bit data is represented by integers (0..255) referred to as Analog Digital Units (ADU). The video source is usually a CCD video camera (Fairchild CCD 3002 - non-integrating, Pulnix TM 840N - integrating) or video from a VCR having been recorded by another camera.

B.Algorithm

The idea of measuring the brightness of a point source in a digital image by summing the values of the digitized pixels seems very simple, except in the problem in distinguishing signal from noise in the image. Any uncertainty in the background level is amplified by the two-dimensional nature of the image.

A major problem in this system includes a large amount of video noise characteristic of RS170 video due to the large bandwidth (5 MHz) and the limited precision (8-bit) of the frame grabber. These problems are addressed by averaging a large number of video frames for each measurement and by storing the subframe averages as floating point numbers. Only the image data within an analysis box, or subframe, is averaged to avoid tying up the processor. Because of the averaging arithmetic, about 4 seconds are required to average and save 30 subframes (one second of real time of size 40 x 40 pixels. Immediately after the acquisition, the averaged subframe is stored on disk as a file of floating point numbers along with a header which contains housekeeping information and analysis results for quick retrieval. A listing of the header fields is found in the appendix.

The algorithm to extract the total brightness of the stellar image consists of subtracting the background, determining a threshold based on the remaining noise level, and summing the total pixel values above that threshold within the subframe. A typical image to be analyzed is shown in Figure 1. This image shows a weak signal of about 20 ADU above the median. It also shows a ripple of about 0.6 ADU rms in the background resulting from the digitizing equipment. Because this ripple is coherent, and runs parallel to the image columns, it can be subtracted. The ripple is read for each column in the subframe by averaging the top 5 rows and the bottom 5 rows for each column. The average ripple for each column is then subtracted from every pixel in the same column. The result is demonstrated in Figure 2. The remaining noise is about 0.16 ADU. The background level is determined from the perimeter of the

Raw image of point source

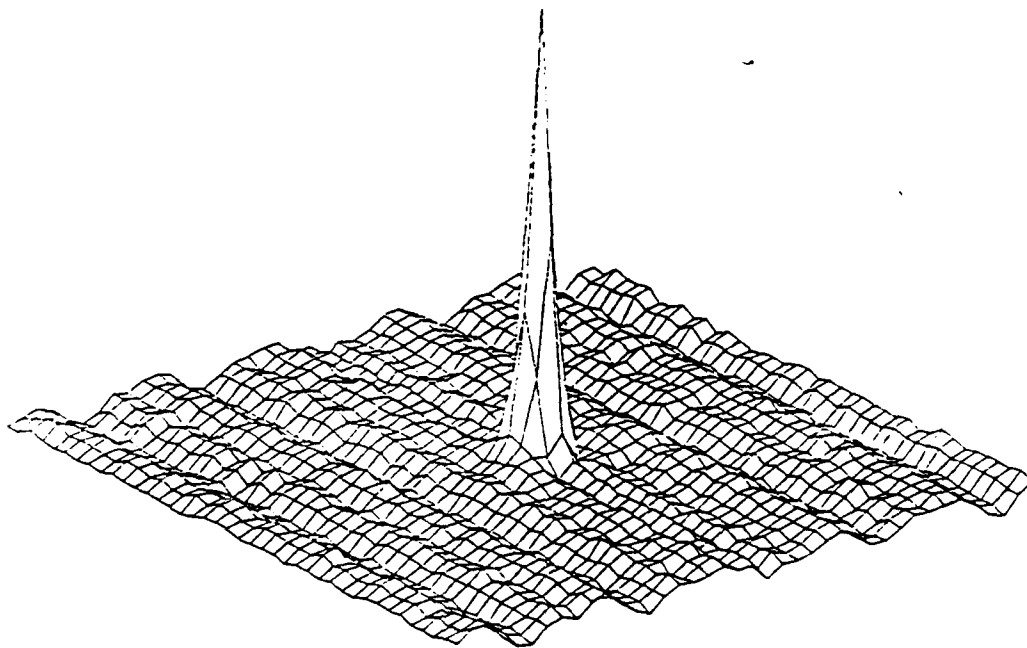


Figure 1. Perspective plot of a point source image showing ripple and random noise.

Point source - ripple 'subtracted

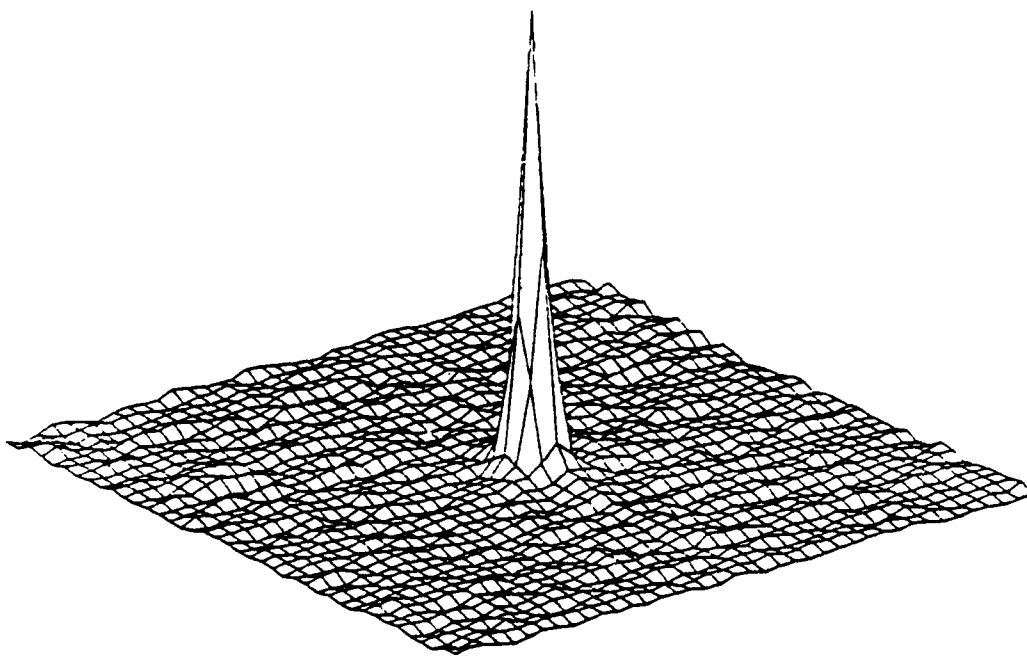


Figure 2. Perspective plot of point source with the ripple subtracted. Remaining noise is 0.16 ADU.

subframe so that a separate image of the blank sky is not needed.

Analysis of the total image brightness in the presence of the remaining noise, though minimized, presents special problems amplified by the 2-dimensional nature of images. To calculate the total signal in the analysis subframe, the background must be determined and subtracted from the input signal. The net signal is then summed over the subframe to determine the integrated intensity. To determine the uncertainty in the integrated signal, the uncertainty in the background is multiplied by the total number of elements in the subframe.

Suppose Σ is the standard deviation of the background. The standard error, δE , of the background is Σ/\sqrt{N} where N is the total number of pixels in the analysis subframe. When subtracting the background, which has an uncertainty of δE , the total uncertainty (standard error) in the integrated signal is

$$\text{S.E.} = \delta E \times N = \Sigma \times \sqrt{N}. \quad (1)$$

Note that the standard deviation is multiplied by \sqrt{N} , where N is the number of pixels in the subframe, rather than divided by \sqrt{N} to obtain the uncertainty of the integrated signal.

In order to eliminate the above uncertainty due to 2-dimensions the images are thresholded - only pixels whose values are at least as large as the threshold contribute to the integrated signal. The threshold is set to three standard deviations above the median. In the absence of a dark frame, the statistics (median and standard deviation)

are determined from the top and bottom 5 rows of the subframe after subtracting the ripple. To account for signals of varying amounts of noise, a constant threshold can be set which is about three standard deviations above the median for the noisiest signals.

To test the linearity of the system and algorithm, a point-source (filament from a miniature lamp) was focused onto the CCD detector. The lamp was placed at various distances from the camera lens, and powered by a regulated power supply. The image of the filament was analyzed by the algorithm described above, and is plotted in Figure 3 which shows linearity over three decades (7.5 stellar magnitudes).

III. USER INTERFACE

Because the algorithm described above works only with a small subframe of the image (usually 40 x 40 pixels), the user must indicate where the analysis should take place. A program was developed in which an analysis box is displayed on the image monitor. The user moves the box around with cursor editing keys and presses the ENTER key when the box is lined-up properly.

Another special problem occurs when digitizing the point-like image of a moving target arising from manual tracking a telescope and a moving source. A program was developed which searches the whole image (about 500 x 500 pixels) of each digitized video frame in order to find the location of the source to perform the analysis on a 60 x 60 pixel subframe. In order to speed up the search for the source, only every fourth pixel was tested to find the maximum. The size of the source is about 10 pixels diameter when this technique is needed. The search algorithm must

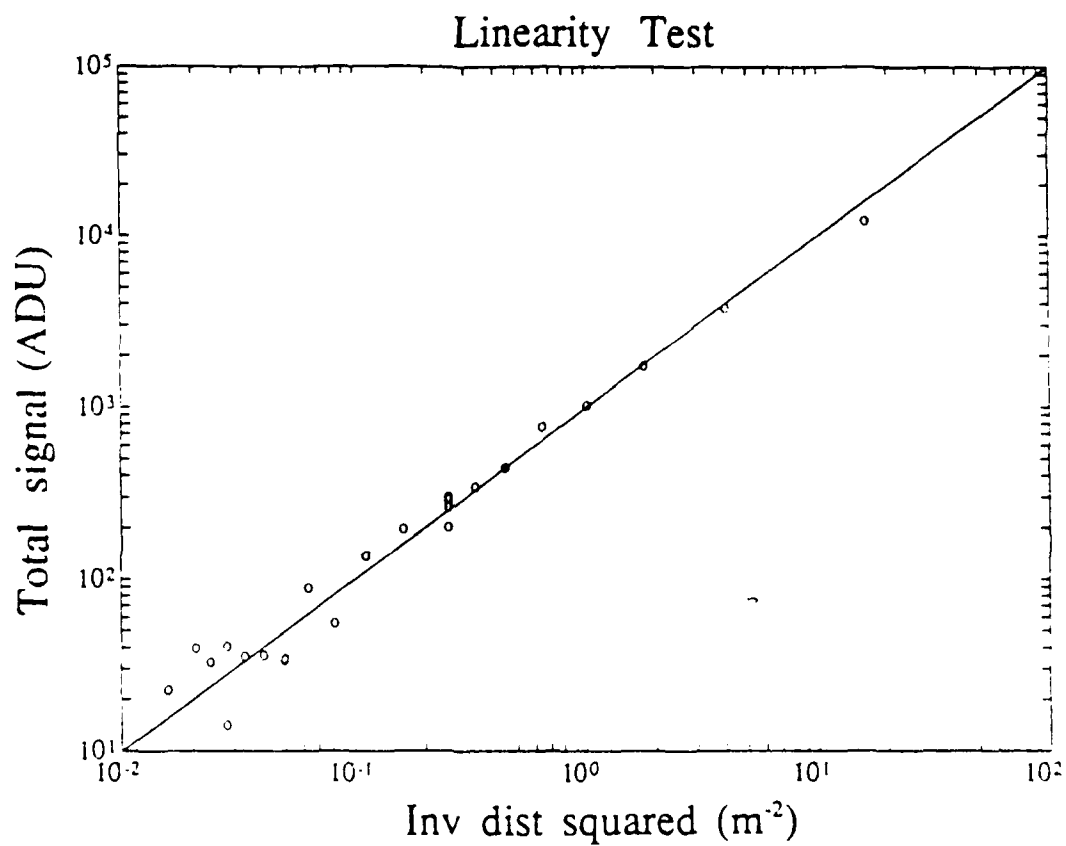


Figure 3. Logarithmic plot of the integrated signal vs. inverse squared distance showing the linearity of the algorithm. The line is drawn for a perfectly linear response (slope = 1).

also distinguish between a source and a "glitch" in the video which is only one or two pixels in diameter.

IV. VARIABLE STAR PHOTOMETRY

A. Introduction

By far the most extensive work with this project has been the development of variable star photometry with the point-source photometry algorithm. Variable star photometry provides a current active area of astronomical observation attainable by colleges with limited observation facilities (Percy, 1986). Studies of variable stars provide great insight into astrophysical processes, require extensive commitments for telescope time over many years, and can be conducted by amateurs as well as professionals with small telescopes.

B. Procedure

A CCD video camera is mounted at the Cassegrain focus of a portable telescope (Celestron 8-inch) and the point-source photometry algorithm applied to a star's image in order to measure the star's brightness. A comparison star close to the variable star is photographed consecutively with the variable star, and the magnitude of the variable is then calculated from the formula

$$m = m_c - 2.5 \log(B/B_c) \quad (2)$$

where m_c is the known magnitude of the comparison star and B and B_c are the photometric brightnesses of the variable star and comparison star respectively measured in ADU by means of the point-source algorithm. Photographing the comparison star compensates for most of variation of atmospheric extinction. A large number of digitized images are averaged to minimize the noise in RS170 video.

Instrumental stellar photometry is traditionally performed using a photomultiplier tube or a PIN photo diode in a reasonably priced photometer (Optec SSP-3, Persha, 1983). With a typical photometer on a small telescope, the observer centers the star on a graticule using a 45 degree mirror and an ocular. Then the mirror is rotated out of the main axis and the starlight falls on the detector to allow an instrumental reading - hopefully with no spurious movement or jarring of the telescope and good clock tracking. The point-source imaging algorithm developed in this study dispenses with the flip-mirror and allows monitoring of the tracking on the image monitor. This monitoring ability while acquiring data is especially valuable with a portable telescope which is susceptible to wind and tracking errors. As long as the star image remains in the analysis box displayed on the monitor, the data is valid. Another advantage of the imaging photometer is that the background reading is obtained from the top and bottom perimeter of the analysis box - making good use of the multi-channel or imaging mode. A separate background measurement is not necessary.

Figure 4 and Figure 5 show the results of Beta Persei (Algol - the brightest known eclipsing binary) and Zeta Geminorum (a Cepheid variable) obtained with the Fairchild camera and the point-source photometer algorithm. No atmospheric corrections besides making use of a comparison star have been applied to this data, hence the relatively large amount of scatter - especially when data from different nights have been combined.

A serious drawback of the CCD detector at video frame rates is the lack of sensitivity to faint stars compared with a photomultiplier or a PIN detector. The Fairchild

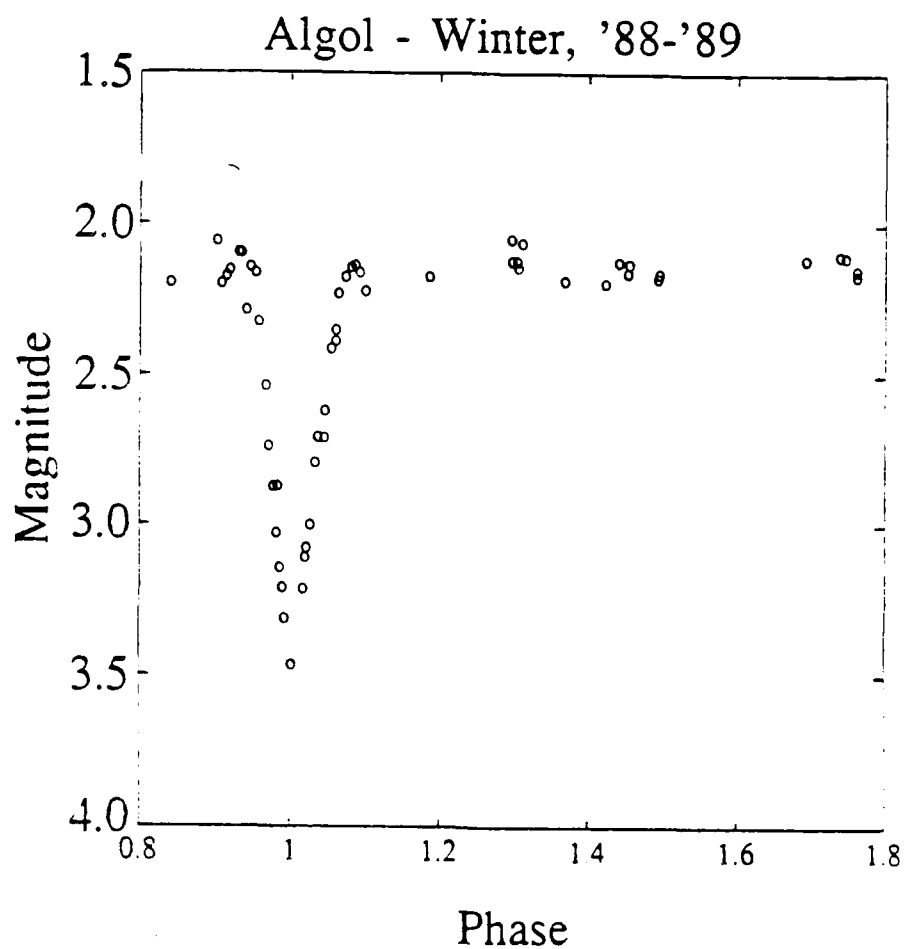


Figure 4. A plot of the eclipsing binary star Algol from fall-winter, 1988-89. The data from many different cycles is combined into phase to show the light curve. The comparison star is Alpha Persei.

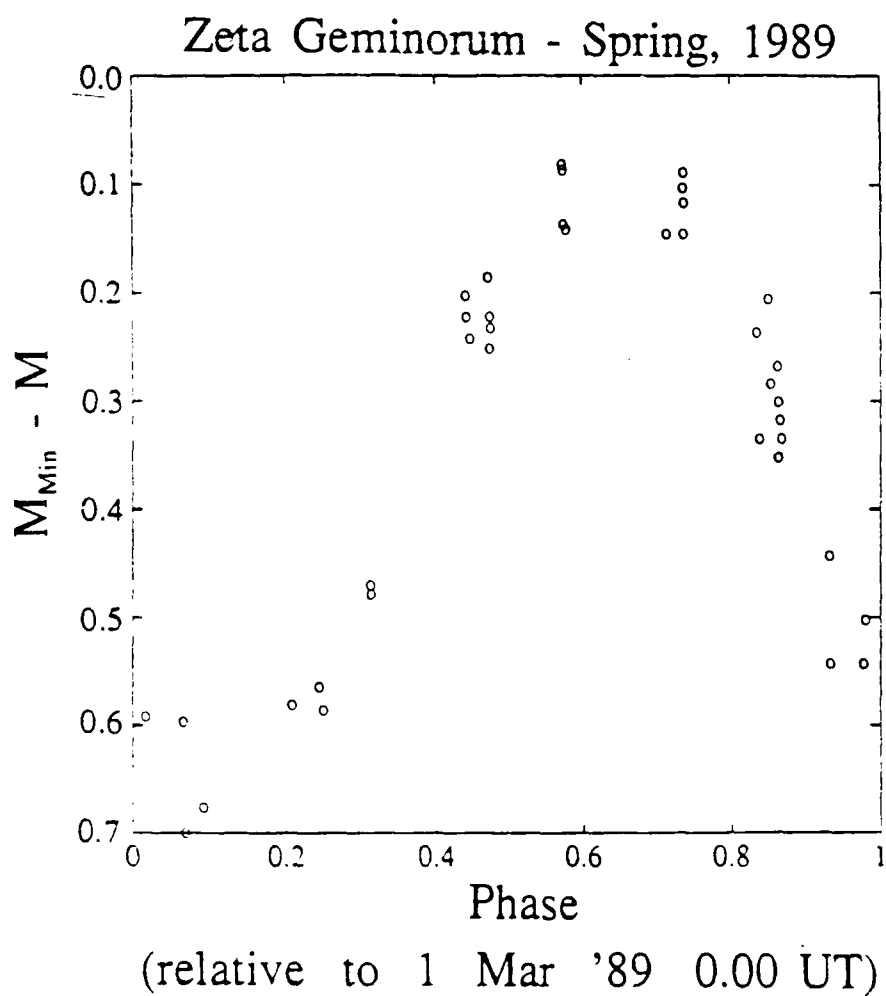


Figure 5. The plot of the Cepheid variable Zeta Geminorum taken with the Fairchild Camera plotted with respect to phase.

3002 camera on the Celestron 8-inch telescope is limited to stars brighter than magnitude 4.0 which precludes the study of many variables and does not permit the use of filters to narrow the optical bandwidth to determine the color index. These data show that the CCD video camera and the point-source photometry algorithm are effective photometry tools for variable stars once the sensitivity to faint stars is improved.

V. INTEGRATING CAMERA

A. Hardware

To develop an increased sensitivity for stellar photometry applications three devices were considered: 1) image intensifier, 2) solid-state photometer, and 3) time-integrating CCD camera. The image intensifier is expensive (\$6,000 for an "inexpensive" surplus type), noisy, and bulky - making the fitting on a small portable telescope difficult. The solid state photometer (SSP-3) has demonstrated its usefulness to astronomers, is inexpensive (under \$2,000), and is fully developed as a measuring instrument. The time integrating camera for RS170 video is also inexpensive (\$2,400), has the advantages of imaging photometry, and allows the monitoring of the image during acquisition. It was decided to obtain the integrating camera and develop the algorithms and techniques for digital image photometry. In addition, many other applications for the integrating camera will be made available besides stellar photometry.

The Pulnix TM-840N is a CCD video camera which allows time-integration with computer control. Among the inexpensive CCD cameras available, this was the only one available at the time which allowed time integration. By allowing integration of up to several seconds, a factor of

100 is obtained in sensitivity compared with the non-integrating camera. This particular camera also possesses the advantage of a frame-storage CCD as opposed to interline storage which is most popular in the inexpensive CCD cameras. With interline storage, half the photosensitive area of each horizontal scan line in the detector is masked and used for storage and read-out - thus reducing the photosensitivity by about 50%.

B. Software

Special software had to be developed to control the integrating camera with the video digitizer. In order to make the integrated field available to the digitizer the integration time had to be controlled for an even number of vertical sync pulses which come at 1/60 second intervals in the interlaced format. In integrated mode, only the even-line field of the interlaced frame is available as a consequence of the frame-storage CCD. It would have been preferable to use non-interlaced video, but frame-storage CCD and non-interlaced video are not compatible. Because the odd video lines are blank when the integrated video is digitized, the picture shows annoying flicker. To eliminate this flicker while the "live" integrated video is monitored, the scroll register in the display section of the video digitizer was incremented and decremented with every 1/60 sec vertical sync signal to fill the blank video lines "on the fly" without having to copy every line from the frame storage memory into the blank lines. Before analyzing an integrated frame, the blank lines are copied over from the adjacent integrated lines - eliminating the need to toggle the scroll register, but adding a redundancy in the image. The point-source photometry algorithm is then applied to the sub-frame as before. Many integrated video frames are still

averaged before storing in order to eliminate the electronic noise associated with RS170 video.

C.Noise

For short integration times the noise is dominated by the video electronics and the ripple discussed earlier. For long integration times, however, the fixed-pattern noise becomes dominant. The fixed-pattern noise is due to small pixel-to-pixel variations in sensitivity and dark level due to variations in pixel size. This fixed-pattern noise may be eliminated by subtracting a dark image for the same integration time ("flat-fielding"). A program to automatically perform the flat-fielding at the discretion of the user by using a blank image on file is currently under development. Tests show that without flat-fielding the spatial standard deviation increases directly with exposure time, whereas after flat-fielding the spatial standard deviation for long exposures is less than twice the standard deviation for a time-averaged single frame. We would expect the noise in the flat-fielded integrated signal to be $\sqrt{2}$ times the noise in the non-integrated video because two readings are made.

D.Linearity

With the integrating camera, the point-source photometry algorithm and a LED source it is easy to test the linearity of the camera by plotting total signal vs. integration time. A red LED is powered by a precision power source in series with a 470 Ohm resistance placed about 3.5 m from the integrating camera. The lamp is focused using a standard camera lens (FL = 25 mm). The brightness of the LED and the lens aperture are adjusted so that the image of the LED saturates the detector in about 2 sec integration time. The total signal obtained from the point-source

photometry algorithm is plotted as a function of exposure time in Figure 6. As can be seen from the plot, the response is non-linear showing a threshold - quite uncharacteristic of CCD behavior. A similar curve is obtained when the peak signal in the image is plotted against exposure time except that the peak clearly saturates and abruptly levels off at 46 frames for the data in Figure 6. The non-linearity is attributed to the video electronics in the camera. The camera had been adjusted manually to produce a near linear response to brightness values. This "reciprocity failure" in the CCD camera may be due to non-linearities in the video electronics to minimize noise in the video image. It is hoped to get this problem corrected. It was attempted to numerically correct for the non-linearity by the use of a table look-up algorithm. Tests show, however, that a complete family of sensitivity curves (such as Figure 6) will be needed - one curve for each intrinsic brightness of a point source. When these curves are normalized to the exposure time to reach saturation, it is expected that they will show different intrinsic shapes.

VI. FILTER SYSTEM

The increased sensitivity of the photometric system by means of the integrating camera permits color measurements by means of wide-band optical filters. It was decided to use the standard U, B, V, R, I system (Ultraviolet, Blue, Visible, Red, Infra-red) (Guinan, et. al., 1986, Kron and Smith, 1951). The U band is not available with the CCD detector. Various filters were selected which when the transmittance was folded with the spectral response of the CCD camera gave wavelengths and bandwidths consistent with the standard B, V, R, I system. The defined wavelengths and bandwidths for this color system are summarized in Table I

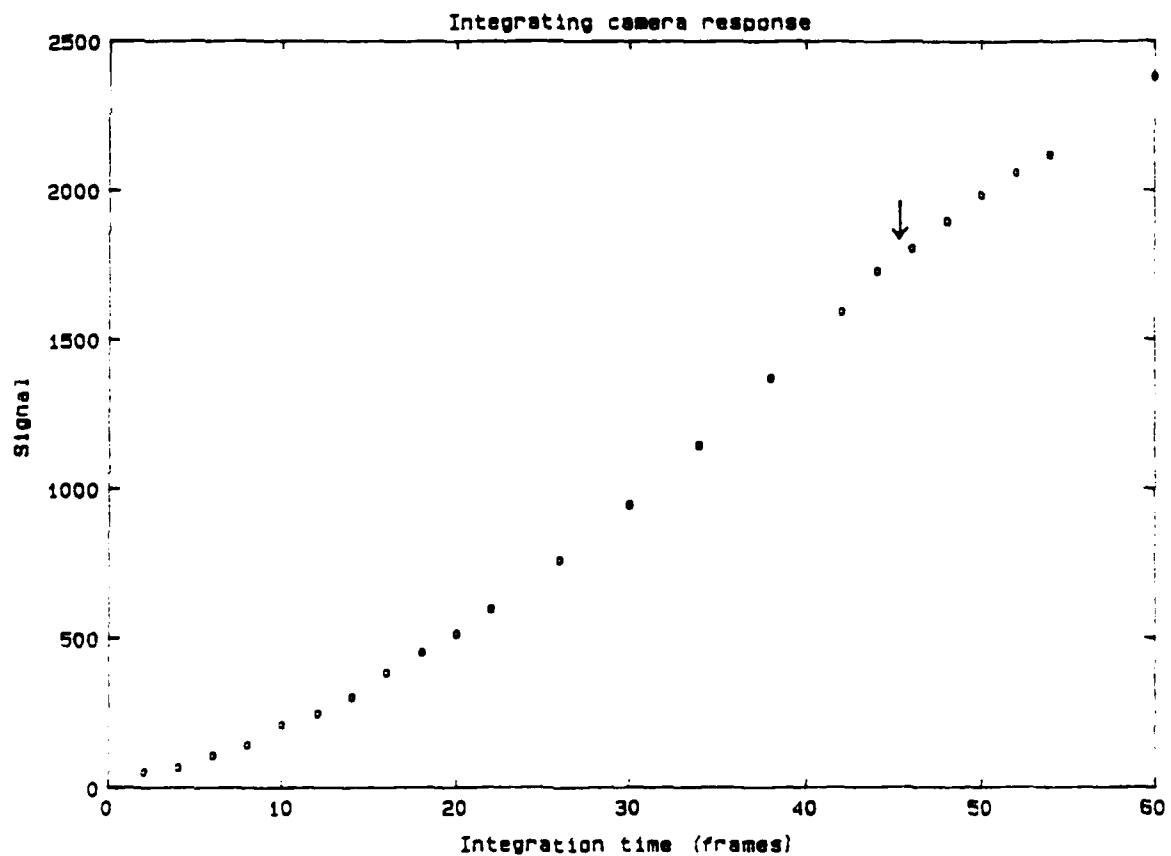


Figure 6. The response to the point-source algorithm of the integrating camera as a function of integration time showing the non-linearity effects. The arrow marks where the CCD becomes saturated at the peak brightness of the signal.

along with the Schott glass types selected and the measured effective wavelengths and sensitivities. The percent transmission of each of the filter configurations was measured with a spectrophotometer, then folded with the Pulnix CCD spectral response. The resultant system spectral response is shown in Figure 7. The effective wavelengths and bandwidths for each band in Figure 7 are calculated and displayed in Table I. The effective wavelength is the centroid for each filter; the bandwidth is the quotient obtained when the peak in sensitivity is divided by the integral of the sensitivity. The relative sensitivity is the integral of each curve in ADU-nm. The filters are mounted in a manually operated 5-position turret between the telescope and the camera.

VII. VARIABLE STAR RESULTS

Three variable stars were observed during the fall of 1989 with the integrating camera and the filter system: Beta Lyrae, R Lyrae, and Beta Persei (Algol). The observing program was the principal activity in a student research project (Alok Aurovillian).

A. Beta Lyrae

Beta Lyrae is an eclipsing binary star, period 12.908 days, whose two components are large, hot, and distorted into elliptical shapes (Petit, 1982). As a result of the distortion of the stellar bodies, the light curves show rather broad minima as opposed to the narrow minimum of Algol. Figure 8 shows the results in the V filter obtained over a 40 day interval (3 cycles) plotted with respect to phase or fraction of a cycle. Essentially one reading per observing night was used to acquire this data. Note the

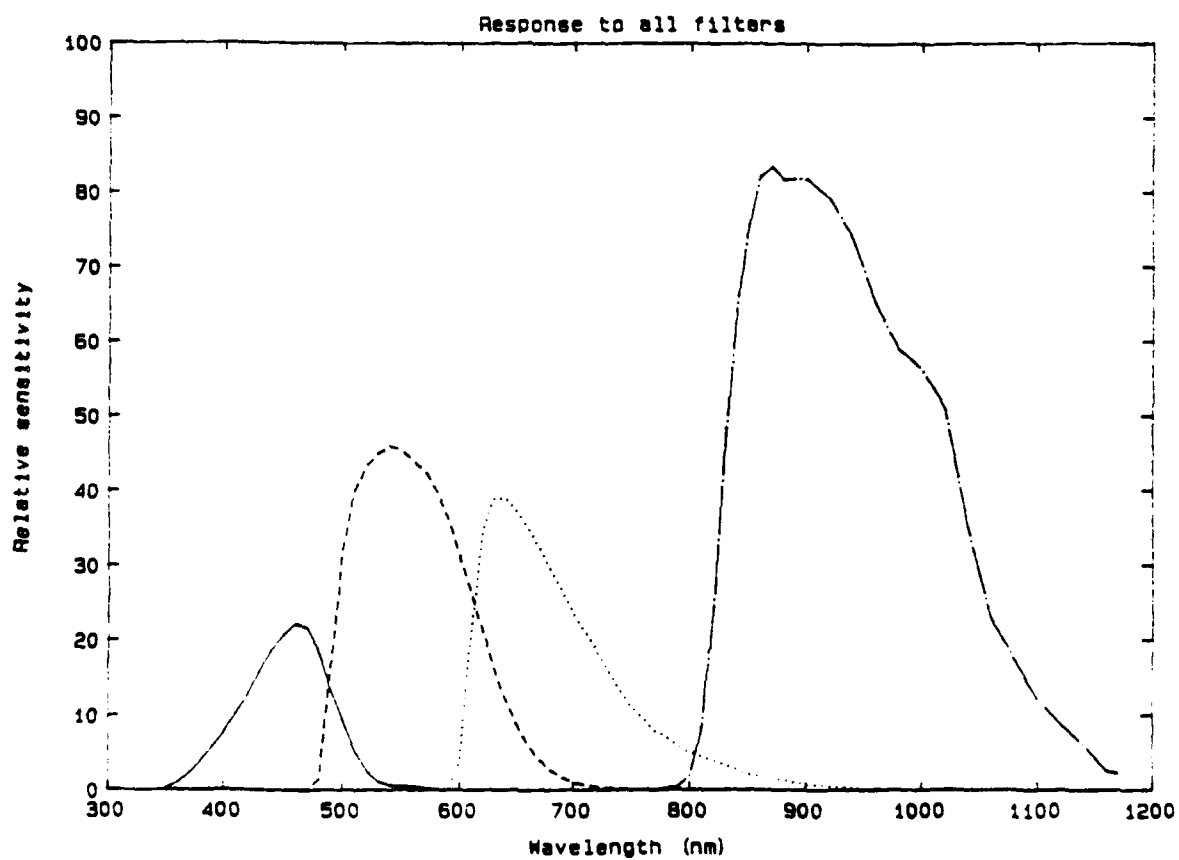


Figure 7. The spectral response of the integrating camera coupled with the various filters for the B, V, R, I bands.

Table I. Summary of the standard photometric optical bands and the measured properties of the filters selected.

Band	Wavelength (nm)	Bandwidth (nm)	Filter Schott	Relative sens	Effective wavelength (nm)	Effective Bandwidth (nm)
U	366	70	---	---	---	---
B	440	97	BG28	194	452	87
V	553	85	GG495 + BG38	564	562	123
R	680	100	KG3 + RG610	463	686	119
I	900		RG830	1164	939	198

broad minima. A similar curve, but with more scatter, is seen using the R filter. The comparison star for these measurements is Gamma Lyrae, magnitude 3.3.

B.R Lyrae

R Lyrae is a semi-regular (SRb) pulsating variable with a period of approximately 50 days with magnitude ranging between 4.0 and 5.0 (Menzel, 1964; Petit, 1982). Stars of this type (SRb) are quasi-periodic in brightness, sometimes showing sudden drops in brightness. Results of our measurements for R Lyrae are shown in Figure 9 and Figure 10 for the V and R bands respectively. Note the high degree of irregularity in the light curve of this variable. The

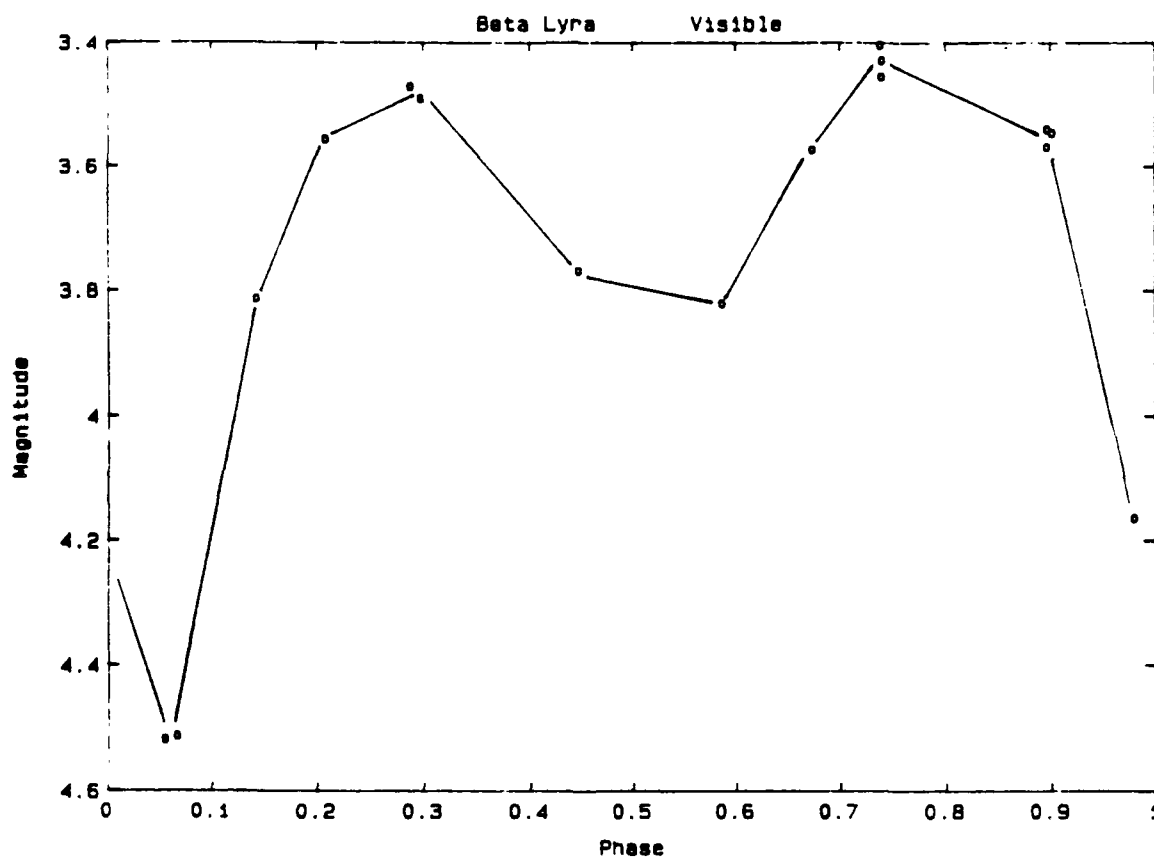


Figure B. A plot of the V magnitude of the eclipsing binary Beta Lyrae whose components are distorted to yield broad minima. The phase is relative to J.D. 2,447,800 (Sept. 30, 1989)

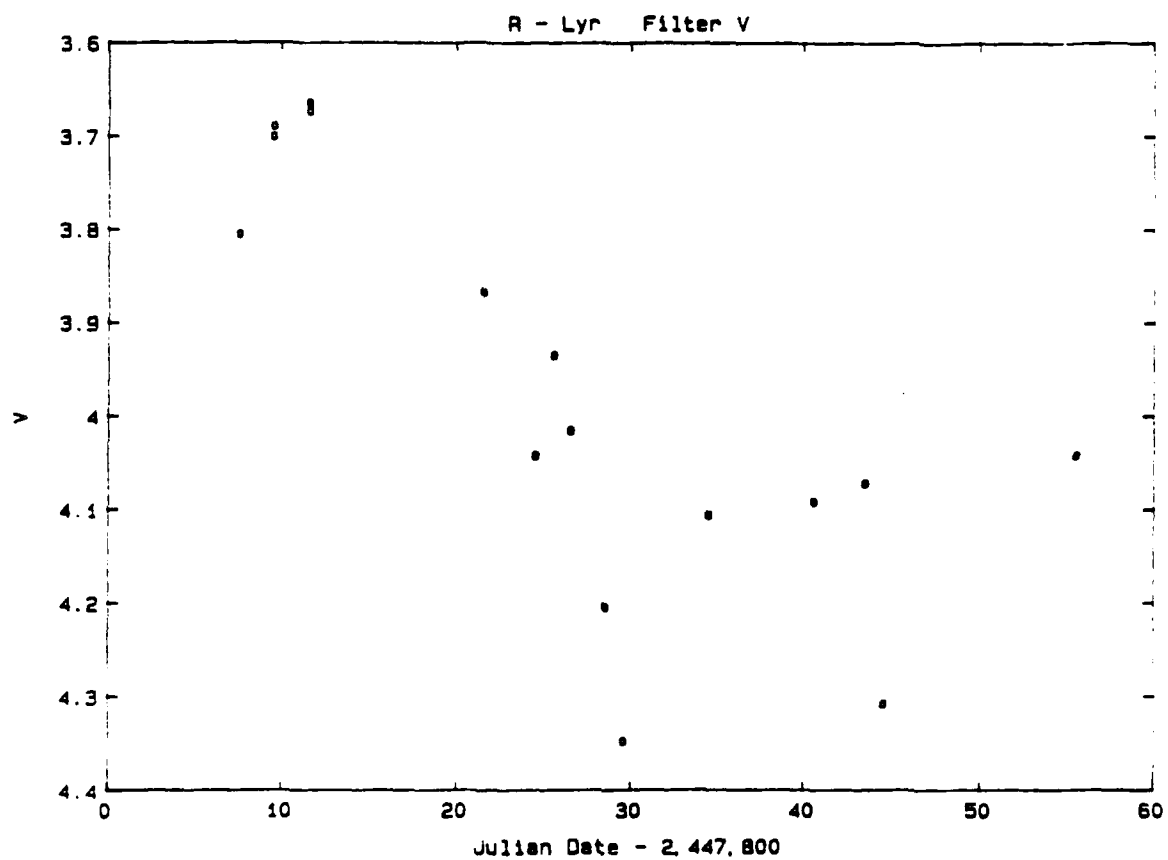


Figure 9. The light curve measured for R Lyræ in the V band.

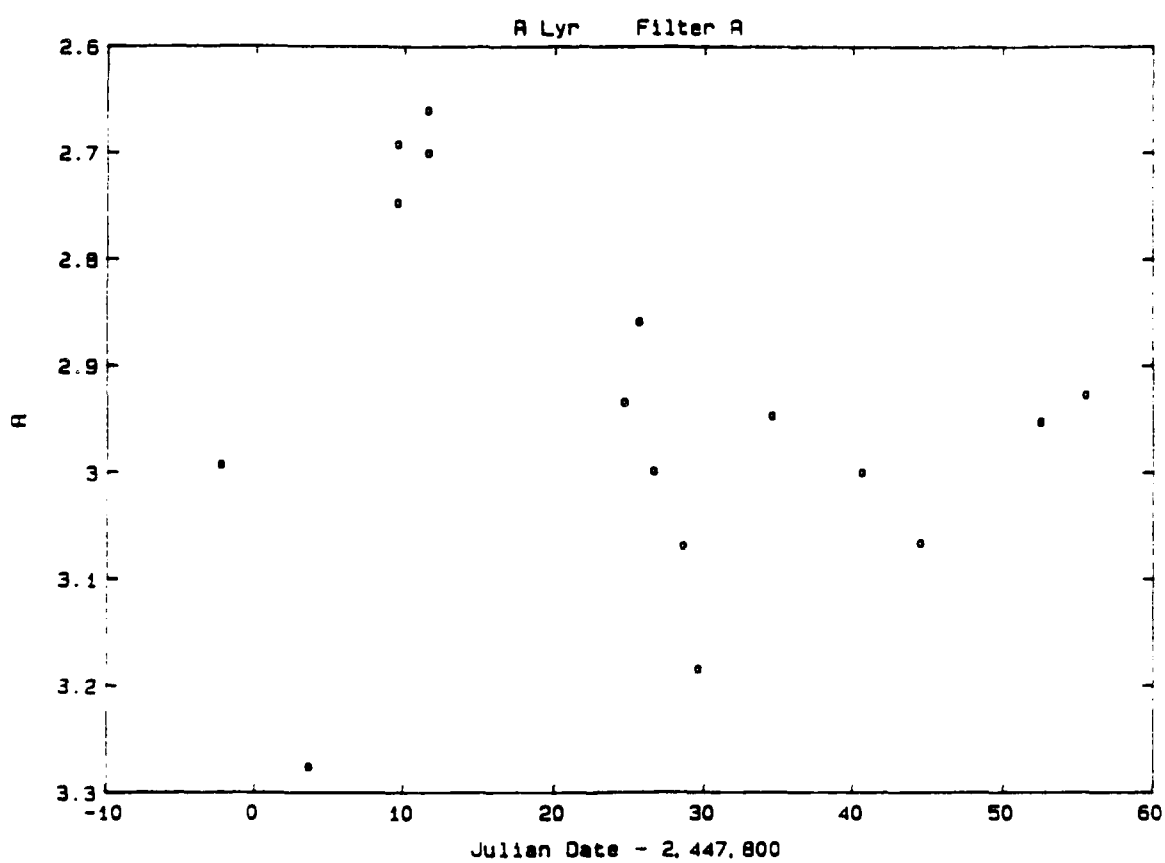


Figure 10. The light curve for R Lyr in the R band.

comparison star for the R Lyrae measurements is an unnamed star suggested by the AAVSO: SAO #047909, magnitude 5.44.

The causes of the large sharp minima in the magnitudes of R Lyrae near days 4, 30, and 44 are not understood. The color dependent atmospheric attenuation has yet to be accounted for and may contribute to the problem. Because there is a large contrast in colors of R Lyrae and the comparison (Spectral type M5 vs. K0 or 3000K vs. 5000K) atmospheric effects are expected to be amplified, especially if the zenith angle changes. When the raw photometric readings are plotted for these two stars (Figure 11) the variation is much smoother. It is also interesting to plot the color index ($V \text{ mag} - R \text{ mag}$) for both R Lyrae and the comparison (Figure 12). One notices a slight decrease in $V - R$ for R Lyrae as R Lyrae approaches its minimum and no trend in the color index for the comparison star. This indicates a constant color index for the atmosphere and a cooling of R Lyrae (redder) in the minimum phase of its cycle.

C. Algol

Beta Persei (Algol) is the oldest known and brightest eclipsing binary star. It is the prototype of eclipsing binaries with narrow minima (see Figure 4). It was decided to concentrate our measurements on Algol in the fall of '89 to measuring the time of maximum eclipses - both for the primary and secondary eclipses. Our apparatus permits the timing of mid-eclipse to a high precision. These results will contribute to the data concerning the period fluctuations in Algol (Mallama, 1982a). In contrast to making measurements on long-term variables which involve a reading about once a night, the photometric measurements on an eclipsing variable of the Algol type require readings

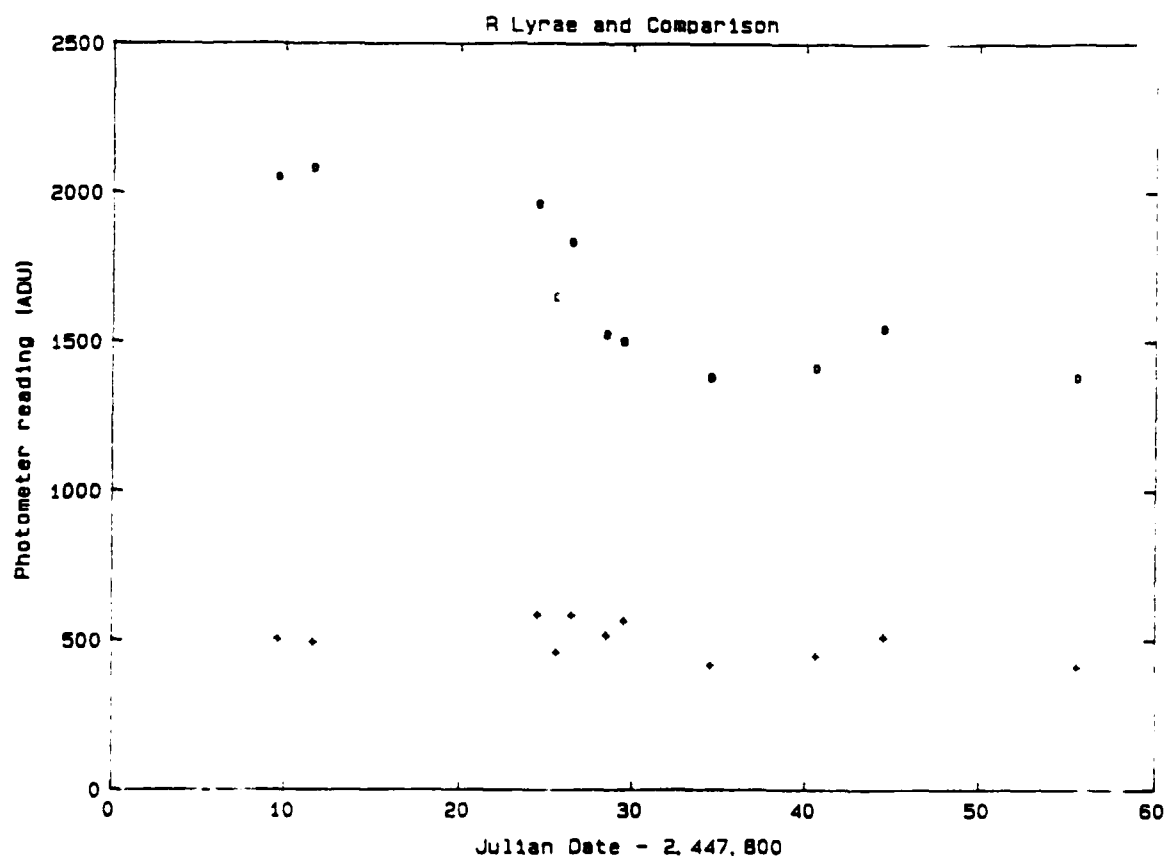


Figure 11. Plot of the raw photometer readings of both R Lyrae and the comparison star.

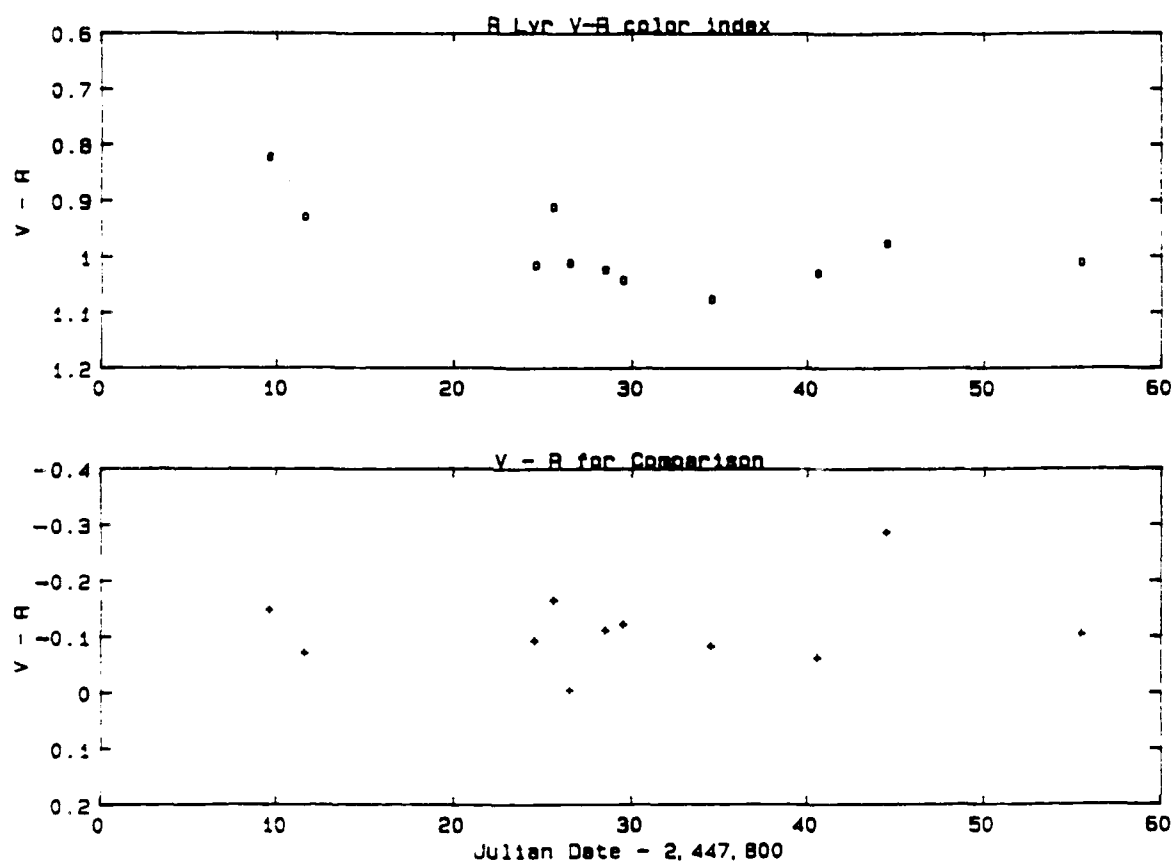


Figure 12 Plots of the color index for both R Lyrae and the comparison star. Note the change in color index for R Lyrae compared to the constant color index for the comparison.

every 5-10 minutes over a span of 4 to 6 hours. Thus the observers are quite busy - especially when taking measurements through different filters. Our best mid-eclipse data for Algol (out of three nights' observations) is shown in Figure 13. The comparison star for the fall, 1989 data is Pi Persei as suggested by Mallama (1982a).

For a better understanding of the physics in the Algol system, it is equally important to measure the smaller amplitude secondary eclipse when the darker star is eclipsed by the brighter star. Because the period of Algol is about three hours less than three days, aliasing allows an observation window about once every three weeks for either eclipse. We are still waiting for the weather to cooperate. The secondary eclipse in Algol has only 0.06 mag amplitude. Judging by the lack of scatter in Figure 13 the small secondary minimum should be detectable with our apparatus.

The fitting of the mid-eclipse minimum will use the Kwee-Van Woerden algorithm (Mallama, 1982b, and Kwee and Van Woerden, 1956) which finds a minimum in the sum of residuals with the curve reflected about each possible time for the minimum. The residuals are the differences in squares of magnitudes on each side of the reflection point. Preliminary attempts at polynomial fitting to find the minimum are inconclusive. The time of minimum varies greatly with the degree of the polynomial used.

VIII. OTHER INVESTIGATIONS

A.Kármán Vortices

Kármán vortices had been noticed by the author to occur in the cryogenic vapors when a rod - having been chilled by liquid nitrogen - is waved slowly through the air. The vortices appear as parallel swirls of visible vapor with

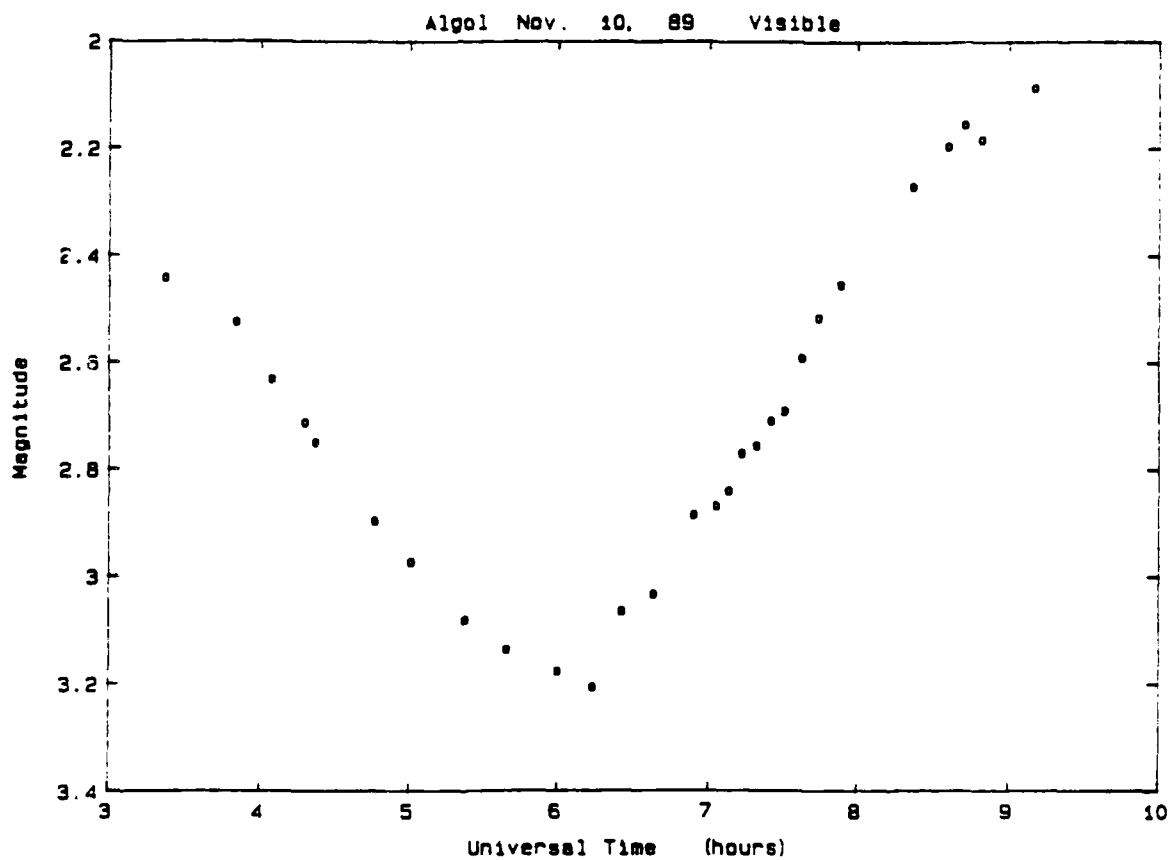


Figure 13. A plot of the magnitude of Algol on Nov. 9-10, 1989 through the V filter.

axes parallel to the axis of the rod. A student's project (Seth Russell) photographed the cryogenic Kármán vortices using the imaging system, made movies, and measured the spacing of the vortices as a function of rod velocity. The purpose of the liquid nitrogen is not only to make the vortices visible, but to bring the Reynolds number into the range where vortices are known to form ($Re = 2000$ to 3000) (Sears, et. al., 1985). The Reynolds number - essentially the ratio of inertial forces divided by viscous forces - is defined as

$$Re = \frac{\text{Density} \times \text{Velocity} \times \text{Characteristic size}}{\text{Viscosity}} \quad (3)$$

At liquid nitrogen temperatures, the density of air is increased and its viscosity is decreased thus increasing the Reynolds number by a factor of 10 needed for the vortex formation. A plot of the vortex spacing shown in Figure 14. The Reynolds number in Figure 14 is obtained using the density and viscosity of air at liquid nitrogen temperatures, the velocity of the rod, and the diameter of the rod. The rod was mounted on a variable speed turntable.

B. Image Analysis Software

Image Pro Image analysis software (Media Cybernetics, Inc) was obtained to evaluate its usefulness to AFGL in its image work. This software is basically menu driven using a mouse. It was found to be quite inflexible for specific image work (inability to drive an integrating camera, no point source photometry). The analysis of auroral images by AFGL are highly specific and generally would not be found in any commercial image analysis package. Acquisition of this pack by AFGL for auroral work is not recommended.

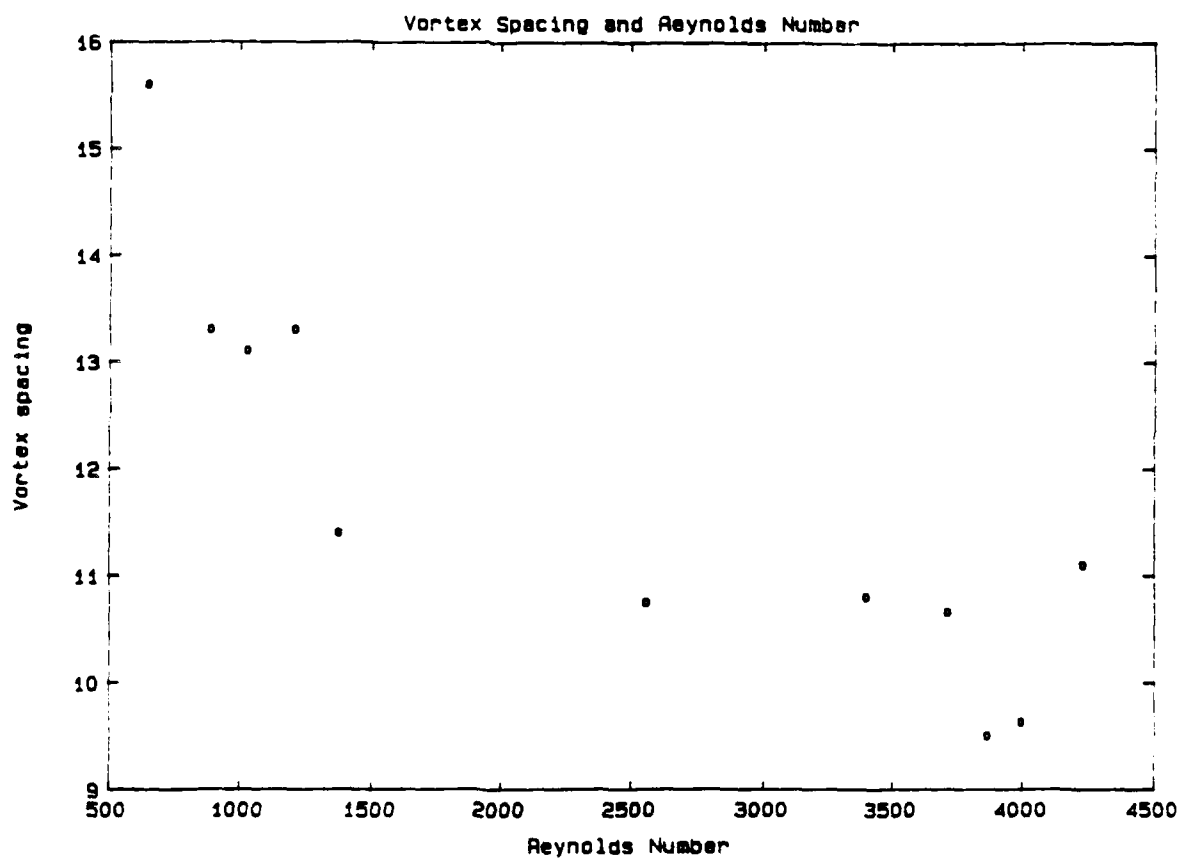


Figure 14. A plot of Kármán vortex spacing obtained from a rod at liquid nitrogen temperatures moving slowly through air.

C. Other Educational Applications

This project supported two student research projects (Kármán vortices in the fall of 1988 and variable star photometry in the fall of 1989 as well as a student worker in the spring of 1989 to write the photometry computer programs. In addition several applications of imaging have been incorporated into introductory physics courses. Old applications include: Lunar and planetary photography; Molecular diffusion photometry; Stellar photography of visual binaries; Photometric analysis of gel-scan electrophoresis; and Photometry of simple diffraction patterns. New applications in college courses include: Strobe photography with the integrating camera; Photography of the Galilean satellites of Jupiter; Imaging spectrophotometer; Sun spot photography and solar rotation measurements; Time lapse microphotography showing amoebae motion.

IX. FUTURE WORK

In addition to continuing with variable star photometry, future work will involve: 1) improving the linearity of the integrating camera and investigating more thoroughly the response curves in order to apply numerical corrections; 2) Developing the methods to correct for variable atmospheric attenuation (Guinan, et. al., 1986). The atmosphere acts like a filter whose bandwidth and spectral response depend on atmospheric conditions and the zenith angle (atmospheric mass). In order to completely understand the atmospheric effects combined with our instruments and to make the appropriate corrections, selected blue-red pairs of standard stars must be measured through the different filters at different zenith angles.

X. CONCLUSION

The point-source imaging algorithm is proving successful to perform stellar photometry on bright stars. The advantages include the monitoring ability, multichannel detector, and the lack of a need for precision tracking (portability). Point-source photometry was also developed to obtain data on a moving target.

REFERENCES

- Collins, D. F., 1989, "Calibration of UV Imagers", Proceedings of the SPIE, 1158, (Aug., 1989).
- Guinan, E. F., George P. McCook, and J. P. McMullin, 1986, "Acquisition, Reduction, and Standardization of Photoelectric Observations", The Study of Variable Stars using Small Telescopes, edited by John R. Percy, Cambridge Univ. Press.
- Huffman, R. E., F. J. LeBlanc, J. C. Larrabee, and D. E. Paulsen, 1980, "Satellite Vacuum Ultraviolet Airglow and Auroral Observations", Journal of Geophysical Research, 85, pp. 2201-2215.
- Kron, G. E. and J. L. Smith, 1951, Ap. J. 113, pp. 324-343.
- Kwee, K. K. and H. Van Woerden, 1956, Bull. Astron. Inst. Neth. 12, 327.
- Mallama, A. D., 1982a, "The Thirty-Two Year Cycle in Algol", Journal of AAVSO 11, No. 1, pp. 1-9.
- Mallama, A. D., 1982b, IAPPP Communications, No.7, pp. 14 - 18.
- Menzel, D. H., 1964, A Field Guide to the Stars and Planets, Houghton Mifflin.
- Percy, John F., editor, 1986, The Study of Variable Stars Using Small Telescopes, Cambridge University Press.
- Persha, Gerald and William Sanders, 1983, "The SSP-3 Photometer", Advances in Photoelectric Photometry, Vol.I, edited by R. C. Wolpert and R. M. Genet, Fairborn Observatory, p. 130.
- Petit, Michel, 1982, Variable Stars, translated from French by W. J. Duffin, Wiley, 1987.
- Sears, F. W., M. Zemansky, and H. Young, 1985, College Physics, Addison-Wesley.

APPENDIX

LISTING OF THE HEADER STRUCTURE FOR STELLAR PHOTOMETRY FILES

```
struct starhdr {  
  
    char    name[16];  
    long    time;  
    int     side;  
    int     frames;  
    int     xcenter;  
    int     ycenter;  
    int     telesc;  
    int     weather;  
    struct scoord coords;  
    float    lat;  
    float    lon;  
    int     nimag;        /* number of averages */  
  
    float    stdev;  
    float    thresh;  
    float    uthresh;  
    double    sum;  
    double    usum;  
    float    zangle;  
    int     nints; /* number of integrations */  
    float    peak; /* peak signal in image */  
    int     filtr; /* filter number used in image */  
    int     xform; /* ccu transform function to compensate  
                  for non-lin */  
    /* xform can take values LINEAR, PULNIX */  
    float    bkg; /* bkground read from perimeter of  
                  subframe */  
    float    darkbkg; /* bkground read from dark frame if  
                      present */  
    char    dum[20];  
};  
  
typedef struct starhdr STARHDR;
```

1987 USAF-UES Research Initiation Program
Submitted to the
AIR FORCE OFFICE OF SCIENTIFIC RESEARCH
Conducted by the
Universal Energy Systems, Inc.
FINAL REPORT
Synthesis of Organometallic Reagents for SIFT Studies of
Electron Attachment Reactions

Prepared by:	Lee A. Flippin
Academic Rank:	Assistant Professor
Department:	Department of Chemistry and Biochemistry
University:	San Francisco State University
Research Location:	SFSU and AFGL-LID, Hanscomb AFB
USAF Researcher:	Dr. John Paulson
Date:	February 23, 1989

Synthesis of Organometallic Reagents for SIFT Studies of Electron Attachment Reactions

by

Lee A. Flippin

A systematic study of the preparation, characterization, and stability of several perfluoroalkylcobalt carbonyls was carried out. The target compounds were all approached via the general scheme: $\text{Co}_2\text{CO}_8 + \text{Na}^0(\text{Hg}) \rightarrow \text{Na}^+\text{CoCO}_4^- + \text{RCOCl} \rightarrow \text{RCOCoCO}_4 + \Delta \rightarrow \text{RCoCO}_4$ (R = perfluoroalkyl).

Trifluoromethylcobalt carbonyl, **1**, was synthesized and shown to have desirable volatility characteristics *vis-a-vis* the proposed SIFT studies that were planned in connection with this project. Compound **1** is also stable at ambient temperatures in the absence of moisture or oxygen, however, exposure to air causes the decomposition of **1** with concomitant formation of several incompletely characterized substances.

Pentafluoroethylcobalt carbonyl, **2**, was also readily prepared by the general scheme. It is somewhat less volatile than compound **1**, however, it is nevertheless suitable for the proposed SIFT studies in terms of its vapor pressure characteristics. Compound **2** is reasonably easy to purify when prepared by the scheme shown above, however, exposure to air at ambient temperatures causes its decomposition.

The reaction of heptafluoro *iso*-butyryl chloride with sodium tetracarbonylcobaltate in ether or THF did not appear to give the expected perfluoroacylcobalt carbonyl intermediate. Therefore, a plan to synthesize and study α -branched perfluoroalkylcobalt carbonyls was not pursued further.

1989 USAF-UES RESEARCH INITIATION PROGRAM

Sponsored by the
AIR FORCE OFFICE OF SCIENTIFIC RESEARCH
Conducted by the
Universal Energy Systems, Inc.

FINAL REPORT

Theoretical and Observational Studies of Geomagnetic Storm-Related Ion and Electron
Heating in the Subauroral Region

Prepared by :	Janet U. Kozyra
Academic Rank:	Assistant Research Scientist
Department and University:	Atmospheric, Oceanic and Space Science Dept., Space Physics Research Laboratory, University of Michigan
Collaborators:	Drs. H. Carlson , C. Valladares, S. Gussenhoven , and W. Swider, Air Force Geophysics Laboratory, Hanscom AFG, MA 01731
Date:	December 31, 1989
Contract No:	S-210-9MG-084

Abstract

Current 3-D ionosphere models specify a zero heat and particle flux as an upper boundary condition in the subauroral region. This is clearly inaccurate limiting the predictive capabilities of these models. The subauroral region of the ionosphere is marked by elevated electron temperatures, enhanced 6300Å emissions (which define a SAR arc), steep plasma density gradients and low electron densities (associated with the main electron density trough). Stable auroral red (SAR) arcs are the optical signature of the subauroral T_e peak, which has a highly variable magnetospheric energy source. Thus ground-based SAR arc observations are a valuable source of information on the long-term variations in the magnetospheric heat flux and the overall energetics of this region. Ground-based photometers indicate that SAR arcs, in general, are weaker in summer than in winter, and are weaker in solar minimum than in solar maximum for comparable magnetic storms (Slater and Kleckner, 1989). A parametric study was carried out to examine these effects. The results from the study indicate that the observed seasonal variation in SAR arc intensities can be explained by seasonal variations in the neutral atmosphere and ionosphere. However, observed solar cycle variations in SAR arc intensity are not consistent with variations predicted solely on the basis of a solar cycle changes in the neutral atmosphere and ionosphere. A reduction of the magnetospheric heat flux by a factor of between 5 and 20 from solar maximum to solar minimum conditions is necessary to bring model electron temperatures and 6300Å emission intensity into agreement with observational results for moderately disturbed conditions ($Dst \sim -80\gamma$). These changes in the magnetospheric energy source are of the same order as changes in the oxygen ion content of the magnetospheric plasma ($E < 17$ keV/e) in the vicinity of geosynchronous orbit presented in the literature. Recent theoretic and observational studies identify Coulomb collisions between ring current oxygen ions and thermal electrons as a major source of SAR arc energy.

Approximations, extrapolations and inadequate observational information associated with the above modelling efforts make it highly desirable to compare actual observations with the parametric results described above. A unique opportunity to examine conditions associated with solar minimum SAR arcs arose in connection with the ETS/GTMS campaign. The Millstone Hill Radar has provided a complete set of data detailing atmospheric and ionospheric conditions during the September 19-24, 1984 magnetic storm, as part of the ETS/GTMS campaign, during the same time period that three solar minimum SAR arcs were observed by the Mobile Automatic Scanning Photometer (MASP) chain in

North America. Additional information on energetic and thermal ion populations at high altitudes is available from the DE-1 and AMPTE/CCE satellites during both the main and recovery phases of the storm. This is the first time that observations of the entire ring current distribution including heavy ions have been available on SAR arc field lines. Estimated column electron heating rates due to Coulomb collisions between energetic and thermal plasma populations are of the correct order to produce the observed 6300Å emissions on all occasions examined. These solar minimum results, along with solar maximum SAR arc observations and models in the literature, provides strong support for the important role played by Coulomb collisions in the SAR arc process (reasonable heating rates are achieved over a broad range of seasonal and solar cycle conditions). In agreement with past studies, energetic O⁺ supplies the bulk of the electron heating during the storm recovery phase; contributions due to H⁺ are negligible. A major new result of the present study is the appearance of an approximately 30 keV H⁺ population during the storm main phase which provides the bulk of the thermal electron heating at this time but is short-lived and is not present during the recovery phase. This limited observational data implies that H⁺ has an important role in producing SAR arcs during the main phase. The observational data and model results for this solar minimum storm and for a number of solar maximum storms in the literature are in basic agreement with the results of the parametric study described above and therefore lend support to the conclusions of that study.

II. INTRODUCTION

The subauroral region of the ionosphere is marked by elevated electron temperatures with associated enhanced 6300Å emissions (SAR arcs), steep plasma density gradients and low electron densities (associated with the main electron density trough), enhanced electron density irregularities, and occasionally, penetration of the convection electric field. At high altitudes, the subauroral ionosphere is overlain by the plasmapause and outer plasmasphere where a warm zone is observed in the ion and electron temperatures. The ion and electron temperatures in the outer plasmasphere and the electron temperatures in the subauroral ionosphere increase with increasing magnetic activity. All of these characteristic structures make the subauroral ionosphere a highly variable environment.

The Air Force Geophysics Laboratory at Hanscom Air Force Base is concerned with the effects of the high altitude environment on radio and radar signals and on spacecraft communications, performance, and lifetime. In order to obtain the capability to predict the

high altitude environment under different seasonal and solar cycle conditions as well as for different levels of magnetic activity, models of the thermosphere-ionosphere system are being assembled and tested against comprehensive measurements of ionospheric and thermospheric parameters. One such effort, made to better understand the response of the thermosphere - ionosphere system to geomagnetic storm conditions, was the ETS/GTMS (Equinox Transition Study/Global Thermospheric Mapping Study) campaign. This campaign involved coordinating the observational efforts of six incoherent scatter radars, 6 polar orbiting satellites, 4 Fabry-Perot interferometers and other supporting instrumentation to obtain a comprehensive set of diagnostics of thermospheric and ionospheric responses to the 19-24 September 1984 magnetic storm.

The Air Force Geophysics Laboratory, Space Physics Division also houses the DMSP data base. The DMSP satellites make extensive observations of ion and electron precipitation. These observations are important diagnostics of regions where energetic magnetospheric populations are undergoing diffusion into the loss cone due to collisions or wave-particle interactions. Such precipitation can cause interesting ionospheric effects.

My research interests lie in understanding the energy source of the ion and electron heating in the subauroral region. Recent theoretical work, by myself and colleagues, indicates that energetic oxygen ions (1 - 200 keV), a component of the earth's ring current, and suprathermal oxygen ions (< 1 keV), that accumulate in the outer plasmasphere during geomagnetic activity, are a significant energy source (possibly the dominant energy source) for elevated electron and ion temperatures, respectively, associated with the subauroral region (Kozyra et al., 1987; Chandler et al., 1988). Energy transfer from the energetic populations to the thermal plasma proceeds as a result of Coulomb interactions in the outer plasmasphere. An understanding of the energy source and its variation with magnetic activity, solar cycle and season as well, as an understanding of the corresponding variation in ionospheric signatures resulting from this high altitude heat source, is paramount to accurate modelling of the subauroral ionosphere and outer plasmasphere, and possible development of forecasting capabilities.

III. RESEARCH OBJECTIVES AND STRATEGIES

(i) Long-Term Objectives

Current three-dimensional ionospheric models specify a zero heat and particle flux as an upper boundary condition in the subauroral region (J. Sojka, private communication). This

is clearly inaccurate. Long term objectives of studies described herein are to understand seasonal, solar cycle, and magnetic-stormtime variations (1) in ion and electron heating and characteristic particle precipitation in the outer plasmasphere and subauroral ionosphere and (2) in the energetic particle environment at high altitudes responsible for this heating. This will allow, among other things, a more accurate specification of heat and particle fluxes in ionospheric models and a more accurate prediction of the plasma environment in the subauroral region at plasmaspheric and ionospheric heights during magnetically active conditions.

(ii) Short-Term Objectives and Research Strategies

Elevated Subauroral Electron Temperatures

Statistical studies of the variation of the intensity and position of the Te peak with magnetic activity have only recently been performed (Kozyra et al., 1986; Buchner et al., 1983; Brace et al., 1988) over limited time intervals. These studies, however, do not contain information on the seasonal and solar cycle variations in the observations. Stable auroral red (SAR) arcs are the optical manifestation at 6300\AA of the subauroral Te peak (see Rees and Roble, 1975 for a discussion of SAR arcs). In the region of the subauroral Te peak, significant populations of thermal electrons with energies in excess of 1.96 eV exist in the high energy tail of the Maxwellian distribution. These electrons are capable of exciting atomic oxygen to the 1D state during a collision. The 1D state relaxes in 110 seconds with the emission of a photon at 6300\AA . The 1D state can also be quenched via collisions with molecular nitrogen. Significant 6300\AA emission only results at altitudes high enough so that collisions with molecular nitrogen are infrequent. The amount of 6300\AA emission which results from this process is dependent on the neutral atmospheric densities of O and N_2 , the N_e density at the F2 peak, the height of the F2 peak, and the electron temperature.

SAR arc observations extend over several solar cycles and contain information on seasonal, solar cycle and magnetic activity variations in the subauroral electron temperature peak and its energy source. SAR arcs occur most frequently during the equinoxes, are rarely observed in June or July (Hoch, 1973), and there is a 2-3 year phase lag between the maximum in the solar cycle and the maximum in SAR arc occurrence frequency (Slater and Smith, 1981). A study of SAR arc intensities over the last solar cycle (1978-1988) indicates that SAR arcs are weaker, on the average, during solar minimum than during solar maximum for the same intensity of ring current as indicated by the D_{st} index (Slater

and Kleckner, 1989). Such variations in SAR arc intensity and occurrence frequency may be due to solar cycle differences in the high altitude heat source or to seasonal and solar cycle changes in the atmosphere and ionosphere resulting in lower electron temperatures for a given heat flux. True seasonal effects are not expected to result from variations in the high altitude heat source since the heat source is equatorial; the same heat source supplies both the winter and summer portions of the flux tube simultaneously. Past studies of SAR arcs have not addressed the question of their solar cycle or seasonal variability and detailed modelling has been done only for solar maximum observations. Short-term objectives are to try to understand and separate the effects of variations in the magnetospheric energy source and the atmosphere/ionosphere system on elevated subauroral electron temperatures.

Task 1: Understand the effects of solar cycle and seasonal variations in the atmosphere/ionosphere system on electron temperatures and SAR arc emissions resulting from a constant magnetospheric energy source.

To provide a framework for interpreting SAR arc and elevated electron temperature measurements during solar minimum and solar maximum magnetic storms, a parametric study is carried out, using a truncated version of an ionosphere model described in Young et al (1980) and typical ionospheric and neutral atmospheric density profiles for each season and for various stages in the solar cycle given by the IRI and MSIS-86 models, respectively. Electron temperature profiles and resulting 6300Å emission intensity were obtained for a variety of model conditions. This study is intended to explore the effect that typical seasonal, solar cycle and magnetic storm-time variations in the neutral atmosphere and ionosphere have on the intensity of SAR arcs by holding the heat flow constant at the upper boundary and allowing only atmospheric and ionospheric parameters to vary. Preliminary results of the SAR arc studies, obtained with funding from the AFOSR/UES Summer Faculty Program, indicate that seasonal variations in SAR arc intensities can be attributed to seasonal variations in the neutral atmosphere and ionosphere but solar cycle variations cannot be explained by normal solar cycle changes in these quantities (Kozyra 1988; Kozyra et al., 1989). The question of how well seasonal and solar cycle changes in the atmosphere and ionosphere are actually represented by this model must be addressed in the present work. Included in this investigation is a look at the effects of a thinner F-layer. A study comparing the IRI-86 model to actual

Millstone Hill observations indicates that IRI-86 consistently predicts a thicker F-layer than is observed (Buonsanto, 1989).

Task 2: Understand the influence of solar cycle changes in the magnetospheric energy source on electron heating rates in the subauroral region.

Part A: In Task 1, the effects of solar cycle and seasonal variations in the atmosphere and ionosphere on SAR arc intensities are examined. The trend, exhibited by SAR arc observations over the last solar cycle (Slater and Kleckner, 1989), is for SAR arc intensities to be lower, on the average, in solar minimum than in solar maximum for comparable magnetic storms (indicated by the D_{st} index). Fok et al. (1989) examined AE satellite observations of the subauroral electron temperature peak during solar minimum and compared these to similar observations by the DE-2 satellite during solar maximum. The authors found no clear solar cycle variation in the correlation between electron temperature and D_{st} in this region. Using information provided by Slater and Kleckner (1989) and Fok et al. (1989) to constrain the model, it is possible to estimate the changes in the magnetospheric heat flux over the solar cycle necessary to bring model results into agreement with observations of the electron temperature and 6300Å emission intensities.

Part B: To determine if observations of solar minimum magnetic storm conditions and SAR arc emissions bear out the results of the parametric study described in Task 1 and Task 2, part A, a particularly well-measured solar minimum magnetic storm will be examined and modelled. The ETS/GTMS campaign, which was carried out during the 19-24 September 1984 magnetic storm, has provided a complete set of data detailing atmospheric and ionospheric conditions during the same time period that three solar minimum SAR arcs were observed by the MASP chain of photometers (D. Slater, private communication). This campaign involved coordinating the observational efforts of six incoherent scatter radars, 6 polar orbiting satellites, 4 Fabry-Perot interferometers and other supporting instrumentation to obtain a comprehensive set of diagnostics of thermospheric and ionospheric responses to the 19-24 September 1984 magnetic storm. The Air Force Geophysics Lab had a major role in coordinating this effort. The solar minimum SAR arc observations during the 19-24 September 1984 storm and models will be interpreted in light

of the results of the parametric study and compared to models and observations of solar maximum SAR arcs, which have appeared in the literature (Rees and Roble, 1975; Kozyra et al., 1982; Kozyra, 1986; Slater et al., 1987), to provide an insight into causes of solar cycle variations in the intensity of SAR arcs.

IV. Parametric Studies of Solar Cycle and Seasonal Variations in SAR arcs - Summary of Results Presented in Kozyra et al. (1989)

SAR arcs are the optical response of the atmosphere to elevated subauroral electron temperatures due to enhanced magnetospheric heat flow in the electron gas during magnetically active conditions. As such, SAR arc statistics (occurrence frequency and intensity) contain information on the variation with season and solar cycle of the magnetospheric energy source for SAR arcs. The interpretation of these statistics is far from straightforward, however. Normal solar cycle and seasonal variations in the neutral atmosphere and ionosphere will dramatically effect the magnitude of the subauroral electron temperature enhancement and the resulting SAR arc intensity, even for a fixed magnetospheric heat flux. Superimposed on trends in SAR arc intensity due to atmospheric and ionospheric changes are variations in the magnetospheric energy source due to solar cycle, seasonal and magnetic activity variations.

This parametric study was undertaken to establish general trends in SAR arc emission intensity due to seasonal and solar cycle changes in the neutral atmosphere and ionosphere using an ionospheric model described in Young et al. (1980), and modified to accept a heat flux upper boundary condition. Variations in the neutral atmosphere were represented by the MSIS-86 model, with suitably chosen input parameters and variations in the ionosphere were represented by the IRI-86 model ionosphere modified to represent magnetically active conditions (i.e., the presence of the main electron density trough). Nightside neutral atmospheric and ionospheric density profiles and topside electron and ion heat fluxes were specified and the ionosphere model was employed to solve for the ion and electron temperature profiles and resulting 6300Å emission intensities. Figure 1 displays ionospheric and atmospheric profiles as well as 6300Å emission intensity resulting from a fixed magnetospheric heat flux, for June and December, solar maximum and solar minimum conditions. Models for September and March were also constructed but are not pictured in Figure 1. Ionospheric and atmospheric profiles fall between those displayed for June and December.

To isolate atmospheric and ionospheric effects the upper boundary electron heat flux was fixed at -2.5×10^{10} eV/cm²/s. In this manner, it was hoped to identify the long-term trends in SAR arc intensity which are attributable to long-term trends in the atmospheric and ionospheric densities and the trends in the intensity which might reasonably require an interpretation in terms of long-term variations in the magnetospheric energy source. Though considerable variation might be expected in SAR arc intensities at any given time just due to the observed daily variations in the neutral atmosphere and ionosphere especially in the region of the main electron density trough, there should be clear long-term trends superimposed on this short-term variability. Information on the magnetospheric energy source may be contained in some of these long-term trends. If such information can be extracted, it places another constraint on proposed mechanisms for the SAR arc magnetospheric energy source with the need to replicate the solar cycle and seasonal variations observed in SAR arc intensities from ground-based photometers.

With the help of recent statistical studies examining variations in the 6300Å emission intensity (Slater and Kleckner, 1989) and the magnitude of the subauroral electron temperature peak (Kozyra et al., 1986; Fok et al., 1989) sufficient constraints are placed on the model results to allow an estimation of the solar cycle variation in the magnetospheric energy source.

The following are the results of the present parametric study:

- (1) There is an obvious seasonal variation in model SAR arc emission intensities, with weakest SAR arcs occurring in June, both in solar maximum and in solar minimum, for a fixed magnetospheric energy flux (see Figure 2). This is consistent with the observed minimum in SAR arc occurrence frequency in the summer months (Hoch, 1973). SAR arc intensities in June reach the threshold for ground-based observations (~50R) less frequently than in other months of the year. Weak summer SAR arcs are also consistent with the statistical study of Slater and Kleckner (1989). Seasonal changes in the ionosphere and atmosphere, represented in the model, are responsible for the seasonal modulation in SAR arc emissions.
- (2) Model SAR arcs are stronger at solar minimum than at solar maximum for a fixed magnetospheric heat flow (see Figure 2). This solar cycle variation in SAR arc intensity, which emerges from the model, results from solar cycle variations in the neutral atmosphere and ionosphere. In order to relate this result to observations,

assumptions regarding the relationship between the ring current energy density and the magnetospheric heat flow must be made. The magnetospheric heat flow results from a transfer of ring current energy to the thermal plasma. If it is assumed that the magnetospheric heat flow varies only with the energy density of the ring current, then ring currents with the same energy density (same D_{st} value) in solar maximum and in solar minimum should provide the same magnetospheric heat flow to the subauroral ionosphere and, according to model results, produce stronger emissions in solar minimum. Contrary to model results, observations indicate a tendency toward weaker SAR arcs during solar minimum than during solar maximum (Slater and Kleckner 1989) for the same D_{st} value. This suggests a solar cycle variation in the efficiency of converting ring current energy into thermal electron heating. The same ring current energy density is linked to a higher magnetospheric heat flux in solar maximum than in solar minimum.

- (3) A factor of 5-20 reduction in the magnetospheric heat flux from solar maximum to solar minimum is required to bring model results (Table 2) into agreement with observations (Table 1). In other words, the model suggests that a moderate magnetic storm characterized by a particular minimum D_{st} value in solar minimum is associated with a factor of 5-20 smaller magnetospheric heat flux than an equivalent storm in solar maximum. Energetic O^+ is predicted to be a major energy source for SAR arcs by Kozyra et al. (1987). Such a variation in the magnetospheric heat flow could reasonably be achieved if the oxygen ion content of the ring current increases significantly with the solar cycle, resulting in large composition changes for a fixed energy density as the solar cycle proceeds. Solar cycle variations in the magnetospheric heat flux required by the model are reasonably consistent with the observed variations in the O^+ content of the magnetospheric plasma with solar cycle (Young et al., 1982).
- (4) The best agreement between model results and 6300Å emission observations is achieved under the assumption that the electron temperature at approximately 500 km does not vary significantly with season or solar cycle but only with magnetic activity. Statistical studies of the electron temperature peak in the altitude range 400-600 km indicates no clear solar cycle variation in this quantity but a dramatic variation with magnetic activity in support of this assumption (Kozyra et al., 1986; Buchner et al., 1983; Fok et al., 1989).

Kozyra et al. (1987) find that Coulomb collisions between thermal electrons and the oxygen ion component of the ring current, heat the electron gas sufficiently to support the elevated electron temperatures observed in the F-region ionosphere during several SAR arcs in solar maximum. The oxygen ion component of the magnetospheric plasma, however, has been observed to decrease in density with the sunspot number by a factor of ~ 10 between solar maximum and solar minimum (Young et al., 1982). A ring current which produces a given depression in the surface magnetic field indicated by the D_{st} index would contain a significantly lower percentage of oxygen during solar minimum than during solar maximum. The electron heating rate resulting from Coulomb collisions with energetic oxygen ions is directly proportional to the flux of the oxygen ions at a given energy. So a reduction in the oxygen ion density by a factor of ~ 10 would produce a corresponding change in the magnetospheric heat flux if the average energy of these oxygen ions remained unchanged with solar cycle. A factor of 20 reduction in the magnetospheric heat flux would require both energy and density changes in the oxygen ion component of the magnetospheric plasma with solar cycle.

The Coulomb collision rate is also directly proportional to the thermal electron density in the outer plasmasphere. Systematic solar cycle variations in the plasmaspheric densities could also be responsible for modulating the magnetospheric heat flow resulting from a given ring current population. However, plasmaspheric densities, inferred from whistler observations, indicate no significant solar cycle variation in the outer plasmasphere but do show a small seasonal variation, with plasmaspheric densities in winter a factor of 1.5 -3 times higher than those in summer (Park et al., 1978).

The apparent lack of solar cycle variability in the subauroral electron temperature peak at F-region heights is an interesting result and one that deserves further comment. Magnetospheric heat fluxes and electron densities are each varying over more than an order of magnitude during the solar cycle. Lower electron densities result in higher electron temperatures for a fixed magnetospheric heat flux. The magnetospheric heat flux is apparently varying in such a way as to maintain the electron temperatures within a fixed range at F-region heights over the solar cycle. It seems highly unlikely that this is happening fortuitously. Rather it may be evidence of the strong ionospheric control over the magnetospheric energy source of Stable Auroral Red arcs and the associated subauroral electron temperature peak.

Recent studies (Kozyra et al., 1987; Chandler et al., 1988) identify energetic oxygen ions as the magnetospheric energy source of SAR arcs. Outflows of heavy ions from the polar cap and auroral ionosphere supply the magnetospheric plasma with heavy ions (cf. Horwitz 1987, Kozyra 1989). These outflows decrease in direct proportion to the solar cycle decrease in the high-latitude ionospheric densities and scale heights. There is a corresponding solar cycle decrease in mid-latitude ionospheric densities. Therefore, the magnetospheric heat source (which varies with high-latitude ionospheric densities and scale heights) and the ionospheric heat sink (which varies with the mid-latitude ionospheric densities) are both decreasing with decreasing solar cycle. This may account for the lack of significant solar cycle variation in the subauroral T_e peak.

V. Observational Study of Three Solar Minimum SAR arcs - Comparison to Predictions of Parametric Study. Summary of Results Presented in Kozyra et al. (1990)

The motivation for this study is to gain insight into solar cycle and magnetic storm phase variations in the SAR arc energy source and emissions as well as to provide an observational test for the parametric study described in Section IV. For the purposes of the present study, the dominant SAR arc energy source was assumed to be Coulomb collisions between ring current ions and thermal electrons at high altitudes on SAR arc field lines. The energy transferred in this manner is transported down the field lines to F-region heights producing elevated electron temperatures and associated enhanced 6300Å emissions which define a SAR arc.

A unique set of observations describing ionospheric conditions, magnetospheric populations and 6300 Å emission intensities on SAR arc field lines during the solar minimum September 19-24, 1984 magnetic storm period prompted an investigation into solar cycle and magnetic storm phase variations in SAR arc emissions and their magnetospheric energy source. Electron heating rates due to Coulomb collisions between ring current ions and thermal electrons were estimated by three separate methods using DE-1/EICS and AMPTE/CCE CHEM observations and thermal plasma properties, in the manner described in Kozyra et al. (1987). The three methods varied with regard to the extrapolation of the energetic population in energy and pitch angle. The three different extrapolations used (1) DE-1 EICS with a loss-cone type distribution, (2) DE-1 EICS with a saddle-type distribution and (2) AMPTE/CCE CHEM with a pitch angle averaged distribution. Further details regarding these extrapolations are given in Kozyra et al. (1990). The electron heating rates were supplied to a plasmasphere model which solves the

coupled continuity, momentum, energy and heat flow equations. The model was solved under conditions necessary to reproduce ionospheric densities measured by the Millstone Hill radar. The model electron temperatures and associated 6300 Å emission intensities were in good agreement with observations of these quantities by the Millstone Hill radar and MASP photometer chain, respectively on September 20 but required some modification of model inputs to bring results into agreement on September 24. The observations and model results were compared to available solar maximum observations and model results to uncover solar cycle variations. In addition, observations and models during the main phase are contrasted with those during the recovery phase to reveal magnetic storm phase variations in relevant quantities. Conclusions are as follows:

- (1) Electron heating rates (Figure 3), calculated using the Coulomb collision model for the magnetospheric energy source and observations of energetic and thermal ion populations, consistently produce model electron temperatures in agreement with observations over a wide variety of conditions (Kozyra et al., 1987; Chandler et al., 1988 and the results of this study). A comparison between observed and modelled electron density and temperature profiles for September 20 and 24 are provided in Figures 4 and 5, respectively. This consistent agreement between models and observations, both in the present study and in other studies in the literature, provides strong support for the Coulomb collision theory of the SAR arc magnetospheric energy source.
- (2) Observations of energetic ion populations on SAR arc field lines during the September 19-24, 1984 magnetic storm period, when compared to energetic populations observed during comparable magnetic storms in solar maximum, indicate approximately a factor of four decrease in the flux of energetic ($E > 1$ keV) oxygen ions in solar minimum on SAR arc field lines. The energetic ($E > 1$ keV) H^+ component, however, exhibits no clear solar cycle variation. This O^+ modulation undoubtedly produces a similar solar cycle variation in the magnetospheric energy source for SAR arcs. This result is illustrated in Figure 6.
- (3) The following differences between main phase and recovery phase ion populations on SAR arc field lines were observed: (1) the energetic ($E \sim 30$ keV) H^+ population was significantly enhanced during the main phase

compared to the recovery phase of the September 19-20, 1984 magnetic storm (Figure 7) and (2) higher thermal plasma densities were observed on SAR arc field lines during the main phase than during the recovery phase of this storm. The net effect of these trends is to increase electron heating during the main phase (See Figure 3). Enhanced heating rates are expected to be short-lived for two reasons: (1) H^+ lifetimes against loss due to charge exchange and Coulomb scattering are less than one day at these energies and (2) the outer plasmaspheric density is eventually depleted as the storm progresses. These difference between main and recovery phase SAR arcs are a major new result of the present study.

This study provides an observational test of the predictions of the parametric study outlined in Section IV. Two questions arise: (1) Is the atmosphere and ionosphere during the well-measured 19-24 September 1984 geomagnetic storm period consistent with conditions adopted in the parametric study for September solar minimum and (2) how do the observed electron temperatures and emissions compare with model results in the parametric study? In general the observed NMF2 on September 20 and 24 was a factor of 2 lower and HMF2 at the low end of the assumed altitude range compared to the Fall solar minimum model used in the parametric study of Kozyra et al. (1989); thus the agreement between the ionospheres in the two cases is fairly good. In the present study, it was found necessary to reduce the neutral O density by 25% to calculate ionospheric densities in agreement with observations. This will reduce column 6300Å emissions calculated in the present study with respect to those obtained in the parametric study. Column electron heating rates and electron temperatures at 500 km are consistent with the results of the parametric study as well. The observational data and model results for this solar minimum storm and for a number of solar maximum storms in the literature are in basic agreement with the results of the parametric study described above and therefore lend support to the conclusions of that study.

VI. Recommendations

The following studies will verify and further develop our understanding of the effects identified in the present work. (1) A statistical look at main versus recovery phase SAR arc emissions and subauroral electron temperatures will clarify the differences in the magnetospheric energy source as the storm progresses. (2) A study of the build-up and

decay of energetic ion populations in the subauroral region during the main and recovery phases of a number of storms would shed light on the relative contributions of various ion subpopulations to the magnetospheric electron heat flux. (3) A comparison of energetic ion populations over the entire ring current energy range on SAR arc field lines in the upcoming solar maximum period (possibly using CRRES observations) with AMPTE/CCE observations from the past solar minimum will test the theory that variations in ring current O^+ with solar cycle is responsible for solar cycle variations in the magnetospheric electron heat flux in the subauroral region.

Studies of the causes of ion heating in the outer plasmasphere to obtain information on the little-understood magnetospheric ion heat flux in the subauroral region are also needed. These studies were postponed in favor of better defining the solar cycle variation in the magnetospheric electron heat flux in the present study. Studies of ion heating in the February 1986 magnetic storm, in collaboration with Drs. S. Gussenhoven and W. Swider of the Air Force Geophysics Laboratory, will be continued, to the extent possible, with funding from other sources.

Acknowledgements

I would like to acknowledge helpful discussions of the present study with Drs. A.F. Nagy and J.-H. Yee of the University of Michigan. The modeling results for the September 19-24, 1984 storm period were a collaborative effort with Dr. M. O. Chandler of NASA/Marshall Space Flight Center, who also supplied and analyzed thermal plasmaspheric ion data for this same time period. Energetic ion datasets, used in the study, were supplied by Dr. W. K. Peterson of Lockheed Corp. and Dr. D. C. Hamilton of the University of Maryland. Special thanks to Dr. Henry Wadzinski for the use of assorted computer program, to Dr. Jurgen Buchau for interesting and helpful discussions on the characteristics of the subauroral ionosphere, to Dr. L. H. Brace for supplying Atmosphere Explorer Langmuir probe observations to guide the selection of model parameters, and to Dr. D. W. Slater for the use of SAR arc statistics from the MASP chain of photometers. Millstone Hill data were acquired and analyzed under support of National Science Foundation cooperative agreement ATM 8808137 to Massachusetts Institute of Technology with the assistance of Dr. M. Buonsanto.

References

- Brace, L. H., C.R. Chappell, M.O. Chandler, R.H. Comfort, J.L. Horwitz, W.R. Hoegy, F-region electron temperature signatures of the plasmapause based on Dynamics Explorer 1 and 2 measurements, *J. Geophys. Res.*, 93, 1896, 1988.
- Buchner, J., H.-R. Lehmann, and J. Rendtel, Properties of the subauroral electron temperature peak observed by Langmuir-probe measurements on board intercosmos-18, *Gerlands Beitr. Geophys.*, 92, 368, 1983.
- Buonsanto, M.J., Comparison of incoherent scatter observations of electron density and electron and ion temperatures at Millstone Hill with the International Reference Ionosphere, *J. Atmos. Terr. Phys.*, 51, 441, 1989.
- Chandler, M.O., J.U. Kozyra, J.L. Horwitz, R.H. Comfort, W.K. Peterson, and L.H. Brace, Modelling of the thermal plasma in the outer plasmasphere: a magnetospheric heat source, *AGU Monograph on Magnetosphere and Ionosphere Plasma Models*, eds., T.E. Moore, J.H. Waite, Jr., and T. Moorhead, 1988.
- Fok, Mei -Ching, J. U. Kozyra and L. H. Brace, Solar cycle variation in the magnitude of the subauroral electron temperature peak: Comparison of AE-C and DE-2 satellite observations, to be submitted to *J. Geophys. Res.*, 1990.
- Hoch, R.J., Stable auroral red arcs, *Rev. Geophys. Space Phys.*, 11, 935, 1973.
- Horwitz, J. L., Core plasma in the magnetosphere, *Rev. of Geophys.*, 25, 579, 1987.
- Kozyra, J.U., T. E. Cravens, A. F. Nagy, M.O. Chandler, L. H. Brace, N. C. Maynard, D. W. Slater, B. A. Emery, and S. D. Shawhan, *Geophys. Res. Lett.*, 9, 973, 1982.
- Kozyra, J.U., L.H. Brace, T.E. Cravens, and A.F. Nagy, A statistical study of the subauroral electron temperature enhancement using Dynamics Explorer 2 Langmuir probe observations, *J. Geophys. Res.*, 91, 11270, 1986.
- Kozyra, J. U., E.G. Shelley, R.H. Comfort, L.H. Brace, T.E. Cravens, and A.F. Nagy, The role of ring current O^+ in the formation of stable auroral red arcs, *J. Geophys. Res.*, 92, 7487, 1987.
- Kozyra, J. U., Theoretical and observational studies of geomagnetic storm-related ion and electron heating in the subauroral region, 1988 USAF-UES Summer Faculty Research Program Final Report, Contract No. F49620-87-R-0004, 1988.
- Kozyra, J.U., C.E. Valladares, H. C. Carlson, M. J. Buonsanto, D. W. Slater, A theoretical study of the seasonal and solar cycle variations of SAR arcs, accepted for publication, *J. Geophys. Res.*, December 1989.

- Kozyra, J. U. , M.O. Chandler, D. Hamilton, W. Peterson, D. W. Slater, M. Buonsanto, H. Carlson, C. Valladares, Stable Auroral Red Arcs during the September 19-24, 1984 Geomagnetic Storm Period - Implications for the Causes of Solar Cycle and Geomagnetic Storm Phase Variations in Intensity, to be submitted to J. Geophys. Res., 1990.
- Park, C.G., D.L. Carpenter, and D.B. Wiggin, Electron density in the plasmasphere: whistler data on solar cycle, annual and diurnal variations, J. Geophys. Res., 83, 3137, 1978.
- Rees, M.H., and R.G. Roble, Observations and theory of the formation of stable auroral red arcs, Rev. Geophys. Space Phys., 13, 201, 1975.
- Slater , D.W. and E.W. Kleckner, Occurrences of stable auroral red arcs detected by the Pacific Northwest Laboratory Photometer Network, 1978-1988, Pacific Northwest Laboratory, Richland, Washington, PNL-7184, 1989.
- Slater, D.W., and L.L. Smith, Modulation of stable auroral red (SAR) arc occurrence rates, J. Geophys. Res., 86, 3669, 1981.
- Slater, D.W., C. Gurgiolo, J.U. Kozyra, E.W. Kleckner, and J.D. Winningham, A possible energy source to power stable auroral red arcs: Precipitating electrons, J. Geophys. Res., 92, 4543, 1987.
- Young, D.T., H. Balsiger, and J. Geiss, Correlations of magnetospheric ion composition with geomagnetic and solar activity, J. Geophys. Res., 87, 9077, 1982.
- Young, E.R., D.G. Torr, P. Richards, and A.F. Nagy, A computer simulation of the mid-latitude plasmasphere and ionosphere, Planet. Space Sci., 28, 881, 1980.

TABLE 1
1978-1988 6300Å INTENSITY STATISTICS
MASP PHOTOMETER CHAIN
(Slater and Kleckner, 1989)

		SPRING			SUMMER			FALL			WINTER		
		Mean	Mean	Emis.	Mean	Mean	Emis.	Mean	Mean	Emis.	Mean	Mean	Emis.
		Dst	Dst		Dst	Dst		Dst	Dst		Dst	Dst	
Solar Min	77.5R	-78 γ	-	-	130R	-68 γ	118R	-79 γ					
Solar Max	315R	-68 γ	106R	-60 γ	300R	-82 γ	164R	-62 γ					
Solar Minimum		Solar Maximum											
Mean Emission	111R	255R											
Mean Dst	-74 γ	-72 γ											

Te STATISTICS

Solar Maximum (DE-2 Statistical Fit)	-80 γ	3155.7 K
(Alt<600 km) (Kozyra et al., 1986)		
Solar Minimum (AE Statistical Fit)	-80 γ	3277.9 K
(Alt< 600 km) (Fok, et al., 1989)		

Table 1: 6300Å and Te observations.

TABLE 2

MODEL 2 RESULTS

No Seasonal or Solar Cycle Variation
of Te at 500 km

	SOLAR MAXIMUM			SOLAR MINIMUM		
	HMF2+50km* IRI HMF2*			HMF2+50km* IRI HMF2*		
	Heat	6300Å	Heat	6300Å	Heat	6300Å
	Flux	Emis.	Flux	Emis.	Flux	Emis.
June	3.4E10	200R	3.4E10	150R	3E9	85R
Equinox	2.5E10	400R	3E10	200R	1.5E9	85R
December	1.5E10	300R	2E10	220R	1.5E9	85R
					5.6E9	80R
					3.3E9	90R
					3.3E9	90R

*Results are presented from models with the height of the F-layer peak density (HMF2) given by the IRI-86 model and with the HMF2 increased by 50 km over the IRI-86 model value.

Table 2: Variation in Heat Flux between solar max and min.

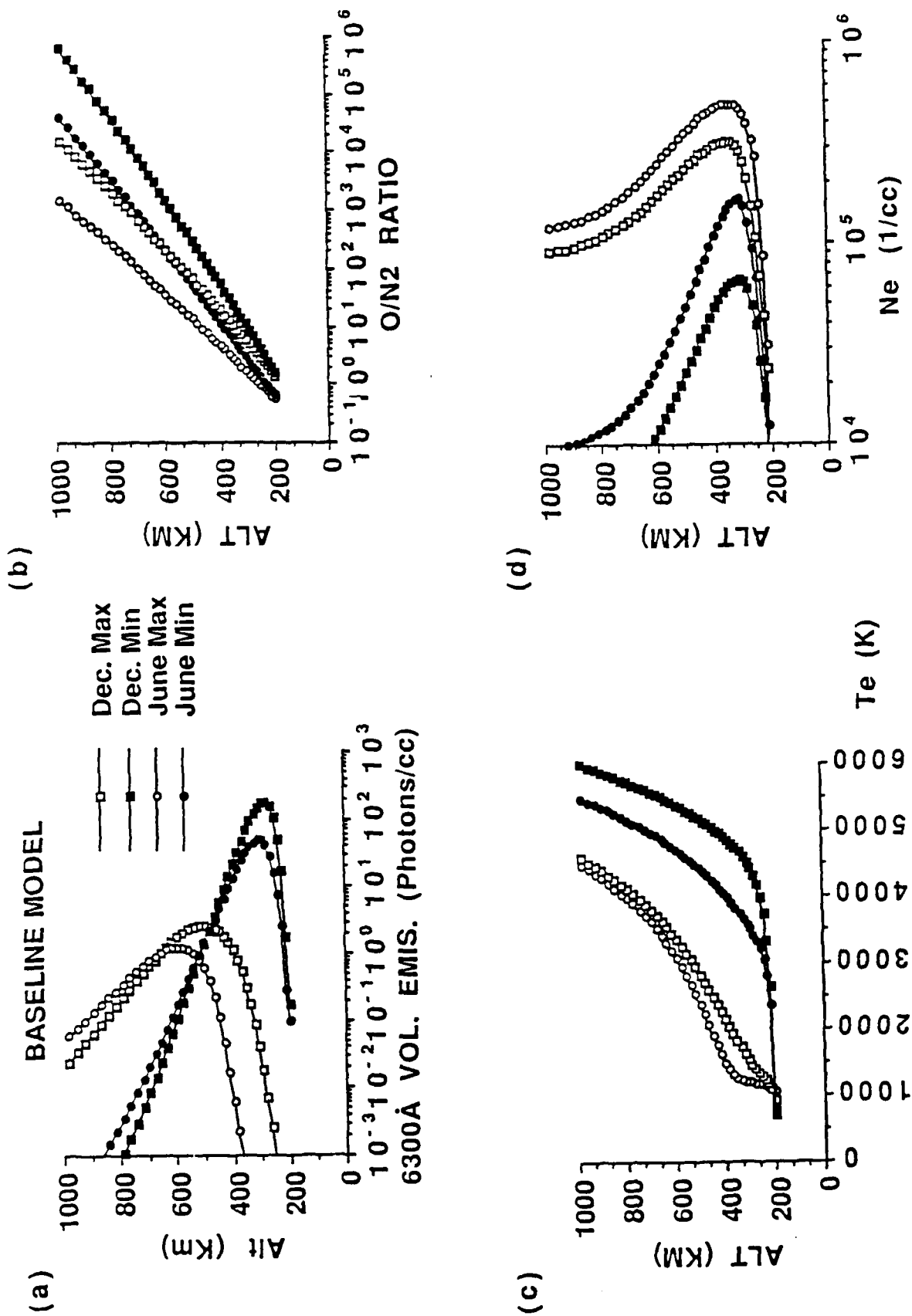


Figure 1: Altitude profiles of (a) 6300Å volume emission rate, (b) O/N₂ ratio from the MSIS-86 model atmosphere, (c) calculated electron temperatures and (d) IRI-86 model electron density for conditions representative of June and December during solar maximum and solar minimum.

STORM MODELS: Magnetospheric Heat **Flux Fixed At $-2.5E10$ ev/cm²/s**

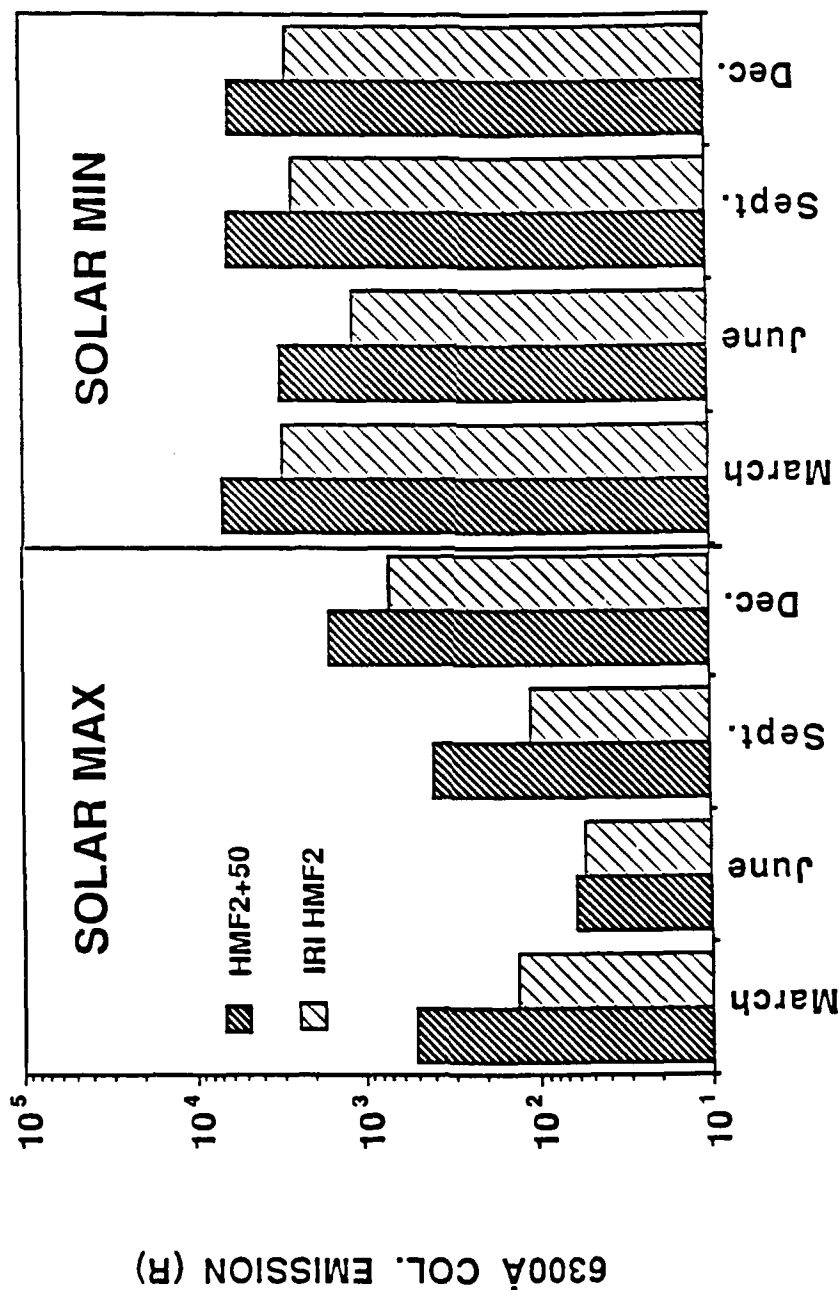


Figure 2: Solar cycle and seasonal variations in 6300 Å emission intensities due to solar cycle and seasonal changes in the neutral atmosphere and ionosphere. The magnetospheric heat flux was held fixed at -2.5×10^{10} eV/cm²/s. Results are shown from models with the IRI-86 HMF2 and with the HMF2 increased by 50 km over the IRI-86 model value. Note there is a seasonal variation in model SAR arc emissions with minimum values occurring in June for a fixed heat flux. The model indicates a trend toward high emission intensities during solar minimum than during solar maximum for a fixed heat flux.

Estimated Column Electron Heating Rates

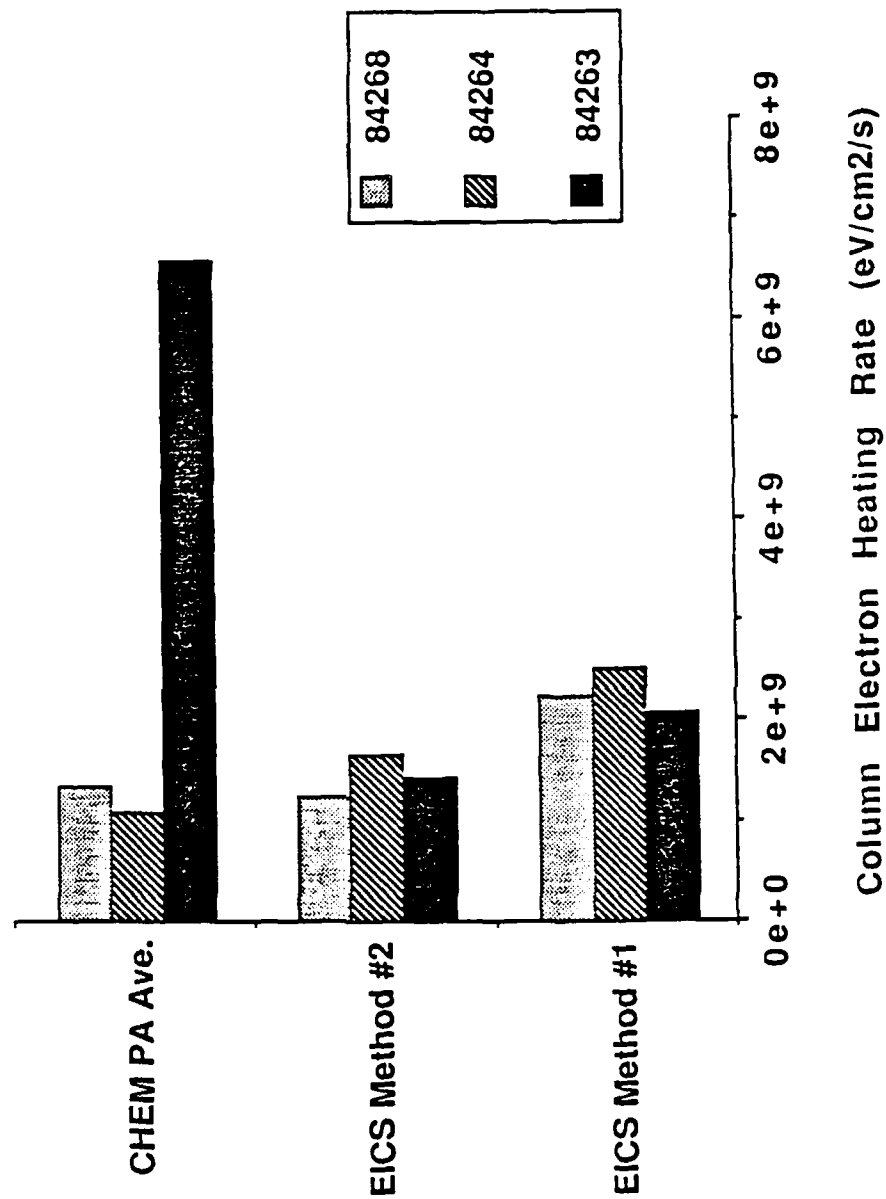


Figure 3: Estimated column electron heating rate using three different methods (described in the text) on SAR arc fields lines during each of the MASP observation periods on September 19, 20, and 24, 1984 (84263, 84264 and 84268, respectively).

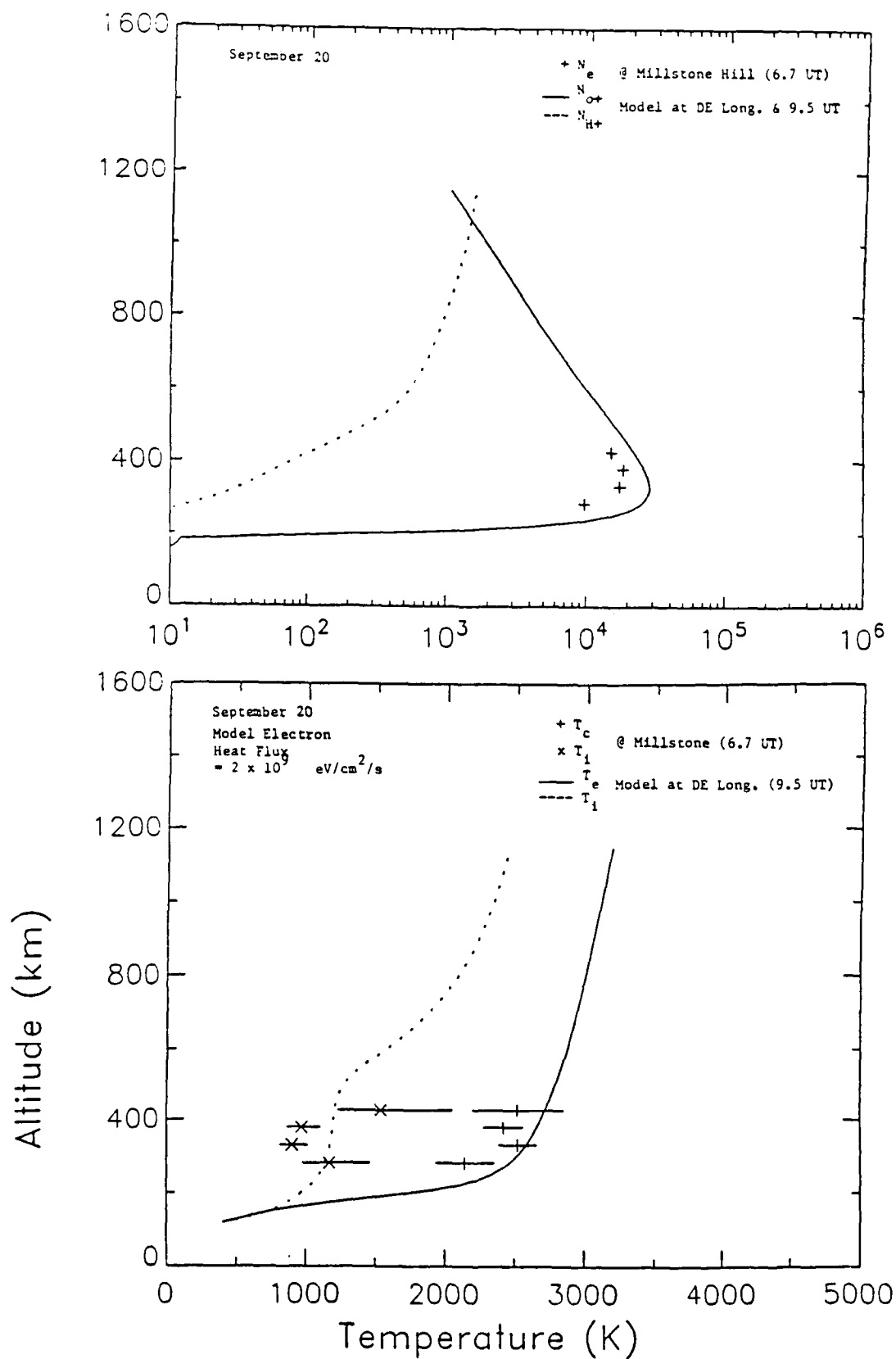


Figure 4: Altitude profiles of model (a) ion densities and (b) electron and ion temperatures on day 84264. Estimated column electron heating rates described in the text were the only energy source included in the model.

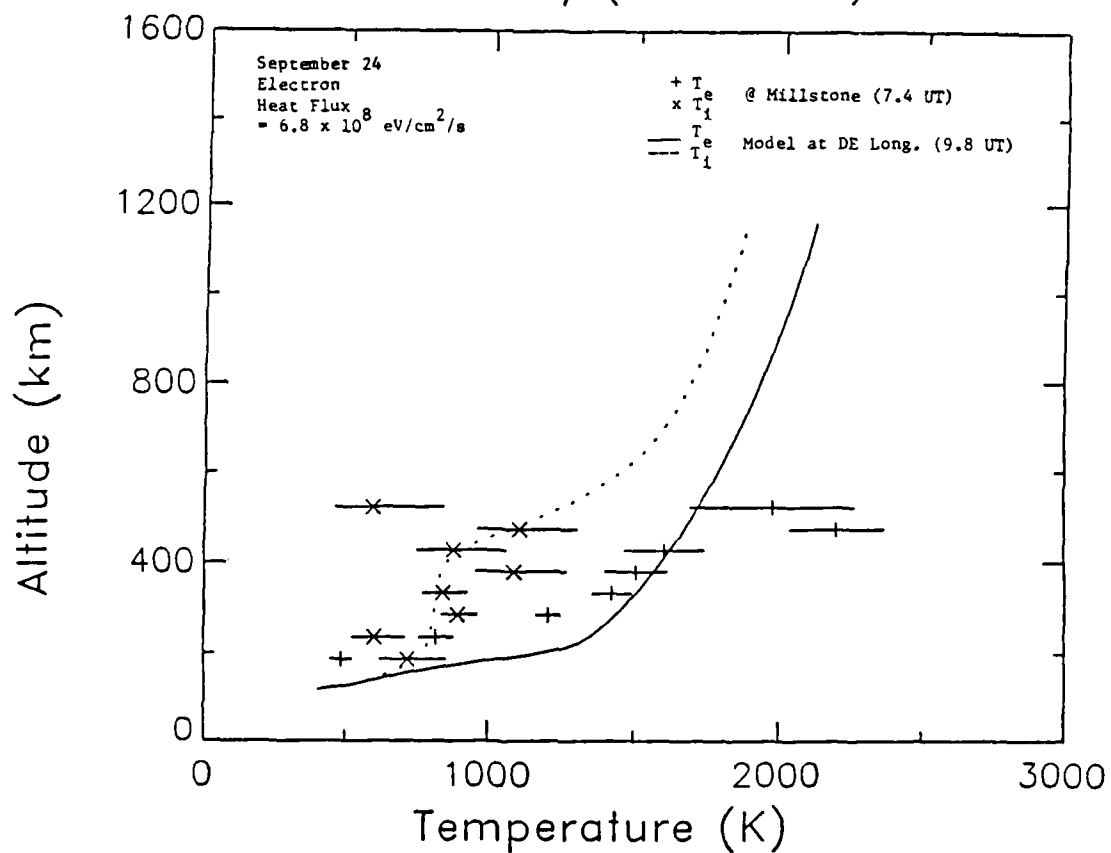
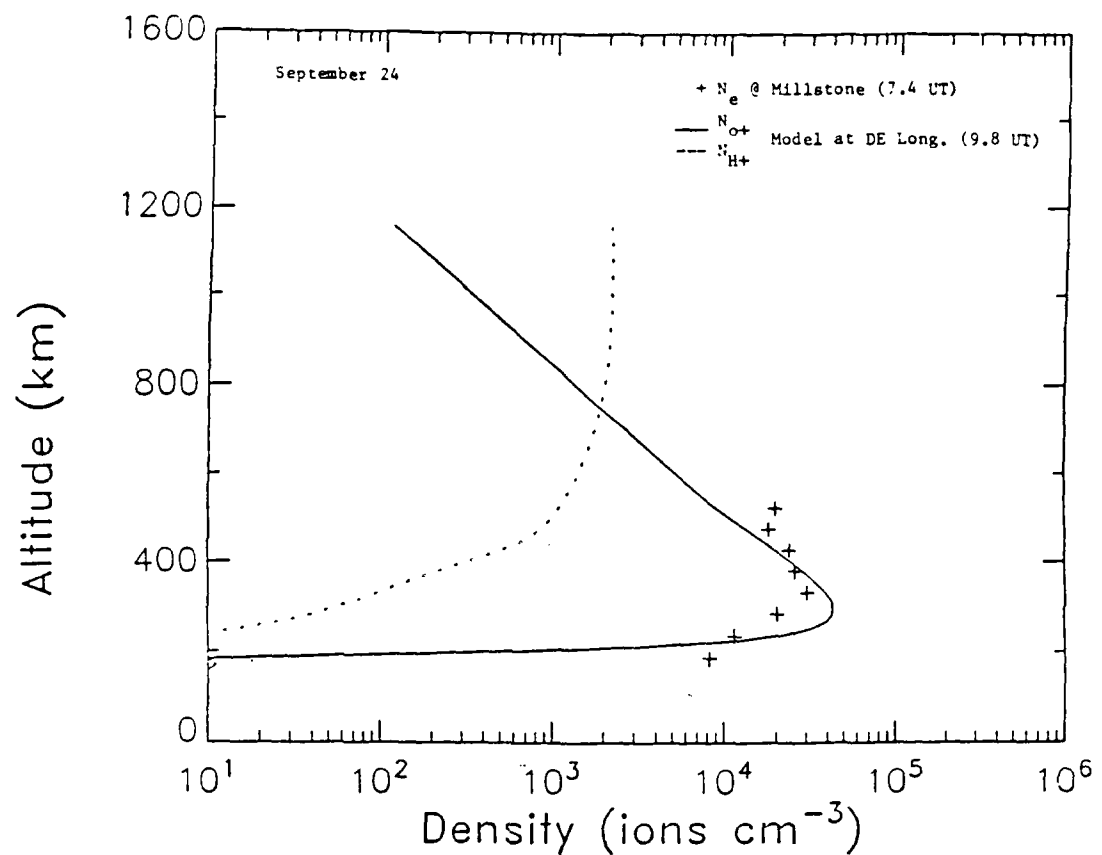


Figure 5: Same as in Figure 4 but for day 84268.

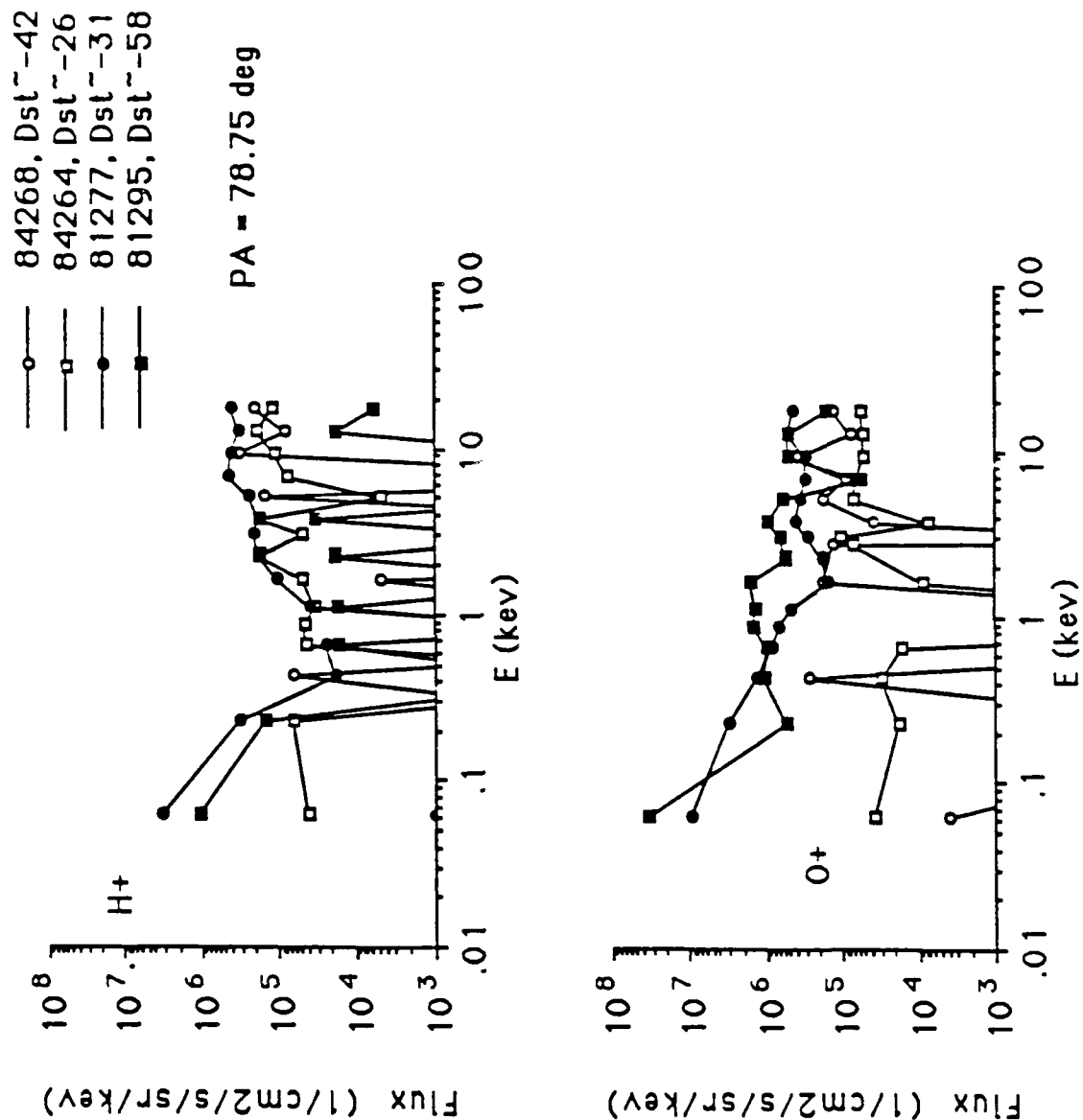
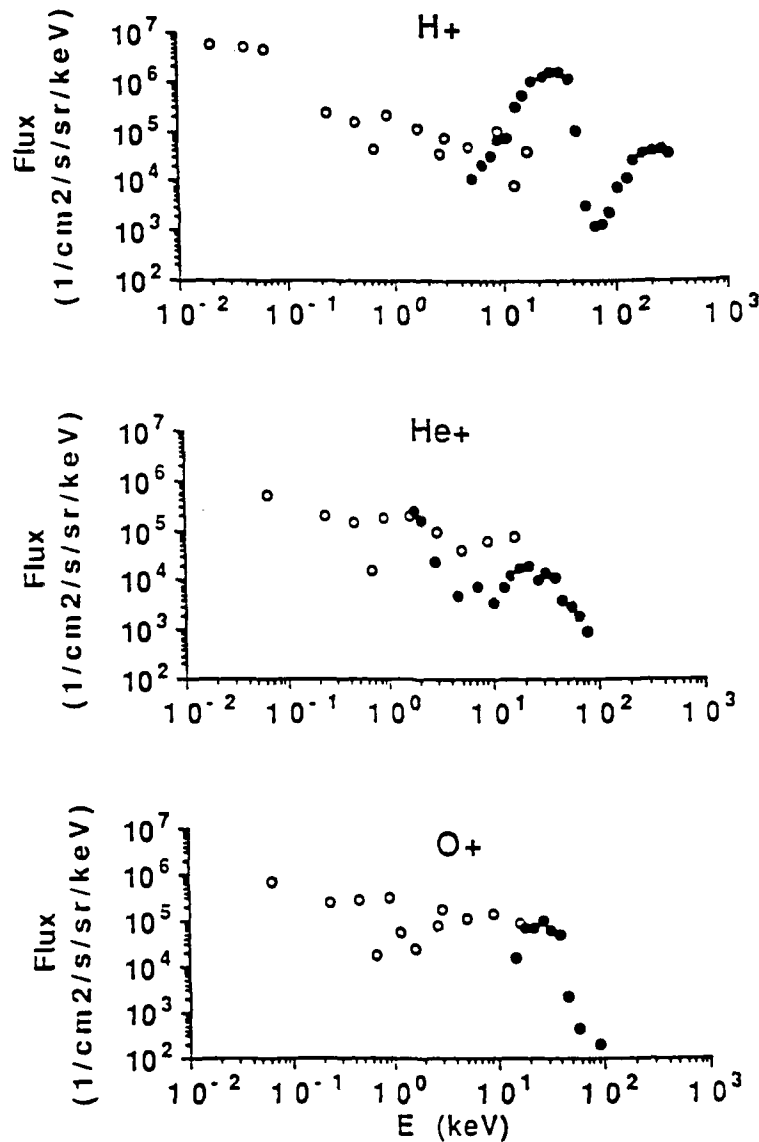


Figure 6: Comparison of the energetic (a) H⁺ and (b) O⁺ observed on field lines which map to the SAR arc peak during selected, comparable geomagnetic storms in solar minimum and solar maximum.

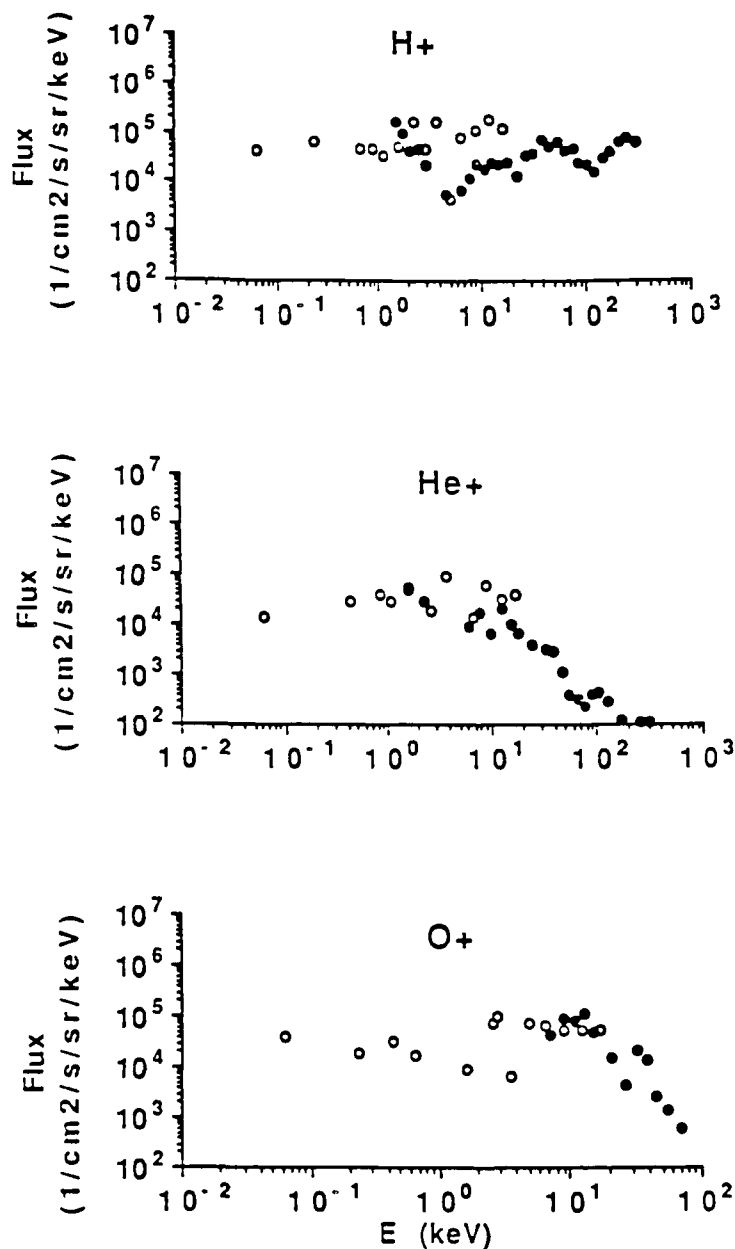
September 19, 1984 (Day 84263)
L=3.3



- DE-1, 22.4MLT, 1021UT, 30 deg MLAT, 78.8 deg PA
- AMPTE/CCE, 17.3MLT, 13UT, -12 deg MLAT, PA ave.

Figure 7a-c: Differential ring current intensity versus energy on SAR arc field lines on (a) September 19, 1984 (main phase), (b) September 20, 1984 (recovery phase) and (c) September 24, 1984 (recovery phase).

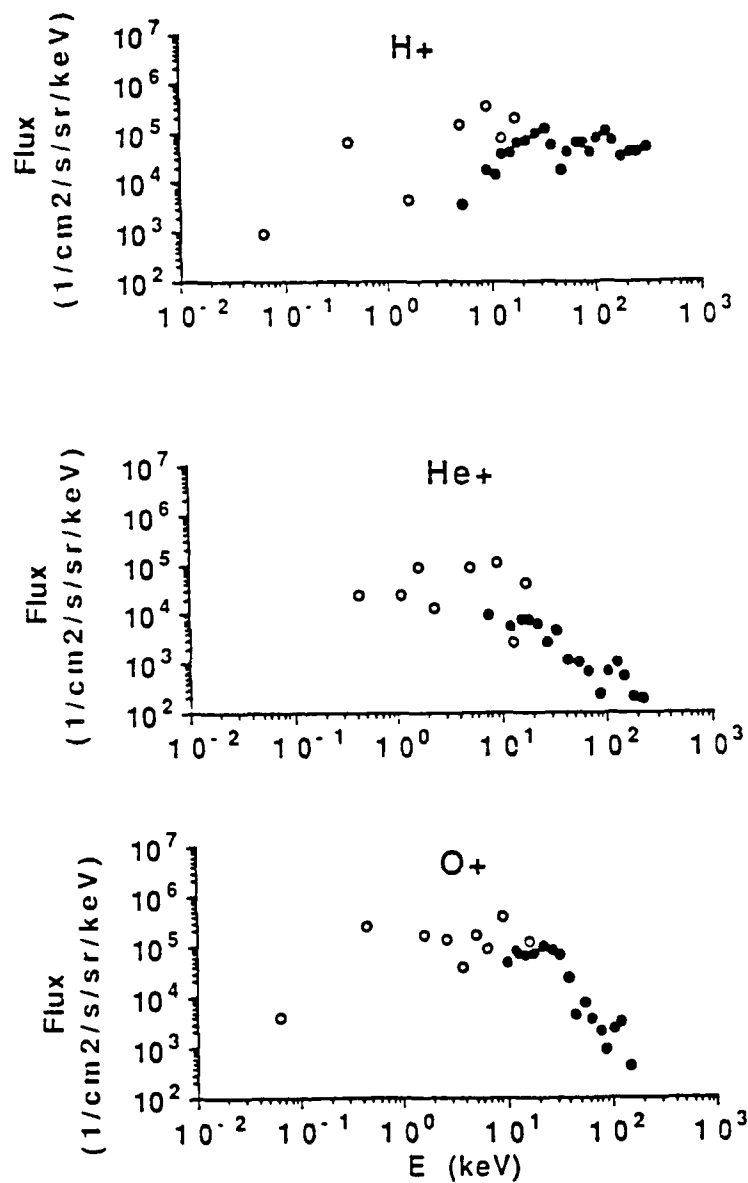
September 24, 1984 (Day 84264)
L=3.4



- DE-1, 22.4MLT, 658UT, 36 deg MLAT, 79 deg PA
- AMPTE/CCE, 17MLT, 432UT, -7.2 deg MLAT, PA ave.

Figure 7b

September 24, 1984 (Day 84268)
L=3.1



- DE-1, 22.5MLT, 648UT, 32 deg MLAT, 79 deg PA
- AMPTE/CCE, 17MLT, 236UT, -13.2 deg MLAT, PA ave.

Figure 7c

1988 AFOSR RESEARCH INITIATION PROGRAM

Sponsored by the

AIR FORCE OFFICE OF SCIENTIFIC RESEARCH

Conducted by the

Universal Energy Systems, Inc.

FINAL REPORT

ALGORITHMS FOR GENERALIZED

EXPONENTIAL INVERSION

Prepared by:	Steven J. Leon
Academic Rank:	Professor
Department and University:	Mathematics Department Southeastern Massachusetts University
USAF Research Supervisor:	Jean I. F. King
Location of Supervisor:	Air Force Geophysics Lab, Atmospheric Sciences Division, Hanscom Air Force Base
Date:	March 28, 1989

ALGORITHMS FOR GENERALIZED EXPONENTIAL INVERSION

Steven J. Leon

Abstract

This paper represents a continuation of the research carried out by S. J. Leon [7] in 1987 as part of the AFOSR Summer Faculty Research Program. During the summer of 1987 Leon and King [5] developed and tested an algorithm for interpolating the radiance function $R(p)$ by a special form of rational function. A new more general algorithm has been developed for interpolating $R(p_i)$, $i = 1, \dots, m$ by a quotient of polynomials $\frac{r(p)}{q(p)}$, where the lead coefficient of r is 1. The interpolating function can be written in a residue form with one polynomial term and several hyperbolic components. The coefficients from the residue form can then be used to construct an exponential representation for the Planck intensity $B(p)$.

1 INTRODUCTION

Transfer theory relates the upwelling intensity of the atmosphere to the integral transform of the Planck intensity $B(p)$. The kernel of the transform can be expressed as a weight function $W(p/\hat{p})$ which peaks at $p = \hat{p}$. If $R(\hat{p})$ denotes the radiance of the sensing channel and $W(z) = ze^{-z}$ then

$$R(\hat{p}) = \int_0^\infty B(p)W(p/\hat{p})dp/\hat{p} \quad (1)$$

If we set $s = \frac{1}{\hat{p}}$, then $B(p)$ can be determined as an inverse Laplace transform

$$B(p) = \mathcal{L}^{-1} \left(\frac{R(\frac{1}{s})}{s} \right)$$

If $R(\hat{p})$ can be represented by a rational function of the form

$$R(\hat{p}) = d_1 + d_2\hat{p} + \dots + d_j\hat{p}^{j-1} + \sum_{i=1}^l \frac{w_i}{1 + c_i\hat{p}} \quad (2)$$

then

$$\frac{R(\frac{1}{s})}{s} = \frac{d_1}{s} + \frac{d_2}{s^2} + \dots + \frac{d_j}{s^j} + \sum_{i=1}^l \frac{w_i}{s + c_i}$$

and it follows that

$$B(p) = d_1 + d_2p + \dots + \frac{d_j}{(j-1)!}p^{j-1} + \sum_{i=1}^l w_i e^{-c_i p} \quad (3)$$

The representation (2) has one polynomial component and l hyperbolic components. The inversion problem then reduces to a problem of finding a rational function of the form (2) which interpolates or approximates the radiance data.

2 GENERALIZED EXPONENTIAL INVERSION

In the generalized exponential inversion proposed by Jean I. F. King it is assumed that

$$W(z) = W_k(z) = \gamma_k z \exp_k(z)$$

where

$$\gamma_k = \frac{1}{k^{1/k} \Gamma(\frac{k+1}{k})}$$

and

$$\exp_k(z) = \exp(-z^k/k)$$

King has shown that if

$$R(\hat{p}) = \int_0^\infty B(p) W_k(p/\hat{p}) \frac{dp}{\hat{p}}$$

and $R(\hat{p})$ is of the form (2), then the Planck intensity $B(p) = B_k(p)$ will be of the form

$$B_k(p) = d_1 + d_2 p + \dots + \frac{d_j}{(j-1)!} p^{j-1} + \sum_{i=1}^l w_i \exp_k(-c_i p) \quad (4)$$

Note that equations (3) and (4) are the same in the case $k = 1$.

3 RATIONAL INTERPOLATION

Given $m = 2l + j$ sensing channels whose weight functions peak at $\hat{p}_1, \hat{p}_2, \dots, \hat{p}_m$, let $R_i = R(\hat{p}_i)$ denote the radiance value at $\hat{p}_i, i = 1, \dots, m$. We will construct a rational function of the form (2) which interpolates the points $(\hat{p}_i, R_i), i = 1, \dots, m$.

If $R(\hat{p}) = \frac{r(\hat{p})}{q(\hat{p})}$ where the degrees of r and q add up to $m - 1$ and the lead coefficient of q is 1, then we can write R in the form

$$R(\hat{p}) = \frac{a_1 \hat{p}^n + a_2 \hat{p}^{n-1} + \dots + a_{n+1}}{\hat{p}^l - a_{n+2} \hat{p}^{l-1} - \dots - a_m} \quad (n + l = m - 1) \quad (5)$$

R interpolates the points (\hat{p}_i, R_i) if and only if

$$a_1 \hat{p}_i^n + a_2 \hat{p}_i^{n-1} + \dots + a_{n+1} + a_{n+2} \hat{p}_i^{l-1} R_i + \dots + a_m R_i = \hat{p}_i^l R_i \quad i = 1, \dots, m \quad (6)$$

Equation (6) represents an $m \times m$ linear system of equations. The coefficients of r and q are determined from the solution to the system. Performing long division on equation (5), we get

$$\frac{r(\hat{p})}{q(\hat{p})} = d(\hat{p}) + \frac{e(\hat{p})}{q(\hat{p})}$$

where

$$d(\hat{p}) = d_1 + d_2 \hat{p} + \dots + d_j \hat{p}^{j-1} \quad (j = n - k + 1)$$

and the degree of $e(\hat{p})$ is less than l .

The long division can be performed numerically using a deconvolution routine. If the roots z_1, \dots, z_l of q are distinct, then we can write $\frac{e(\hat{p})}{q(\hat{p})}$ in terms of partial fractions

$$\frac{b_1}{\hat{p} - z_1} + \frac{b_2}{\hat{p} - z_2} + \dots + \frac{b_l}{\hat{p} - z_l}$$

If

$$q(\hat{p}) = q_i(\hat{p})(\hat{p} - z_i)$$

then it follows that

$$b_i = \frac{r(z_i)}{q_i(z_i)} \quad i = 1, \dots, l$$

Thus if we set

$$c_i = -\frac{1}{z_i} \text{ and } w_i = c_i b_i \quad i = 1, \dots, l$$

then $R(\hat{p})$ can be represented in the form (2).

In the unlikely case that q has a multiple root the form of the partial fraction expansion of e/q will change. In this case the b_i 's can be determined by solving a $l \times l$ linear system.

A routine has been developed for computing the interpolating function using the methods described. Input for the routine consists of

1. A vector \mathbf{x} of the m values of \hat{p}
2. A vector \mathbf{y} of the corresponding radiance values
3. The degree n of the numerator of the rational function
4. A vector \mathbf{t} corresponding to a partition of the domain of the radiance function

Output for the routine consists of

1. Vectors \mathbf{c} and \mathbf{w} containing the coefficients of the hyperbolic components
2. A vector \mathbf{d} consisting of the coefficients of the polynomial component
3. A vector \mathbf{R} of the values of the interpolating function at the partition points \mathbf{t}

A second routine was developed to compute the Planck intensity using forms (3) and (4). Input for the second routine consists of

1. The vectors \mathbf{d} , \mathbf{c} , and \mathbf{w} that define the rational interpolating function.
2. The scalar k that determines the generalized weighting function
3. A vector \mathbf{p} of pressure values ranging from 1 to 1000 millibars

Output consists of a vector \mathbf{B} containing the computed values of the Planck intensity corresponding to the pressures p_i .

4 STABILITY

In practice not many sensing channels are needed to determine $R(\hat{p})$ and $B(p)$. If too many channels are used, then $R(\hat{p})$ will have more hyperbolic components than necessary. The poles of these extraneous components are quite sensitive to perturbations. It is likely that some of them will be positive even though it is impossible for the actual radiance profile to have a positive pole. To avoid these extraneous positive poles the number of sensing channels should be limited to 4, 5, 6, or 7. This corresponds to 1 or 2 hyperbolic components and a polynomial component of degree 0, 1, or 2. The \hat{p}_i values corresponding to the sensing channels should be well separated. If the \hat{p}_i values for two sensing channels are not well separated, then errors smaller than the precision of the sensing instruments can cause one or more positive poles. Thus it is necessary to have at least four channels with well separated \hat{p}_i values. If more than seven channels are available, a subset should be chosen to give a wide range of well separated \hat{p}_i 's. With these restrictions the computations of $R(\hat{p})$ and $B(p)$ are both quite stable.

Actually the interpolation is more stable than the calculation of the poles z_i and the coefficients w_i . For small perturbations in the data, the differences in the values of the interpolating functions will be much less significant than the differences in their poles z_i and in their coefficients w_i . Because the poles are more sensitive, larger perturbations in the data may result in positive poles. For example, if one of the sensing channels was faulty and produced results that were significantly in error, then it is probable that the interpolating function will have a positive pole z_p that is close to the \hat{p}_i corresponding to the faulty channel. Even in the case of a positive pole z_p , the interpolating function will do a good job of approximating the radiance profile except for a small neighborhood about z_p .

5 TEST RESULTS

The algorithm was first tested on the radiance data in the paper by McClatchey [8]. This data consisted of eighteen sets of radiance values. Each of these sets consisted of six radiance values corresponding to the peaks \hat{p}_i of six sensing channels. The data was normalized and interpolating functions with one linear component and two hyperbolic components were computed. In each of the eighteen cases the rational interpolating function had a single positive pole whose coefficient w_p was small relative to the coefficient of the other hyperbolic component. In light of the preceding discussion this would indicate that one of the sensing channels involved significant errors. Indeed, in twelve cases \hat{p}_5 , the data point corresponding to the fifth sensing channel, was the closest \hat{p}_i to the pole. In five cases \hat{p}_4 was the closest and in the remaining case it was \hat{p}_6 . This seems to suggest that the fifth channel is faulty. Indeed, it does appear upon further

examination that the results for this channel were not processed properly.

One way to eliminate the positive pole is to set $w_p = 0$. The resulting function no longer interpolates the data points, but it does approximate them closely. This function will be referred to as the zero weight approximating function. If it is used to approximate the radiance profile, then its exact inverse can be used to approximate the Planck function.

Alternatively, one can eliminate the data corresponding to the faulty channel and fit a rational function to the remaining points. Since there are five degrees of freedom for each such data set, the rational function could consist of either a quadratic polynomial and one hyperbolic component or a constant polynomial and two hyperbolic components. In either case the resulting functions interpolate the data to machine precision and the functions are so close that their graphs are indistinguishable.

The interpolation and inversion algorithms were also tested on data from the NOAA TIROS Operational Vertical Sounder (TOVS). This data, likewise, consisted of six sensing channels that were in the appropriate range. However, two of the \hat{p}_i values, \hat{p}_2 and \hat{p}_3 were not well separated. Since $\hat{p}_2 - \hat{p}_1 < \hat{p}_4 - \hat{p}_3$, the data points corresponding to the second channel were eliminated. The remaining five points were fitted in the same manner as the McClatchey data.

6 CONCLUSIONS

An algorithm was designed and tested for interpolating radiance data by rational functions. The Planck intensity can then be computed as the exact inverse of the rational function. If the \hat{p}_i values corresponding to the sensing channels are well separated and not too many hyperbolic components are used, then the interpolating function should not have any positive poles. If, however, in such a case a positive pole is computed, then that would be evidence of a faulty sensing channel.

References

- [1] S. Chandrasekhar. *Radiative Transfer*. Oxford University Press, London, 1950.
- [2] L.M. Delves and J. Walsh. *Numerical Solution of Integral Equations*. Clarendon Press, Oxford, 1974.
- [3] Robert G. Holfeld, Ronald F. Wachtman, and James C. Kilian. *Application and Evaluation of a Differential Inversion Technique for Remote Temperature Sensing*. Technical Report 88-0138, AFGL, Hanscom AFB, Massachusetts 01731, 1988.

- [4] Jean I. F. King. Theory and application of differential inversion to remote sensing. In A. Deepak et al., editors, *Advances in Remote Sensing*, A. Deepak Publishing, Hampton, Virginia, 1985.
- [5] Jean I. F. King and Steven J. Leon. A smart algorithm for nonlinear interpolation and noise discrimination. In A. Deepak et al., editors, *Remote Sensing Retrieval Methods*, A. Deepak Publishing, Hampton, Virginia, 1987.
- [6] Jean I. F. King and Steven J. Leon. Smooth profile inferencing from noisy radiance data: the phasarc algorithm. 1989. In preparation.
- [7] Steven J. Leon. *A Hyperbolic Interpolation Algorithm for Modelling Radiance Data*. AFOSR SFRP Final Report, AFGL, Universal Energy Systems, Dayton Ohio. 1987.
- [8] Robert A. McClatchey. *Satellite Temperature Sounding of the Atmosphere: Ground Truth Analysis*. Technical Report 76-0279, Air Force Geophysics Lab, Hanscom AFB, Massachusetts 01731, 1979.

FINAL REPORT NUMBER 50
REPORT NOT AVAILABLE AT THIS TIME
Dr. John P. McHugh
210-9MG-125

Trajectory calculations of high temperature and kinetic energy dependent
ion-polar molecule collision rate constants

Hu Cheng Bei^a, Pradip K. Bhowmik^b and Timothy Su
Department of Chemistry
Southeastern Massachusetts University
North Dartmouth, Massachusetts 02747

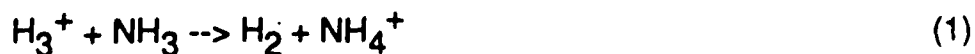
- a. Present address: Department of Chemistry, Boston College, Chestnut Hill,
Massachusetts 02167
- b. Present address: Department of Chemistry, University of Massachusetts,
Amherst, Massachusetts 01003

ABSTRACT

The trajectory method is used to calculate high temperature and kinetic energy dependent ion-polar molecule collision rate constants. A new ion-polar molecule interaction potential energy surface is derived which takes into account the average hard sphere diameter of the colliding partners and the dimensions of the permanent dipole and the induced dipole vectors. A model system, $\text{H}_3^+ + \text{NH}_3$ is chosen for the calculation. The calculated results show that at low temperatures and kinetic energies, the effects of the size of the ion-molecule partners and the dimensions of the dipole vectors on the collision rate constant are small. At high temperatures and high relative kinetic energies, however, these effects are significant. The calculated results are in good agreement with existing experimental kinetic energy dependent reaction rate constants.

INTRODUCTION

Theoretical treatments of ion-polar molecule collision dynamics have been an area of interest. A number of theoretical treatments in calculating ion-polar molecule capture rate constants have been developed in recent years, including: the "average dipole orientation" (ADO) theory of Su and Bowers,¹ the "average energy" theory of Barker and Ridge,² the "average free energy" or "activated complex" theory of Celii, Weddle and Ridge,³ the thermodynamic theory of Turluski and Forys,⁴ the "microcanonical variational transition state" theory of Chesnavich, Su and Bowers,⁵ the classical trajectory calculations of Su, Chesnavich and Bowers,^{5,6} the "adiabatic invariance" theory of Bates,⁷ the "perturbed rotational state" theory of Sakimoto,⁸ the "total energy and angular momentum conserved average charge-dipole interaction" (TEAMS) theory of Hasieh and Castleman,⁹ the "adiabatic capture and centrifugal sudden approximation" (ACCSA) theory of Clary¹⁰ and the "statistical adiabatic channel model" of Troe¹¹. The ion-polar molecule intermolecular potential energy used in all these theoretical approaches was derived assuming that the ion-molecule separation is much larger than the size of the particles (point particle assumption). While this assumption may be a good approximation for calculating collision rate constants at thermal or near thermal relative translational energies at low temperatures (where the capture radii are large), it may not yield accurate results at higher temperatures or higher relative kinetic energies. In this paper, a more accurate ion-polar molecule interaction potential energy is derived. Since the trajectory method is a powerful tool in treating collision dynamics¹², it is used in this work to calculate high temperature and nonthermal kinetic energy ion-polar molecule collision rate constants. High temperature (ca. 3000K) ion-molecule reactions are of importance in new engine exhaust systems and in studies on missile re-entry phenomena. Calculations of high temperature ion-molecule rate constants are desirable since it is difficult to measure high temperature rate constants in the laboratory. A model ion-molecule system, $\text{H}_3^+ + \text{NH}_3$, is chosen for the calculation. The calculated rate constants are compared with existing experimental results. This system is chosen because the reaction is a simple exothermic proton transfer.



Most exothermic proton transfer reactions are fast and are believed to proceed with near collision rate constants¹³.

THEORY

A. Ion-polar molecule intermolecular potential energy

(a) Ion-induced dipole potential energy

Consider a dipole induced on a neutral molecule by an ion with a charge e and at a distance r from the center of mass of the molecule as shown in Fig. 1. The induced dipole is assumed to consist of two opposite charges, $+q$ and $-q$, separated by a distance of $2d$. The center of mass of the molecule is assumed to be at the mid-point of the two poles. The distances r_1 and r_2 are measured from the ion to the negative and the positive ends of the induced dipole respectively. The force at the ion is then

$$F(r) = -qe/r_1^2 + qe/r_2^2 \quad (2)$$

The induced dipole moment μ' is

$$\mu' = \alpha E = 2dq \quad (3)$$

where E is the average electric field at the molecule:

$$E = \frac{1}{2} \left(\frac{e}{r_1^2} + \frac{e}{r_2^2} \right) \quad (4)$$

Combining Eqs. (2), (3) and (4), the force at a given ion-molecule separation becomes

$$F(r) = -\frac{\alpha e^2}{4d} \left(\frac{1}{r_1^4} - \frac{1}{r_2^4} \right) \quad (5)$$

The potential energy of the system is then

$$V_{\text{ind}}(r) = -\frac{\alpha e^2}{4d} \left[\int_{r_1}^{\infty} \frac{dr}{r_1^4} - \int_{r_2}^{\infty} \frac{dr}{r_2^4} \right] \quad (6)$$

or

$$V_{\text{ind}}(r) = -\frac{\alpha e^2 (3r^2 + d^2)}{6(r^2 - d^2)^3} \quad (7)$$

Note that as $r \rightarrow \infty$, $V_{\text{ind}}(r) = -\alpha e^2 / 2r^4$, which is the conventional ion-induced dipole potential energy.

(b). Ion-permanent dipole potential energy

Consider an ion with a charge e and at a distance r from a polar molecule with an orientation angle θ as shown in Fig. 2. In Fig. 2, $+q$ and $-q$ are the charges on the positive and the negative poles of the polar molecule, respectively, d_1 is the distance from the center of mass of the neutral molecule to its negative pole (or the pole with a charge opposite in sign to the charge on the ion), and d_2 is the distance from the center of mass to the positive pole. Since the dipole moment of the polar molecule is

$$\mu_D = q(d_1 + d_2), \quad (8)$$

the potential energy is given by Eq. (9).

$$V_D = \frac{e\mu_D}{d_1 + d_2} \left(\frac{1}{r_2} - \frac{1}{r_1} \right) \quad (9)$$

where r_1 and r_2 are the distances from the ion to the negative and the positive poles, respectively, and are given by

$$r_1 = (r^2 + d_1^2 - 2rd_1 \cos \theta)^{1/2} \quad (9a)$$

and $r_2 = (r^2 + d_2^2 + 2rd_2 \cos \theta)^{1/2}. \quad (9b)$

It can be shown that if $r \gg d_1$ and d_2 , Eq. (9) is reduced to $-\epsilon\mu_D \cos \theta / r^2$ which is the point dipole approximation.

For simplicity, it is assumed that the center of mass of the polar molecule is at the mid-point of the poles. It is also assumed that the distance between the positive and negative poles of the dipole is the same as the distance between the positive and the negative poles of the induced dipole discussed in the last section. That is, it is assumed that $d_1 = d_2 = d$. This assumption is made so that there is only one adjustable parameter (see Results).

(c) Over all potential energy surface

It is assumed that (i) prior to collision, the ion-polar molecule interaction potential is governed by the combination of $V_{ind}(r)$ and $V_D(r)$, and (ii) a capture collision occurs when the ion and the molecule approach to a distance equal to the ion-molecule average hard sphere diameter r_H . Thus the total potential energy of the system is given by

$$V_{total} = \begin{cases} V_{ind}(r) + V_D(r); & r > r_H \\ \infty; & r \leq r_H \end{cases} \quad (10)$$

B. Treatment of trajectories

The system Hamiltonian (with the motion of the center of mass removed) for $r > r_H$ is given by

$$H = p_r^2 / 2\mu + L^2 / 2\mu r^2 + B j^2 + V_{ind}(r) + V_D(r) \quad (11)$$

where p_r is the radial momentum of the collision partners, L is their orbital angular momentum, and μ is the reduced mass of the colliding pair. The angular momentum and the moment of inertial of the rotor are given by j and I , respectively. The reactive trajectories are obtained by solving the equation of motion to determine which trajectories lead to collision. In

Hamiltonian form, the equation of motion for the canonical pair $[p_i, q_i]$ are

$$\frac{\partial H}{\partial p_i} = \dot{q}_i; \quad \frac{\partial H}{\partial q_i} = -\dot{p}_i \quad (12)$$

where p_i and q_i represent momentum and coordinate, respectively, of the i^{th} component. The trajectories are begun at 63 Å and are integrated to $r = r_H$. The thermal energy collision rate constant at a given temperature T is determined from the expression

$$k_{\text{coll}}(T) = \frac{1}{2Ik_B T (2\pi\mu k_B T)^{3/2}} \int \chi_r(p, q) e^{-E/k_B T} d\gamma_L d\gamma_j dL dJ dE \quad (13)$$

where k_B is the Boltzmann constant, J is the total angular momentum, and γ_L and γ_j are Euler angles. The term $\chi_r[p, q]$ is the characteristic function which labels the trajectory with initial conditions $[p, q]$ on r as reactive or nonreactive.

The collision rate constant at a given relative translational energy E_t and T is given by

$$k_{\text{coll}}(E_t, T) = \frac{1}{2\pi k_B T (8\mu^3 E_t)^{1/2}} \int \chi_r(p, q) e^{-E/k_B T} d\gamma_L d\gamma_j 2L dL dE_r \quad (14)$$

RESULTS

Figure 3 compares theoretical kinetic energy dependent collision rate constants with experimental results for reaction (1) at 300K. The experimental results are taken from the data obtained by Lindinger, et al¹⁴ and are represented by solid circles. Curve (a) is the point particle theoretical collision rate constants as a function of relative ion-molecule translational energy. Curve (b) is the theoretical results which takes into account the ion-molecule average hard sphere diameter, but assumes that both of the dimension of the dipole (the distance between the positive and the negative poles) and the dimension of the induced dipole are small

compared to r , i.e. $d \rightarrow 0$. Curve (c) is the theoretical result which considers both the average ion-molecule hard sphere diameter and the dimension of the dipole and the induced dipole. It is not easy to estimate the value of d . In this work, it is considered as an adjustable parameter. The best value of d is found to be 1.0\AA . (In fact, the dipole moment should be calculated by integrating the charge distribution on the molecule. For simplicity, here we assume that the dipole consists of two opposite charges separated by a distant d .) The hard sphere diameter of NH_3 is 3.2\AA ¹⁵. The hard sphere diameter of H_3^+ is estimated from the structure of H_3^+ ¹⁶ to be 3.0\AA . Thus the average hard sphere diameter, r_H , of the ion-molecule system $\text{H}_3^+ + \text{NH}_3$ is 3.1\AA . The dipole moment and polarizability of NH_3 are 1.47 Debye and 2.26\AA^3 respectively^{17,18}. Table I shows the theoretical thermal energy collision rate constants at 300K and 3000K under various assumptions.

DISCUSSION

A. Kinetic energy dependence of collision rate constants

From Fig. 3, several phenomena are apparent. At thermal energies, the point particle theoretical rate constant is in good agreement with the reaction rate constant measured experimentally. However, at higher relative kinetic energies, the point particle theoretical predicted collision rate constants are lower than experimental results. [see curve (a)]. Curve (b) is the result from calculations using the point particle potential energy, but assuming that when the ion-molecule pair approach each other to a distance equal to the average hard sphere diameter, a capture collision occurs. Curve (b) is slightly higher than curve (a) at thermal energies. It becomes significantly higher than curve (a) at higher relative kinetic energies. While curve (b) agrees well with experiment results at near thermal energies, it is still significantly lower than experimental values at higher relative kinetic energies. In curve (c), in addition to considering the average hard sphere diameter, the more accurate ion-molecule potential energy [Eq.(10)] is used which assumes that the dimensions of the permanent dipole and the induced dipole are both 1.00\AA . Curve (c) is in good agreement with experimental results through out the range of relative kinetic energy reported. Figure 3 indicates that at low relative kinetic

energies the ion-molecule pair can be treated as point particles. However, the size of the colliding partners and the dimensions of the permanent dipole and the induced dipole should be considered in calculating collision rate constants at higher relative kinetic energies.

It should be noted that in Fig. 3, we are comparing reaction rate constants with collision rate constants. While collision rate constants are upper bounds to reaction rate constants, we believe that in this case the reaction rate constants are very close to the collision rate constants. Proton transfer reactions involve a simple step. Exothermic proton transfer reactions like reaction (1) often are fast and proceed near collision rate constants¹³. Figure 4 is a plot of the relative number of trajectories versus the collision angle at 300K and at relative kinetic energies 0.5 and 1.0 eV. The collision angle is the angle θ when the ion-molecule pair approach to a distance equal to r_H (when they collide). It is observed (theoretically) that almost all the collisions result in a collision angle $< 90^\circ$ and most of the collision angles are $< 45^\circ$. This means that in most collisions, even at the highest relative kinetic energy reported here, the nitrogen end (the negative end) of NH_3 is directed toward the positive ion H_3^+ , a favorable orientation for proton transfer to occur. At lower relative kinetic energies, the fraction of favorable orientations is even higher.

B. Temperature dependence of collision rate constants.

Since the theoretical kinetic energy dependent rate constants are in good agreement with experimental results, it suggests that the present theoretical approach predicts quite accurately the collision rate constant for ion-polar molecule interactions from thermal energies at 300K to at least several tenth of an eV relative kinetic energy. We can argue that the same approach should also accurately predict high temperature thermal energy collision rate constants. This is the main purpose of this research since high temperature reaction rate constants are difficult to measure. Table I, presents theoretical thermal energy rate constants at 300K and 3000K. The first column shows the point particle theoretical rate constants. The last column shows the theoretical results of the present approach. At 300K, as pointed out before, the difference between the point particle theoretical rate constant and the rate constant calculated from the the present improved treatment is insignificant. At 3000K, however, the effects of the

average hard sphere diameter and the dimensions of the dipole vectors become significant. The second column shows the results of theoretical rate constants that only takes into account the dimensions of the dipole vectors but not the average hard sphere diameter. That is, only those trajectories that reach $r = 0$ are counted as collisions. This calculation is done only to see how much it would affect the calculated rate constant when only the dimensions of the dipole vectors are considered. It is shown from table I that while the effect is small at room temperature, at high temperatures, the effect is significant.

Figure 5 is a plot of the relative number of trajectories versus collision angle at thermal energies. It is shown that even at 3000K, most collisions (when the ion-molecule separation reaches the average hard sphere diameter) have small collision angles. Therefore the theoretical collision rate constant at 3000K is probably close to the reaction rate constant.

CONCLUSION

In conclusion, ion-molecule collision rate constants can be accurately estimated by trajectory calculations. At low temperatures and low relative kinetic energies, the point particle assumption is a good approximation. At high temperatures and high relative kinetic energies, however, the effect of the size of the colliding partners and the effect of the dimensions of the permanent dipole and the ion-induced dipole become significant. This is because at high kinetic energies, the question of capture is settled at small distances. Thus the dimensions of the dipole vectors and the size of the ion-molecule partners become comparable to the ion-molecule separation. Also, the capture radius may become less than the average hard sphere diameter of the ion-molecule pair. In this case the collision criterion is governed by the hard sphere diameter instead of the capture radius. Therefore, both the size of the colliding partners and the dimensions of the dipole vectors should not be ignored when calculating collision rate constants of ion-polar molecule interactions at high temperatures or high relative kinetic energies.

ACKNOWLEDGEMENT

Research sponsored by the Air Force Office of Scientific Research/AFSC,

United States Air Force, under Contract F49620-85-C-0013. The authors also thank Dr. John F. Paulson and his research group at Hanscom Air Force Base for their suggestions and input.

REFERENCES

1. (a) Su, T. and M. T. Bowers, *J. Chem. Phys.*, **58**, 3027 (1973); (b) Su, T. and M. T. Bowers, *Int. J. Mass Spectrom. Ion Phys.*, **12**, 347 (1973).
2. Barker, R. A. and D. P. Ridge, *J. Chem. Phys.*, **64**, 4411 (1976).
3. Celii, F., G. Weddle and D. P. Ridge, *J. Chem. Phys.*, **73**, 801, (1980).
4. Turluski, J. and M. Forsys, *J. Phys. Chem.*, **83**, 2815 (1979).
5. Chesnavich, W. J., T. Su and M. T. Bowers, *J. Chem. Phys.*, **72**, 2641 (1980).
6. Su, T. and W. J. Chesnavich, *J. Chem. Phys.*, **76**, 5183 (1982).
7. (a) Bates, D. R., *Chem. Phys. Lett.*, **82**, 396 (1981); (b) Bates, D. R., *Proc. R. Soc. Lond. A* **384**, 289 (1982); (c) Bates, D. R., *Chem. Phys. Lett.*, **111**, 428 (1984); (d) Morgan, W. L. and D. R. Bates, *Astrophys. J.*, **314**, 817 (1987).
8. (a) Sakimoto, K. and K. Takayanagi, *J. Phys. Soc. Japan*, **43**, 2076 (1980); (b) Sakimoto, K., *Chem. Phys.*, **63**, 419 (1981); (c) Sakimoto, K., *Chem. Phys.*, **85**, 273 (1984).
9. Hsieh, E. T. and A. W. Castleman, Jr., *Int. J. Mass Spectrom. and Ion Phys.*, **40**, 295 (1981).
10. (a) Clary, D. C., *Mol. Phys.*, **53**, 3 (1984); (b) Clary, D. C., *Mol. Phys.*, **54**, 605 (1985); (c) Clary, D. C., D. Smith and N. G. Adams, *Chem. Phys. Lett.*, **119**, 320 (1985).
11. (a) Troe, J., *Chem. Phys. Lett.*, **122**, 425 (1985); (b) Troe, J., *J. Chem. Phys.*, in press.
12. D. P. Ridge, in "Structure/Reactivity and Thermochemistry of Ions", Ausloos, P. and S. G. Lias Eds., D. Reidel Publishing Company, 1986.

13. See, for example, (a) G. I. Mackay, C. D. Betowski, J. D. Payzant, H. I. Schiff and D. K. Bohme, *J. Phys. Chem.*, 80, 2919 (1976); (b) D. Betowski, J. D. Payzant, G. I. Mackay and D. K. Bohme, *Chem. Phys. Lett.*, 31, 321 (1975)
14. W. Lindinger, D. L. Albritton, F. C. Fehsenfeld, A. L. Schmeltekopf and E. E. Ferguson, *J. Chem. Phys.*, 62, 3549 (1975)
15. "Molecular Theory of Gasses and Liquids", Hirschfelder, Curtiss and Bird, John Wiley & Sons, Inc., 1954, p1200.
16. (a) R. K. Preston and J. C. Tully, *J. Chem. Phys.*, 54, 4297 (1971); (b) K. Kawaoka and R. F. Borkman, *J. Chem. Phys.*, 55, 4637 (1971)
17. R. D. Nelson, Jr., D. R. Lide Jr. and A.A. Maryott, NSRDS-NBS, (1966) 10.
18. H. H. Landolt and R. Bornstein, "Zahlenwerte und Funktionen", 6 Auflage, "Atom und Molecular Physik", 3 Teil, Springer-Verlag, Berlin, 150, p. 509.

Table I. Thermal energy collision rate constants for the model ion-molecule system $\text{H}_3^+ + \text{NH}_3$ with $d = 1.0\text{\AA}$ (all rate constants $\times 10^9\text{cm}^3\text{sec}^{-1}$)

K	point particles	$r_{\text{H}} = 0.0\text{\AA}$	$r_{\text{H}} = 3.1\text{\AA}$
300	5.02	5.07	5.13
3000	2.67	3.02	3.24

FIGURE CAPTIONS

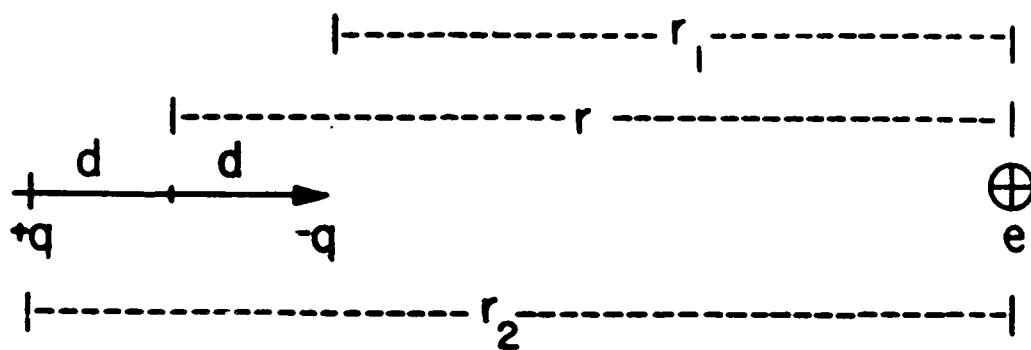
Figure 1. Ion Induced dipole interaction

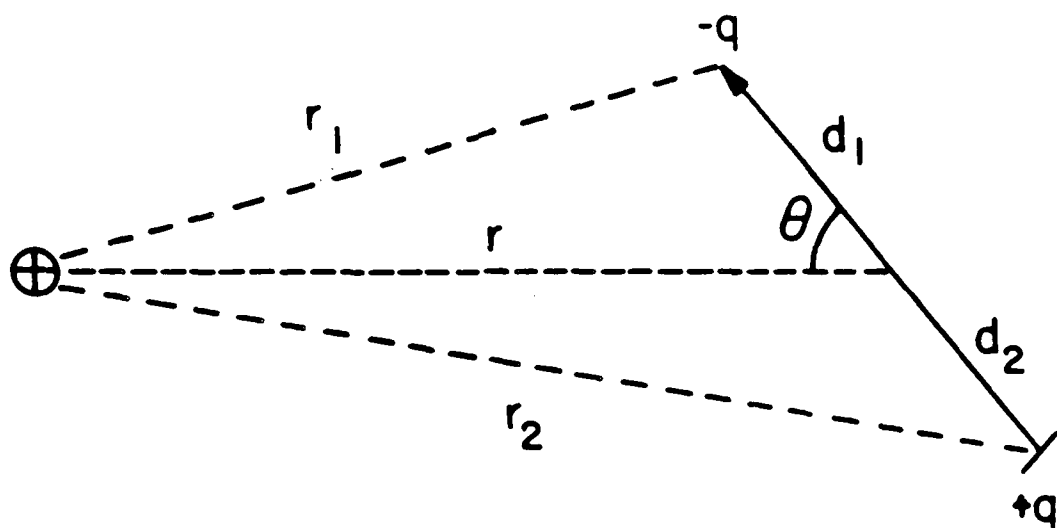
Figure 2. Ion permanent dipole interaction

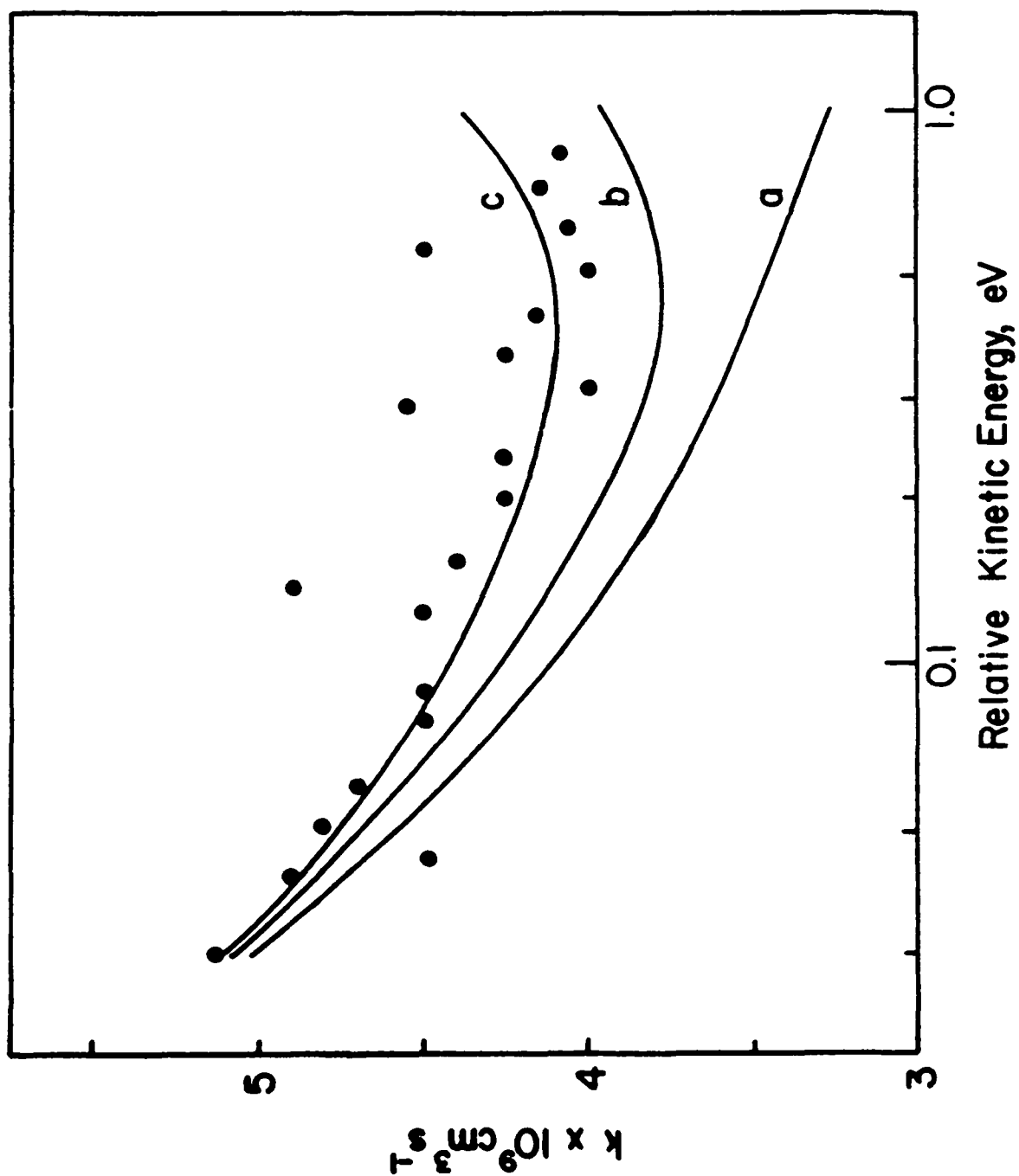
Figure 3. Rate Constant as a Function of Relative Kinetic Energy. Solid circles: experimental results. Curve (a): point particle approximation. Curve (b): $d \rightarrow 0$, $r_H = 3.1$. Curve (c): $d = 1.0 \text{ \AA}$, $r_H = 3.1$

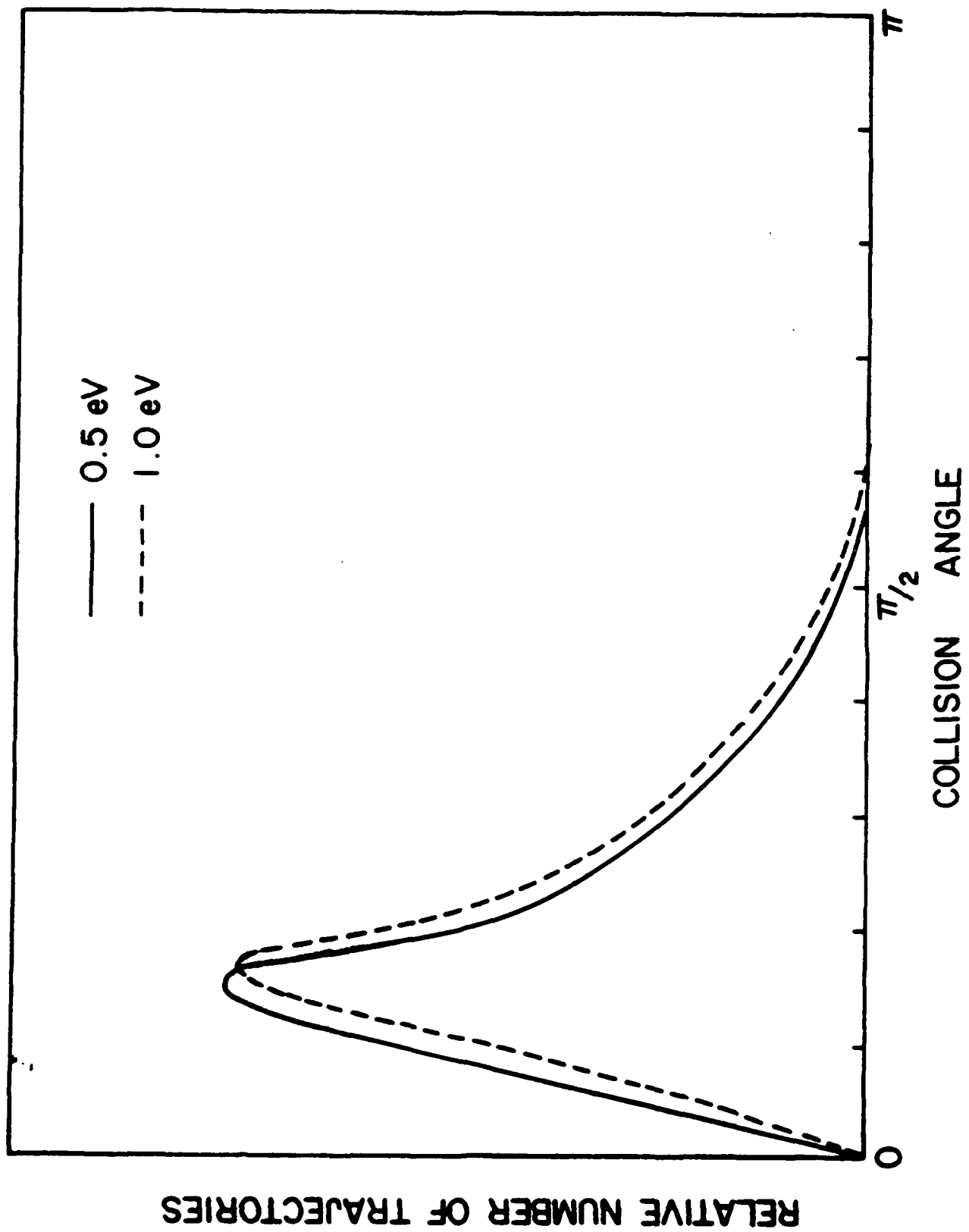
Figure 4. Collision Orientation (θ at $r=r_H$) at 0.5 and 1.0 eV Relative Kinetic Energies

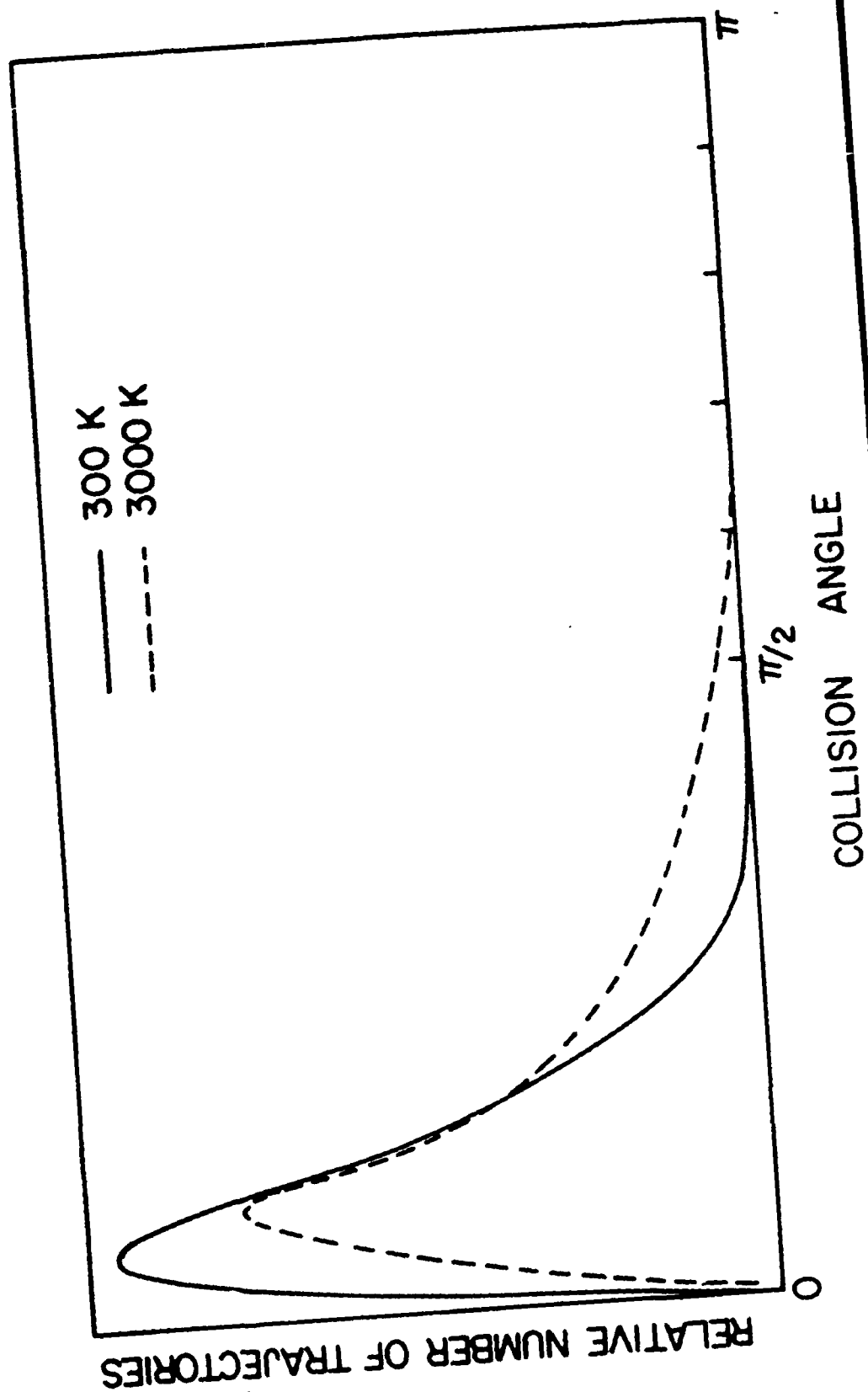
Figure 5. Collision Orientation (θ at $r=r_H$) at 300K and 3000K.











1988 USAF-UES RESEARCH INITIATION PROGRAM

Sponsored by the
AIR FORCE OFFICE OF SCIENTIFIC RESEARCH

Conducted by the
Universal Energy Systems, Inc.

FINAL REPORT

AGING STUDIES OF GaAs SCHOTTKY BARRIERS

Prepared by:	Keith A. Christianson
Academic Rank:	Assistant Professor
Department:	Electrical Engineering Department
University:	University of Maine
USAF Researchers:	A.L. Tamburrino, M. Walter
Date:	December 12, 1989
Contract no:	F49620-88-C 0053

AGING STUDIES OF GaAs SCHOTTKY BARRIERS

by

Keith A. Christianson

ABSTRACT

A recent series of measurements has shown that the barrier height of Schottky diodes on GaAs may change under long term biasing conditions. The aging has been found to occur under reverse bias conditions with a logarithmic dependence on time. This study has been concerned with looking at the deep level and interface/surface state configuration of these diodes using transient capacitance and conductance techniques to see if state generation/destruction plays any role in this aging process. Measurements of the steady state I-V characteristics as a function of temperature were also made to examine the transport mechanism and the role of interface/surface states and/or deep levels in the current transport.

Two groups of diodes, Au/W/GaAs and Au/Pt/Ti/GaAs, were studied. Both of these diode types are contained within power MESFET structures. As has been reported elsewhere, the Au/W/GaAs diodes exhibit pronounced aging effects, while the Au/Pt/Ti/GaAs diodes show this effect only slightly.

Steady state I-V measurements showed that at room temperature thermionic emission controlled for both the Au/W/GaAs and Au/Pt/Ti/GaAs diodes, as has been assumed previously. For the most part the reverse bias characteristics were controlled by thermionic-field (TF) emission, except for selected Au/W/GaAs samples where it was possible to see the influence of interface-states over a small reverse voltage range. Evaluation of the

characteristics gave an average interface-state density of $10^{13}/\text{cm}^2\text{-eV}$, which then increased after aging. Evaluation of the experimental Richardson constant for the Au/W/GaAs samples also gave a value for A^{**} far from the theoretical value, which is characteristic for interface-state dominated devices.

Conductance DLTS measurements of the Au/W/GaAs devices showed "hole trap" like response, which has recently been interpreted to arise from surface states between the gate and source and/or drain. Two separate bands of these states were noted, and they are presumably located at different places in the energy gap. Both bands were seen to increase in amplitude after aging. It is believed these surface states are separate and distinct from the interface-states which have been observed via I-V characteristics and forward bias capacitance spectroscopy. Thus, reverse bias aging has been seen to result in an increase of both surface and interface related trapping states.

Conductance DLTS results of the Au/Pt/Ti/GaAs devices showed a single bulk electron trap located at approximately $E_C - 0.5 \text{ eV}$. This particular trapping state has been seen before in other conductance DLTS studies of GaAs MESFET devices. No evidence of surface states was observed. The characteristics of this electron trap did not change after reverse bias aging.

ACKNOWLEDGEMENTS

I wish to thank the Air Force Systems Command and the Air Force Office of Scientific Research for sponsoring this research. Also, special thanks to Universal Energy Systems for their management of the Research Initiation Program.

At the University of Maine I would like to thank Jim Rioux who helped set up the I-V measurement system, and Rafiqul Murshed who helped configure the DLTS measurement system for this latest series of measurements. Also, thanks to Andy Alexander, Seth Spiller, and Peter Gaboury who in years past have helped build the instrumentation systems in the semiconductor lab.

I. INTRODUCTION

Metal/semiconductor contacts are a fundamental part of all discrete semiconductor devices and integrated circuits. Two main types can be distinguished: the ohmic (low resistance) and the Schottky (rectifying) type contacts. Despite the widespread usage of these contacts some fundamental properties are still not well understood, particularly those involving Schottky contacts on compound semiconductors.

For example, there is the question of barrier height. It is not understood why the barrier height of a metal on GaAs is relatively insensitive to the work function of the metal. A wide variety of metals give a barrier height of about 0.75 eV above the valance band for n-type GaAs, and about 0.5 eV above the valance band edge for p-type GaAs.¹ A number of theories have been proposed to explain the pinning of the Fermi level, including the unified defect model by Spicer^{2,3} and the effective work function model by Woodall.⁴ There is no general agreement at this point on the responsible mechanism.

In addition to not understanding what causes the barrier height to be fixed at relatively constant level, a new series of experiments have changed the barrier height, temporarily, after photochemical and/or chemical treatments.^{5,6} Also, a recent series of measurements have shown that the barrier height of Schottky diodes on GaAs may change under biasing conditions. The effect has been most pronounced for Ag/GaAs and W/GaAs diodes, but has also been observed in Au/GaAs and Ti/GaAs diodes.^{7,8} The aging has been found to occur under reverse bias conditions with a logarithmic dependence on time. Recovery of the barrier height was found to occur within a few days of removal of the bias, or in an accelerated manner under forward bias. The slow time constant associated with this process

suggests that creation/destruction of interface/surface states and/or deep levels is occurring.

The understanding of the mechanism(s) behind this barrier height shift will require the careful characterization of the trapping states (either interface, surface or deep) present in those devices which show this instability. In general these characterization techniques rely on analysis in either the frequency or time domain. The most common variation of frequency domain analysis is admittance spectroscopy,⁹⁻¹¹ which, in its classical form, characterizes the trapping at the interface-states as an induced displacement current in the oxide. Variations of this model have been applied to Schottky barriers without an interfacial layer,¹² but as Werner et al.¹³ have pointed out this model does not allow for current flow across the oxide in the forward bias direction (i.e. the most characteristic feature of the Schottky barrier). More recently, Wu and Yang¹⁴ have modeled the diode capacitance as the modulation of the effective barrier height by the interface charge. The characterization of devices which show these aging effects with frequency domain techniques as per Wu and Yang has been addressed in a separate effort funded by RADC/RBRP.¹⁵

The time domain techniques include Hall effect transient spectroscopy,¹⁶ photo-induced transient spectroscopy (PITS),¹⁷ capacitive deep level transient spectroscopy¹⁸ and conductive deep level transient spectroscopy.¹⁹ Of these four the most directly useful for device measurements are the two deep level transient spectroscopy (DLTS) techniques. These techniques are widely used for the analysis of bulk trapping levels, but the interpretation of the results becomes much more difficult for interface-states. Conductance mode DLTS is typically used for small structures, which have a very small gate capacitance making

capacitance mode transients difficult to measure. However, it has not been clear until recently¹⁹ that capacitance and conductance mode DLTS measure the same parameters.

The great advantage of the time domain techniques is that they readily provide the energy levels and capture cross sections if the states being observed are bulk like. This advantage comes at a price, though, since the most common means of analysis assume the time response is exponential. Such an assumption is not justified in many cases.²⁰ Also, as has been mentioned previously, the determination of interface-state parameters by DLTS is not straightforward. One early attempt used an Arrhenius plot method usually reserved for single bulk levels.²¹ A more recent project used DLTS to characterize the interface-states present at the Au/GaAs interface.²² Both of these projects assumed an intimate interface, which was obviously not true for these high vacuum fabricated diodes. As a recent article from Platen²³ has pointed out, it should not be possible to see these interface states without the existence of an interfacial layer.

It is also possible in certain cases to evaluate for interface-state characteristics from the current-voltage characteristics, in a manner recently expanded on by Horvath.²⁴ Here, interface-state energy distributions and the interfacial layer thickness relative to its dielectric constant may be evaluated if it is possible to estimate the contribution of the interface-states to the slope of the forward and reverse I-V characteristics.

II. OBJECTIVES

The major objective of the proposed research was to determine the mechanism which causes the observed variations in barrier height of Au/W/GaAs and Au/Pt/Ti/GaAs Schottky barriers upon prolonged reverse bias

conditions. In order to determine the mechanism, answers to the following questions were sought. Are the variations due to a changing of the occupation of existing deep levels and/or interface/surface states, or are new states being created by this process of reverse bias? What are the parameters of these states? Is their creation/occupation related to the non-ideality of the reverse bias characteristics?

These characteristics were to be measured using capacitance and conductance mode DLTS, both before and after aging. In addition, I-V characteristics were to be taken as a function of temperature, both as a check to be sure if thermionic emission was taking place at room temperature, and also as an alternate way of evaluating interface-state characteristics as per Horvath.²⁴

III. EXPERIMENTAL PROCEDURE

A. Samples

The same two groups of samples previously evaluated in the barrier height aging study were used in this study. The first group were GaAs power MESFETs, designed for two watts output at 7.5 GHz. They have 24 gate fingers, each 200 μm wide by 1 μm width, for a total gate width of 4.8 mm. The metalization system for these was Au/W/GaAs. The second group of samples were also GaAs power MESFETs, however this group of samples was designed for two watts output at 4 GHz. Their structure has six gate fingers, each 1 μm length, for a total gate width of 1.7 mm. The metalization system for these is Au/Pt/Ti/GaAs. Further details about these samples may be found in references (8) and (15).

B. I-V measurements

The I-V characteristics of the Schottky diodes were measured using a Keithley 485 picoammeter and HP 3478A multimeter with the samples mounted in a Cryosystems cryostat. Biasing was provided by the filtered output of an SRS SR-245 computer interface. The entire system was automated under IEEE-488 control.

C. Transient capacitance/current measurements

The DLTS measurements were made in an existing system. Samples were mounted in a Cryosystems closed cycle cryostat. Injection to the samples was electrically supplied through an HP pulse generator. Waveform analysis was done by a Stanford Research Systems single channel boxcar analyzer, which was configured under software control to emulate a dual-channel boxcar.

Two types of measurements were attempted. Capacitance transients were measured between the gate and the channel as connected to by the source or drain. These transients were measured using a Boonton 72A capacitance bridge. Conductance measurements were made by pulsing the gate voltage while measuring the drain current. The drain to source voltage was kept small and constant (approximately 50 mV). The resulting channel current transients were measured using an Ithaco 1211 preamplifier. Once again the entire system was under IEEE-488 control from an IBM PC.

IV. EXPERIMENTAL RESULTS AND DISCUSSION

A. Au/W/GaAs Schottky barriers

1. I-V measurements

As has been reported previously⁸ for room temperature the I-V characteristics of the Au/W/GaAs Schottky barriers are fairly uncomplicated, in that only a single barrier is present. As can be seen from the straight line behavior of Figure 1 for sample #38, thermionic emission controls over a wide

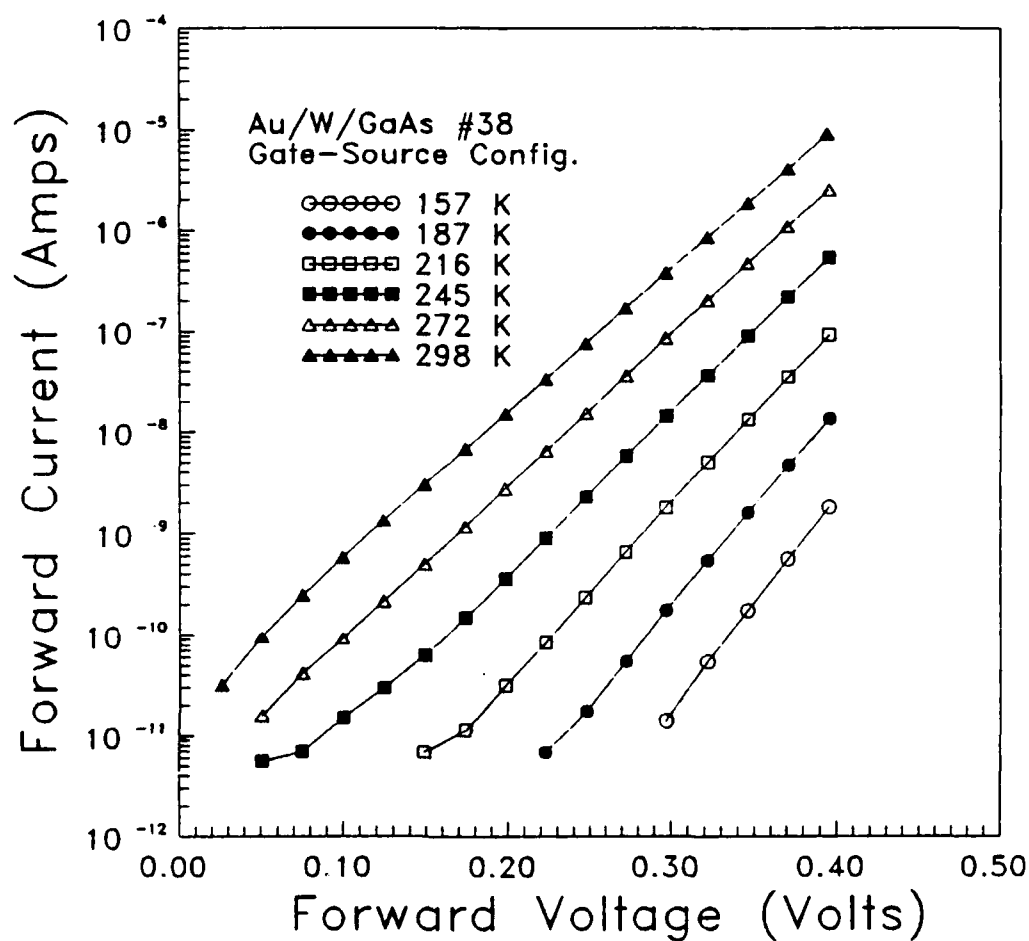


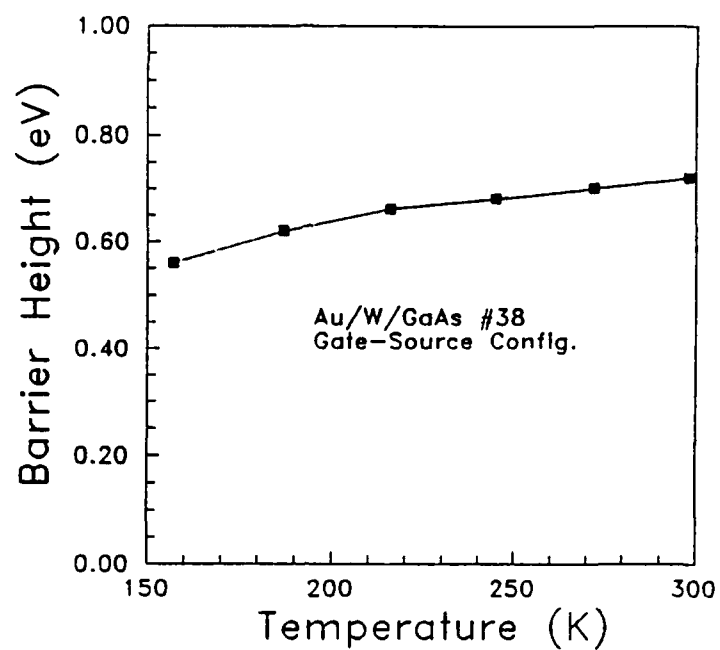
Fig. 1. Forward I-V characteristics of Au/W/GaAs sample #38 as a function of temperature. The sample was measured between the gate and source. The lines connecting the data points are eye aids only, with the barrier height and ideality factor determined as described in reference (8).

temperature range. The barrier height and ideality factor as a function of temperature were then evaluated from these characteristics, using the procedure described in reference (8). The barrier height was found to decrease and ideality factor was found to increase with decreasing temperature. This transition is gradual in nature, as is seen in Figure 2, indicating a smooth transition into thermionic-field emission. For this group of samples the assumption of thermionic emission controlling at room temperature seems to be valid.

By plotting the saturation current in the form of a Richardson plot (I_s/T^2 vs. $1000/T$) and evaluating the Y intercept the experimental Richardson constant was determined. Figure 3 shows an example plot for sample #38. The experimental constant evaluated, approximately 10^{-4} , is orders of magnitude smaller than the theoretical constant, 8.1. Variations of the Richardson constant away from the theoretical value are typically described as being due to interface-states, however, the theory has not been developed.²⁵

The reverse I-V characteristics were also evaluated. The current flow could not be explained in terms of thermionic (T) emission, including the use of image force barrier height lowering. However, at room temperature the current could be successfully modeled using thermionic-field (TF) emission^{26,27} at reverse voltages greater than two volts with the following additional assumptions. First, there is a slight lowering of the barrier height due to the edge effects of the MESFET structure. Second, a bias dependent component of the barrier height was included to account for the movement of the depletion region across the channel and towards the channel-substrate interface. Figure 4 shows a comparison of experiment with modified TF theory for sample #38 for reverse voltages in the range of 2 to 10 Volts.

a)



b)

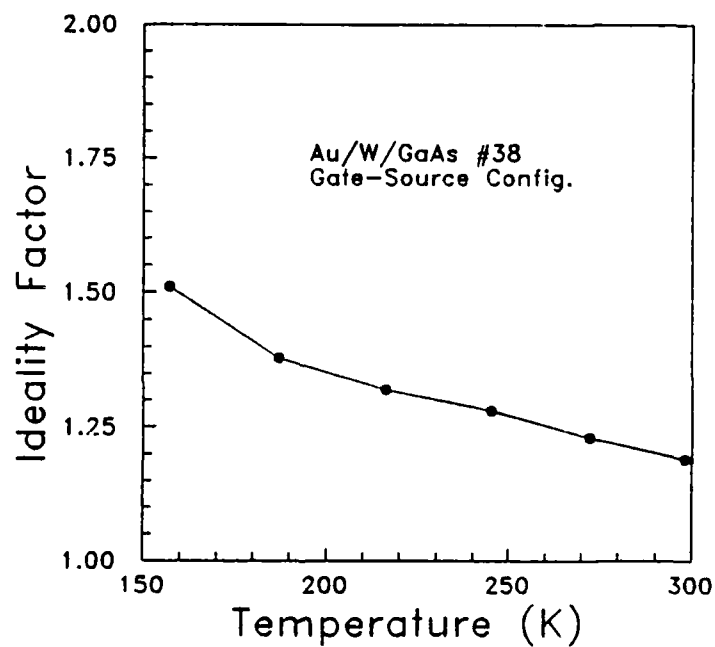


Fig. 2. (a) Barrier height and (b) ideality factor of Au/W/GaAs sample #38 as a function of temperature. The sample was measured between the gate and source. The lines connecting the data points are eye aids only.

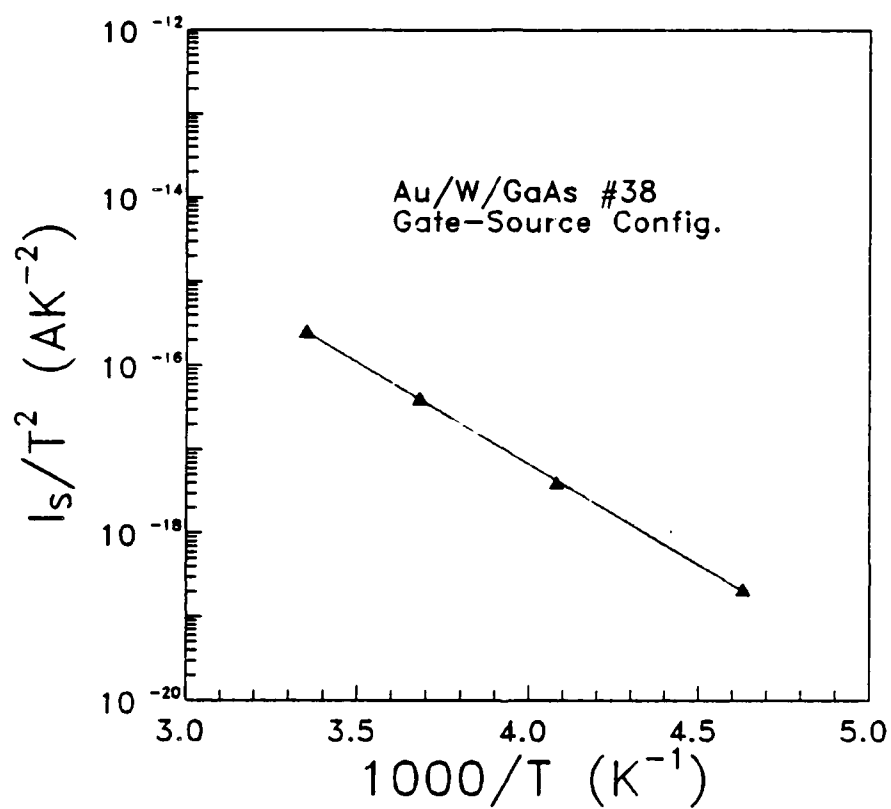


Fig. 3. Richardson plot of Au/W/GaAs sample #38. The sample was measured between the gate and source. The line between data points is best exponential fit.

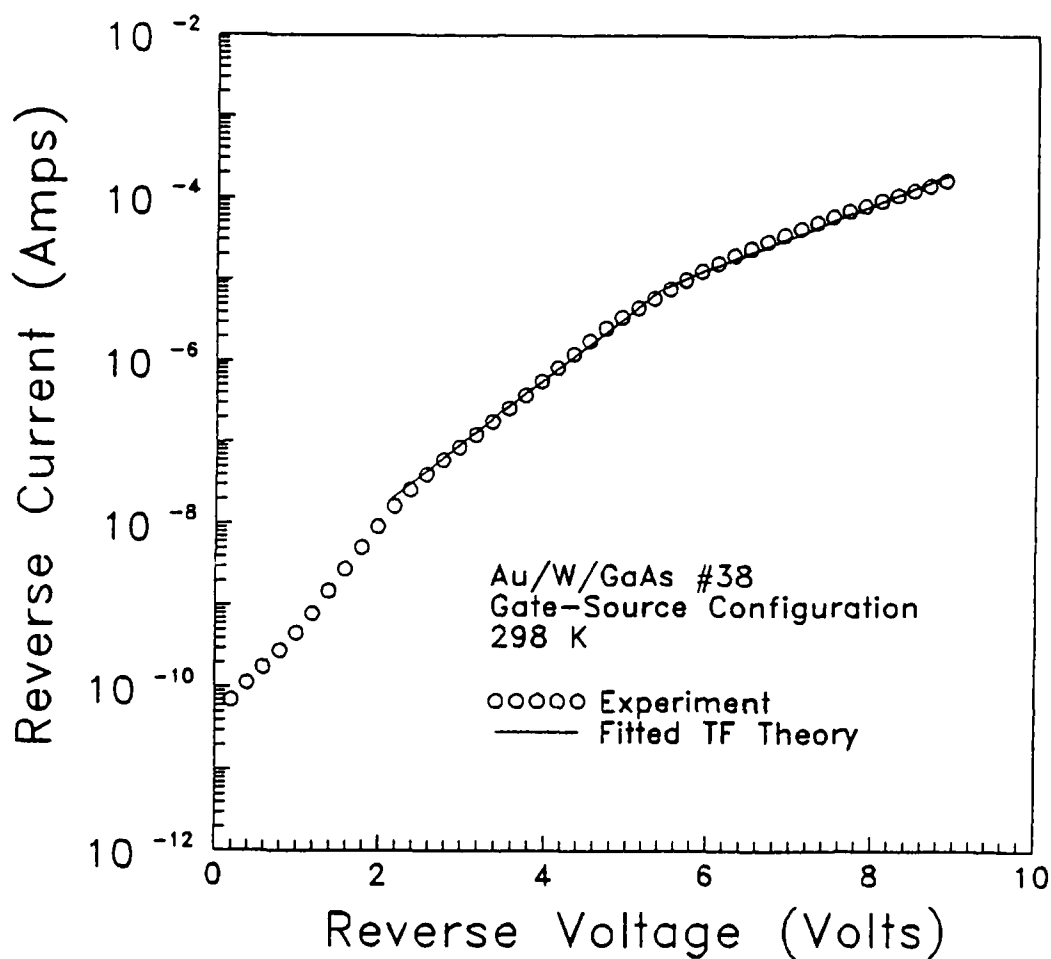


Fig. 4. Reverse I-V characteristics of Au/W/GaAs sample #38 showing the fit between experiment and thermionic field theory. As was explained in the text, this theory was fitted by assuming a slight lowering of the barrier height due to edge effects. Additionally, a bias dependent component was included. The sample was measured between the gate and source.

At voltages below two volts, the I-V characteristics were found to be substantially determined by the contribution of the interfacial layer to the barrier height lowering. This dependence allowed for an evaluation of the interface-state density as per Horvath.²⁴ The appropriate expression for this evaluation is from Horvath's model A, where the interface-state density may be determined from:

$$D_s = \frac{\epsilon_0}{n_i q} \left(\frac{\epsilon_s}{w_R} \left(\frac{q}{s_i kT} - 1 \right) (n_i - 1) - \frac{\epsilon_s}{w_F} \right) \quad (1)$$

where D_s is the interface-state density, n_i is the ideality factor in the forward direction due to interface states, w_R and w_F are the widths of the depletion regions under reverse and forward bias conditions, s_i is the contribution of the interface-states to the slope of the reverse bias characteristics, and with all other terms having their usual meaning.

The major difficulty in this evaluation was obtaining a value for s_i . As has been mentioned, for reverse voltages greater than 2 volts TF emission controls. Thus a reverse voltage range of 3 to 4 volts was used to establish s_{TF} , i.e. the slope due to thermionic-field emission. For reverse voltages less than one volt is believed that not all the interface-states may be filled, thus the reverse voltage range of one to two volts was used to establish s_{Total} , i.e. the sum of s_i and s_{TF} . For sample #38 in the non-aged condition s_{Total} was evaluated to be 3.47, s_{TF} was evaluated to be 1.90, so s_i was found to be 1.57.

For this calculation n was assumed to be the same as n_i , i.e. the non-ideality of forward characteristics was assumed to be due to the presence of interface-states. After evaluating w_R at a reverse voltage of 1.5 V, w_F at 0.3 V, then substitution into equation (1) yielded an average interface-state density

of approximately $10^{13}/\text{cm}^2\text{-eV}$. After aging with a gate to source voltage of -10 volts for 12 hours, n_i increased to 1.30, s_{TF} was virtually unchanged at 2.01, s_T was 3, and so s_i was now found to be 0.99. Evaluation via equation (1) now gave an average interface-state density of $3 \times 10^{13}/\text{cm}^2\text{-eV}$. An increase in interface-state density after aging has also been seen using forward bias capacitance.¹⁵

2. Transient capacitance/current measurements

It was initially attempted to use capacitance mode DLTS to look for the influence of deep traps and/or interface/surface states in these devices. It was believed the relatively large gate area, and thus relatively large sample capacitance (approximately 5 pF) would allow this procedure. However, all attempts to use capacitance mode spectroscopy were not successful.

It was thus decided to use current mode spectroscopy for the remainder of the evaluation of these samples. An example for sample #38 is shown in Figure 5. Let us concentrate initially on the not aged (solid line) data. Note that two features are readily apparent. One is a poorly defined peak occurring at approximately 225 K. The second is a well defined peak occurring at approximately 320 K. From the definition of $t(1)$ and $t(2)$ this second feature is a "hole trap," and an Arrhenius plot gives an activation energy of 0.43 eV.

"Hole traps" of this form have been seen before in transient conductance studies of GaAs MESFETs. Initial explanations dealt with hole traps in the semi-insulating substrate,²⁸ but it is now widely believed the response is due to surface states located in the ungated region between the gate and either the source or drain.²⁹⁻³¹ The signal is inverted because we are monitoring the re-injection of electrons into surface states that were emptied during the voltage pulse (i.e. we are watching a capture process, rather than an emission process). The very slow capture process observed for these states

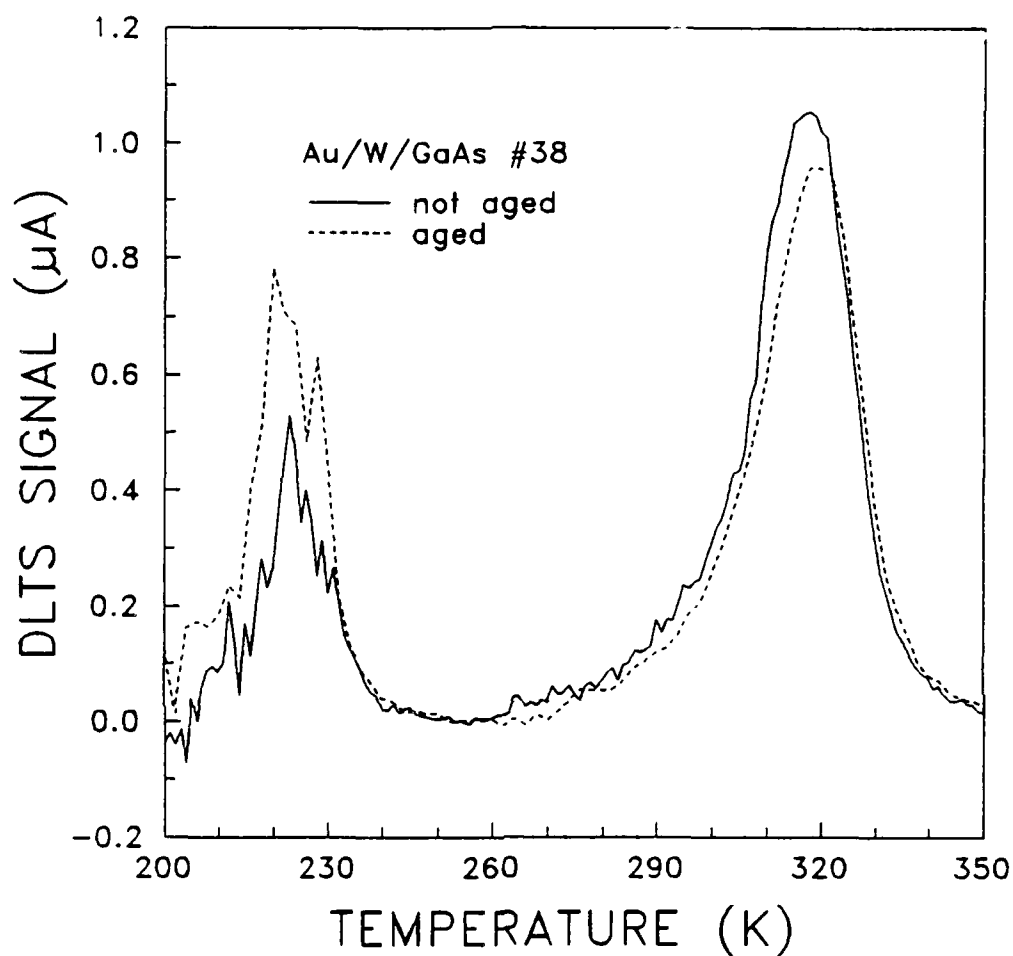


Fig. 5. Conductance DLTS plot of Au/W/GaAs sample #38 measured from 200 to 350 K. Data was taken both before (solid line) and after (dotted line) aging gate to source with -10 V for 12 hours. The spectrum was taken with a time constant τ of 2.73 ms. The reverse bias was 4.8 V and the voltage during the pulse was + 0.4 V. Note the large feature above room temperature, as well as a poorly defined feature peaking at around 225 K.

(it required greater than 10 μ s for observation, and capture was not complete even for times greater than 100 μ s) also points to the fact that these are surface states.^{30,31} These states are observed in conductance mode since in a MESFET device the ungated area of the device can become as large as the surface area located under the gate electrode. After a filling pulse the response of these states becomes critical in determining the channel conductance. This is fundamentally different than in capacitance mode DLTS, where the sampled area is located in the depletion region directly under the gate, and thus these surface states do not play a major role in determining the response.

Thus it is believed the feature located at approximately 320 K is related to the presence of surface states located either side of the gate region. Is this also true for the feature located at 225 K? Once again, the direction of the feature peak implies a hole trap. But the response is poorly defined, compared to the nearly Gaussian shape of the higher temperature peak. At first it was thought the ragged appearance indicated an interface-state distribution, but the peak is inverted from what it should be for the anticipated donor type interface-states located in the upper half of the bandgap.¹⁵ A very important clue comes again from the very slow capture time, which required 100 μ s or greater of pulse before the low temperature response was seen. Also, although Figure 5 was recorded with a voltage pulse which extended into the forward bias regime, the response could be seen equally as well without ever going into forward bias, which is not anticipated for an interface-state distribution.^{2,3} Thus the low temperature feature also represents the contribution from surface states located between the gate and source or drain.

Presumably any response from electron traps (bulk and/or interface-state related) are buried beneath this surface state response. Attempts to look

for the contribution of these by reducing the filling pulse width to 1 μ s were not successful.

An examination of the aging results (dotted line of Figure 5) is also quite interesting. An increase in signal for both of the surface state peaks is observed, although the lower temperature peak seems to change more drastically. This points to an increase in density of both surface related states following the aging process, although again the lower temperature peak seems to have been more dramatically affected.

At this point the obvious question is whether these surface states are the same states previously identified as interface-states in both the I-V characterization (previous section of this paper) and in the forward bias capacitance results.¹⁵ It would seem unlikely these are the same, because the depletion layer edge should be far removed from the location of the surface states, unless the depletion layer is highly skewed by the biasing arrangement. For this reason it is believed the aging process is resulting in both an increase of interface-state density (as observed through the I-V characteristics of this study and through the forward bias capacitance measurements of a previous study¹⁵) and also an increase in surface state density. Such an increase in surface state density has also been recently seen in degradation studies of HEMTs.³²

B. Au/Pt/Ti/GaAs Schottky barriers

1. I-V measurements

Figure 6 shows the forward I-V characteristics as a function of temperature for a typical Au/Pt/Ti/GaAs sample. As has been seen before⁸ at room temperature there are two separate linear regions, corresponding to two barriers in parallel, with the lower barrier dominating at the lower biasing voltages. The higher energy barrier corresponds to the thermionic emission

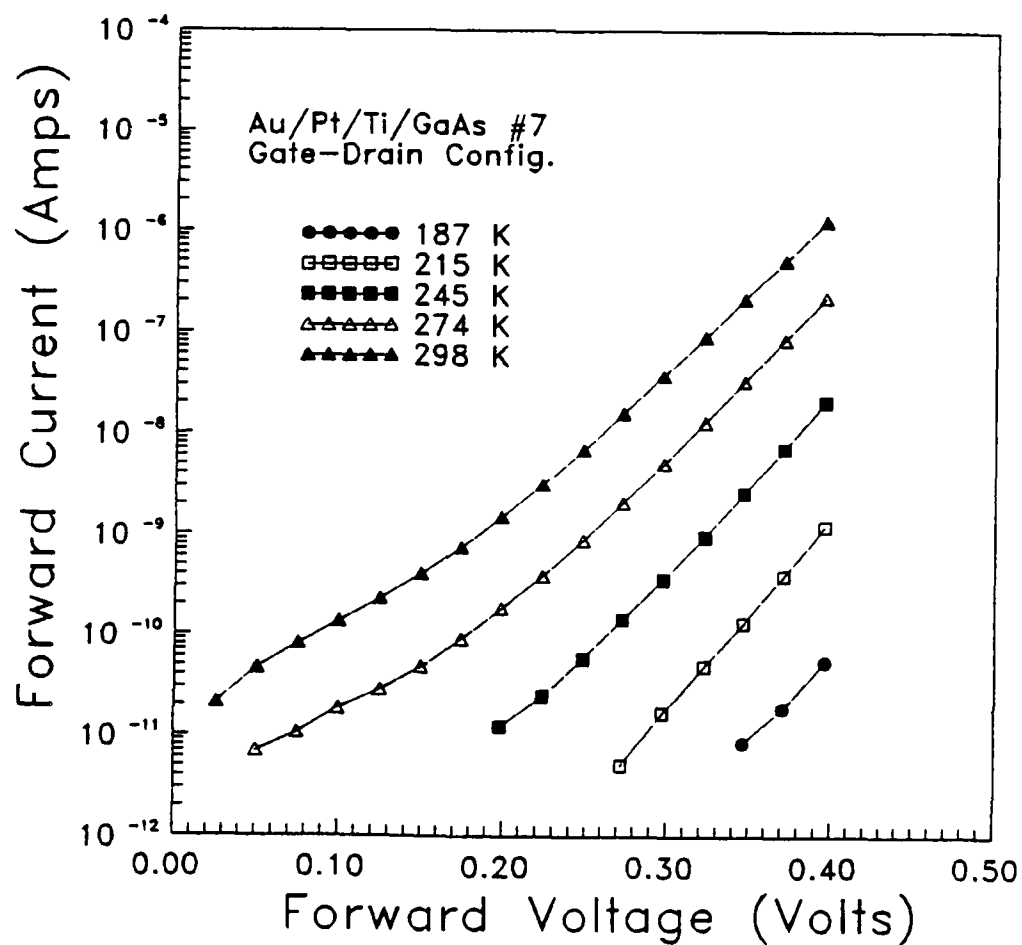


Fig. 6. Forward I-V characteristics of Au/Pt/Ti/GaAs sample #7 as a function of temperature. The sample was measured between the gate and drain. The lines connecting the data points are eye aids only, with the barrier height and ideality factor determined as described in reference (8).

barrier. As the temperature is lowered the second barrier decreases in importance, until finally only the thermionic emission barrier controls in the temperature region of approximately 200 to 250 K.

Figure 7 shows the barrier height and ideality factor as a function of temperature for sample #7. These were evaluated from the slope and intercept of the higher voltage straight line portion of the curve as has been explained in reference (8). Based upon the rapid increase of the ideality factor near 200 K the current at that temperature is probably being conducted by a mixed thermionic-field emission mode.

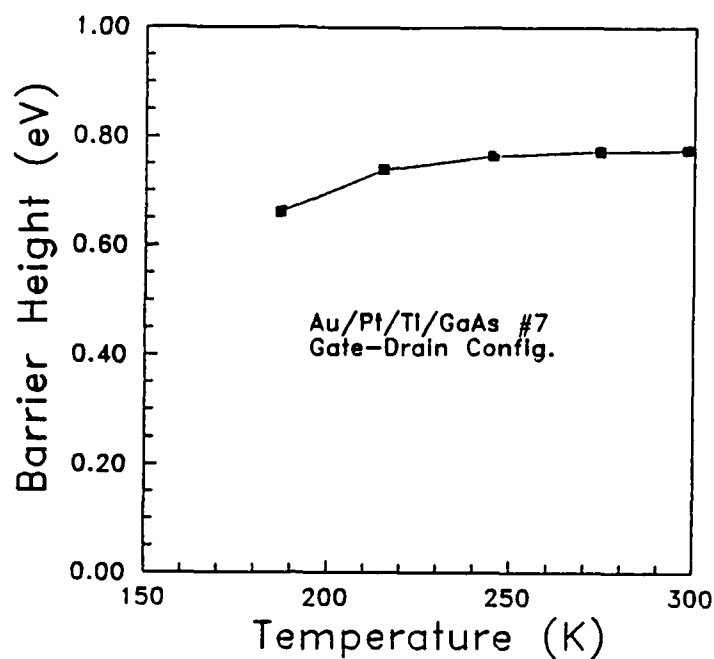
By plotting the saturation current in the form of a Richardson plot (I_s/T^2 vs. $1000/T$) and evaluating the Y intercept the experimental Richardson constant was determined. Figure 8 shows such a plot for sample #7. An evaluation of the plot gives A^{**} approximately 1, versus 8.1 theoretical. The closer value of the experimental Richardson constant to the theoretical value as compared to the Au/W/GaAs samples indicates a reduced influence of interface-states.

Figure 9 shows a comparison between experiment and fitted thermionic field theory for sample #7 over the reverse voltage range from 0 to 10 Volts, using the same fitting procedure as described previously. Because of the domination of TF emission in the reverse characteristics it was not possible to evaluate for interface-state characteristics from the I-V characteristics, such as was possible for selected Au/W/GaAs samples.

2. Transient capacitance/current measurements

As with the Au/W/GaAs samples, capacitance mode DLTS measurements of the Au/Pt/Ti/GaAs samples did not show anything of significance. Thus, interest was centered on conductance mode measurements. Figure 10 shows the response from a typical sample, #4. There was noted a single prominent

a)



b)

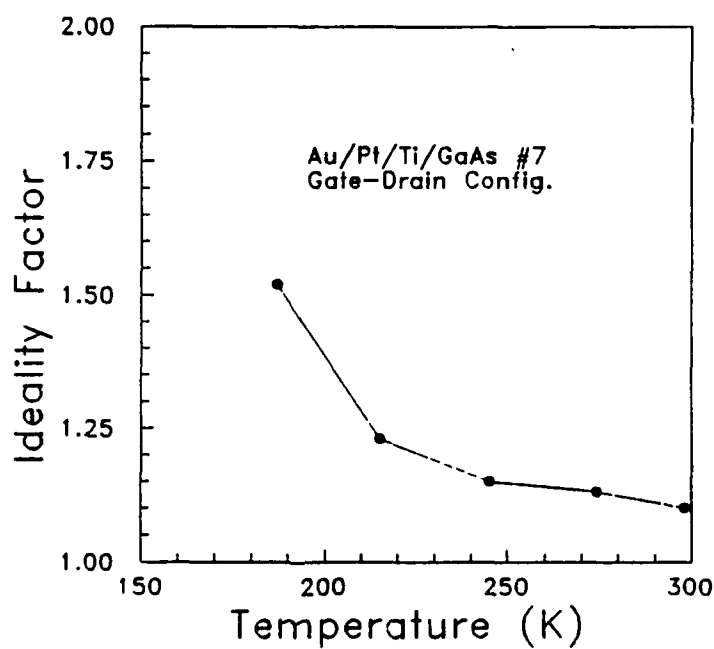


Fig. 7. (a) Barrier height and (b) ideality factor of Au/Pt/Ti/GaAs sample #7 as a function of temperature. The sample was measured between the gate and drain. The lines connecting the data points are eye aids only.

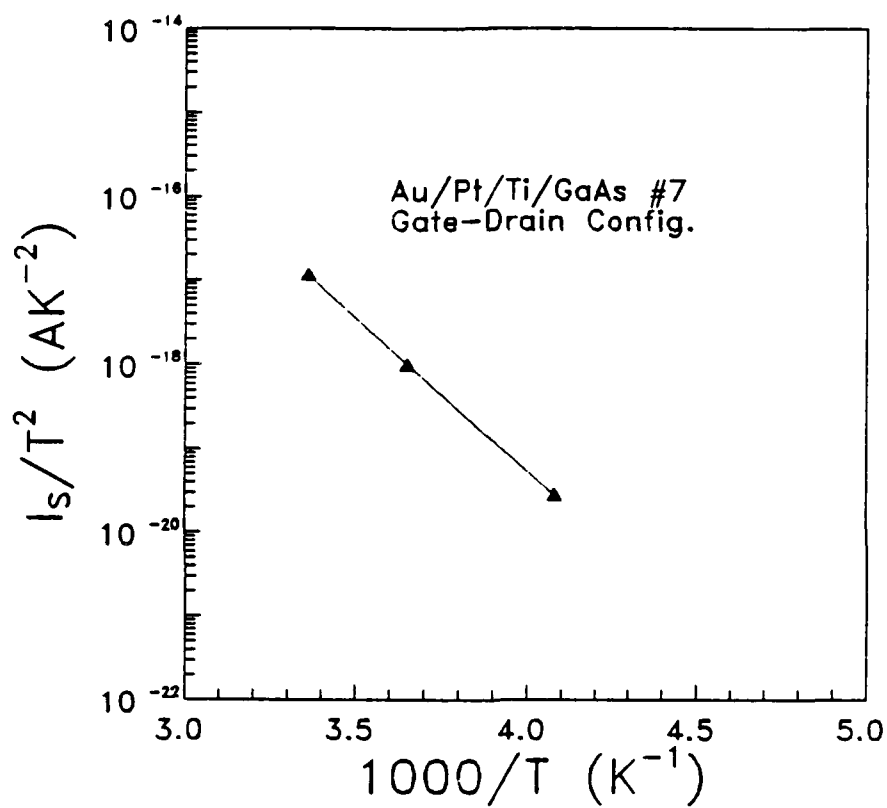


Fig. 8. Richardson plot of Au/Pt/Ti/GaAs sample #7. The sample was measured between the gate and drain. The line between data points is best exponential fit.

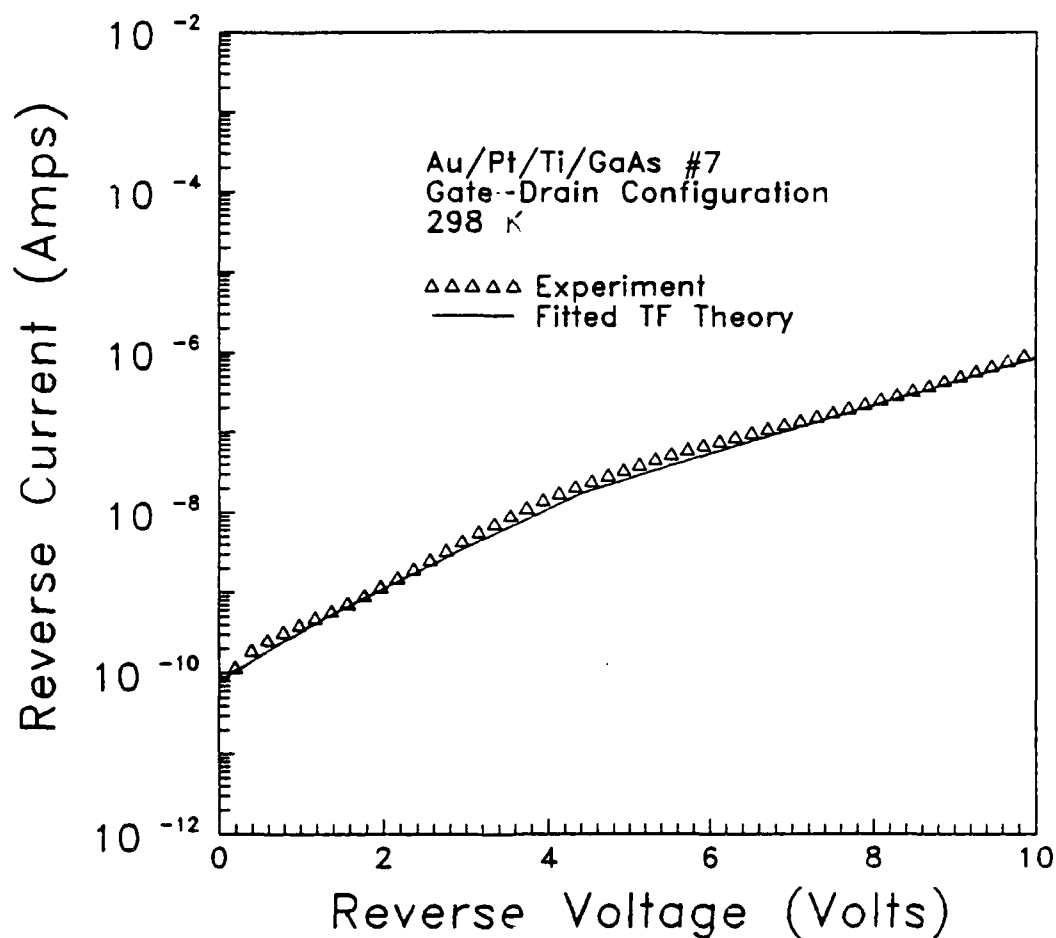


Fig. 9. Reverse I-V characteristics of Au/Pt/Ti/GaAs sample #7 showing the fit between experiment and thermionic field theory. As was explained in the text, this theory was fitted by assuming a slight lowering of the barrier height due to edge effects. Additionally, a bias dependent component was included. The sample was measured between the gate and drain.

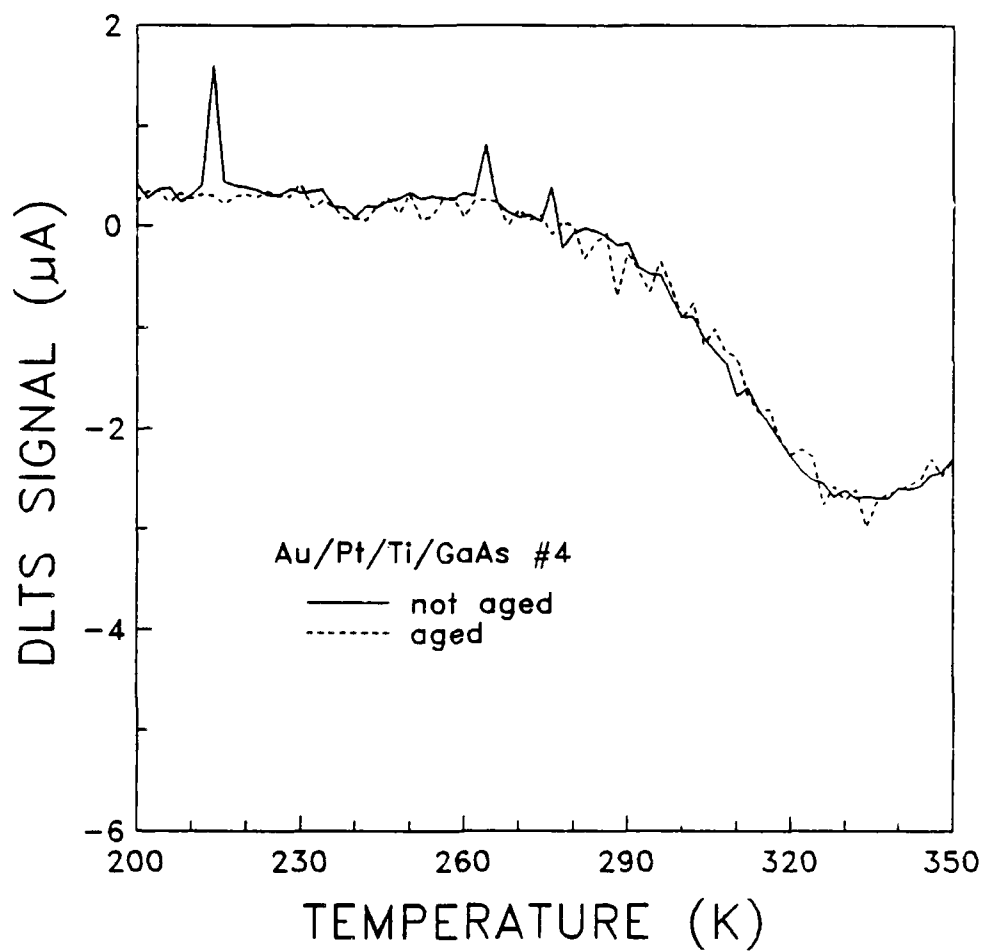


Fig. 10. Conductance DLTS plot of Au/Pt/Ti/GaAs sample #4 measured from 200 to 350 K. Plot shows both before (solid line) and after (dotted line) aging gate to drain with -10 V for 18 hours. The spectrum was taken with a time constant τ of 4.33 ms. The reverse bias was 5.0 V and the voltage during the pulse was + 0.4 V.

peak located slightly above room temperature. The carrier capture at this center was seen to occur very rapidly, with virtually the same response whether the filling pulse was 1 μ s or 1 ms wide (the spectrum shown was taken with a 100 μ s wide filling pulse). This fast carrier capture is indicative of a true bulk trapping level.²⁹⁻³¹ An Arrhenius plot of e_n/T^2 (see Figure 11) gave an apparent activation energy of 0.56 eV, which is quite close to the energy (0.53 eV) reported for a characteristic electron trap in conductance studies of GaAs MESFETs.³³

Thus the second group of samples were found to have only a single electron trap, located at $E_c - 0.56$ eV, which could be seen only by conductance mode DLTS. Apparently the passivation problem with its associated surface states is not of significance in this group of samples. Also, if we examine the DLTS response after aging we see that it is unchanged (dotted line of Figure 10), which is consistent with the very slight barrier height changes seen after aging with this group of samples,⁸ and also with the absence of changes in the forward bias capacitance results after aging.¹⁵

V. CONCLUSIONS AND RECOMMENDATIONS

In this work the reasons why the barrier height changes in Au/W/GaAs (and to a much lesser extent Au/Pt/Ti/GaAs) MESFET Schottky barriers after prolonged reverse bias aging were examined. In particular the role of various types of states (bulk, interface, and surface) was examined. This was done through a combination of steady state I-V measurements and transient conductance measurements.

The steady state I-V measurements showed that at room temperature thermionic emission controlled for both the Au/W/GaAs and Au/Pt/Ti/GaAs diodes, as has been assumed previously.⁸ For the most part the reverse bias

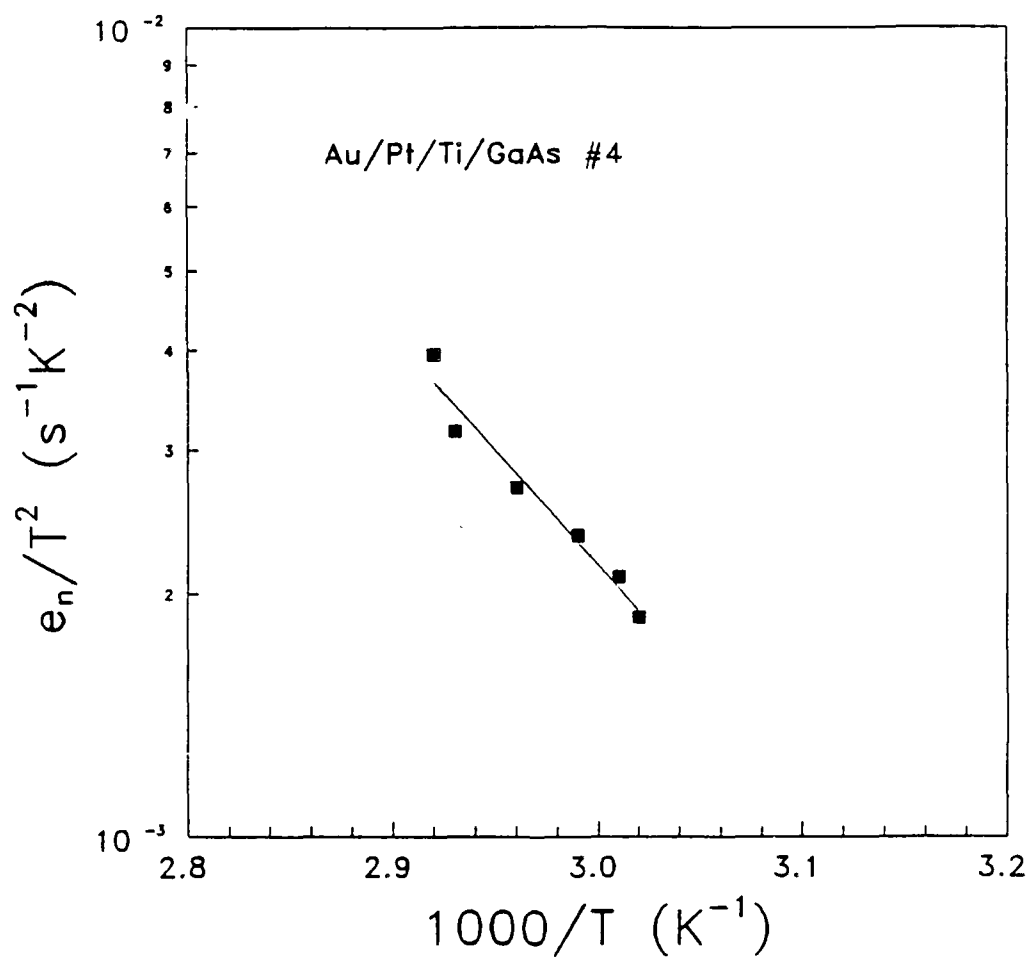


Fig. 11. Arrhenius plot of the prominent feature appearing at approximately 335 K in Au/Pt/Ti/GaAs sample #4. An evaluation of this plot gives an effective trap depth of 0.56 eV.

characteristics were controlled by thermionic-field (TF) emission, except for selected Au/W/GaAs samples where it was possible to see the influence of interface-states over a small reverse voltage range. Evaluation of the characteristics gave an average interface-state density of $10^{13}/\text{cm}^2\text{-eV}$, which then increased after aging. Evaluation of the experimental Richardson constant for the Au/W/GaAs samples also gave a value far removed from the theoretical for A^{**} , which is characteristic for interface-state dominated devices. The experimental Richardson constant seems to be a particularly sensitive indicator of the amount of interface (surface?) states present in these barriers, however the theoretical link is currently missing. The author has been working on this, however, there remains much work to be done.

Conductance DLTS measurements of the Au/W/GaAs devices showed "hole trap" like response, which has recently been interpreted to arising from surface states between the gate and source and/or drain.²⁹⁻³¹ Two separate bands of these states were noted, and they are presumably located at different places in the energy gap. Both bands were seen to increase in amplitude after aging.

Conductance DLTS results of the Au/Pt/Ti/GaAs devices showed a single bulk electron trap located at approximately $E_C - 0.5 \text{ eV}$. This particular trapping state has been seen before in other conductance DLTS studies of GaAs MESFET devices.³³ No evidence of surface states was observed. The characteristics of this trap did not change after reverse bias aging.

The persistent question remains as whether the states observed by I-V and forward bias capacitance (which have been labeled interface) and the states observed by DLTS (labeled surface) are the same entity. It is believed that these bands are separate and distinct because it is assumed that the measurement techniques are really looking at two different areas. But, if this

is true, then why are the DLTS studies not able to see the interface-states that are so readily observable under forward bias spectroscopy, when both of these techniques are presumably looking at the same place? Perhaps a modeling study using PISCES or similar program is in order to locate precisely where the depletion region is located in these different measuring techniques. Such a study might also reveal why there are differences in aging characteristics depending on whether the aging is done gate to source, gate to drain, or gate relative to source and drain connected.⁸

VI. REFERENCES

- 1) J.R. Waldrop, Appl. Phys. Lett. 44, 1002 (1984).
- 2) W.E. Spicer, I. Lindau, P. Skeath, C.Y. Su, and I. Lindau, J. Vac. Sci. Technol. 17, 1019 (1980).
- 3) W.E. Spicer, P.W. Chye, P.R. Skeath, C.Y. Su, and I. Lindau, J. Vac. Sci. Technol. 16, 1422 (1979).
- 4) J. M. Woodall and J.L. Freeout, J. Vac. Sci. Technol. 19, 794 (1981).
- 5) S.D. Offsey, J.M. Woodall, A.C. Warren, P.D. Kirchner, T.I. Chappel, and G.D. Petit, Appl. Phys. Lett. 48, 475 (1986).
- 6) M.S. Carpenter, M.R. Mellach, and T.E. Dungan, Appl. Phys. Lett. 53, 66 (1988).
- 7) A. Miret, N. Newman, E.R. Weber, Z. Lilientiel-Weber, J. Washburn, and W.E. Spicer, J. Appl. Phys. 63, 2206 (1988).
- 8) K.A. Christianson, in Proceedings of the 27th Annual International Reliability Physics Symposium, p. 65 (IEEE Press, 1989).
- 9) E. Shibi and A.G. Milnes, Solid State Elect. 11, 323 (1968).
- 10) W.G. Oldham and S.S. Naik, Solid State Elect. 15, 1985 (1972).
- 11) C.F. Smiley, L.D. Law, and C.T. Sah, Solid State Elect. 16, 895 (1973).
- 12) P.S. Ho, E.S. Yang, H.L. Evans, and X. Wu, Phys. Rev. Lett. 56, 177 (1986).
- 13) J. Werner, K. Ploog, and H.J. Queisser, Phys. Rev. Lett. 57, 1080 (1986).
- 14) X. Wu and E. Yang, J. Appl. Phys. 65, 3560 (1989).
- 15) "Interface-State Measurements of GaAs Schottky Barriers Using Admittance Techniques: Relationship to Barrier Height Instability," final report for RADC task number N-9-5940 (Sept. 15, 1989).
- 16) Z. Kachwalla and D. Miller, Appl. Phys. Lett. 50, 1438 (1987).
- 17) R.E. Kremer, M.C. Arikan, J.C. Abele, and J.S. Blakemore, J. Appl. Phys. 62, 2424 (1987).
- 18) D.V. Lang, J. Appl. Phys. 45, 3023 (1974).
- 19) I.D. Hawkins and A.R. Peaker, Appl. Phys. Lett. 48, 227 (1986).
- 20) P.D. Kirchner, W.J. Schatt, G.N. Maracas, L.F. Eastman, T.I. Chappell, and C.M. Ranson, J. Appl. Phys. 52, 6462 (1981).

- 21) H. Lim, G. Sagnes, and G. Bastide, J. Appl. Phys. 53, 7450 (1982).
- 22) H. Zhang, Y. Aoyagi, S. Iwai, and S. Naraba, Appl. Phys. Lett. 50, 341 (1987).
- 23) W. Platen, H.J. Schmutzler, D. Kohl, K.A. Brauchle, and K. Wolter, J. Appl. Phys. 64, 218 (1988).
- 24) Zs. J. Horvath, J. Appl. Phys. 63, 976 (1988).
- 25) A.K. Srivastava, B.M. Arora, and S. Guha, Solid State Elect. 24, 185 (1981).
- 26) F.A. Padovani and R. Stratton, Solid State Elect. 2, 695 (1966).
- 27) Zs. J. Horvath, J. Appl. Phys. 64, 6780 (1988).
- 28) A. Zylbersztejn, G. Bert, and G. Nuzillat, Instit. Phys. Conf. Ser. 45, 315 (1979).
- 29) R.H. Wallis, A. Faucher, D. Pons, and P.R. Jay, Instit. Phys. Conf. Ser. 74, 287 (1984).
- 30) S. Blight, R. Wallis, and H. Thomas, IEEE Trans. Elect. Dev. ED-33, 1447 (1986).
- 31) J.P. Harrang, A. Tardella, M. Rosso, P. Alnot, and J.F. Peray, J. Appl. Phys. 61, 1931 (1987).
- 32) R. Magno, R. Shelby, and W.T. Anderson, J. Appl. Phys. 66, 5613 (1989).
- 33) S. Sriram, and M. Das, IEEE Trans. Elect. Dev. ED-30, 586 (1983).

FINAL REPORT NUMBER 53
REPORT NOT AVAILABLE AT THIS TIME
Dr. Hugh K. Donaghy
210-9MG-094

**FINAL REPORT NUMBER 54
NEURAL NETWORK FOR AIDING
INTELLIGENT ANALYSIS
PENDING APPROVAL
Dr. Oleg G. Jakubowicz
210-9MG-124**

SUPPLY LINE TESTING IN CMOS DIGITAL CIRCUITS

FINAL REPORT

August 1, 1989

by

Ker-Jen Hsu
Louis G. Johnson

ABSTRACT

This report describes progress made toward the goal of demonstrating the supply line testing of a CMOS chip fabricated with modern processing techniques and extending its application to general dynamic CMOS design styles.

A further exploration showed that with proper test pattern arrangement, most stuck-open faults can be detected by power line testing. Applications of supply line testing directly on psuedo-two phase CMOS logic and on domino CMOS logic have been simulated successfully for stuck open faults. This means that it is highly possible to extend supply line testing for stuck open faults to general dynamic CMOS logic. To demonstrate its feasibility, a real CMOS test chip with intentionally embedded faults has been laid out and well simulated.

I. INTRODUCTION

With the advent of VLSI, the importance of CMOS technology has increased. Among various fabrication processes, CMOS has emerged as a promising technology for the future design of densely-packed low power VLSI circuits. Therefore, testability of CMOS devices has assumed great significance.

While conventional testing, which will be referred to as voltage-sensitive testing in this paper, worked well for SSI and MSI devices, it has many weaknesses when applied to LSI and VLSI circuits. Voltage-sensitive testing detects faults in terms of different output voltages on output pins of the chip under test. In VLSI, the circuits get more and more complex while the ratio of the number of pins on the chip to the number of elements inside the chip becomes smaller and smaller. In CMOS circuits, stuck-open faults can make matters worse by making a sequential network out of a combinational one.

In contrast to voltage-sensitive testing. Supply line testing will be called current-sensitive testing in our discussion because it observes faults by excess leakage supply current on the power line of the chip. The underlying principle of the current-sensitive testing is based on the nominally zero static supply current of CMOS devices, a unique characteristic of CMOS logic. The current-sensitive method makes testing simplified by providing us with current-sensitive primary outputs, the supply lines which are directly connected to gates inside the chip. However, the current-sensitive testing has its weak points as well.

The current-sensitive testing and the voltage-sensitive testing should not exclude each other but complement each other. The best way

is to use both test schemes which gives us more flexibility and more fault-coverage.

II. SUPPLY LINE MODULATION

In earlier research work [1,4], it has been shown that stuck-open faults may be supply line testable, if the capacitive coupling between the power line and a floating node allows a modulating voltage on the power line to drive the floating node to the desired mid-range value where both the pull-up and pull-down transistors are on. It has also been pointed out that for any given fabrication process, there exists a maximum tolerable capacitance ratio (MTCR) beyond which it will be impossible to detect open faults. This maximum tolerable capacitance ratio must satisfy the following inequality,

$$BV - V_{p1} > WV > \max \{ (1 + C_n/C_p)V_{tn}, (1 + C_p/C_n)|V_{tp}| \}$$

where

BV is the break down voltage of the FET's,

$WV = (V_{ph} - V_{p1})$, the magnitude of the modulation
of the power line voltage,

C_n and C_p are the coupling capacitances from Figure 1, and

V_{tn} and V_{tp} are the threshold voltage of the n-FET
and p-FET respectively.

After further investigation, we made some interesting observations relating to the MTCR. Even though the capacitance ratio on the open node is over the limitation of the MTCR, it may still be possible to detect open-faults by current-sensitive methods if we apply a current-sensitive two-pattern test and choose V_{p1} so that

$$V_{p1} > V_{tn} + |V_{tp}|,$$

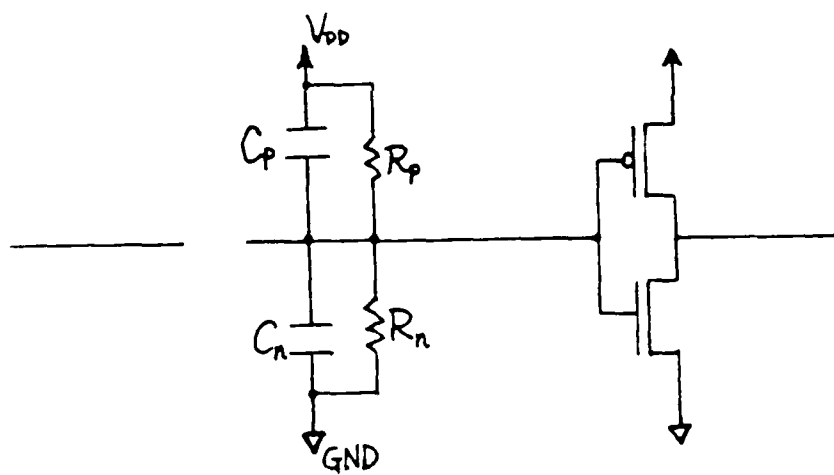


Figure 1. Circuit model of an open in CMOS.

For the purpose of comparison, we introduce the voltage-sensitive two-pattern test, which was first used by Wadsack [2] to detect stuck-open faults in CMOS circuits.

Suppose that the good gate implements a function

$$G: X \rightarrow \{0, 1\}$$

while the faulty (stuck-open) gate implements a function

$$F: x \rightarrow \{0, 1, M\}$$

where $X = \{0, 1\}^n$ the input space of the gate, and M denotes an output which is floating. A voltage-sensitive two-pattern test is a pair (t_1, t_2) such that

$$(t_1, t_2) \in X_1 \times X_M^F \text{ when n-FET is stuck-open}$$

$$(t_1, t_2) \in X_0 \times X_M^F \text{ when p-FET is stuck-open}$$

where $X_0 = G^{-1}(0)$, $X_1 = G^{-1}(1)$, and $X_M^F = F^{-1}(M)$.

A current-sensitive two-pattern test is a pair (t_1, t_2) such that

$$(t_1, t_2) \in X_1^F \times X_M^F \text{ when } C_n/C_p > \text{MTCR}$$

$$(t_1, t_2) \in X_0^F \times X_M^F \text{ when } C_p/C_n > \text{MTCR}$$

where $X_0^F = F^{-1}(0)$ and $X_1^F = F^{-1}(1)$. If X_0^F and X_1^F exist, then the two pattern test should detect stuck-open faults when the capacitance ratio is above the MTCR. If the capacitance ratio is under the limitation,

$$\max \{ C_n/C_p, C_p/C_n \} < \text{MTCR},$$

then a single pattern $t \in X_M^F$ will be sufficient.

III. APPLICATION TO DYNAMIC LOGIC

A general dynamic CMOS logic can possess a clock-controlled transmission gate, or a non-complementary gate. Both of them can cause open nodes during normal operation. It complicates the current-sensitive testing by mixing the current from open faults with that from the intentionally open nodes.

One of the reasons why the current-sensitive testing is more efficient is that it eliminates fault propagation problems by providing every gate a current-sensitive primary output. A gate with an intentionally floating output does not gain this sort of benefit. So, to detect faults that happen at floating output gates, we have to find some way to propagate the faults either to a current-sensitive primary output or to a voltage-sensitive primary output, depending on which one is closest to that faulty node.

We deal with dynamic logic using a modified by D-algorithm [7]. The step-by-step procedures for applying current-sensitive testing to general dynamic logic are as follows:

- . Find all propagation D-cubes for the circuits between the fault and node and the closest current-sensitive primary output.
- . Search for an entry which has current-sensitive D-cube on the output and D or D entry matching the signal on the fault node.
- . If fail to find such cube, we have to try voltage-sensitive test method.
- . Modulate power line.

- . Right after modulating power line, control clocks such that every intentionally open node is driven to a definite 0 or 1 value.
- . Then, the excess current will come just from faulty nodes.

Two of our simulated examples which apply the above algorithm are illustrated below.

A. Psuedo-two phase logic

A CMOS shift register with psuedo-two phase clocking is shown in Figure 2 and a timing diagram which is shown in Figure 3 shows the application of power line testing to this circuit. The half of the circuit with inputs clocked by ϕ_1 may be tested by bringing the power line high during ϕ_1 . At the end of ϕ_1 , current is flowing in all inverters driven by floating nodes including the intentionally floating nodes clocked by ϕ_2 . If the power line retains the high value through the whole period of ϕ_2 , then the nodes clocked by ϕ_2 no longer float during ϕ_2 and the only remaining current during ϕ_2 is caused by floating nodes from open faults. The other half of the circuit with inputs clocked by ϕ_2 may be tested by shifting the modulation of the power line voltage to ϕ_2 . The current for a SPICE simulation of a CMOS process is shown on the bottom of Figure 3.

B. Domino logic

A simple stage of domino logic is shown in Figure 4. The test pattern and the current waveform for a SPICE simulation is shown in Figure 5. We find a current-sensitive propagation D-cube for the circuit between the open-fault node and the primary current output (complement inverter gate) which has a D entry matching the signal on

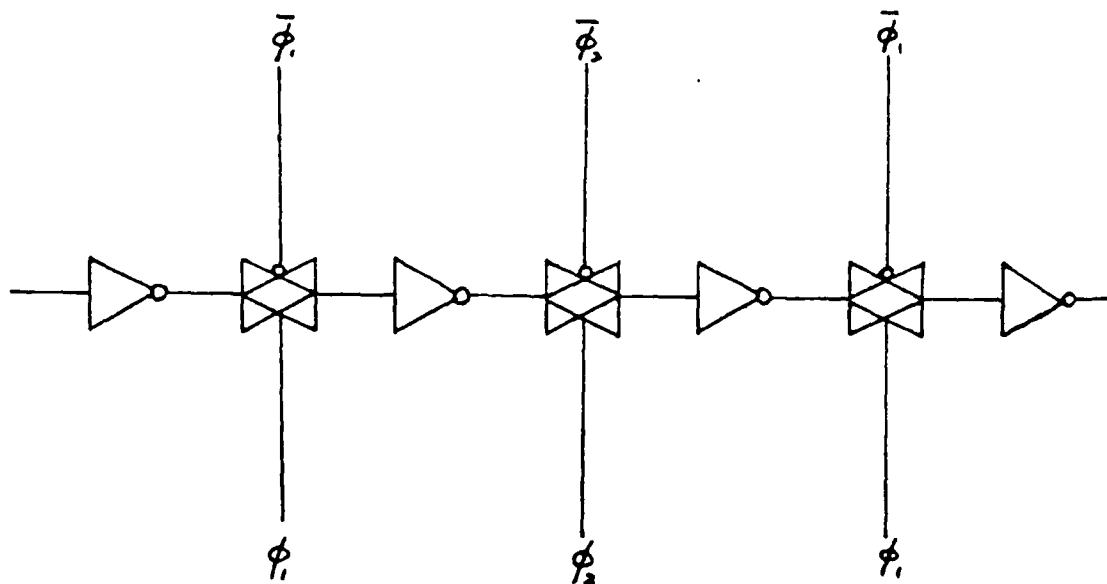


Figure 2. A dynamic CMOS shift register with a pseudo-two phase clocking scheme.

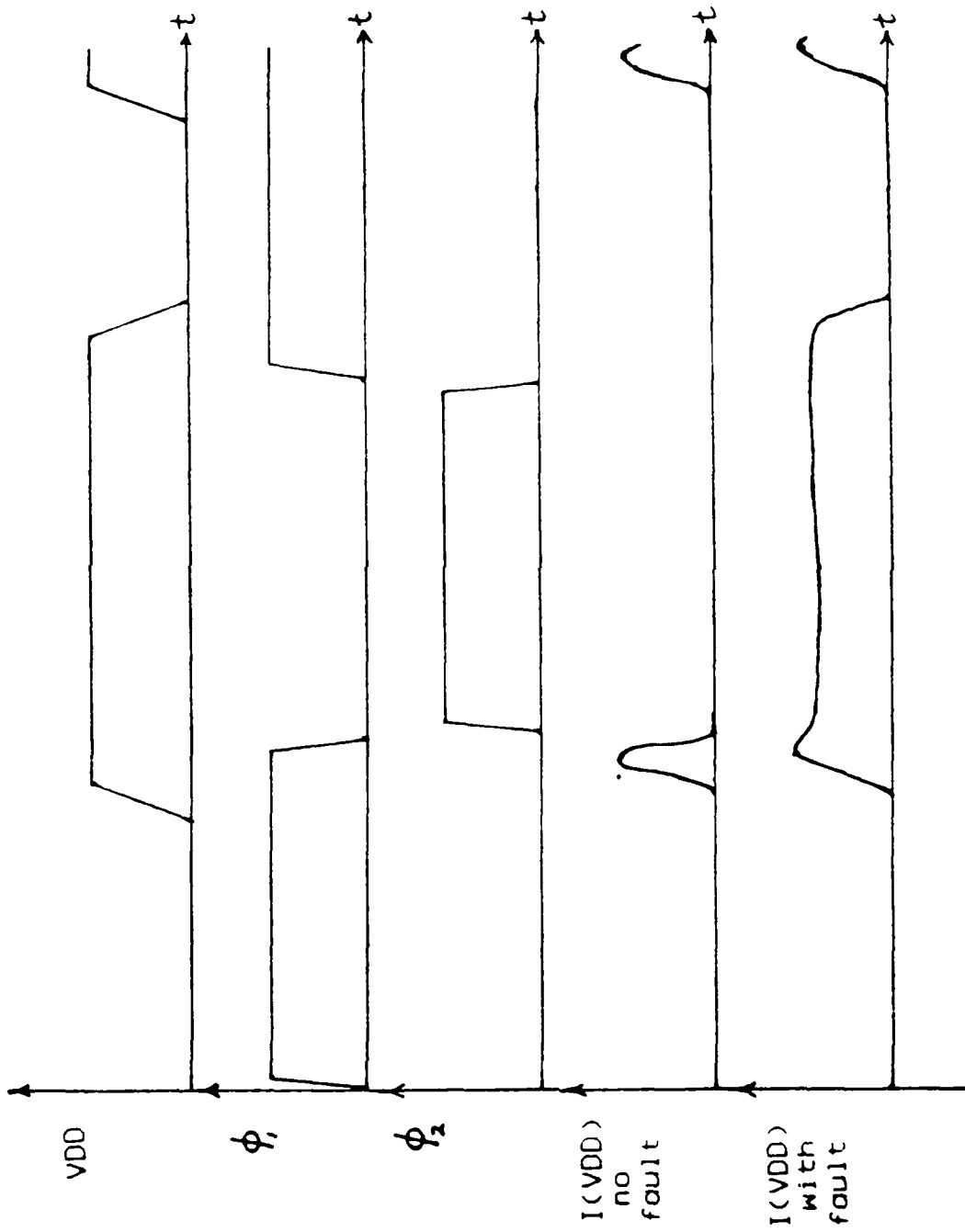
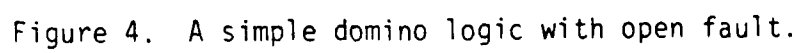


Figure 3. Waveforms for applying power line testing to the shift register.
 The currents were predicted by the SPICE simulations when given the voltage inputs.



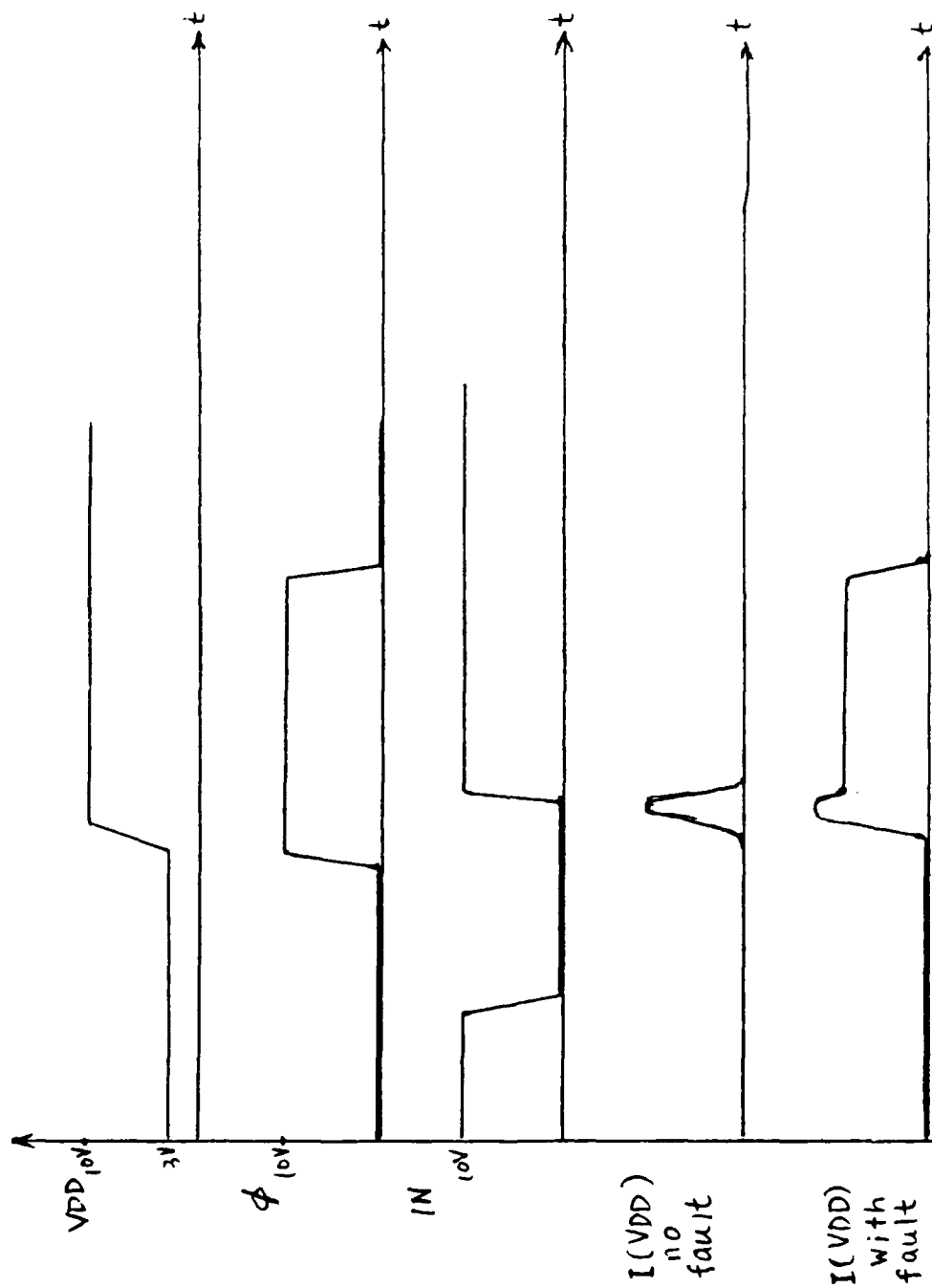


Figure 5. Waveforms for applying power line testing to the domino logic. The currents were predicted by the SPICE simulation when given the voltage inputs.

the fault node when a 0 is applied on input A. After modulating the power line, both dynamic gates, one with an open fault and one intentionally open, will cause excess current to flow through the driven inverters. After we change the signal on input A to 1, the intentionally open node will be connected. Thereafter, the remaining current is contributed only by the open fault.

IV TESTING DEMONSTRATION

One of our research objectives is to demonstrate the current-sensitive test scheme on integrated circuits fabricated with modern processing techniques to verify that a single fault may be detected over the leakage background current on the power input. We have laid out and simulated our design for a test chip. The test chip is composed of 32 test blocks, one decoder, and two long-chained shift registers. In each test block is an intentionally embedded single fault. The long shift registers provide overall background leakage current. We can selectively supply power to only one test block at a time, in addition to the long shift registers, by using the decoder such that excess current will just come from a single fault. The test blocks cover both the static and dynamic logic. The detail documentation of the test chip is provided in the appendix of this report.

V. CONCLUSIONS

While the current-sensitive testing has several advantages over the voltage-sensitive techniques, it does have some blind spots, such as faults in psuedo-nMOS logic, shorted output faults on pre-charge logic, and the combined short and open faults which cause the "floating" input to short with another gate output. This does point out that the current-sensitive method and the voltage-sensitive method do not totally replace each other but complement each other.

An integral combination scheme, if well developed, will provide us with more flexibility and more fault-coverage. However, the details of employing this hybrid scheme on general CMOS logic are not systemized yet.

We hope to be given the opportunity to continue this research. In particular, we propose to do the following:

- (1) To achieve the goal of demonstration, we need to have the test chip fabricated. All our theoretical discussion will be verified by this practical implementation.
- (2) Experimentally determine what capacitance ratios are really critical to the current-sensitive testing. This parameter will be a useful reference for IC designers.
- (3) Work out a new test generation algorithm which should efficiently take advantage of all available primary current or voltage output for the combination test scheme.

REFERENCES

- [1] L.G. Johnson, "Contribution of the value assignment problem to the complexity of test generation in combinational logic circuits and power line testing of CMOS digital logic circuits," Final Report 1987 USAF-UES Summer Faculty Research Program, Sept. 1987.
- [2] R.L. Wadsack, "Fault modeling and logic simulators of CMOS and MOS integrated circuits," Bell System Tech. J., Vol. 57, pp. 1449-1473, May-June 1978.
- [3] M.W. Levi, "CMOS is most testable," Proc. of 1981 Intl. Test Conf., pp. 217-220, Oct. 1981.
- [4] Yashwant K. Malaiya, et al. "Testability of VLSI Leakage Faults in CMOS," Rome Air Development Center, RADC-TR-83-202, Sept. 1983.
- [5] S.D. Sherlekar, et al. "Conditionally Robust Two-Pattern Tests and CMOS Design of Testability," IEEE Trans. CAD-7, pp. 325-332, March 1988.
- [6] Y.M. Elzig, et al. "Functional-Level Test Generation for Stuck-Open Faults in CMOS VLSI," Proc. of 1981 Intl. Test Conf., pp. 536-546, Oct. 1981.
- [7] A. MICZO, Digital Logic Testing and Simulation, Harper & Row, publisher. 1986.
- [8] H.H. Chen, et al., "Test Generation for MOS Circuits," in Proc. 1984 Intl. Test Conf., pp. 44-49.
- [9] K.J. Hsu, "Power Line Testing in CMOS Digital Circuits," ECEN 6050 Proposal, Oklahoma State University, May 1988.

Appendices can be obtained from
Universal Energy Systems, Inc.

RESEARCH INITIATION PROGRAM

Sponsored by the

AIR FORCE OFFICE OF SCIENTIFIC RESEARCH

Conducted by the
Universal Energy Systems, Inc.

FINAL REPORT

CHARACTERIZATION OF DETECTORS FOR OPTICAL PATTERN
RECOGNITION

Prepared by:	Samuel P. Kozaitis
Department:	Department of Electrical and Computer Engineering
University:	Florida Institute of Technology Melbourne, FL 32901
Period of Performance:	1 Jan 89-30 Dec 89
Contract No:	F49620-88-C-0053

Abstract

Two-dimensional sensors are examined for their use in optical pattern recognition. These devices may be fabricated with a variety of pixel sizes, on-chip circuitry and ever increasing sizes of arrays. The compatibility with semiconductor manufacturing allows large high-quality image sensing devices to be made.

The devices of interest here have applications to optical pattern recognition. In short, this application demands high-resolution two-dimensional devices with video frame rates and a reasonable cost to sample the output of an optical processing system. These types of devices commonly form the basis of camera systems.

There are primarily three technologies from which solid-state image sensors are fabricated. They are: diode array; charge injection (CID) array; and charge coupled array (CCD). These sensor technologies all have in common the principle of charge storage. The main difference between these sensors is their method of reading out information.

In order to select an image sensor for a particular application, the terms and quantities for characterizing sensors must be understood. Performance parameters used to characterize sensors are described.

Several high resolution arrays for optical pattern recognition are examined. They represent some of the latest and advanced devices. The best way to evaluate these sensors is simply use them. Evaluation board or supporting electronics should be purchased which take advantage of a particular array.

Table of Contents

1. Introduction
2. Solid state image sensors
 - 2.1 Charge storage
 - 2.2 Diode array
 - 2.3 Charge injection device (CID) array
 - 2.4 Charge-coupled device (CCD) array
3. Performance parameters
 - 3.1 Responsivity
 - 3.2 Charge to voltage conversion
 - 3.3 Spectral response
 - 3.4 Photoresponse non-uniformity
 - 3.5 Linearity
 - 3.6 Charge transfer efficiency
 - 3.7 Saturation voltage
 - 3.8 Dark signal
 - 3.9 Dynamic range
 - 3.10 Resolution (modulation transfer function)
 - 3.11 Antiblooming
 - 3.12 Output data rate
 - 3.13 Noise
4. Devices
 - 4.1 EG&G Reticon RA0256B (256x256 photodiode array)
 - 4.2 Texas Instruments TC213 (1024x512 CCD image sensor)
 - 4.3 Sony ICX018-K (510x492 CCD color image sensor)
 - 4.4 Thompson-CSF THX 31156 (1024x1024 CCD image sensor)
 - 4.5 Fairchild CCD 222 (488x380 CCD image sensor)
 - 4.6 Dalsa IA-D2-0512 (512x512 CCD image sensor) and IA-A3-0128 (128x128 wide dynamic range image sensor)
5. Conclusion

List of figures

- Figure 1 Photodiode structure
- Figure 2 One-dimensional photodiode array
- Figure 3 Two-dimensional photodiode array
- Figure 4 MOS photosensing device
- Figure 5 CID array
- Figure 6 Surface channel CCD array
- Figure 7 Buried layer CCD array
- Figure 8 Typical spectral response of image-sensing devices
- Figure 9 Spectral response of RA0256B
- Figure 10 Block diagram of EG&G Reticon RA0256B (256x256 photodiode array)
- Figure 11 Block diagram of Texas Instruments TC213 (1024x512 CCD image sensor)
- Figure 12 Block diagram of Sony ICX018-K (510x492 CCD color image sensor)
- Figure 13 Block diagram of Thompson-CSF THX 31156 (1024x1024 CCD image sensor)
- Figure 14 Block diagram of Fairchild CCD 222 (488x380 CCD image sensor)
- Figure 15 Block diagram of Dalsa IA-D2-0512 (512x512 image sensor)
- Figure 16 Block diagram of Dalsa IA-A3-0128 (128x128 wide dynamic range image sensor)
- Figure 17a Basic structure of the DYNASENSOR™ device b) potential profile c) equivalent circuit

1. Introduction

Image-sensing devices have become important elements in optical signal processing due to recent advances in technology. They convert optical information into electronic information which can be manipulated by a computer. The optical information is usually an image so that spatial, as well as intensity information is retained. Image-sensing devices are used to analyze or to sample the output of a optical system for display or for further processing. They may be used within a camera, frame grabber, or interfaced directly to an electronic circuit.

Image-sensing devices are used in a variety of applications such as astronomy, machine vision, and pattern recognition. The different requirement of these applications makes some image sensing devices better suited for a particular application than others. For example, for astronomical use a high-resolution array with a large dynamic range and a small dark current may be needed. This type of device may need to be cryogenically cooled and may not have the ability to be sampled at video rates. This type of sensor may not be suited to an environment where high-speed and binary data is needed. Other applications may need a particular type shape or size pixel. In some machine vision applications, circular or linear scanning is needed, or a large dynamic range is not required. Devices with a variety of characteristics are available due to the mature nature of the technology for fabrication.

Although image-sensing devices are available with a variety of specifications, they share a similar fabrication process. Furthermore, the fabrication of image-sensing devices is generally the same as for silicon integrated circuits. Devices may be fabricated with a variety of pixel sizes, on-chip circuitry and ever increasing sizes of arrays. The compatibility with semiconductor manufacturing allows large high-quality image sensing devices to be made.

The devices of interest here have applications to optical pattern recognition. In short, this application demands high-resolution two-dimensional devices with video frame rates and a reasonable cost to sample the output of an optical processing system. These types of devices commonly form the basis of camera systems. Linear arrays and circular arrays are not considered because their geometry. Furthermore, high resolution (2Kx2K) arrays for astronomy which need cryogenic cooling are also not considered. These devices are

very expensive, and need substantial support.

The three main technologies which image-sensing devices are fabricated from are discussed in the next section. The theory and major advantages and disadvantages are also discussed. A discussion of the performance parameters which are usually measured follows. Finally, a sampling of some of the latest devices are examined.

2. Solid state image sensors

There are primarily three technologies from which solid-state image sensors are fabricated. They are: diode array; charge injection (CID) array; and charge coupled array (CCD). These sensor technologies all have in common the principle of charge storage.

The main difference between these sensors is their method of reading out information. For example, the diode array technology multiplexes each signal charge into a common video line. The CID array injects charge into a sense node while the CCD array shifts the signal charge in series to an output sensing node.

2.1 Charge storage

An image sensing device basically consists of photosensitive elements and some drive circuitry. The photosensitive elements are usually photodiodes or MOS capacitors. In both elements, light is converted to charge by the same process. When a photon enters silicon, an electron-hole pair is generated. The electron is collected in the depletion zone of the diode or MOS device and the hole is recombined in the silicon substrate. Image sensing is performed by collecting and saving these electrons.

Charge-storage operation is based on the fact that charge is stored in the depletion layer of a p-n junction. A p-n junction is first reversed biased such that a charge accumulates in the depletion region. The junction is then open-circuited so the stored charge will decay at a rate proportional to the incident light intensity. In the dark, the generation-recombination current (dark current) discharges the charge in the depletion layer.

The light-generated current of a sensing device is directly proportional to the illumination level. That is to say, the amount of charge removed from the depletion region is proportional to the integral of light for a given amount of time. By monitoring the

amount of charge needed to refresh the depletion region, a signal proportional to the incident light may be obtained.

Two elements are needed to realize this process.

1. A charge-storage element is needed. In a diode array, a p-n diode is used. For CID or CCD arrays, a MOS junction is used.
2. A charge reset and sensing circuit.

2.2 Diode array

A photodiode structure is created by a n^+ region implemented in a p-type substrate. This process effectively creates a diode. The diode is reverse biased by depositing a polysilicon gate to create a depletion zone where electrons are to be separated from holes. A diagram of the geometry is shown in Fig.1. This device forms the basis of a diode image-sensing array.

The basic diode array device consists of a row of photodiodes and a shift register on a silicon chip. A one-dimensional array is shown in Fig. 2. A MOS transistor switch is located between each photodiode and the video line. The shift register contains all 0's and one 1. The 1 is shifted from one end of the the shift register to the other. The effect is that each MOS switch is turned on successively one at a time. When the switch is on, the photodiode is connected to the video line. The resulting video signal is a train of charge pulses, each having a magnitude proportional to the the light intensity on the respective photodiode. The same structured can be modified for two-dimensional operation.

Two-dimensional diode arrays with the resolution of commercial television cameras have been developed. These structures use two MOS switches for every photodiode in an array as shown in Fig. 3. A vertical shift register selects a single row and the row is read out exactly like the one-dimensional array. Additional rows are selected one at a time and each row is read out as before.

The main advantages and disadvantages of diode arrays are:

- (a) Full spectral response of silicon can be used due to the high quantum efficiency.
- (b) Ease of manufacturing due to the compatibility with MOS

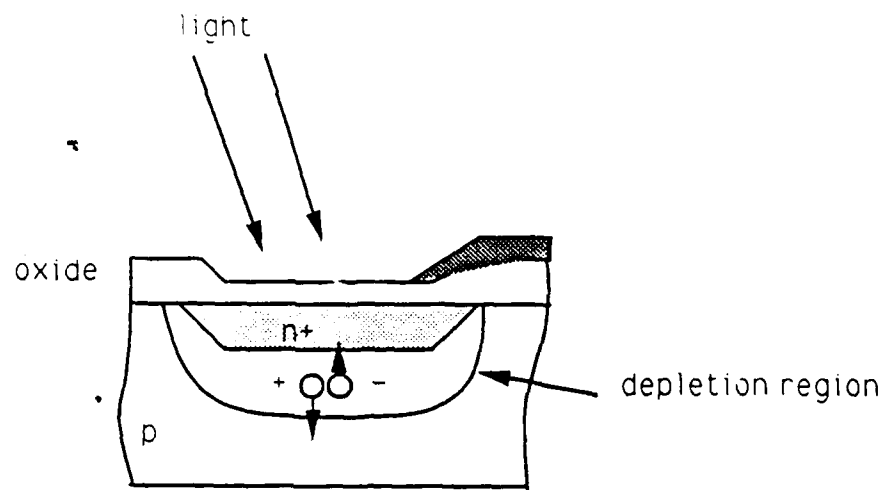


Figure 1 Photodiode structure

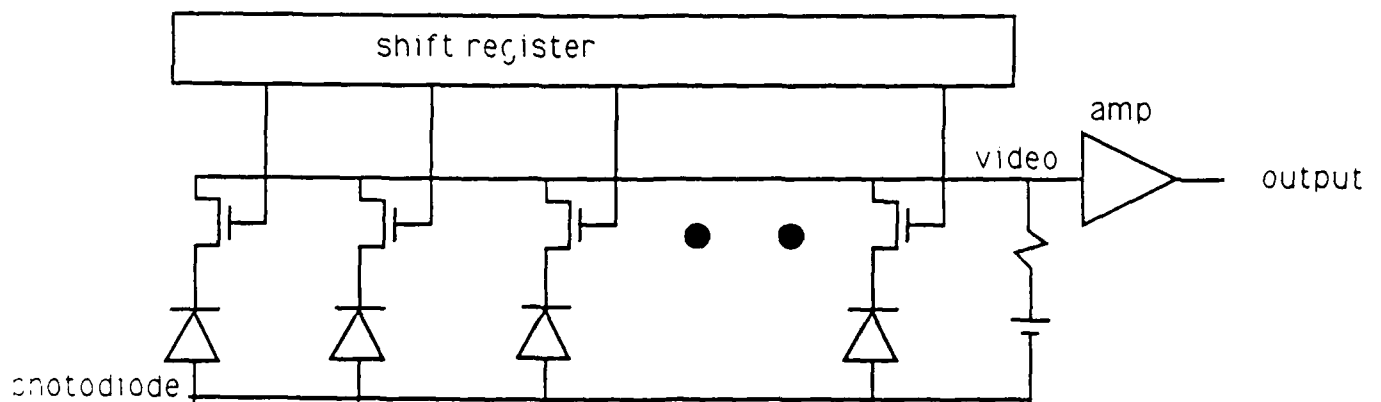


Figure 2 One-dimensional photodiode array

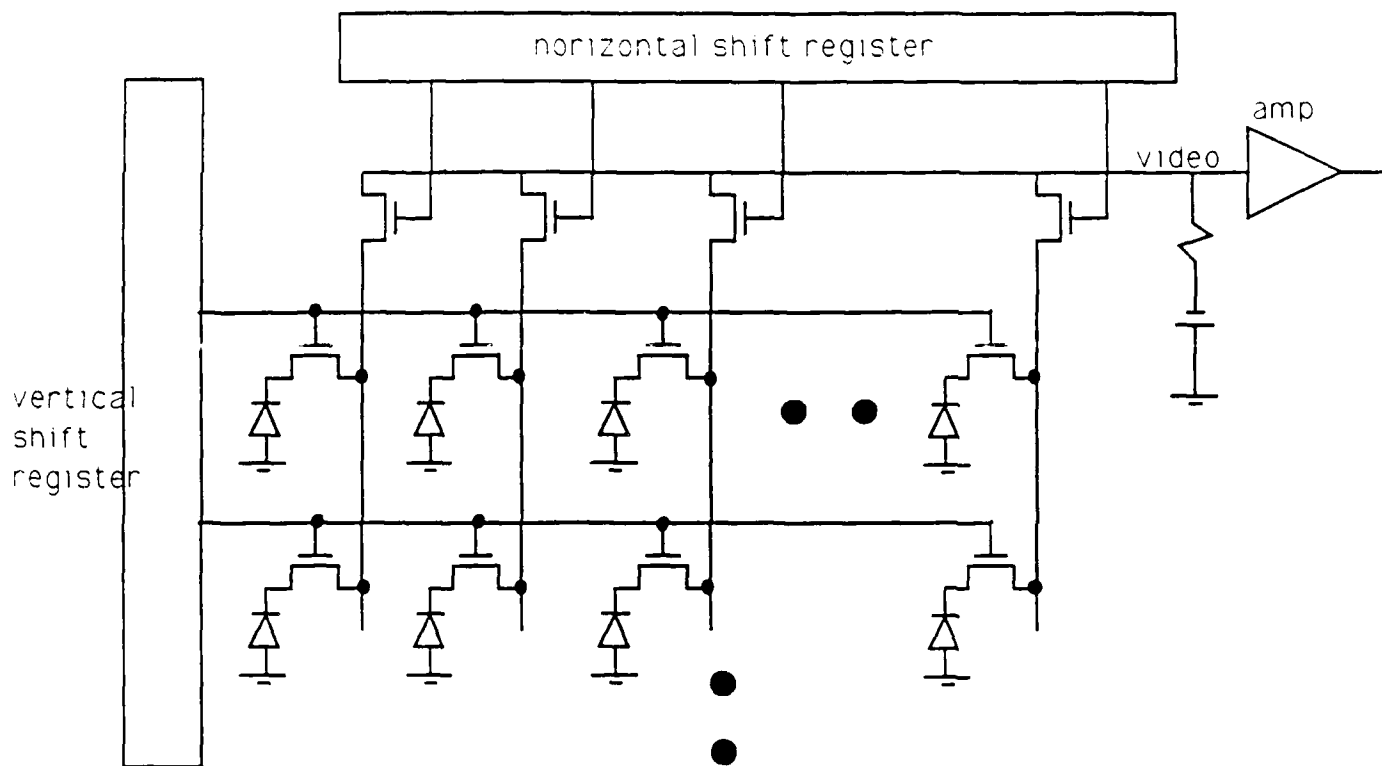


Figure 3 Two-dimensional photodiode array

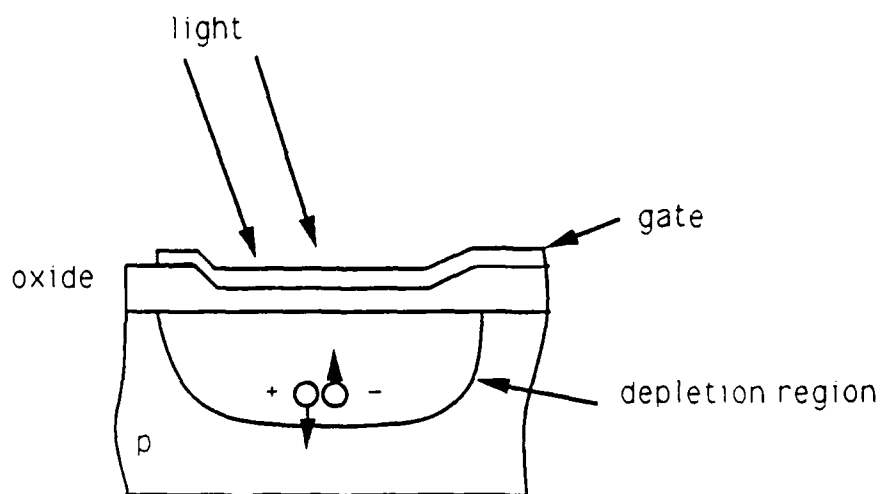


Figure 4 MOS photosensing device

technology.

(c) Low dark current.

(d) Flexibility of design due to the fact that the photodiode can be made in any shape.

(e) No smearing of shading problem resulting from charge transfer.

(f) Less of a blooming problem because diodes are isolated from each other.

(g) Entire active area is sensitive to light.

The disadvantages are:

(a) Fixed-pattern noise.

(b) Low level imaging difficult due to large video line capacitance.

2.3 Charge injection device (CID) array

A MOS capacitor is used as a photosensitive device in both CID and CCD arrays. In a MOS capacitor, the depletion region is induced by a polysilicon gate overlying a thin oxide layer. Charge accumulates in the inversion layer of the capacitor after electron-hole generation. The structure of a MOS capacitor is shown in Fig. 4.

In a CID array, the charge collected during illumination is stored in a potential well formed by two MOS capacitors. Such a structure is shown in Fig. 5. When the voltage is removed from only one of the electrodes, charge is transferred to the other potential well and is not injected into the substrate. The output signal results from measuring the charge transfer between the two storage capacitors at each sensing site of an array.

In a X-Y matrix format, the charge transfer along an entire row can be performed in parallel. After charge transfer, a row may be cleared by injecting the charge into the substrate. Alternatively, the injection may be omitted and the voltage reapplied to the row. This keeps the signal charge at the site and comprises a nondestructive readout operation.

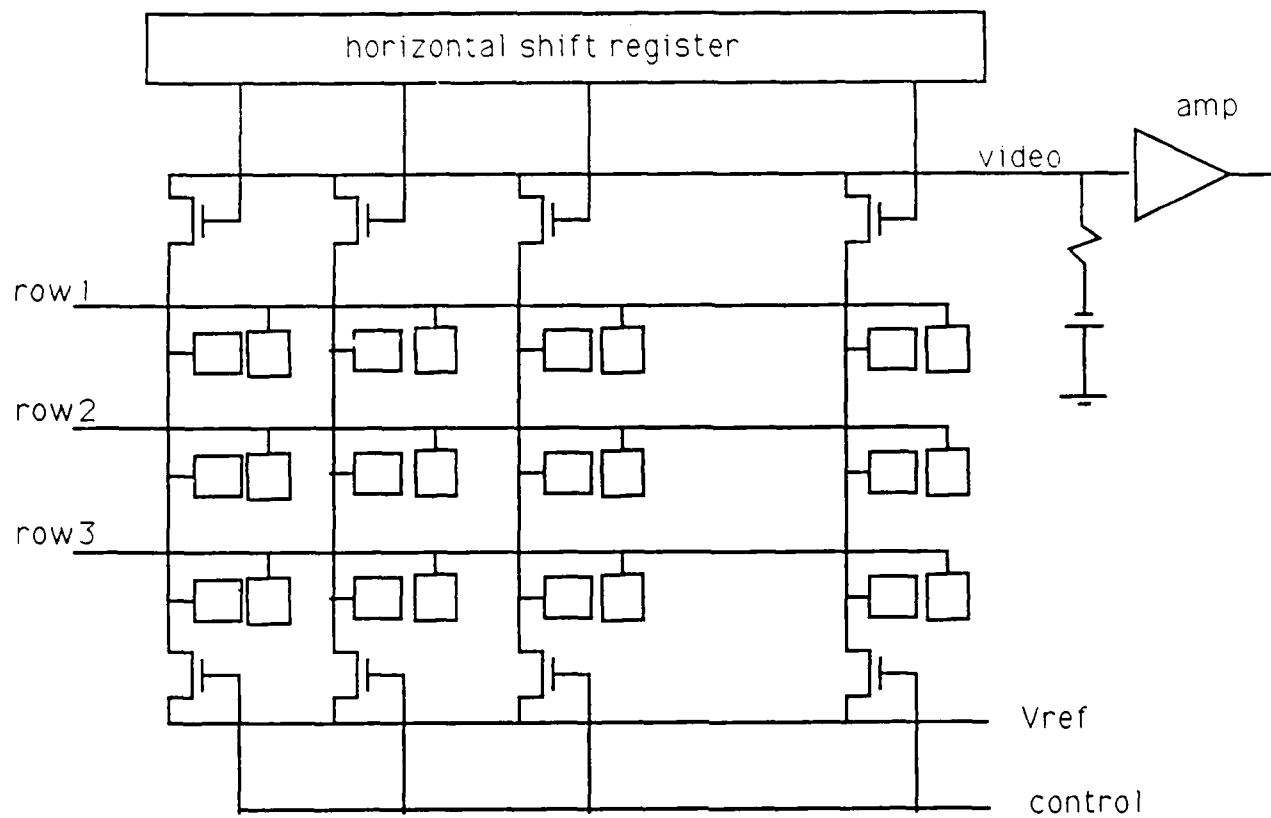


Figure 5 Two-dimensional CID array

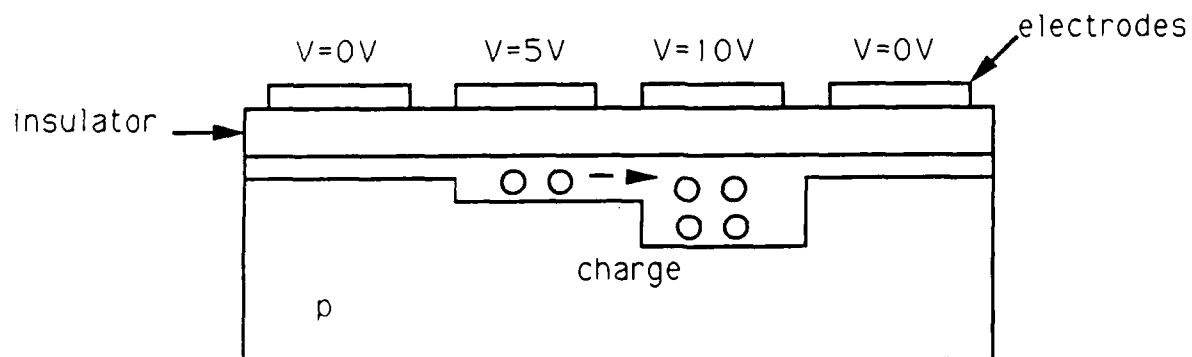


Figure 6 Surface channel CCD array

The readout operation of the CID is as follows. Both row and column lines are set to a reference voltage and the array is exposed to illumination. A row is read out by setting the common row electrode to zero. The charge is then transferred to the column electrode. The voltage on the column electrode changes in proportion to the amount of charge transferred. The voltage on each column line is then shifted out through the horizontal shift register through an amplifier.

Ultimately the charge in the array must be discharged through the substrate. The charge must recombine or be collected so it does not interfere with future readouts. Recombination is usually not suitable due to the relatively long lifetimes encountered in substrates. Therefore, most CID arrays are fabricated on epitaxial materials. An epitaxial junction lies under the entire array and acts as a buried collector for the array. If the thickness of the epitaxial layer is comparable to the distance between sensing sites, then the charge will primarily be collected in the reversed-biased epitaxial junction and cross-talk between sensing sites will be minimized.

The main advantages and disadvantages of diode arrays are:

- (a) Small blooming problem due to collection of charge in epitaxial structure.
- (b) Flexibility of operation such as both destructive and nondestructive readout mode.
- (c) Flexibility of design-can be implemented in a random access structure.
- (d) Low dark current.
- (e) No smearing of shading problem resulting from charge transfer.
- (f) Entire active area is sensitive to light.

The main disadvantages of CID arrays are:

- (a) Fixed-pattern noise.

- (b) Low level imaging difficult due to large video line capacitance.
- (c) Poor spectral response due to absorption of long wavelength photons by polysilicon gates.
- (d) Requires epitaxial structure which is not a standard MOS process.
- (e) Loss of sensitivity due to absorption of photons by epitaxial layer.

2.4 Charge-coupled device (CCD) array

CCD devices transfer the signal charge by manipulation of MOS potential wells. A CCD consists of closely spaced capacitors on an isolated surface of a semiconductor as shown in Fig. 6. When a voltage is applied to one of the electrodes, a potential well forms under the electrode. If two adjacent electrodes (capacitors) are turned on with the same voltage, a charge packet will evenly distribute underneath the electrodes.

Charge is moved under the electrodes by manipulating the voltages on the electrodes. There are a few different ways including multiple clocking schemes and/or different electrode geometry. Basically, the general operation is as follows. Consider three adjacent electrodes. With electrodes 1 and 2 on at the same potential, a charge packet evenly distributes underneath the electrodes. When electrode 1 is turned off, all the charge will appear under the electrode 2. To continue the process, electrode 3 is turned on. The charge evenly distributes itself between electrodes 2 and 3, and the process may continue as before. In this way, charge may be transferred along a device.

In most devices the charge is not actually moved along the surface of the Si-SiO₂ interface, but moved within the substrate. The Si-SiO₂ interface is usually avoided due to interaction of the charge and interface. When the charge transfer is moved away from the interface, transfer efficiency and noise is usually reduced. The result is a bulk-channel or buried-channel CCD as opposed to the surface-channel CCD. The buried-channel is created with an epitaxial layer or ion-implanted silicon layer of opposite polarity of

the substrate. A diagram of a buried-layer CCD is shown in Fig. 7.

In general, a CCD image sensor consists of isolated photosensors and a light-shielded CCD readout register. The photosensors are simply MOS capacitors. After illumination, the charge from the photosensors is shifted to a CCD shift register. The shift register begins to shift out the charge to an amplifier which produces an output signal. While the shift register is shifting out data, the photosensors are being illuminated with the next frame of data.

For an image-sensing CCD array, a frame-transfer structure is common. In this configuration, both a sensing and storage area is needed. After illumination, all the data in the photosensors are shifted into the light-shielded storage area. The information is then readout one row at a time while the photosensors are being illuminated. This method is also referred to as a TV mode frame transfer sensor. A full-frame frame transfer device does not have a storage area. The charge is shifted out directly from the photosensitive portion of the array.

The main advantages and disadvantages of CCD arrays are:

- (a) Low dark current.
- (b) Low-level light imaging due to low noise and high sensitivity.
- (c) Structure good for high resolution sensor integration.
- (d) Good spectral response for some devices.

The main disadvantages of CCD arrays are:

- (a) Larger blooming problem than other sensors.
- (b) Larger smearing problem than other sensors.
- (c) Less flexibility of design than other sensors.
- (d) Poor spectral response for some devices.
- (e) Requires more complicated fabrication process than other sensors.

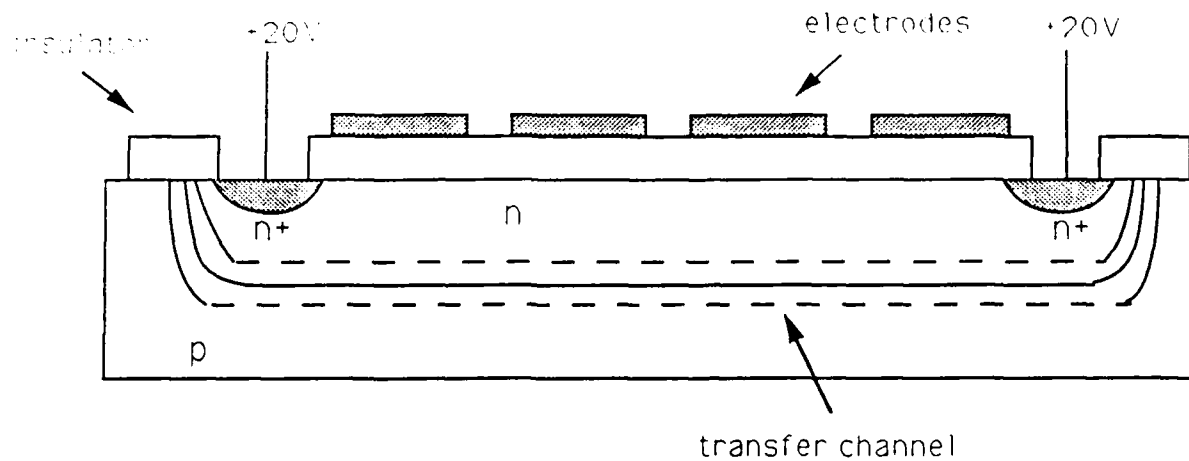


Figure 7. Buried channel CCD array

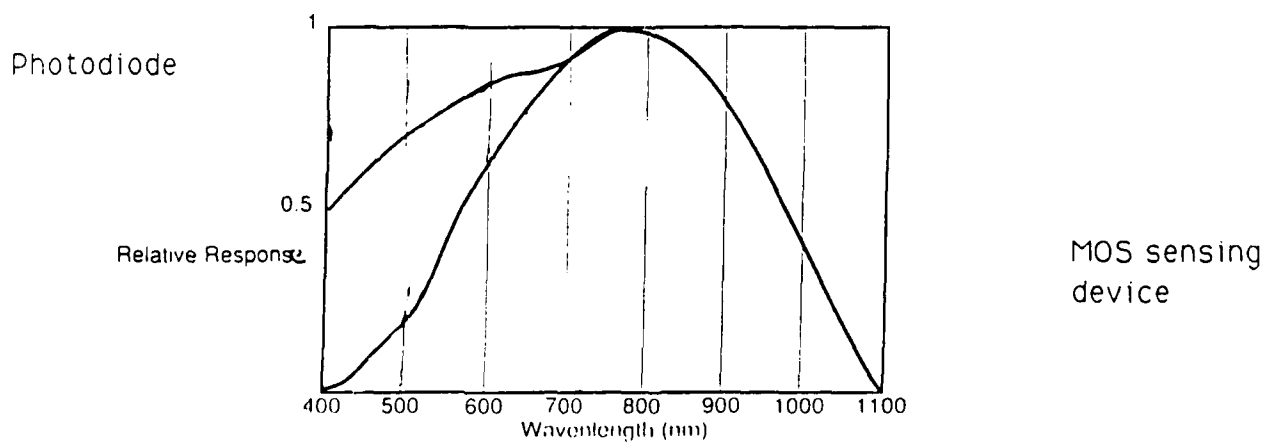


Figure 8 Typical spectral response of image-sensing devices

(f) Large dark current for buried channel devices.

3. Performance parameters

The ultimate goal of an image sensing device is to obtain a clean fast video signal within a particular spectrum range. With the aid of VLSI technology, high-resolution sensors can be made with impressive resolution. In order to select an image sensor for a particular application, the terms and quantities for characterizing sensors must be understood. Quantities used to characterize sensors are described in this section.

3.1 Responsivity

The responsivity R , is the ratio of the output voltage to the corresponding exposure ($\mu\text{J}/\text{cm}^2$). It is measured at $V_{\text{sat}}/2$. The quantum efficiency S , is defined as the ratio:

$$\frac{\text{number of carriers contributing to charge formation}}{\text{number of incident photons on pixel area}} \quad (1)$$

The quantum efficiency can depend on a few factors. For example, S is a function of wavelength. Furthermore, an entire pixel may be not be photosensitive due to the space used by the electronic circuitry. The pixel aperture is the ratio of the photosensitive area to the pixel area and affects S .

The quantum efficiency is related to the responsivity through:

$$R = nKA/hc \quad (\text{V}/\text{J}/\text{m}^2) \quad (2)$$

independent of integration time, where n is the quantum efficiency, K is a conversion factor discussed below, A is the pixel area, λ is the wavelength, hc is the product of Planck's constant and the speed of light.

CCD devices are well-suited to working at low-light levels which is very desirable. In general, the noise at room temperature generates a signal equivalent to about 100 electrons per/pixel with responsivity of $.5\text{V}/\mu\text{J}/\text{cm}^2$. CCD imagers usually work well in the range of 500-500,000 electrons/pixel. They also provide a good

response under low-level light conditions of 100-1000 electrons/pixel.

3.2 Charge to voltage conversion

The charge to voltage conversion factor (K) is determined by the readout amplifier. K is measured in $\mu\text{V}/e^-$ and is given as:

$$K=qG/C \quad (3)$$

Where q is the charge on an electron, G is the gain of the readout amplifier which is usually around .7 and C is the capacitance of the readout element. The relationship between the number of electrons and output voltage is $V_{out}=KN$, where N is the number of electrons/pixel.

3.3 Spectral response

The spectral response of an image-sensing device depends on the type of silicon substrate being used and the photosensing structure. The typical spectral response for a photodiode, MOS sensing device, and human eye is shown in Fig 8. The quantum efficiency of the two photosensing structures are nearly the same for wavelengths greater than 700nm (near-infrared). For wavelengths below 700nm, the response differs substantially, especially in the blue-light region.

Most of the solid state image-sensing devices are made from silicon. The general response is in the 400-1100nm range with a peak at around 750nm.

The distance from the surface of the device where electron-hole combinations are created is a function of wavelength. Longer wavelengths are absorbed deeper into the silicon. Above 1100nm, the photons do not have enough energy to be absorbed.

The shorter the wavelength, the closer to the surface photons are absorbed. Below 400nm the photons are absorbed very close to the surface where recombination times are short. Many carriers recombine before being collected in the depletion region.

The response of the MOS sensing device is lower in the blue region because of the polysilicon gates used as electrodes. Light must usually pass through these gates before entering the silicon. The blue response can be improved by making the electrodes thinner,

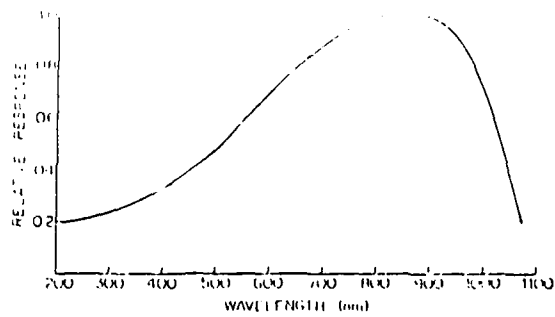


Figure 9 Spectral response of RA0256B

or by illuminating the device from the opposite (backside) side.

3.4 Photoresponse non-uniformity

The photoresponse non-uniformity is the peak-to-peak difference in response between the most and least sensitive elements with respect to the average response. This effect occurs because the charge collected from pixel to pixel may change across a device. The non-uniformity increases with increasing light intensity and is measured as a percentage of the output. This fact is caused by variations in geometry of different pixels. The geometry changes may be in any one of three dimensions including different layer thicknesses. The non-uniformity depends on the wavelength and sensing structure. In general, infrared light penetrates deeper into the silicon and exaggerates the effect.

The fixed pattern non-uniformity is independent of light intensity. It may also be referred to as fixed pattern noise and is usually measured in mV.

3.5 Linearity

The linearity of an image-sensing device is a measure of how well the output signal is proportional to exposure. The linearity, indicated by a gamma factor, is equal to one if the output signal is directly proportional to exposure. The linearity is usually close to one but can be limited by primarily the output amplifier nonlinearity, and the readout capacitance non-linearity. These factors usually result in non-linearity factors of less than 1%. When nearing saturation, the linearity is reduced rapidly.

Gamma is the value of the exponent in the following equation for two close points on the nonsaturated portion of the transfer function curve:

$$\frac{[\text{Exposure}(2)]^{\text{gamma}}}{[\text{Exposure}(1)]} = \frac{[\text{outputsignal}(2)]}{[\text{outputsignal}(1)]} \quad (4)$$

3.6 Charge-transfer efficiency

The charge transfer efficiency measures the percentage of charge transferred from one site to the next. In general the result is that the first pixels shifted out will have a greater resolution than that of the last ones shifted out. The charge transfer efficiency is usually a trade-off between the maximum operating frequency and gate length in CCDs. This fact occurs because the maximum clock frequency is inversely proportional to gate length. The result is that the pixel size may decrease to operate at high speed, but the efficiency also decreases.

3.7 Saturation voltage

Saturation is the condition in which further increases in exposure does not lead to a further increase in output signal. The saturation voltage is the maximum output signal voltage an image-sensing device can deliver. It is limited by the output amplifier, reset voltage, output capacitance, and storage capacitance of a photosensing element.

The maximum amount of charge a photosensing device depends on several interdependent factors. In general MOS devices can handle more charge than photodiodes and the larger the device the more charge it can hold. In short, the saturation level depends on photoelement capacity of output capacitance. Other factors such as clocking schemes, clocking voltages, and geometry affects the saturation voltage. The corresponding light level is the saturation exposure E_{sat} , the exposure is increased until the output voltage no longer increases.

3.8 Dark current

The dark signal is the video signal in the absence of any illumination. The dark current or signal is due to thermal generation of charges when the device is not illuminated. As the temperature increases, the dark current increases. The dark current doubles about every 10°C above 25°C . As the charge due to thermal generation increases, the room for signal charge decreases.

A dark signal is created during charge transfer between sites as well as within the site itself. A significant dark signal will accumulate if the clocking of the output is too slow. The dynamic range of a sensor is limit by the dark current and transfer

efficiency. Furthermore, the small area of a photosensing element may cause low levels of charge to be collected resulting in a low dynamic range.

3.9 Dynamic range

The dynamic range is defined as the ratio of the saturation voltage to the signal in the dark (temporal noise). The equation is expressed as:

$$\text{dynamicrange} = -20 \log \frac{[\langle \text{noise} \rangle]}{[V_{\text{sat}}]} \quad (5)$$

where $\langle \text{noise} \rangle$ is the mean noise signal, and V_{sat} is the saturation output signal.

An imaging device should have a low noise component to extend its low end of operation. It must also have the ability to detect high illumination levels without saturating. A larger dynamic range increases the number of gray levels its spatial resolution. The result is an increase in the quality of an image.

In CCD image sensors, an rms noise of 400 electrons and a saturating signal of 10^6 electrons gives a dynamic range of some quality devices of 2500:1. In some MOS image sensors the noise can be much higher such that the dynamic range is limited to about 300:1. Dalsa Inc. has developed a sensor with a logarithmic output which gives a dynamic range of 10^6 :1.

3.10 Resolution (modulation transfer function)

High resolution and a good modulation transfer function (MTF) is needed so fine detailed can be detected. The resolution of an image-sensing device is measured in terms of spatial frequency. An upper limit is the Nyquist frequency which is 1/2 of the distance between pixels. The value of the contrast of a pattern is reduced as the spatial frequency of the pattern increases. This is comparable to the MTF of a lens. The MTF is usually plotted as the contrast vs. f/f_N , where f is the spatial frequency, and f_N is the Nyquist frequency. In addition to the geometry of the sensing element, other factors contribute to the decrease of the MTF. They are: crosstalk, from the diffusion of charges between sensing sites, and transfer inefficiency, from transferring charges between sites.

3.11 Antiblooming

Blooming is the phenomenon of charges spilling over from one site to another. More specifically it is the condition in which charge is induced in an element by light incident on an adjacent element. It usually occurs due to a strong illumination signal caused by many factors such as exposure period and aperture setting. Blooming appears as a spot or streak on a monitor. Antiblooming is the ability of a device to prevent blooming. Blooming overload ratio is the blooming exposure relative to saturation exposure.

An antiblooming diode is often used to prevent blooming. Excess charge flows through this diode rather than spilling into another site. An antiblooming gate may determine the antiblooming level.

Many devices do not have a sufficient anti-blooming capability. A wide dynamic range can in effect improve the anti-blooming performance of a sensor.

3.12 Output data rate

The maximum output data rate of an image-sensing device is limited by internal circuitry or the output amplifier bandwidth. In addition, photodiodes have a phenomenon called lag which limits the data rate. Lag is the effect of having residue charges left in a diode after transferring the charge to another site.

Image sensing devices have an analogy with a DRAM (dynamic random access memory). Continuous high-frequency operational pulses must be supplied for capturing an image in the form of charge and transferring them. Fast frame reset or fast scan resetting is needed for new frame sensing.

Most image sensors have data rates of about 5 to 20 MHz. This usually allows for frame rates at video frequencies. For signal processing, higher rates up to 250 Mhz are sometimes required. The larger the size of the array, the faster the data rate needs to be to obtain video frame rates. Some larger arrays cannot achieve video frame rates.

Interlacing is used by some sensors. Interlacing is achieved by shifting the position of the odd and even field by one-half pixel height.

3.13 Noise

There are several kinds of noise which all contribute to the degradation of performance of the image-sensing device. Shot noise is due to the nature of light as is dominant at low illumination levels.

The temporal noise is the time-fluctuation of a signal of a pixel in the dark. It is usually given as an RMS value. The main contributions to temporal noise are from a variety of sources. Noise sources are from amplifier noise, charge transfer noise, and reset noise.

The fixed-pattern noise is the time-independent noise from fluctuations in the video signal. Dark signal fluctuations usually come from inhomogeneities in the substrate. Other contributions come from voltage transients associated with clocks, power supplies, or other external sources. Furthermore, the physical topology of the pixel area for image sensing caused undesirable optical noise. These effects limit the dynamic range of the sensor.

4.0 Devices

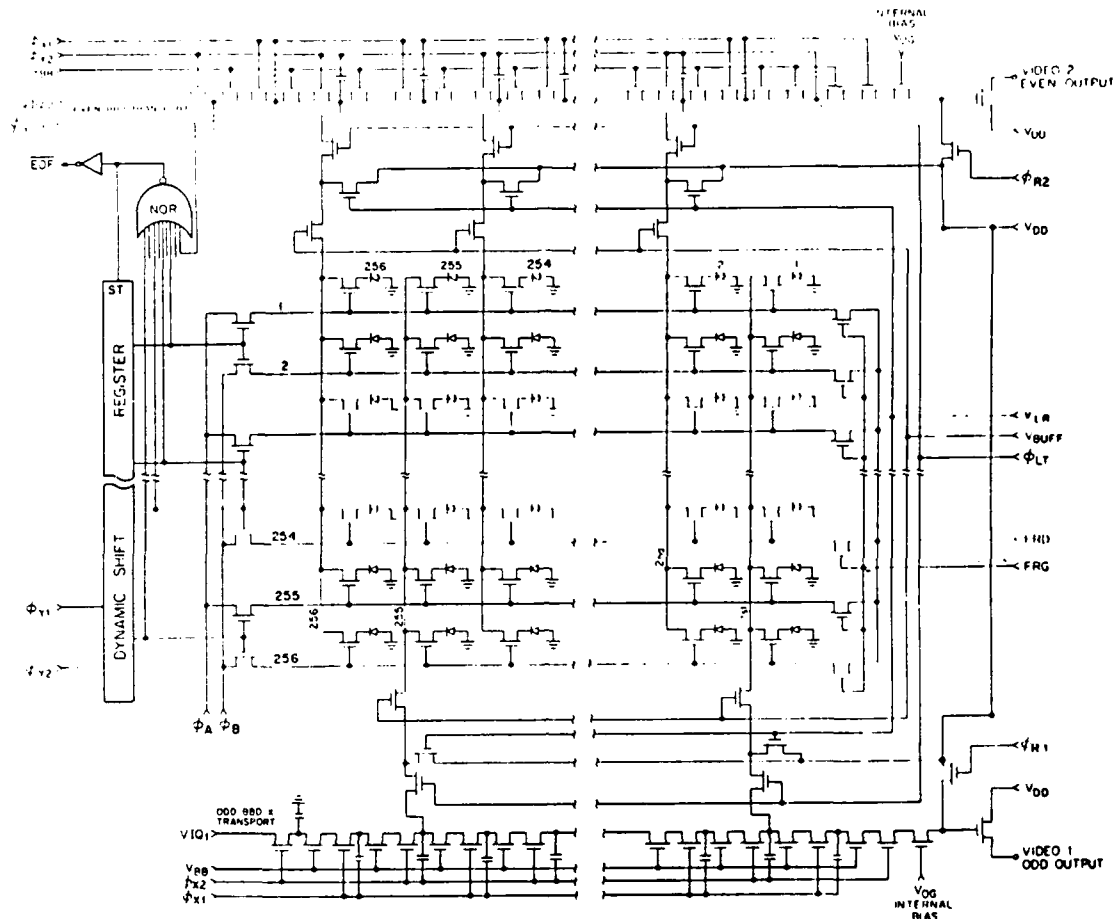
The following are data supplied by the manufacturer for several high resolution arrays for optical pattern recognition. They represent some of the latest and advanced devices.

4.1 EG&G Reticon RA0256B (256x256 array)

The RA0256B is a 256x256 photodiode array. The array does not require a surface electrode as in CCD arrays. The result is that there is no interference pattern or light loss from the electrode to decrease sensitivity. An entire line of information is loaded in parallel into an analog shift register. The data is then shifted out serially. This process is repeated 256 times to obtain an entire frame. Every other row can be shifted out to give interlace operation.

The device contains the diode array, access and reset switches, and horizontal and vertical read-out shift registers. The schematic diagram of the RA0256B adopted from the EG&G Image Sensing Products databook is shown in Fig. 10.

A shift register sequentially selects rows of diodes while two bucket brigade devices (BBD) select the columns. The shift register and BBD together process the signal. The shift register selects two rows, each of which is selected by an A or B clock. Transfer gates



Definition	Symbol
X Direction	ϕ_{X1}
Transport Shift Reg.	ϕ_{X2}
Y Direction	ϕ_{Y1}
Digital Shift Reg.	ϕ_{Y2}
Y Shift Reg. Reset	ϕ_{YST}
Line Transfer	ϕ_{LT}
Line Reset	V_{LR}
X Transport Input Bias Odd	V_{IQ1}
X Transport Input Bias Even	V_{IQ2}
Video Reset 2 (Even)	VR_1
Video Reset 2 (Even)	VR_2
Frame Reset Gate	FRG
Frame Reset Drain	FRD
Isolation Gate	$VBUFF$
DC Supply	V_{DD}
DC Current	I_{DD}
X Transport Tetraode Gate Bias	V_{GB}
Multiplex Clock	ϕ_A
Multiplex Clock	ϕ_B
Substrate Bias	V_{SUB}

Figure 10 Block diagram of EG&G Reticon RA0256B (256x256 photodiode array)

are used to load the BBD in parallel. One BBD obtains information from odd-numbered diode columns and the other BBD obtains information from even-numbered diode columns. The even video information is shifted a half cycle so that alternating odd and even signals are transferred to corresponding output ports.

Mechanical characteristics

Number of sensing elements: 65,536

X,Y center-to-center spacing: 40um

Sensing area: 912um²

Performance characteristics

Dynamic range: 100:1

Photoresponse non-uniformity: $\pm 10\%$

Average dark signal: 1%

Responsivity: 4 V/uj/cm²

Saturation output signal (Vsat): 1.6V

Output impedance: 1K Ω

Video sample rate: 2Mhz

Frame rate: 30hz

The spectral response is shown in Fig. 9.

4.2 Texas Instruments TC213 (1024x512 CCD image sensor)

The TC213 is a frame-transfer CCD image sensor with 12um square pixels. The image area contains 510 active lines with 1000 active pixels per line. Two additional dark reference lines give a total of 512 lines, and 24 dark reference pixels per line give a total of 1024 pixels per line.

Charge generated in the image area is transferred to a storage section in less than 500ns. This storage area is protected from exposure to light by an aluminum shield.

After an image is captured, it is readout by transferring charge, one line at a time into two registers. One register clocks out charge generated in odd-numbered column while the other register clocks out charge generated in even-numbered columns. The typical register transfer data rate is 10Mpixels/sec. The two registers can provide a data rate of 20Mpixels/sec when combined off chip. An output of 30 frames per second is typical.

The antiblooming protection is activated by supplying clocking pulses to the antiblooming gate, which is an integral part of each image sending element. Figure 11 shows the functional block diagram and the pin functional description of the TC213. Figure 11 was adopted from the Texas Instruments data sheet.

Mechanical characteristics

Number of sensing elements: 510,000

Sensing area: $144\mu\text{m}^2$

Pixel size: $12\mu\text{m} \times 12\mu\text{m}$

Performance characteristics

Dynamic range: 60db

Charge conversion: $6\mu\text{V}/e$

Gamma: .98

Photoresponse non-uniformity: $\pm 15\%$

Average dark signal: 5mV

Saturation output signal: .39V

Sensitivity: 518 mV/lx

Output impedance: $.6\text{K}\Omega$

Video sample rate: 10Mhz

Frame rate: 30hz

Antiblooming control

4.3 Sony ICX018-K (510x492 CCD color image sensor)

The Sony ICX018-K is an interline transfer CCD image device for NTSC color TV systems. Little information could be found on this device other than the specifications found in the data sheet. A block diagram of the device is shown in Fig. 12 which was taken from the data sheet.

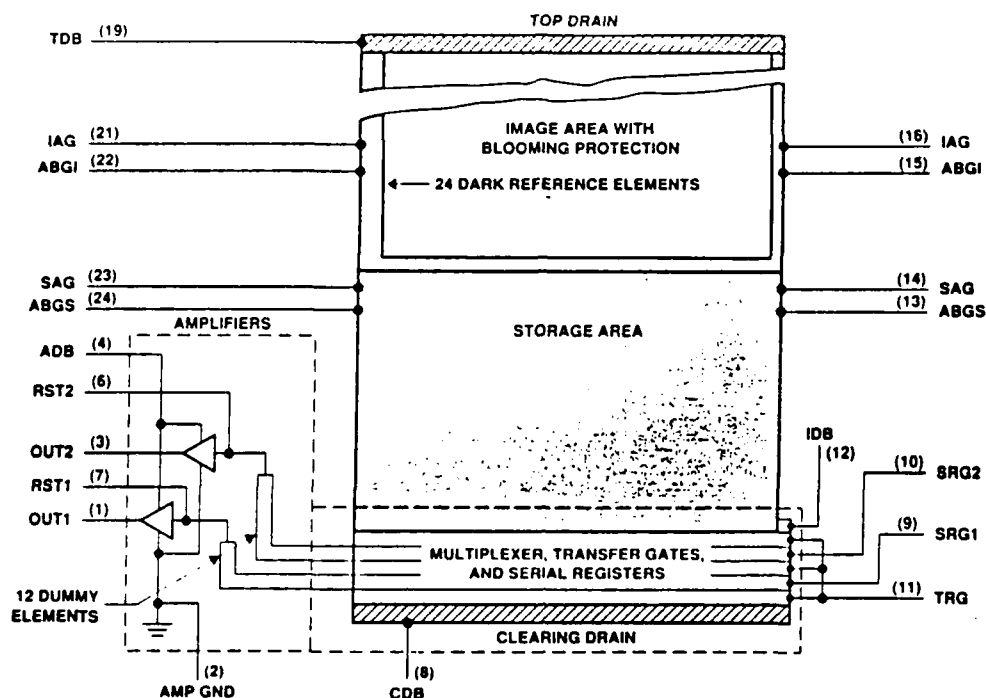
Mechanical characteristics

Number of sensing elements: 250,920

$17\mu\text{m}(\text{H}) \times 13\mu\text{m}(\text{V})$

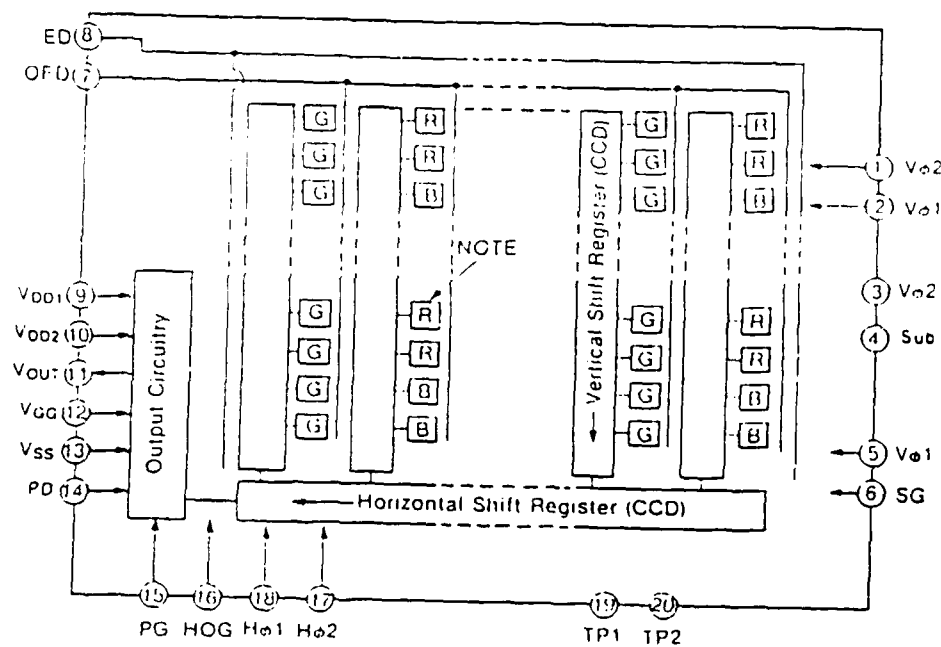
Sensing area: $221\mu\text{m}^2$

functional block diagram



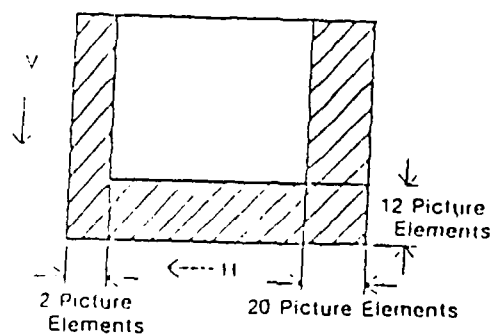
PIN	NAME	NO	DESCRIPTION	INPUT/OUTPUT (I/O)
	ABG1 [†]	15	Antiblooming gate for image area	I
	ABG1 [†]	22	Antiblooming gate for image area	I
	ABGS [†]	13	Antiblooming gate for storage area	I
	ABGS [†]	24	Antiblooming gate for storage area	I
	ADB	4	Supply voltage for amplifier drain bias	I
	AMP GND	2	Amplifier ground	
	CDB	8	Supply voltage for clearing drain bias	I
	IAG [†]	16	Image area gate	I
	IAG [†]	21	Image area gate	I
	IDB	12	Supply voltage for input diode bias	I
	OUT1	1	Output signal 1	O
	OUT2	3	Output signal 2	O
	RST1	7	Reset gate 1	I
	RST2	6	Reset gate 2	I
	SAG [†]	14	Storage area gate	I
	SAG [†]	23	Storage area gate	I
	SRG1	9	Serial register gate 1	I
	SRG2	10	Serial register gate 2	I
	SUB [†]	5	Substrate and clock return	
	SUB [†]	17	Substrate and clock return	
	SUB [†]	18	Substrate and clock return	
	SUB [†]	20	Substrate and clock return	
	TDB	19	Supply voltage for top drain bias	I
	TRG	11	Transfer gate	I

Figure 11 Block diagram of Texas Instruments TC213 (1024x512 CCD image sensor)



NOTE:  Photodiode

Layout of Optical Black Spots



No.	Symbol	Description	No.	Symbol	Description
1	Vφ4	Vertical register transfer clock input	11	Vout	Signal output
2	Vφ3	"	12	VGG	Output amplifier gate bias
3	Vφ2	"	13	VSS	Output amplifier source bias
4	SUB	Substrate	14	PD	Precharge drain bias
5	Vφ1	Vertical register transfer clock input	15	PG	Precharge clock input
6	SG	Sensor gate bias	16	HOG	Horizontal register read out control bias
7	OFD	Antiblooming bias	17	Hφ2	Horizontal register transfer clock input
8	ED	Edge drain bias	18	Hφ1	"
9	VDD1	Power supply	19	TP1	Test pin
10	VDD2	"	20	TP2	"

Figure 12 Block diagram of Sony ICX018-K (510x492 CCD color image sensor)

Performance characteristics

Dynamic range: 50db

Gamma: 1

Photoresponse non-uniformity: 11%

Non-uniformity between color signals: 8%

Dark signal: 14mV

Sensitivity: 110 mV

Saturation signal (Vsat): 530mV

Frame rate: 30hz

Antiblooming control

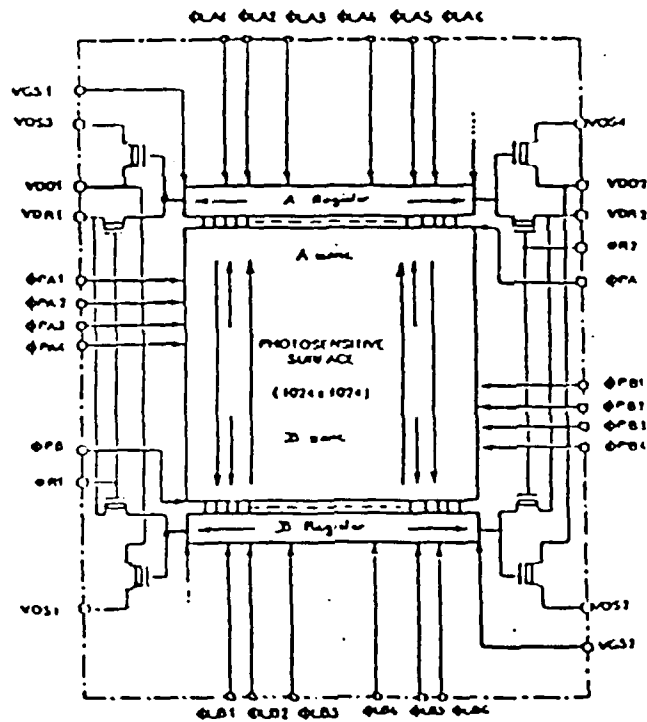
4.4 Thompson-CSF THX 31156 (1024x1024 CCD image sensor)

The THX 31156 is a 1024x1024 CCD image sensor with a frame transfer organization for single-field operation without a memory zone. There are 1024x1024 active elements with several additional blank elements at the beginning and end of each line to establish a dark reference.

The pixels are square with dimensions 19umx19um. They have an aperture of 100% but do not have antiblooming capability.

The THX 31156 has two readout registers, one on each side of the device. These registers each have two outputs, one on each side. These outputs allow one fourth an image to be readout. The driving signals are designed such that the entire image may be readout by one, two, or four outputs.

An image may be readout in three ways. In mode 1, the entire image is readout line by line (lines 1 to 1028)-the useful lines are lines 3 to 1026. In mode two, the top half and the bottom half of the image is readout at different outputs. Lines 1 to 514 (1 to 512 are useful) are readout one output, and lines 1028 to 515 are readout another output (lines 1026 to 515 are useful). In mode three, the same lines as in mode 2 are used; but, some pixels of the line are readout of one output and other pixels are readout another. useful pixels 1 to 512 are readout of two outputs, and useful pixels 1024 to 513 are readout two other outputs.



Pin	Symbol	Function
1	VCS1	Package body and package contact
2	VCS2	Video output signal 2
3	VCS3	Drain supply 3
4	VCS4	Transfer gate clock (B zone)
5	VCS5	Readout shift register gate voltage 2
6	VCS6	Readout shift register gate voltage 2
7	VCS7	Reset clock 2
8	VCS8	Reset transistor drain voltage 2
9	VCS9	Reset transistor drain voltage 2
10	VCS10	Temperature test 2
11	VCS11	Video output signal 4
12	VCS12	Video output signal 4
13	VCS13	Serial transfer phase 2 (A side register)
14	VCS14	Serial transfer phase 2 (A side register)
15	VCS15	Parallel transfer phase 2 (A zone)
16	VCS16	Parallel transfer phase 2 (A zone)
17	VCS17	Serial transfer phase 2 (A side register)
18	VCS18	Serial transfer phase 2 (A side register)
19	VCS19	Parallel transfer phase 2 (A zone)
20	VCS20	Parallel transfer phase 2 (A zone)
21	VCS21	Serial transfer phase 2 (A side register)
22	VCS22	Serial transfer phase 2 (A side register)
23	VCS23	Video output signal 3
24	VCS24	Video output signal 3
25	VCS25	Drain supply 1
26	VCS26	Transfer gate clock (A zone)
27	VCS27	Readout shift register gate voltage 1
28	VCS28	Readout shift register gate voltage 1
29	VCS29	Reset clock 1
30	VCS30	Reset transistor drain voltage 1
31	VCS31	Reset transistor drain voltage 1
32	VCS32	Temperature test 1
33	VCS33	Video output signal 1
34	VCS34	Video output signal 1
35	VCS35	Serial transfer phase 1 (B side register)
36	VCS36	Serial transfer phase 1 (B side register)
37	VCS37	Parallel transfer phase 1 (B zone)
38	VCS38	Parallel transfer phase 1 (B zone)
39	VCS39	Serial transfer phase 1 (B side register)
40	VCS40	Serial transfer phase 1 (B side register)
41	VCS41	Parallel transfer phase 1 (B zone)
42	VCS42	Parallel transfer phase 1 (B zone)
43	VCS43	Serial transfer phase 1 (B side register)
44	VCS44	Serial transfer phase 1 (B side register)

Figure 13 Block diagram of Thompson-CSF THX 31156 (1024x1024 CCD image sensor)

Mechanical characteristics

Number of sensing elements: 1,048,576

Pixel size: 19 μ m \times 19 μ m

Sensing area: 361 μ m²

MTF: .7 at 26 lp/mm

Performance characteristics

Quantum efficiency: 40% at 700nm

Responsivity: 3.3 V/ μ J/cm²

Charge conversion: 1 μ V/e

Average dark signal: 1nA/cm²

Dark signal uniformity: 300mV

Video sample rate: 40Mhz

Frame rate: 30hz

4.5 Fairchild CCD 222 (488x380 CCD image sensor)

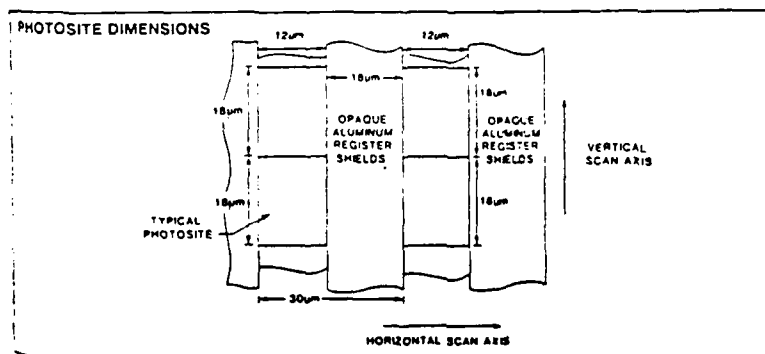
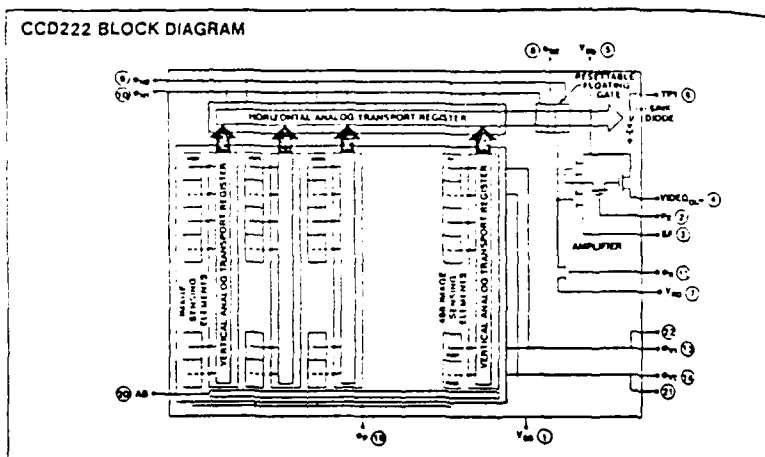
The CCD222 is a 488x380 element CCD area image sensor for use in TV compatible systems. It is arranged as a matrix of standard TV aspect ratio size pixels (4:3) so that the pixels are not square. The functional block diagram of the CCD222 adopted from the Fairchild databook is shown in Fig. 14.

Photons pass through a transparent polysilicon gate and are absorbed in the substrate. Electrons are collected at the photosites during the integration period.

The architecture of the CCD222 provides video information in two sequential fields of 244 lines each. At the end of an integration period, information from odd-numbered sites are transferred to the vertical transport registers for an odd-field readout. Data is then transferred line by line into the horizontal output register. The same process is then repeated to read out even-numbered sites.

The horizontal output register (horizontal analog transport register in Fig. 14) is a 285 element, two-phase register which receives data from the vertical transport registers line by line. After each line of information is moved to the horizontal register, it is moved through the output amplifier.

The resultant video output signal is a analog signal representing the spatial distribution of the exposure level at the sensor surface.



Symbol	Parameter	Range			Unit	Remarks
		Min	Nom	Max		
V_{oPL}	Photogate Clock LOW	-6.0	0.0		V	Note 2, 8
V_{oPH}	Photogate Clock HIGH	3.0	5.0	7.0	V	Note 2
V_{oSEL}	Bias Electrode of FGA Clock LOW	-3.0	0.0	0.0	V	
V_{oEDH}	Bias Electrode of FGA Clock HIGH	0.0	5.0	7.0	V	Note 1
V_{oH1L}	Horizontal Transport Clock LOW	-5.0	0.0	0.0	V	Note 3
V_{oH1H}	Horizontal Transport Clock HIGH	5.0	10.0	12.0	V	Note 1, 3
V_{oV1L}	Vertical Transport Clock LOW	-6.0	0.0	0.0	V	Note 2, 9
V_{oV1H}	Vertical Transport Clock HIGH	5.0	7.0	12.0	V	Note 4
V_{oSL}	Sample-and-Hold Clock LOW	-3.0	0.0	0.0	V	
V_{oSH}	Sample-and-Hold Clock HIGH	3.0	5.0	7.0	V	
V_{oRL}	Reset Clock LOW	-6.0	0.0	0.0	V	
V_{oRH}	Reset Clock HIGH	5.0	7.0	12.0	V	
f_{oH1}	Horizontal Transport Clock Frequency		7.2	20.0	MHz	Note 5

Symbol	Parameter	Range			Unit	Remarks
		Min	Nom	Max		
V_{DD}	DC Supply Voltage	12.0	15.0	16.0	V	
V_{AB}	Anti-Blooming Bias Voltage		12.0		V	
V_{REF}	Source of Floating Gate Amplifier	4.0	7.0	10.0	V	Note 1
V_{SD}	Reset Drain Voltage		4.0		V	
TP_1	Test Point		V_{DD}		V	
TP_2, TP_4	Test Points		0.0		V	
TP_3	Test Point		V_{AB}		V	Note 10
I_{DD}	DC Supply (V_{DD}) Current		35		mA	
I_{SP}	Current at Pin SP		50		µA	

Figure 14 Block diagram of Fairchild CCD 222 (488x380 CCD image sensor)

Mechanical characteristics

Number of sensing elements: 185,440

X,Y center-to-center spacing: 30umH, 18umV

Pixel size: 12umH, 18umV

Sensing area: 216um²

Performance characteristics

Dynamic range: 1000:1

Gamma: 1

Saturation output signal: 700mV

Output impedance: 1K Ω

Video sample rate: 20Mhz

Frame rate: 90hz

Antiblooming control

4.6 Dalsa IA-D2-0512 (512x512 CCD image sensor) and IA-A3-0128 (128x128 wide dynamic range CCD image sensor)

Dalsa Inc. has gained attention for fabricating CCD arrays with a wide dynamic range ($>10^7$). Only some of their products claim this type of performance. A largest image sensing device made by Dalsa (part no. IA-D2-0512) is a 512x512 CCD array. Its dynamic range is about 2000:1. A schematic diagram of the device is shown in Fig. 15. An image sensing CCD array with a dynamic range of 10^6 :1 is available in a 128x128 array (part no. IA-A3-0128). Its schematic diagram is shown in Fig. 16.

The devices with the wide dynamic range are ones that use a photodetector developed by Dalsa Inc.. Some image sensing devices are use this detector called the DYNASENSOR™, which is responsible for the large dynamic ranges of their devices. This photodetector device provides an analog signal of about 1-3V when the incident optical intensity varies over a range of 10^6 . The DYNASENSOR™ has been used in several linear arrays, but only one two-dimensional array.

The basic structure of the DYNASENSOR™ device is shown in Fig. 17a. The potential profile is shown in Fig. 17b, and the equivalent circuit is shown in Fig. 17c. The sensor is basically a photodiode in series with a MOS transistor where the transistor is biased as

$V_{ds}=V_{gs}$ on the edge of saturation. The characteristics of this biasing arrangement do not look like typical curves for V_{gs} . Instead, they resemble the logarithmic curve of a forward biased diode.

Light incident on the photodiode portion of the sensor generates a current like most photodiodes. The current is injected under the gate region of the MOS transistor in Fig. 17a. The injection of carriers is a natural logarithmic process which causes the voltage across the photodiode to change logarithmically. For a wide range of incident intensity, the output will change by only a few volts.

IA-A3-0128 128x128 wide dynamic range sensor

The IA-A3-0128 is a wide dynamic range image sensing device with 128x128 pixels. The output is logarithmic with respect to input light intensity at high light intensities and linear at low light levels. It has square 50um pixels. The response of the photoelements can be controlled by the user by variation of the photoelement clock and bias voltages to give the desired response.

A CCD shift register is located adjacent to the sensors as shown in Fig. 16. Charge is transferred into the shift register in parallel and each shift register is readout one line at a time.

Mechanical characteristics

Number of sensing elements: 16,384

Pixel size: 50um x50um

Sensing area: 250um²

Performance characteristics

Dynamic range: 100,000:1

Saturation output signal: 500mV

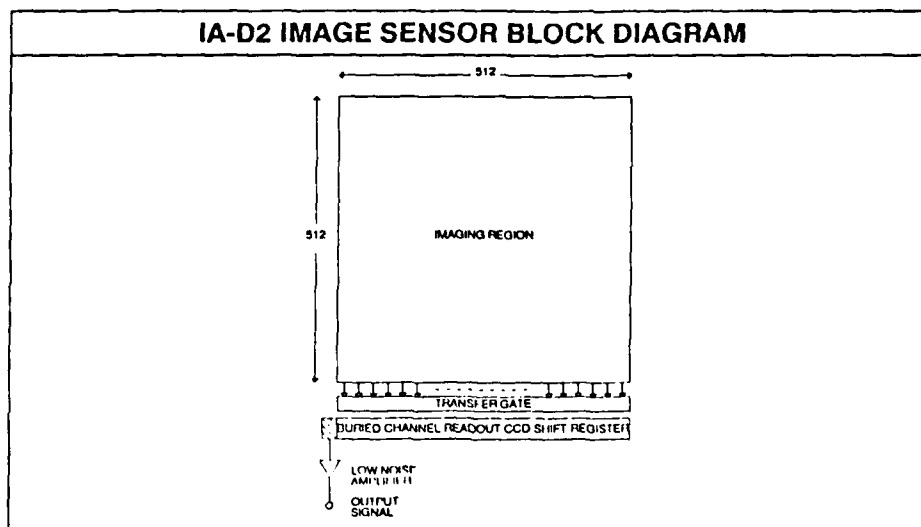
Uniformity: 10%

Saturation voltage: .5V

Output noise voltage: .075V

IA-D2-0512 (512x512 CCD image sensor)

The IA-D2-0512 is a 512x512 element image sensing array. It is designed for output data rates of 16Mhz. It has square pixels of 10umx10um. The linear output has a dynamic range of 2000:1 which is more than many other manufacturers but not near the wide dynamic range of the DYNASENSOR™ devices. The device is readout



IA-D2 PIN FUNCTIONAL DESCRIPTION		
PIN	SYMBOL	NAME
1	CI1	Image Region Clock, phase 1
2	CI2	Image Region Clock, phase 2
3	CI3	Image Region Clock, phase 3
4	CI4	Image Region Clock, phase 4
5	VBB	Substrate bias
6	VSET	Output node set voltage
7	RST	Output node reset clock
8	VDD	Output node drain bias
9	VDD	Amplifier supply
10	OS	Output signal
11	VA	Amplifier bias
12	VSS	Ground reference
13	VBB	Substrate bias
14	CR2	Readout clock, phase 2
15	CR1	Readout clock, phase 1
16	TCK	Transfer clock
17	VBB	Substrate bias
18	VBB	Substrate bias
19	VBB	Substrate bias
20	VBB	Substrate bias
21	CI4	Image Clock, Phase 4
22	CI3	Image Clock, Phase 3
23	CI2	Image Clock, Phase 2
24	CI1	Image Clock, Phase 1

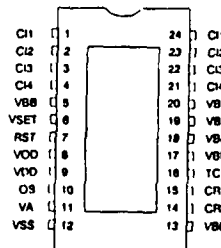


Figure 15 Block diagram of Dalsa IA-D2-0512 (512x512 image sensor)

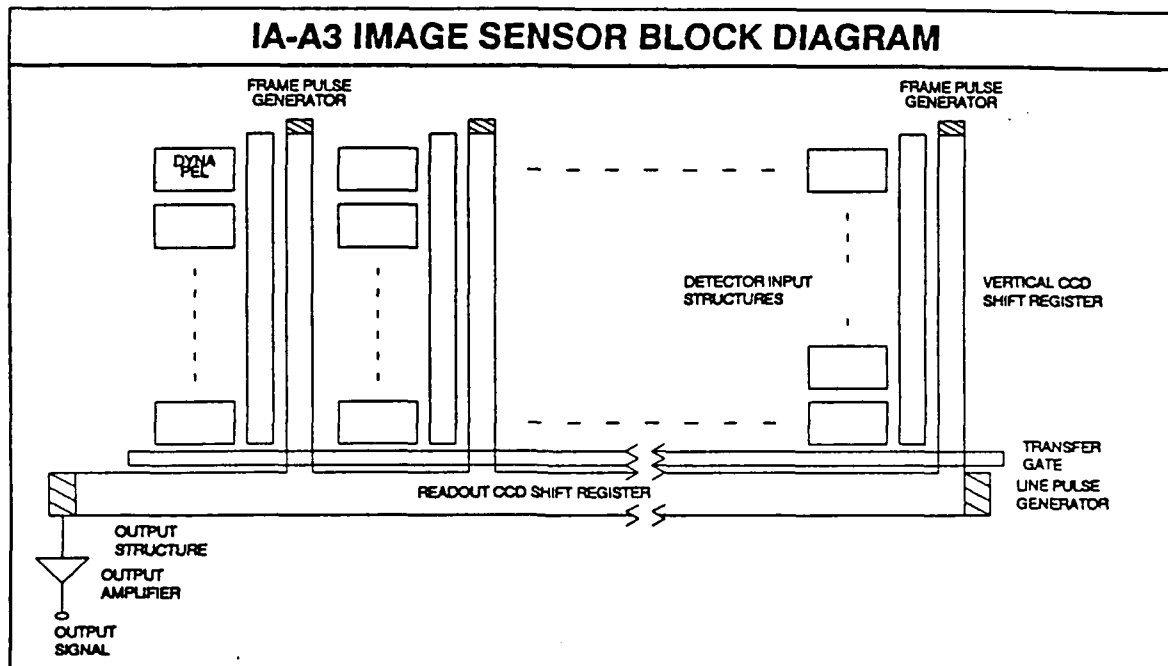


Figure 16 Block diagram of Dalsa IA-A3-0128 (128x128 wide dynamic range image sensor)

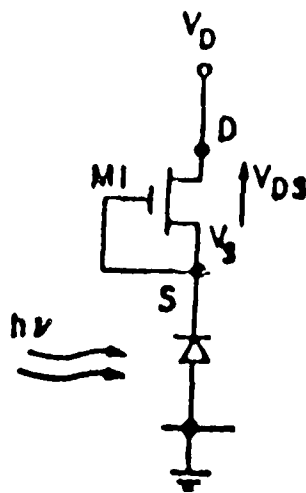
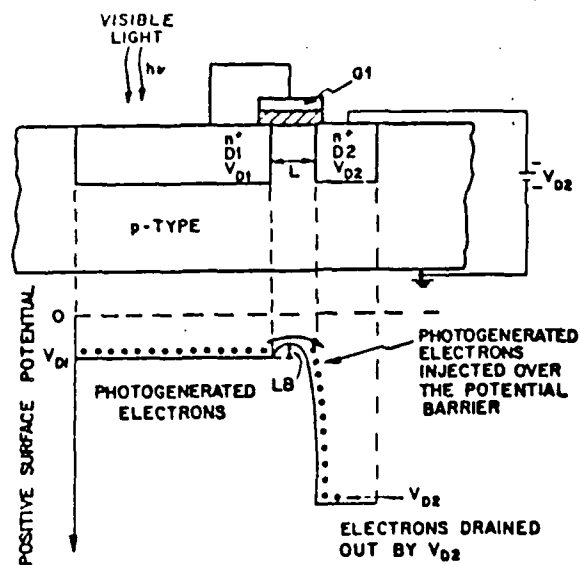


Figure 17a Basic structure of the DYNASENSOR™ device b) potential profile c) equivalent circuit

one line at a time through a high speed shift register.

Mechanical characteristics

Number of sensing elements: 262,144

Pixel size: 10um x10um

Sensing area: 100um²

Performance characteristics

Quantum efficiency: 40% at $\lambda=630\text{nm}$

Sensitivity: 6.76 V/uJ/cm²

Uniformity: 10%

Saturation voltage: .5V

Output noise voltage: .041V

Dynamic range: 2000:1

Video sample rate: 15Mhz

5. Conclusion

There are many factors to consider when evaluating the performance or choosing an image sensing device. CCDs seem to dominate the market, but there are other technologies which should be considered. The most important factor in the choice of an image sensing device is the application for which it is intended. Care must be taken because a sensor could be used in a system which is not able to exploit the capabilities of that sensor.

The sensors investigated here are to be used in a system where an image is ultimately to reside in the memory of a digital computer. There are primarily two paths to take to achieve this goal. A popular way is that a sensor can be used as part of camera system which can be interfaced to a computer. Another way is to use dedicated electronics to interface directly to a computer. In either case the interfacing to a computer is very important.

Cameras are emphasized here because of the large amount of support circuitry available. Although, video circuits require a major effort to design, there are many proven products available. Given a camera, it only takes a frame grabber to get the information into a computer.

An image sensing device is not a camera. There are major differences between these devices. Many image sensors, including the ones investigated can be used as the basis for a camera. The

circuitry of a camera requires a major effort to design. It must also take into account the specifications and quirks of an array. Fortunately, some manufacturers offer the necessary supporting devices to use their arrays in a camera. In addition, evaluation boards are often available from manufacturers to help measure parameters of interest and evaluate sensors. Some vendors also offer complete cameras for a particular array. This type of support is very useful when considering an image sensing array.

Care must be taken when interfacing to a computer with a video camera. Most frame grabbers digitize to 8 bits. If the dynamic range of a sensor is greater than 256:1, it can not be utilized to its full potential. Although cameras and video circuitry are available to interface to a computer, the requirements of a specific application should be examined in great detail.

An image sensing array may be interfaced directly to a computer. At sometime an analog to digital (A/D) conversion must take place. This type of circuit also requires a substantial effort to design. Fortunately some vendors offer complete circuits to help accomplish the task. If the A/D is to be performed at video rates, a real-time digitizer circuit must be used. Again, the specific needs of the system must be examined when designing the interfacing circuitry.

In many optical pattern recognition experiments, such as with a correlator, filters or other components are being examined and evaluated. The sensor required for this application may differ from a real-time implementation of a correlator. When evaluating components in a testbed, a very high quality sensor is required. One with high resolution so the shape of the response can be seen in detail. A sensor must have high resolution for the same reason. Furthermore, a sensor that works well under low light conditions must usually be considered since many optical devices are highly attenuating. Real-time operation might not be needed for all applications.

When considering a pattern recognition system, different parameters may take on more importance and others may take on less importance. For example, for high resolution array, the Airy disk of a lens may be larger than the pixel size. The shape of a correlation peak may or may not be as important if the entire system has already been characterized. The resolution is important for another reason, the more pixels, the more data which must be

processed.

Much information is missing from a company's data sheet. Values for one parameter of a device may not be available for another. Furthermore, not all parameters are measured under exactly the same conditions or use slightly different definitions.

The best way to evaluate these types of sensors is simply use them. Evaluation board or supporting electronics should be purchased which take advantage of a particular array.

**FINAL REPORT NUMBER 57
FIBER OPTIC DISTRIBUTION SYSTEM FOR PHASED
ARRAY ANTENNAS
PENDING APPROVAL
Dr. David Sumberg
760-7MG-113**

FINAL REPORT

Submitted to

Universal Energy Systems, Inc.

4401 Dayton-Xenia Road

Dayton, Ohio 45432-1984

Continuation Study of the Effect of Nonlinearities of

High Speed Analog-to-Digital Converters on

Digital Beamforming Arrays

Prepared by:	Donald R. Ucci, Ph.D. / Jian-Ren Wang
Academic Rank:	Associate Professor / Research Assistant
Department and	Electrical and Computer Engineering Department
University:	Illinois Institute of Technology
Research Location:	RADC/EEA
	Hanscom Air Force Base
	Bedford, MA 01731-5000
USAF Researcher:	Dr. Hans Steyskal
Date:	January 31, 1990
Contract No:	F49620-88-C-0053/SB5881-0378
Subcontract No.	S-210-9MG-040

ACKNOWLEDGMENT

We express our thanks and appreciation to the Air Force Systems command, the Air Force Office of Scientific Research, the Rome Air Development Center, and Universal Energy Systems for making the research in this report possible. In particular, we wish to thank Dr. Hans Steyskal, our research colleague, at RADC, Dr. Rodney C. Darrah, Director of the UES Faculty Research Program, and the staff of both these organizations.

We also thank Mr. David P. Miller and Mr. Robert G. Petroit for their assistance in obtaining some of the results presented in this report.

ABSTRACT

This Final Report documents the research on the effects of an Analog-to-Digital Converter (ADC) nonlinearity on a Digital Beam Former (DBF). The results show that a third order power law is sufficient to model the nonlinearity. The ADC's Input-Output Characteristic (IOC) and its deviation from a truly linear behavior is presented. Two major results of this work are that some degradation is experienced by the DBF, and that an adaptive DBF employing a Sampled Matrix Inversion (SMI) technique is not substantially degraded by the nonlinearity. Two techniques for reducing the degradation in the standard DBF case are examined. The power constraint method trades off input dynamic range for improved performance. The adaptive compensator scheme trades off system complexity for reduced distortion.

Continuation Study of The Effect of Nonlinearities of High Speed Analog-to-Digital Converters on Digital Beamforming Arrays

I. Introduction

This report studies the effects of a nonlinearity of an Analog-to-Digital Converter (ADC) on the performance of a Digital BeamFormer (DBF). In order to evaluate the distortion caused by the ADC, a measurement based on the normalized Average Power Pattern Error (APPE) is used. A simplistic mathematical model of the ADC which is based upon the data supplied by the Rome Air Development Center (RADC) is also established.

We note that the available data describe the frequency response of the ADC to a fixed level sinusoidal wave at a single frequency only. The model of the ADC and the measurement of the output performance are made based upon the following two assumptions: First, the ADCs have the same frequency characteristics over the entire spectrum, and second, the ADCs applied at each antenna element are identical. In practice, these assumptions are true only to a certain degree. An average characteristic would be more applicable. To properly complete the study, further research needs to be performed using this average characteristic which would be obtained by accumulating data from a large sample of typical ADCs.

The study reveals that only the first few harmonic components contribute significantly to the beamformer degradation. This is intuitively appealing since these harmonics have values on the same order of magnitude while succeeding harmonics are far below this nominal value.

To eliminate the degradation in the DBF resulting from the nonlinearity of the ADC, two approaches have been studied. The first approach examines the effect of reducing the input signal level or, equivalently, the signal power to the ADC. (This is similar to the approach used in High Power Amplifiers (HPAs) in which the signal level is "backed off".) The results of this method show that the reduction of the input intensity decreases the effect of the nonlinearity, but it also decreases the available resolution. The second method uses a compensator constructed as an Infinite Impulse Response (IIR) adaptive filter to decrease level of the harmonics generated by the ADC nonlinearity. The results for this approach show that the adaptive compensator effectively eliminates the higher order harmonics. Since the compensator is adaptable, no prior knowledge of the input signals or the ADC characteristics is required. There is, however, an increase in system complexity.

A further study of an adaptive array using digital techniques and a Sampled Matrix

Inversion (SMI) algorithm reveals another interesting result. Because of the nulling capability of the adaptive array, the performance is imperceptibly affected by the presence of the nonlinearity.

II. Objectives

This study was undertaken to determine the effects of nonlinearities of an ADC on an adaptive DBF, and recommend ways to mitigate any detrimental effects which arose. To accomplish this task several objectives were proposed. The first objective was to determine the effective order of the nonlinearity, that is the order which causes significant degradation in some defined performance measure. A second objective was to determine and evaluate methods for reducing incongruities in the DBF pattern. A final objective was to evaluate the performance (in terms of degradation at the output) of a digitally implemented adaptive array. These objectives have been accomplished.

In pursuit of these goals, several other tasks were outlined. One task was to develop an input-output characteristic for the ADC. Another task was to determine the effect of multiple jammers on the DBF pattern. An additional task was to examine the effect of arrival angle on performance. These effects are shown by means of computer simulation. Other questions which were not addressed were:

- Development of equations for the output beam pattern in the case of multiple interferers. This task was deemed unnecessary as no additional information would be obtained. It is clear that in this case, the intermodulation products will create "pseudo-interferers". These can be seen in the output beam patterns.
- Base band/Intermediate Frequency Analysis equivalence. This issue was not addressed since evidence of its applicability is available in the literature [COMP87], [BART80].
- Effect of a Tapped-Delay-Line (TDL) processor for improved performance. This investigation was unnecessary at this time because the results of the adaptive processor study, using the SMI algorithm, revealed that the degradation incurred was minimal. That is, the adaptive algorithm itself, mitigated the ADC nonlinearity's effect.

III. Problem Formulation

Effective Order of Nonlinearity

In determining the effective order of the nonlinearity, a performance criterion based on the normalized Average Power Pattern Error is chosen. To describe this measure we

proceed as follows [UCCI89].

Consider the structure of an M-element array with half wavelength spacing of $d=\lambda_d/2$, where λ_d is the wavelength of the desired signal of radian frequency $\omega_d=2\pi f_d$, as shown in Fig. 1. The signal received by the m^{th} antenna element is x_m and y_m is the corresponding output from the ADC. Accordingly, with an ADC which has a K^{th} order nonlinearity, y_m can be represented as

$$y_m(t) = \sum_{k=0}^K a_k x_m^k(t), \quad (1)$$

where a_k is the coefficient of the k^{th} power law relationship. For a single tone sinusoidal input signal, $x_m(t)$, the output of the ADC can be described by

$$y_m(t) = \sum_{k=0}^K A_k x_m^k(t). \quad (2)$$

where the set $\{A_k\}$ is a set of coefficients of a harmonic law model and are related to the set $\{a_k\}$ [UCCI88]. The values of these harmonic components were supplied RADC [UCCI89] and are shown in Fig. 2. The signal, $x_m(kt)$, is the k^{th} harmonic of $x(t)$ with maximum index K . Define the m^{th} antenna element quiescent weight as $w_m = b_m \exp[j(m-1)\pi \sin \theta]$ where b_m denotes the amplitude weighting and θ is the quiescent beam pattern look direction. Denote the desired signal time delay at the m^{th} element as Δ_{dm} . The output of the m^{th} weight is then $z_m(t) = w_m y_m(t)$, given by

$$z_m(t) = \sum_{k=0}^K A_k b_m e^{jk[\omega_d t - \phi_{dm} + \psi_d + (m-1)\pi \sin \theta]}, \quad (3)$$

where $\phi_{dm} = \omega_d \Delta_{dm} = (m-1)\pi \sin \theta_d$ is the interelement phase shift, ψ_d is an arbitrary phase shift and θ_d is the arrival angle of the desired signal. The array output is the weighted sum of the ADC outputs, thus

$$Z(t; \theta) = \sum_{m=1}^M z_m(t), \quad (4)$$

Notice that the output is parameterized by the angle θ .

For a generalized array output, $u(t; \theta)$, the Beam Pattern Power Gain (BPPG) is given

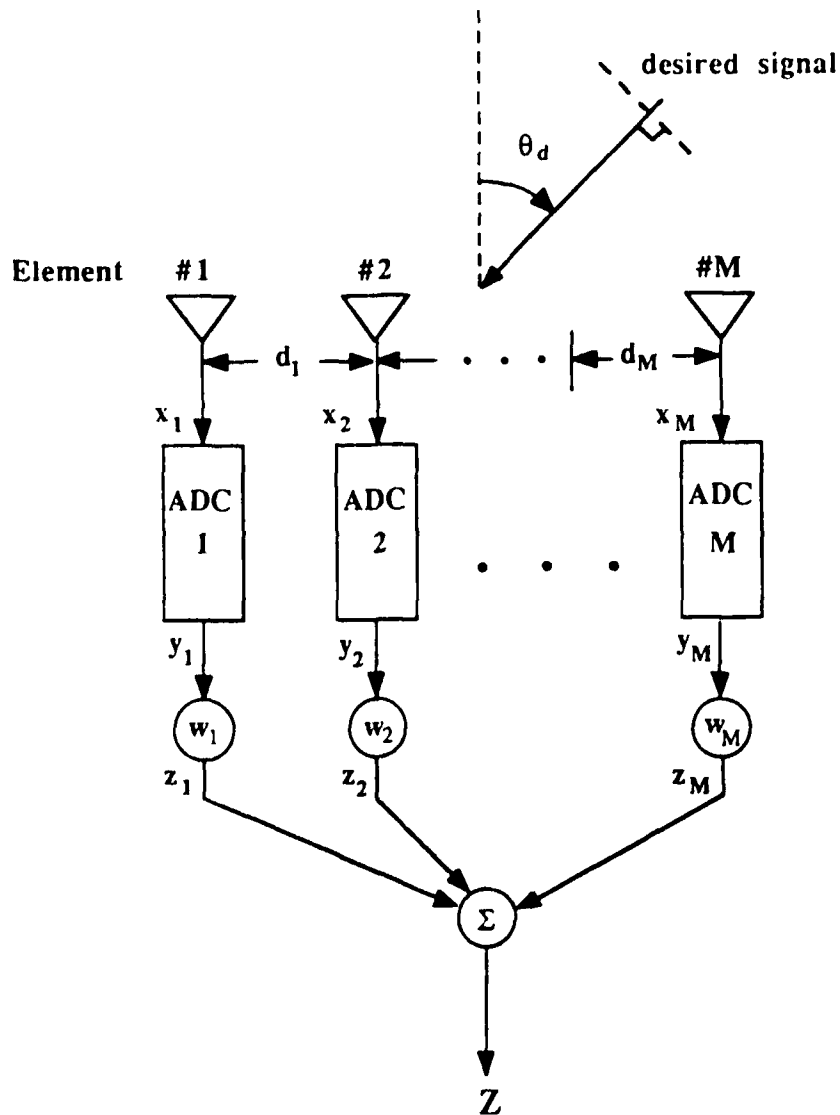
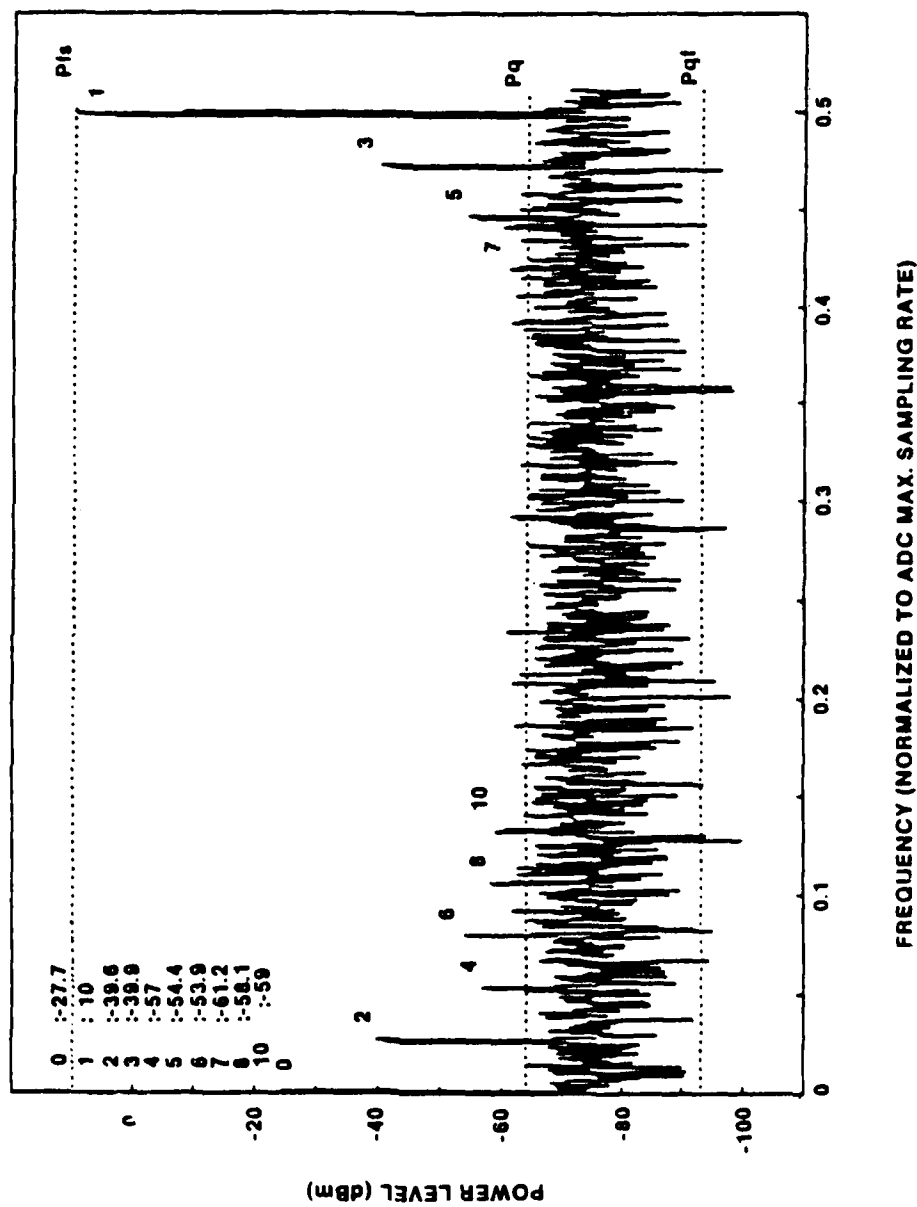


Fig. 1 Structure of the Digital Beamformer

Fig. 2 ADC Spectral Response to Pure Sine-Wave



the intensity of the harmonic components,) can be decreased or suppressed by compensating the nonlinear characteristic of the ADC. There are several techniques for compensation of the nonlinearity's effect. We discuss two methods in the following section.

Power Constraint Method

A simple compensation technique is to place constraints on the input signal's dynamic range thus allowing the ADC to operate more linearly. As consequence of this approach, the ADC bit utilization and signal to quantization noise is decreased at the expense of dynamic range and signal resolution.

Adaptive Compensator

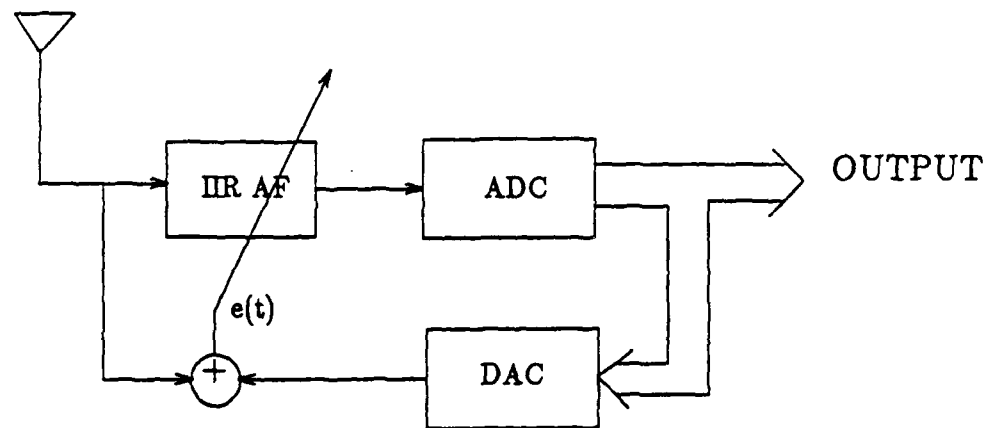
An alternative approach for reducing the effect of the nonlinearity is to use an adaptive compensator. The compensator is designed to adapt itself to minimize the Mean Square Error (MSE) between the input and output signals of the ADC therefore, it can be applied to various ADCs without a priori knowledge of the nonlinear characteristic. The structure of the adaptive compensator, as shown in Fig. 3, is constructed as an IIR filter which in turn is composed of two adaptive Finite Impulse Response (FIR) filters [WIDR85]. We assume that the Digital-to-Analog Converter (DAC) does not possess a nonlinearity. The technique by which the adaptive compensator reduces the distortion is to form an inverse model of the ADC operating characteristic. Thus, the error between the input and output of the ADC can be minimized although we incur increased system complexity.

V. Results

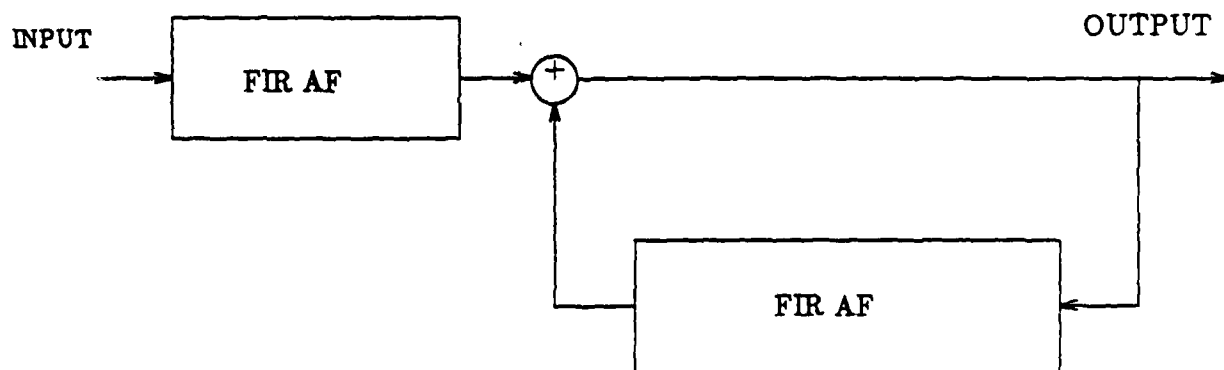
We now present the results of our study. First we investigate the effective order of the nonlinearity. Second, we will discuss the IOC. Third, we examine the effect of the compensation methods. Last, we present the outcome of the SMI study.

Effective Order of Nonlinearity

In this study we examine the following system. We assume uniform linear array which uses one-half wavelength spacing at the desired signal wavelength. The number of elements in the array is 10 and we use Chebyshev weighting with -20 dB sidelobes. The desired signal has unity amplitude and is located at broadside. There are either one or two jammers present. The first jammer is located at 15° and has a frequency 1.5 times that of the desired signal. The second jammer is located at -20° and has a frequency of 0.9 times that of the desired signal. In the single jammer case only the first jammer is assumed



(a) Configuration of compensator



(b) Structure of IIR adaptive filter

Fig. 3 Structure of the Adaptive Compensator

present. Both jammers have power which is 40 dB above the signal power. For averaging we use eight samples for each cycle of the desired signal. Figure 4 illustrates the Average Power Pattern Error, ϵ_h , vs. order of nonlinearity, h , or the APPE curve. Note that the highest order of the nonlinearity is 18. This number is merely an index which is greater (by one) than the actual order of the nonlinearity considered. Thus, the true order is 17, corresponding to the 17 harmonics above the noise floor in Fig. 2 [UCCI88]. The average pattern error, ϵ_h , as given by Eq. 10, is plotted as the ordinate. This is a relative value and we are only interested in significant changes seen in the curve. By observing the variation of ϵ_h in Fig. 4 it is clear that the plot saturates at about -20 dB very quickly, reaching its last most significant change at $h=4$. This corresponds to a harmonic number, and therefore a significant power law, of 3. This result is intuitively pleasing since, from Fig. 2, we see that the 2nd and 3rd harmonic components are of the same order (40 dB below the fundamental) and all higher order harmonics are far below this number.

Next we examine several types of power and error patterns. Based on our previous work, as illustrated in Fig. 4, we consider only a 4th order nonlinearity (please note again that our definition of order here is one more than the value of k in Eq. (1)). In all figures time is normalized.

Figure 5 presents two patterns for the ideal case, that is only the fundamental component present. In Fig. 5a we plot the instantaneous normalized power pattern, or BBPG, $F_i(\theta)$, at time $t=0$ for only the jammer present. Notice that the value at 0° is approximately -70 dB. In Fig. 5b we include the desired signal. Note that the value at 0° is now 20 dB higher. This shows that the BPPG is dominated by the higher power jammer. This pattern is used as a reference to obtain the error pattern.

Figure 6 illustrates the BPPG and TAPPE for 2nd, 3rd and 4th order nonlinearities. In Fig. 6a, we examine the instantaneous pattern for $t=0$. As expected, we note the appearance of the pseudo-interferers in proportion to the nonlinearity. For the case of a 2nd order nonlinearity (i.e. d.c. and fundamental present), as indicated by the dashed line, there is only one main lobe (this pattern is very similar to that of the reference pattern as will be seen from Fig. 6d); for a 3rd order nonlinearity, as indicated by the solid line, we see two large lobes; also, for the 4th order nonlinearity, as indicated by the dash-dot line, we see three large lobes. A similar phenomenon is seen in Fig. 6b for time $t=3$, which also indicates the temporal variation caused by the intermodulation products. In Fig. 6c we show the time averaged patterns for this case.

Using Figs. 5b and 6c we determine the TAPPE, $\langle \epsilon_h(\theta) \rangle$ as given by Eq. (8) and shown in Fig. 6d. Note that, for the 2nd order nonlinearity, the error is very small as compared to the 3rd and 4th order errors. In Fig. 7 we examine the BPPG and TAPPE for

Fig. 4 Average Power Pattern Error vs. Order of Nonlinearity

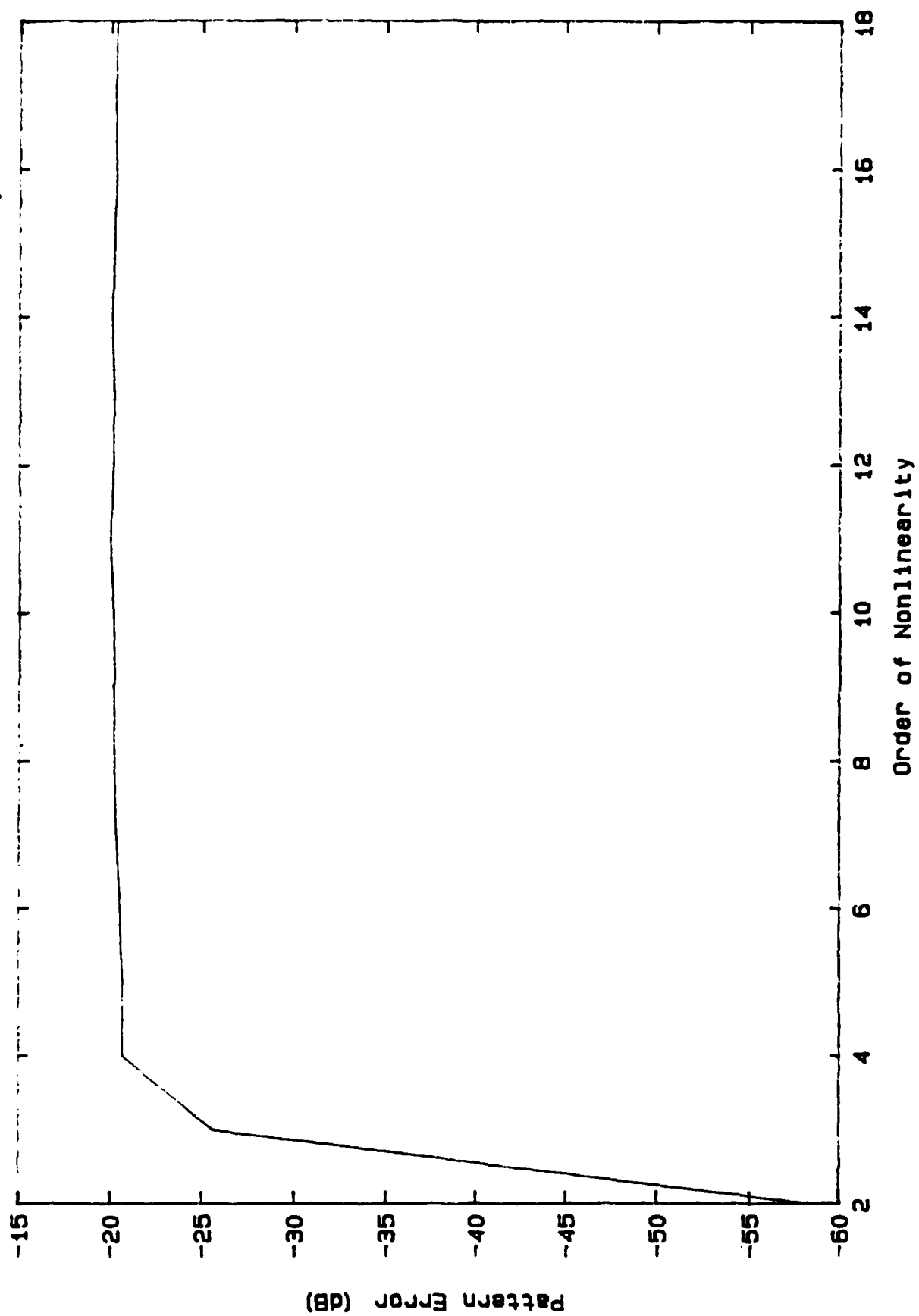


Fig. 5a

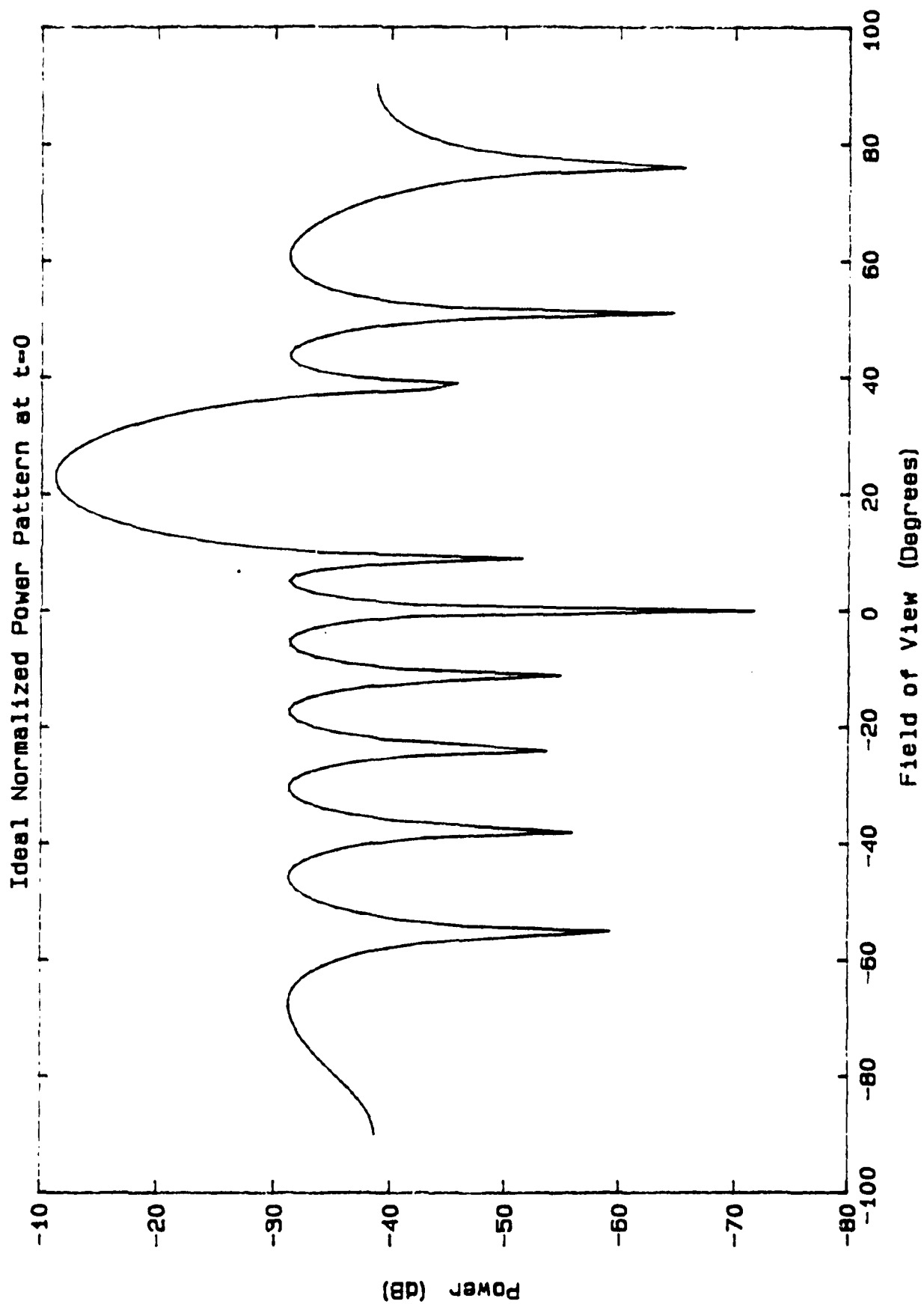


Fig. 5b

Ideal Normalized Power Pattern

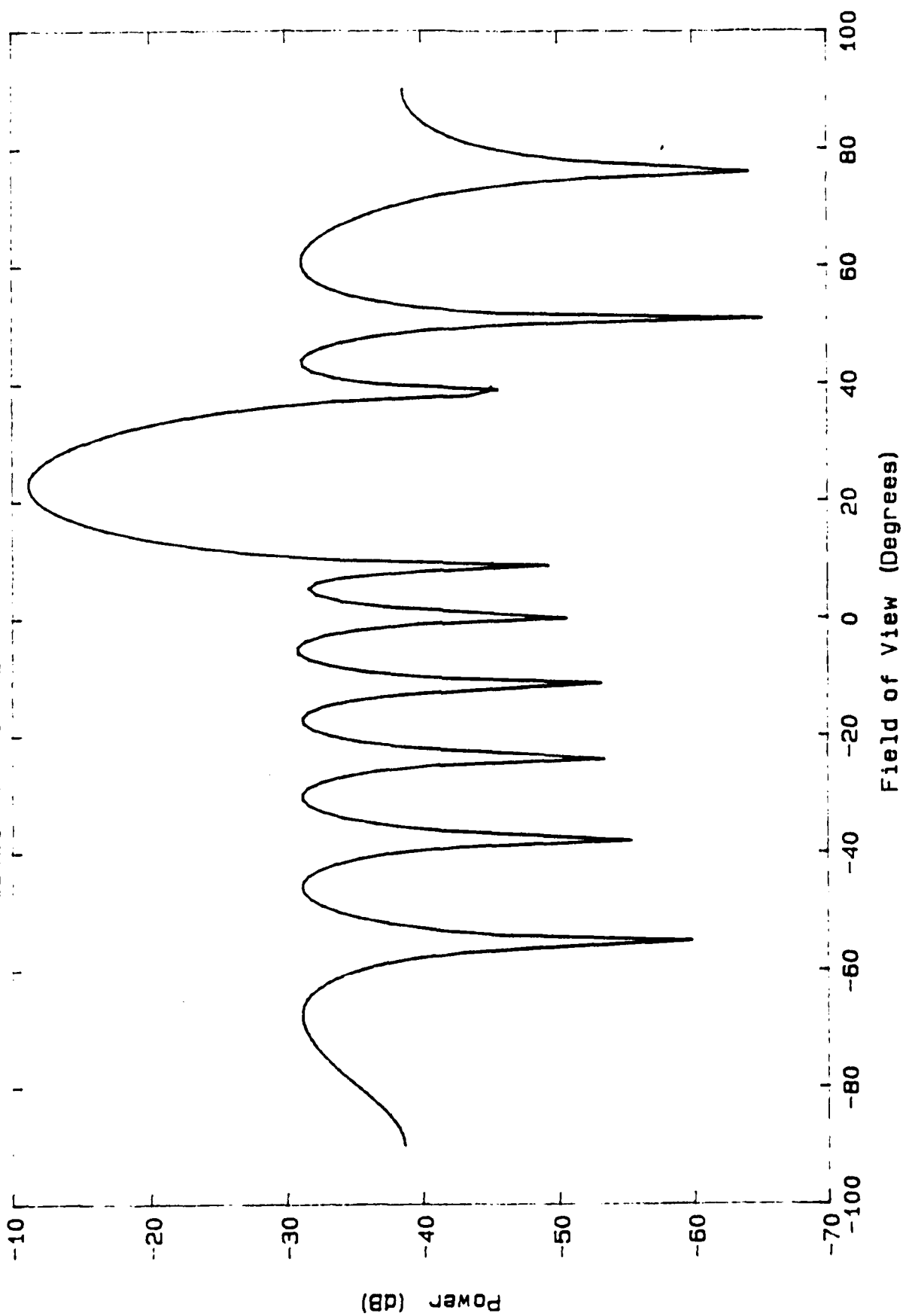


Fig. 6a

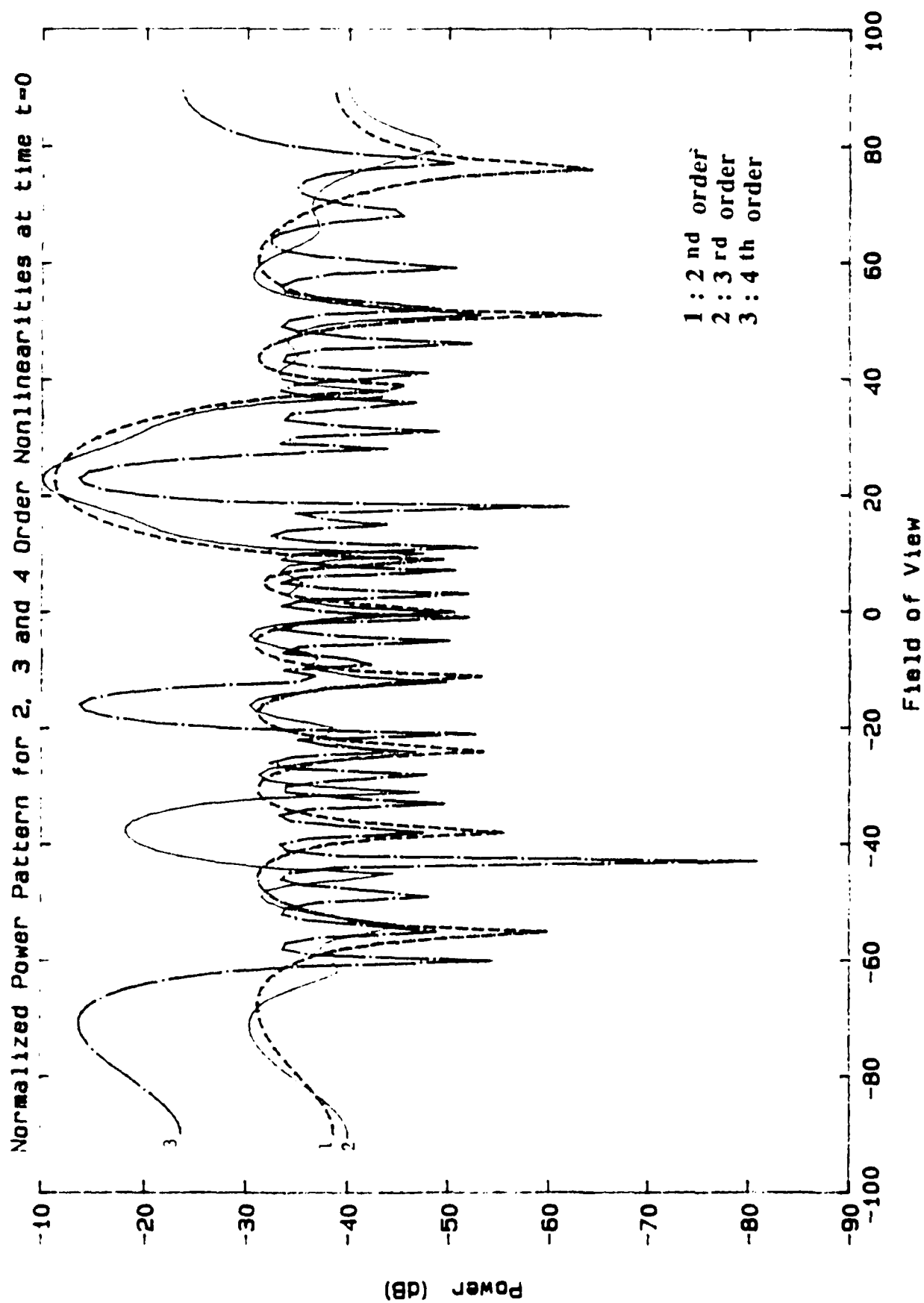


Fig. 6b

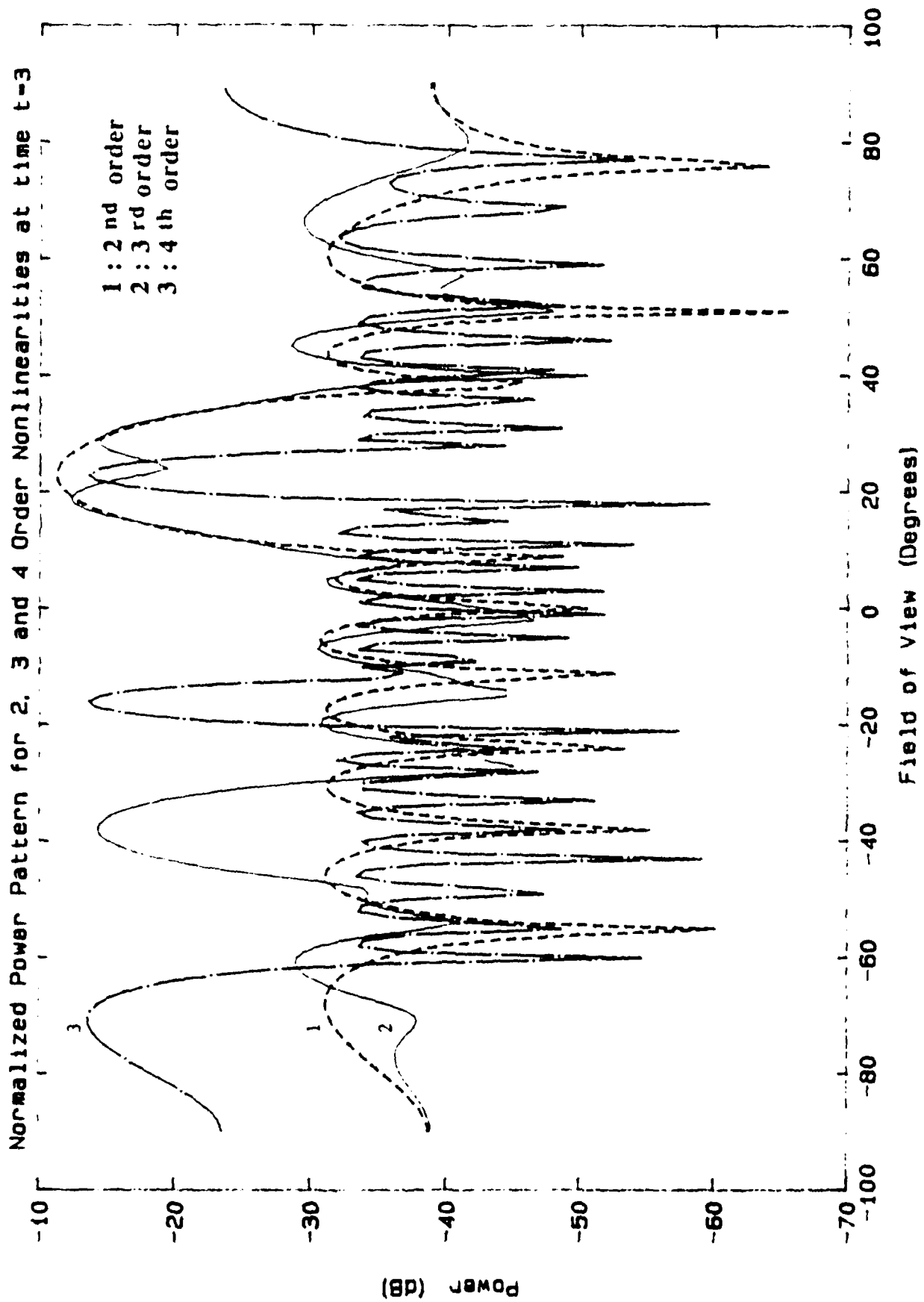


Fig. 6c

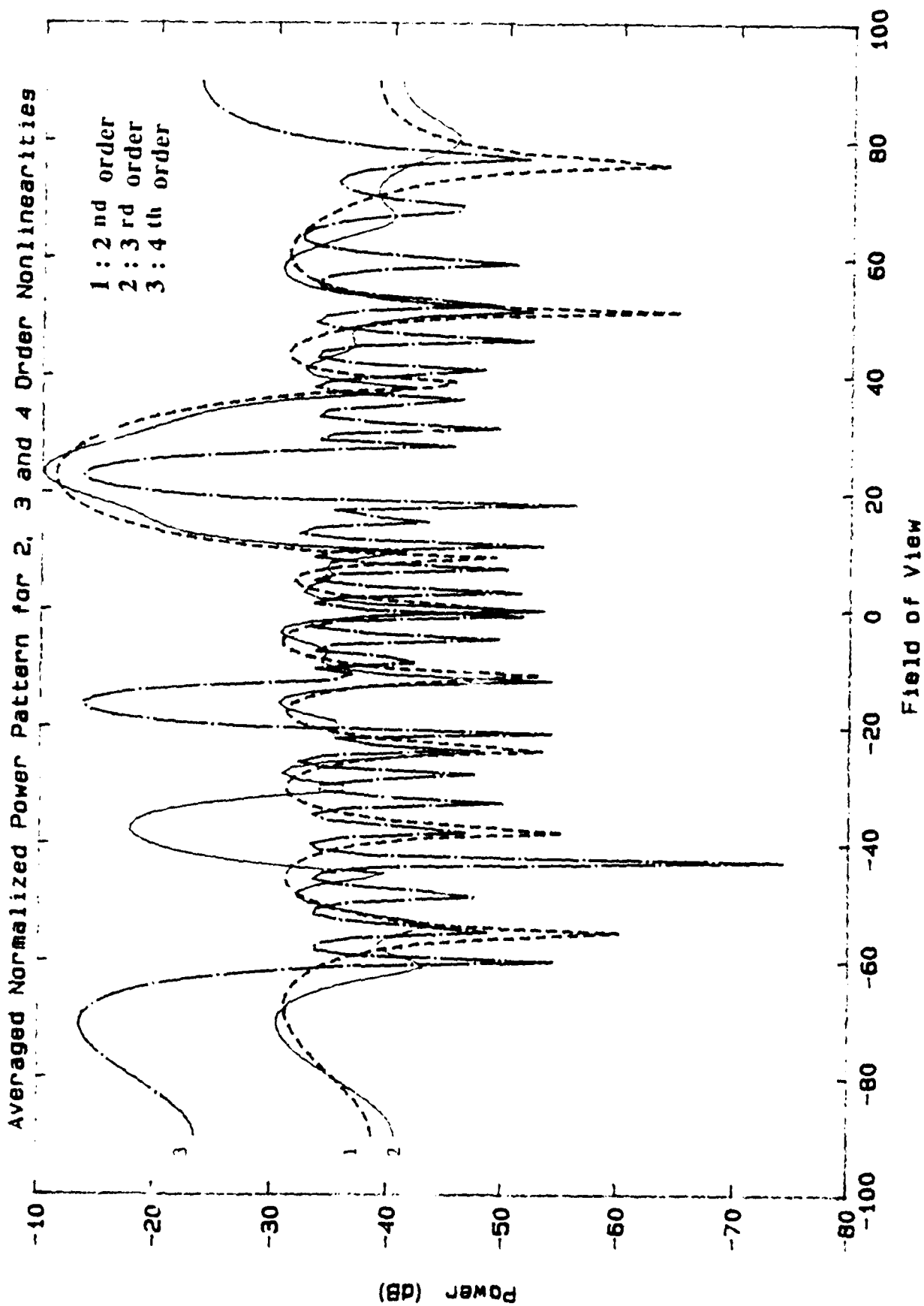


Fig. 6d

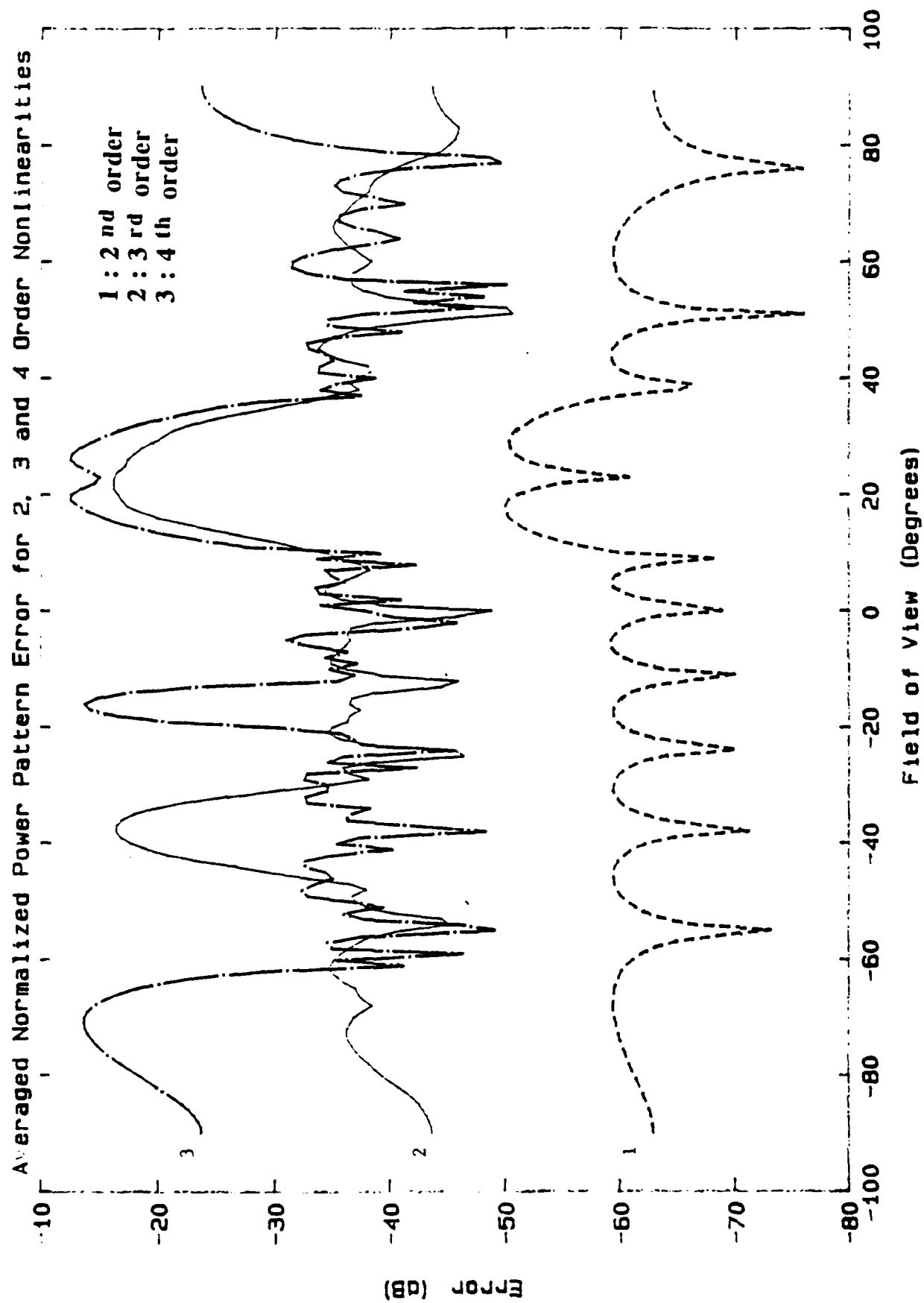


Fig. 7a

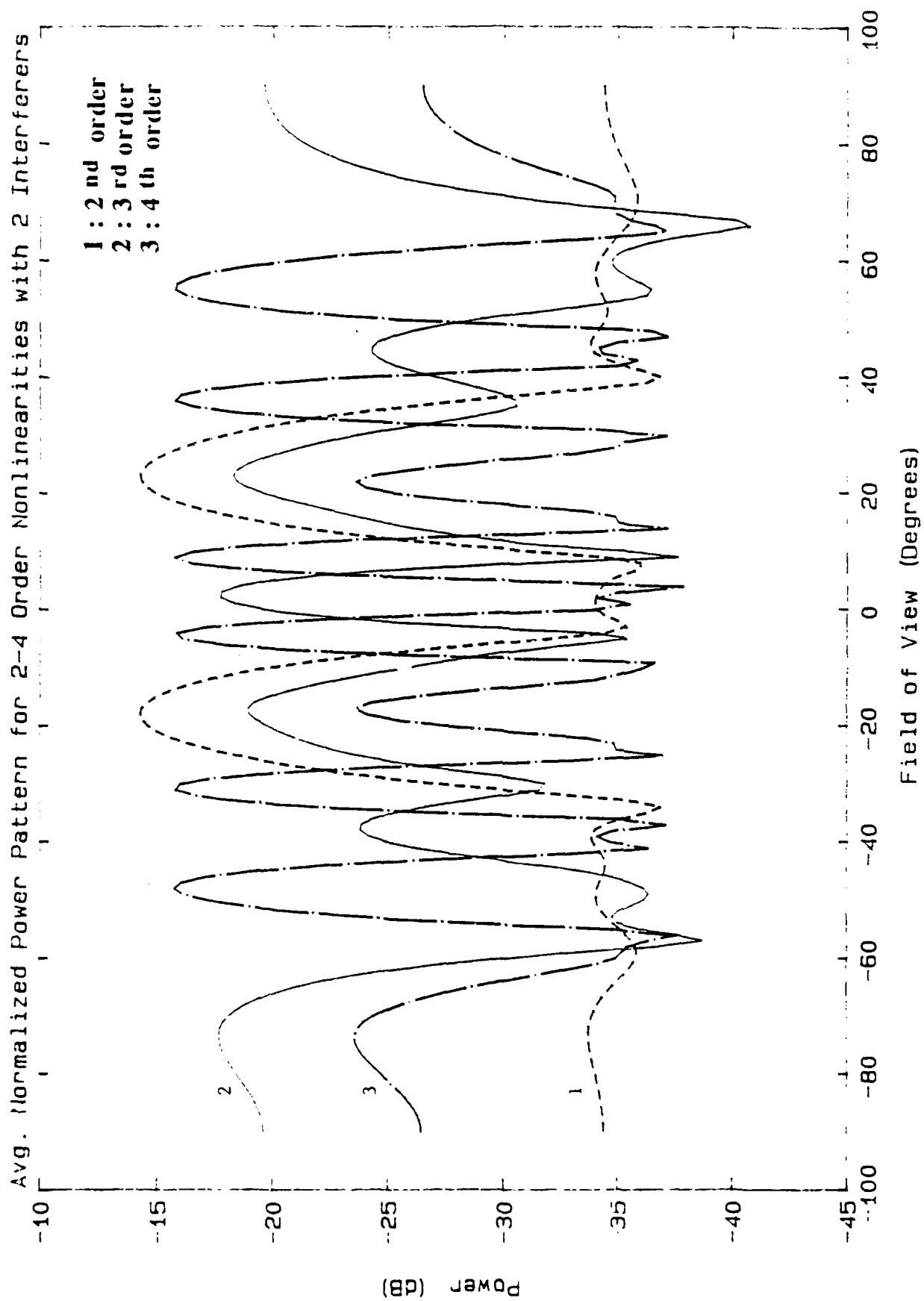
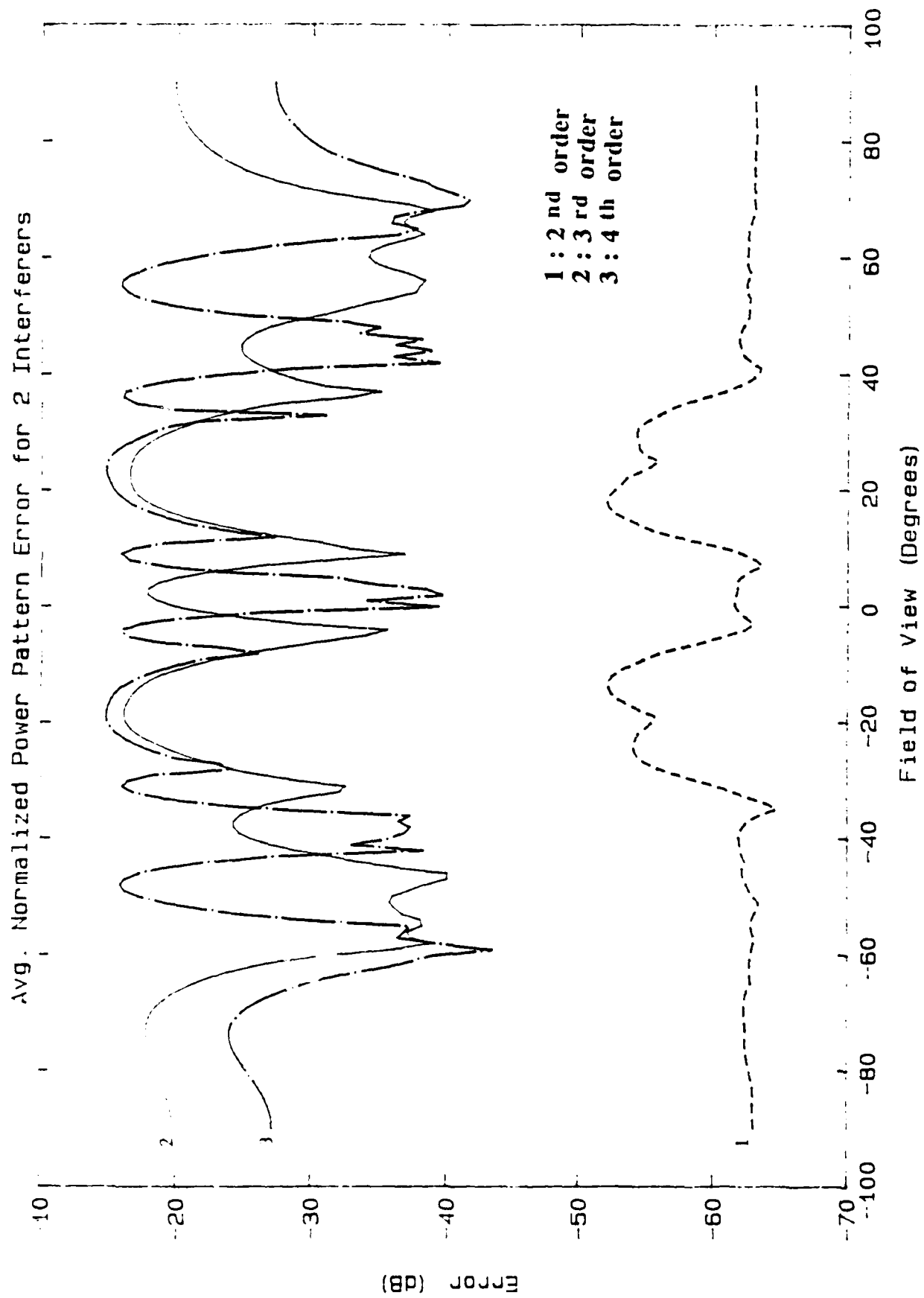


Fig. 7b



the case of two interferers. In Fig. 7a we show the BPPG for 2nd, 3rd and 4th order nonlinearity. Note again the appearance of the pseudo-interferers. In this case, since there are two jammers, the number of "large lobes" in each case is doubled, as is seen in the figure. In Fig. 7b we plot the TAPPE. We again see similarity in the overall behavior as was seen in Fig. 6d. Note the trend: as the number of real jammers increase, we see a "flattening" in the TAPPE. As the number of jammers, and therefore the number of pseudo-jammers increase, the environment becomes white-noise-like.

Angle of Arrival

In Fig. 8, we investigate the effect of the angle of arrival of the desired signal and interference on the TAPPE. Initially, we set the desired signal at -10° and the interferer at 15° in Fig. 8a. Then, in Fig. 8b we move the jammer to 25° . Comparing the curves, we observe a similar trend and conclude that angle of arrival is not critical provided there is sufficient separation between the signals. This would be true in a standard beamformer.

Input-Output Characteristic

Next we determine the IOC, or transfer function, of the Analog-to-Digital converter as shown in Fig. 9. Figure 9a illustrates the overall transfer function for the full range of 17 harmonics whereas Fig. 9b presents this result using only harmonics up to the third order. Both curves appear to be linear; however, when compared to a true linear curve an error is seen. Illustrated in Fig. 9c is the error using all orders of the nonlinearity. In Fig. 9d we show the error using only the components up to the effective order of the nonlinearity. By comparing the two error functions we detect a strong similarity. Thus, the error functions of the IOC provide further credence to our previous evaluation of the effective order of the nonlinearity.

Methods of Compensation

We now evaluate the effectiveness of the two techniques of compensation. First, we examined the power constraint method using the ADC output harmonic content as a measure of performance. Figure 10a shows a plot of the ADC output versus normalized frequency (here we ignore quantization noise). This plot was obtained using our model, and compares well with Fig. 2 which illustrates the measured response. In Fig. 10b and 10c we display the output when the input power is reduced by 3 dB and 6 dB, respectively. Notice the drastically reduced levels of the harmonic components with respect to the fundamental. Of course, the decrease is greater for the 6 dB power reduction. From our preceding analysis and simulation we conclude that this method is an effective means to

Fig. 8a

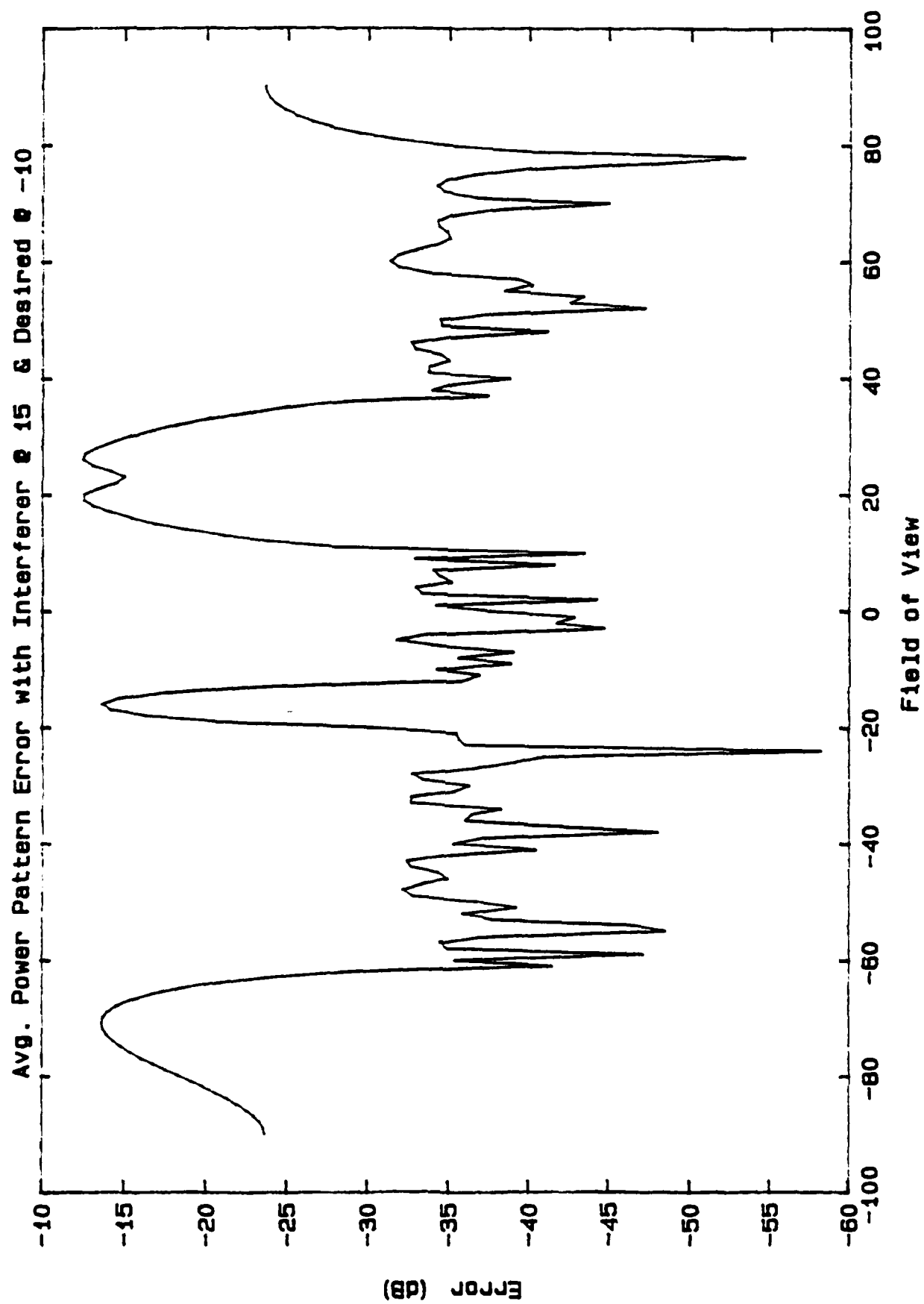


Fig. 8b

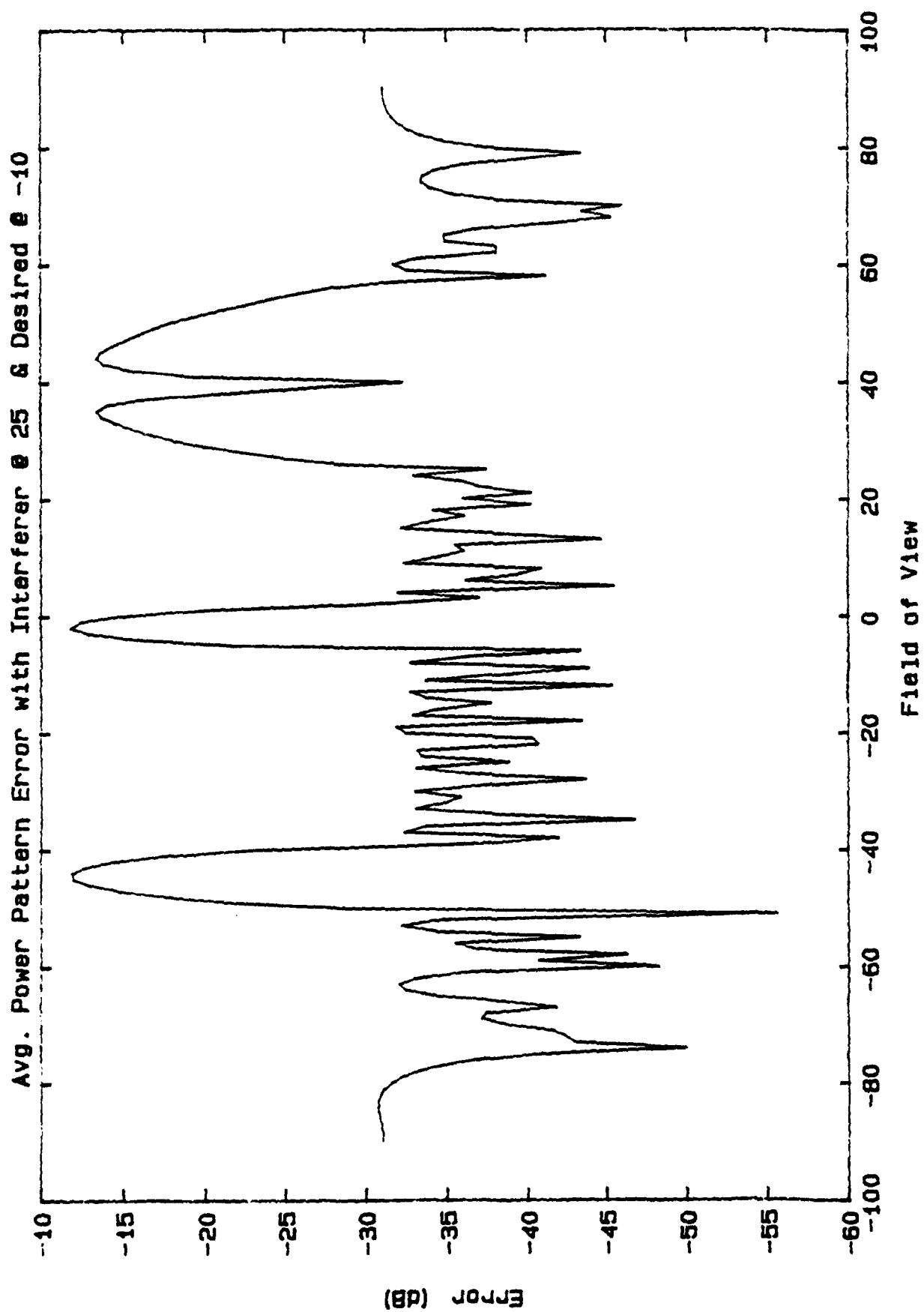


Fig. 9a
ADC Transfer Function

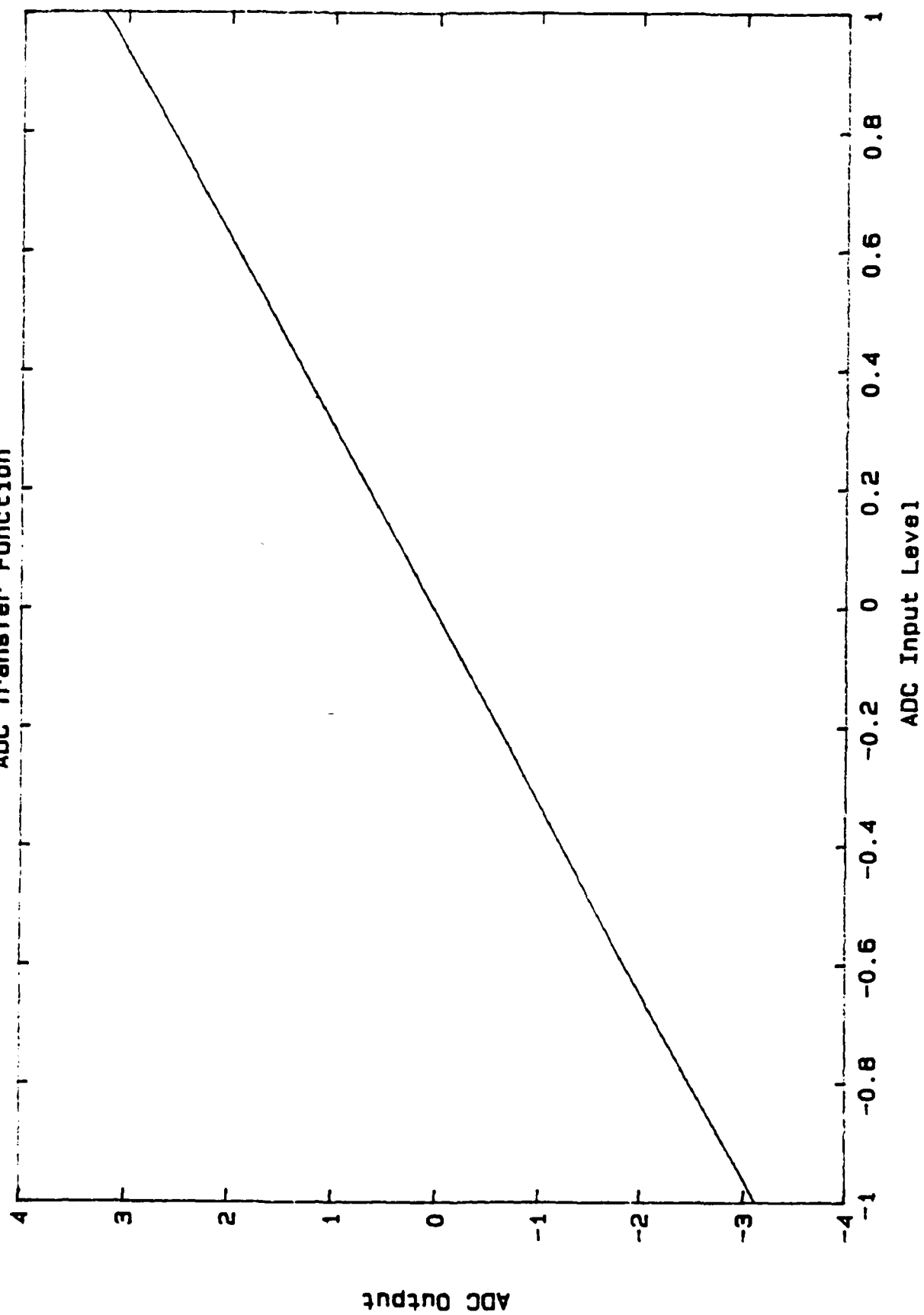


Fig. 9b

ADC Transfer Function with up to 3rd Harmonic Present

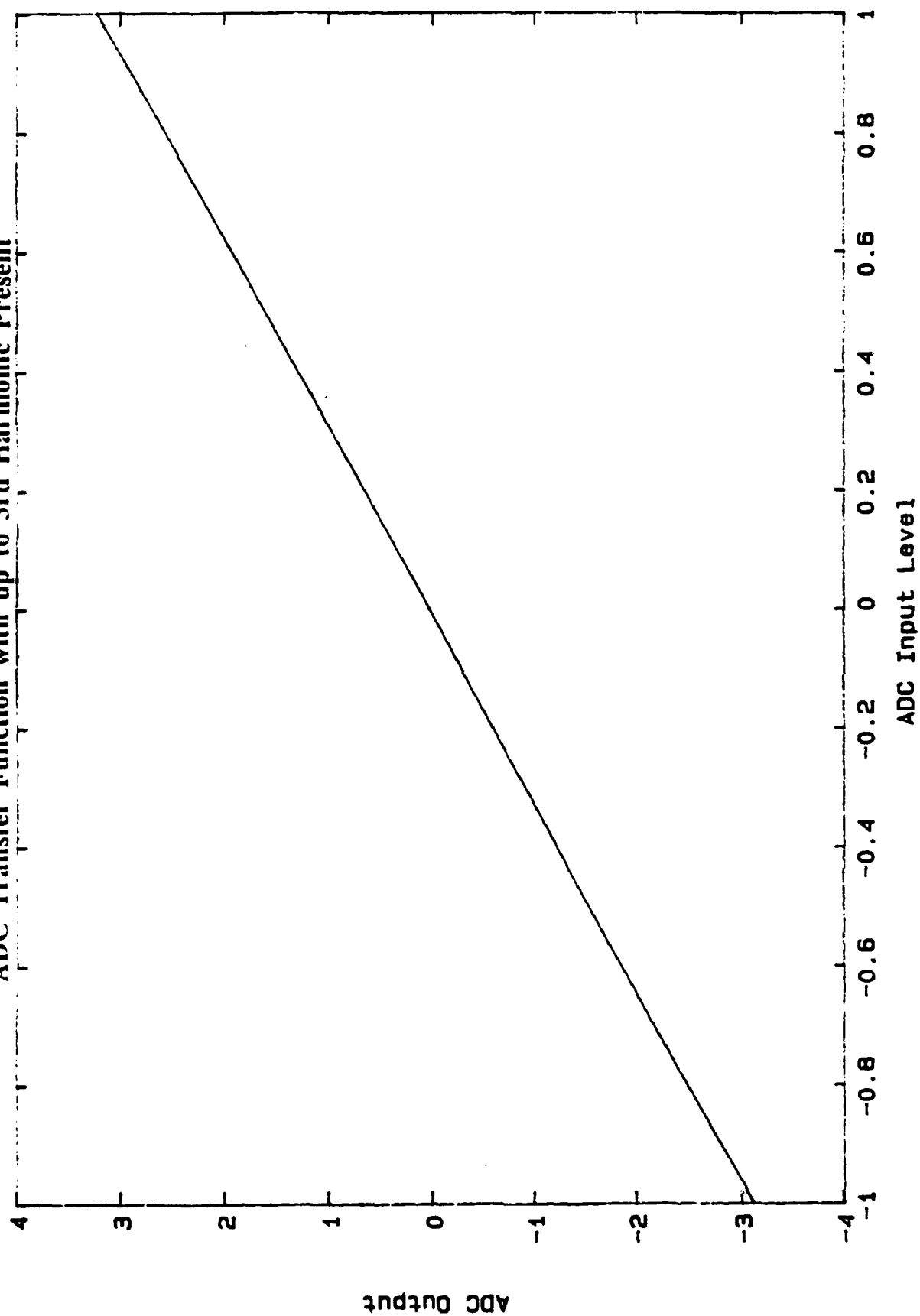


Fig. 9c
ADC Transfer Function Error

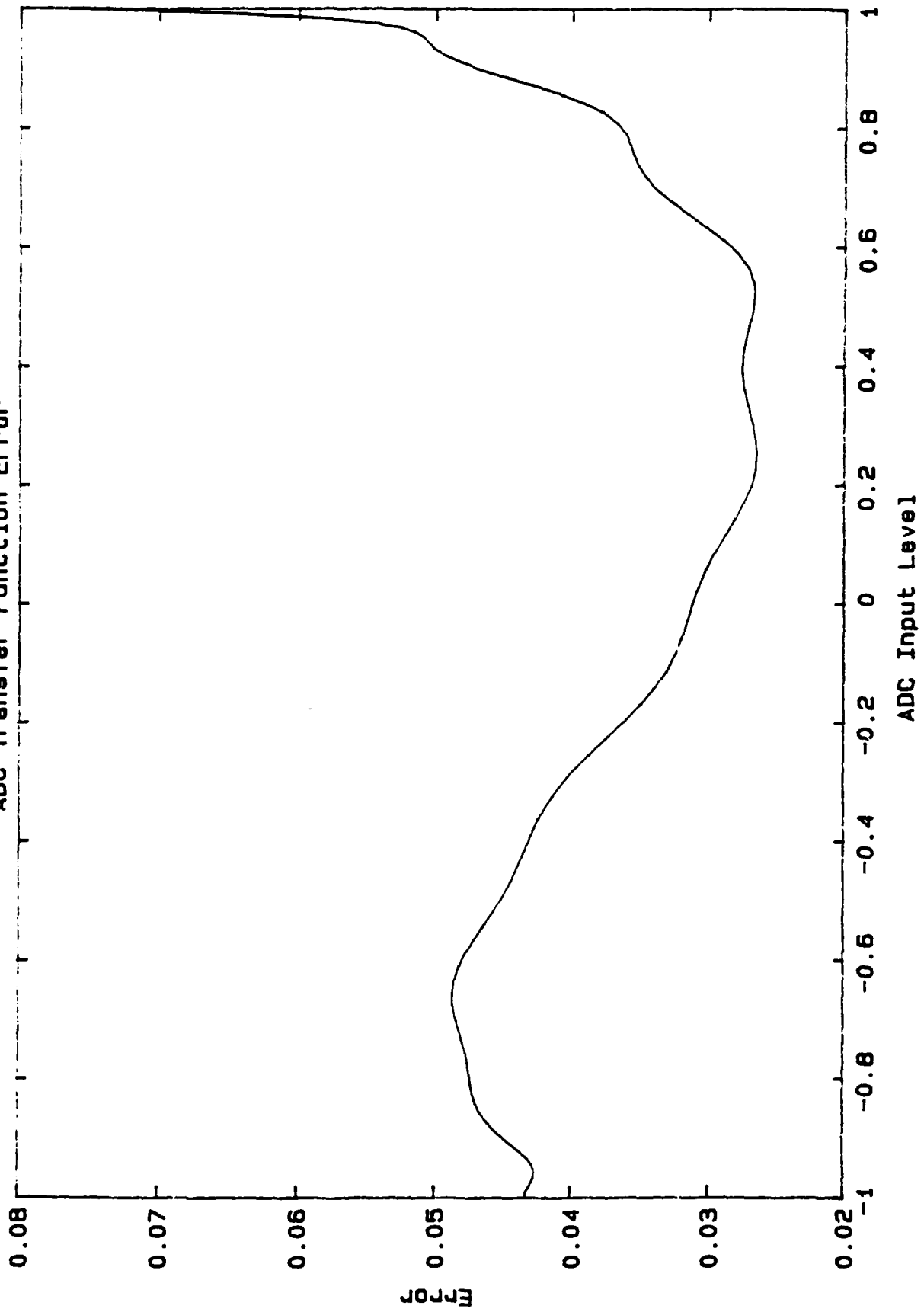


Fig. 9d

ADC Transfer Function Error with DC, 2 and 3 Harmonic Present

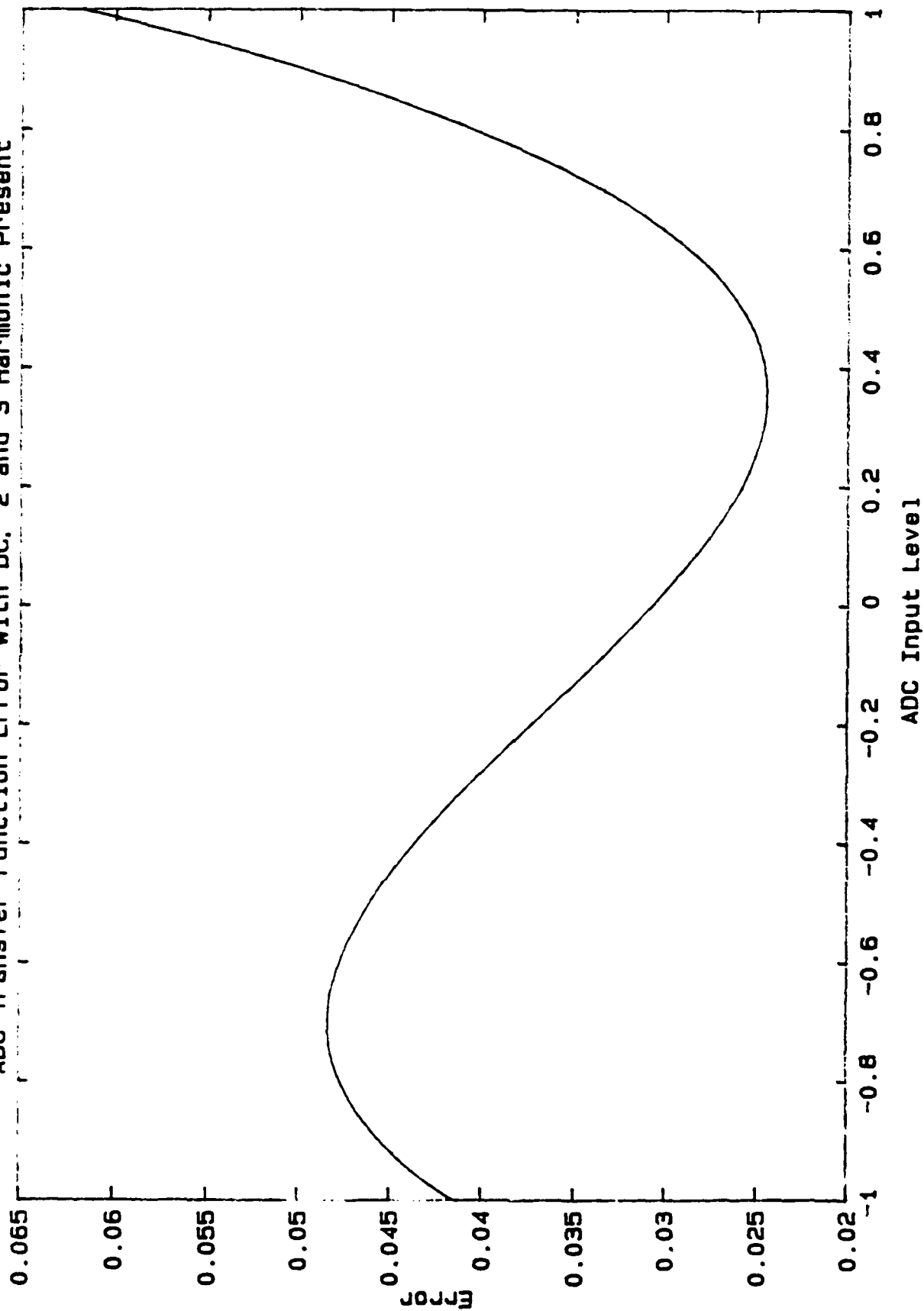


Fig. 10a

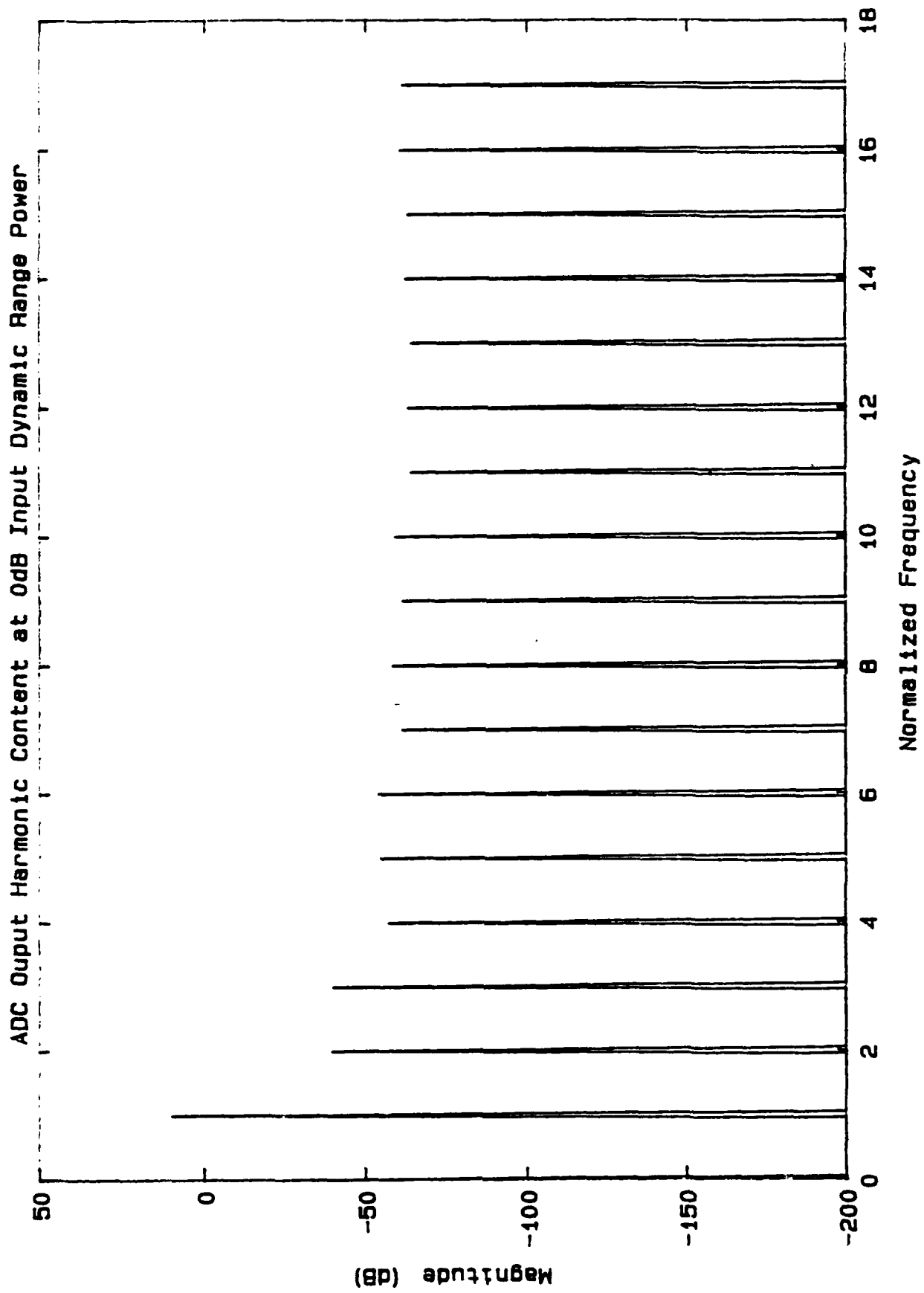


Fig. 10b

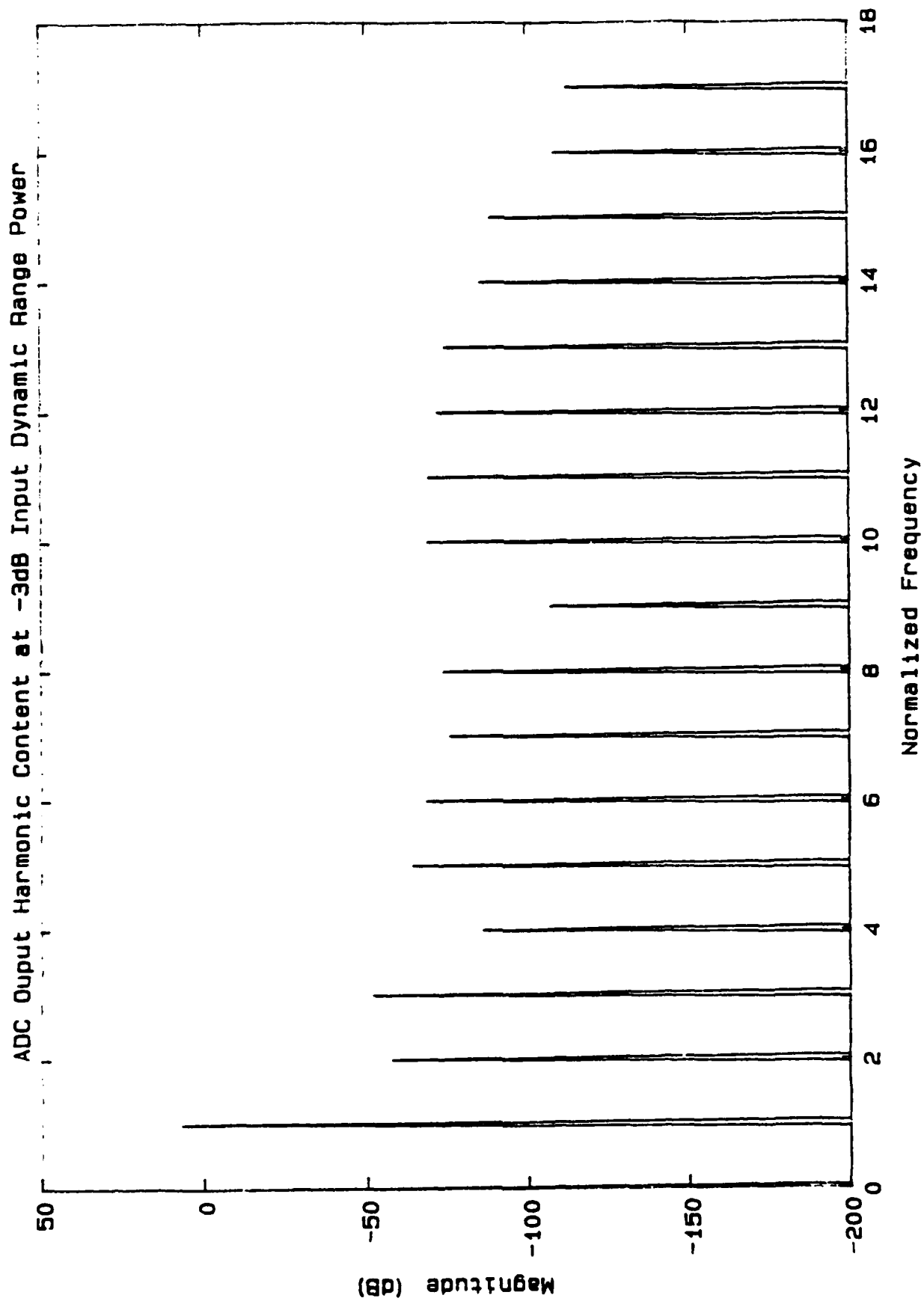
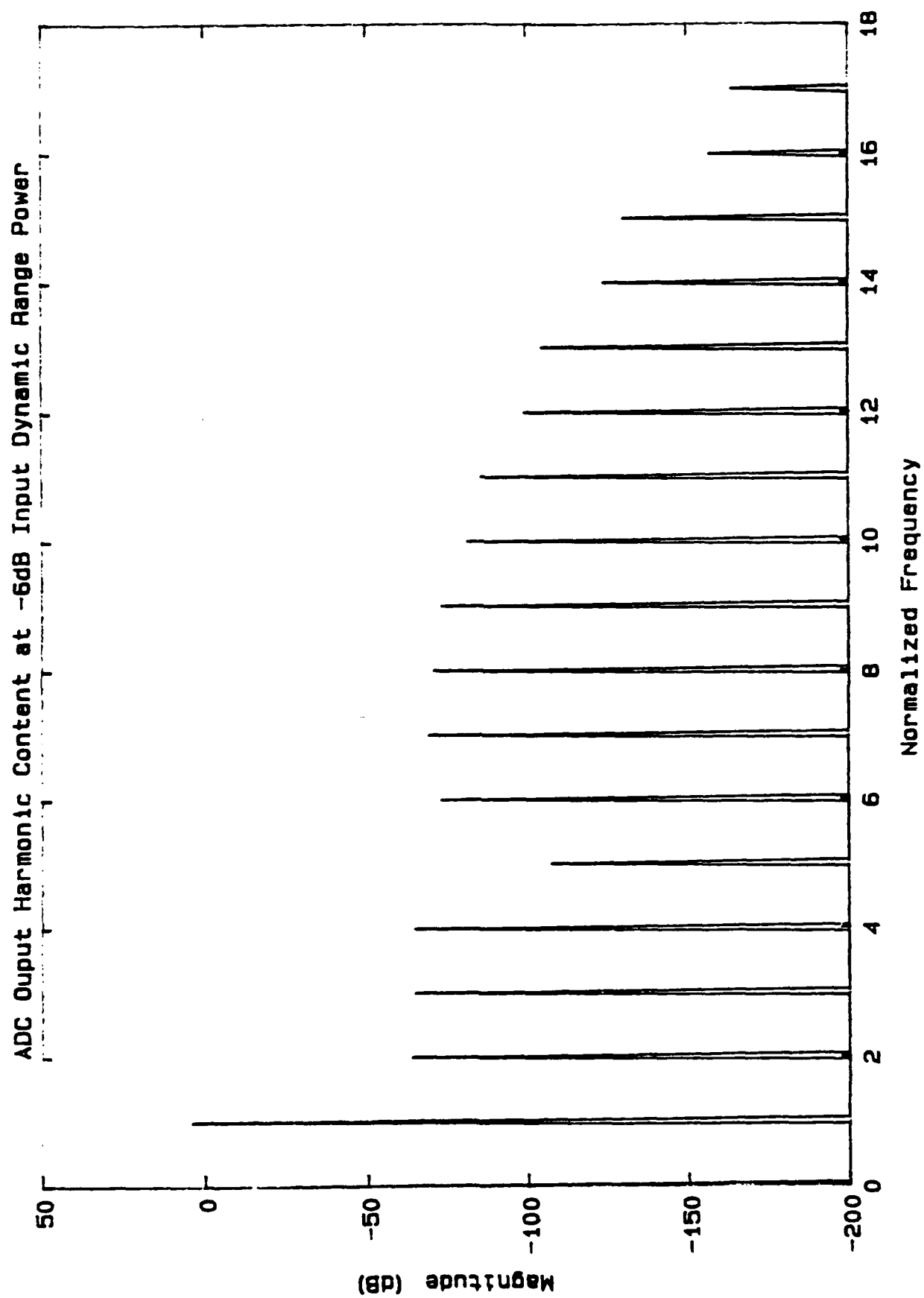


Fig. 10c



alleviate the error caused by the nonlinearity. However, we are trading off ADC resolution for reduced error.

Next, we explore the adaptive compensator's performance. Figure 11 demonstrates the effectiveness of this approach. In Fig. 11a we present a plot of the harmonic components with the fundamental suppressed (with quantization noise present) for the case of an uncompensated and compensated ADC. Note in the compensated case all the harmonics have been suppressed below the quantization noise level of -72 dB, except for the d.c. term which is reduced by approximately 5 dB. The d.c. term, however, does not create catastrophic degradation. In Fig. 11b and c we compare the uncompensated and compensated ADC output for the case of two interferers. The interferers have a frequency of $1.05 \omega_d$ and $0.95 \omega_d$, respectively. Again we see that the compensator annihilated the harmonics greater than order three, significantly reduced the second and third harmonics, and slightly reduced the d.c. component. Thus, we conclude that the adaptive compensator is an effective means for reducing degradation at the cost of complexity.

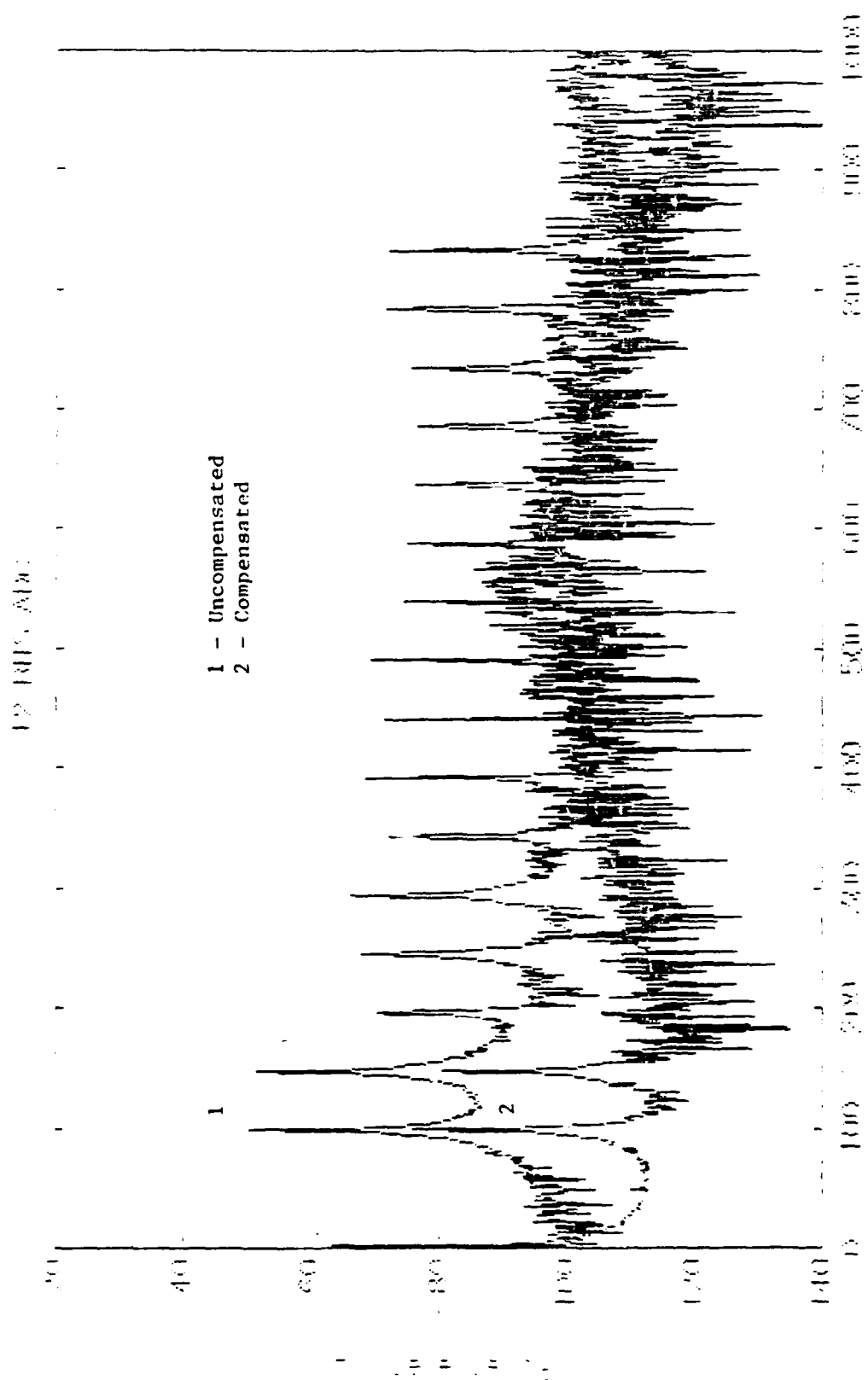
An SMI Adaptive Array

To evaluate the extent to which the ADC nonlinearity affects the performance of an adaptive antenna, we examine an array using the Sampled Matrix Inversion technique to adapt the array weights. The configuration of an m -element half-wavelength spaced array with SMI adaptive algorithm [REED74] is illustrated in Fig. 12. Consider a 5-element adaptive array with a desired signal arrival angle of 50° . To calculate the covariance matrix 150 incoming signal samples were used. We consider two cases for which the input SNR is 55 dB and 15 dB, respectively. (To increase the SNR we reduce the noise power.) For each of these cases we plot the ideal case and the worst case model of seventeen harmonics. In both cases we assume that the power of the desired signal is 5 dB below a sinusoidal waveform which has amplitude equal to the maximum input power of the ADC.

The antenna patterns with and without harmonics are shown in Fig. 13. We see that the harmonic components only cause a slight difference in the antenna patterns. Note that the gain in the look direction in both cases is the same. Although the gain is higher in some non-look direction for the SNR=55 dB case, the output performance will be similar to the SNR=15 dB case. This is because the background noise is much lower in the SNR=55dB case.

In the next example we use the same array with the background thermal noise power equal to -10 dB with respect to the maximum input power, an interference source at 20° with respect to broad side and with frequency $1.7\omega_d$. We again consider two cases for which the input Signal-to-Interference Ratio (SIR) is set to be equal to 0 and 5 dB for both

Fig. 11a



Spectrum of butene-1

Fig. 11b

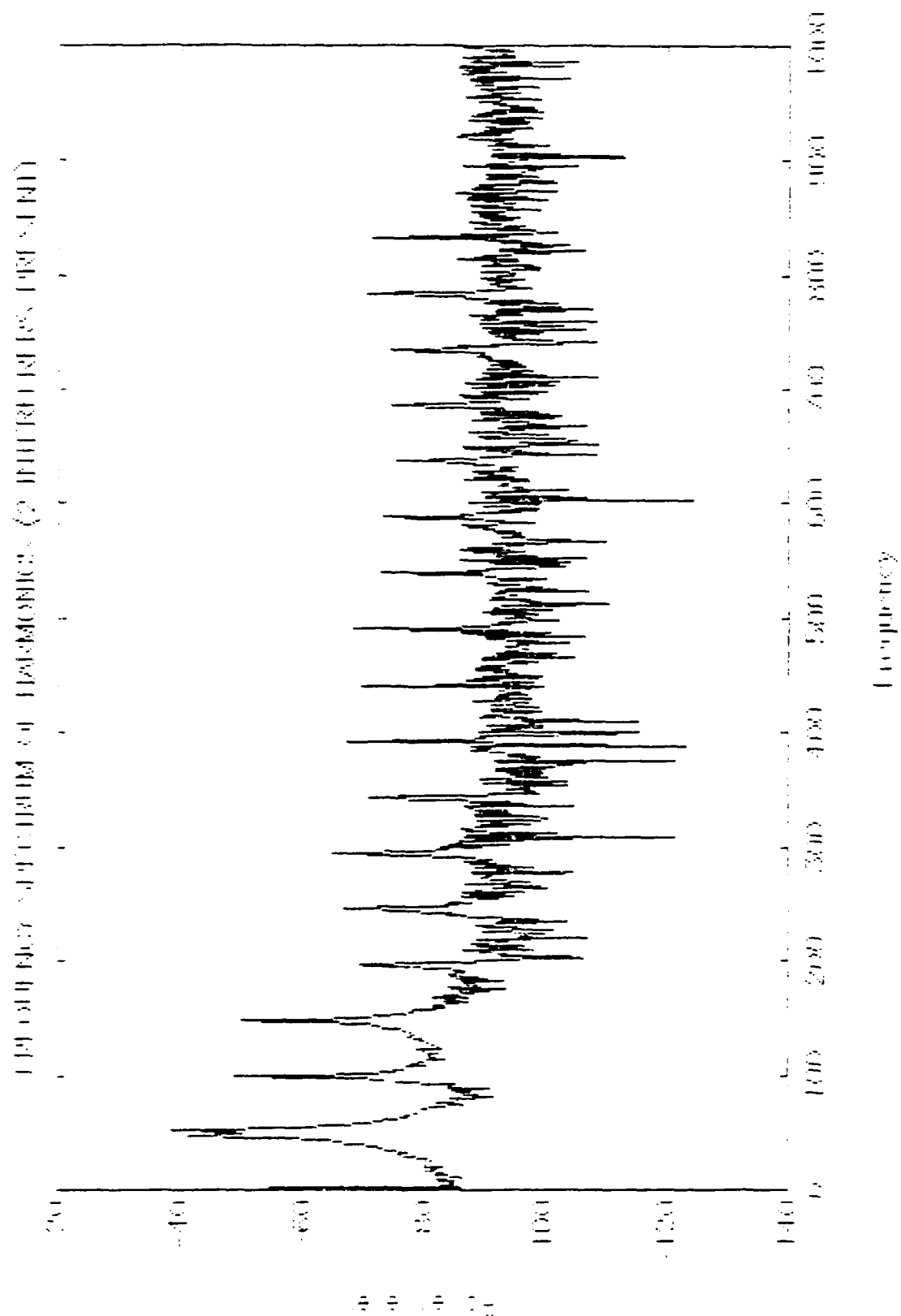
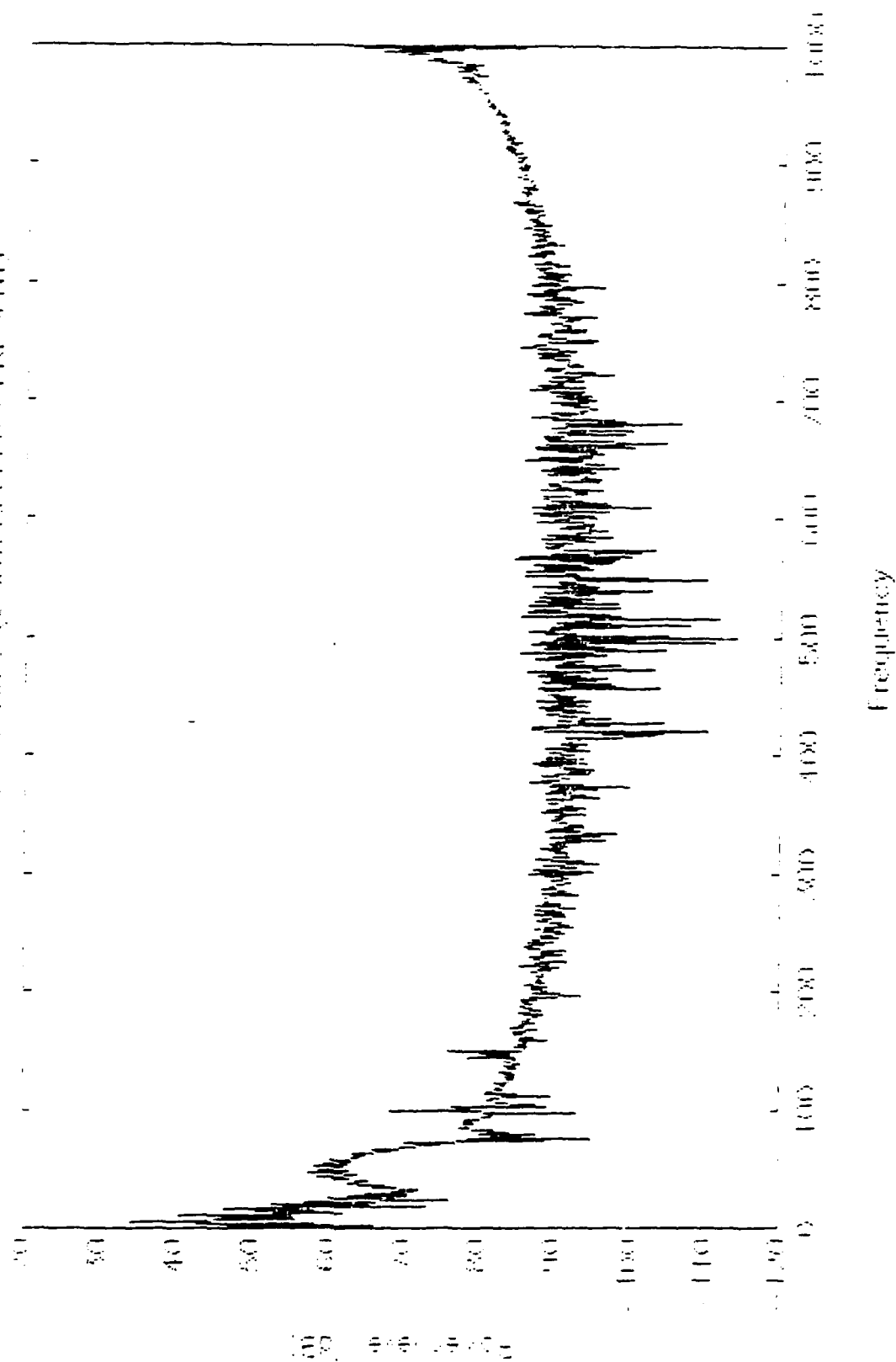


Fig. 11c

SPECTRUM OF HARMONICS (2 HUNDREDS PER SECOND)



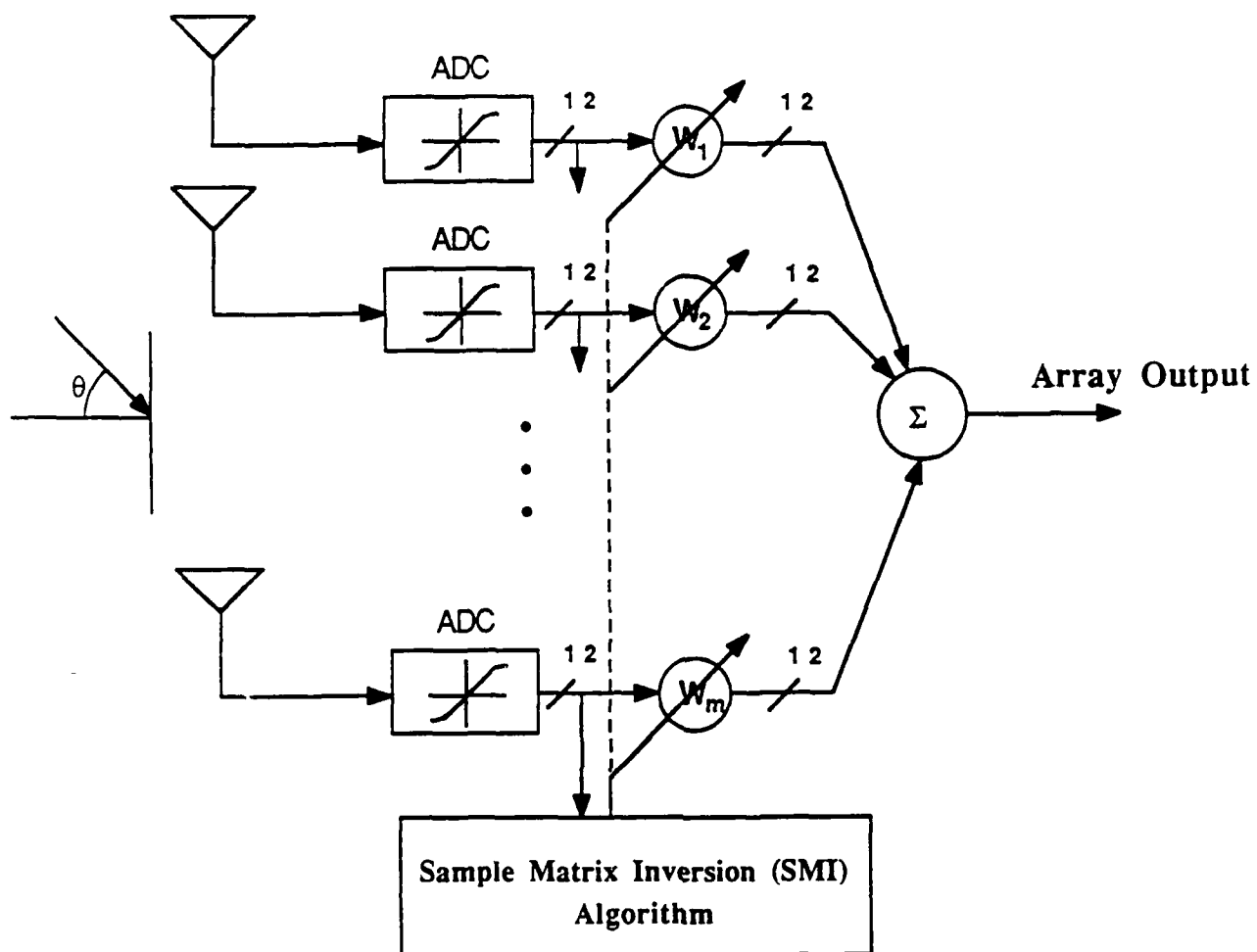
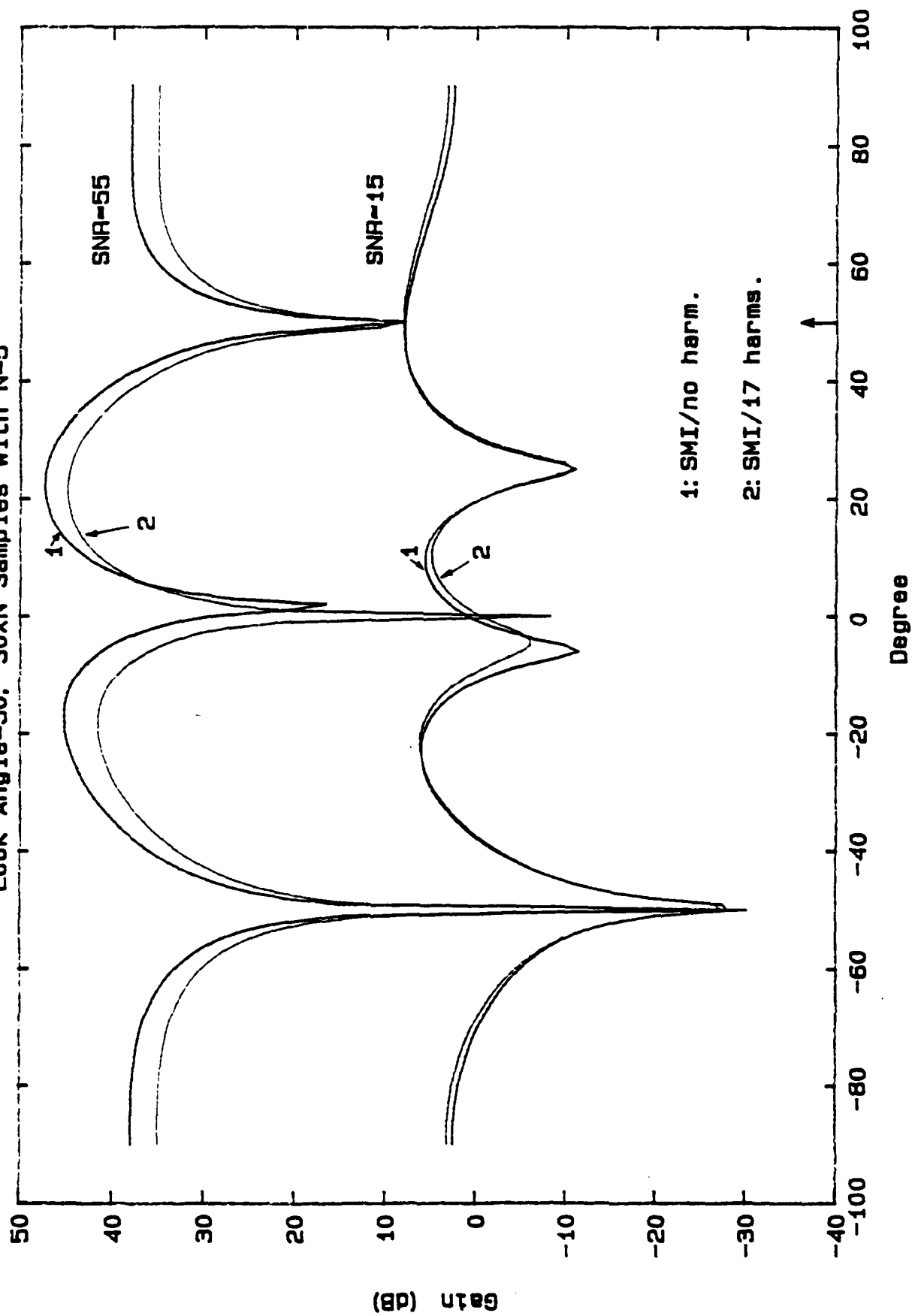


Fig. 12 Configuration of the Digital BeamFormer (DBF)

Fig. 13

Look Angle=50, 30xN Samples with N=5



the ideal and non-ideal systems. The antenna patterns are shown in Fig. 14. We note, in both cases, that the antenna patterns with and without harmonics are almost exact matches. The reason for the similarity is that when the total input signal power, (i.e. the desired signal, interference and the background noise) is large with respect to the power of the harmonic components, the effects caused by the harmonics become negligible. In addition, the antenna patterns in these cases all have a null at an angle of 35° instead of 20° . This is because a signal at 20° with a frequency of $1.7\omega_d$ is electrically equivalent to a signal at 35° with frequency ω_d .

An example illustrating the effect of the nonlinearity on different size arrays also was investigated. Consider an array with a look direction of 50° and the interferer impinging upon the array from 20° with respect to broad side. The input SIR is -10 dB and has a signal power equal to 0 dB with respect to the maximum input power. Again, we use $N=150$. The antenna patterns for the cases of 2-element and 4-element arrays are shown in Fig. 15 for both the ideal and non-ideal systems. We note that in both cases the curves almost completely coincide. The fact that these patterns virtually overlap for each case indicates that the nonlinearity of the ADCs has an insignificant effect on the performance of the DBF employing an SMI adaptive algorithm. The reason that the 2-element array does not put a null at the arrival angle of the interference is because it lacks sufficient of the degrees of freedom (DOF).

The computer simulations indicate that unless the input power of the background noise and interference is smaller than the power of the harmonic components generated by the nonlinearity of the ADCs, the effects of the nonlinearity upon the output performance of the adaptive array is negligible.

VI. Conclusions

The outcome of the study indicates two major results. First, for a typical DBF, there will be error introduced in the output because of the effect of the pseudo-interferers. The amount of degradation is scenario dependent since the contribution to the DBF output power by these artificial interferers is related to the arrival angles of the desired signal and the true interferer(s), their relative frequencies and power levels. For a given case, one can linearize the system by determining the effective position and power level of the pseudo-interferers on the quiescent or steered array pattern and compute the resulting SINR. This can be compared with the ideal case to determine the amount of degradation as a function, for example, of arrival angle of an interferer.

Fig. 14

Look Angle=50, 1 Interferer, 30xN Samples with N=5

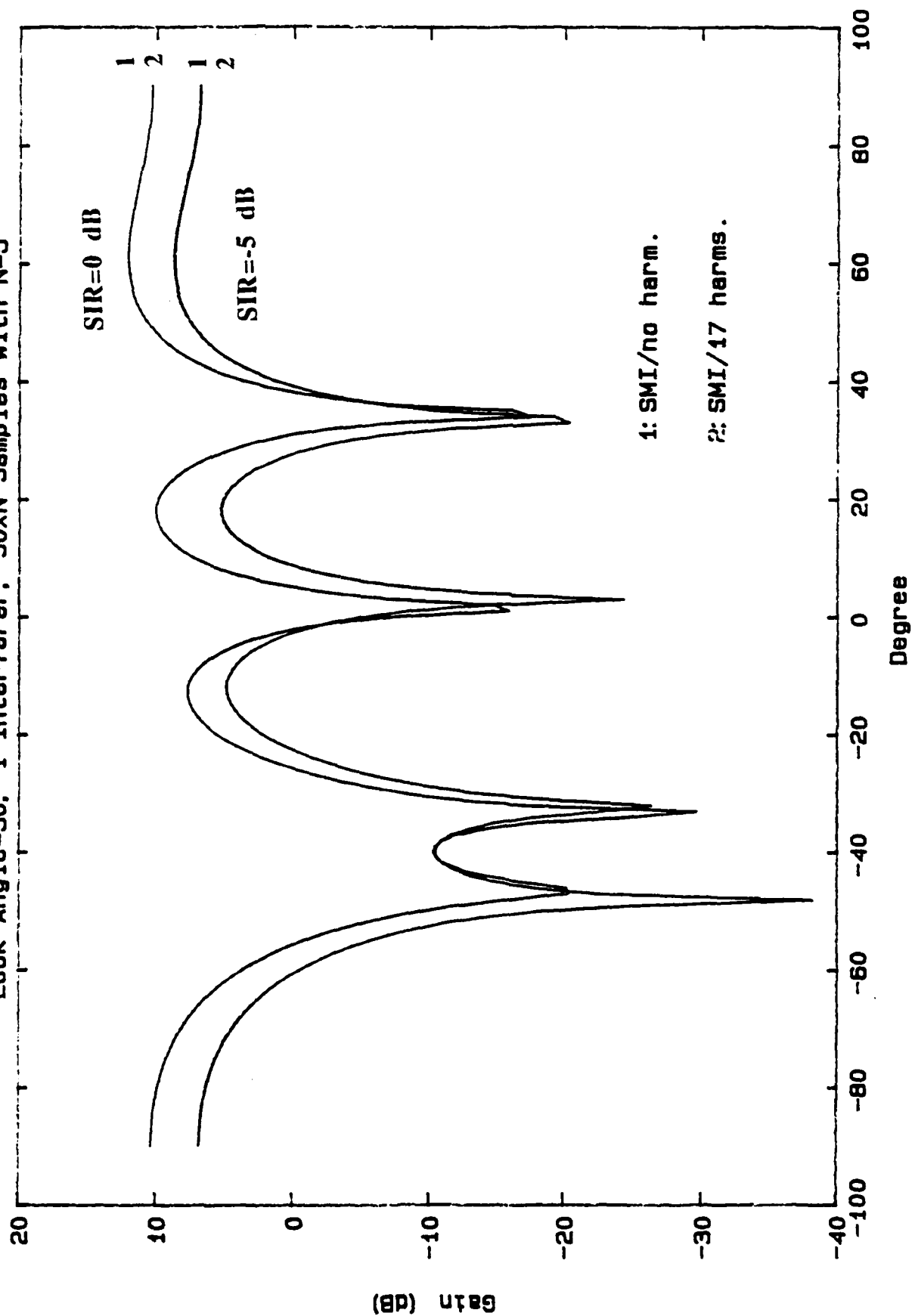
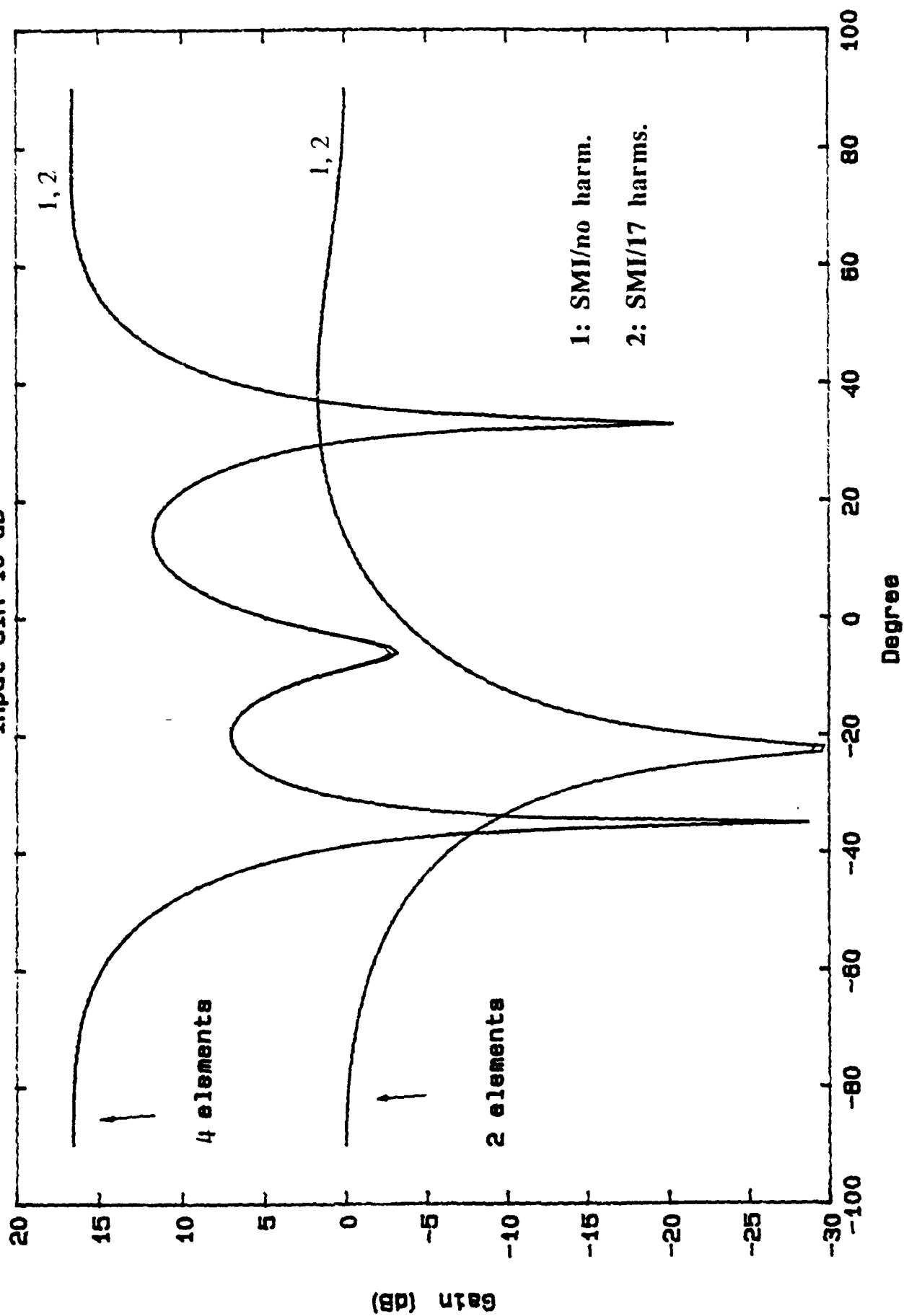


Fig. 15
Input SIR-10 dB



Second, for an adaptive system, the results indicate that there is very little degradation. There are two possibilities to be considered. In the first case, the pseudo-interference power is small compared to the thermal noise; thus, there is little or no degradation. In the second case, the pseudo-interference power is larger than the other signal power and will be nulled by the adaptive algorithm provided that the adaptive DBF has sufficient degrees of freedom.

VII. Recommendations

The completion of this study has left open several problems which need to be addressed. These unanswered questions are outlined below with our recommendations.

The results of this study are predicated on the models developed for the ADC. The model is based upon limited data. A study to verify this model needs to be undertaken. As a first step, an experimental investigation of many typical ADCs of interest to RADC should be performed to validate the assumed harmonic model. In addition, the spectral content of the ADC output needs to be found for the cases of (a) different input frequency, (b) different input power level, and most importantly (c) multi-signal input scenarios. The first case will allow for a better representation of the spectral envelope of the ADC. The second case will verify the IOC curve and conclusions drawn from the power constraint approach. The third case will prove the intermodulation concept for signal plus jammer(s).

The effect of finite bandwidth has not been examined. The nonlinear process results in signal mixing producing many harmonics and intermodulation products. However, in a real system only signals which fall within the passband of the components will pass unattenuated. Furthermore, in any feedback system there will be additional bandwidth limitations. Thus, the overall degrading effects described in this report may be diminished.

The topic of coherent jamming which was not examined in this study, needs to be investigated. It is known that coherent jammers cause severe degradation in adaptive arrays. The potential for a decrease in performance certainly exists in an adaptive DBF. This needs to be quantified.

The SMI, open loop method, was the only adaptive technique studied in this research. Closed loop techniques such as the Least Mean Squares (LMS) the Applebaum feedback, and the Recursive Least Squares (RLS) approaches need to be pursued as to their performance in this degraded environment. In particular, convergence rates should be examined.

Finally, we recommend the development of an experimental simulator system using

several ADCs and digital weights. This will allow for real-time testing of actual signals, reveal problems with channel mismatch caused by dissimilarities in different ADCs and corroborate the results of this study.

As a baseline system, we can simulate the input signal using real signal generators, thus alleviating the need for antennas and an antenna range or anechoic chamber. The effect of different angles of arrival can be simulated by using several (variable) delay elements. Background noise can be simulated by use of noise generators. The signal processing can be performed by a high speed DSP processor such as the Motorola 56000 series. This would be a cost effective means for examining system performance.

REFERENCES

- [UCCI88] Ucci, D. R. and Petroit, R. G., "The Effects of Nonlinearities of High-Speed Analog-to-Digital Converters on Digital Beam Forming Arrays," UES Final Report, Aug. 1988. Contract Nos: F49620-87-R-004 / F49620-88-C-0053, UES, Inc. Dayton, OH.
- [UCCI89] Ucci, D. R. and Petroit, R. G., "The Effects of ADC Nonlinearities on Digital Beamformers," IEEE Proc. of MILCOM, vol. 1, Oct. 1989, pp. 13.3.1-13.33.5.
- [COMP88] Compton, R. T., Adaptive Antennas: Concept and Performance, Prentice Hall, New Jersey, 1988.
- [WIDR85] Widrow, B. and Stearns, S.D., Adaptive Signal Processing, Prentice Hall, New Jersey, 1985.
- [BART80] Barton, P., "Digital Beamforming for Radar," IEE Proc., Vol. 127, Pt. F., No. 4, Aug. 1980, pp. 266-277.
- [REED74] Reed, I. S., Mallet, J. D. and Brennan, L. E., "Rapid Convergence Rate in Adaptive Arrays," IEEE Trans. on Aerosp. and EI. Sys., Vol. AES-10, No. 6, Nov. 1974, pp. 853-863.

ANALYSIS OF MICROWAVE SURFACE IMPEDANCE OF HIGH
TEMPERATURE SUPERCONDUCTORS

Final Report

P. J. Walsh

Fairleigh Dickinson University

Contract: F49620-88-C0053/SB5881-0378

Feb. 25 1990

Abstract

An analytic expression has been developed which gives the Mattis-Bardeen surface resistance for an isotropic superconductor in the local limit for a wide range of scaled frequency $v = hf/k_B T_C$, temperature $t = T/T_C$ and coherence, or free path, parameter $s = Lk_B T_C/hv_F$. The frequency, temperature and free path are f , T and L while T_C and v_F are the transition temperature and Fermi velocity. The parameter ranges tested were $0.003 < v < 0.13$, $0.6 < t < 1.0$ and $0 < s < 10$. Within these ranges, the ratio R_S/R_N of superconductor surface resistance to the normal state resistance spans almost five decades but the analytic expression has an average RMS deviation less than 3.5%. The analytic expression is $R_S/R_N = 1/[1 + H]$, with $H = B[(1-t)/t^2]Y[a/\tanh(av)]^X$. The dependence on temperature and frequency separates but not that on s . Expressions are given for B and a , which depend strongly on s , and for x and y which are weak functions of s . The analytic expression has been used to determine the minimum superconducting surface resistance in an isotropic superconductor possible under variation of the free path or s . The surface resistance is within 10% of the minimum over the range $0.03 < s < 0.20$.

1. Introduction

The rigorous theory of the surface resistance of a superconductor is quite complicated. As first given by Mattis and Bardeen¹ the full theory involved a quadruple integration. In his thesis Turneaure was able to reduce the integration to a double numerical integration for isotropic superconductors. Since the new high temperature are firmly in the local limit where the penetration depth is much larger than the superconducting pair coherence length and collision free path, the double numerical integration can be replaced by a single one as discussed in my first report. Even in this case access to a desk computer is still needed to derive rigorous theoretical estimates of the surface resistance of a particular superconductor for a given temperature and frequency and possibly unknown material free path. The widespread use of rigorous estimates of superconducting surface resistance would be greatly enhanced if an analytic formula were available which gives the surface resistance in terms of the operating and material parameters.

This report presents an accurate analytic expression which yields the Mattis-Bardeen surface resistance in the local limit for isotropic superconductors and illustrates how the expression may be used to determine the minimum surface resistance of a superconductor attainable by varying the material free path of the material while keeping other superconducting properties unchanged. While this report applies only to isotropic superconductors, the techniques used in developing the basic single numerical integration and subsequent analytic form should be applicable to anisotropic superconductors.

2. Dependence of Superconductor Surface Resistance on Frequency, Temperature, and Material Parameters.

The microwave surface resistance of superconductors can be determined, in principle, from the Mattis-Bardeen theory¹ of surface impedance, which has been well-tested². In the general theory, the surface impedance depends on four scaled parameters.^{3,4} These parameters are

$$v = hf/k_B T_C, \quad t = T/T_C, \quad s = Lk_B T_C / \hbar v_f \quad (1)$$

and

$$\beta = 3L^2/2d^2. \quad (2)$$

Here \hbar is Planck's constant divided by 2π and k_B is Boltzmann's constant, f is the microwave frequency, T the temperature, T_C the superconductor critical temperature, v_f the carrier Fermi velocity and L the carrier mean free path, and d is the skin depth of the normal metal. Appendix I gives the Mattis-Bardeen equations for the case of diffuse specular surface reflection for reference.

The parameter v scales the microwave frequency to the transition temperature while t scales the operating temperature in a similar manner. The parameter s may be expressed in terms of the intrinsic coherence length⁵, $\xi_0 = 0.18\hbar v_f / k_B T_C$. Hence $s = 0.18L/\xi_0$ and increases when scattering reduces the coherence of the scattered pair wave compared to their original state. When s is very small scattering leaves the super pairs in phase with their original state and resistive effects are as small as possible. I will term the limit $s = 0$ the fully coherent limit.

The parameter β indicates the spatial change in the microwave field during a free path of the carriers in the superconductor. In the high temperature superconductors β is very small and the theory is quite local,

with the supercarriers scattering before they experience a substantial spatial change in field. When b is much greater than unity, as in some low temperature superconductors, the theory is in the anomalous range and pairs travel through a substantial change in field between scattering collisions. The extreme anomalous range implies that the coherence length is long compared to the penetration depth and this in turn implies that the coherence parameter s approaches zero. This was a special case treated by Mattis and Bardeen and the term anomalous limit has been applied to the small s case, when, in fact, the limit $s = 0$ also exists also in the local limit typical of high temperature superconductors. As noted I refer to the limit $s = 0$ as the fully coherent limit to prevent confusion.

In the local limit Nam^6 gave equations from which the surface resistance may be obtained for all values of s , u and t . I programmed these equations, as discussed in the last report, and have used them to obtain the surface resistance of high temperature superconductors for a wide range of coherence parameters, frequencies and temperatures. The program assumes an isotropic superconductor, with a BCS-like gap given by the convenient analytic form of Shridhar.⁷ Modifications to anisotropic superconductors and non-BCS gaps are not difficult.

The surface resistance, scaled to the surface resistance in the normal metal was calculated for a wide range of scaled parameters. The values of s were 0, 0.1, 0.3, 1.0, 3.0, and 10, those for v were 0.00327, 0.00900, 0.02073, 0.0484 and 0.1284 and for t were 0.6, 0.7, 0.8, 0.9, and 1.0, giving a total of 150 combinations. The values for the scaled frequency correspond to the frequency range from about 17 GHz to 245 GHz for a 92 K superconductor. The value $t = 1.0$ was used as a check on the calculations. Additional checks were made against the results given in Refs. 2, 3 and 7 and against the full Mattis-Bardeen program of Turneaure which is not

restricted to the local case. All checks agree within a few percent, which is approximately the error involved in the numerical calculations used here and in the references cited.

From the results of these calculations a single analytical formula was derived which gives the frequency and temperature dependence of the superconducting surface resistance for the entire range of coherence parameters investigated. The average RMS deviation of the all the calculations was approximately 3.5% even though the range of scaled surface resistance covered was nearly 10^5 . The analytic formula is the following:

$$R_s/R_n = 1/[1 + H(s,v,t)] \quad (3)$$

with

$$H(s,v,t) = B(s)[(1-t)/t^2]Y(s)[a(s)/\tanh(a(s)v)]X(s) \quad (4)$$

$$B(s) = [1.2866/(s + 0.03715)]^{0.782}[1 + 0.213\sin\theta(s)] \quad (5)$$

$$\theta(s) = 2\pi \ln[(s/0.03715) + 1]/\ln[(10/0.03715) + 1] \quad (6)$$

$$y(s) = 0.9917 + 0.02546[s(11.0 - s)]^{1/2} \quad (7)$$

$$a(s) = 4.53 + 1.87s \quad (8)$$

$$x(s) = 1.3355 - 0.032601s^{0.85} \quad (9)$$

Note that the resistance ratio is equal to the reciprocal of H when H is large, i.e. when the resistance ratio is small, and is unity when H is zero.

When s is small the composite dependence simplifies since the exponents x and y are substantially constant. Indeed, at $s = 0$, a appears to equal $3\pi/2$, y is quite close to unity, x is almost exactly $4/3$ while θ is

zero. Hence, the following more approximate, but suggestive, formula describes the fully coherent case $s = 0$ with a 3.2% RMS accuracy:

$$H(0, v, t) = 16[(1-t)/t^2][((3\pi/2)/\tanh((3\pi/2)v))]^{4/3} \quad (4')$$

When the R_n/R_n is small, that ratio is simply the reciprocal of H . Even at small values of s , the surface resistance rises quite sharply above the fully coherent case described in Eq. (4') and the dependencies upon s are necessary, especially in B and a . The formula for R_n is given in the next section which discusses the analysis that lead up to the analytic formula.

3. Choice of Functional Form for Resistance Ratio

Fig. 1 illustrates the ratio R_S/R_N calculated in the local limit calculations for the range of scaled parameters tested. The local limit value of R_N is given by the standard formula

$$R_N = \text{Re}[i\omega\mu/\sigma_N]^{1/2} \quad (10)$$

where σ_N is the complex normal state conductivity. In the collision approximation the normal state conductivity is $ne^2\tau/m[1 + i\omega\tau]$, with n the carrier density, m its mass and τ the collision time. Then

$$R_N = [2\omega\mu m/ne^2\tau]^{1/2}[1 + \omega^2\tau^2]^{1/4}\cos(\phi/2), \quad \tan\phi = [1/(-\omega\tau)] \quad (11)$$

We note that $\omega\tau = sv$. At the higher frequencies and larger s the inertial collision factor $\omega\tau$ plays a role in determining R_N and also appears in the ratio R_S/R_N as noted below. Our numerical calculations were checked against the functional forms in Eqs. (10) and (11) to which the numerical integrations must reduce at $t = 1$ where the superconducting gap vanishes.

To obtain a calculated value for R_S the result in Eq. (11) must be used with the calculations illustrated in Fig. 1. The range of the resistance ratio is nearly 5 orders of magnitude at $s = 0$ but gradually diminishes as s increases. By the time s is 10 the range has reduced to 2 orders. The wide range in the resistance ratio and in the parameters on which it depends made the task of fitting the calculations formidable and the final accuracy achieved was gratifying.

One important point to note concerning the variation of R_S/R_N is that the ratio cannot exceed unity despite the wide range of variation in both s and v , in their product and in the possible functional variation with

temperature. This immediately suggests that the ratio may be expressed as a function of $1/[1 + H(s, v, t)]$ where the range of H is unlimited. Large H will yield a small ratio R_S/R_N while small H produces the unity limit on the ratio.

At low values of s , where coherence is strong, the superconducting surface resistance ratio falls orders of magnitude below unity, increasing as a simple power of the scaled frequency v when v increases. The power exponent is a function of s but not of the scaled temperature and so the temperature and frequency dependencies separate from each other, although both dependencies are functions of the coherence parameter s . When the product $sv = wt$ is near unity, the exponent in the power law dependence on v decreases as inertial factor sv approaches unity. These facts concerning the v dependence suggests the $[a(s)/\tanh(a(s)v)]^{x(s)}$ multiplier in H . At small $a(s)v$ the multiplier produces a power dependence of H and R_S/R_N on v while the v dependence saturates at large $a(s)v$. To replicate the calculations in the $s = 0$ coherent limit, $a(0)$ should be a constant while $a(s)$ should be linear in s at large s so that $a(s)v$ behaves as $sv = wt$ at large sv . These expectations were fulfilled in the fitting process carried out.

The temperature dependence of H was assumed to separate from the frequency dependence. Several forms of the type $[(1-t^n)/t^m]^{x(s)}$ were investigated in the manner discussed below and the choices $n = 1$ and $m = 2$ were near optimum.

Finally, the multiplier $B(s)$ was necessary, of course, to replicate the strong dependence of the resistance ratio on the coherence parameter. Here the general increase in the resistance ratio with increase in s suggests an inverse dependence of H upon s . Since the resistance ratio is finite at the fully coherent limit $s = 0$, the denominator of $H(s)$ must include an additive constant with s . However, this inverse dependence,

raised to the power $y(s)$, leaves an oscillatory departure in the fit to the calculated resistance values. The departure oscillates with $\ln s$ rather than s with about one cycle of nearly 20% departure for $0 < s < 10$. It was thus necessary to include the multiplicative logarithmic oscillatory factor in $B(s)$ to get a truly accurate fit over the full range of s .

4. Fitting Procedure

A wide range of B , a , y and x values were scanned at each s to determine the minimum RMS deviation of the 25 calculated resistance ratios at the s value investigated. The form of R_s/R_n in Eq. (3) along with that of H in Eq. (4) guarantee that the ratio is exact at $t = 0$. Table 1 presents the values of the four fitting parameters, for the six values of s , and the RMS deviation d in percent. True minima were found in the deviation in the

s	B	a	x	y	d
n	n	n	n	n	n
0	15.99	4.53	1.3285	0.9917	2.8
0.1	7.052	4.665	1.3322	1.0274	2.9
0.3	3.182	4.96	1.3315	1.0517	3.1
1	1.048	6.43	1.3087	1.087	2.8
3	0.4042	10.89	1.2431	1.1001	2.3
10	0.2006	23.23	1.1047	1.0722	4.2

Table I. Fitting parameters for analytic surface resistance ratio, Eqs. 3 and 4, and RMS deviation d in %.

four dimensional space of the four variables subject to the functional form of Eqs. (1) and (4). However, it has not been determined if other local minima may exist with smaller deviations in this complicated variable space.

With the values of B , a , x and y which minimize the deviation of the fitting relation to the calculated surface resistance at each of the six values of the coherence parameter it was then possible to choose functional dependencies on s which minimized the overall deviation in the fitted R_s/R_n with s . The functional forms discussed for $B(s)$ and $a(s)$ were employed along with a power law decrease in $x(s)$ with increasing s and a simple

parabolic dependence of $y(s)$ on s to affect a maximum in $y(s)$. The maximum deviation in fitted resistance ratio occurs at $s = 10$ (4.2 %, Table 1) and so the functional forms were all adjusted to give the exact values of B , a , x and y at $s = 10$. The remaining choices in the functional dependencies were adjusted to give nearly uniform deviations at the other five values of s .

The result of the global fitting of B , a , x and y to s is illustrated in Fig. 2. Note that both B and a cover extended ranges, while the variations of x and y are limited by comparison. The open circles are the values of Table 1 and the solid lines are the final functional forms which were presented in Eqs. (5) through (9). The oscillatory behavior noted for B is quite evident in Fig. 2. The RMS deviation over the range of s from 0 to 10 was slightly less than 3.6 % which might be compared to an RMS deviation using the optimum values Table 1 of slightly over 3.0 %. At $s = 1, 0.1, 0.3, 1, 3$ and the individual deviations are 3.8, 3.0, 3.4, 3.3 and 4.2 %, respectively, in the global fit. A comparison of final analytic form with the calculated surface resistance ratio is given in Fig. 3. To prevent confusion in the plotted points only the resistance ratios for the s values, $s = 0, 1$ and 10 , which have the poorest fit, are presented in Fig. 3.

5. Minimum Surface Resistance

A simple application of the analytic formula presented here for the surface resistance is the calculation of the minimum surface resistance possible for the superconductor at a given temperature and frequency. We assume that the mean free path, hence s , is a variable with other superconducting properties remaining constant. Of course, the actual surface resistance may have a field dependence and may have a residual resistance component and we assume both quantities remain unchanged.

As the free path, proportional to s , is decreased the resistance ratio decreases toward its minimum value at the coherent limit $s = 0$. Meanwhile, the normal state resistance increases toward infinity since the collision rate is inverse in s and so a minimum surface resistance exists at an intermediate s . The minimum surface resistance was determined by using the analytic ratio from Eq. (3) with the normal state surface resistance of Eq. (11) and determining the minimum of the product as s varies. The value of s which gives the minimum is almost independent of t and increases approximately linearly with the logarithm of v from 0.73 at $v = 0.00326$ to 0.85 at $v = 0.1284$. In all cases, however, the minimum is quite shallow and over a range in s from about 0.03 to 0.20 the value of the surface resistance is within 10% of the minimum value. Fig. 4 illustrates the relative variation of surface resistance with s for $t = 0.6$ and $v = 0.02073$.

As an example of the numerical value at the minimum, a 80 K superconductor held at 77K and at 245 GHz will have a 0.014 ohm minimum surface resistance (about 1/5 that of copper) if the effective electron mass is 3 and the carrier concentration about $5.7 \cdot 10^{27}/m^3$. While YBCO is

not isotropic. the calculation might be representative of the lowest possible surface resistance for that material oriented so the c axis is normal to the surface.

It is noteworthy that minimum superconducting surface resistance is obtained at high pair collision rates rather than at low collision rates desirable in a normal metal. The reason is, of course, that coherence can survive the coherent phase shifts involved in numerous collisions within a coherence length but not infrequent, incoherent collisions outside the coherence length. The result is quite analogous to the passage of light through a clear liquid such as water. The light suffers continual, strong, but coherent, interactions with the liquid atoms as witnessed by the decrease in velocity by about one quarter in water. Nevertheless, the beam is unscattered. However, the addition of only a small fraction of dispersive material will break up the light beam because of the sparse, but incoherent, interactions over the large distances between the dispersing atoms.

REFERENCES

- (1) D. C. Mattis and J. Bardeen, "Theory of the Anomalous Skin Effect of Normal and Superconducting Metals," Phys. Rev., 111, 412-417, 1958.
- (2) J. P. Turneaure and I. Weissman, J. Appl. Phys. 39 4417-4427, (1968).
- (3) P. B. Miller, "Surface Impedance of Superconductors," Phys. Rev. 118, 928-934 (1960).
- (4) P. J. Walsh and V. T. Tomaselli, to appear Amer. J. Phys. (1990).
- (5) T. VanDuzer and C. W. Turner, Principles of Superconductive Devices and Circuits, Elsevier, N. Y. (1981).
- (6) S. B. Nam, "Theory of Electromagnetic Properties of Superconducting and Normal Systems. I," Phys. Rev. 136, 470-486 (1967).
- (7) S. Shridhar, C. A. Shiffman and H. Hamdeh, "Dynamic Response of $Y_1Ba_2Cu_3O_y$ and $La_{1.83}Sr_{0.15}Cu_4-d$ in the Superconducting State," Phys. Rev. B 36 (1989).

FIGURE CAPTIONS

1. Local limit calculations (open squares, values computed by single numerical integration) of the ratio of superconductor surface resistance to normal state surface resistance at various values of s , v , t , the scaled free path, frequency and temperature, respectively.
2. Values of the analytical fitting parameters B , a , x and y . The open circles are the best values of these parameters, as given in Table 1, at the six values of s investigated. The solid lines are the functional forms of Eqs. (5) - (9).
3. Comparison of analytic expression for the surface resistance ratio with the numerical calculations for three values of s .
4. Variation of superconducting surface resistance, in arbitrary units, with s for $t = 0.6$ and $v = 0.2073$.

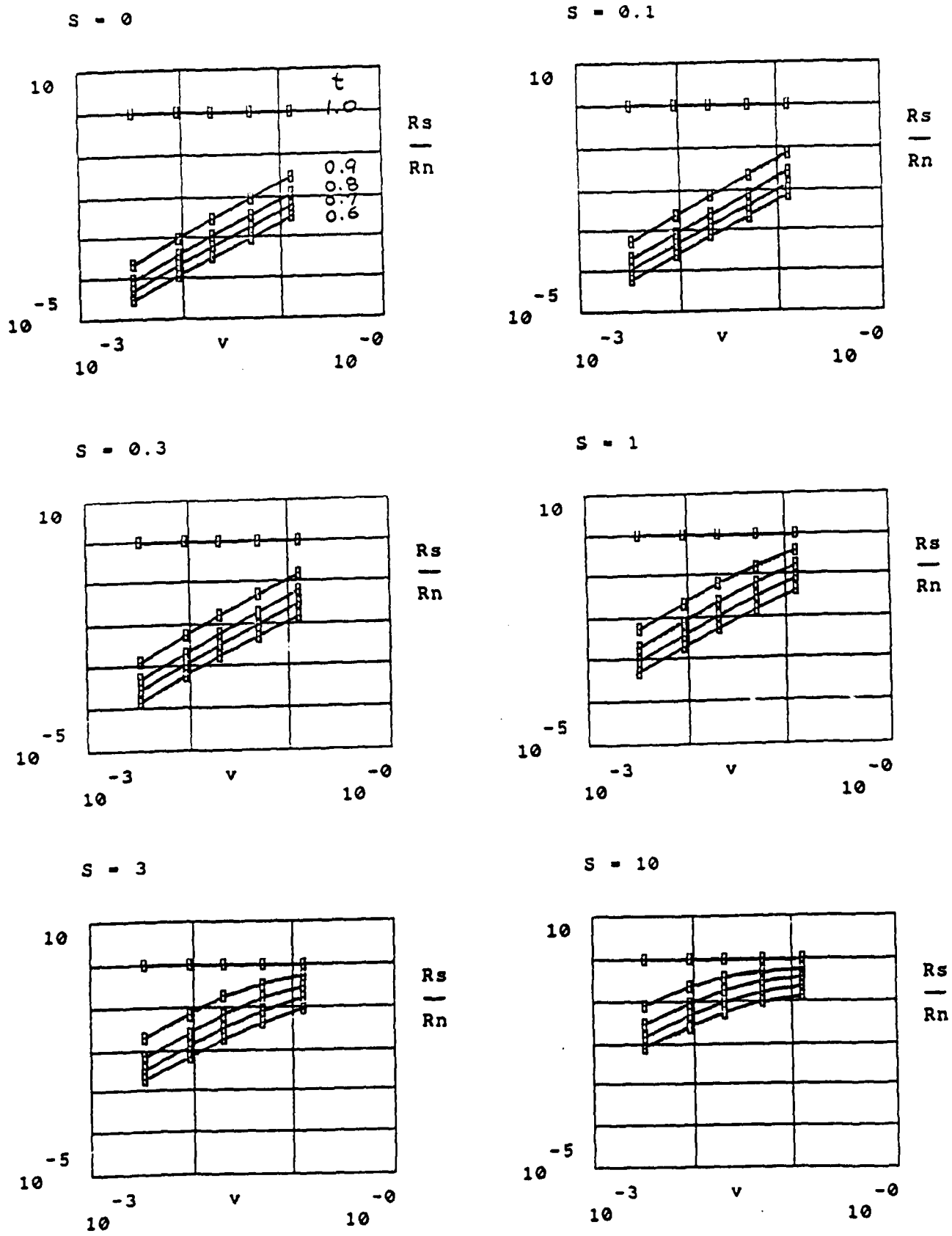


FIG. 1

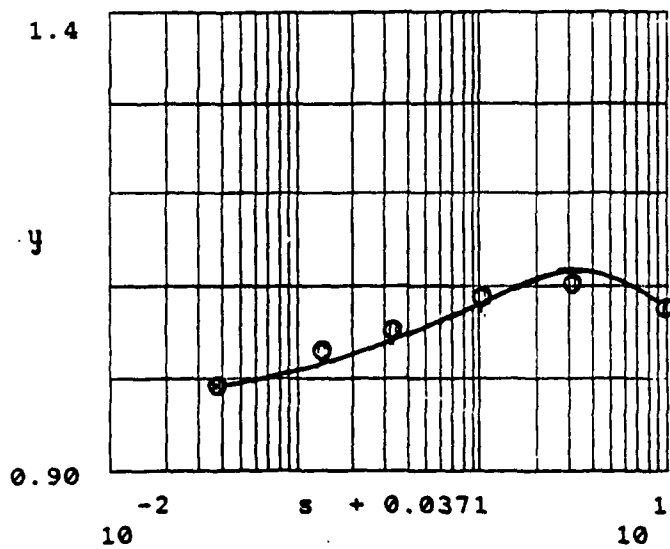
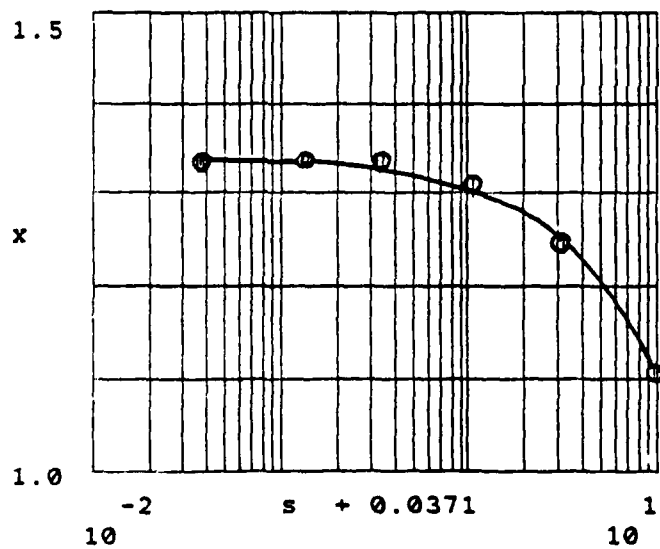
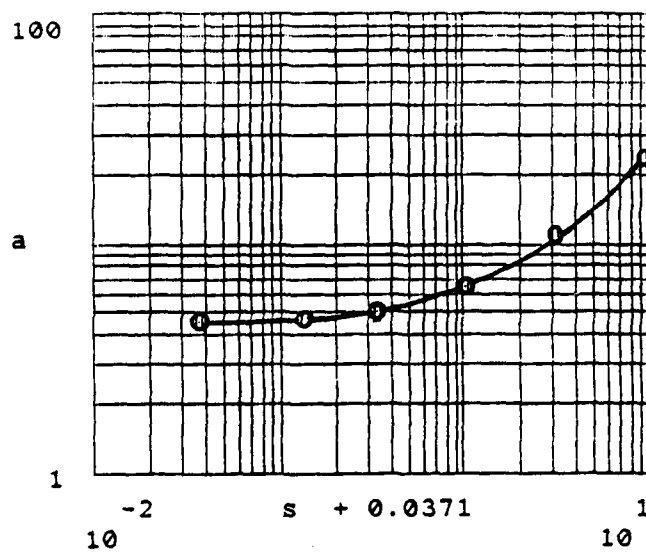
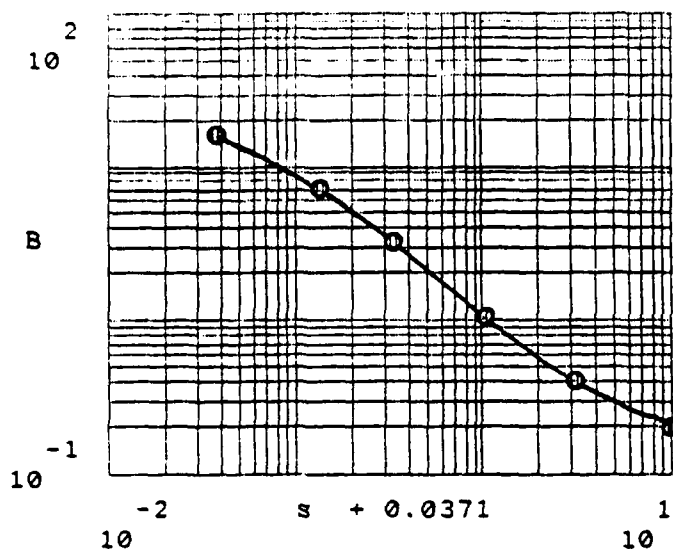


FIG. 2

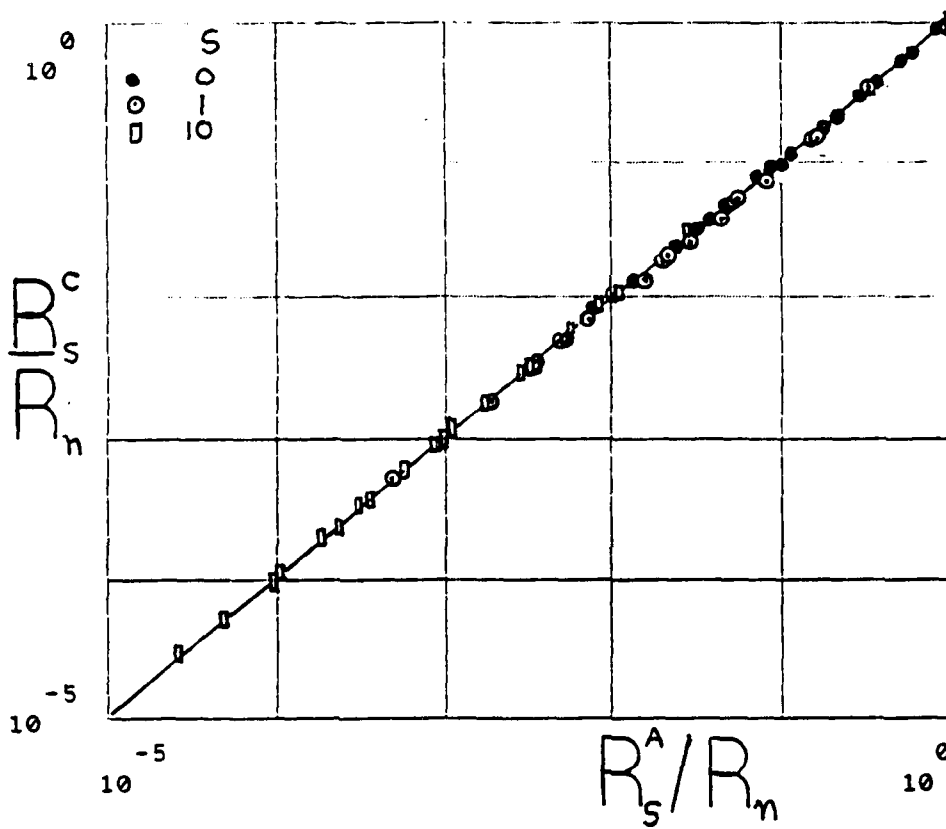


FIG. 3

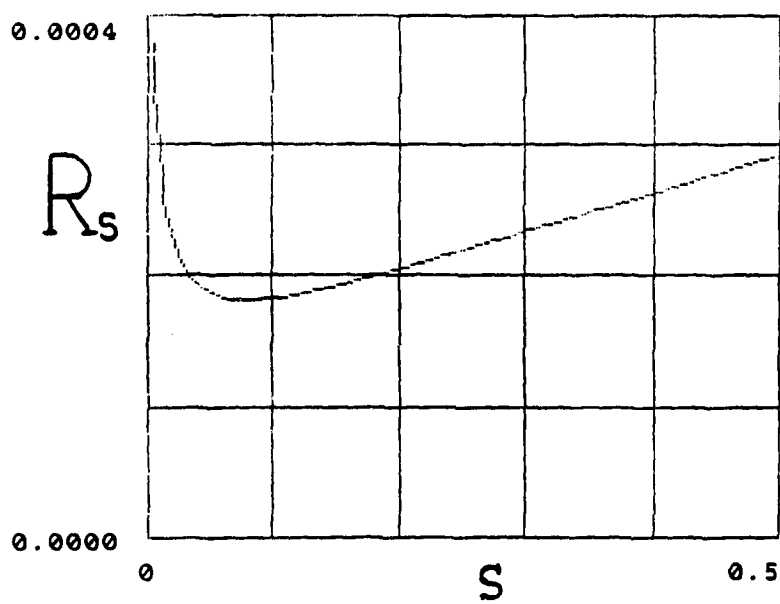


FIG. 4

FINAL REPORT NUMBER 60
REPORT NOT AVAILABLE AT THIS TIME
Dr. Kenneth L. Walter
210-9MG-113

1989 USAF-UES RESEARCH INITIATION PROGRAM MINI-GRANT

Sponsored by the
AIR FORCE OFFICE OF SCIENTIFIC RESEARCH
Conducted by the
Universal Energy Systems , Inc.
FINAL REPORT

Prepared by:	Gwo-Ching Wang, Ph. D.
Academic Rank:	Associate Professor
Department and	Physics Department
University:	Rensselaer Polytechnic Institute
Research Location:	Rensselaer Polytechnic Institute Troy, New York 12180-3590
USAF Researcher:	Alvin J. Drehman
Date:	November 30, 1989
Contract No:	F49620-88-C-0053/SB5881-0378

X-RAY POLE-FIGURE ANALYSIS OF $\text{YBa}_2\text{Cu}_3\text{O}_{7-x}$ THIN FILM ON $\text{SrTiO}_3(100)$ PREPARED BY RF DIODE SPUTTERING

Abstract

The structural properties of high temperature superconducting textured $\text{YBa}_2\text{Cu}_3\text{O}_{7-x}$ thin film on $\text{SrTiO}_3(100)$ substrate have been studied by employing the reflection X-ray pole figure method, which is extremely powerful in studying the nature and degree of preferred orientations of the crystallites in polycrystalline materials as well as the relative orientations and lateral lattice alignments of the film with respect to the substrate. The specimen was fabricated on $\text{SrTiO}_3(100)$ substrate by RF diode sputter deposition and subsequent furnace annealing in flowing oxygen. The film was found to be more preferentially a-axis oriented than c-axis oriented with a grain ratio of about 4:1. The a-axis oriented grains have been determined to be heavily twinned and the twinning structure has been identified as reflection class with the (013) reflection plane. Nevertheless, the crystal axes of both types of oriented grains are aligned with those of the substrate. The possible twinning structure of the c-axis oriented grains and the interface matching of the film with respect to the substrate are discussed.

Acknowledgements

I would like to thank the Air Force Systems Command, the Air Force Office of Scientific Research, the Solid State Sciences Division at Rome Air Development Center, Hanscom, and the Universal Energy System for sponsorship of this Research Initiation Program.

The research program on high temperature superconducting film was challenging and rewarding. We thank Dr. Alvin Drehman at Hanscom who provided us with valuable samples of high temperature superconducting $\text{YBa}_2\text{Cu}_3\text{O}_{7-x}$ thin films.

1. Introduction

Since the discovery of the high-temperature superconductivity in Y-Ba-Cu-O compounds [1-4], extensive studies covering a variety of aspects have been carried out. It is well accepted that the superconductivity is closely related to the structural properties of the films. Massive efforts have been put in the epitaxial growth of the $\text{YBa}_2\text{Cu}_3\text{O}_{7-x}$ (YBCO) materials [5] and many important techniques such as X-ray θ - 2θ diffraction, electron microscopy and electron diffraction have been employed to characterize the structural properties [e.g., 6-8]. Recently, Knorr and Livingston have reported the X-ray pole figure study on the preferred orientations of magnetically aligned, sintered compacts of $\text{RBa}_2\text{Cu}_3\text{O}_{7-x}$ [9]. We have found the X-ray pole figure analysis method is not only an effective way to study the texture of YBCO film but especially also an excellent way to quantify the lattice alignments between the film and the substrate.

2. Objective of the Research Effort

The research objective is to characterize the structural properties of YBCO film and its lattice alignments with respect to the $\text{SrTiO}_3(100)$ substrate using the X-ray pole figure analysis method.

3. Experimental

The YBCO film was prepared by RF diode sputtering of a Y-Ba-Cu oxide target with compositional ratios of 1:3:4. The sputter gas consisted of 1×10^{-2} Torr argon and 2×10^{-3} oxygen. The target was approximately 5 cm in diameter, and was located 3 cm above the SrTiO_3 substrate holder. The sputtering power was 160 Watts, and a 30 volt negative bias was applied to the substrate holder. The DC current flowing from the substrate holder through the plasma and then to the ground was maintained at a constant. The film was deposited on $\text{SrTiO}_3(100)$ substrate at a

substrate temperature of $\sim 400 \pm 25$ K. The film thickness was determined to be ~ 1 μm . The as-grown film was amorphous, and subsequently was crystallized in a tube furnace by heating at 1120 K for 30 min. in flowing oxygen and then cooling to below 470 K at a rate of ~ 3 K/min..

The oxygen stoichiometry has been studied by using nuclear scattering of 3 MeV protons [10], in which the oxygen concentration determined is 6.59. The transition temperature, T_c , of the films was determined to be ~ 87 K by four probe resistive measurements. The transition width is about 8 K.

X-ray θ -2 θ diffraction scans were produced by a Philips PW1710 diffractometer using Cu $K\alpha$ radiation. X-ray pole figures were obtained with the Schulz method [11]. Fig. 1 is a scheme of the Schulz geometry. The method requires a special specimen holder which tilts the sample with a horizontal axis, BB', while rotating it in its own plane about an axis, AA', normal to its surface. The horizontal axis lies on the specimen surface and is initially adjusted by a rotation about the diffractometer axis to make equal Bragg angles with the incident and diffracted beams [12]. A horizontal slit is placed at D, half way between the radiation source and the specimen, to ensure the constancy of the absorption in a wide range of latitudinal rotation. The studies were performed by employing a Siemens 018-003 pole-figure goniometer, with which the latitudinal and the longitudinal rotations are provided by a vertical circle and a small horizontal azimuth circle, respectively. The latitudinal rotation, measured by an angle of ϕ , can be varied from 0 to 90° , while the azimuthal scan, vs. an angle of β , can be simultaneously taken from 0 to 360° . In our experiments, however, the ϕ -angles were usually set at preselected values, at which the longitudinal β -scans were made from 0 to 360° .

4. Results and Discussion

4.1 X-Ray θ -2 θ Diffraction

Fig. 2 shows an X-ray θ -2 θ scan for the YBCO film on $\text{SrTiO}_3(100)$ substrate. The (100), (200) and (005) peak intensities are "relatively" much stronger than that of the strongest

(110)/(103) powder diffraction peak (the (110) and (103) Bragg peaks overlap with each other since the (110) and (103) planes have about the same interplanar spacings, hence, the same Bragg angles). According to the study of powder diffraction [13], the relative powder diffraction intensities (normalized to the (110)/(103) peak intensity) for (100), (200) and (005) reflections were determined to be 0.04, 0.13 and 0.11, respectively, where the relative intensity of (110)/(103) was assumed to be 1.00. The appreciably stronger intensities of (100) and (200) reflections indicate preferential orientation of the YBCO film with the a-axis "normal" to the substrate, meanwhile, the considerable intensity of (005) reflection indicates that a fraction of grains in YBCO film are preferentially oriented with the c-axis "normal" to the substrate. In contrast, the much lower intensities of (110)/(103) reflections might suggest that the grains producing these reflections are randomly oriented and the fraction of the randomly oriented grains is fairly small. However, the θ - 2θ diffraction studies do not provide further information about the orientational perfection of the film to the substrate normal and the lateral lattice alignment of the film with respect to the substrate near the interface. Such properties are mostly amenable to study by the X-ray pole figure analysis method.

4.2 X-Ray Pole Figure Analyses and Film Orientations

The X-ray pole figure analysis is a traditional technique. The method is adapted from a single-crystal stereographic projection which is derived from a spherical projection and has been widely used for the description and analysis in geometrical crystallography. To prepare a spherical projection, the crystal is assumed to be placed at the center of a hollow, transparent sphere. With the centers of the crystal and sphere coincident, normals are drawn from the common center to each atomic plane and further extended to the spherical surface. The intersects of the normals and spherical surface are then referred to as the poles of the atomic planes. One of the most useful features of the spherical projection is the ease with which angular measurements can be made on it through a system of angular coordinates, which is analogous to the lines of latitude and longitude used on the globe of the earth. The angle between two poles, i.e., between the normals of two

atomic planes, can be simply measured on the spherical projection as the number of degrees on a great circle passing through both the poles. However, it is more convenient to work on a piece of flat paper with the angular relationship on the spherical surface. A stereographic projection is the most important scheme to map out the spherical projections without destroying any angular relation. The projection is built up with intersects of lines passing through both the south pole and the spherical projections with any plane, which is normal to the diameter connecting the north and south poles and is also located in the northern hemisphere [12]. In brief, a pole figure is a map of the statistical distribution of the atomic plane normals of a single crystalline or a polycrystalline sample and, therefore, it provides a complete picture of the texture of the sample.

As mentioned before, the θ - 2θ reflection data does not contain enough information regarding the accurate degree of alignment between the crystal orientations and the substrate normal. However, the pole figures do provide the conclusive evidence. Fig. 3 shows the azimuthal scans of the SrTiO_3 (200), and YBCO (200), (005) poles, where the specimen was slightly tilted at an angle (ϕ) of about 2.0° . Any deviation greater than 0.5° from the setting ϕ value decreases the peak intensities. The data shows that all the poles coincide at the same azimuthal angle (β). The coincidence of both the ϕ and β angles is expected if the poles of the film and that of the substrate are parallel to each other. Accordingly, we conclude that the a-axis of one type of grains and the c-axis of another type of grains in YBCO film are aligned, respectively, with the normal of the substrate well within the experimental error ($\sim 0.5^\circ$). Based on this finding, the ratio of the a- to c-axis oriented grains is estimated to be about 4:1 from the relative peak intensities of (200), (100) and (005) reflections.

The film orientations with respect to the substrate have been reported to be essentially related to the preparation conditions, especially to the substrate temperature and oxygen partial pressure [7]. However, due to the slight difference in lattice constants of a (3.8214 \AA) and b (3.8877 \AA) we might also expect a fraction of b-axis oriented grains to exist, even though b-axis orientation might be energetically less favored than a-axis orientation since a-axis has a lattice mismatch (to the substrate whose lattice constant is 3.9050 \AA) of about 2.1 % which is much higher than that of the

b-axis ($\sim 0.4\%$). An approach to detect the possible b-axis oriented grains is to monitor the (020) pole of the film since it has an appreciable relative intensity (0.20) and is distinguishable from the (200) pole due to the $\sim 1^\circ$ difference in Bragg 2θ angles. However, the (020) and other possible $\{0k0\}$ poles are completely obscured by those of the substrate since the ratio of their lattice constants is about 0.996 which only makes a slight difference of about 0.3° in 2θ between their Bragg reflections. In addition, similar to a different approach to be presented later, the detection of the possible b-axis oriented grains might also be realized by studying other $\{hkl\}$ poles in the [010] projection. However, due to the tiny difference, or even an overlapping, in Bragg reflections and latitudinal angles resulting from the slight difference in lattice constants of a and b, a distinction between the a-axis and the possible b-axis oriented grains is beyond the present instrumental resolution.

4.3 Pole Figures of the Substrate

In the study of film growth, there always exists a question regarding the lattice alignment of the film with respect to the substrate at the interface. The X-ray pole figure analysis is particularly capable of answering this question, provided that the film is thin enough for X-ray to penetrate and to be diffracted by the substrate lattice. Our YBCO film has a vertical thickness of $\sim 1\ \mu\text{m}$. Therefore, the X-ray pole figure can be used to detect the reflections from the substrate as already shown in the θ - 2θ scans.

SrTiO_3 crystal is well known to have a perovskite structure with a Sr atom at the center of its cubic unit cell, whose lattice parameter is $3.9050\ \text{\AA}$, a Ti atom at the corners and three oxygen atoms at the centers of the faces. Hence, a four-fold symmetry is expected. The relative azimuthal angle of the reflection from the film with respect to that of the substrate will conclusively indicate the in-plane alignment between the crystal lattices of the film and substrate [14]. Therefore, we have monitored various poles of the substrate. All of these poles consistently indicate the cubic structure of SrTiO_3 . For comparison, only the line profile of the $\{111\}$ pole family, referred to as "form", of the substrate is presented in Fig. 4(a). During the scan, the latitudinal angle was set at ϕ

$= 55.0^\circ$ and the azimuthal angle was referenced with the same meridians as used for the pole figure studies of the film. The $\{111\}$ poles appear at azimuthal angles (β) of 45° , 135° , 225° and 315° , respectively. The four-fold symmetry as observed is essentially a characteristic of a cubic single crystal.

4.4 a-Axis Oriented Grains

a) [100] Projection

The crystallographic unit cell of YBCO is shown in Fig. 5. It is conveniently described as oxygen-deficient perovskites with tripled unit cells due to the Y-Ba ordering along the c-axis. The analysis of the neutron powder diffraction profile indicates that the unit cell of $\text{YBa}_2\text{Cu}_3\text{O}_7$ is orthorhombic (Pmmm) with $a = 3.8198(1) \text{ \AA}$, $b = 3.8849(1) \text{ \AA}$ and $c = 11.6762(3) \text{ \AA}$ [15]. It is well accepted that the $\text{YBa}_2\text{Cu}_3\text{O}_{7-x}$ phases differ from that of $\text{YBa}_2\text{Cu}_3\text{O}_7$ by a random distribution of oxygen vacancies on the b-axis (i.e., O(1) sites) [16,17]. The slightly oxygen-deficient phases ($x \ll 1$) still possess the same point group, i.e., mmm. X-ray powder diffraction studies essentially indicate that the unit cell of $\text{YBa}_2\text{Cu}_3\text{O}_{6.8}$ is orthorhombic (Pmmm) with $a = 3.8214(7) \text{ \AA}$, $b = 3.8877(6) \text{ \AA}$ and $c = 11.693(2) \text{ \AA}$ [13]. The X-ray powder diffraction results are compatible with those of a neutron powder diffraction study in a polymorphous $\text{YBa}_2\text{Cu}_3\text{O}_{7-x}$ sample [18] and have been used in our studies. Accordingly, a general form $\{hkl\}$ has a multiplicity of eight since the repetition operation of the point group (mmm) on the initial pole (hkl) produces eight crystallographically identical poles. However, only half of them which have positive h-indices, i.e., $(h\bar{k}l)$, (hkl) , $(h\bar{k}\bar{l})$ and (hkl) , appear in the stereographic projection on the (100) plane. There also exist special forms, such as $\{100\}$, $\{010\}$, $\{001\}$ and $\{0kl\}$ etc., whose multiplicities are less than those of the general forms. For example, the special form $\{100\}$ only has two multiplicities, namely, (100) and $(\bar{1}00)$, and only the projection of the former exists in the [100] projection. The stereographic projections of YBCO in the [100] projection are shown in Fig. 6a) as open circles where the (200) is projected at the center for convenience. The calculated projection angles are listed in Table 1.

b) Pole Figure and the Twinning Structure

As shown with open circles in Fig. 6a), the special forms of $\{h0l\}$ possess a multiplicity of two lying on the big circle which contains both (200) and (001) poles and also showing a two-fold symmetry. A general form has four multiplicities, i.e., poles. For example, the $\{112\}$ form possesses a multiplicity of four and each of them is located with an azimuthal angle of 112.76° or 67.24° apart from its two adjacent multiplicities, respectively. Again, the multiplicities possess a two-fold symmetry. In other words, the $\{112\}$ form consists of two pairs of poles each of them containing two poles with 67.24° apart (or 112.76° apart for other two equivalently combined pairs) and the two pairs of poles are identical with an azimuthally angular rotation of 180° . Experimentally, however, a four-fold symmetry in pole pairs was observed as shown in Fig. 4(b), where the angles between two poles within each pair remain as $\sim 67.2^\circ$, but, two more identical pairs of poles appear with a 90° shift in azimuthal positions from those expected in a single crystal calculation. The same symmetry was also observed for various other $\{hkl\}$ forms with k and l not simultaneously being zero, shown as solid circles in Fig. 6a). In brief, the [100] projection from experimental measurements (solid circles) consists of two identical calculated projections (open circles) with an azimuthally angular rotation of 90° from each other. The four-fold symmetry conclusively indicates a twinning structure, which might be identified as reflection type with a twin plane of (013).

It will be discussed later that the (110) twin has been reported in the literature [19-23]. Models have been proposed to describe the twinning structure [17,21,22]. In our work reported here, we found the a-axis oriented grains are similarly twinned with a composition plane of (013). As to be discussed later, the major oriented fraction may result mainly from the coincidence of lattices of SrTiO_3 (3.9050 Å) and orthorhombic YBCO (3.8877 and 11.6932 Å), which give lattice mismatches of 0.4% and 0.2% (three to one matching), respectively. Furthermore, due to the isotropy of the substrate lattice arrangement, there exist equal possibilities for the film to align along two perpendicular directions. This gives rise to the twinning formation with an equal fraction of twinning lamellae. This argument is consistent with the experimental observation in which the

relative X-ray reflection intensities of poles are equal. The equally diffracted peak intensities essentially suggest an equal fraction (50%) of the twinned lamellae. Accordingly, we have proposed a possible schematic representation of the twinning structure as shown in Fig. 6b). The twin boundary, indicated by the solid line, is apparently the (013) plane. Within each domain the atom chains along b- and c-axes are parallel while across the boundary the b-axis and c-axis are "switched"; i.e., the grains are crystallographically reflected with respect to the (013) plane, which is similar to those findings reported for the c-axis oriented grains.

c) In-Plane Alignment

As discussed above, the relative azimuthal angular relation between the film and the substrate will conclusively indicate the lattice alignment at the interface. Comparing any YBCO form, for example, {112} with any SrTiO₃ form, say, {111} as shown in Figs 4(b) and 4(a), one can see that each of the {111} poles falls right at the halfway point between adjacent {112} pole pairs. Therefore, the angles from each of {112} poles to the nearest {111} pole of SrTiO₃ are determined to be $\sim 11.4^\circ$. If we designate the zone which contains both (200) and (010) poles to be the origin (where $\beta = 0$) of the azimuthal coordinate as we have already assumed in the plots, then the (112) pole appears azimuthally at $\beta = 56.4^\circ$, which is in agreement with the calculated value (56.38°) as given in Table 1. Therefore, the observed azimuthal angle agrees with a lattice arrangement in which both b- and c-axes are aligned with those of the substrate. Accordingly, we propose a schematic representation of crystal structures at the boundary of the a-axis oriented grains near the interface in Fig. 6c), where the 90° twinning relationship is also presented. Despite the twinning structure, all of the YBCO crystal axes (now labeled as X, Y and Z) are oriented parallel to those of the substrate as discussed above.

4.5 c-Axis Oriented Grains

a) [001] Projection and the Pole Figures

As indicated by both the θ - 2θ and pole figure data, besides the more preferential a-axis oriented grains, the film also consists of a smaller fraction (4:1) of c-axis oriented grains.

Similarly, a [001] stereographic projection is shown as open circles in Fig. 7a) where the (005) pole is projected at the center. Again, a two-fold symmetry is expected. A general form, for example {117}, is expected to show a multiplicity of four, but it still has a two-fold symmetry since the lattice parameters, a and b, are different. However, the calculation indicates that the azimuthal angles between the multiplicities differ by only $< 1^\circ$ as presented in Table 1.

Fig. 4(c) is a line profile of the {117} poles. During the scan, the latitudinal angle was set at 35.5° . The four poles all appear as expected. However, the differences in the azimuthal angles are less than $\sim 1^\circ$ so that the observation of the tiny differences is marginal. Individual textured YBCO films have been reported to be heavily twinned with a (110) twin plane [19-23]. The twin boundaries were observed by either electron or optical microscopy. Furthermore, Zhu and Suenaga *et al* [22] reported their observation on twin boundary layers in pure and alloyed $\text{YBa}_2\text{Cu}_3\text{O}_{7-x}$ film by using electron diffraction technique. The (110) twinning structure is highly likely to exist in the c-axis oriented grains since our specimen is also heavily textured. Therefore, the line profile of the {hkl} poles might be an overlap of those reflections from two types of perpendicularly twinned lamellae, whose lattice axes are rotated by 90° across the twin boundary. Another possibility for the formation of the line profiles of {hkl} poles is that the profiles may consist of the overlaps of {hkl} and {khl} poles. Since the lattice constants of a and b are slightly different with a ratio of ~ 0.98 , the detection of this small difference is marginal due to the low instrumental resolution.

b) In-Plane Alignment

Even though there exists difficulty in determining the possible (110) twinning structure, we can still compare the YBCO poles in its [001] projection with the SrTiO_3 poles to study the in-plane alignment. To do so, we examine the line profiles of YBCO {117} and SrTiO_3 {111} poles in Figs. 4(a) and 4(c), respectively. The experimental data is consistent with the in-plane alignment where a- and b-axes are all parallel to those of the substrate. The same conclusion also could be drawn by comparing the {111} poles with various other YBCO poles as measured and presented in Fig. 7a). A possible structure at the boundary between the c-axis oriented grains and the

substrate is shown in Fig. 7b). All of the YBCO axes (labeled as X, Y and Z) are oriented parallel to those of the substrate as discussed above.

4.6 Interface Matching

The YBCO unit cell consists of three stacked perovskite structures which differ only slightly in lengths of the sides and in oxygen atomic positions. Since the lattice constant of SrTiO_3 is very close to those of the YBCO perovskite structures, it might be energetically favored for the film lattices to align with those of the substrate at the growth stage or during the annealing.

As discussed above, the YBCO film mainly consists of a-axis and c-axis oriented grains. All of the crystal axes are oriented parallel to those of the substrate. It seems natural to discuss the interfacial lattice matching between the film and substrate. For the a-axis oriented grains, the mismatches are calculated to be 0.4 % and 0.2 % in b-axis and c-axis directions, respectively. The lattice mismatches (< 0.4 %) are well below the thermal vibrational amplitude. Therefore, the a-axis oriented fraction may match very well with the substrate. It is likely that no atom dislocation may occur over the twin lamellar dimension. However, for the c-axis oriented grains, a mismatch of 2.1 % arise in the direction of a-axis. An edge dislocation or a strain may occur over about 50 unit cells in the a-axis direction since the observed twin lamellar dimension usually exceeds 50 Å [23].

5. Conclusion

The high temperature superconducting textured YBCO thin film has been investigated by applying reflection X-ray pole figure analyses. The method is traditional but extremely suitable for studying preferentially oriented textures and especially the lattice alignments between the film and the substrate. The $\text{YBa}_2\text{Cu}_3\text{O}_{7-x}$ film (with $x = 0.41$) was found to consist mainly of a-axis and c-axis oriented grains. The crystal axes of both types of oriented grains are aligned with those of the substrate at the interface. Furthermore, the a-axis oriented grains are twinned. The twinning

structure has been identified as reflection type with the (013) reflection plane. While a similar twinning structure is highly likely to exist in the c-axis oriented grains, it was indistinguishable in the pole figure due to the limited angular resolution of the instrument. The twinning structure may arise partially from the symmetry of the substrate as indicated in the observed equal diffracted intensities.

6. Recommendations

We have demonstrated that the X-ray pole figure analysis is a powerful method to study the preferred orientations in the YBCO film and the lattice alignments between the film and the substrate. We can use the method to characterize the stability and reproducibility of the YBCO films. Further research efforts should be focused on the correlation between structural properties (microstructure and epitaxial orientation), chemical composition and electrical properties ($R(T)$, T_c and J_c) using multiple technique approach. A joint proposal combining expertises of Hanscom Air Force Base (thin film growth), R. P. I. (X-ray pole figure) and Brooklyn college of City University at New York (nuclear scattering) will be submitted to the Air Force to further study the high temperature superconducting thin films.

Table 1 The Bragg and stereographic projection angles (in degree) of the $\text{YBa}_2\text{Cu}_3\text{O}_{6.8}$. In the calculation, Cu $K\alpha$ radiation wavelength and the YBCO lattice constants obtained from the X-ray powder diffraction study were used. The latitudinal angles $\phi[100]$, $\phi[010]$ and $\phi[001]$ are designated as those for the $[100]$, $[010]$ and $[001]$ projections, respectively. The azimuthal angles $\beta[100]$ and $\beta[001]$ represent those for the $[100]$ and $[001]$ projections, respectively. The azimuthal angular references are assumed as follows, in the $[100]$ projection the zone containing both the (200) and (001) poles, while, in the $[001]$ projection that containing both the (005) and (010) poles has an azimuthal angle of 0° .

hkl	2 θ	$\phi[100]$	$\phi[010]$	$\phi[001]$	$\beta[100]$	$\beta[001]$
012	27.53	90.00	33.62	56.38	56.38	0
102	27.83	33.17	90.00	56.83	0	90.00
110	32.81	44.50	45.49	90.00	90.00	45.49
103	32.81	44.43	90.00	45.57	0	90.00
112	36.33	49.73	50.55	65.01	56.38	45.49
005	38.45					
014	38.45	90.00	53.06	36.94	36.94	0
104	38.78	52.58	90.00	37.42	0	90.00
020	46.71					
200	47.58					
115	51.47	62.33	62.83	40.63	31.03	45.49
122	55.24	64.23	31.29	73.49	71.61	26.96
124	62.24	67.04	39.94	59.35	56.38	26.96
117	65.50	68.12	68.51	35.51	23.25	45.49
108	68.67	69.07	90.00		0	90.00
128	87.15	73.00	54.92	40.15	36.94	26.96

Figure Captions

- Fig. 1. A schematic representation of the Schulz geometry used in the X-ray pole figure analysis. Bragg angle can be adjusted by rotating the sample about the diffractometer axis. The specimen can be simultaneously rotated latitudinally and azimuthally around the BB' and AA' axes, respectively.
- Fig. 2. X-ray θ - 2θ diffractions of the YBCO film on the $\text{SrTiO}_3(100)$ substrate. The spectrum indicates that the film is preferentially a-axis and c-axis oriented with respect to the substrate. The diffuse peaks near 30° are diffracted from impurity phases.
- Fig. 3. Line profiles of $\text{SrTiO}_3(200)$, YBCO (200) and YBCO (005) poles. All the latitudinal angles are set at $\phi = 2.0^\circ$. The pole positions coincide at the same azimuthal angle. The symbols such as x7 and x38 represent the intensities are reduced by a factor of 7 and 38 in the presentation, respectively.
- Fig. 4. Line profiles of representative poles of the film and substrate. The references of the azimuthal angular measurements are defined in Table 1. (a) $\text{SrTiO}_3\{111\}$ poles, (b) YBCO $\{112\}$ poles and (c) YBCO $\{117\}$ poles.
- Fig. 5. A schematic representation of the YBCO unit cell. The cell consists of three stacked oxygen-deficient perovskites. Atom sites are labeled for the convenience in discussion.
- Fig. 6a). $[100]$ stereographic projection of the YBCO film. The (200) pole is projected at the center for convenience. Open circles: calculated projections for which the calculated angles are listed in Table 1. Solid circles: poles measured from X-ray diffraction

which consists of two identical maps of the calculated projections with a 90° azimuthal rotation from each other. A open circle with a solid circle at the center simply represents an overlap of a calculated and a measured poles.

- b). Proposed twinning structure of a-axis oriented grains in the YBCO film. The twin boundary is presented with a solid line and the unit cells on either sides of the boundary are shown as rectangles in which the lattice parameters are labeled. The Y and Ba atoms are positioned either above or below the plane of the plot.
- c). A schematic diagram showing the relationship of lattice alignments between the a-axis oriented YBCO grains and $\text{SrTiO}_3(100)$ substrate at the interface. The 90° twinning scheme is also presented. X is labeled for the a-axis direction, while, Y, similarly Z, is labeled for either b- or c-axis direction.

Fig. 7a). [001] stereographic projection of the YBCO film. The (005) pole is projected at the center for convenience. Open circles: calculated projections for which the corresponding angles are listed in Table 1. Solid circles: poles measured from X-ray diffraction. A open circle with a solid circle at center simply represents a overlap of a calculated and a measured poles.

- b). A schematic diagram showing the relationship of lattice alignments between the c-axis oriented YBCO grains and $\text{SrTiO}_3(100)$ substrate at the interface. X is labeled for the a-axis direction, while, Y, similarly Z, is labeled for either b- or c-axis direction.

References:

- [1] M. K. Wu, J. R. Ashburn, and C. J. Torng, P. H. Hor, R. L. Meng, L. Gao, Z. J. Huang, Y. Q. Wang, and C. W. Zhu, *Phys. Rev. Lett.* **58**, 908 (1987).
- [2] R. J. Cava, B. Batlogg, R. B. van Dover, D. W. Murphy, S. Sunshine, T. Siegrist, J. P. Remeika, E. A. Rietman, S. Zahurak, and G. P. Espinosa, *Phys. Rev. Lett.* **58**, 1676 (1987).
- [3] S. Hikami, T. Hirai, and S. Kagoshima, *Jpn. J. Appl. Phys.* **26**, L314 (1987).
- [4] H. Takagi, S. Uchida, K. Kishio, K. Kitazawa, K. Fueki, and S. Tanaka, *Jpn. J. Appl. Phys.* **26**, L320 (1987).
- [5] for example, T. Aida, T. Fukazawa, K. Takagi, and K. Miyauchi, *Jpn. J. Appl. Phys.* **26**, L1489 (1987); T. Yamaguchi, S. Aoki, N. Sadakata, O. Kohno, and H. Osanai, *Appl. Phys. Lett.* **55**, 1581 (1989); G. C. Xiong, and S. Z. Wang, *Appl. Phys. Lett.* **55**, 902 (1989); E. A. Hayri, M. Greenblatt, K. V. Ramanujachary, M. Nagano, J. Oliver, M. J. Miceli, and R. Gerhardt, *J. Mater. Res.* **4**, 1099 (1989).
- [6] M. Tomita, T. Hayashi, H. Takaoka, Y. Ishii, Y. Enomoto, and T. Murakami, *Jpn. J. Appl. Phys.* **27**, L636 (1988).
- [7] Y. Terashima, M. Sagoi, K. Kubo, Y. Mizutani, T. Miura, J. Yoshida, and K. Mizushima, *Jpn. J. Appl. Phys.* **28**, L653 (1989); M. Sagoi, Y. Terashima, K. Kubo, Y. Mizutani, T. Miura, J. Yoshida, and K. Mizushima, *Jpn. J. Appl. Phys.* **28**, L444 (1989).
- [8] L. A. Tietz, C. B. Carter, D. K. Lathrop, S. E. Russek, R. A. Buhrman, and J. R. Michael, *J. Mater. Res.* **4**, 1072 (1989).
- [9] D. B. Knorr, and J. D. Livingston, *Supercond. Sci. Technol.* **1**, 302 (1989).
- [10] H.-S. Jin, H. Homma, D. Yan, A. J. Drehman, and G.-C. Wang, *Mat. Res. Soc. Symp.* to be published.
- [11] L. G. Schulz, *J. Appl. Phys.* **20**, 1030 (1949).
- [12] B. D. Cullity, **Elements of X-Ray Diffraction**, Addison-Wesley, 1978.
- [13] W. Wong-Ng, R. S. Roth, L. J. Swartzendruber, L. H. Bennett, C. K. Chiang, F. Beech, and C. R. Hubbard, *Adv. Ceramic Mater.* **2**, 565, (1987).
- [14] K.-H. Park, H.-S. Jin, L. Luo, W. M. Gibson, G.-C. Wang, and T.-M. Lu, *Mat. Res. Soc. Symp. Proc.* **102**, 271 (1988); K.-H. Park, D. C. McKenna, H.-S. Jin, G.-C. Wang, K. Rajan, G. Smith, L. Luo, and W. M. Gibson, *Mat. Res. Soc. Symp. Proc.* **138**, 545 (1989).
- [15] F. Beech, S. Miraglia, A. Santoro, and R. S. Roth, *Phys. Rev. B* **35**, 8778 (1987).

- [16] S. Miraglia, F. Beech, A. Santoro, D. Tran Qui, S. A. Sunshine, and D. W. Murphy, *Mat. Res. Bull.* **22**, 1733 (1987).
- [17] D. W. Murphy, S. A. Sunshine, P. K. Gallagher, H. M. O'Bryan, R. J. Cava, B. Batlogg, R. B. van Dover, L. F. Schneemeyer, and S. M. Zahurak, **Chemistry of High-Temperature Superconductors**, edited by D. L. Nelson, M. S. Whittingham, and T. F. George, ACS Symp. Series **351**, 181 (1987).
- [18] F. Izumi, H. Asano, T. Ishigaki, E. Takayama-Muromachi, Y. Uchida, N. Watanabe, and T. Nishikawa, *Jpn. J. Appl. Phys.* **26**, L649 (1987).
- [19] A. Mogro-Campero, L. G. Turner, and E. L. Hall, **Superconductivity and Its Applications**, edited by H. S. Kwok, and D. T. Shaw, Elsevier, 1988, p.168.
- [20] S. Iijima, T. Ichihashi, Y. Kubo, and J. Tabuchi, *Jpn. J. Appl. Phys.* **26**, L1478 (1987).
- [21] S. Iijima, T. Ichihashi, Y. Kubo, and J. Tabuchi, *Jpn. J. Appl. Phys.* **26**, L1790 (1987).
- [22] Y. Zhu, M. Suenaga, Y. Xu, R. L. Sabatini, and A. R. Moodenbaugh, *Appl. Phys. Lett.* **54**, 374 (1989).
- [23] S. Nakahara, T. Boone, M. F. Yan, G. J. Fisanick, and D. W. Johnson, Jr., *J. Appl. Phys.* **63**, 451 (1988).

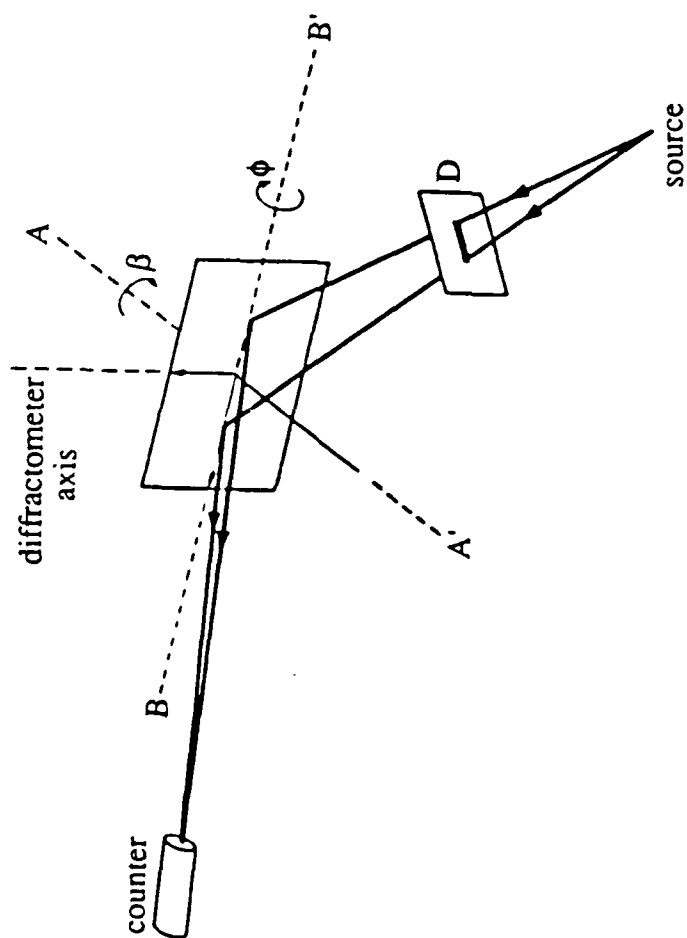


Fig. 1

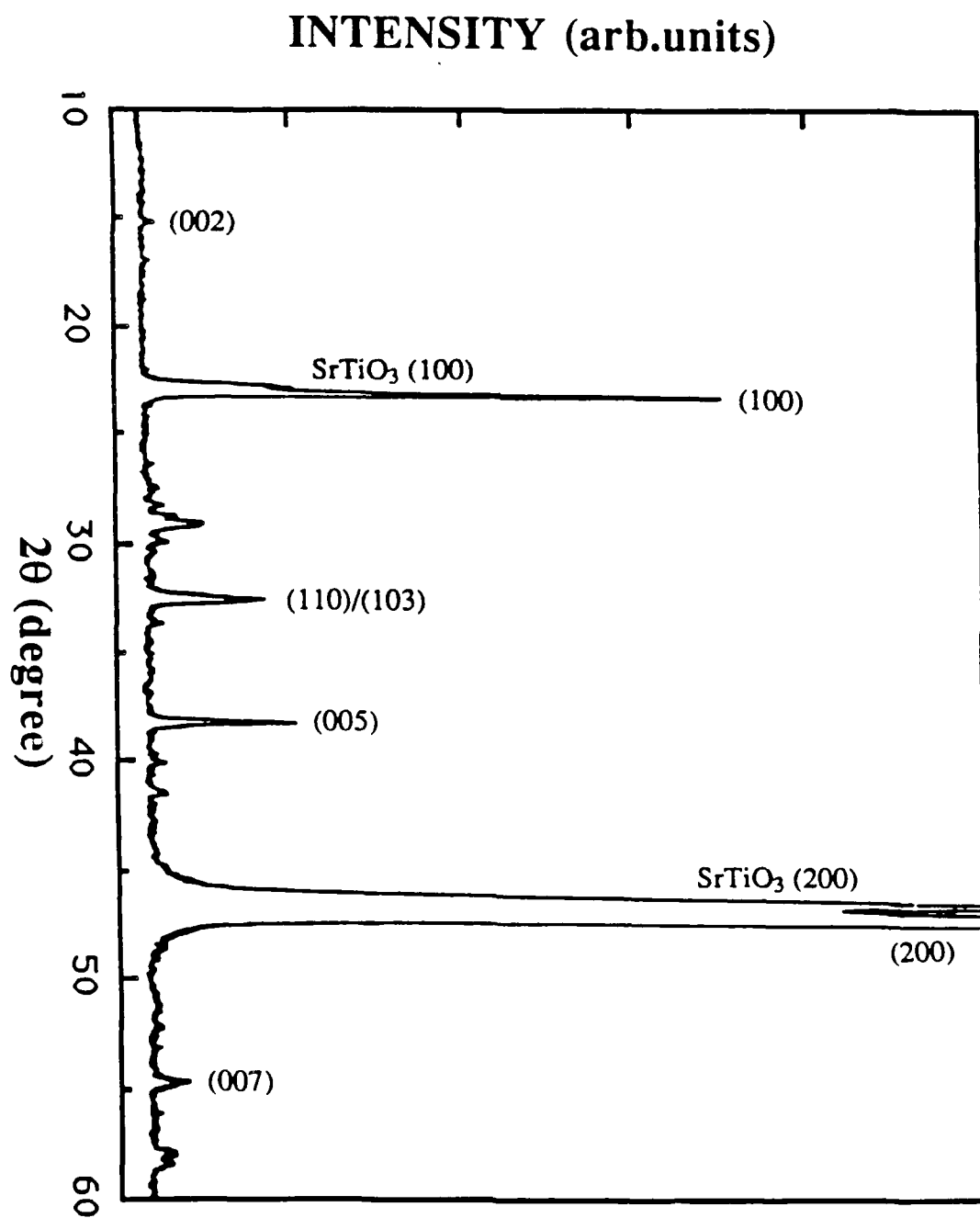
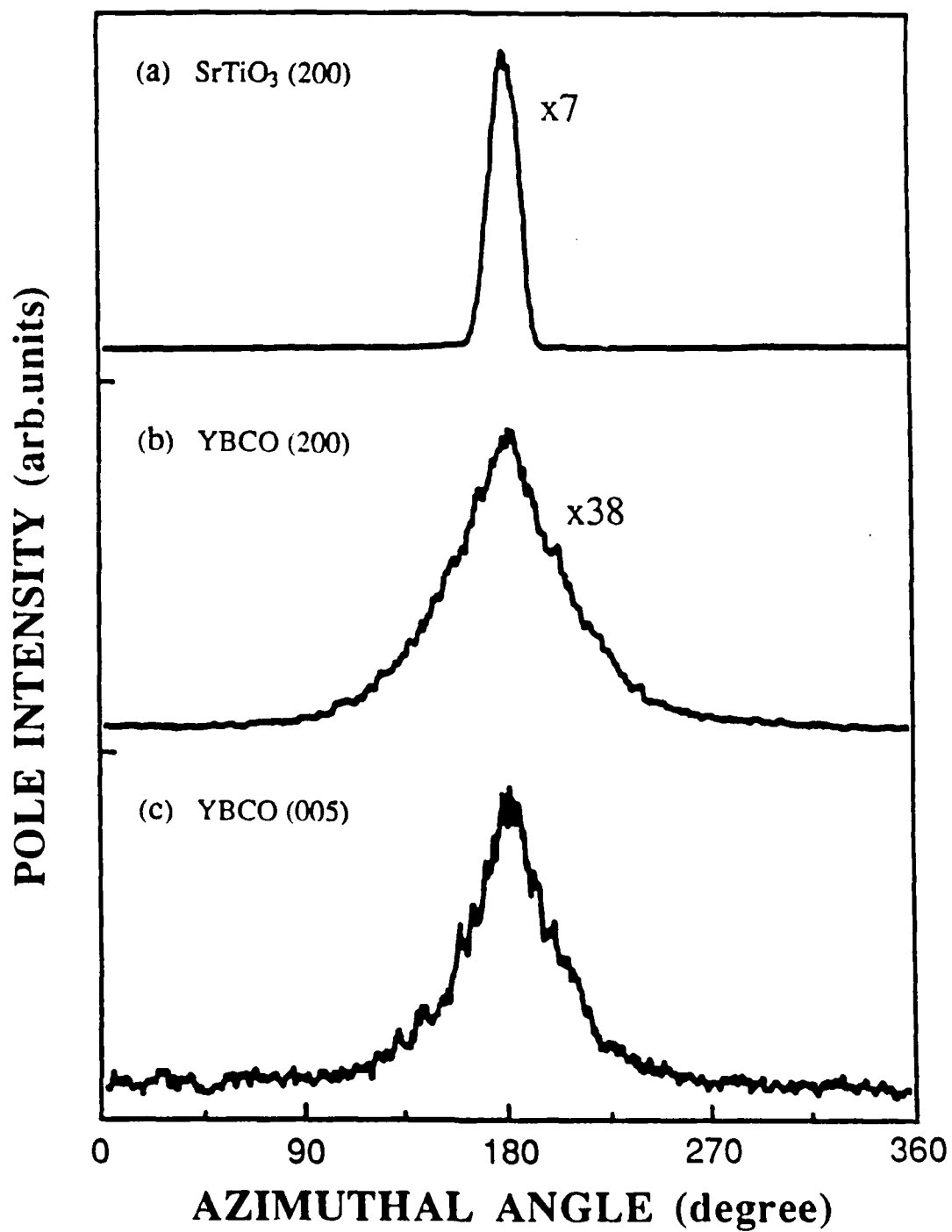


Fig. 2



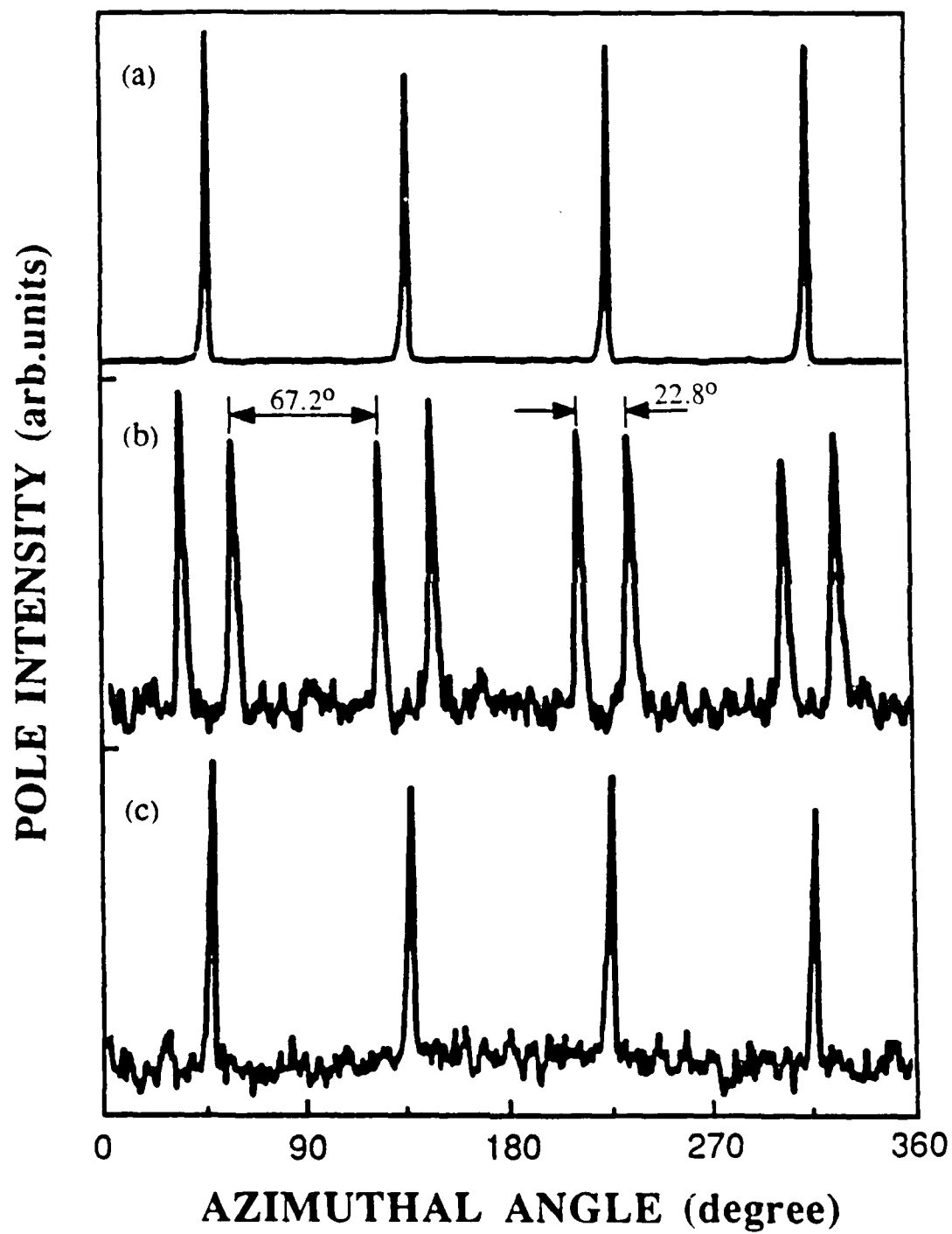


Fig. 4

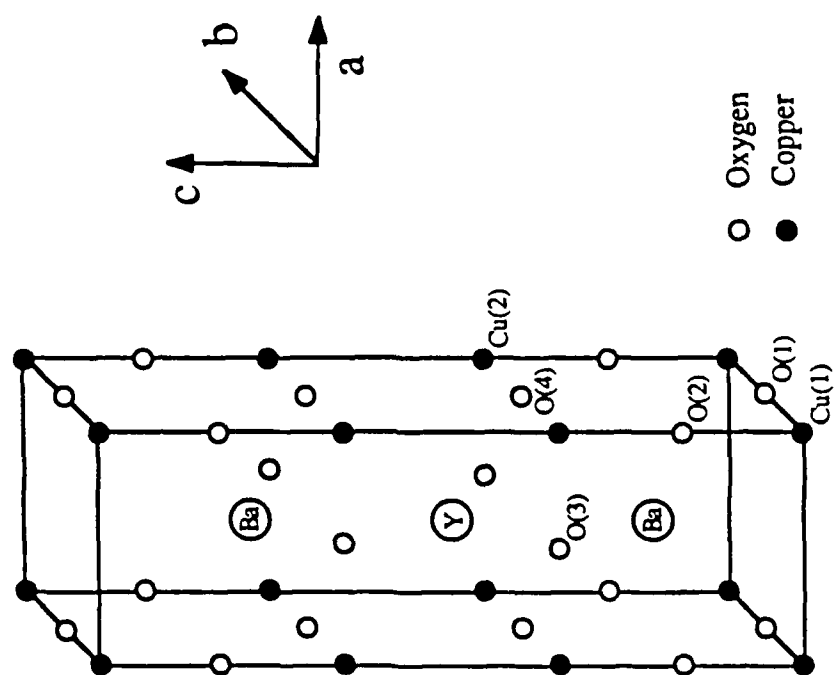


Fig. 5

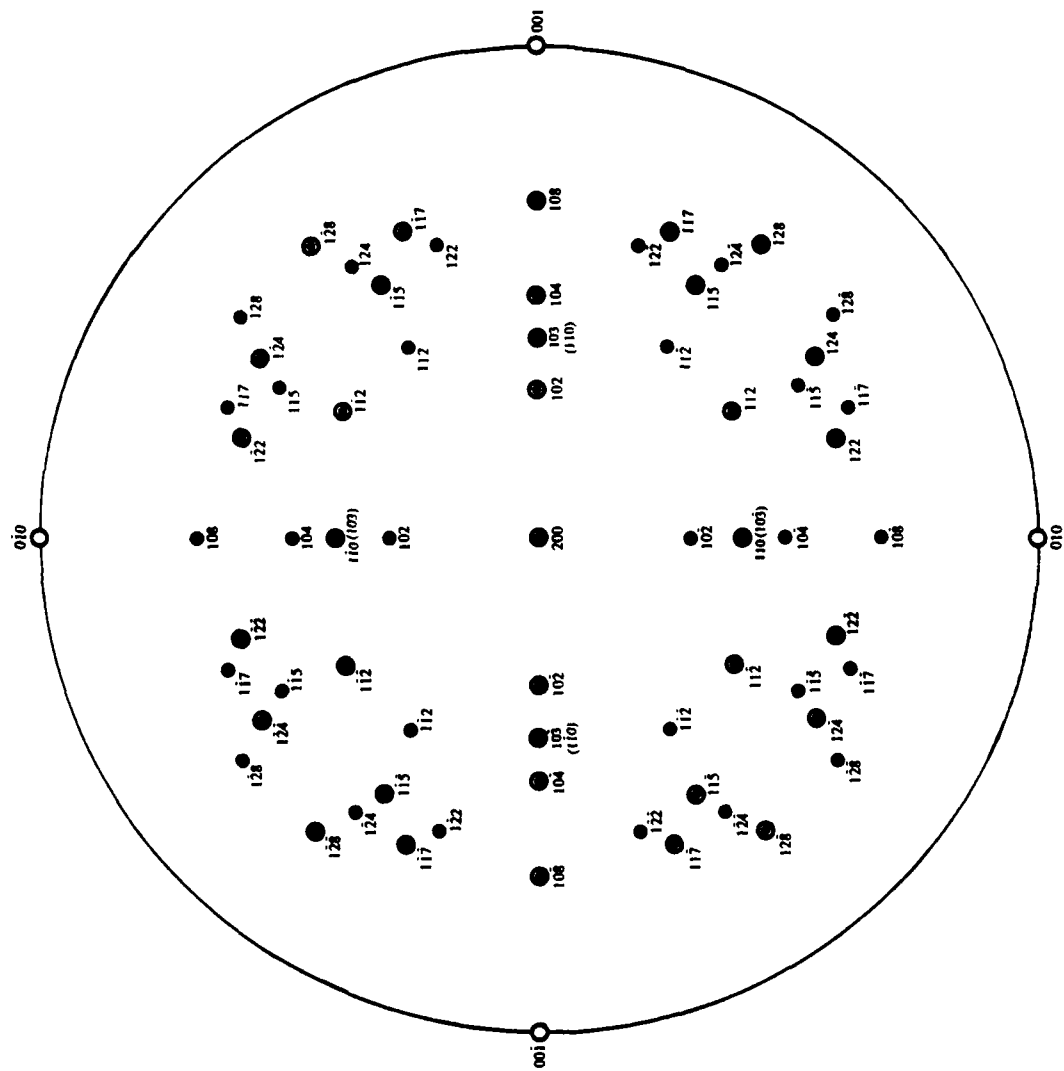


Fig. 6a)

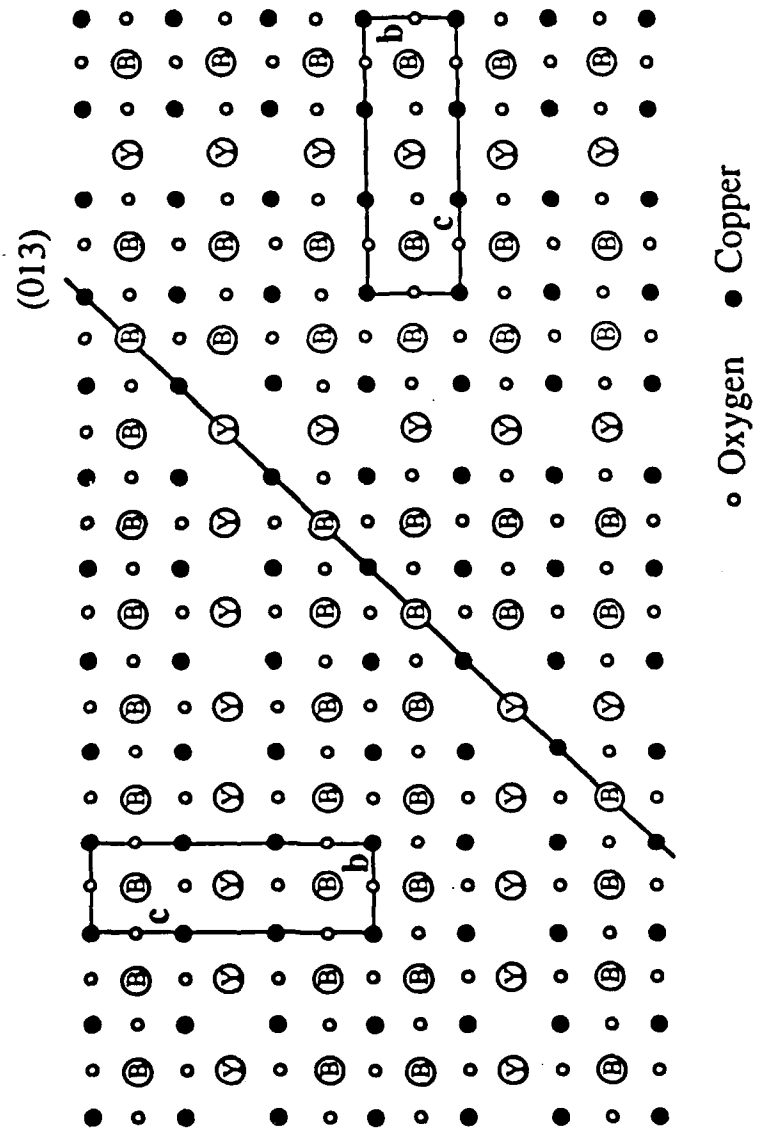


Fig. 6b)

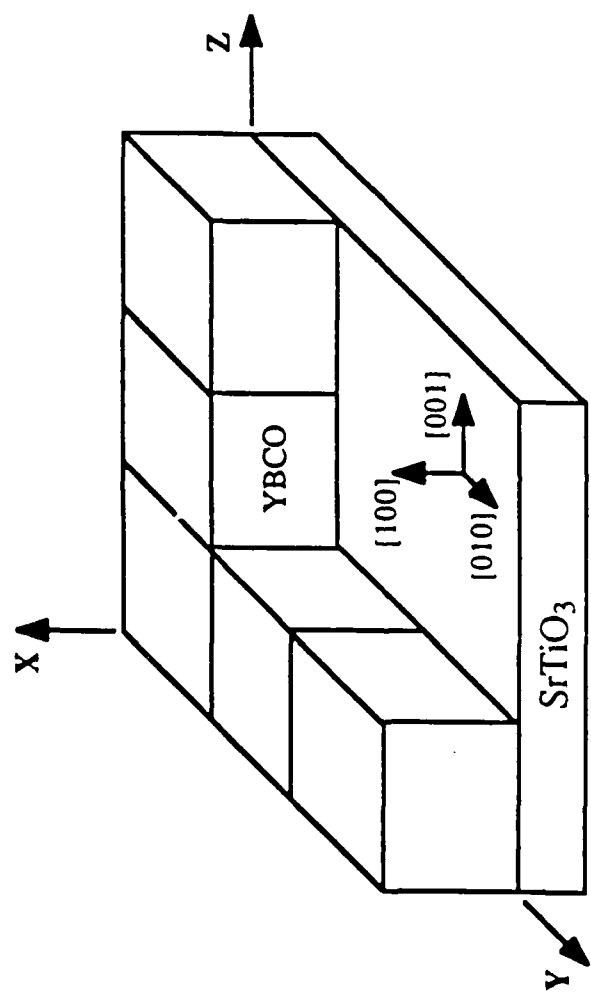


Fig. 6c)

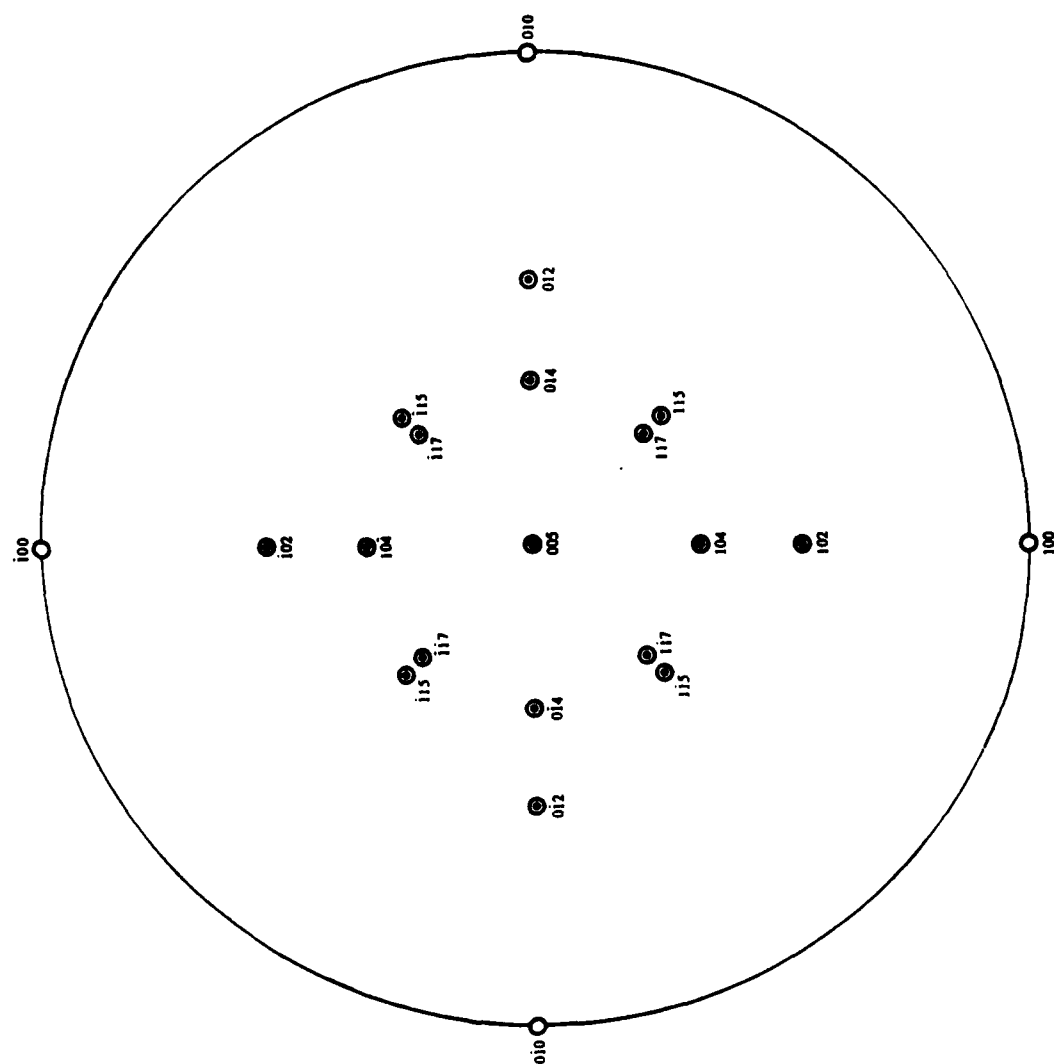


Fig. 7a)

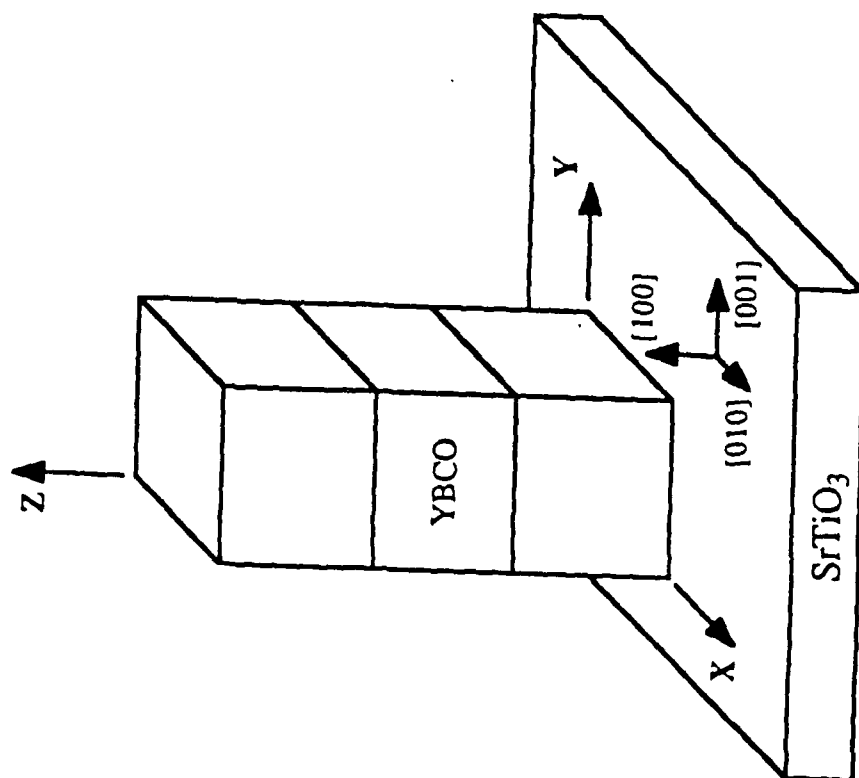


Fig. 7b)

FINAL REPORT

SLOW WAVE TRANSMISSION LINE TRANSFORMERS

by

Albert W. Biggs

Electrical Engineering Department

College of Engineering

University of Alabama in Huntsville

Huntsville, Alabama 35899, USA

prepared for

Universal Energy Systems, Incorporated

Dayton, Ohio, USA

UES Project 760

Purchase Order S-760-6MG-072

October 1989

ABSTRACT

The development of a periodic structure is described. It couples a slow wave transmission line to a fast wave transmission line. The slow wave line is a coaxial line with rectangular corrugations on the outer conductor of the line and with a smooth metallic wall for the inner conductor. The fast wave structure is a coaxial line with smooth inner and outer conductors, or with outer conductors where the depths of corrugations approach zero. The unit cells, or quarter wave sections, are developed for both binomial and Chebyshev coefficients. The Chebyshev transformer is designed for arbitrary bandwidths from 1.0 to larger numbers. For bandwidths, where bandwidth is equal to $f(\text{upper})$ divided by $f(\text{lower})$, equal to 1.0, the binomial and Chebyshev transformers are the same.

The Chebyshev coefficients are determined with unpublished methods. They are then applied in calculating characteristic impedances for prescribed input and output line impedances. For slow wave structures, the characteristic impedances are found to be proportional to slow or fast wave phase velocities. This is the modification to previous work with binomial and Chebyshev transformers.

SLOW WAVE TRANSMISSION LINE TRANSFORMERS

Albert W. Biggs

University of Alabama in Huntsville

Huntsville, Alabama 35899 USA

Summary - This report is a continuation of studies made during the summer of 1986. It describes the development of a periodic structure which couples a slow wave transmission line to a fast wave transmission line. The slow wave transmission line is a coaxial line with periodic square wave metallic corrugations on the outer coaxial conductor and a smooth metallic wall for the inner conductor. The fast wave structure is a coaxial transmission line with smooth metallic walls for the outer and inner coaxial conductors. The periodic transition structure is developed with use of Chebyshev filters.

Designs of transformer sections which match transmission lines with different characteristic impedances over a predetermined bandwidth are described in subsequent sections.

1. INTRODUCTION

In this report a method of design will be given for transformer structures which are capable of matching slow wave transmission lines of different characteristic impedances over given bandwidths. The design techniques were developed originally by Cohn [1] for fast wave transmission lines. The differences are in the modification of Cohn's techniques for a slow wave transmission line. The structure consists of a succession of

different characteristic impedances spaced by equal electrical lengths of slow wave line. The slow wave line may be coaxial, waveguide, or parallel planes. With a given number of steps, the modified method yields the maximum bandwidth for a given VSWR, or a minimum VSWR for a given bandwidth. It is called the Chebyshev transformer because the Chebyshev polynomial is used.

2. QUARTER WAVE TRANSFORMERS AND SMALL REFLECTIONS

Quarter wave transformers are found as intermediate matching sections connecting two transmission lines (waveguides, coaxial lines, microstrip or stripline transmission lines) of different characteristic impedances. When matching two transmission lines over a narrow band of frequencies, one transformer section is usually adequate. When matching over a wide bandwidth, several intermediate transformer sections may be present to achieve the same overall standing wave ratio (VSWR).

The design of a quarter wave transformer section is described by matching a transmission line of real characteristic impedance Z_1 to a resistive load impedance Z_3 . The transformer section with a characteristic impedance Z_2 and a quarter wavelength long connects the transmission line and the load, shown in Fig. 2.1.

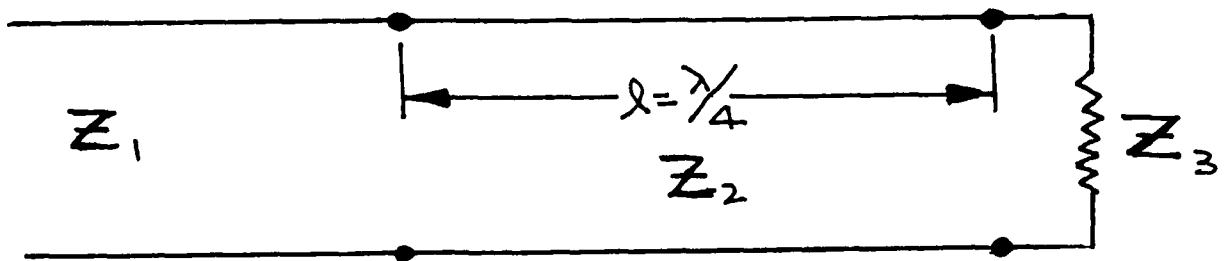


Fig. 2.1. A quarter wave transformer.

The effective load impedance Z seen by the main line when $l = \lambda/4$ is

$$Z = Z_2 \frac{Z_3 \cos \beta l + j Z_2 \sin \beta l}{Z \cos \beta l + j Z_3 \sin \beta l}$$

$$= Z_2 \frac{Z_2}{Z_3} = \frac{Z_2^2}{Z_3}, \quad (2.1)$$

where β is the phase constant. If Z_2 is selected to equal $\sqrt{Z_1 Z_3}$, then Z equals Z_1 and the load impedance is matched to the characteristic impedance of the main transmission line. For frequencies or transformer lengths where βl is not a quarter wavelength, or lengths not equal to $(n\lambda/2 + \lambda/4)$, the reflection coefficient is

$$\Gamma = \frac{Z - Z_1}{Z + Z_1} = \frac{Z_3 - Z_1}{Z_1 + Z_3 + j 2 \sqrt{Z_1 Z_3} \tan \beta l}, \quad (2.2)$$

where Eq. (2.1) and $Z_2^2 = Z_1 Z_3$ were used.

When applied to many intermediate transformer sections, the reflection coefficients for several reflecting impedances are developed because they provide simpler approximations for finding the overall reflection coefficient. The approximations are made by considering only first order reflections and dropping terms with multiply reflected waves.

In Fig. 2.2, the reflection coefficients $\Gamma_1, \Gamma_2, \Gamma_3$, and transmission coefficients T_{12}, T_{21} are

$$\Gamma_1 = \frac{Z_2 - Z_1}{Z_2 + Z_1}, \quad \Gamma_2 = -\Gamma_1, \quad (2.3)$$

$$T_{21} = 1 + \Gamma_1 = \frac{2Z_2}{Z_1 + Z_2},$$

$$T_{12} = 1 + \Gamma_2 = \frac{2Z_1}{Z_1 + Z_2} \quad (2.4)$$

$$\Gamma_3 = \frac{Z_3 - Z_2}{Z_3 + Z_2} \quad (2.5)$$

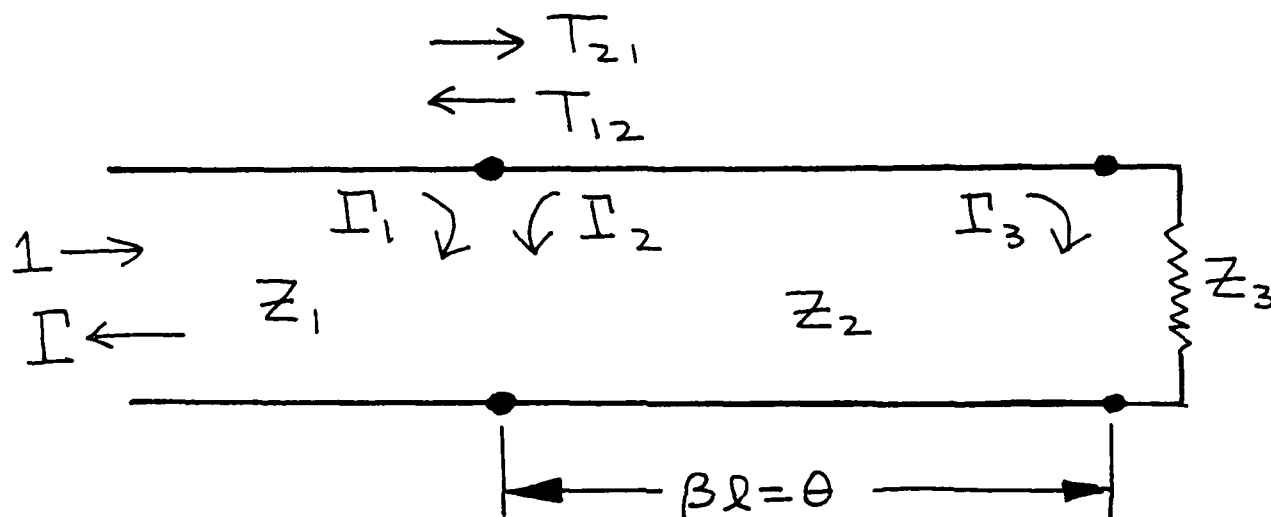


Fig. 2.2. Transformer with two reflecting junctions.

The incident electric field has unit amplitude and the reflected field has a complex amplitude Γ . When the incident field reaches the first junction, the first partial reflected and transmitted waves are Γ_1 and T_{21} , respectively. When this partial transmitted wave reaches the second junction or load, part of the wave is reflected with a reflection coefficient Γ_3 to create a wave,

$$\Gamma_3 T_{21} e^{-j2\theta}, \quad (2.6a)$$

incident upon the first junction from the load. The exponent indicates an electrical distance $\beta l = \theta$ from first to second junction, and the same distance $\beta l = \theta$ from second to first junction, for a total distance $2\beta l = 2\theta$. Part of the wave is

transmitted and becomes part of the overall reflection coefficient.

$$T_{12} T_{21} \Gamma_3 e^{-j2\theta}, \quad (2.6b)$$

and part is reflected back to the load,

$$T_{21} \Gamma_2 \Gamma_3 e^{-j2\theta}. \quad (2.6c)$$

This reflected wave travels to the load and part of the wave is reflected back to the first junction with amplitude,

$$T_{21} \Gamma_2 \Gamma_3^2 e^{-j4\theta}, \quad (2.6d)$$

and at this junction, the transmitted wave,

$$T_{12} T_{21} \Gamma_2 \Gamma_3^2 e^{-j4\theta}, \quad (2.6e)$$

with a wave reflected toward the load,

$$T_{21} \Gamma_2^2 \Gamma_3^2 e^{-j4\theta}, \quad (2.6f)$$

after reflection at the load is incident upon the first junction with amplitude,

$$T_{21} \Gamma_2^2 \Gamma_3^3 e^{-j6\theta}, \quad (2.6g)$$

creating another part of the overall reflection coefficient,

$$T_{12} T_{21} \Gamma_2^2 \Gamma_3^3 e^{-j6\theta}.$$

(2.6h)

This reflection and transmission continues forever. The infinite sum of reflected waves becomes the overall reflection coefficient

$$\begin{aligned} \Gamma &= \Gamma_1 + T_{12} T_{21} \Gamma_3 e^{-j2\theta} + T_{12} T_{21} \Gamma_3^2 \Gamma_2 e^{-j4\theta} \\ &+ T_{12} T_{21} \Gamma_3^3 \Gamma_2^2 e^{-j6\theta} + T_{12} T_{21} \Gamma_3^4 \Gamma_2^3 e^{-j8\theta} \\ &+ T_{12} T_{21} \Gamma_3^5 \Gamma_2^4 e^{-j10\theta} + \dots + \\ &= \Gamma_1 + T_{12} T_{21} \Gamma_3 e^{-j2\theta} \sum_{n=0}^{\infty} \Gamma_1^n \Gamma_3^n e^{-j2n\theta}, \end{aligned}$$

(2.7)

and with the series

$$\sum_{n=0}^{\infty} x^n = (1-x)^{-1}, \quad x < 1,$$

(2.8)

the reflection coefficient is

$$\Gamma = \Gamma_1 + \frac{T_{12} T_{21} \Gamma_3 e^{-j2\theta}}{1 - \Gamma_2 \Gamma_3 e^{-j2\theta}},$$

(2.9)

and replacing T_{12} by $1 - \Gamma_1$ and T_{21} by $1 + \Gamma_1$,

$$\Gamma = \frac{\Gamma_1 + \Gamma_3 e^{-j2\theta}}{1 + \Gamma_1 \Gamma_3 e^{-j2\theta}}.$$

(2.10)

If the product of the magnitudes Γ_1 and Γ_3 is much less than 1.0,

Γ is approximated by

$$\Gamma = \Gamma_1 + \Gamma_3 e^{-j2\theta} \quad (2.11)$$

so that when reflection magnitudes are less than 0.3, for example, the error in Γ is less than 8 percent.

3. MULTISECTION QUARTER WAVE TRANSFORMERS

For an n-section quarter wave transformer, the reflection coefficients Γ_m at each junction or step are ($m = 1, 2, \dots, n$)

$$\Gamma_1 = \frac{Z_2 - Z_1}{Z_2 + Z_1} = \rho_1, \quad (3.1a)$$

⋮

$$\Gamma_m = \frac{Z_{m+1} - Z_m}{Z_{m+1} + Z_m} = \rho_m, \quad (3.1b)$$

⋮

$$\Gamma_n = \frac{Z_{n+1} - Z_n}{Z_{n+1} + Z_n} = \rho_n, \quad (3.1c)$$

where $Z_1, Z_2, \dots, Z_m, \dots, Z_{n+1}$ are characteristic impedances of the waveguide, stripline or microstrip transmission line, or slow wave structure. These appear in Fig. 3.1,

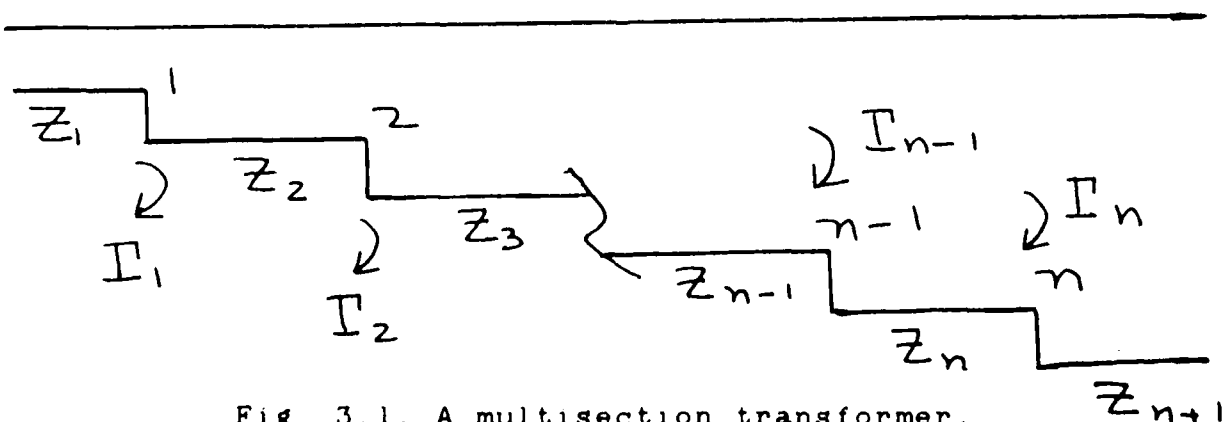


Fig. 3.1. A multisection transformer.

Each section has the same length $\beta l = \theta$, where l is a quarter wavelength at the matching frequency. The load impedance Z_{n+1} is a resistance or the impedance of the last part of the line. The characteristic impedances are real and

$$Z_{n+1} > Z_n > \dots > Z_m > \dots > Z_2 > Z_1, \quad (3.2)$$

so that Γ_m are replaced by ρ_m , the magnitudes of Γ_m . If the above impedances are reversed in 'greater than,' the ρ_m 's are negative real terms. We will assume the inequalities above, so that the overall reflection coefficient Γ is

$$\Gamma = \rho_1 + \rho_2 e^{-j2\theta} + \dots + \rho_m e^{-j2(m-1)\theta} + \dots + \rho_n e^{-j2(n-1)\theta}, \quad (3.3)$$

where $\exp(-j 2[m-1]\theta)$ describes the distance traveled by the m th partial wave. With symmetry,

$$\rho_1 = \rho_n, \rho_2 = \rho_{n-1}, \rho_3 = \rho_{n-2}, \dots, \quad (3.4)$$

so that Γ becomes

$$\begin{aligned} \Gamma &= e^{-j(n-1)\theta} \left[\rho_1 (e^{j(n-1)\theta} + e^{-j(n-1)\theta}) + \rho_2 (e^{j(n-3)\theta} + e^{-j(n-3)\theta}) + \dots + \rho_{(n+1)/2} \right] \\ &= e^{-j(n-1)\theta} \left[\sum_{m=1}^{(n+1)/2} \rho_m (e^{j(n-2m+1)\theta} + e^{-j(n-2m+1)\theta}) + \rho_{(n+1)/2} \right], \end{aligned} \quad (3.5a)$$

for odd values of n , and when n is even, the result is

$$\begin{aligned} &\dots + \rho_{n/2} (e^{j\theta} + e^{-j\theta}) \\ &= e^{-j(n-1)\theta} \sum_{m=1}^{n/2} \rho_m (e^{j(n-2m+1)\theta} + e^{-j(n-2m+1)\theta}). \end{aligned} \quad (3.5b)$$

With the symmetrical transformer, Γ is

$$\begin{aligned}\Gamma &= 2e^{-j(n-1)\theta} \left[p_1 \cos(n-1)\theta + p_2 \cos(n-3)\theta \right. \\ &\quad \left. + \dots + p_m \cos(n-2m+1)\theta + \dots + \frac{1}{2} p_{(n+1)/2} \right] \\ &= 2e^{-j(n-1)\theta} \left[\sum_{m=1}^{(n-1)/2} p_m \cos(n-2m+1)\theta + \frac{1}{2} p_{(n+1)/2} \right]\end{aligned}$$

(3.6a)

for odd values of n , and when n is even, the result is

$$\begin{aligned}&+ \dots + p_m \cos(n-2m+1)\theta + \dots + p_{n/2} \cos \theta] \\ &= 2e^{-j(n-1)\theta} \sum_{m=1}^{n/2} p_m \cos(n-2m+1)\theta.\end{aligned}$$

(3.6b)

4. BINOMIAL TRANSFORMERS

The accepted method for designing transformer structures was Hansen's binomial coefficient design prior to development of the Chebyshev or optimul stepped transformer. The binomial transformer is obtained from the Chebyshev transformers for unity bandwidth ratios.

Maximally flat passband responses are achieved when equals the magnitude of Γ and when the first $(n-1)$ derivatives with respect to frequency or angle θ vanish at the matching frequency where $\beta\ell = \theta = \pi/2$. These are realized with the function,

$$\Gamma = A(1 + e^{-j2\theta})^{n-1},$$

(4.1)

where p is the magnitude of Γ ,

$$p = |\Gamma| = |A 2^{n-1} (\cos \theta)^{n-1}|,$$

(4.2)

and where n is the number of junctions or steps. The constant A is found at $\theta = 0$ or π , where

$$A(2^{n-1}) = \frac{z_{n+1} - z_1}{z_{n+1} + z_1}, \quad A = 2^{-(n-1)} \frac{z_{n+1} - z_1}{z_{n+1} + z_1} \quad (4.3)$$

With A obtained from Eq. (4.3), Eq. (3.1) is expanded by the Binomial Theorem,

$$\begin{aligned} \Gamma &= 2^{-(n-1)} \frac{z_{n+1} - z_1}{z_{n+1} + z_1} (1 + e^{-j2\theta})^{n-1} \\ &= 2^{-(n-1)} \frac{z_{n+1} - z_1}{z_{n+1} + z_1} \left[1 + (n-1)e^{-j2\theta} \right. \\ &\quad + \frac{(n-1)(n-2)}{2!} e^{-j4\theta} + \dots + \frac{(n-1)(n-2)\dots(n-m+1)}{(m-1)!} \\ &\quad \cdot e^{-j2(m-1)\theta} + \dots + \frac{(n-1)(n-2)}{2!} e^{-j2(n-3)\theta} \\ &\quad \left. + (n-1)e^{-j2(n-2)\theta} + e^{-j2(n-1)\theta} \right] \\ &= 2^{-(n-1)} \frac{z_{n+1} - z_1}{z_{n+1} + z_1} \sum_{m=1}^n \frac{(n-1)(n-2)\dots(n-m+1)}{(m-1)!} \\ &\quad \cdot e^{-j2(m-1)\theta} \\ &= \sum_{m=1}^n p_m e^{-j2(m-1)\theta}, \end{aligned}$$

(4.4)

where the binomial coefficients $\binom{n-1}{m-1}$ are

$$\binom{n-1}{m-1} = \frac{(n-1)(n-2)\dots(n-m+1)}{(m-1)!}$$

$$= \frac{(n-1)!}{(n-m)!(m-1)!} = \binom{n-1}{n-m},$$

(4.5)

and some simple terms have the forms

$$\binom{n-1}{0} = \binom{n-1}{n-1} = \frac{(n-1)!}{(n-1)! 0!} = 1,$$

$$\binom{n-1}{1} = \binom{n-1}{n-2} = \frac{(n-1)!}{(n-2)! 1!} = (n-1). \quad (4.6)$$

Another simplification is made with the series

$$\ln x = 2 \frac{x-1}{x+1} + \frac{2}{3} \left(\frac{x-1}{x+1} \right)^3 + \dots + \frac{2}{(2m+1)} \left(\frac{x-1}{x+1} \right)^{2m+1} + \dots \simeq 2 \frac{x-1}{x+1}, \quad m=1, 2, 3, \dots, \quad (4.7)$$

applied to $x = Z_{n+1}/Z_1$ and $x = Z_{m+1}/Z_1$. The above approximations are 9 percent in error when $x = 3$, and 3 percent when $x = 2$.

Symmetry provides the terms,

$$\rho_m = 2^{-n} \frac{Z_{n+1} - Z_1}{Z_{n+1} + Z_1} \binom{n-1}{m-1} = 2^{-n} \ln \frac{Z_{n+1}}{Z_1} \binom{n-1}{m-1}$$

$$= 2^{-n} \ln \frac{Z_{n+1}}{Z_1} \binom{n-1}{n-m} = \rho_{n-m+1}, \quad (4.8)$$

and with Eq. (4.7),

$$\rho_m = \frac{Z_{m+1} - Z_m}{Z_{m+1} + Z_m} \simeq \frac{1}{2} \ln \frac{Z_{m+1}}{Z_m}. \quad (4.9)$$

Combining Eqs. (4.8) and (4.9) yield

$$\rho_m = 2^{-n} \ln \frac{Z_{n+1}}{Z_1} \binom{n-1}{m-1} = \frac{1}{2} \ln \frac{Z_{m+1}}{Z_m}, \quad (4.10)$$

which is the solution for the logarithmic ratios of the characteristic impedances for adjacent transformer sections m and $m + 1$, where $m = 1, 2, 3, \dots, n$. The logarithmic ratios are proportional to the binomial coefficients and a constant given by

$$\binom{n-1}{m-1} 2^{-n} \ln \frac{Z_{n+1}}{Z_1},$$

(4.11)

since Z_1 is the characteristic impedance of the main line at the transformer input, Z_{n+1} is the load or characteristic impedance of the line at the end of the transformer, and n is the number of steps or junctions.

The reflection coefficient is expressed in two forms with

Eqs. (4.4) and (4.10),

$$\begin{aligned} \rho &= \sum_{m=1}^n \rho_m e^{-j 2 m \theta} = \frac{1}{2} \sum_{m=1}^n \ln \frac{Z_{m+1}}{Z_m} e^{-j 2(m-1)\theta} \\ &= 2^{-n} \ln \frac{Z_{n+1}}{Z_1} \sum_{m=1}^n \binom{n-1}{m-1} e^{-j 2(m-1)\theta}. \end{aligned}$$

(4.12)

When Eq. (4.10) is divided by Eq. (4.12) for $\theta = 0$, the result is

$$\frac{\frac{1}{2} \ln \frac{Z_{m+1}}{Z_m}}{\frac{1}{2} \sum_{m=1}^n \ln \frac{Z_{m+1}}{Z_m}} = \frac{2^{-n} \ln \frac{Z_{n+1}}{Z_1} \binom{n-1}{m-1}}{2^{-n} \ln \frac{Z_{n+1}}{Z_1} \sum_{m=1}^n \binom{n-1}{m-1}}, \quad (4.13)$$

and when like terms are cancelled, and with the reduction of a sum of logarithms,

$$\begin{aligned} \sum_{m=1}^n \ln \frac{Z_{m+1}}{Z_m} &= \ln \frac{Z_2}{Z_1} + \ln \frac{Z_3}{Z_2} + \dots + \ln \frac{Z_{n+1}}{Z_n} \\ &= \ln \frac{Z_2}{Z_1} \frac{Z_3}{Z_2} \dots \frac{Z_{m+1}}{Z_m} \dots + \ln \frac{Z_{n+1}}{Z_n} \\ &= \ln \frac{Z_{n+1}}{Z_1}, \end{aligned}$$

(4.14)

so that Eq. (4.13) becomes

$$\ln \frac{Z_{m+1}}{Z_m} = \frac{\binom{n-1}{m-1} \ln \frac{Z_{n+1}}{Z_1}}{\sum_{m=1}^n \binom{n-1}{m-1}} \quad (4.15)$$

5. CHEBYSHEV TRANSFORMERS

Hansen's [2] binomial-coefficient design for transmission line transformer sections was described in the preceding section. In his design, the logarithms of the characteristic impedance ratios of adjacent sections were made to be in the ratio of the binomial coefficients.

In this section, the design method calculates the logarithms of the characteristic impedance ratios so that the VSWR has the characteristic "equal ripple" response of a Chebyshev polynomial. Instead of the maximally flat passband characteristic, the Chebyshev transformer provides a variation of reflection coefficient ρ to vary or oscillate between 0 and ρ_m across the passband. Since the equal ripple response makes ρ behave like a Chebyshev polynomial, it is named the Chebyshev transformer. The reflection coefficient is zero at as many different frequencies in the passband as there are transformer sections.

Use of the Chebyshev polynomials can be better understood by looking at the generation and properties of these polynomials. In the differential equation,

$$(1-x^2) \frac{d^2 y}{dx^2} - x \frac{dy}{dx} + n^2 y = 0, \quad (5.1)$$

where n is an integer, the general solution is a linear

combination of the first kind $T_n(x)$, and the second kind $U_n(x)$.

$$y = C_1 T_n(x) + C_2 U_n(x), \quad (5.2)$$

where we will use the first kind $T_n(x)$. The functional forms of the Chebyshev polynomials are

$$\begin{aligned} T_n(x) &= \cos(n \cos^{-1} x) = x^n - \binom{n}{2} x^{n-2} (1-x^2) \\ &+ \binom{n}{4} x^{n-4} (1-x^2)^2 - \binom{n}{6} x^{n-6} (1-x^2)^3 + \\ &\dots (-1)^m \binom{n}{2m} x^{n-2m} (1-x^2)^m + \dots + \\ &(-1)^{n/2} \binom{n}{n} (1-x^2)^{n/2}, \quad n \text{ even, and} \\ &(-1)^{(n-1)/2} \binom{n}{n-1} x (1-x^2)^{(n-1)/2}, \quad n \text{ odd,} \end{aligned}$$

$$\begin{aligned} U_n(x) &= \sin(n \sin^{-1} x) = \sqrt{1-x^2} \left[\binom{n}{1} x^{n-1} \right. \\ &- \binom{n}{3} x^{n-3} (1-x^2) + \dots (-1)^{m-1} \binom{n}{2m-1} x^{n-2m+1} \\ &\cdot (1-x^2)^{m-1} + \dots + (-1)^{\frac{n-2}{2}} \binom{n}{n-1} x (1-x^2)^{\frac{n-2}{2}}, \\ &n \text{ even, and } (-1)^{\frac{n-1}{2}} \binom{n}{n} (1-x^2)^{\frac{n-1}{2}}, \\ &n \text{ odd.} \end{aligned} \quad (5.3)$$

If $x = \cos \theta$ in Eq. (5.3) and $x = \sin \theta$ in Eq. (5.4), other forms for $T_n(x)$ and $U_n(x)$ are

$$T_n(\cos \theta) = \cos n\theta, \quad (5.5)$$

$$U_n(\sin \theta) = \sin n \theta.$$

(5.6)

As functions of x , the first few terms of $T(x)$ and $U(x)$ are

$$\begin{aligned} T_0(x) &= 1, T_1(x) = x, T_2(x) = 2x^2 - 1, \\ T_3(x) &= 4x^3 - 3x, T_4(x) = 8x^4 - 8x^2 + 1, \\ T_5(x) &= 16x^5 - 20x^3 + 5x, \dots, \\ T_m(x) &= 2xT_{m-1}(x) - T_{m-2}(x). \end{aligned} \quad (5.7)$$

$$\begin{aligned} U_0(x) &= 0, U_1(x) = \sqrt{1-x^2}, U_2(x) = 2x\sqrt{1-x^2}, \\ U_3(x) &= [4x^2-1]\sqrt{1-x^2}, U_4(x) = [8x^3-4x] \cdot \\ &\cdot \sqrt{1-x^2}, U_5(x) = [16x^4-12x+1]\sqrt{1-x^2}, \\ U_6(x) &= [32x^5-32x^3+6x]\sqrt{1-x^2}, \\ \dots, U_m(x) &= 2xU_{m-1}(x) - U_{m-2}(x), \end{aligned} \quad (5.8)$$

where a few properties of these Chebyshev functions may be noted.

When $x = 1$, or $\theta = 0$,

$$T_1(1) = T_2(1) = \dots = T_m(1) = 1, \quad (5.9)$$

and when $x = -1$, or $\theta = \pi$, for odd orders,

$$T_1(-1) = T_{2m+1}(-1) = -1, \quad (5.10)$$

and for even orders,

$$T_2(-1) = T_{2m}(-1) = +1, \quad (5.11)$$

resulting in an increasing number of oscillations between -1 and

+1 (or 0 and 180 degrees) as m increases, while the absolute value of $T_m(x)$ increases asymptotically with increasing absolute values of x (greater than 1) as

$$T_m(x) \rightarrow 2^{m-1} x^m, \quad (5.12)$$

so that the 'equal ripple' is encountered.

With $U_m(x)$, the function is not defined for the absolute value of x greater than one. For $x = +1$ or -1 ($\theta = 0$ or 180 degrees),

$$U_0(\pm 1) = U_m(\pm 1) = 0, \quad m = 0, 1, \dots \quad (5.13)$$

and for $x = 0$,

$$\begin{aligned} U_{4m-3}(0) &= 1, \\ U_{4m-1}(0) &= -1, \quad m = 1, 2, 3, \dots \end{aligned} \quad (5.14)$$

where $U_m(x)$ oscillates between +1 and -1, with oscillations increasing with m . It is not suitable for equal ripple filters, antennas, or transformers because of the region outside of x equal to +1 and -1.

The suitable function for equal ripple is the Chebyshev polynomial of the first kind $T_m(x)$, with x replaced by $\cos \theta$ in Eq. (5.5). As θ varies from 0 to 180 degrees, the range of x varies from +1 to -1. If the bandwidth or equal ripple characteristic is chosen from θ_1 to 180 degrees - θ_1 , we must choose

$$T_m\left(\frac{\cos \theta}{\cos \theta_1}\right) = \cos m \left(\cos^{-1} \frac{\cos \theta}{\cos \theta_1} \right), \quad (5.15)$$

where the argument is unity when $\theta = \theta_1$, and less than unity for $\theta_1 < \theta < \pi - \theta_1$. This defines the bandwidth B by

$$B = \frac{f_2}{f_1} = \frac{\theta_2}{\theta_1} = \frac{180^\circ - \theta_1}{\theta_1} \quad (5.16)$$

in coaxial or two conductor transmissine lines, and in waveguides by

$$B = \frac{\theta_2}{\theta_1} = \frac{\lambda_{\text{GUIDE 1}}}{\lambda_{\text{GUIDE 2}}} \quad (5.17)$$

For a given value of B, θ_1 is found with

$$\theta_1 = \frac{180^\circ}{1+B} \quad (5.18)$$

When $B = 1.0$, then $\theta_2 = \theta_1$ and both are 90 degrees. But with $B = 2.0$, f_2 equals $2f_1$, satisfied by a typical range of 200 and 400 MHz, or 3 and 6 GHz. With a narrower B, such as 1.2, we have 3 and 3.6 GHz, or 200 and 240 MHz. The frequency band for a given bandwidth ratio is

$$\Delta f = f_2 - f_1 = (B - 1) f_1, \quad (5.19)$$

or with the center frequency f_0 .

$$\begin{aligned} f_0 &= (f_1 + f_2) / 2 \\ &= f_1 (1+B) / 2 \\ &= f_2 (1+B) / 2B. \end{aligned} \quad (5.20)$$

With the above descriptions of Chebyshev polynomials and bandwidth, we return to the overall reflection coefficient in Eq. (3.3) for all multisection quarter wave transformers with small reflections at each step,

$$\begin{aligned}
 \Gamma &= p_1 + p_2 e^{-j2\theta} + p_3 e^{-j4\theta} + \dots + p_m e^{-j2(m-1)\theta} \\
 &\quad + \dots + p_n e^{-j2(n-1)\theta} \\
 &= e^{-j(n-1)\theta} \left[p_1 e^{j(n-1)\theta} + p_2 e^{j(n-3)\theta} + \dots + \right. \\
 &\quad \left. p_m e^{-j(n-2m+1)\theta} + \dots + p_n e^{-j(n-1)\theta} \right]
 \end{aligned}
 \tag{5.21}$$

and the magnitude of the reflection coefficient is

$$\begin{aligned}
 \rho = |\Gamma| &= p_1 e^{j(n-1)\theta} + p_2 e^{j(n-3)\theta} + \dots + \\
 &\quad p_m e^{-j(n-2m+1)\theta} + \dots + p_n e^{-j(n-1)\theta}
 \end{aligned}
 \tag{5.22}$$

and with the same symmetry as that expressed in Eq. (3.4), the above expression is

$$\begin{aligned}
 \rho &= 2p_1 \cos(n-1)\theta + 2p_2 \cos(n-3)\theta + \dots + \\
 &\quad 2p_m \cos(n-2m+1)\theta + \dots + p_{(n+1)/2}
 \end{aligned}
 \tag{5.23}$$

when n is odd, like 1, 3, 5, ... and

$$= 2p_1 \cos(n-1)\theta + \dots + 2p_{n/2} \cos \theta,
 \tag{5.24}$$

for n even, like 2, 4, 6, ... In order to have the Chebyshev form of equal ripple across the bandwidth of the antenna, we first adjust with the bandwidth ratio B with

$$y = \cos \theta, \quad x \cos \theta_1 = y,
 \tag{5.25}$$

so that the cosine functions become

$$\cos \theta = y = x \cos \theta_1,
 \tag{5.26a}$$

$$\cos 2\theta = 2y^2 - 1 = 2x^2 \cos^2 \theta_1 - 1,$$

$$\cos 3\theta = 4y^3 - 3y = 4x^3 \cos^3 \theta_1 - 3x \cos \theta_1, \quad (5.26b)$$

$$\cos 4\theta = 8y^4 - 8y^2 + 1 = 8x^4 \cos^4 \theta_1 - 8x^2 \cos^2 \theta_1 + 1, \quad (5.26c)$$

$$\cos 5\theta = 16y^5 - 20y^3 + 5y = 16x^5 \cos^5 \theta_1 - 20x^3 \cos^3 \theta_1 + 5x \cos \theta_1, \quad (5.26d)$$

$$\cos 6\theta_1 = 32y^6 - 48y^4 + 18y^2 - 1 \quad (5.26e)$$

$$= 32x^6 \cos^6 \theta_1 - 48x^4 \cos^4 \theta_1 + 18x^2 \cos^2 \theta_1 - 1, \quad (5.26f)$$

and so on. We now match powers of x in Eq. (5.26a) to (5.26f) with powers of x in $\alpha(n) T_{n-1}(x)$ to evaluate the arbitrary constants p_1, p_2, \dots, p_n . The term $\alpha(n)$ is

$$\alpha(n) = \frac{\frac{1}{2} \ln \bar{z}_{n+1} / \bar{z}_1}{T_{n-1}(1/\cos \theta_1)}. \quad (5.27)$$

When $n = 1$, p_m are found with Eq. (5.23),

$$\begin{aligned} p = p_1 &= \alpha(1) T_0(x) = \frac{\frac{1}{2} \ln \frac{\bar{z}_2}{\bar{z}_1}}{T_0(1/\cos \theta_1)} T_0(x) \\ &= \frac{\frac{1}{2} \ln \frac{\bar{z}_2}{\bar{z}_1}}{1} \cdot 1 = \frac{1}{2} \ln \frac{\bar{z}_2}{\bar{z}_1}, \end{aligned} \quad (5.28)$$

and when $n = 2$, p_m are found with Eq. (5.24),

$$\begin{aligned} p &= 2 p_1 \cos \theta = 2 p_1 x \cos \theta_1 = \alpha(2) T_1(x) \\ &= \frac{\frac{1}{2} \ln \frac{\bar{z}_3}{\bar{z}_1}}{T_1(1/\cos \theta_1)} x, \end{aligned} \quad (5.29)$$

so that coefficients of x are equated.

$$\begin{aligned}
 \rho_1 &= \frac{1}{2 \cos \theta_1} \frac{\frac{1}{2} \ln \frac{z_3}{z_1}}{T_1\left(\frac{1}{\cos \theta_1}\right)} \\
 &= \frac{\ln \frac{z_3}{z_1}}{4 \cos \theta_1 T_1\left(\frac{1}{\cos \theta_1}\right)} = \frac{1}{4} \ln \frac{z_3}{z_1},
 \end{aligned}
 \tag{5.30}$$

from $T_1(B) = B = 1./\cos \theta_1$. With $n = 3$, ρ_m are found with Eq. (5.23),

$$\begin{aligned}
 \rho &= 2 \rho_1 \cos 2\theta + \rho_2 = \rho_1 [(4 \cos^2 \theta_1) x^2 - 2] + \rho_2 \\
 &= \alpha(3) T_2(x) = \frac{\frac{1}{2} \ln \frac{z_4}{z_1}}{T_2\left(\frac{1}{\cos \theta_1}\right)} (2x^2 - 1),
 \end{aligned}
 \tag{5.31}$$

and when coefficients of powers of x are equated,

$$\rho_1 = \frac{1}{4 \cos^2 \theta_1} \frac{\ln \frac{z_4}{z_1}}{T_2(B)} = \frac{B^2 \ln \frac{z_4}{z_1}}{4 T_2(B)},
 \tag{5.32a}$$

$$\rho_2 = \frac{\ln \frac{z_4}{z_1}}{2 T_2(B)} [B^2 - 1].
 \tag{5.32b}$$

When $B = 2.0$, the reflection coefficients are

$$\rho_1 = \frac{B^2 \ln \frac{z_4}{z_1}}{8 T_2(B)} = \frac{\ln \frac{z_4}{z_1}}{2 [2B^2 - 1]} = \frac{\ln \frac{z_4}{z_1}}{14},
 \tag{5.33a}$$

$$\rho_2 = \frac{\ln \frac{z_4}{z_1}}{14} \left(\frac{3}{2}\right),
 \tag{5.33b}$$

and the ratios of reflection coefficients are

$$\rho_1 : \rho_2 : \rho_3 = 1.0 : 1.5 : 1.0.
 \tag{5.34}$$

With four steps, the ratios of reflection coefficients become

$$P_1 : P_2 : P_3 : P_4 = 1.0 : 2.25 : 2.25 : 1.0. \quad (5.35)$$

Derivation of subsequent reflection coefficients becomes increasingly tedious but logically straightforward. A simplified method for calculating these coefficients was developed for antenna arrays by Ross E. Graves, Stanford University, in an unpublished report.

Grave's method is similar to that employed with Pascal's triangle for binomial coefficients. Pascal's triangle is formed by always inserting a number 1.0 in the first row. In the second row, another number 1.0 is always placed to the left of the element above and the same number 1.0 is always placed to the right of the element above. This ritual for element placement is described above because a similar ritual is followed with Grave's pyramid. In successive rows, elements are formed by adding the two elements on the left and right in the row above. When elements are absent, they are assumed to be zero. Pascal's triangle appears in Table I for several rows.

				1				
			1		1			
		1		2		1		
	1		3		3		1	
	1	4		6		4	1	
1		5	10		10	5		1
1	6	15	20	15	6			1

Table I. Pascal's Triangle for Binomial Coefficients.

Grave's pyramid is formed by always inserting a number 2.0 in the first row. In the second row another number B, representing the bandwidth described earlier, is always placed to the left of the element above and the same number B is always placed to the right of the element above. In successive rows, elements are formed by adding the two elements on the left and right in the row above, multiplying the sum by B, and subtracting the element in the second row above the entry being calculated from this product. When elements are absent, they are assumed to be zero. Grave's pyramid appears in Table II as a function of B.

		2		
		B		B
	B**2		2*B**2-2	B**2
B**3		3*B**3-3*B	3*B**3-3*B	B**3

Table II. Grave's Pyramid for Chebyshev Coefficients.

When B = 2.0, Grave's Pyramid has the values seen in Table III.

			2			
			2		2	
		4		6		4
	8		16		16	8
	16	48		66	48	16
32		120	210		210	120
64	288	612	774	612	288	64

Table III. Grave's Pyramid for Chebyshev Coefficients. B = 2.0.

When the elements of Table III are normalized with respect to the elements at the ends, we have the reflection coefficient ratios.

			1.0			
			1.0		1.0	
		1.0		1.5		1.0
	1.0		2.25		2.25	1.0
	1.0	3.0		4.125	3.0	1.0
1.0		3.75		6.5675	6.5675	3.75
	1.0		9.5625	12.0938	9.5625	4.51
						1.0

Table IV. Grave's Pyramid for Normalized
Chebyshev Coefficients, $B = 2.0$.

6. MATCHING OF PERIODIC STRUCTURES

The binomial coefficients and the Chebyshev coefficients described in Sections 4.0 and 5.0 are used to match one transmission line or waveguide to another transmission line or waveguide with different characteristic impedances. The first unloaded line or guide may be a slow wave periodic structure, a fast wave structure, or a two conductor transmission line such as coaxial lines, parallel wire lines, shielded pairs, parallel plates, or parallel bars. The input guide or loaded line may be any of the above.

Slow wave structures are waveguides and transmission lines loaded at periodic intervals with identical obstacles such as a reactive element like a diaphragm. The diaphragm may be a rectangular serration in the form of a thin fin or a thick rectangu-

lar or square shape. This type of waveguide structure has two important properties, which are passband-stopband characteristics and support of electromagnetic waves with phase velocities much slower than the velocity of light. An excellent physical picture of slow waves is found in the serpentine or sinusoidal serrated slow wave structure, where the periodic obstacles look like a roller coaster track. The electromagnetic waves follow the serpentine path with the velocity of light, but their velocities along the axis of the guide are much less. Another example is the helical wire in a traveling wave tube (TWT), where the waves travel along the surface of the wire with the velocity of light, but their axial velocities are much slower.

The passband-stopband characteristic is the presence of frequency bands in which waves propagate with negligible attenuation separated by frequency bands in which the waves are cut off and do not propagate. The former is a passband, and the latter is a stopband. The passband-stopband is useful for frequency filtering.

The property of periodic structures to support slow waves with phase velocities slower than that of light, is applied in the designs of linear magnetron type (M type) TWTs with magnetically focussed electron beams and a slow wave structure of periodic annular cavities, ordinary type (O type) TWTs with a slow wave structure in the form of a helix, resistance wall amplifiers with a slow wave structure made with resistive linings, and related structures. Other applications are found in transmission lines coupling TWTs to slow wave antennas, where the periodic structure continues from source to antenna.

Metallic waveguides are one example of fast wave structures. In waveguides, modal waves are obliquely incident on the guide walls as they propagate along the guide. As frequency decreases toward cutoff, the angle of incidence approaches zero. With frequencies increasing above cutoff, the angle of incidence increases. If we observe the velocity of the wave front parallel to the direction of propagation, the phase velocity is greater than the velocity measured normal to the wave front. It will be greater in any oblique direction. As the angle of incidence approaches zero and the frequency approaches the cutoff frequency for the propagating mode, the phase velocity measured in the direction propagation approaches infinity. For this reason, this guide is a "fast wave" guide. The same phenomena occurs in dielectric and insular waveguides.

In most designs for matching slow to fast wave guides, the fast wave guide is identical to the slow wave guide when the obstacles are removed. In this Section we consider a slow wave coaxial line with square wave serrations on the outer conductor, while the smooth coaxial line has a phase velocity equal to that of light.

The inner and outer conductor radii of the coaxial line are R_I and R_O , respectively, with $R_O = 6.5$ cm and $R_I = 8.2$ cm. The characteristic impedance Z_0 of the smooth coaxial line is

$$Z_0 = \frac{\eta}{2\pi} \ln \frac{R_O}{R_I} = 60 \ln \frac{R_O}{R_I}, \quad (6.1)$$

where η is the intrinsic impedance of free space (or air), 120π ohms. The characteristic impedance Z_s of the slow wave

coaxial line is

$$Z_s = \left(\frac{C}{V} \right) \frac{\eta}{2\pi} \ln \frac{R_0}{R_I} = \left(\frac{C}{V} \right) 60 \ln \frac{R_0}{R_I}, \quad (6.2)$$

where (C/V) is the ratio of the phase velocity of light to that of the slow wave structure. Figure 6.1 depicts the slow wave and fast wave guides to be matched.

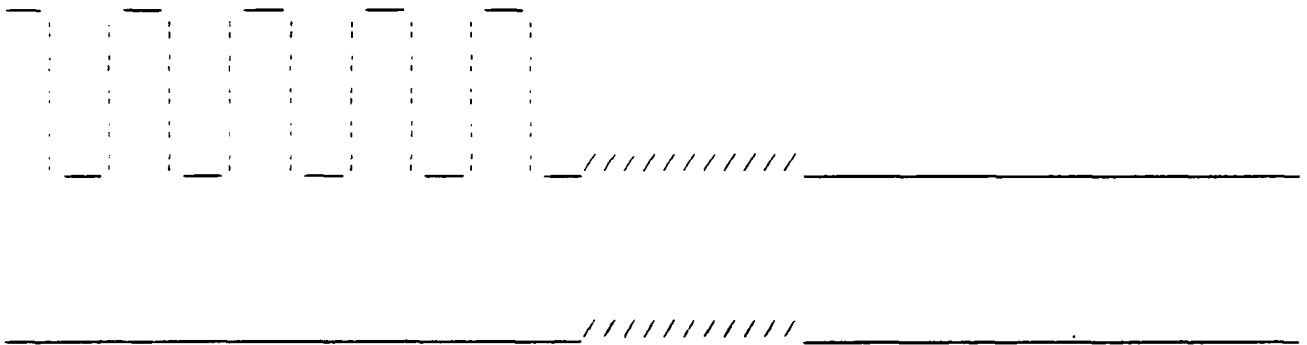


Fig. 6.1. Slow and fast wave structures.

A more detailed picture of the slow wave structure is seen in Fig. 6.2, which describes the coordinate system. The teeth are rectangular or square. The inner conductor is located at $y = -h$, where h is the distance between inner conductor R_I and outer conductor R_0 of the coaxial line.

Although the actual slow wave structure is a coaxial line with the outer corrugated surface radius R_0 of 8.2 cm to the teeth surfaces, a planar model yields similar results when the teeth surfaces, a planar model yields similar results when the corrugation parameters are the same because of the relatively close spacing between outer and inner conductors. Although $d = 1.4$ cm, $b = 0.7$ cm, and $\lambda = 1.8$ cm, the results are valid for any combination of these parameters.

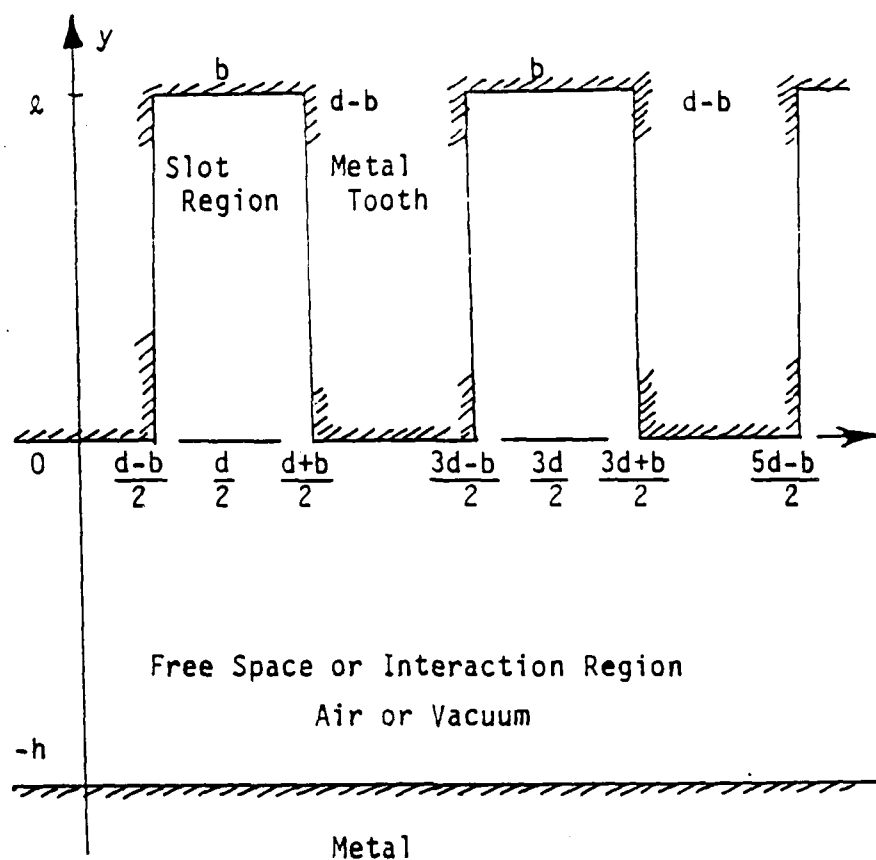


Fig. 6.2. Coordinate system for the slow wave structure.

In designing the transformer sections, the characteristic impedance $Z(1)$ of the first section is equal to the slow wave impedance in Eq. (6.2), while the characteristic impedance of the last section $Z(N+1)$ is equal to the characteristic impedance of the smooth coaxial line in Eq. (6.1). Since coaxial lines have no cutoff frequencies for TEM modes, they are only fast wave guides for modes higher than TEM modes.

Binomial and Chebyshev transformers will be developed in subsequent paragraphs to match the characteristic impedance $Z(1)$ to match the characteristic impedance $Z(N+1)$ of the output or load section $(N+1)$ in an N -step transformer. In order to find

$Z(1)$ as a function of slow wave guide geometry, the ratio of phase velocity of light in an infinite dielectric space to slow wave phase velocity in the same dielectric material between coaxial conductors must be found in section (1) of the transformer. These ratios are $C/V(M)$, where $M=1, \dots, N+1$. (The notation for sections is changed here to identify parameters more closely with section properties.).

$C/V(1)$ is calculated with equating slow wave and transmission line impedances in the drift space for electron beam and electromagnetic wave interactions. If a slow wave transmission line with phase velocity ratio $C/V(M)$ is introduced, the series impedance per unit length, $Z_S(M)$, is

$$Z_S(M) = j \left(C/V(M) \right)^2 \frac{\omega \mu}{2\pi} \ln \frac{R_O}{R_I} \text{ ohms/m,} \quad (6.3)$$

while the parallel susceptance $Y_P(M)$ is

$$Y_P(M) = j \frac{2\pi \omega \epsilon}{\ln \frac{R_O}{R_I}} \text{ mhos/m.} \quad (6.4)$$

Equations (6.3) and (6.4) can be combined to obtain the characteristic impedance in Eq. (6.2),

$$Z(M) = \sqrt{\frac{Z_S(M)}{Y_P(M)}} = \frac{C}{V(M)} \frac{\eta}{2\pi} \ln \frac{R_O}{R_I} \text{ ohms,} \quad (6.5)$$

and the phase velocity $V(M)$ is

$$\begin{aligned} V(M) &= \frac{1}{\sqrt{Z_S(M) Y_P(M)}} = \frac{1}{\sqrt{\left(C/V(M) \right)^2 \mu \epsilon}} \\ &= \frac{C}{C/V(M)} = V(M). \end{aligned} \quad (6.6)$$

For the short circuited radial transmission line, formed by to circular, parallel, infinitely conducting planes or tooth

walls, with radial length $l(M)$ and width $b(M)$, the input impedance Z_{slot} is

$$\begin{aligned} Z_{\text{slot}}(M) &= j Z_0(M) \tan kl(M) \\ &= j \frac{d(M)}{2\pi R_0} \eta \tan kl(M), \end{aligned} \quad (6.7)$$

where $d(M)$ is the width of a unit cell (M) or section (M) .

The series impedance per unit length for a unit cell with $l(M) = 0.0$ (in a smooth wall coaxial line) is

$$Z(M) = j \frac{\omega \mu}{2\pi} \ln \frac{R_0}{R_I} \text{ ohms/m}, \quad (6.8)$$

so that the slow wave impedance due to radial cavities are the difference between Eqs. (6.3) and (6.8), multiplied by the cavity width $b(M)$.

$$Z_{\text{slot}}(M) = j \left[\left(\frac{C}{V(M)} \right)^2 - 1 \right] \frac{\omega \mu}{2\pi} b(M) \ln \frac{R_0}{R_I}, \quad (6.9)$$

and when Eqs. (6.7) and (6.9) are equated,

$$\begin{aligned} j \frac{d(M)}{2\pi R_0} \eta \tan kl(M) \\ = j \left[\left(\frac{C}{V(M)} \right)^2 - 1 \right] \frac{\omega \mu}{2\pi} b(M) \ln \frac{R_0}{R_I}, \end{aligned} \quad (6.10)$$

and with $\omega \mu = k\eta$, and cancelling terms,

$$\frac{d(M)}{R_0} \tan kl(M) = \left[\left(\frac{C}{V(M)} \right)^2 - 1 \right] k b(M) \ln \frac{R_0}{R_I},$$

$$\tan kl(M) = \left[\left(\frac{C}{V(M)} \right)^2 - 1 \right] \frac{b(M)}{d(M)} k R_0 \ln \frac{R_0}{R_I},$$

$$l(M) = \frac{1}{k} \tan^{-1} \left[\frac{C^2}{V(M)^2} - 1 \right] \frac{b}{d} k R O \ln \frac{R O}{R I}, \quad (6.11)$$

$$\frac{C^2}{V(M)^2} = 1 + \left[\frac{d}{k d R O \ln(R O / R I)} \right] \tan k l(M), \quad (6.12)$$

where $b(M)/d(M) = b/d$ in the first section (1). When the expression $C/V(1)$ is obtained for the input section (1) of the slow wave guide, the slow wave characteristic impedance $Z(1)$ is found with Eq. (6.5).

With $d = 1.40$ cm, $b = 0.70$ cm, $l(1) = 1.80$ cm, $\lambda = 8.12$ cm ($F = 6.69$ GHz), the ratio $V(1)/C$ is 0.342. If the ratio $V(1)/C$ is chosen to be 0.34 (based on computer simulation results), $l(1)$ is 1.8032 cm. This correlation with simulation results indicates a good approximation to the dispersion curve with Eqs. (6.11) and (6.12).

The characteristic impedances of the N-step or N-junction transformers are calculated with Eqs. (4.10) and (4.14),

$$\begin{aligned} \ln \frac{Z(M+1)}{Z(M)} &= 2 p(M) = 2 p(M) \frac{\ln [Z(N+1)/Z(1)]}{\ln [Z(N+1)/Z(1)]} \\ &= p(M) \frac{\ln [Z(N+1)/Z(1)]}{\sum_{M=1}^N \frac{1}{2} \ln \frac{Z(M+1)}{Z(M)}} \\ &= p(M) \frac{\ln [Z(N+1)/Z(1)]}{p(1) + p(2) + \dots + p(N)}. \quad (6.13) \end{aligned}$$

With $p(M)$ known from Pascal's Triangle and Grave's Pyramid, the characteristic impedances can be obtained for the binomial and Chebyshev transformers. Since $Z(1)$ is known from the ratio $C/V(1)$, $Z(2)$ is calculated. After $Z(2)$ is found, $Z(3)$ is next calculated. This procedure continues until the

remaining $Z(M)$ are found, with $m = 4, 5, \dots, N$. The procedure for finding binomial and Chebyshev coefficients simplifies calculating characteristic impedances for both sets of sections.

With the values of $Z(M)$ calculated, the subsequent values of the $C/V(M)$ ratios are then found with

$$C/V(M) = Z(M) / 60 \ln \frac{R_0}{R_I},$$

$$M = 2, 3, \dots, N, N+1. \quad (6.14)$$

The widths $d(M)$ of the unit cells are equal to a half wavelength of the slow waves,

$$d(M) = \frac{C}{2 * FR * C/V(M)}, \quad (6.15)$$

which are found with $C/V(M)$ ratios. The cavity widths $b(M)$ are proportional to $d(M)$ with

$$b(M) = \frac{b}{d} d(M), \quad (6.16)$$

when we do not have square waves (teeth may be thin fins or fat teeth with negligible gaps).

The inductance L and capacitance C per unit length are relatively simpler.

$$L = (C/V(M))^2 \frac{\mu}{2\pi} \ln \frac{R_0}{R_I} \text{ h/m}, \quad (6.17)$$

$$C = \frac{2\pi\epsilon}{\ln \frac{R_0}{R_I}} \text{ f/m}. \quad (6.18)$$

Adjustments for compatibility between teeth periods $b(1)$, phase velocity ratios $V(1)/C$, and cavity or tooth gap lengths (1) , and frequency F create minor departures from simulated

Sect	Z(M,N)	V/C	Tooth	X (Slot)	Tooth	L/Cell	C/Cell
	ohms		Period	ohms	Ht. cm	nH	pF
1	40.9998	0.3400	1.3804	113.91	1.8032	5.549	3.301
2	40.8388	0.3413	1.3858	113.35	1.8012	5.527	3.314
3	39.7690	0.3505	1.4231	109.59	1.7873	5.382	3.403
4	36.4819	0.3821	1.5513	97.88	1.7355	4.937	3.710
5	30.5985	0.4556	1.8496	76.18	1.5888	4.141	4.423
6	23.9068	0.5831	2.3674	49.57	1.2417	3.235	5.661
7	18.6785	0.7463	3.0300	26.00	0.6853	2.528	7.245
8	15.6662	0.8898	3.6126	10.25	0.2475	2.120	8.638
9	14.3713	0.9700	3.9381	2.67	0.0598	1.945	9.417
10	13.9948	0.9961	4.0441	0.34	0.0075	1.894	9.670
11	13.9399	1.0000	4.0600	0.00	0.0000	1.886	9.708

Table VI. Transition Summary for 11 Sections and 10 Steps.

Sect	Z(M,N)	V/C	Tooth	X (Slot)	Tooth	L/Cell	C/Cell
	ohms		Period	ohms	Ht. cm	nH	pF
1	40.9998	0.3400	1.3804	113.91	1.8032	5.549	3.301
2	40.7000	0.3425	1.3906	112.86	1.7995	5.508	3.325
3	38.9468	0.3579	1.4532	106.68	1.7757	5.271	3.475
4	34.3159	0.4062	1.6493	90.02	1.6915	4.644	3.944
5	27.3838	0.5091	2.0668	63.73	1.4574	3.706	4.942
6	20.8712	0.6679	2.7117	36.32	0.9578	2.825	6.484
7	16.6551	0.8370	3.3981	15.67	0.3945	2.254	8.126
8	14.5747	0.9499	3.8567	4.50	0.1029	1.986	9.222
9	14.0426	0.9927	4.0303	0.64	0.0598	1.900	9.637
10	13.9399	1.0000	4.0600	0.00	0.0000	1.986	9.708

Table VII. Transition Summary for 10 Sections and 9 Steps.

Sect	Z(M,N)	V/C	Tooth	X (Slot)	Tooth	L/Cell	C/Cell
	ohms		Period	ohms	Ht. cm	nH	pF
1	40.9998	0.3400	1.3804	113.91	1.8032	5.549	3.301
2	40.4421	0.3447	1.3994	111.95	1.7962	5.473	3.346
3	37.6367	0.3704	1.5037	102.02	1.7554	5.094	3.596
4	31.4453	0.4433	1.7998	79.39	1.6159	4.256	4.304
5	23.9068	0.5831	2.3674	49.57	1.2417	3.235	5.661
6	18.1755	0.7670	3.1139	22.51	0.6156	2.440	7.446
7	15.1855	0.9180	3.7270	7.51	0.1767	2.055	8.912
8	14.1321	0.9864	4.0048	1.20	0.0264	1.912	9.576
9	13.9399	1.0000	4.0600	0.00	0.0000	1.886	9.708

Table VIII. Transition Summary for 9 Sections and 8 Steps.

Sect	Z(M,N)	V/C	Tooth	X (Slot)	Tooth	L/Cell	C/Cell
	ohms		Period	ohms	Ht. cm	nH	pF
1	40.9998	0.3400	1.3804	113.91	1.8032	5.549	3.301
2	39.9654	0.3488	1.4161	110.28	1.7899	5.409	3.386
3	35.6242	0.3913	1.5887	94.78	1.7191	4.821	3.799
4	27.9014	0.4996	2.0284	65.77	1.4821	3.776	4.850
5	20.4848	0.6805	2.7629	34.55	0.9138	2.772	6.607
6	16.0434	0.8689	3.5277	12.35	0.3035	2.171	8.436
7	14.3007	0.9748	3.9576	2.23	0.0499	1.935	9.463
8	13.9399	1.0000	4.0600	0.00	0.0000	1.886	9.708

Table IX. Transition Summary for 8 Sections and 7 Steps.

Sect	Z(M,N)	V/C	Tooth	X (Slot)	Tooth	L/Cell	C/Cell
	ohms		Period	ohms	Ht. cm	nH	pF
1	40.9998	0.3400	1.3804	113.91	1.8032	5.549	3.301
2	39.0907	0.3566	1.4478	107.19	1.7778	5.290	3.462
3	32.6902	0.4264	1.7313	84.02	1.6515	4.424	4.140
4	23.9068	0.5831	2.3674	49.77	1.2417	3.235	5.661
5	17.4833	0.7973	3.2371	20.01	0.5164	2.366	7.741
6	14.6207	0.9534	3.8710	4.18	0.0951	1.979	9.256
7	13.9399	1.0000	4.0600	0.00	0.0000	1.886	9.708

Table X. Transition Summary for 7 Sections and 6 Steps.

Sect	Z(M,N)	V/C	Tooth	X (Slot)	Tooth	L/Cell	C/Cell
	ohms		Period	ohms	Ht. cm	nH	pF
1	40.9998	0.3400	1.3804	113.91	1.8032	5.549	3.301
2	37.5094	0.3716	1.5088	101.56	1.7533	5.076	3.608
3	28.7222	0.4853	1.9705	69.98	1.5193	3.887	4.712
4	19.8987	0.7005	2.8442	31.83	0.8438	2.693	6.801
5	15.2371	0.9149	3.7144	7.80	0.1843	2.062	8.882
6	13.9399	1.0000	4.0600	0.00	0.0000	1.886	9.708

Table XI. Transition Summary for 6 Sections and 5 Steps.

Sect	Z(M,N)	V/C	Tooth	X (Slot)	Tooth	L/Cell	C/Cell
	ohms		Period	ohms	Ht. cm	nH	pF
1	40.9998	0.3400	1.3804	113.91	1.8032	5.549	3.301
2	34.7297	0.4014	1.6296	91.56	1.7006	4.700	3.897
3	23.9068	0.5831	2.3674	49.57	1.2417	3.235	5.661
4	16.4566	0.8471	3.4391	14.60	0.3650	2.227	8.224
5	13.9399	1.0000	4.0600	0.00	0.0000	1.886	9.708

Table XII. Transition Summary for 5 Sections and 4 Steps.

Sect	Z(M,N)	V/C	Tooth	X (Slot)	Tooth	L/Cell	C/Cell
	ohms		Period	ohms	Ht, cm	nH	pF
1	40.9998	0.3400	1.3804	113.91	1.8032	5.549	3.301
2	30.1244	0.4627	1.8787	74.37	1.5724	4.077	4.492
3	18.9724	0.7347	2.9831	27.43	0.7249	2.568	7.133
4	13.9399	1.0000	4.0600	0.00	0.0000	1.886	9.708

Table XIII. Transition Summary for 4 Sections and 3 Steps.

Sect	Z(M,N)	V/C	Tooth	X (Slot)	Tooth	L/Cell	C/Cell
	ohms		Period	ohms	Ht, cm	nH	pF
1	40.9998	0.3400	1.3804	113.91	1.8032	5.549	3.301
2	23.9068	0.5831	2.3674	49.57	1.2417	3.235	5.661
3	13.9399	1.0000	4.0600	0.00	0.0000	1.886	9.708

Table XIV. Transition Summary for 3 Sections and 2 Steps.

Sect	Z(M,N)	V/C	Tooth	X (Slot)	Tooth	L/Cell	C/Cell
	ohms		Period	ohms	Ht, cm	nH	pF
1	40.9998	0.3400	1.3804	113.91	1.8032	5.549	3.301
2	13.9399	1.0000	4.0600	0.00	0.0000	1.886	9.708

Table XV. Transition Summary for 2 Sections and 1 Step.

The following Tables indicate the slow wave structure design for a Binomial transformer with 11 or less sections, and 10 or less steps. Table XVI is Pascal's Triangle for the successive Tables with 11 to 2 sections.

1									
	1								
2		1							
	3		1						
6		4		1					
	10		5		1				
20		15		6		1			
	35		21		7		1		
70		56		28		8		1	
	126		84		36		9		1

Table XVI. Pascal's Triangle or Graves' Pyramid
for 10 Steps and Normalized Binomial Coefficients,
with Bandwidth = 1.0.

In the following sequence, Table XVII starts with the transition summary for 11 sections and 10 steps and continues to Table XXVI, transition summary for 2 sections and 1 step. Bandwidth is 1.0, and columns indicate section (M), characteristic impedances $Z(M,N)$ for steps (N) in the transformer, the step (M), ratio of slow wave phase velocity to velocity of light (V/C), tooth period $d(M)$ and height $h(M)$, cavity reactance $X(M)$, and inductance $L(M)$ and capacitance $C(M)$ per unit cell.

Sect	Z(M.N)	V/C	Tooth	X (Slot)	Tooth	L/Cell	C/Cell
	ohms		Period	ohms	Ht. cm	nH	pF
1	40.9998	0.3400	1.3804	113.91	1.8032	5.549	3.301
2	40.9135	0.3407	1.3833	113.61	1.8021	5.537	3.308
3	40.1448	0.3472	1.4098	110.91	1.7923	5.433	3.371
4	37.2122	0.3746	1.5209	100.50	1.7483	5.036	3.637
5	31.1759	0.4471	1.8154	78.36	1.6076	4.219	4.341
6	23.9068	0.5831	2.3674	49.57	1.2417	3.235	5.661
7	18.3325	0.7404	3.0872	24.29	0.6376	2.481	7.382
8	15.3587	0.9076	3.6849	8.50	0.2021	2.078	8.812
9	14.2368	0.9791	3.9753	1.85	0.0410	1.927	9.506
10	13.9693	0.9979	4.0515	0.18	0.0040	1.890	9.688
11	13.9399	1.0000	4.0600	0.00	0.0000	1.886	9.708

Table XVII. Transition Summary for 11 Sections and 10 Steps.

Sect	Z(M.N)	V/C	Tooth	X (Slot)	Tooth	L/Cell	C/Cell
	ohms		Period	ohms	Ht. cm	nH	pF
1	40.9998	0.3400	1.3804	113.91	1.8032	5.549	3.301
2	40.8273	0.3414	1.3862	113.31	1.8011	5.525	3.315
3	39.4738	0.3531	1.4338	108.54	1.7832	5.342	3.428
4	35.0803	0.3974	1.6133	92.81	1.7081	4.748	3.858
5	27.7061	0.5031	2.0427	65.01	1.4730	3.750	4.885
6	20.6284	0.6758	2.7436	35.21	0.9304	2.792	6.560
7	16.2921	0.8556	3.4738	13.71	0.3405	2.205	8.307
8	14.4788	0.9628	3.9089	3.32	0.0750	1.960	9.347
9	13.9988	0.9958	4.0429	0.37	0.0081	1.894	9.668
10	13.9399	1.0000	4.0600	0.00	0.0000	1.886	9.708

Table XVIII. Transition Summary for 10 Sections and 9 Steps.

Sect	Z(M,N)	V/C	Tooth	X (Slot)	Tooth	L/Cell	C/Cell
	ohms		Period	ohms	Ht, cm	nH	pF
1	40.9998	0.3400	1.3804	113.91	1.8032	5.549	3.301
2	40.6556	0.3429	1.3921	112.71	1.7989	5.502	3.329
3	38.3263	0.3637	1.4767	104.48	1.7664	5.189	3.531
4	32.1092	0.4341	1.7626	81.86	1.6355	4.346	4.215
5	23.9068	0.5831	2.3674	49.57	1.2417	3.235	5.661
6	17.7997	0.7832	3.1796	32.62	0.5622	2.409	7.603
7	14.9123	0.9348	3.7953	5.91	0.1370	2.018	9.075
8	14.0579	0.9916	4.0259	0.74	0.0162	1.902	9.627
9	13.9399	1.0000	4.0600	0.00	0.0000	1.886	9.708

Table XIX. Transition Summary for 9 Sections and 8 Steps.

Sect	Z(M,N)	V/C	Tooth	X (Slot)	Tooth	L/Cell	C/Cell
	ohms		Period	ohms	Ht, cm	nH	pF
1	40.9998	0.3400	1.3804	113.91	1.8032	5.549	3.301
2	40.3144	0.3458	1.4039	111.51	1.7945	5.456	3.357
3	36.4363	0.3826	1.5533	97.71	1.7346	4.931	3.714
4	28.2961	0.4926	2.0001	67.32	1.5000	3.829	4.783
5	20.1983	0.6902	2.8020	33.23	0.8802	2.734	6.700
6	15.6858	0.8887	3.6081	10.34	0.2504	2.123	8.628
7	14.1769	0.9933	3.9921	1.48	0.0327	1.919	9.546
8	13.9399	1.0000	4.0600	0.00	0.0000	1.886	9.708

Table XX. Transition Summary for 8 Sections and 7 Steps.

Sect	Z(M,N)	V/C	Tooth	X (Slot)	Tooth	L/Cell	C/Cell
	ohms		Period	ohms	Ht, cm	nH	pF
1	40.9998	0.3400	1.3804	113.91	1.8032	5.549	3.301
2	39.6405	0.3517	1.4277	109.13	1.7855	5.365	3.414
3	33.4913	0.4162	1.6899	86.99	1.6720	4.532	4.041
4	23.9068	0.5831	2.3674	49.77	1.2417	3.235	5.661
5	17.0652	0.8169	3.3165	17.84	0.4552	2.310	7.930
6	14.4179	0.9668	3.9254	2.95	0.0664	1.951	9.386
7	13.9399	1.0000	4.0600	0.00	0.0000	1.886	9.708

Table XXI. Transition Summary for 7 Sections and 6 Steps.

Sect	Z(M,N)	V/C	Tooth	X (Slot)	Tooth	L/Cell	C/Cell
	ohms		Period	ohms	Ht, cm	nH	pF
1	40.9998	0.3400	1.3804	113.91	1.8032	5.549	3.301
2	38.3263	0.3637	1.4767	104.48	1.7664	5.189	3.531
3	29.2662	0.4763	1.9338	71.08	1.5403	3.961	4.624
4	19.5288	0.7138	2.8981	30.09	0.7975	2.643	6.930
5	14.9123	0.9348	3.7953	5.91	0.1370	2.018	9.075
6	13.9399	1.0000	4.0600	0.00	0.0000	1.886	9.708

Table XXII. Transition Summary for 6 Sections and 5 Steps.

Sect	Z(M,N)	V/C	Tooth	X (Slot)	Tooth	L/Cell	C/Cell
	ohms		Period	ohms	Ht, cm	nH	pF
1	40.9998	0.3400	1.3804	113.91	1.8032	5.549	3.301
2	35.8273	0.3981	1.5797	95.52	1.7231	4.849	3.777
3	23.9068	0.5831	2.3674	49.57	1.2417	3.235	5.661
4	15.9525	0.8738	3.5478	11.85	0.2899	2.159	8.484
5	13.9399	1.0000	4.0600	0.00	0.0000	1.886	9.708

Table XXIII. Transition Summary for 5 Sections and 4 Steps.

Sect	Z(M,N)	V/C	Tooth	X (Slot)	Tooth	L/Cell	C/Cell
	ohms		Period	ohms	Ht. cm	nH	pF
1	40.9998	0.3400	1.3804	113.91	1.8032	5.549	3.301
2	31.3074	0.4453	1.8078	78.86	1.6117	4.237	4.323
3	18.2555	0.7636	3.1002	23.91	0.6268	2.471	7.413
4	13.9399	1.0000	4.0600	0.00	0.0000	1.886	9.708

Table XXIV. Transition Summary for 4 Sections and 3 Steps.

Sect	Z(M,N)	V/C	Tooth	X (Slot)	Tooth	L/Cell	C/Cell
	ohms		Period	ohms	Ht. cm	nH	pF
1	40.9998	0.3400	1.3804	113.91	1.8032	5.549	3.301
2	23.9068	0.5831	2.3674	49.57	1.2417	3.235	5.661
3	13.9399	1.0000	4.0600	0.00	0.0000	1.886	9.708

Table XXV. Transition Summary for 3 Sections and 2 Steps.

Sect	Z(M,N)	V/C	Tooth	X (Slot)	Tooth	L/Cell	C/Cell
	ohms		Period	ohms	Ht. cm	nH	pF
1	40.9998	0.3400	1.3804	113.91	1.8032	5.549	3.301
2	13.9399	1.0000	4.0600	0.00	0.0000	1.886	9.708

Table XXVI. Transition Summary for 2 Sections and 1 Step.

7. CONCLUSIONS

This paper describes the use of binomial coefficients and Chebyshev coefficients in the design of multisection quarter wave transformers. To reduce the sidelobe level of linear in-phase broadside antenna arrays, John Stone Stone [1] proposed that the sources have amplitudes proportional to the coefficients of a

binomial coefficients. After John Stone Stone's work, Charles Dolph [2] then applied Chebyshev coefficients to sidelobe reduction in antenna arrays in 1946, and Seymour Cohn [3] applied Dolph's results to electromagnetic filters in 1955. Examples with both binomial and Chebyshev coefficients are presented in slow to faster wave guides or transmission lines. The modification to the work by Stone Stone, Dolph, and Cohn is derivation of characteristic impedances $Z(M)$ for each unit cell (M) with binomial and Chebyshev coefficients, and then equating these $Z(M)$ to the product of the ratio of the phase velocity of light, C , to the slow wave phase velocity in unit cell (M) , $C/V(M)$, given by

$$Z(M) = Z(N+1) * C/V(M) \quad (7.1)$$

where $Z(N+1)$ is the characteristic impedance of the fast wave guide or line at the transformer output.

Although the slow wave velocity $V(1)$ was found from circuit concepts for the input line, unit cell (1) , more exact results will be developed with methods based on matching boundary conditions between waves in the radial cavities or teeth slots and the guiding region between inner smooth conductor and outer serrated conductor.

8. ACKNOWLEDGMENTS

Acknowledgments are made to Dr. Ray Lemke, who provided many questions and answers for my many answers and questions, and to Dr. Carl E. Baum, who provided similar responses. Both provided many valuable discussions which aided my studies.

9. REFERENCES

- [1] John Stone Stone, U.S. Patents 1,643,323 and 1,715,433.
- [2] C.L. Dolph, "A Current Distribution for Broadside Arrays which Optimizes the Relationship between Beam Width and Side-Lobe Level, Proc. IRE, vol. 34, pp. 335-348, June 1946.
- [3] S.B. Cohn, "Optimum Design of Stepped Transmission Line Transformers," IRE Trans. Microwave Theory & Techniques, vol. MTT-3, pp. 16-21, April 1955.

```

C      PROGRAM MILLI
C      PROGRAM FOR SUMMARY OF MULTISECTION TRANSFORMERS FOR
C      SLOW AND FAST WAVE TRANSMISSION LINES BASED USE OF
C      BINOMIAL AND CHEBYSHEV COEFFICIENTS
      REAL*8 A(25,25),AM(25,25),AMN(25,25),AN(25,25),BAND
      REAL*8 DE,DEC,FR,KO,L(26,25),LEN,LW(26,25)
      REAL*8 PI,RAZ(26,25),SUM(25),VC(26,25),VC1(1,25)
      REAL*8 SI(51,26,25),SLFA
      REAL*8 Z(26,25)
      INTEGER*4 LM,LN,M,ML,N,NF,NN,NNF,NL,NLN,NNL

      OPEN(UNIT=10,FILE='MILLI.DAT',STATUS='NEW')

      WRITE(6,*)' IF INPUT IS A SLOW WAVE AND OUTPUT IS
1 A SLOW WAVE, WRITE SLFA=11. IF INPUT IS SLOW AND OUTPUT
2 IS FAST, WRITE SLFA=12. IF INPUT IS FAST AND OUTPUT
3 IS FAST, WRITE SLFA=22. '
      READ(5,12)SLFA
      WRITE(6,*)' THE NUMBER OF STEPS, NF, IS '
      READ(5,10)NF
      WRITE(6,*)' THE BANDWIDTH P IS '
      READ(5,12)P
      WRITE(6,35)
      WRITE(10,35)
      WRITE(6,15)P,NF
      WRITE(10,15)P,NF
      WRITE(6,80)
      WRITE(10,80)
      N=NF
8      CONTINUE
10     FORMAT(I4)
12     FORMAT(F10.4)
15     FORMAT(' THE BANDWIDTH RATIO P IS ',F6.3,', THE LARGEST NUMBER
1 OF SECTIONS IS ',I2)
18     FORMAT(5X,' THE TRANSITION SUMMARY FOR ',I2,' SECTIONS
1 FOR ',I2,' STEPS')

C      P IS THE BANDWIDTH RATIO,F2/F1, OR (180 DEGREES-PHI1)/PHI1. IF THE
C      REQUIRED FREQUENCY RANGE IS 1 TO 2 GHZ, P = 2.0.
35     FORMAT(2X,130('='))

      PI=2.0*ASIN(1.0)
      KO=2.*PI/WL

      A(1,1)=2.0
      A(2,2)=1.0/COS(PI/(1.0+P))

      DO N=3,NF
          A(1,N)=2.0*A(2,2)*A(2,(N-1))-A(1,(N-2))
          DO M=2,N
              A(M,N)=A(2,2)*(A((M+1),(N-1))+A((M-1),(N-1)))-A(M,(N-2))
          END DO
      END DO

      DO 75 N=1,NF
          IF((N/2)*2-N)40,60,40

40     CONTINUE
      M=0

```

```

45      AM(M+1,N)=A((N-2*M),N)
C      NORMALIZE AM WITH RESPECT TO AM(1,N)
      AMN(M+1,N)=AM(M+1,N)/AM(1,N)

      M=M+1
      IF((2*M).LT.N)GOTO 45
50      AM(M+1,N)=A((2*M-N+2),N)
C      NORMALIZE AM WITH RESPECT TO AM(1,N)
      AMN(M+1,N)=AM(M+1,N)/AM(1,N)
      M=M+1
      IF((2*M).LT.(2*N-1))GOTO 50
      GOTO 75

60      M=0
65      AM(M+1,N)=A((N-2*M),N)
C      NORMALIZE AM WITH RESPECT TO AM(1,N)
      AMN(M+1,N)=AM(M+1,N)/AM(1,N)
      M=M+1
      IF((2*M+1).LT.N)GOTO 65
70      AM(M+1,N)=A((2*M-N+2),N)
C      NORMALIZE AM WITH RESPECT TO AM(1,N)
      AMN(M+1,N)=AM(M+1,N)/AM(1,N)
      M=M+1
      IF((2*M+1).LT.(2*N)) GOTO 70
75      CONTINUE

      DO 102 N=1,NF-1

      IF(N.GT.6)GOTO 81

      WRITE(6,77)N
      WRITE(10,77)N
77      FORMAT(' THE NUMBER OF STEPS N IS ',I2)
      WRITE(6,79)(AM(M+1,N),M=0,(N-1))
      WRITE(10,79)(AM(M+1,N),M=0,(N-1))
79      FORMAT(<N>(F18.2,2X),/)
      WRITE(6,80)
      WRITE(10,80)
80      FORMAT(2X,130(' - '))
      GOTO 102
81      CONTINUE
      NL=N/6
      LN=N-(N/6)*6
      IF(LN.EQ.0)GOTO 84
      GOTO 93
84      CONTINUE
      WRITE(6,77)N
      WRITE(10,77)N
87      WRITE(6,90)(AM(M+1,N),M=0,(N-1))
      WRITE(10,90)(AM(M+1,N),M=0,(N-1))
90      FORMAT(<NL>(6(F18.2,2X),/))
      WRITE(6,80)
      WRITE(10,80)
      GOTO 102

93      CONTINUE
      WRITE(6,77)N
      WRITE(10,77)N
      WRITE(6,99)(AM(M+1,N),M=0,(N-1))
      WRITE(10,99)(AM(M+1,N),M=0,(N-1))

```

```

WRITE(6,80)
WRITE(10,80)

102    CONTINUE

      DO 202 N=NF

      IF(N.GT.6)GOTO 101

      WRITE(6,77)N
      WRITE(10,77)N
      WRITE(6,79)(AM(M+1,N),M=0,(N-1))
      WRITE(10,79)(AM(M+1,N),M=0,(N-1))
      WRITE(6,35)
      WRITE(10,35)
      GOTO 122
101    CONTINUE
      NL=N/6
      LN=N-(N/6)*6
      IF(LN.EQ.0)GOTO 104
      GOTO 113
104    CONTINUE
      WRITE(6,77)N
      WRITE(10,77)N
      WRITE(6,90)(AM(M+1,N),M=0,(N-1))
      WRITE(10,90)(AM(M+1,N),M=0,(N-1))
      WRITE(6,35)
      WRITE(10,35)
      GOTO 122

113    CONTINUE
      WRITE(6,77)N
      WRITE(10,77)N
116    WRITE(6,99)(AM(M+1,N),M=0,(N-1))
      WRITE(10,99)(AM(M+1,N),M=0,(N-1))
      WRITE(6,35)
      WRITE(10,35)

122    CONTINUE

C      WRITE(6,35)
C      WRITE(10,35)
      WRITE(6,155)P
      WRITE(10,155)P
155    FORMAT(20X,' THE NORMALIZED Am VALUES FOR P = ',F6.3)
      WRITE(6,35)
      WRITE(10,35)

      DO 180 N=1,NF-1

      IF(N.GT.10)GOTO 161

      WRITE(6,77)N
      WRITE(10,77)N
      WRITE(6,158)(AMN(M+1,N),M=0,(N-1))
      WRITE(10,158)(AMN(M+1,N),M=0,(N-1))
158    FORMAT(<N>(F12.4,X))

```



```

        WRITE(10,80)
        GOTO 180
161      CONTINUE
       >NNL=N/10
       >NNLN=N-(N/10)*10
       >IF(NLN.EQ.0)GOTO 164
       >GOTO 173

164      CONTINUE
       >WRITE(6,77)N
       >WRITE(10,77)N
       >WRITE(6,170)(AMN(M+1,N),M=0,(N-1))
       >WRITE(10,170)(AMN(M+1,N),M=0,(N-1))
170      FORMAT(<NNL>(10(F12.4,X)))
       >WRITE(6,80)
       >WRITE(10,80)
       >GOTO 180

173      CONTINUE
       >WRITE(6,77)N
       >WRITE(10,77)N
       >WRITE(6,179)(AMN(M+1,N),M=0,(N-1))
       >WRITE(10,179)(AMN(M+1,N),M=0,(N-1))
179      FORMAT(<NNL>(10(F12.4,X)),</>,<NLN>(F12.4,X))
       >WRITE(6,80)
       >WRITE(10,80)

180      CONTINUE

        DO 210 N=NF

        IF(N.GT.10)GOTO 191

        WRITE(6,77)N
        WRITE(10,77)N
        WRITE(6,158)(AMN(M+1,N),M=0,(N-1))
        WRITE(10,158)(AMN(M+1,N),M=0,(N-1))
        *      WRITE(6,35)
        *      WRITE(10,35)
        GOTO 210
191      CONTINUE
       >NNL=N/10
       >NNLN=N-(N/10)*10
       >IF(NLN.EQ.0)GOTO 194
       >GOTO 203

194      CONTINUE
       >WRITE(6,77)N
       >WRITE(10,77)N
       >WRITE(6,170)(AMN(M+1,N),M=0,(N-1))
       >WRITE(10,170)(AMN(M+1,N),M=0,(N-1))
        *      WRITE(6,35)
        *      WRITE(10,35)
       >GOTO 210

203      CONTINUE

```

```

      WRITE(10,77)N
      WRITE(6,179)(AMN(M+1,N),M=0,(N-1))
      WRITE(10,179)(AMN(M+1,N),M=0,(N-1))
*      WRITE(6,35)
*      WRITE(10,35)

210      CONTINUE

      SUM(1)=AMN(1,1)
      DO N=2,NF
        M=1
        SUM(N)=AMN(M,N)
212      M=M+1
        SUM(N)=SUM(N)+AMN(M,N)
        IF(M.LT.N)GOTO 212
      END DO
C      THE CHARACTERISTIC IMPEDANCE OF THE FIRST SECTION, M = 1, IN
C      AN N-STEP TRANSITION, IS Z(1,N). THE LAST SECTION HAS AN
C      IMPEDANCE Z(N+1,N).

C      RAZ(M,N) IS THE RATIO OF CHARACTERISTIC IMPEDANCE Z(M+1,N) OF THE
C      LAST SECTION, M+1, TO THE PRECEDING CHARACTERISTIC IMPEDANCE
C      Z(M,N) OF THE PRECEDING SECTION M, IN AN N STEP TRANSITION.

      IF(SLFA.EQ.22.)GOTO 220
      GOTO 225

220      CONTINUE
      WRITE(6,*)' THE CHARACTERISTIC IMPEDANCE OF SECTION
1 ONE IS '
      READ(5,12)Z(1,1)
      WRITE(6,*)' THE CHARACTERISTIC IMPEDANCE OF SECTION
1 N+1 IS '
      READ(5,12)Z(2,1)

      DO N=1,NF
        Z(1,N)=Z(1,1)
        Z(N+1,N)=Z(2,1)
      END DO

225      CONTINUE
      DO N=1,NF
        DO M=1,N
C          WRITE(6,226)SUM(N),N
C          WRITE(10,226)SUM(N),N
226      FORMAT(' 226SUM(N) = ',F10.4,' AND N = ',I4,/)
          RAZ(M,N)=EXP((AMN(M,N)*LOG(Z(N+1,N)/Z(1,N)))/SUM(N))
          END DO
        END DO

C      WITH RAZ(M,N), WE CAN FIND Z(M+1,N) WHEN Z(M,N) IS KNOWN.
      DO N=1,NF
        DO M=1,N
          Z(M+1,N)=RAZ(M,N)*Z(M,N)
        END DO
      END DO

```

```

: PHASE VELOCITY RATIO IS FOUND WITH CHARACTERISTIC IMPEDANCE
: Z(M,N) FOR SECTION M IN N STEPS AND CHARACTERISTIC IMPEDANCE
: Z(N+1,N) FOR A SMOOTH COAXIAL CYLINDER WAVEGUIDE, 60 LN (RO/RI).
:   DO N=1,NF
:     DO M=1,N+1
:       VC(M,N)=60.0*(LOG(RO/RI))/Z(M,N)
:     END DO
:   END DO

: PHASE CONSTANT BETA IS RELATED TO WAVELENGTH IN FREE SPACE*RATIO OF
: PHASE VELOCITY TO VELOCITY OF LIGHT.  WL IS IN CM.

*   DO N=1,NF
*     DO M=1,N+1
*       L(M,N)=2.E-1*LOG(RO/RI)/(VC(M,N)**2)
*     END DO
*   END DO
DO N=1,NF

WRITE(6,35)
WRITE(10,35)
WRITE(6,250)N+1,N
WRITE(10,250)N+1,N
250  FORMAT(5X,' THE TRANSITION SUMMARY FOR ',I2,' SECTIONS
1  FOR ',I2,' STEPS')
WRITE(6,35)
WRITE(10,35)
WRITE(6,252)
WRITE(10,252)
252  FORMAT(' SECT ',Z(M,N), OHMS ',X,' RATIO, V/C ',
2X,' L/CELL, NH ',3X,' C/CELL, pF ')
WRITE(6,35)
WRITE(10,35)
DO M=1,N
253  WRITE(6,255)M,Z(M,N),VC(M,N)
WRITE(10,255)M,Z(M,N),VC(M,N)
255  FORMAT(2X,I2,3X,F10.4,5X,F7.3)
WRITE(6,80)
WRITE(10,80)
END DO
M=N+1
WRITE(6,255)M,Z(M,N),VC(M,N)
WRITE(10,255)M,Z(M,N),VC(M,N)
END DO
WRITE(6,35)
WRITE(10,35)
END

```

FINAL REPORT NUMBER 63
REPORT NOT AVAILABLE AT THIS TIME
Dr. Lane Clark
210-9MG-119

Vibrational Energy Transfer in Sulfur Monoxide

Final Report

Contract No. F49620-88-C-0053/SB5881-0378

Prepared for Universal Energy Systems, Inc.

by

David A. Dolson, Ph.D.
Chemistry Department
Wright State University
Dayton, OH 45435

February 3, 1990

Vibrational Energy Transfer in Sulfur Monoxide

by

David A. Dolson, Ph.D.
Chemistry Department
Wright State University

ABSTRACT

A pulsed laser photolysis experiment has been conducted to measure the rate coefficient, k_1 , for vibrational energy transfer (VET) from $\text{SO}(v=1)$ to SO_2 . Low pressures of SO_2 (0.1 - 0.3 torr) were subjected to photolysis at 213 nm with the fifth harmonic of a Nd:YAG laser in order to generate $\text{SO}(v=1)$. Time-dependent infrared fluorescence observations from $\text{SO}_2(v_3)$ have been obtained at 7.4 μm . A kinetic scheme has been used in an attempt to extract the initial VET rate from the $\text{SO}_2(v_3)$ observations. The preliminary results and a consideration of theory suggest that $k_1 > 2 \times 10^{-11} \text{ cm}^3 \text{ molecule}^{-1} \text{ s}^{-1}$, but a slower rate constant cannot be discounted without further investigation. This work is continuing with efforts to observe $\text{SO}(v=1)$ directly.

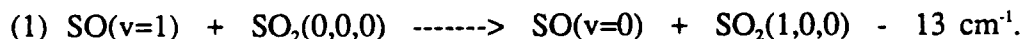
I. INTRODUCTION

The molecular radical, sulfur monoxide (SO), is currently being evaluated by the Advanced Radiation Branch of the Air Force Weapons Laboratory (AFWL) as a gas phase chemical laser candidate. A sulfur monoxide chemical laser operating on the A-X electronic transition would generate near ultraviolet output.¹ Rapid vibrational energy transfer (VET) in the ground electronic state (X) is crucial for removing population from the lower level of the laser transition in order to maintain the required population inversion. Knowledge of VET rates for collisions of SO in vibrational levels of the X state with several molecular and atomic collision partners is extremely important to the evaluation of the SO (A-X) transition as a potential chemical laser system.

This report presents preliminary results from an infrared fluorescence study of VET from SO(v=1) to SO₂. Progress on this work during the contract period was slower than expected due to construction delays in the renovation of new laboratory space. However, the work has begun, and these first results were generated very quickly. This investigation will continue as a Masters degree thesis project. The preliminary results have suggested a small modification in the experimental design that is expected to simplify the kinetic observations. Continuation of this work to study VET rates for SO(v=1) with other collision partners is planned.

II. EXPERIMENTAL CONSIDERATIONS

The objective of this study is to measure the bimolecular VET rate constant, k_1 , at 298K for deactivation of SO(v=1) by SO₂. Energy considerations suggest that the most likely pathway for VET in this system is



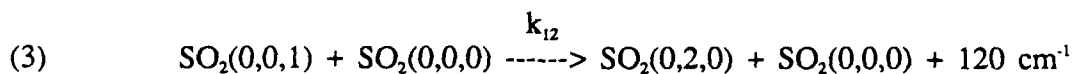
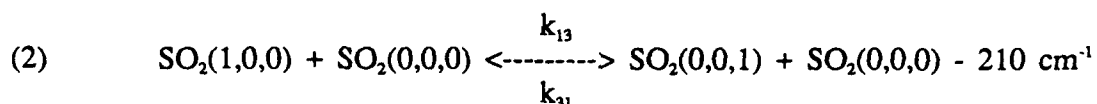
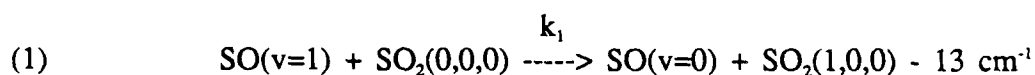
The experimental approach is to prepare SO(v=1), at time $t=0$, in the presence of a larger quantity of SO₂ so that pseudo first-order kinetic conditions are satisfied. Kinetic measurements of k_1 may be made from real time observations of infrared fluorescence from SO(v=1) or from SO₂(v) excited by VET from the initially prepared sulfur monoxide.

Ultraviolet pulsed laser photolysis of SO₂ was chosen to prepare SO(v=1). Experimental studies have shown that the onset of SO₂ dissociation occurs in the C-X transition at 219 nm.² The S-O bond length change from 1.56Å in SO₂(C) to 1.43Å in SO(X)

suggests that some vibrational excitation of the sulfur monoxide fragment is likely. Two independent groups^{3,4} have demonstrated that 193 nm photolysis of SO₂ produces SO predominantly in $v=2$ (67%) and $v=1$ (24%), with lesser amounts in levels $v=0$ and $v=3-6$. 212.9 nm photolysis of SO₂ (5th harmonic, YAG laser) is energetic enough only for SO($v=1$) production. This is a much simpler kinetic environment in which to study VET with infrared fluorescence observations.

The most straightforward method to obtain k_1 is to observe the exponential decay of the 8.8 μm emission from the excited SO($v=1$) radicals. In the SO/SO₂ system emission from SO($v=1$) would be overlapped by emission from the symmetric stretch vibration of SO₂(v_1). It may be possible to remove the SO₂(v_1) fluorescence from such observations by using a filter cell filled with SO₂; however, during the planning of this investigation it was felt that it would be better to ensure the observation of only one emitting species. Consequently attention was turned to observing SO₂(v_3) emission at 7.4 μm , excited by VET from SO($v=1$).

The kinetic scheme is expected to involve the following bimolecular processes:



The time evolution of 7.4 μm fluorescence is directly proportional to the concentration of SO₂(v_3), which (for pseudo-first order conditions) is given by

$$(4) \quad [\text{SO}_2(0,0,1)] = P_1 \exp(-k_1[\text{SO}_2]t) + P_2 \exp(-k_+[\text{SO}_2]t) + P_3 \exp(-k_-[\text{SO}_2]t)$$

The first term is due to VET from SO($v=1$) to SO₂. The second term arises from the equilibrium between the two stretching modes of SO₂. The third term describes the loss of vibrational energy to the bending mode of SO₂, which is finally deactivated by V-T,R processes.

The constants, k_+ and k_- , have been determined by the careful work of Flynn and coworkers.^{5,6,7} The near resonance of SO($v=1$) and SO₂(v_1) energy levels suggests that k_1 will

be larger than $k_- \approx k_{13} + k_{31}$, which is larger than $k_+ \approx k_{12}$. If the time constants of Eqn. (4) are well enough separated, infrared observations of ν_3 emission from SO_2 should exhibit three distinctive time constants. k_1 would then be obtained from measuring the appropriate time constant as a function of SO_2 concentration. The initial experiments in this project have been conducted according to the considerations presented here.

III. EXPERIMENTAL METHOD

A pulsed YAG laser (Spectra Physics, Quanta-Ray DCR-11-3 and HG-2) was used with standard KD*P crystals to generate collinear output at 1064nm, 532nm, and 266nm. A BBO crystal (8mm x 8mm x 7mm, 57.1° cut with respect to the z-axis) was used to generate the fifth harmonic at 212.9nm by sum frequency mixing of the fundamental and fourth harmonic beams. Ten mJ/pulse of the fifth harmonic could be produced from about 50 mJ/pulse of fourth harmonic energy. The input to the crystal was not focussed. The harmonics were separated with a Pellin-Broca prism, and the fifth harmonic beam was selected with a 90° turning prism and directed through the photolysis cell. Both prisms were of UV grade fused silica.

The glass photolysis cell, 40mm in diameter and 20cm in length, was equipped with fused silica windows on either end and a sodium chloride observation window centered on one side of the cell. SO_2 flow through the cell was regulated with a fine needle valve, and the pressure was measured with a 10 torr capacitance manometer. A 77K trap collected SO_2 downstream from the cell for subsequent disposal.

Infrared fluorescence from $\text{SO}_2(0,0,1)$ passed out of the cell through the sodium chloride window and a narrow-band interference filter to a 77K photoconductive HgCdTe detector (Infrared Associates, 4mm x 4mm active area). The filter transmission, centered at 7.355 μm with a 0.21 μm bandpass, passes $\text{SO}_2(\nu_3)$ fluorescence. Following amplification, the signal is directed to a digital oscilloscope (LeCroy 9400) for digitization and signal averaging. The fluorescence vs. time signals presented in this report are the result of 10,000 laser pulses with SO_2 in the cell minus 10,000 laser pulses with an empty cell. The empty cell data was required because of the presence of reproducible background signals generated upon laser firing. The time-dependent fluorescence signals were analyzed to measure the exponential time constants.

IV. RESULTS

Infrared chemiluminescence results from the room temperature 212.9nm photolysis of sulfur dioxide are presented in Fig. 1 and Fig. 2 for sample pressures of 0.10 and 0.30 torr, respectively. The remaining "noise" spikes in these figures result from imperfect background subtraction and indicate the firings of the flashlamp (about .3 ms before time=0) and of the Pockles cell to Q-switch the laser (at time=0). A visual inspection of the fluorescence suggested that the 0.10 torr result might be explained with a difference of only two exponentials, while it appeared that the 0.30 torr curve exhibited two time constants in the decay.

The fluorescence signals were analyzed by an exponential stripping method to obtain time constants and pre-exponential intensity coefficients. The results of this preliminary treatment are presented in Table 1. The fluorescence obtained at 0.30 torr rises with a single exponential time constant of 49 usec and falls with a 219 usec fast decay followed by a 2,380 usec slower decay. The pre-exponential coefficients are consistent with the functional form for the time-dependent intensity given in equation (5). This function is plotted as the solid line

$$(5) \quad I(t) = A \exp(-t/219 \text{ usec}) + B \exp(-t/2380 \text{ usec}) + (A+B) \exp(-t/49.0 \text{ usec})$$

in Fig. 1. The pre-exponential factor for the rise agrees with the sum of those for the two decay terms within three percent.

It was not possible to discern the presence of more than one exponential decay in the 0.10 torr observation. Consequently only two time constants are reported in Table 1, and the signal is approximated by the difference of exponential terms presented in equation (6). This

$$(6) \quad I(t) = A (\exp(-t/2040 \text{ usec}) - \exp(-t/116 \text{ usec}))$$

function is plotted as the solid line in Fig. 2. It may be that three exponential terms more correctly describes the signal; however, the quality of the present data does not justify using more than two exponential terms.

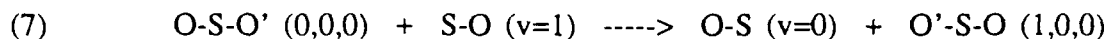
V. DISCUSSION

The rising portions of the fluorescence signals can be attributed to the approach to equilibrium between the v_1 and v_3 modes of SO_2 . The average rate coefficient from the rise is seen to be $k_- = 2.3 \times 10^{-12} \text{ cm}^3 \text{ molecule}^{-1} \text{ s}^{-1}$ as compared to $1.9 \times 10^{-12} \text{ cm}^3 \text{ molecule}^{-1} \text{ s}^{-1}$ (60 msec $^{-1}$ torr $^{-1}$) from West et al.⁶ The v_1 to v_2 energy transfer process in pure SO_2 proceeds with a rate coefficient of $1.0 \times 10^{-13} \text{ cm}^3 \text{ molecule}^{-1} \text{ s}^{-1}$ (3.1 msec $^{-1}$ torr $^{-1}$)⁶. The exponential decay at 0.10 torr (Fig. 2.) most closely matches this value. The fast and slow decays at 0.30 torr (Fig. 1.) lie on either side of the literature value.

The results satisfy expectations about the v_1 - v_3 intermode equilibrium; however, there are serious deficiencies in regards to the expected exponential decay times. Although this is of interest and demands further study, the immediate interest is focussed on identifying the initial VET process represented in Eqn. (1) and obtaining a rate coefficient for the process.

It is not clear that the $\text{SO}(v=1)$ to $\text{SO}_2(1,0,0)$ VET step is observable in either figure. One possible explanation is that this process is faster than the observed rise such that it is indistinguishable from direct excitation of $\text{SO}_2(1,0,0)$ on the time scale of our observation. If so, $k_1 \gtrsim 2 \times 10^{-11} \text{ cm}^3 \text{ molecule}^{-1} \text{ s}^{-1}$ would appear to be a reasonable lower limit (ten-fold faster than the observed rise). An alternative explanation would require a fortuitous near equality in k_1 and k_- such that they are inseparable and indistinguishable from a single exponential rise. In this case, $k_1 \gtrsim 2 \times 10^{-12} \text{ cm}^3 \text{ molecule}^{-1} \text{ s}^{-1}$. A final argument would state that the unexpected decay time is due to the initial $\text{SO}(v=1) + \text{SO}_2$ energy transfer, though this would seem to have less support from VET theory.

Long range dipole-dipole interactions between SO and SO_2 are expected to play a role in the VET efficiency. The theory⁸ for such interactions is consistent with a probability of transfer (per collision), $\langle\langle P \rangle\rangle = 0.7$, for exact resonance. A marked reduction is predicted in $\langle\langle P \rangle\rangle$ for small energy gaps ($\langle\langle P \rangle\rangle = 0.01$ for $\Delta E = 13 \text{ cm}^{-1}$), but rotational degrees of freedom have been omitted in this simple theoretical treatment. The exact resonance predictions agree with the experimental VET cross-sections for several non-resonant cases: $\text{CO}_2\text{-SF}_6$ ($\Delta E = 13 \text{ cm}^{-1}$), $\text{CO}_2\text{-CO}^{18}\text{O}$ ($\Delta E = 18 \text{ cm}^{-1}$), and for $\text{CO}_2\text{-}^{13}\text{CO}_2$ ($\Delta E = 66 \text{ cm}^{-1}$). This good agreement, even for systems in which the collision partners are dissimilar ($\text{CO}_2\text{-SF}_6$), suggests that the exact resonance prediction may also hold for the SO-SO_2 system. The possibility for O atom exchange via process (7) provides an additional mechanism for VET.



Reactive exchange is particularly effective in the relaxation of hydrogen halides by halogen atoms. The stronger theoretical evidence argues for fast VET ($\langle\langle P \rangle\rangle \sim 0.1$) from $\text{SO}(v=1)$ to SO_2 . An attempt to verify this in the $\text{SO}_2(v_3)$ rise would require experiments at lower pressures where the signal-to-noise values are poorer. Consequently an alternative experimental approach will be taken.

We have planned continuing experiments in this study that involve direct observation of emission from $\text{SO}(v=1)$. Broadband observations of 5-14 μm fluorescence following 213 nm photolysis of SO_2 yields some prompt emission that is not viewed through the 7.4 μm filter. It is probable that this prompt emission is from $\text{SO}(v=1)$. We will attempt to isolate the SO fluorescence with an 8.8 μm filter. A cold gas filter cell⁹ containing SO_2 will be used to resonantly absorb the $\text{SO}_2(v_1)$ fluorescence excited in the initial VET step. The exponential decay of the observed signal will give k_1 directly according to Eqn. (8). This approach,

$$(8) \quad I(t) = I_0 \exp(-k_1[\text{SO}_2]t)$$

though previously considered, was omitted in favor of the $\text{SO}_2(v_3)$ observations presented here. It now appears as if the direct $\text{SO}(v=1)$ observation holds the greater promise.

REFERENCES

1. Huber, K. P. and G. Herzberg, *Molecular Spectra and Molecular Structure IV. Constants of Diatomic Molecules*, Van Nostrand Reinhold, New York (1979).
2. Okabe, H., *Photochemistry of Small Molecules*, Wiley-Interscience, New York (1978).
3. Felder, P., C. S. Effenjauser, B. M. Haas, and J. R. Huber, "Photodissociation of Sulfur Dioxide at 193 nm," *Chem. Phys. Lett.*, **1988**, 148, 417-22.
4. Kanamori, J., J. E. Butler, K. Kawaguchi, C. Yamada, and E. Hirota, "Spin Polarization in SO Photochemically Generated from SO₂," *J. Chem. Phys.*, **1985**, 83, 611-15.
5. Seibert, D. and G. Flynn, "Vibration-Vibration Energy Transfer in Laser Excited SO₂: Further Evidence for a Slow V-V Step," *J. Chem. Phys.*, **1975**, 62, 1212-20.
6. West, G. A., R. E. Weston, and G. W. Flynn, "Deactivation of Vibrationally Excited SO₂ by O(³P) Atoms," *J. Chem. Phys.*, **1977**, 67, 4873-9.
7. Lester, M. I. and G. W. Flynn, "Intermolecule Vibrational Energy Transfer Dynamics in IR Laser Pumped SO₂/¹⁸O₂ Mixtures," *J. Chem. Phys.*, **1980**, 72, 6424-36.
8. Yardley, J. T., *Introduction to Molecular Energy Transfer*, Academic Press, New York (1980).
9. Vlahoyannis, Y. P., M. Koshi, and R. J. Gordon, "Use of a Cold Gas Filter to Characterize Polyatomic Vibrational State Distributions: Application to SF₆ + N₂O," *Chem. Phys. Lett.*, **1985**, 118, 179-85.

Table 1.
Exponential Stripping Results for 7.355 μm Fluorescence from SO_2
Following 213 nm Photolysis

Sample Pressure (torr)	Pre-Exponential Coefficient (arbitrary units)	Time Constant (usec)	Rate Coefficient $\text{cm}^3 \text{ molecule}^{-1} \text{ s}^{-1}$
0.30	591 **	49.0 **	2.1×10^{-12} **
	372	219	4.7×10^{-13}
	233	2,380	4.3×10^{-14}
0.10	216 **	116 **	2.6×10^{-12} **
	210	2,040	1.5×10^{-13}

** Denotes rising exponential term

INFRARED CHEMILUMINESCENCE IN
213 nm PHOTOLYSIS OF SULFUR DIOXIDE

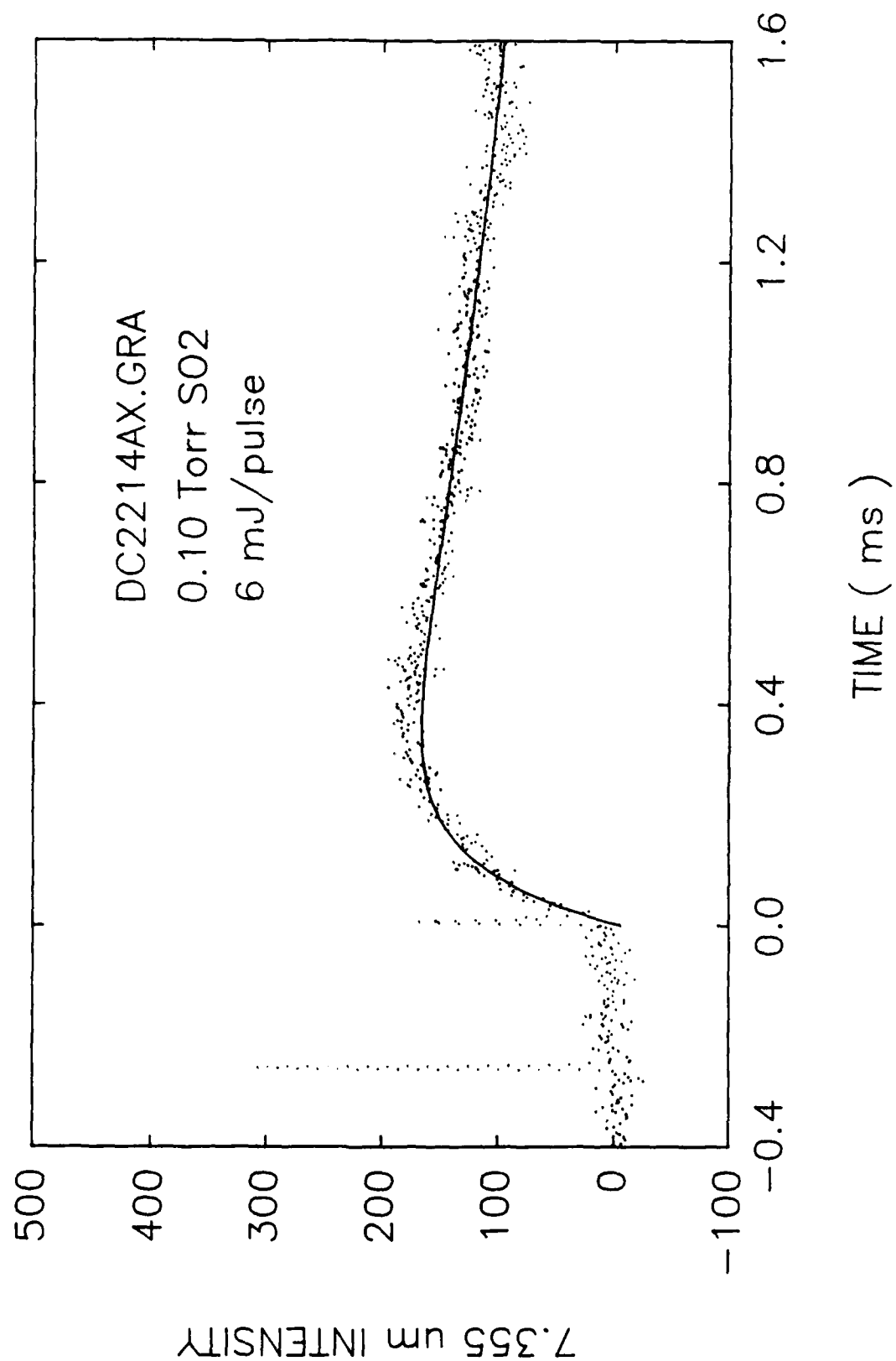


Figure 1

INFRARED CHEMILUMINESCENCE IN
213 nm PHOTOLYSIS OF SULFUR DIOXIDE

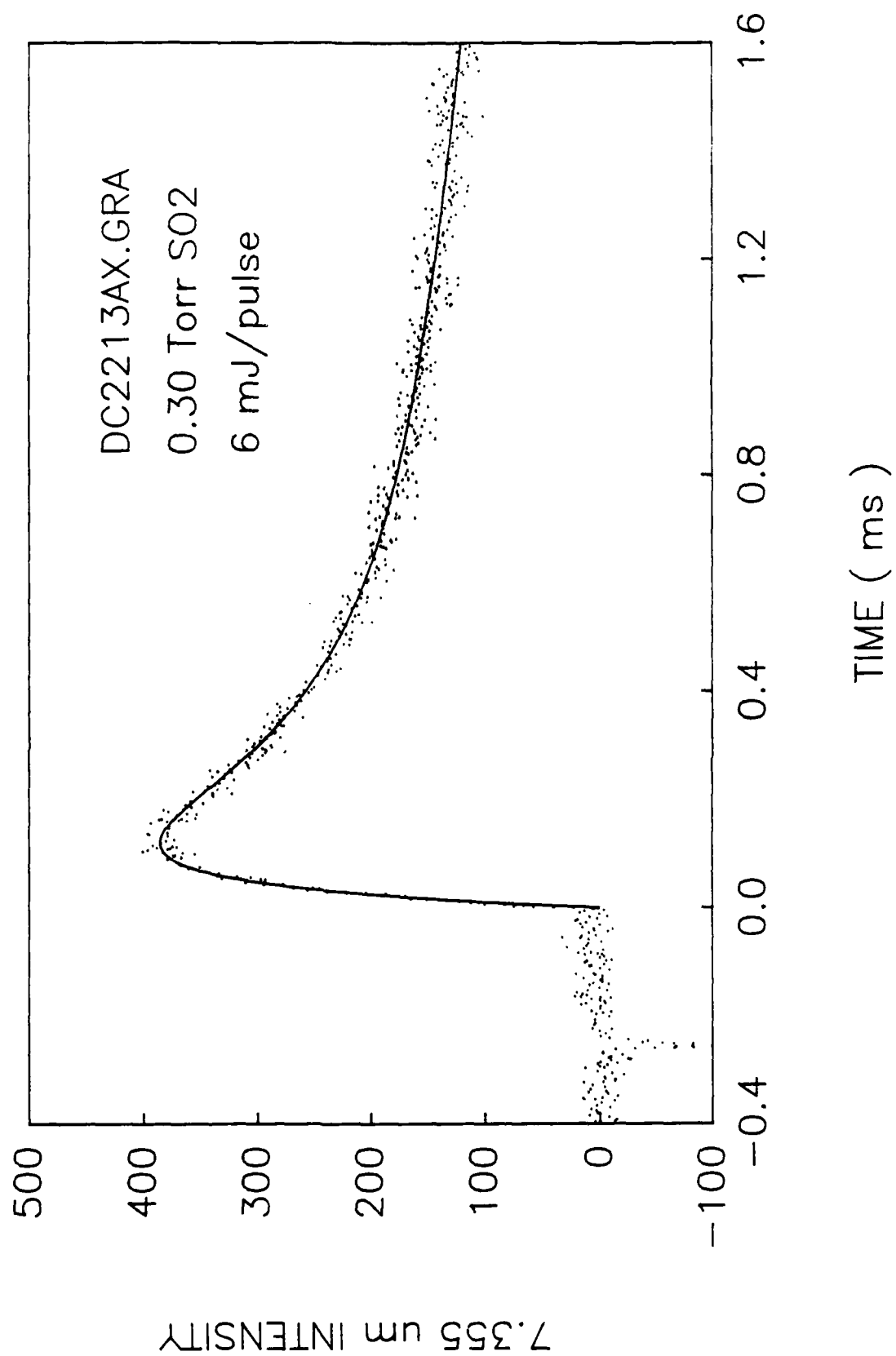


Figure 2

1988 U.S.A.F.--U.E.S. Research Initiation Program

Sponsored by the

AIR FORCE OFFICE OF SCIENTIFIC RESEARCH

Conducted by

Universal Energy Systems, Inc.

FINAL REPORT

Development of an Experimental
Program to Evaluate Laser Composite
Material Damage Models

Prepared by: William M. Jordan, Ph.D, P.E.

Academic rank: Associate Professor

Department and University: Mechanical and Industrial
Engineering Department
Louisiana Tech University
Ruston, LA 71272

U.S.A.F. Researcher: Jorge Beraun

Date: December 29, 1989

Contract No.: F49620-88-C-0053

ABSTRACT

Development of an Experimental Program to Evaluate Laser Composite Material Damage Models

by

William M. Jordan, Ph.D., P.E.

This research project had two major tasks. The first task was to evaluate several different laser composite material damage models being developed by the Air Force. The second task was to develop an experimental program to evaluate the predictive capability of these models. One criticism of several of the models is that they are just empirical curve fits to data, able to predict what occurs only on previously tested systems.

The recommended experimental program had three major parts. The first part was recommendations for experiments to be done by the Weapons Laboratory itself. The second part was recommended experiments that could be performed by a university, but for which there was not enough time or budget to do so during this minigrant.

The third part dealt with the issue of whether local delamination around the laser damaged region plays a significant role. This is important for several laser damaged models have ignored local delamination. This was evaluated by performing delamination testing and notch strength testing on materials with different toughnesses. The experimental results indicate that local delamination does not play a major role in the global failure process. Therefore, the models that ignored local delamination made the correct choice. (It must be noted that they made this choice without having experimental evidence to back up the choice.)

Acknowledgements

The author wishes to acknowledge the financial support of the:

Air Force Office of Scientific Research
Bolling AFB, D.C.

The contract was administered by Universal Energy Systems, Inc. Their support is also gratefully acknowledged.

He also wishes to acknowledge the support given by the Air Force Weapons Lab, particularly, Mr. Jorge Beraun and Dr. Pat Vail.

The author wishes to thank the following students who aided in the development of the experimental program and in mechanical testing of the composites:

Hisham Hegab

David Henry

Tina Williams

Robbie Jordan

ME 484--Senior Laboratory class, fall 1989

Final Report
December 29, 1989

**DEVELOPMENT OF AN EXPERIMENTAL PROGRAM TO
EVALUATE LASER COMPOSITE MATERIAL DAMAGE MODELS**

by

William M. Jordan, Ph.D., P.E.
Mechanical and Industrial Engineering Department
Louisiana Tech University
Ruston, LA 71272

**I. INTRODUCTION: THE RELATIONSHIP OF THIS PROJECT TO THE
GOALS OF THE RESEARCH INITIATION PROGRAM**

The principal investigator had two major goals in this research program. The first goal was to continue the work begun during his time in the Summer Faculty Research Program. The second goal was to use this project to begin a federally sponsored research career. Both of these goals were accomplished. There was a set of research goals that dealt with the technical portion of the work and visibility goals that demonstrated the capability of the principal investigator.

Dr. Jordan has extensive research experience in this area. Dr. Jordan has shown that he can do excellent research. However, he has not had enough experience to be able to demonstrate this to many funding agencies. This program allowed him to demonstrate his capability to do research on his own. Coupled with the excellent background he obtained at Texas A & M University, this should allow him to become nationally competitive in the composite materials field.

To obtain federally sponsored research funding there are three basic criteria that must be met. The researcher must propose something of interest to the agency. The researcher and his institution must be qualified to do the research. The last criterion is that the researcher must be perceived to be qualified to do the research by the agency. This last criterion is often the hardest to accomplish for a young researcher cannot prove his capability until some agency first believes in him and gives him funding. One of the goals of the Research Initiation Program is to provide younger researchers with the opportunity to begin such a federally sponsored research career. The successful completion of this project should help the principal investigator to obtain other sponsored research.

II. OBJECTIVES OF THIS RESEARCH PROGRAM

Laser irradiation of composite materials is a concern to the Air Force for two related reasons. Composites are increasingly used as structural parts in aerospace vehicles and lasers can be used as effective weapons against composite materials. Various models of how laser irradiation damages composite materials have been proposed. Many of them have been largely empirical, able to predict what will occur in a specific system. Their capability to predict the interaction in different systems is less clear. This study began by evaluating some of the proposed laser damage models.

The overall research goals of this project were to design, build, and test experimental methods to evaluate the limits where the proposed models could be applied.

To meet these goals there were three main objectives. The first objective was to analyze the various models that

have been proposed to predict the laser/composite material interaction. A key aspect of this was to understand what assumptions were made in the development of each model. A distinction was made as to what parts of each model were empirical (a curve fit to the data) and what parts were based on fundamental parameters.

The second objective was to examine what sort of input data the models need to make their predictions. This led to some suggested new flat plate tests that could provide additional input data for the models. One of the problems with evaluating the present models is that not all of the required input data is known. Some of the material properties have to be assumed. This can lead to the temptation to assume values that will allow the model to predict the results that were experimentally determined.

The third objective was to design an experimental program that could yield the proper information so the accuracy of the above models can be examined. The different models do not make the same starting assumptions and they cannot all be reasonably accurate. For a model to be used confidently the researcher must know under which conditions it will function and under which conditions it will not function. The goal was for the models to be examined in enough detail to determine what experiments might be used to verify (or refute) their predictive capability. Included in this design phase was the building of required test fixtures. A few sample tests were run to verify this test methodology functions as designed. The minigrant budget was not large enough to support all of the experimental tests that should be run to evaluate all the models. It is anticipated that this experimental program could be continued in a future project to be funded by the Weapons Laboratory.

The visibility goals of this research program were to

show to the federal research community the capability of the principal investigator to conduct sponsored research. A significant goal of this Research Initiation Program is to allow new investigators the chance to show their capability. Outside of programs like this, this is very difficult to do because it is hard for new investigators to compete with more established workers. This project allowed him to demonstrate his capability in such a way that future sponsored research will be more easily obtained. For additional details, see the publication plans section of this report.

III. ANALYSIS OF VARIOUS MODELS FOR LASER INDUCED COMPOSITE FAILURE

Various modelling approaches to laser damage of composite materials have been tried. Among the approaches that have were analyzed are the three shown below:

- (1) An attempt to model the deformation and crack growth by using the viscoelastic properties of the composite material. This is the work being done by R.D.A. [1].
- (2) A modified two dimensional fracture mechanics approach that recognizes some of the damage is actually a three dimensional phenomenon. This is the work done by Southwest Research Institute [1].
- (3) A semi-empirical "hybrid model" that incorporates two key damage parameters Q_D and D_D . Q_D is a measure of the depth of thermal damage in the composite while D_D is a measure of the length of the damaged region. This is the model now being developed by Lockheed [1].

These three models described above were examined in more detail during this research project. They are the ones being developed (and refined) by contractors to the Air

Force.

(1) ANALYSIS OF LASER DAMAGE MODELS

One of the goals was to develop a model that could evaluate whether the failure assumptions of the Hybrid model and SWRI model are correct. They both assumed a version of the maximum stress theory. To aid this evaluation an attempt has been made to develop a finite element model for the failure of a biaxially loaded composite containing a hole. The original attempts were made using a personal computer based finite element software by the name of Algor. This software was not sophisticated enough. A more sophisticated main-frame computer based system was then tried. This was done using MSC/NASTRAN and the university's main frame computer. This has been more difficult than anticipated and results now are not conclusive. The complexity of the finite element analysis appears beyond the scope of what can be accomplished on this small project. The main effort on the remaining time of the project was concentrated on the mechanical testing methodology.

Layups were developed that should have the same unnotched strength but different toughnesses. When a center notched specimen is loaded, some delamination will occur near the hole. If center notched samples fail at the same loads then those models' assumptions (ignoring delamination) were reasonable. If they fail at different loads, then their ignoring of delamination failure may be a significant error.

Failure of these composites was also analyzed using a composite materials based software. This software uses traditional composite mechanics equations for its analysis (it is not a finite element based software) [2]. It is anticipated that this will yield similar answers to the finite element analysis. This is because the logical individual finite element would have the thickness of one

ply.

To aid in future work requiring significant computing power the department has enhanced its computer labs with seven SUN SPARC Engineering workstations with 12.5 MIPS processing speed. Three workstations are GX models with 19 inch color monitors, 2D/3D wireframe bit graphics accelerators, 16 Mbytes RAM, 2x104 Mbytes hard disks, and 3.5 inch floppy drives. The remaining four workstations are with 19 inch black and white monitors, 2x104 Mbytes hard disks, and 3.5 inch floppy drives. One of the four black and white workstations has 16 Mbytes of RAM while others are with 12 Mbytes. Software packages contained in this laboratory include FORTRAN, C, SUN COMMON LISP, SUN word processing package, and DOS WINDOW. Finite element analysis software will be bought in the near future. These workstations are faster than the university's main frame computer and would be used in future computing oriented projects.

(2) NEEDS OF ASSISTANCE FROM WEAPONS LABORATORY

After the analytical and experimental work have been suitably refined, these results need to be compared to the models of interest to the Weapons Lab.

To test experimentally these models, some specific data from those models is needed, so this current analysis can be compared with the previous work. An example of this would be some values of D_D and Q_D for the Hybrid Model. Included with this would be the stress that was applied to the pressure vessel wall at the time of the laser testing. For the viscoelastic model, values of their calculated viscoelastic components as well as the actual pressures are needed. For the S.W.R.I. model, some values of the depth at which local instability occurs are needed before it could be evaluated. Some of the data may be classified, but

a lot of the data the principal investigator evaluated in 1988 was only in the limited distribution category. However, it was not possible to obtain the necessary data to complete this portion of the project during calendar year 1989.

The principal investigator is very willing to continue this effort in a follow-on project from the Weapon's Laboratory. One possibility would be for the principal investigator to spend some time at the Weapon's Lab (perhaps during summer of 1990) and then finish the project at Louisiana Tech University.

With the approval of the Militarily Critical Technical Data agreement, non-classified (but still sensitive) material can be handled at Louisiana Tech University. In addition, the University has a location approved where even classified data can be stored. These two clearances will make it easier for us to handle securely any data that might be needed to evaluate the legitimacy of the various models.

IV. SUGGESTIONS FOR AN EXPERIMENTAL PROGRAM THAT COULD BE USED TO EVALUATE THE PREDICTIVE CAPABILITY OF THE MODELS

The goal of the analysis was to design an experimental program that will yield the proper information so the predictive capability of the models can be examined. The different models do not make the same starting assumptions and they cannot all predict the same answer. One of the problems with some of the current models is their empirical nature. For example, the "hybrid model" appears to work satisfactorily for the specific systems used in its development. While it can predict the results for the specific systems studied, the boundaries defining where it

will work (or won't work) are not clear.

In this study, emphasis was placed on the viscoelastic model, the Southwest Research Institute model and the Lockheed hybrid model since they are the subject of current research.

(1) OUTLINE OF EXPERIMENTAL PROGRAM THAT NEEDS TO BE
DESIGNED

This experimental program should include tests that would allow discrimination to be made among the various models. It would be most desirable to design tests where one model would predict one result and another model would predict a different result.

Included in the desired experimental program would be some materials characterization tests as well. These would provide the proper toughness values to be input into the various models. This portion of the study would involve the determination of a mixed mode failure envelope for the materials in question. This type of work is necessary if the models are to be properly evaluated. It is not solely being done for its own sake. The scope of this project was not large enough (in time or money) to allow for this to be done.

The following descriptions are the tests that the principal investigator recommends be done. Some of them could only be done at the Weapon's Lab itself. There was not enough time nor money in this project to perform all of the rest of the recommended experiments. Section V of this report will describe the experiments that were actually performed on this project. The principal investigator is very willing to perform the remainder of the recommended experimental program in future contracts with the Air Force.

(2) EXPERIMENTAL TESTS THAT COULD BE USED TO EVALUATE THE

VISCOELASTIC MODEL

This work was started after an apparent viscoelastic effect was noticed in the pressurization data of the ten inch bottle tests. There are some questions about the quality of the viscoelastic data that has been provided to them to use as a basis for their evaluation. More tests probably need to be made to provide them with better data for them to analyze. This will involve some bottle pressurization tests as well as flat plate tests.

Two problems occurred during the first tests on the 10 inch bottles which made data analysis more difficult. They should be corrected during this study. The first change should be that all tests should be run to the same final pressure. On the 10 inch bottle tests, the two different pressurization rates were done up to two different final pressures. This may introduce complicating factors that could be avoided during the next test series. The second change is that within each test, the pressurization rate should be maintained constant (it was not constant during the 10 inch pressurization tests). This will require some additional fixtures to be designed and built.

The types of suggested tests are shown below:

(1) Viscoelastic bottle tests can be performed in the following fashion. Several bottle pressurization tests can be run at different pressurization rates but with the same maximum pressure. One problem with doing tests like this is that each bottle may be slightly different in such crucial areas as percentage resin content. This would make it difficult to compare results of different pressurization rates on different bottles.

One way to deal with this problem would be to pressurize a bottle at one rate, depressurize it, and then repressurize it at another rate. This removes the problem of differences between bottles but may produce an additional

problem. It is possible that the first pressurization somehow damaged the composite, so the repressurization would be done with a damaged bottle that might behave differently. One way to deal with this would be to test two bottles. The first bottle should be pressurized at one rate, depressurized, and then repressurized at the same rate. Any differences between the two tests would be the result of the type of damage induced by the first pressurization. On a second bottle, pressurize it at one rate, depressurize it, and then repressurize it at a different rate. Using the data from the first bottle, the effect of any damage can be removed, leaving only the result of the viscoelastic behavior of the composite bottle. By having the two different rate tests done on one bottle, the effect of the different bottles can be lessened.

The above described bottle tests will be performed separately from this research effort.

(2) Viscoelastic tests performed on several of flat plate specimens to verify if there is a significant viscoelastic effect at the stress levels in question. The plates can be loaded up to the pressurization stresses at different rates and then held at those stress levels. The strain in the composite could then be monitored as a function of time.

(3) Tensile tests on unnotched specimens to determine the elastic constants of the material (may also be done using a 3 point test geometry). These tests should be performed both on samples that have been irradiated by the laser and on samples that have not.

(4) Tensile tests on samples with center cracks to determine the load at which crack growth begins. This should be done for several different sizes of initial cracks. The size of the plastic zone could be calculated from a knowledge gained of the tensile properties. These tests should be performed both on samples that have been

irradiated by the laser and on samples that have not.

During this program the tests described in item (2) were not performed. In addition, the tests described on irradiated samples described in items (3) and (4) were not performed.

(3) EXPERIMENTAL TESTS THAT COULD BE USED TO EVALUATE THE
SOUTHWEST RESEARCH INSTITUTE MODEL

This model uses fracture toughness and the maximum stress failure theory to try to predict when local failure of the composite will occur. They used a modified 2-D model that considers the three dimensional nature of the stress state near the crack. They used maximum stress failure theory to predict when each ply would break. Part of their input requirements include the fracture toughness of the composite. They admit that they ignored the issue of delamination.

The experiments described below will try to analyze whether delamination is significant or not in the structures in question. The experiments will also attempt to determine the mixed mode fracture toughness of the composite to use as an input into the model. The use of an experimentally derived fracture failure criteria can be used to better evaluate the predictions of this model.

The types of suggested tests are shown below:

(1) The legitimacy of using the maximum stress failure theory could be evaluated in the following fashion. Make up two sets of composites having the same layups (fiber orientations) and the same amount of fibers. Fabricate them in such a way that a different percentage of resin will result in the system. If maximum stress theory holds true then they should both have the same tensile strength when tested with a center crack. If they do not fail with the same stress value, then they probably have different amounts

of delamination occurring in the systems. This is because delamination toughness is usually very dependent upon the resin content, while tensile strength is relatively independent of resin content. Separate mode I and mode II delamination tests can be performed on these materials to verify that their delamination behavior is different.

An alternative method might be to cure two sets of composites differently such that one set has some small voids present. The presence of the voids would not change the tensile strength of a center cracked composite but would change the delamination toughness of the composite. This alternative method could also be used to evaluate the legitimacy of using the maximum stress theory in this specific structural system.

(2) Tensile tests on unnotched specimens to determine the elastic constants of the material (may also be done using a 3 point test geometry). These tests should be done both on samples that have been irradiated and on samples that have not.

For some composite systems, a change in percentage resin content will also change the strength of the composite by affecting the bonding between the fibers and the resin. By tensile testing both systems with unnotched samples, the effect of resin content (if any) can be separated from the effect of amount of delamination. This is because delamination would not be expected during a tensile test on an unnotched specimen.

(3) Mixed mode delamination tests to evaluate the shape of the "failure envelope" predicted from finite element model. These tests should be done both on samples that have been irradiated and on samples that have not. This will partially overlap with the delamination tests that will be done under (1) above. This is needed for these authors used fracture toughness as one of their input variables, but did

not define which fracture toughness was required. It would be tempting to use whatever fracture toughness that would fit the data that was already obtained. By determining a mixed mode fracture toughness, an independent value of the toughness could be used to test how well the model predicted the experimentally observed results.

(4) The extent of delamination during mechanical loading of the composite could be measured. This could be done with free edge delamination tests or on the center cracked tensile samples mentioned earlier. This might involve using a dye penetrant, followed by an ultrasonic analysis of the sample.

The experiments described in items (1) and (2) were done in this program. The experiments in item (3) could be done at Louisiana Tech University but there was not time to do so. The experiments in item (4) were not done, but it still may be possible to do them by examining the fractured samples from items (1) and (2).

(4) EXPERIMENTAL TESTS THAT COULD BE USED TO EVALUATE THE "HYBRID" MODEL

This is a semi-empirical model that seeks to determine the critical value of damage that is required for bursting of the pressurized of cylinder to occur. They have tried to predict when this occurs analytically. In their prediction of the critical damage parameter, D_D , they require as input the fracture toughness of the composite, K_C (or G_C), and the bulge correction factor, M_T . One problem with this model has been that K_C and M_T have not been known very precisely. They are either back-calculated from the burst tests or typical values are assumed. As long as these methods are used to determine the critical input parameters, this theory runs the risk of being considered only a curve fit to the data. The limits where this theory

may be applied appear to be the systems that have already been tested. The experiments described below are an attempt to provide an independent source for the fracture toughness so the true predictive capability of the model may be examined.

One of the areas of concern with this model is the uncertainty in the value of Q_D at low irradiance levels. At low irradiance levels, the amount of thermal damage near the spot size increases as the laser no longer has enough energy to remove material by ablation. Q_D now includes the thermal damage near the laser spot. To analyze the effect of this laser damage on mechanical properties, it is proposed to test flat plate samples that have been irradiated at these lower intensity levels. These results should be compared with results from those that have not been irradiated. The specific tests to be performed are shown in the list below.

This model assumed a typical value for the fracture toughness. It does not appear to deal with the mixed mode loading that occurs near the laser spot region. This means that some mixed mode fracture toughness failure envelope needs to be determined so the appropriate fracture toughness value can be used as input to the theory. This model also uses the maximum stress failure theory, and the experiments described under the discussion of the Southwest Research Institute model also apply here.

It is suggested flat plate tests be done on both Kevlar based composites as well as the graphite composites that will be used in the 20 inch tests. This will provide enough experimental data to evaluate whether this model did, in fact, predict the actual results obtained on the 10 inch bottle tests.

The types of suggested tests are shown below:

- (1) Tensile tests on unnotched specimens to determine the

elastic constants of the material. This may also be done using a 3 point test geometry.

(2) Tensile tests on samples with center cracks to determine the load at which crack growth begins. This should be done for several different size of initial cracks. The size of the plastic zone could be calculated from a knowledge gained of the tensile properties.

(3) Load up some small samples with center cracks and measure the size of the damaged zone in a scanning electron microscope.

(4) Mixed mode delamination tests to evaluate the shape of the "failure envelope" predicted from finite element model.

(5) The extent of delamination during mechanical loading of the composite could be measured. This could be done with free edge delamination tests or on the center cracked tensile samples mentioned earlier. This might involve using a dye penetrant, followed by an ultrasonic analysis of the sample.

(6) The legitimacy of this group using the maximum stress failure theory could be evaluated as described above in the discussion of the Southwest Research Institute model.

(7) Perform tests (2), (3), (4), and (5) above on both an irradiated specimen and on a specimen that has not been irradiated.

The experiments described in items (1), (2), and (6) have been completed. The experiments described in items (3), (4), and (5) have not been performed. The tests on laser irradiated samples described in item (7) have not been performed.

V. EXPERIMENTAL PROGRAM PERFORMED ON THIS PROJECT

This proceeded in two areas, design of a means to cure composite materials, and design of a means to mechanically test composite materials. A small press type autoclave (that can be used to produce flat plate panels) has been designed and built. This small press is then inserted into an existing furnace which will apply the required temperature cycle. This current press can be used to cure rectangular shaped composite panels with dimensions of about 9 inches by 12 inches. Successful panels were cured for the first time in late September. Drawings of the press type autoclave are attached to this report (see Figures 1-3).

Now that this methodology has been shown to be a success, a press that would produce larger panels could then be designed and built. This larger press would have the heating elements embedded in the press itself and would not require an additional furnace. Building of this larger press/autoclave could occur only after additional funding had been obtained.

The second area of experimental work lies in the design of test fixtures to mechanically test the composite materials. The most important equipment, an M.T.S. model 810 tensile test machine and a personal computer based Keithley data acquisition system are already on hand. The fixtures required for the fracture toughness tests have been built and were used during the later portion of this project.

One of the goals to this portion of the work is to evaluate experimentally whether the failure assumptions of the Hybrid model and SWRI model are correct. They both assumed a version of the maximum stress theory. Panels were cured that had the same fiber content and orientation

but different toughnesses. If the center notched samples fail at the same loads then those models' assumptions were reasonable. If they fail at different loads, then this ignoring of delamination failure may be a significant error.

The issue of whether delamination plays a role in the global failure (burst) condition is being evaluated in this way. Several quasi-isotropic panels have been cured using the same prepreg material and the same layup. They were cured with different temperature, pressure and vacuum cycles so they have different toughnesses. Since the strength of the composite is mostly dependent upon the fibers, the strength of the different panels would be expected to be the same. If delamination plays a significant role, then the notched strengths would be expected to be different. If delamination does not play a significant role, then the notched strengths would be expected to be very similar.

When the principal investigator was at the Weapons Lab in 1988, it was indicated that some actual applications used angle ply layups (same number of plus and minus angles) rather than quasi-isotropic layups (which have equal numbers of +-45 degrees, 0 degrees and 90 degrees). Therefore, several angle ply panels have been cured in such a way as to provide different toughnesses. They were tested in December as a further evaluation of the effect of delamination upon failure of composite structures that contain circular holes.

OTHER EXPERIMENTAL WORK RELATED TO THIS PROJECT

A paper very relevant to this work has recently appeared in the *Journal of Materials Science* [3]. Its title is "Notch sensitivity of thermoset and thermoplastic laminates loaded in tension." In this paper the authors compared the notch sensitivity of two graphite fiber based composite materials, one of them a thermoset (Hercules' 3501-6) and the other a thermoplastic (ICI's APC-2 [PEEK]).

Quasi-isotropic layups of these materials exhibited similar notch sensitivity, but when angle ply layups (± 45 degree) were examined, the more ductile PEEK material exhibited greater notch sensitivity. The bottle layups I was told about when I was at the Weapons Lab are typically of this angle ply type.

Their results show that the toughness of the material may play a role in the failure of specimens with holes in them. This is the type of tests performed on this project, analyzing the effect of toughness on notched strength for several layups that should have the same unnotched strengths. If toughness does play a role in failure of the material, then the amount of delamination would be different for different toughness materials. This would indicate that it would be unwise to ignore the issue of delamination, as is done by some of the laser damage models being proposed.

The analytical approach used in the above paper was followed in the experimental portion of this project.

EXPERIMENTAL TEST PROGRAM

Tensile tests on both notched and unnotched specimens were performed on the following layups of Hexcel's T6T145/F155 graphite/epoxy system:

[-45(2)/0(2)/45(2)/90(4)/45(2)/0(2)/-45(2)]

[-45(4)/45(8)/-45(4)]

Both of the above layups are balanced and symmetric so there is no coupling between bending and stretching. The first layup is a quasi-isotropic one, which means that it has isotropic mechanical properties. The second layup is an angle-ply one, which is like the layups used in the actual applications of concern to this project.

The notched and unnotched tensile tests were performed on the department's Detroit Tensile Test machine. The tensile test procedure and calculation methodology is shown

in references [3] and [4]. To evaluate the effect of differing delamination toughnesses, two panels of each layup were made. One of the panels was cured according to the manufacturer's suggested temperature and pressure cycle. The second panel of each layup was cured according to the manufacturer's recommended temperature cycle, but without any external pressure being applied. This resulted in the presence of voids in the system. As discussed elsewhere, this would be expected to change the toughness of the composite material [5, 6, 7].

Double-cantilevered mode I toughness tests were performed on a model 810 M.T.S. tensile test machine. The test fixtures were designed and built at Louisiana Tech University. A Keithley digital data acquisition system was used to record the load-displacement data. The method used to calculate the toughness is shown in reference [8].

Three-point bend tests were performed to measure the modulus of the composite. Mode II tests were also performed using a three point bend test geometry (only now the sample has a pre-existing crack within it). The method used to calculate the toughness is shown in reference [8].

VI. EXPERIMENTAL RESULTS AND DISCUSSION

Modulus and toughness test results are shown in Table I. As expected, the panel that was cured under pressure had a higher modulus. Curing without pressure induced some voids into the composite at the ply interfaces. These voids acted as filler material (with a zero modulus) to lower the overall modulus of the composite. This change in the composite changed the toughness of the composite (as also shown in Table I).

When voids were introduced into a brittle composite

material, they acted as crack arrestors (increasing the radius of curvature at the crack tip). This resulted in an increase in toughness of the composite [5,6]. With this more ductile material the presence of voids at the interface acted to decrease the toughness of the composite. This appears related to the interfacial strength of the composite being lowered by the presence of the voids. This made crack growth easier, thus lowering the toughness of the composite.

The different curing cycles (with or without pressure) did have the desired effect of changing the toughness of the composite. This allowed the effect of toughness on notch strength to be examined, which is one of the main experimental goals of this project.

Table II shows the notched strength for quasi-isotropic layups of Hexcel's T6T145/F155 graphite/epoxy material. The presence of the voids (in the no pressure cure panel) decreased both the unnotched and notched strength of the composite material. It was noted that the failure process around the notch began by delamination in the notch vicinity before the entire sample finally failed.

The most important result in Table II is the column at the far right of the table. The lower toughness material had a ratio of its unnotched strength to that of the higher toughness material of .713. However, the ratio of its notched strength material to that of the higher toughness material varied from .778 to .845. This means that the unnotched strength was more sensitive to variations in delamination toughness than was the notched strength.

Table III shows the notched strength for angle ply layups of Hexcel's T6T145/F155 graphite/epoxy material. The presence of the voids (in the no pressure cure panel) decreased both the unnotched and notched strength of the composite material. It was noted that the failure process around the notch began by delamination in the notch vicinity

before the entire sample finally failed.

The most important result in Table III is the column at the far right of the table. The lower toughness material had a ratio of its unnotched strength to that of the higher toughness material of .545. However, the ratio of its notched strength material to that of the higher toughness material varied from .640 to .656. This means that the unnotched strength was more sensitive to variations in delamination toughness than was the notched strength.

This means, that for the angle ply layups shown in Table III, the effect of delamination around the hole was not as significant as the effect of toughness variations in the entire specimen.

In summary, the effect of delamination around the hole that occurred as a result of differences in material toughness does not appear to be significant. The differences in the basic toughness of the composite material is significant, but variation in delamination that occurs near the hole does not appear to be significant. This means that the choice to ignore delamination near the laser damaged spot will not significantly affect the accuracy of the model. This choice, which was made by both the SWRI model and the hybrid model, appears to be the correct one. The principal investigator remains convinced that the choice to ignore delamination effects, while correct, was made prematurely when there was not yet experimental evidence to back up that choice.

VII. PUBLICATION PLANS

It is Dr.Jordan's desire to publish relevant portions of this work in the open literature. This will require some delicacy, recognizing the sensitive nature of some of the

related Weapons Laboratory work.

The issue of whether delamination plays a role in the global failure (burst) condition can be evaluated by fabricating several panels that have different toughnesses but about the same strength. Since the strength of the composite is mostly dependent upon the fibers, the strength of the different panels would be expected to be the same.

The next step would be performing notched strength tests on the composites (tensile tests on flat plates that have holes in them). Some delamination will be initiated around the edges of the hole. The amount of delamination would be different for each panel because of their different toughnesses. If delamination plays a significant role, then the notched strengths would be expected to be different. A tentative title for this paper is **The Effect of Toughness on the Notched Strength of Graphite/Epoxy Composite Materials**. This paper would be relevant to the work of the Weapons Lab, but it would not compromise any of the laser damage models because they would not be directly mentioned in the text.

VIII. OTHER RELATED WORK BY WILLIAM JORDAN

To increase his knowledge on additional aspects of composite material design and failure analysis, Dr. Jordan attended a short class on Metal Matrix Composites, sponsored by ASM International, in early August. This class involved the use of Militarily Critical Technical Data. The appropriate clearances for the use of this were obtained.

In September 1989 Dr. Jordan presented a paper at the Fifth Annual Advanced Composites Conference-Exposition sponsored by the Engineering Society of Detroit and ASM International. The title of the presentation was "Using Variations in Stacking Sequence To Improve Delamination

Toughness" [9]. He published a paper that overlaps with the present work in the September 1989 issue of the Journal of Composite Materials [10]. Its title was "Relating Resin Mechanical Properties to Composite Delamination Fracture Toughness."

In December 1989, Dr. Jordan travelled to Tbilisi, Georgia, U.S.S.R., to present several seminars at the invitation of the Academy of Sciences of the U.S.S.R. The papers are shown as references [11, 12, 13]. This trip also allowed him to observe engineering education and university based research in the Soviet Union.

IX. RECOMMENDATIONS

This work answered one of the basic questions, namely, was it legitimate to ignore the effects of delamination near the laser damage region in calculating predictions of failure. However, there are several other experimental suggestions made in section IV that ought to be followed up. (All the principal investigator's questions about the legitimacy of some of the models have not been answered.)

The first recommendation the principal investigator will follow up on out of his own interest in the issue. This recommendation involves running a few more mechanical tests (such as mode I tests on quasi-isotropic layups and mode II tests on the angle ply layups) so some of the (partially) loose ends can be tied together. Then the principal investigator will submit a manuscript for publication, as described in the publication plans section.

The remaining recommendations are mostly for continuing to perform the experiments suggested in section IV. Among these are the following:

To evaluate the viscoelastic model

- (1) Viscoelastic tests on flat plate specimens.
- (2) Notched tensile tests on irradiated specimens.
- (3) Tensile tests on irradiated specimens.

To evaluate the Southwest Research Institute model

- (1) Mixed mode delamination tests to evaluate the mixed mode failure envelope.
- (2) Measure the extent of delamination near the vicinity of the notch during notched tensile tests.

To evaluate the "Hybrid" model

- (1) Measure size of damage zone near the notch by using a scanning electron microscope.
- (2) Mixed mode delamination tests to evaluate the mixed mode failure envelope.
- (3) Perform the above tests, as well as notched tensile tests on samples that have been irradiated.

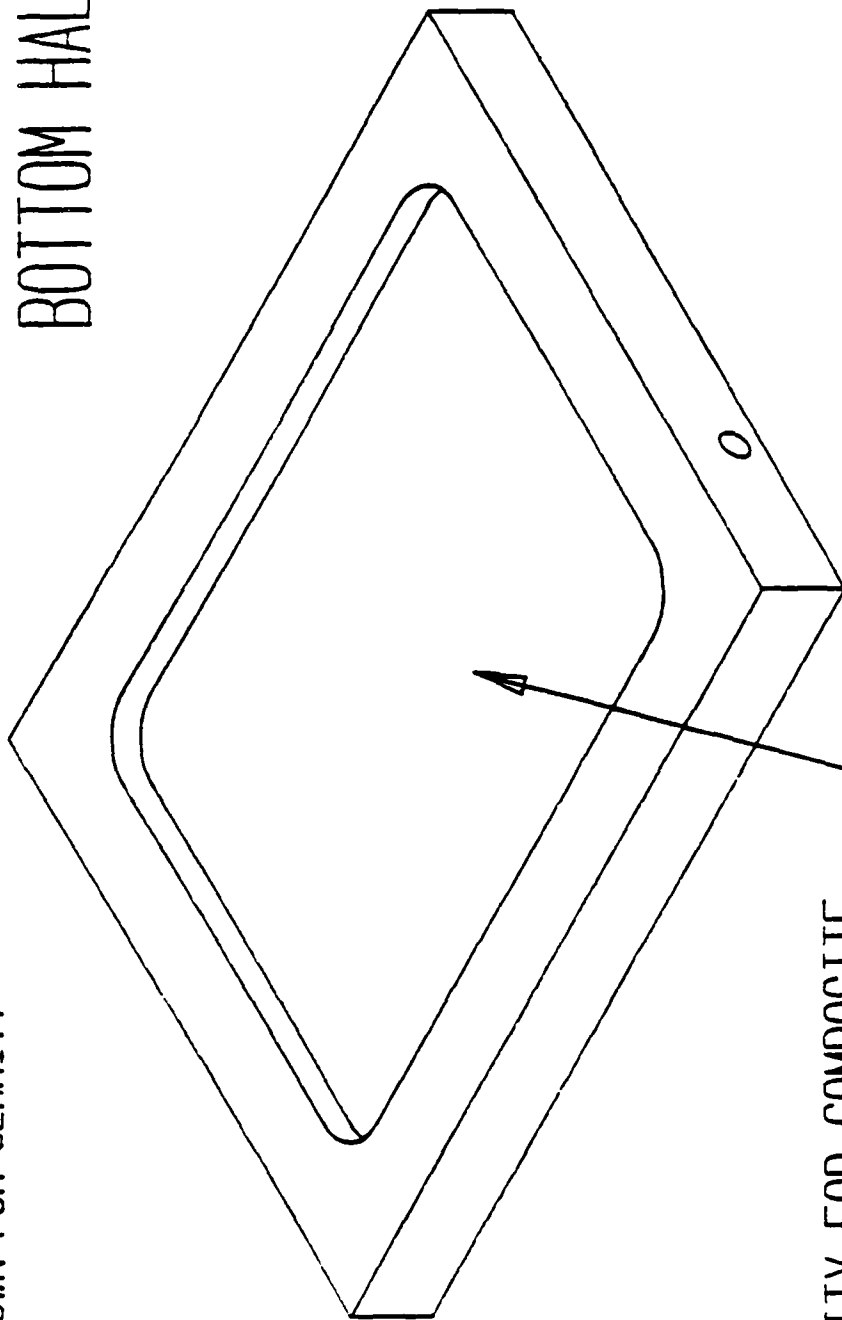
To perform these tests will require some help from the Weapon's Lab in two areas:

- (1) Obtaining of the relevant composite materials to test.
- (2) Irradiating some samples so further mechanical tests might be performed on them.

The principal investigator is interested in pursuing some (or all) of the above recommendations in a separate research program with the Weapon's Laboratory.

BOLT HOLES NOT
SHOWN FOR CLARITY

BOTTOM HALF



CAVITY FOR COMPOSITE

ALUMINUM AUTOCLAVE

DR. WILLIAM JORDAN

SIZE	FIG. NO.	REV.

SCALE	SHEET
4" = 1"	1 OF 3

HOLE FOR CONNECTING BOLTS

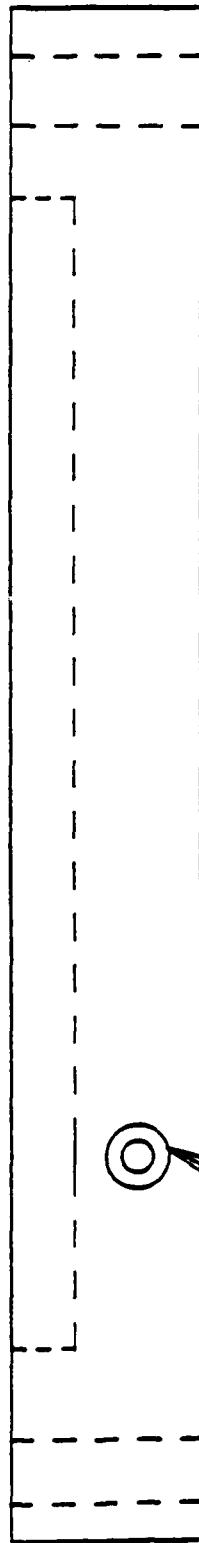
PRESSURE PORT

TOP PIECE



VACUUM PORT

BOTTOM PIECE



RIGHT-SIDE
VIEW

ALUMINUM AUTOCLAVE

DR. WILLIAM JORDAN

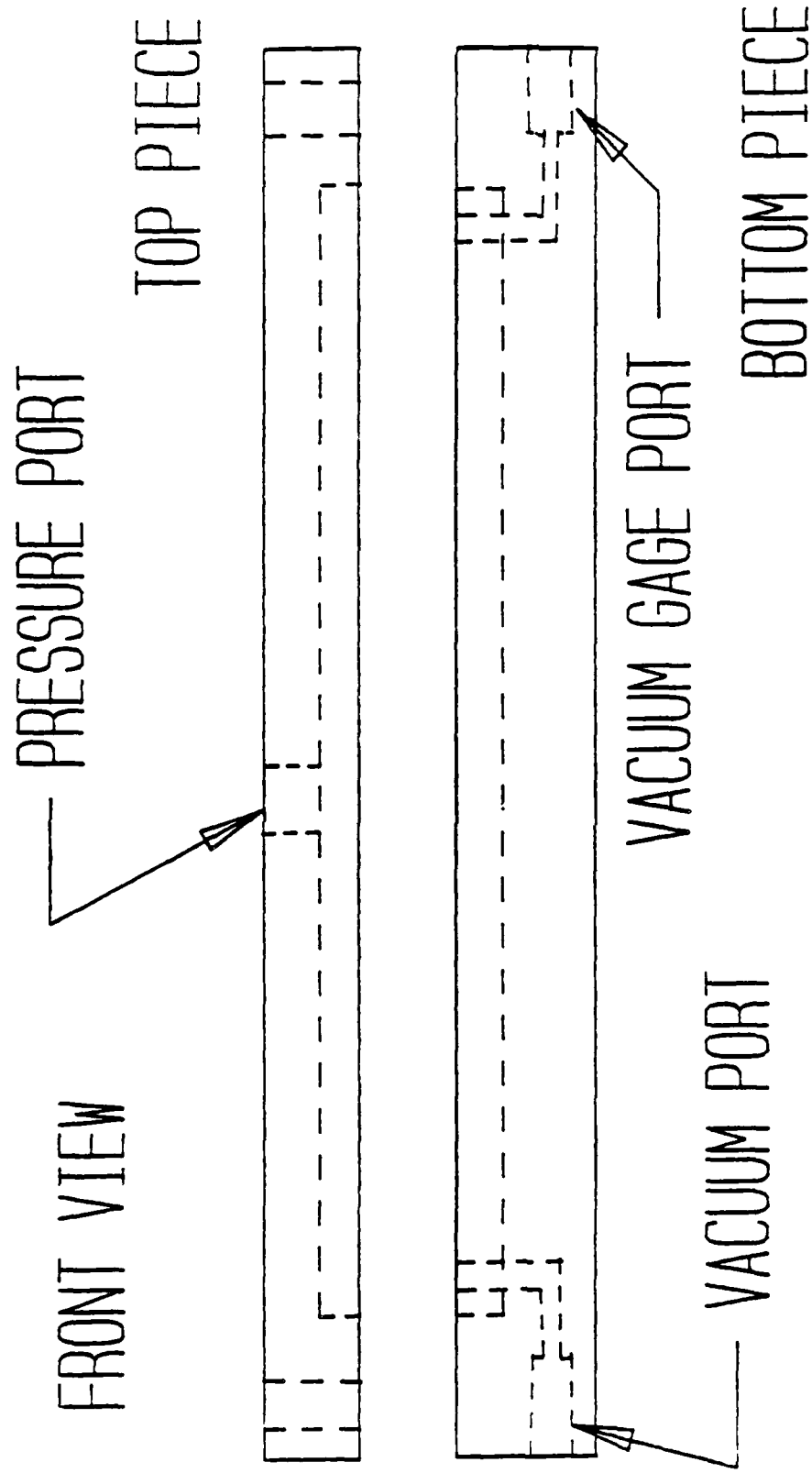
SIZE PSCH NO.

DRG NO.

REV

SCALE .75"=1"

SHEET 2 OF 3



BOLT HOLES WERE
OMITTED IN BOTTOM
PIECE FOR CLARITY.

ALUMINUM AUTOCLAVE			
DR. WILLIAM JORDAN			
SIZE	FSCH NO.	DOB NO.	REV
SCALE .6"=1"	SHEET 3 OF 3		

TABLE I

Modulus and Toughness of Hexcel T6T145/F155
Graphite Epoxy Composite

[-45(2)/0(2)/45(2)/90(4)/45(2)/0(2)/-45(2)]

Pressure During Cure	Theoretical Modulus (10 ⁶ psi)	Mode II Toughness (J/m ²)
Yes	5.71	4540
No	5.71	2520

[-45(4)/45(8)/-45(4)]

Pressure During Cure	Theoretical Modulus (10 ⁶ psi)	Experimental Modulus (10 ⁶ psi)	Mode I Toughness (J/m ²)
Yes	.881	.884	679
No	.881	.824	561

TABLE II

Notch Strength of Hexcel T6T145/F155
Graphite Epoxy Composite

[-45(2)/0(2)/45(2)/90(4)/45(2)/0(2)/-45(2)]

Pressure During Cure	Hole Diameter (in)	Failure Stress (psi)	Ratio of notched to unnotched	Ratio of Unpressure Cure Results to Pressure Cure Results
Yes	None	52,000		
Yes	.25	33,100	.637	
Yes	.375	36,100	.694	
No	None	37,100		.713
No	.25	28,300	.763	.845
No	.375	28,100	.757	.778

TABLE III

Notch Strength of Hexcel T6T145/F155
Graphite Epoxy Composite

[-45(4)/45(8)/-45(4)]

Pressure During Cure	Hole Diameter (in)	Failure Stress (psi)	Ratio of notched to unnotched	Ratio of Unpressure Cure Results to Pressure Cure Results
Yes	None	20,000		
Yes	.25	15,700	.785	
Yes	.375	16,100	.805	
No	None	10,900		.545
No	.25	10,300	.945	.656
No	.375	10,300	.945	.640

REFERENCES

1. These models were described in distribution limited reports and are, as such, not listed in this open report. For details on these models, the reader should contact:
Mr. Jorge Beraun
WL/TALE
Kirtland Air Force Base, New Mexico 87117
2. CEMCAL: Composite Experimental Mechanics Calculations User's Manual, University of Delaware, Technomic Publishing Co., Lancaster, PA, 1987, 41 pages.
3. Carlsson, Leif, Aronsson, Carl-Gustaf, and Backlund, Jan, "Notch sensitivity of thermoset and thermoplastic laminates loaded in tension", *Journal of Materials Science* (Vol. 24, pp. 1670-1682).
4. Carlsson, Leif, and Pipes, R. Byron, *Experimental Characterization of Advanced Composite Materials*, Prentice-Hall, Inc., Englewood Cliffs, New Jersey, 1987, 197 pages.
5. Jordan, William, "The Toughness of Damaged or Imperfect Laminates", in *Proceedings of the American Society for Composites, Third Technical Conference*, Technomic Publishing Co., Lancaster, PA, 1988, pp. 495-504.
6. Harper, B.D., Staab, G.H., and Chen, R.S., "A Note on the Effects of Voids Upon the Hygral and Mechanical Properties of AS4/3502", *Journal of Composite Materials*, Vol. 21, March 1987, pp. 280-289.
7. Tang, J., Lee, W.I., and Springer, G.S., "Effects of Cure Pressure on Resin Flow, Voids, and Mechanical Properties", *Journal of Composite Materials*, Vol. 21, May 1987, pp. 421-440.

8. Jordan, W.M., and Bradley, W.L., "Micromechanisms of Fracture in Toughened Graphite-Epoxy Laminates", in *Toughened Composites*, ASTM STP 937, Norman Johnston, Ed., American Society for Testing and Materials, Philadelphia, PA, 1987, pp. 950-114.
9. Jordan, W.M., "Using Variations in Stacking Sequence to Improve Delamination Toughness", presented at the Fifth Advanced Composites Conference/Exposition in Dearborn, Michigan, September 25-28, 1989. In *Design and Manufacturing of Advanced Composites*, ASM International, Metals Park, Ohio, 1989, pp. 1-10.
10. Jordan, W.M., and Bradley, W.L., "Relating Resin Mechanical Properties to Composite Delamination Fracture Toughness", *Journal of Composite Materials*, Vol. 23, No. 9, September 1989, pp. 923-943.
11. Jordan, W.M., "Engineering Ethics", presented to the Institute of Metallurgy of the Academy of Sciences of the Georgian S.S.R. (on December 4, 1989) and to the Georgian Lenin Polytechnic Institute (on December 5, 1989), both in Tbilisi, Georgia, U.S.S.R.
12. Jordan, W.M., "Origins of Modern Science", presented to the Institute of Metallurgy of the Academy of Sciences of the Georgian S.S.R. (on December 6, 1989), Tbilisi, Georgia, U.S.S.R.
13. Jordan, W.M., "Fracture of Composite Materials", presented to the Institute of Metallurgy of the Academy of Sciences of the Georgian S.S.R. (on December 7, 1989), Tbilisi, Georgia, U.S.S.R.

FINAL REPORT NUMBER 66
REPORT NOT AVAILABLE AT THIS TIME
Dr. Arkady Kheyfets
210-9MG-114

FINAL REPORT NUMBER 67
REPORT NOT AVAILABLE AT THIS TIME
Dr. Barry McConnell
760-7MG-047

FINAL REPORT

SLOW TO FAST WAVE TRANSITION ANALYSIS

by

W. Perry Wheless, Jr.

Electrical Engineering Department

College of Engineering

The University of Alabama

Prepared for

Universal Energy Systems, Inc.

Dayton, Ohio

Contract No. F49620-85-C-0013/SB5851-0360

UES Project 760

Purchase Order S-760-7MG-068

May 1989

BER Report No. 462-62

ABSTRACT

Techniques for the analysis of electromagnetic slow to fast wave transition structures have been investigated by The University of Alabama for the Air Force Office of Scientific Research (AFOSR) through Project S-760-7MG-068 of Universal Energy Systems, Inc., acting on behalf of AFOSR. This study emphasizes computer-assisted and lumped-element equivalent circuit aids for the analysis of coaxial slow wave structures with corrugated outer conductors, and excludes synthesis techniques. This report includes an algorithm for determination of phase velocity in planar magnetrons which is also applicable to many coaxial devices, a method of moments (MOM) analysis technique for coaxial transitions (with corrugated outer conductors), and discussion of research into broadband lumped-element equivalent circuit models.

TABLE OF CONTENTS
FINAL REPORT

SLOW TO FAST WAVE TRANSITION ANALYSIS

ABSTRACT

TABLE OF CONTENTS

LIST OF FIGURES

LIST OF TABLES

- 1 A classical view re-visited
 - 1.1 Introduction
 - 1.2 Theory
 - 1.3 Numerical solution
 - 1.4 Application to cylindrical structures
- 2 First-order analysis
 - 2.1 Basis
 - 2.2 Estimation of planar discontinuity
 susceptances
 - 2.3 An application example
 - 2.4 Limitations of the formulation
- 3 Extended MOM numerical analysis
 - 3.1 Basis
 - 3.2 Program for multiple apertures
 - 3.3 Application example
 - 3.4 Limitations of the MOM analysis
- 4 Lumped-element equivalent circuits
 - 4.1 General discussion
 - 4.2 Procedure
 - 4.3 Illustrative example

Summary and Conclusions

Acknowledgement

References

LIST OF FIGURES

- Fig. 1.1 Planar magnetron geometry
- 1.2 Solution dependence on maximum function evaluations
- 1.3 Solution dependence on number of series terms
- 1.4 Solution dependence on b-to-L ratio
- 2.1 Step discontinuity in the outer conductor of a coaxial waveguide
- 3.1 Slow to fast wave transition for analysis by program NSLOTS.FOR
- 3.2 Session listing for NSLOTS execution
- 4.1 Generic slow wave unit cell
- 4.2 Lumped-element equivalent circuits
- 4.3 TAME data files
- 4.4 Input reflection coefficient, initial analysis
- 4.5 Forward transmission coefficient, initial analysis
- 4.6 Input reflection coefficient, final analysis
- 4.7 Forward transmission coefficient, final analysis

Appendices

- A. Listing of MULLER.FOR
- B. Listing of GMULLER.FOR
- C. Listing of CELL6.FOR
- D. Listing of CELL8.FOR
- E. Listing of STPOUT.FOR
- F. Listing of COAXRT.FOR
- G. Listing of GELG.FOR
- H. Listing of NSLOTS.FOR
- I. Listing of CDMLR.FOR
- J. Listing of OUTSTP.FOR

LIST OF TABLES

- 3.1 Analysis of slow to fast wave transition
by program NSLOTS
- 4.1 Sample equivalent circuit phase velocity
results

CHAPTER 1

A CLASSICAL VIEW RE-VISITED

1.1 Introduction

Coaxial slow wave structures with comparable outer and inner conductor radii may be analyzed successfully via approximation by a planar magnetron geometry. A schematic representation of the planar magnetron family under discussion is given in Figure 1.1. The fundamental governing equations are known [1], with more advanced electron beam considerations available in references such as [2].

Rectangular (square wave profile) corrugations such as those depicted in the upper conductor of Figure 1.1, cause the phase velocity v_p of +z-propagating electromagnetic waves to be less than the speed of light, c . An electron beam space charge wave interacts with the slow wave structure when their respective velocities are matched, so that energy is extracted from the electron beam and deposited into the high frequency electromagnetic fields.

As an analysis exercise, this report assumes that a desired phase velocity v_p ($v_p < c$) is already known from separate ballistic or hydrodynamical treatment of the electron beam dynamics, and the objective here is a computer-based analysis aid for use in determination of the slow wave structure dimensions to realize the requisite v_p .

An analytical model is next described and, afterward, a numerical algorithm is detailed which can analyze the slow

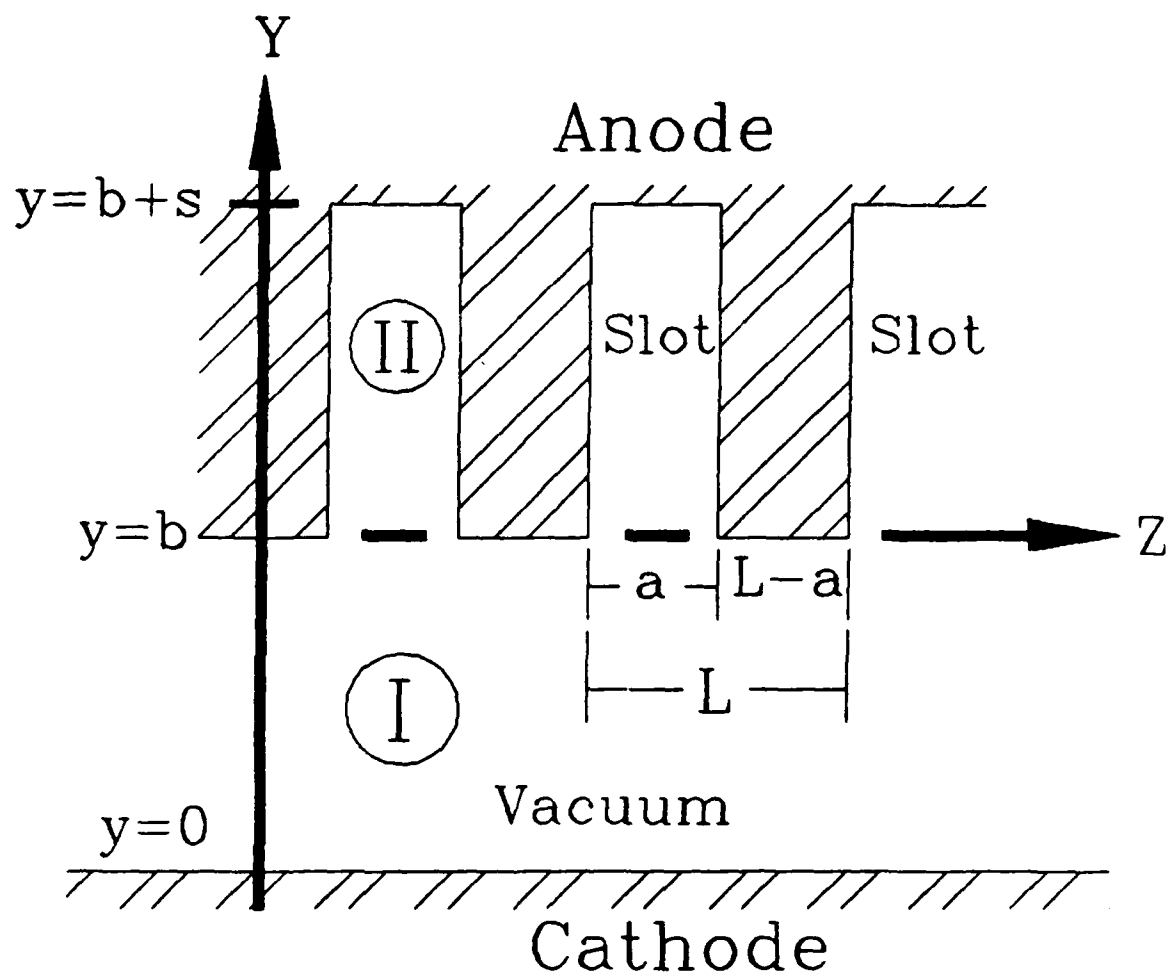


Figure 1.1. Planar magnetron geometry.

wave propagation in this class of electromagnetic structures.

1.2 Theory

The specific case under consideration is that of a parallel-plane transmission line with corrugations, or periodic slots, in one plate as illustrated in Figure 1.1. The corrugation parameters are cell length L , slot depth s , and slot width a . The upper surface of the cathode is taken to reside at $y = 0$ with machined slots in the anode extending from mouths in the plane at $y = b$ to metallic backs at $y = b + s$. Dimension b is referred to as the gap between cathode and anode.

The problem is formulated as invariant with respect to coordinate x (edge effects due to finite extent in x are ignored). Region I refers to the gap region below the corrugated anode in Figure 1.1, while Region II is in the slots.

A large z -directed electric field is necessary for magnetron operation, and the correct field construction is, indeed, transverse magnetic (TM) allowing for propagation in the z direction and evanescence in y . The electromagnetic boundary conditions can be satisfied for variable slot and metal tooth widths, as well as variable slot depth, through the use of series expansions for the field components (the terms of which are called space harmonics). One finds three non-zero field components in Region I, which may be written [3]:

$$H_x^I = -\frac{1}{\eta} \sum_{n=-\infty}^{n=+\infty} A_n \frac{k}{\kappa_{cn}} \cosh(\kappa_{cn} y) e^{j(\omega t - \beta_n z)} \quad (1.1)$$

$$E_z^I = \sum_{n=-\infty}^{n=+\infty} A_n \sinh(\kappa_{cn} y) e^{j(\omega t - \beta_n z)} \quad (1.2)$$

and

$$E_y^I = j \sum_{n=-\infty}^{n=+\infty} A_n \frac{\beta_n}{\kappa_{cn}} \cosh(\kappa_{cn} y) e^{j(\omega t - \beta_n z)} \quad (1.3)$$

with (1.2) and (1.3) following the construction of (1.1) by direct application of Maxwell's equations, where A_n is the amplitude of mode TM_{0n} ,

$$\kappa_{cn}^2 = \beta_n^2 - k^2, \quad (1.4)$$

and

$$\beta_n = \frac{\omega}{v_{pn}} = \beta_0 + \frac{2\pi n}{L}. \quad (1.5)$$

β_0 is the axial wavenumber for the fundamental component, which is normally selected for excitation by space-charge wave interaction. k is the customary wavenumber,

$$k = \omega \sqrt{\mu_0 \epsilon_0} = \frac{\omega}{c}. \quad (1.6)$$

The axial wavenumber relation, (1.5), is in accord with Floquet's theorem [4]. Floquet's theorem allows solution for the entire periodic structure through consideration of a

single slot.

The fields in the slots (Region II) are assumed to be TEM mode. An electromagnetic boundary condition is that $E_z^{II}(y = b + s) = 0$, as the slots are backed with metal, and a standing wave results in the slot region. The z-component of TEM electric field in the slots hence varies as $\sin(s + b - y)$, so that E_z^{II} has value zero at $y = b + s$. The Region II field components may be expressed as [3]:

$$E_z^{II} = A_{z,b}^{II} \frac{\sin k(s + b - y)}{\sin(ks)} e^{j(\omega t - m\phi)} \quad (1.7)$$

$$E_y^{II} = 0 \quad (1.8)$$

and

$$H_x^{II} = -j \frac{A_{z,b}^{II}}{\eta} \frac{\cos k(s + b - y)}{\sin(ks)} e^{j(\omega t - m\phi)}, \quad (1.9)$$

with the phase angle $m\phi$ of the wave in slot m arbitrary at this point.

Continuity of the field components must be appropriately enforced in the slot mouths at $y = b$, where Region I interfaces with Region II. The following relation results:

$$\frac{1}{\frac{\epsilon}{c} \tan \left[\frac{\omega}{c} s \right]} = \frac{a}{L} \sum_{n=-\infty}^{+\infty} \left[\frac{\sin \left[\beta_n a/2 \right]}{\left[\beta_n a/2 \right]} \right]^2 \frac{L}{(\beta_n L) \tanh[\beta_n b]} \quad (1.10)$$

which compares favorably with equation (7-125) of reference [3]. It is important to note that (1.10) results from matching fields at $y = b$ under the assumption that the phase velocity v_p is small in comparison to c (only a slow wave solution is sought), which allows the approximation $\beta_n^2 \approx \kappa_{cn}^2$ to be applied. Thus, it should be anticipated that the solutions to (1.10) will become irrelevant if v_p is allowed to approach c . Equation (1.10) is generally referred to as the "dispersion relation" for the slow wave structure.

1.3. Numerical Solution

Dispersion relation (1.10) is solved with the aid of a personal computer. A zero-finding routine, preferably fast as well as reliable, is essential. There are numerous excellent routines in commercially available mathematical software libraries. The source code for such library routines, however, is proprietary and unavailable to the user. It is desirable here to have the source code for the chosen algorithm accessible for study and possible modification.

Müller's method, with FORTRAN source code as given by [5], is utilized in this particular study. The Conte and de Boor coding of the algorithm is efficient and dependable. The source code listing for the basic program may be seen in Appendix A. A modified version, listed in Appendix B, has been developed to allow a "scan" analysis over a user-input range of slot depths. The data output from the Appendix B

program is to a file named GMULLER.M, which may be directly used by PC-MATLAB to graphically depict the output data.

One input parameter to the Müller routine is the maximum number of function evaluations allowed per zero (MAXIT). The matter of an acceptable lower limit for this parameter has been investigated, and the results depicted in Figure 1.2 are representative. Figure 1.2 data is for the frequency 2.0 GHz, with cell width 2.5 cm, gap 3.125 cm, and slot width 1.25 cm. Slot depth is allowed to vary so that the ks product ranges from 0.01 to 1.3. The horizontal axis is the $\beta_0 L$ solution to (1.10).

A MAXIT selection of sixty or greater has been found satisfactory for the function of (1.10). In Figure 1.2, the results for MAXIT = 60, 80, and 100 are indistinguishable.

The infinite summation in the dispersion relation (1.10) elicits concern for the effect of higher order terms on the solution. For practical frequencies and physical dimensions, it turns out that only a few terms are required. The results from an example case regarding the influence of higher order terms may be seen in Figure 1.3, where the system parameters are the same as for Figure 1.2. As before, ks is varied from 0.01 to 1.3. The fundamental term ($n = 0$) alone is not sufficient. Including three terms ($n = 1$) in the evaluation is definitely better, but remains inadequate for a reliable solution, as the dotted $n = 1$ locus becomes distinct at higher ks values. The solutions for $n = 2$ (five terms) and $n > 2$ are essentially identical. The lower (solid

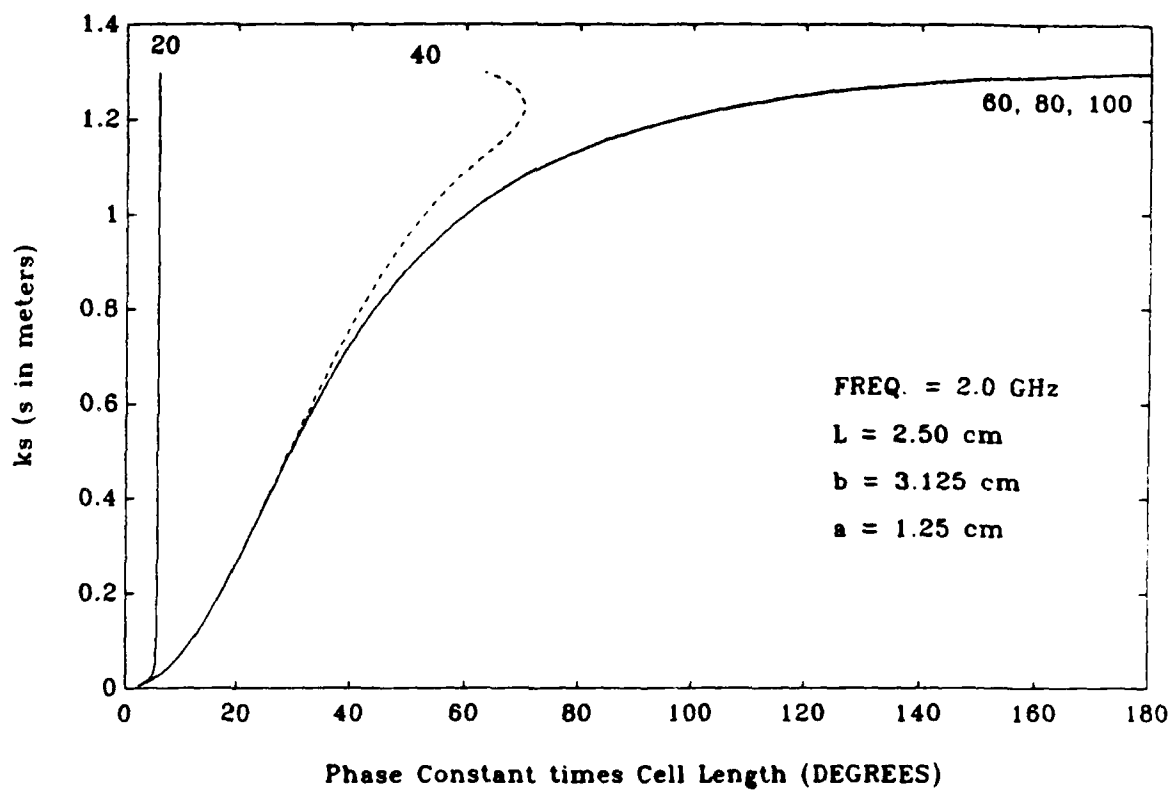


Figure 1.2. Solution dependence on maximum function evaluations.

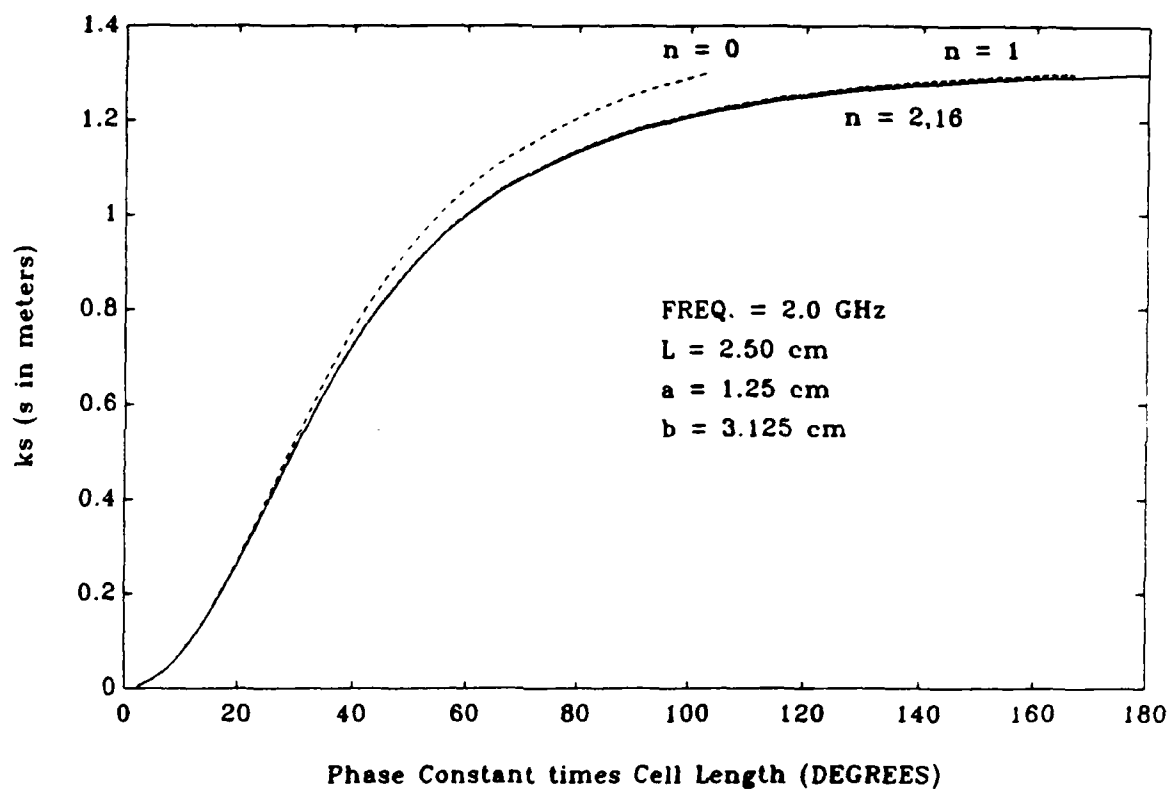


Figure 1.3. Solution dependence on number of series terms.

line) plot in Figure 1.3 is actually two solution cases, $n = 2$ and $n = 16$. Generally, it has been found that $n = 4$ is a conservative selection, with higher terms inconsequential.

The ratio of gap to cell width (b/L) resides between 0.5 and 4 in most practical designs. Figure 1.4 shows the effect on $\beta_0 L$ for three common b -to- L ratios. Each curve plotted in Figure 1.4 is based on one hundred equally spaced (in ks) data points, which is also the case for Figures 1.2 and 1.3.

Numerous specific solutions from the numerical procedure have been compared against the nomograph Figure 7-20 of [3], and found to be consistent in all cases. For example, [3] gives $\beta_0 L \approx 80^\circ$ for frequency 5.0 GHz, $ks = 1.35$, $s/L = 4$, $b/L = 0.5$ and $a/L = 0.5$. The solution by computer is 79.0° .

Dispersion curves for structures of this type also appear in Figure 18.18 of [6]. For example: frequency = 6.0 GHz, $ks = 94.29$, $\lambda_0/L = 100$, $s/L = 15$, $b/L = 0.3$, and $a/L = 0.5$ gives a $\beta_0 L$ solution of 21.8° by computer. From [6], $c/v_p \approx 6$ so that the expected phase constant times cell width product increases from 3.6° for velocity c to 21.6° for the indicated v_p .

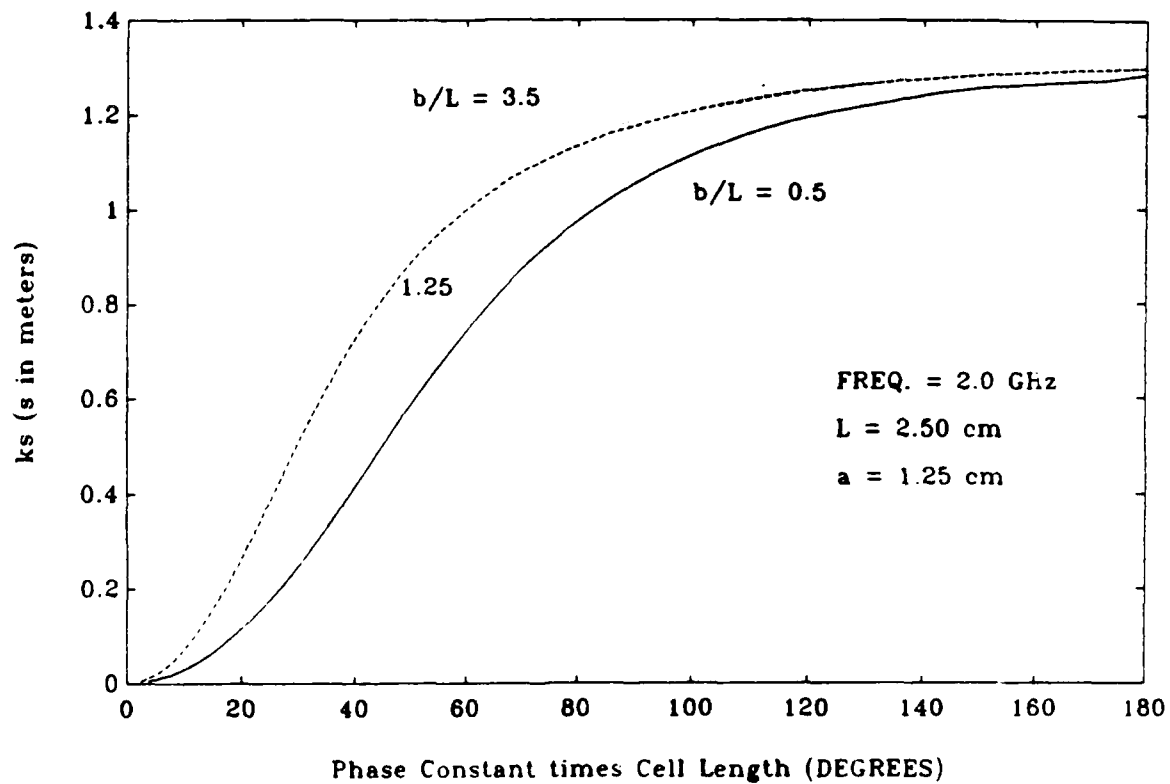


Figure 1.4. Solution dependence on b-to-L ratio.

1.4 Application to Cylindrical Structures

The numerical procedure above is also applicable to coaxial slow wave structures with corrugated outer conductors in cases of small outer-to-inner conductor radius ratios (ratios typically less than two). In those cases, the geometrical relation between cathode and anode locally approximates the planar geometry considered here.

To illustrate an application of the procedure to a cylindrical slow wave structure, consider: frequency = 3.6 GHz, $k_s = 1.357$, $\lambda_0/L = 5.95$, $s/L = 1.286$, $b/L = 1.214$, and $a/L = 0.500$. Specifically, the inner conductor radius is 6.5 cm, the inner dimension of the outer conductor is 8.2 cm while the outer dimension is 10.0 cm, cell width is 1.4 cm with 0.7 cm each in the tooth and slot. The computer-assisted analysis described here gives the solution $v_p/c = 0.336$. The analysis of [7] concludes that v_p is 0.398c, and quotes an experimental value of 0.34c.

CHAPTER 2

FIRST-ORDER ANALYSIS

2.1 Basis

It is noted in [8] that an important class of high-frequency filters utilizes a cascade connection of short transmission lines having alternately low and high characteristic impedances. The transmission matrix description of [8] is now more commonly referred to as an ABCD matrix description. A cascade connection of two-ports, each with a known ABCD matrix description, is characterized simply by the ordered product of the respective two-port matrices. For a short section of transmission line of electrical length θ and characteristic impedance Z_0 , taken to be lossless, the ABCD matrix description is

$$\begin{bmatrix} \cos \theta & jZ_0 \sin \theta \\ j \frac{\sin \theta}{Z_0} & \cos \theta \end{bmatrix}. \quad (2.1)$$

The characteristic impedance for an vacuum-filled coaxial line is

$$Z_0 = 60 \ln \frac{b}{a}, \quad (2.2)$$

where b is the outer conductor radius and a is the radius of the inner conductor.

For example, for a corrugated coaxial line with inner radius 6.5 cm, small outer radius of 8.2 cm, and large outer radius of 10. cm, the line may be viewed as comprised of

alternating sections of impedance

$$Z_1 = 60 \ln \frac{8.2}{6.5} = 13.94 \Omega \quad (2.3)$$

and

$$Z_2 = 60 \ln \frac{10.}{6.5} = 25.85 \Omega. \quad (2.4)$$

This straightforward circuit analysis obviously ignores the cavity effect associated with the outer conductor slots and/or the discontinuity reactances associated with the step changes in outer conductor radius. However, it is a simple modification to add into the formulation the ABCD matrix for a shunt susceptance at each discontinuity point. A Method of Moments (MOM) program has been developed (see next section) to assist with estimating such discontinuity susceptances.

Two FORTRAN programs have been written which will execute this analysis. The first (called CELL6), which has its source code documented in Appendix C, treats each slot and metal tooth as an entity. The second (CELL8, with source code in Appendix D) recognizes that the actual system has distributed parameters and is not actually in such coarse lengths. Toward a more realistic analysis, then, the second program decomposes each cell (one slot width plus one tooth width) into nine sub-intervals. Both programs provide for the interactive input of shunt capacitive discontinuity associated with the outer conductor's step change in radius. Without an approximate value available, "0" shunt capacitance (reactance ∞) may be entered, but the program then yields a v_p approximately equal to c , because the simplified model is

based on TEM line sections which indeed support propagation at velocity c .

2.2 Estimation of Planar Discontinuity Susceptance

The matter of planar discontinuities in coaxial waveguides has been studied in detail over a period of years by Dr. Michael G. Harrison, with his engineering analysis strategy and results thoroughly detailed in [9]. The formulation in [9] is the well known Method of Moments (MOM), which is capable of quite accurate predictions when properly applied. Dr. Harrison has treated, among other cases, that of a single step change in outer conductor radius. The situation addressed by Dr. Harrison's MOM code is illustrated in Figure 2.1. With permission, his code has been applied to the problem at hand and, further, is listed in Appendices E, F, and G (the main program STPOUT appears in Appendix E, with essential subroutines COAXRT in Appendix F and GELG in Appendix G).

2.3 An Example Application

For illustration, the earlier geometry of inner conductor radius $a = 6.5$ cm, smaller outer radius $b = 8.2$ cm, larger outer radius $c = 10.$ cm, slot and tooth width of 0.7 cm each, and frequency 3.6 GHz is considered again.

The program STPOUT, executed for twelve MOM pulses in the aperture at the radius step change and with four terms in the Bessel function series, gives a normalized shunt

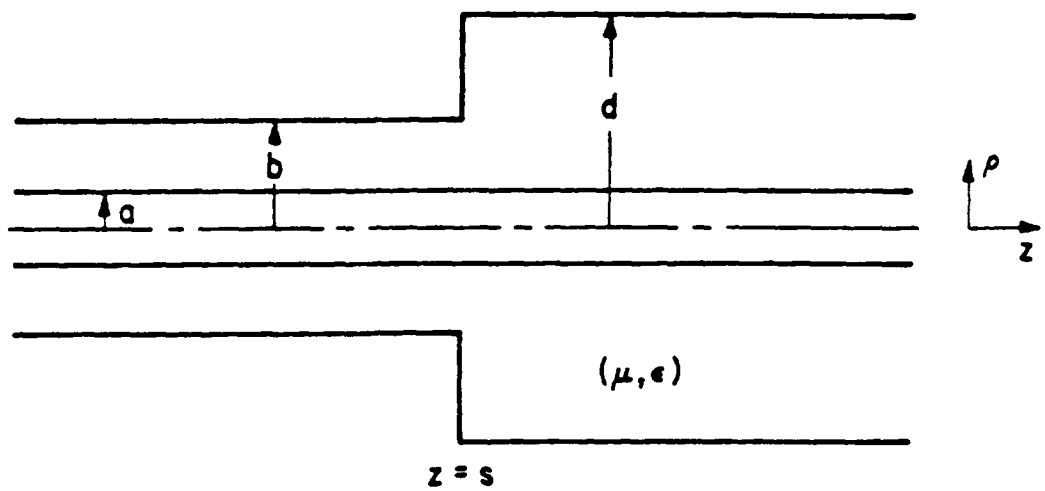


Figure 2.1. Step discontinuity in the outer conductor of a coaxial waveguide.

susceptance prediction of 0.522. The normalization is the admittance of the coaxial section with inner radius 6.5 cm and outer radius 8.2 cm. The de-normalized shunt susceptance is thus 0.0375, which in turn gives the following conclusions:

$$\text{From CELL6} - v_p \approx 0.616c \quad (2.5)$$

$$\text{From CELL8} - v_p \approx 0.453c. \quad (2.6)$$

The sub-interval program CELL8 results are encouragingly closer to the accepted value 0.34c, and one immediately wonders if further subdivision of the slot and tooth widths would be productive. This has been investigated with a program based on eighteen sub-intervals; however, the improvement turns out to be trivial when more than nine subdivisions are used.

2.4 Limitation of the Formulation

The formulation of this chapter takes into account only a single step discontinuity, analyzed in isolation from other perturbations of the outer conductor dimension. In reality, there is a succession of such discontinuities, each in rather close electrical proximity to its neighbors. Hence, the discontinuities interact with each other electromagnetically. Also, the slots act as cavities in addition to their basic transmission line section behaviors, which is not taken into account by a single-aperture evaluation.

CHAPTER 3

EXTENDED MOM NUMERICAL ANALYSIS

3.1 Basis

It is straightforward to extend the analysis of program STPOUT from a single aperture to multiple apertures. The background theory is documented at length in [9], and the reader is referred to that reference for the formulation details.

3.2 Program for Multiple Apertures

The extended program, named NSLOTS, has the source code listing in Appendix H. Two new additional subroutines are required to support this main program - CDMLR and OUTSTP. The source code listing for CDMLR is given in Appendix I, while that for OUTSTP appears in Appendix J. This program requires a minimum input of two apertures. The present array dimensions may be increased if the user desires more than eighty (total, for all apertures) MOM pulses.

Work with this program to date indicates that it is computationally reliable. Although NSLOTS accepts necessary input data from the operator by rather self-explanatory questions, a specific application is now documented.

3.3 Application Example

Consider the hypothetical slow to fast wave transition geometry shown in Figure 3.1. This circuit represents a

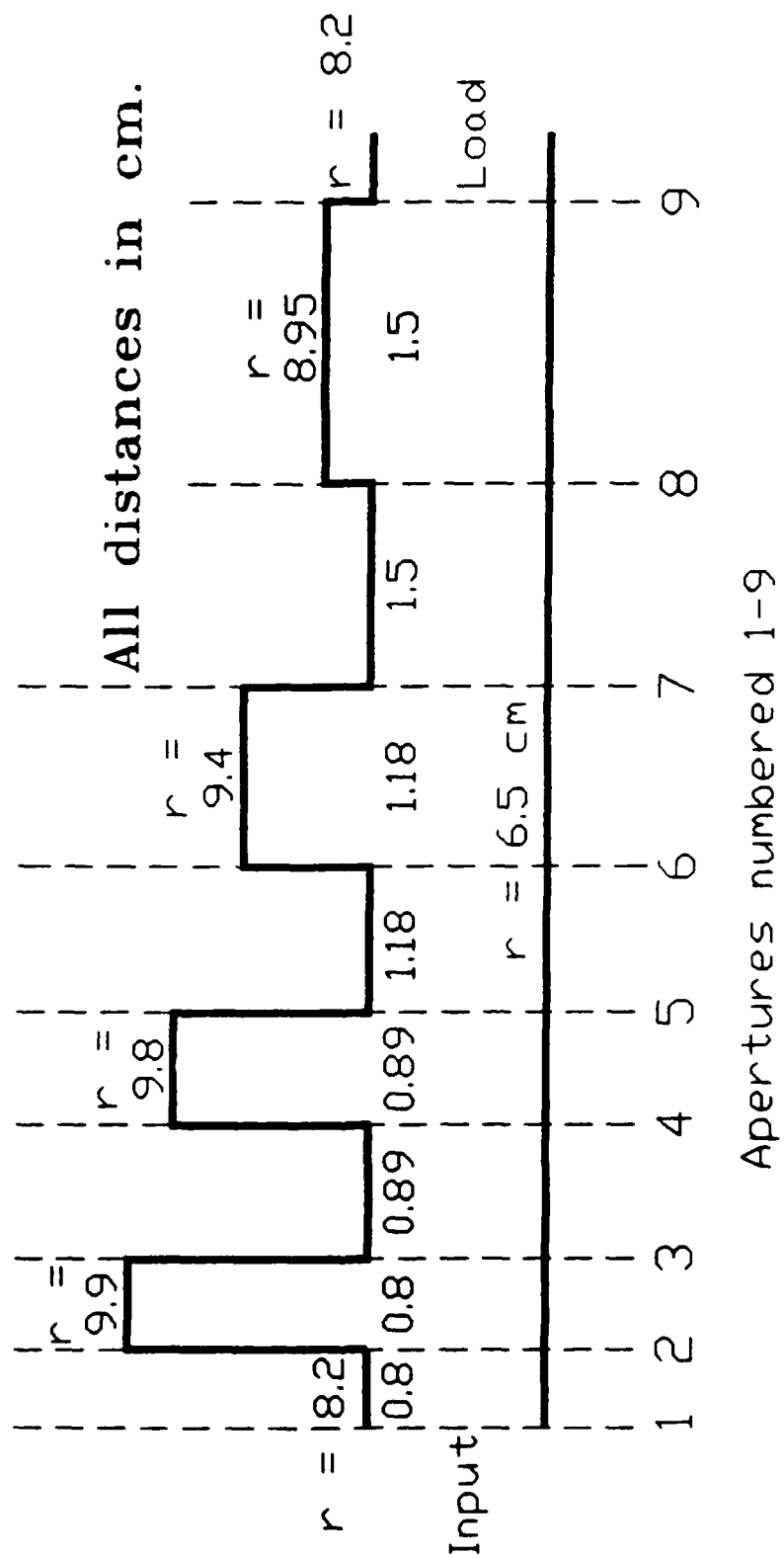


Figure 3.1. Slow to fast wave transition for analysis by program NSLOTS.FOR.

proposed transition design, and the objective is to predict the input impedance/SWR of the transition at various frequencies prior to physical construction of the device.

The operator commands necessary to invoke execution of NSLOTS and to enter the requisite input data are found in the session listing of Figure 3.2, for 3.6 GHz. Results of the program executions are summarized in Table 3.1 for frequencies from 1.8 to 10.8 GHz in steps of 1.8 GHz. At certain frequencies, the input impedance is seen to present a rather good match to the source, while there is large mismatch at others. This is expected, as the transition region is expected to function basically as a high-frequency filter circuit.

3.4 Limitations of the MOM Analysis

In its present form, the MOM program NSLOTS outputs an analysis only for one aperture, at the input end of the structure. Furthermore, this analysis is for the *total* electric field, which is comprised of the original incident field superimposed with the scattered fields from points farther down (+z) the structure.

The MOM analysis strategy appears excellent for analysis of a transition in a composite sense. On the other hand, the fact that the MOM solution gives a total field solution apparently makes it impossible to extract individual susceptances associated with the various planar discontinuities. This, in turn, makes development of a

lumped-element equivalent circuit model extremely difficult.


```

nslots
  APMULT1.FOR OUTPUT - PROGRAM TO COMPUTE APERTURE FIELDS FOR TWO-PORT
                      COAXIAL LINE WITH GROOVES
INPUT THE NUMBER OF APERTURES
9
INPUT THE NUMBER OF PULSES IN EACH OF THE 9 APERTURES
7,7,7,7,7,7,7,7,7
INPUT THE NUMBER OF TERMS IN THE BESSEL FUNCTION SERIES
4
INPUT INNER RADIUS (IN METERS)
.065
INPUT 10 OUTER RADII (IN METERS)
.082,.082,.099,.082,.098,.082,.094,.082,.0895,.082
INPUT 8 SECTION WIDTHS (IN METERS)
.008,.008,.0089,.0089,.0118,.0118,.015,.015
INPUT FREQUENCY IN HERTZ
3.6e9

```

Figure 3.2. Session listing for NSLOTS execution.

TABLE 3.1
ANALYSIS OF SLOW TO FAST WAVE TRANSITION
BY PROGRAM NSLOTS

FREQUENCY (GHZ)	INPUT ADMITTANCE (S)	REFLECTION COEFFICIENT ρ	SWR
1.80	0.0554 + j0.0003	0.130	1.300
3.60	0.0372 + j0.0008	0.319	1.937
5.40	0.0255 + j0.0128	0.680	5.248
7.20	0.0958 + j0.0267	0.851	12.385
9.00	0.4108 - j0.0226	0.704	5.753
10.80	0.1093 - j0.0336	0.688	5.411

CHAPTER 4

LUMPED-ELEMENT EQUIVALENT CIRCUITS

4.1 General Discussion

A generic slow wave unit cell is illustrated in Figure 4.1. In the course of this study, over three hundred man-hours were devoted to investigation of possible broadband lumped-element equivalent circuits for the individual slow wave circuit unit cells.

Such equivalent circuits, if possible to develop, would be useful both for faster analysis of the cell at new frequencies of interest intermediate to those of the original analysis, and for the physical insight into the workings of the slow wave unit cell. Circuit analysis computer programs are plentiful and most execute quickly in comparison to the Method of Moments electromagnetics code described earlier.

The equivalent circuits should be applicable through at least the third harmonic of the frequency of interest, as slow to fast wave transition behavior at second and third harmonic frequencies is always a concern of the transition designer.

4.2 Procedure

It soon becomes apparent that a manual (analytical) approach to the modelling problem is not feasible. The most practical approach which has evolved in this study has been

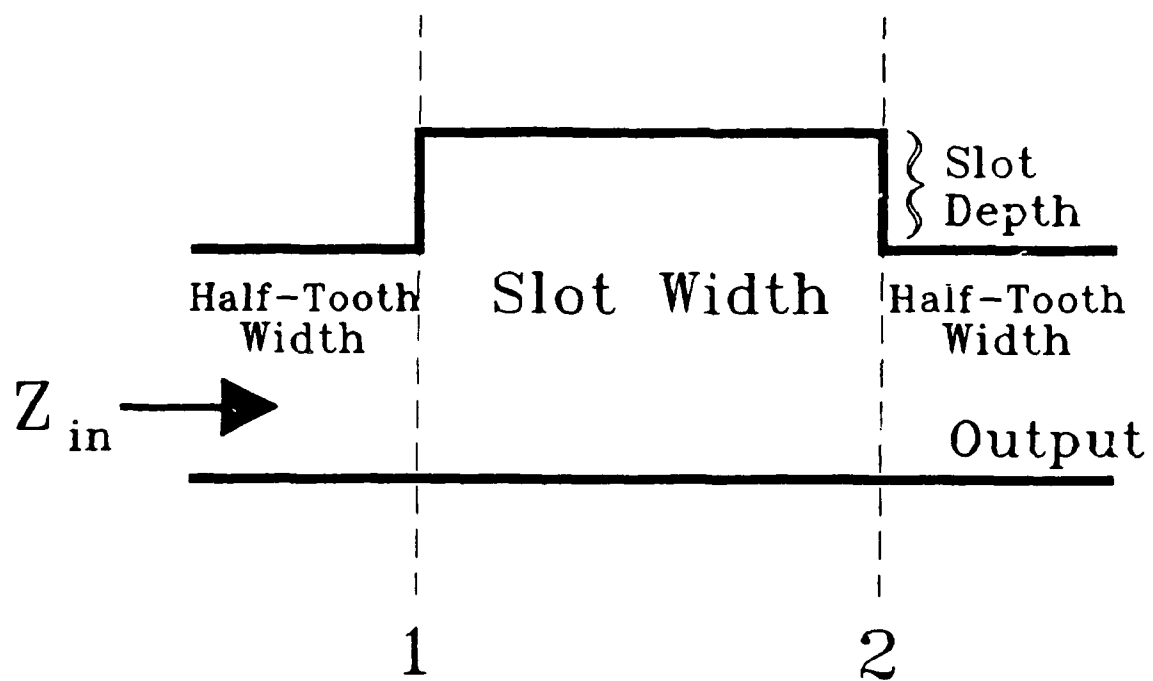


Figure 4.1. Generic slow wave unit cell.

to fit a circuit containing appropriate elements (transmission line sections, capacitances, etc.) to the cell input impedance data obtained at a few selected frequencies across the relevant frequency span with the aid of the MOM code.

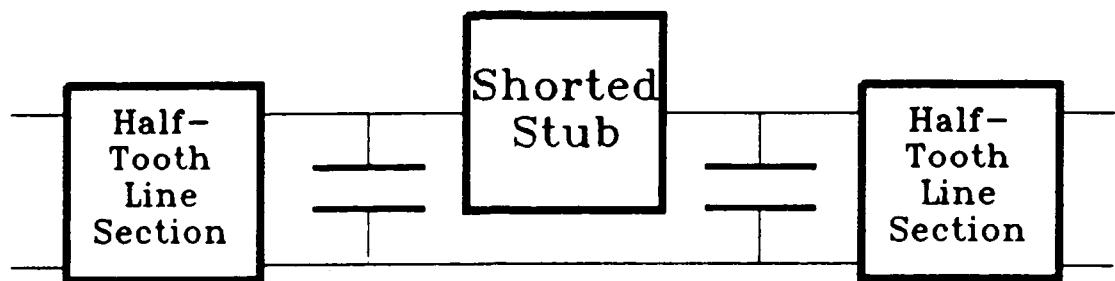
Dozens of possible equivalent circuit forms have been actively studied. For example, the circuits of Figure 4.2(a)-(1) are a subset of those considered. Note that half-slot line sections are not shown in Figure 4.2 in order to avoid excessive clutter of the diagrams. Slot equivalents were considered both with and without half-slot line sections included.

4.3 Illustrative Example

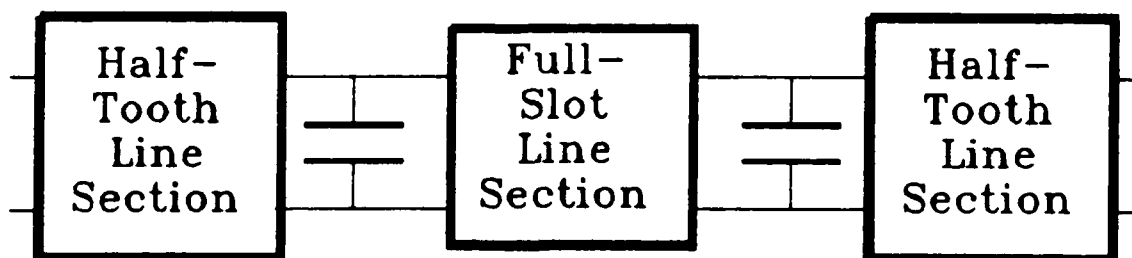
The cell of Figure 4.1 with half-tooth width of 0.8 cm, slot width of 1.8 cm, slot depth of 0.2 cm, cathode-anode gap of 1.7 cm, and frequencies from 1.8 to 10.8 GHz illustrates typical results from this study. For this shallow slot geometry, the phase velocity will closely approximate that of light and, for simplification of the example, is taken to be $0.98c$ over the specified frequency range.

The input impedance of the cell at discrete frequencies 1.8, 2.7, 3.6, 4.5, 5.4, 6.3, 7.2, 8.1, 9.0, 9.9, and 10.8 GHz was calculated by first finding the impedance at aperture 1 with the MOM code, and then translating that impedance to the input plane shown in Figure 4.1 by means of

Slow-wave cell



(a)

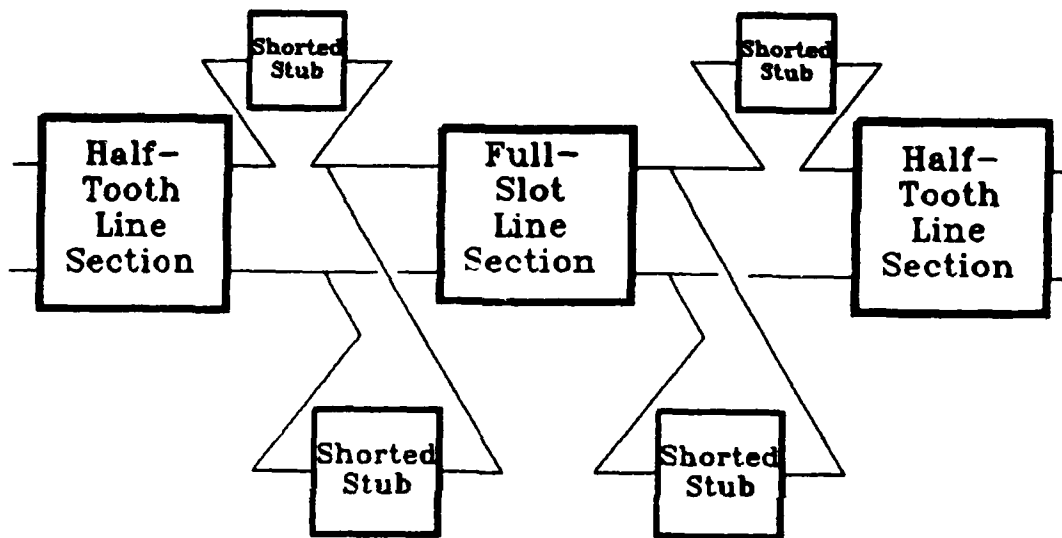


(b)

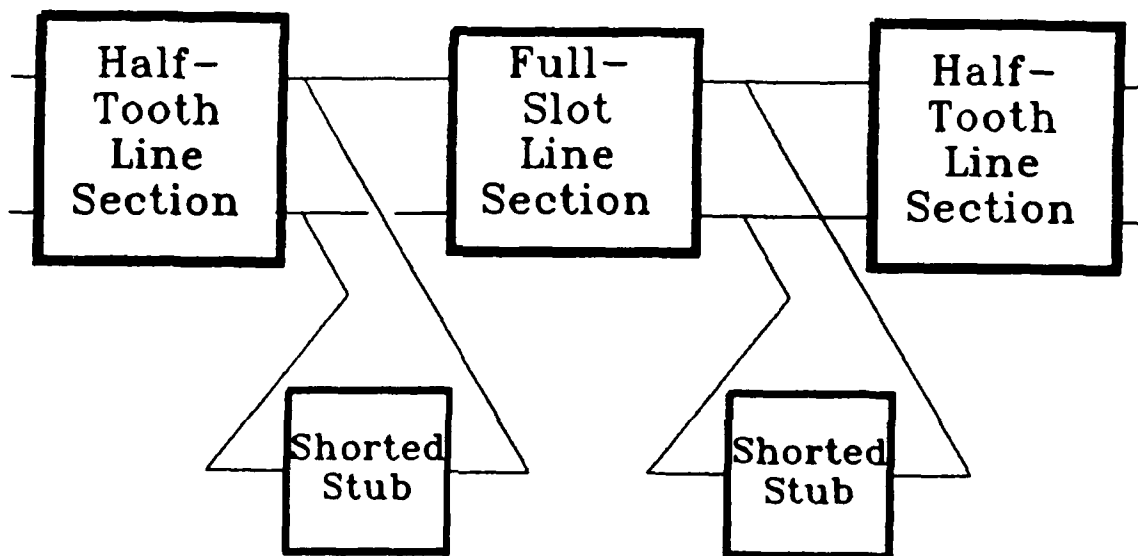
Figure 4.2. Lumped-element equivalent circuits.

Slow-wave cell

Slot



(c)

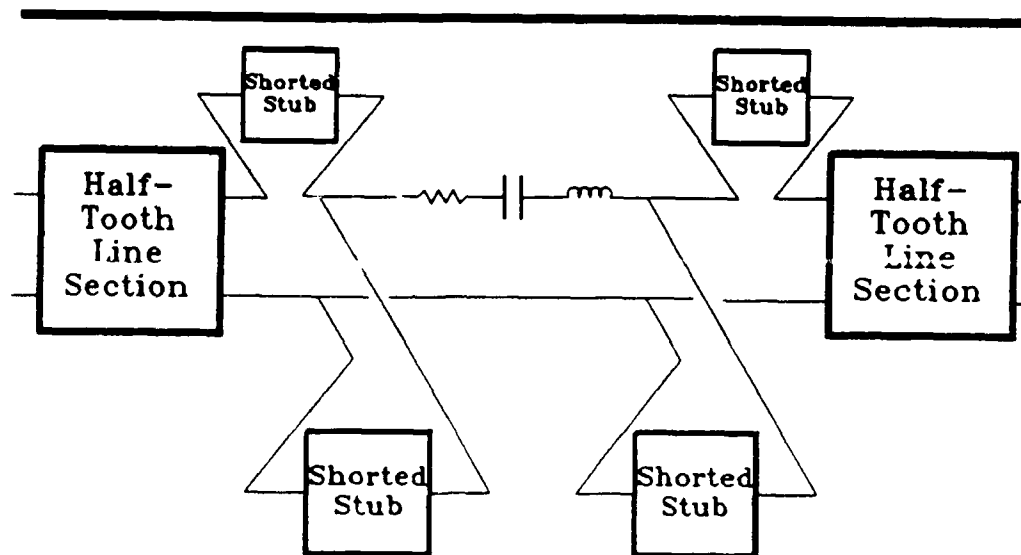


(d)

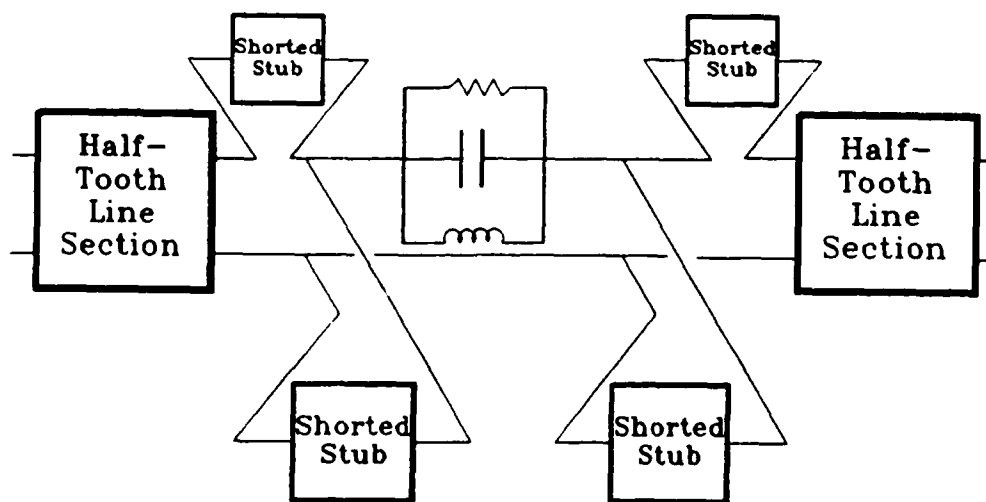
Figure 4.2 (continued) Lumped-element equivalent circuits.

Slow-wave cell

Slot



(e)

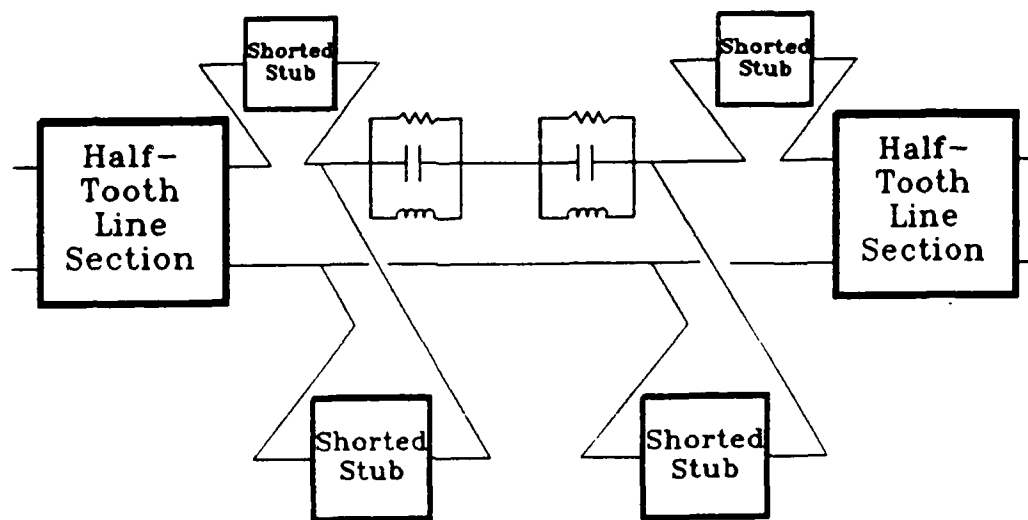


(f)

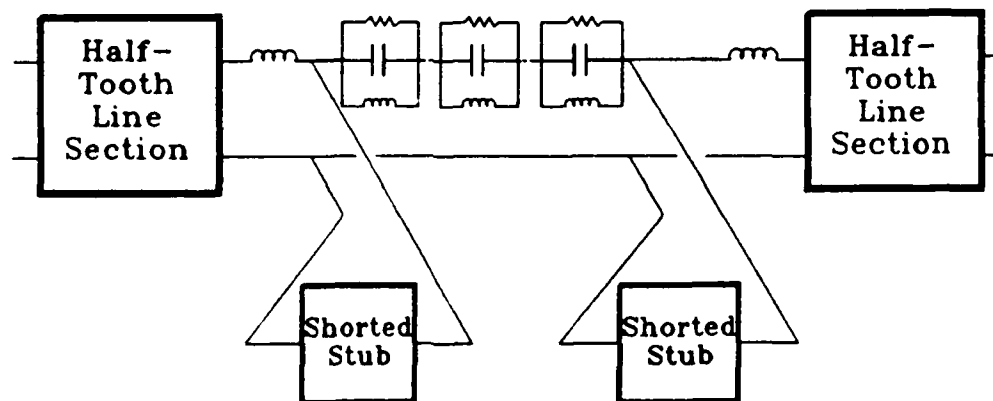
Figure 4.2 (continued) Lumped-element equivalent circuits.

Slow-wave cell

Slot



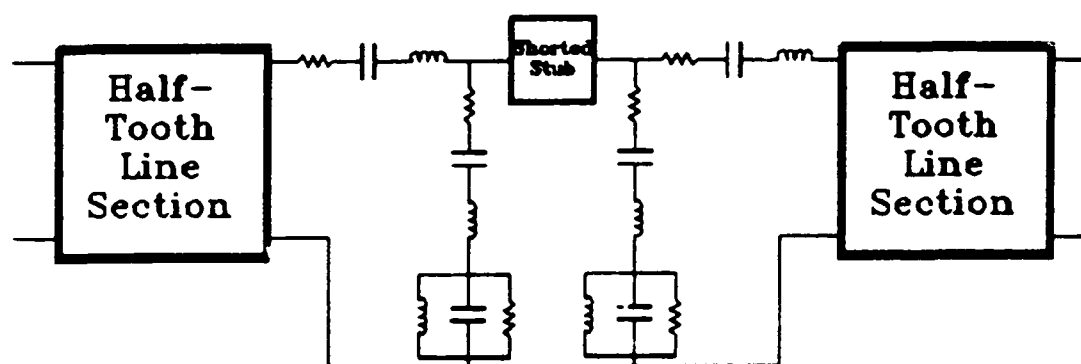
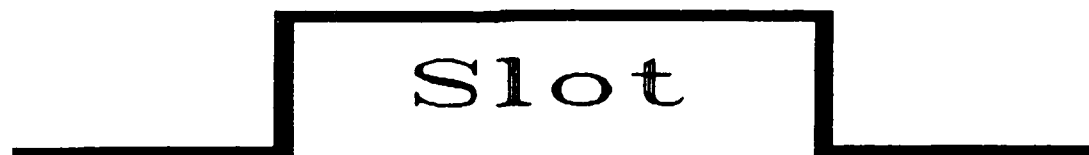
(g)



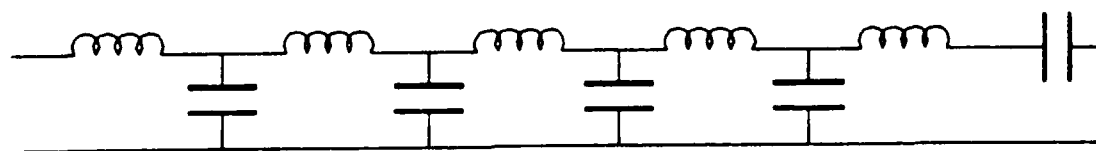
(h)

Figure 4.2 (continued) Lumped-element equivalent circuits.

Slow-wave cell



(i)

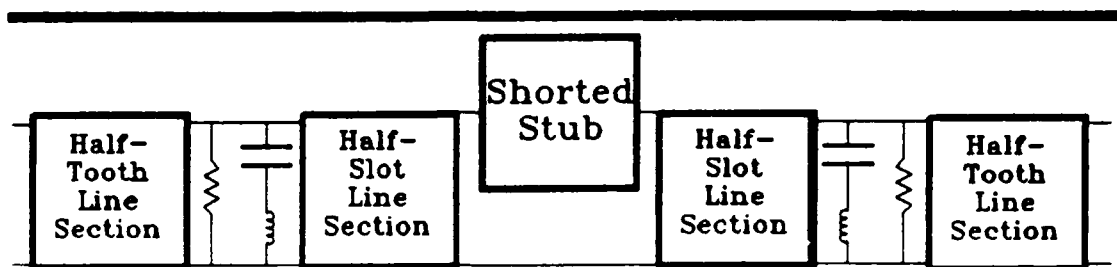


(j)

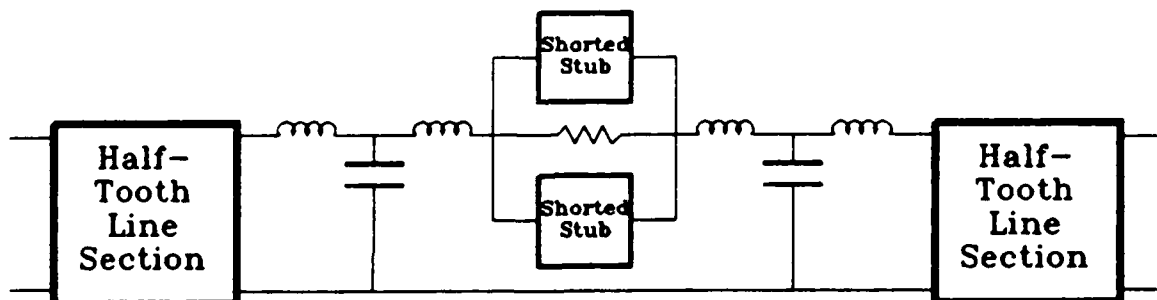
Figure 4.2 (continued) Lumped-element equivalent circuits.

Slow-wave cell

Slot



(k)



(l)

Figure 4.2 (continued) Lumped-element equivalent circuits.

the standard transmission line equation.

In this case, the circuit analysis/optimization program *TANE* [10] was applied to optimize the fit of the equivalent circuit elements from Figure 4.2(1), with the minor deletion of one shorted stub, to the impedance data. *TANE* utilizes the Davidson-Fletcher-Powell optimization technique, which is widely recognized as effective in such optimization applications. The initial data file for the program is given in Figure 4.3(a) while the modified circuit element values, after optimization, are output by the program to a new file which is given for convenient reference as Figure 4.3(b). The circuit node numbering scheme is clear from the data files.

Initial plots of the input reflection coefficient S_{11} , both magnitude and phase, may be seen in Figure 4.4. Similar plots for the transmission coefficient S_{21} are found in Figure 4.5. The initial circuit element choices give a particularly bad fit to the data at 2.7 and 8.1 GHz. After approximately three hundred optimization iterations, the equivalent circuit fit progresses to the condition graphically depicted in Figures 4.6 (S_{11} final magnitude and phase) and 4.7 (S_{21} final magnitude and phase).

From Figure 4.6, it is seen that with the exception of 8.1 GHz, the fit of the equivalent circuit to the electromagnetics code data is quite good. Even at 8.1 GHz, the "mismatch" from a power viewpoint is only $(0.125)^2 \times 100\% = 1.56\%$.

```

TRL * 1 0 2 0 13.94 34.5 3.6E9 0.
IND* 2 3 5.E-11
CAP* 3 0 0.6E-12
IND* 3 4 9.E-11
TRL * 4 0 5 0 15.4 31. 3.6E9 0.
RES* 5 6 1000.
SST** 5 6 4.4 120. 3.6E9 0.
TRL * 6 0 7 0 15.4 33. 3.6E9 0.
IND* 7 8 9.E-11
CAP* 8 0 0.9E-12
IND* 8 9 8.E-11
TRL 9 0 10 0 13.94 34.5 3.6E9 0.
PORT1 1 0 TABLE1
PORT2 10 0 13.94
PERFORM TWOPORT OPTIMIZATION MAGNITUDE
GRAPHICS ON SM11 BLACK
END
1.8E9 2.7E9 3.6E9 \ 1 0 0 0
4.5E9 5.4E9 6.3E9 \ 1 0 0 0
7.2E9 8.1E9 9.E9 \ 1 0 0 0
9.9E9 10.8E9 \ 1 0 0 0
END
TABLE1 ZPARAM
15.5 -0.5
16.1 0.8
15.3 2.4
13.5 2.8
12.1 2.0
11.5 0.5
11.7 -0.9
12.3 2.9
14.3 -0.9
13.3 0.9
12.3 0.2
END

```

Figure 4.3(a). Initial data file for circuit analysis by TAME.

```

TRL * 1 0 2 0 1.394E+001 2.507E+001Deg. 3.600E+009 0.000E+000
IND* 2 3 4.171E-011
CAP* 3 0 5.738E-013
IND* 3 4 7.842E-011
TRL * 4 0 5 0 1.540E+001 2.230E+001Deg. 3.600E+009 0.000E+000
RES* 5 6 8.787E+002
SST** 5 6 6.238E-002 2.595E+002Deg. 3.600E+009 0.000E+000
TRL * 6 0 7 0 1.540E+001 3.404E+001Deg. 3.600E+009 0.000E+000
IND* 7 8 9.697E-011
CAP* 8 0 7.148E-013
IND* 8 9 8.744E-011
TRL 9 0 10 0 1.394E+001 3.450E+001Deg. 3.600E+009 0.000E+000
PORT1 1 0 TABLE1
PORT2 10 0 1.394E+001
PERFORM TWOPORT OPTIMIZATION MAGNITUDE
GRAPHICS ON SP21 Black
END
1.8E9 2.7E9 3.6E9 \ 1 0 0 0
4.5E9 5.4E9 6.3E9 \ 1 0 0 0
7.2E9 8.1E9 9.E9 \ 1 0 0 0
9.9E9 10.8E9 \ 1 0 0 0
END

TABLE1 ZPARAM
15.5 -0.5
16.1 0.8
15.3 2.4
13.5 2.8
12.1 2.0
11.5 0.5
11.7 -0.9
12.3 2.9
14.3 -0.9
13.3 0.9
12.3 0.2

END

```

Figure 4.3(b). TAME output file showing optimized element values.

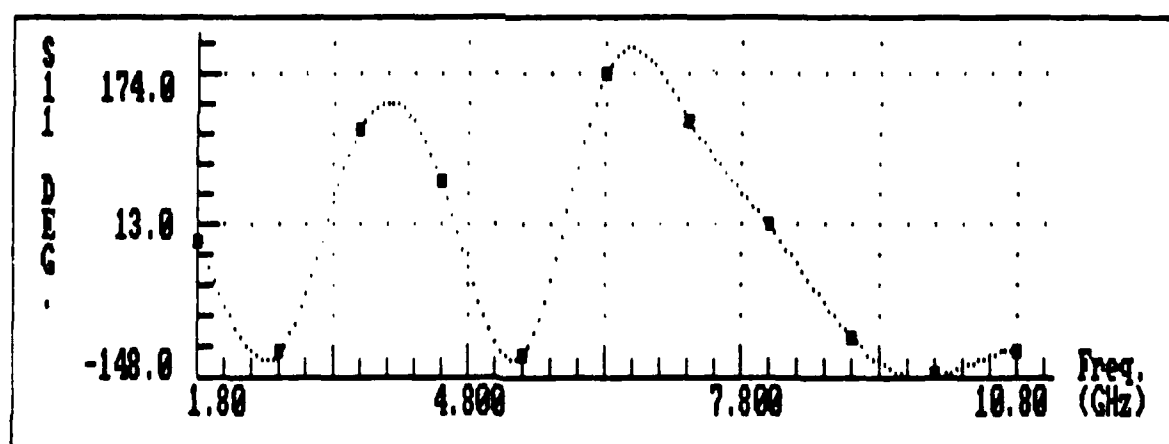
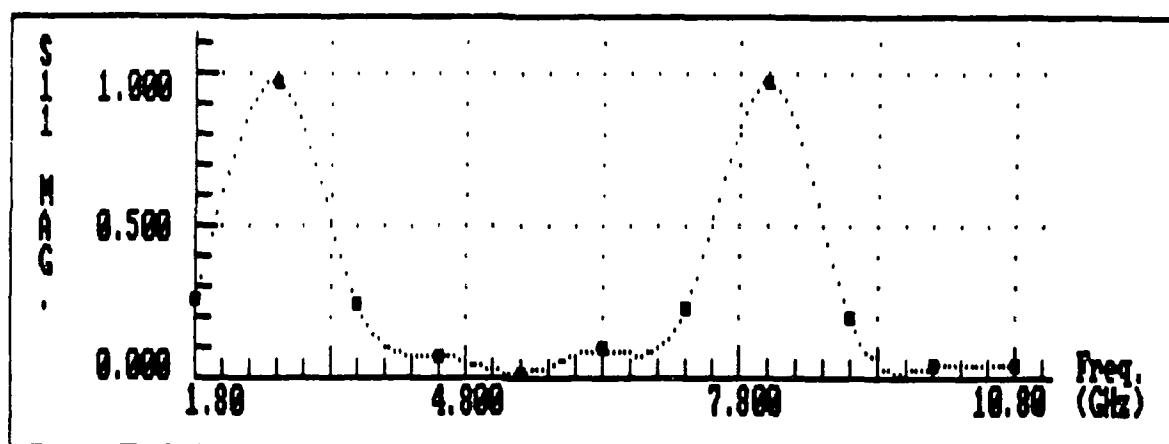


Figure 4.4. Input reflection coefficient, initial analysis.

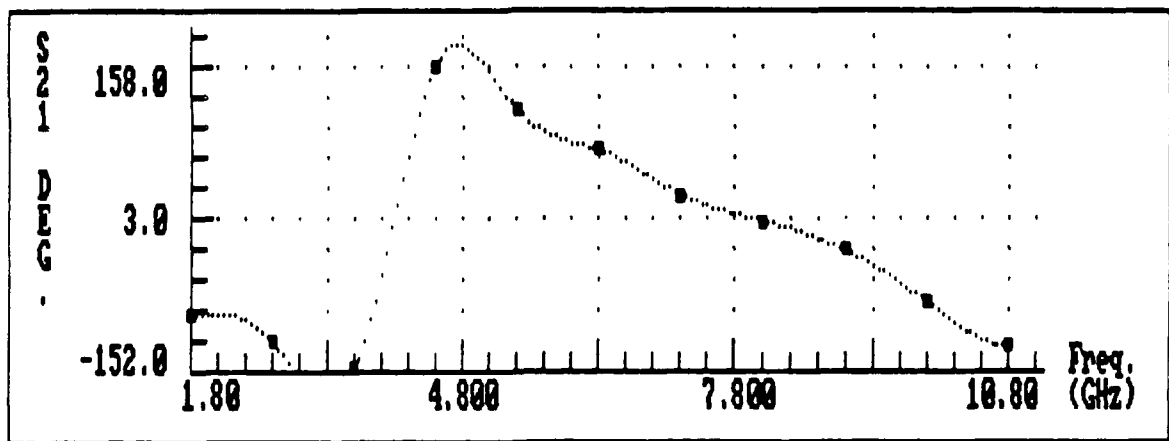
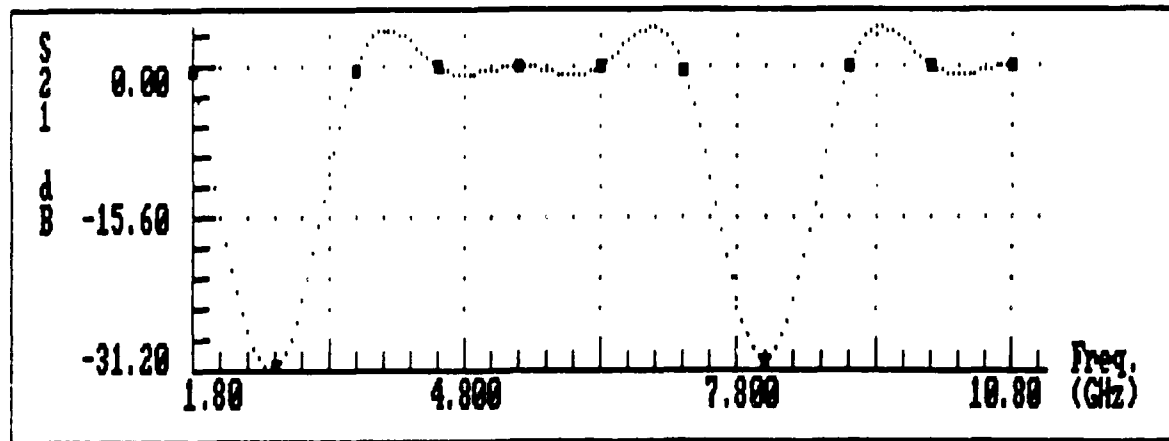


Figure 4.5. Forward transmission coefficient, initial analysis.

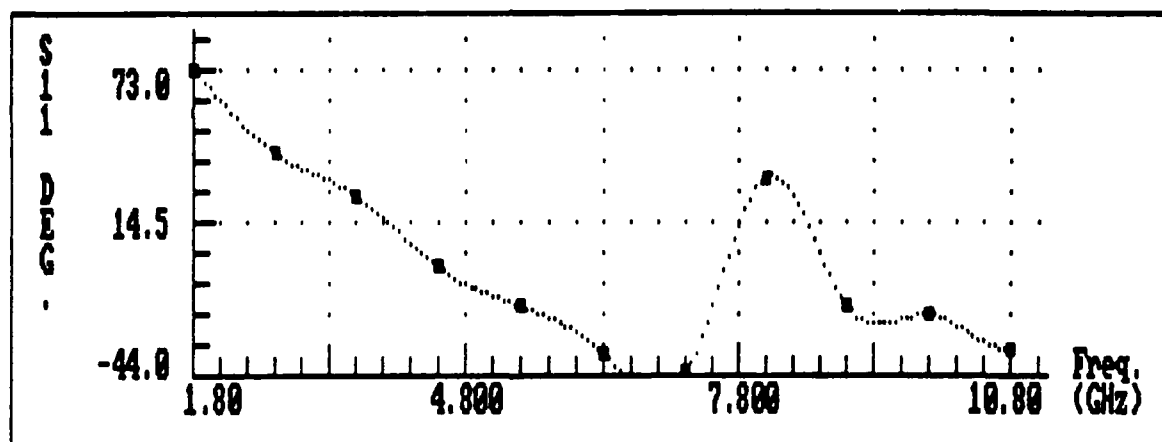
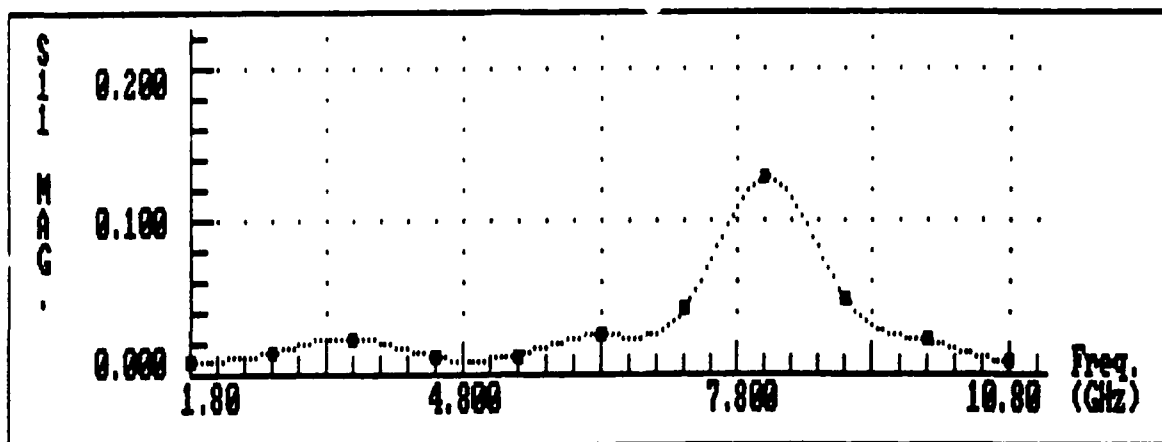


Figure 4.6. Input reflection coefficient, final analysis.

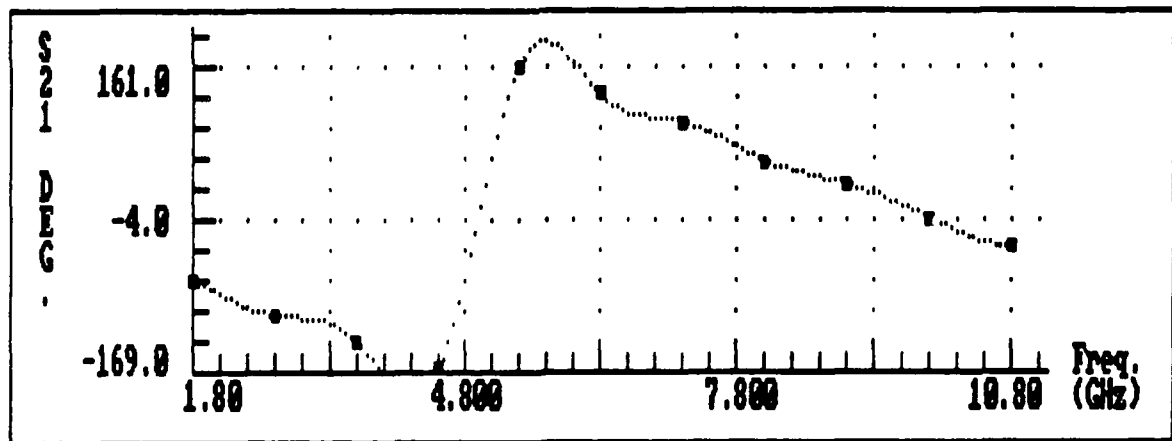
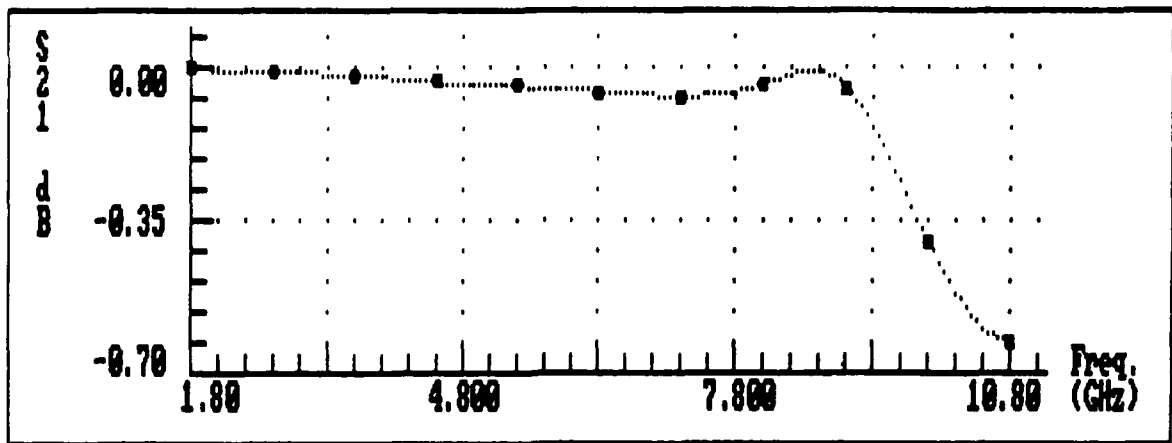


Figure 4.7. Forward transmission coefficient, final analysis.

Primary interest lies with the final S_{21} phase values. From these "phase shift across the unit cell" numbers, the phase velocity v_p follows directly. The results are summarized in Table 4.1.

The average error for this equivalent circuit's v_p is about 10% at eleven frequencies from 1.8 to 10.8 GHz. For design purposes, an average error more on the order of 2% would be highly desirable. In some cases, a better fit to the impedance data was obtained, with the S_{11} plot having a maximum magnitude of 0.050 over a similar frequency range. On the other hand, worse results were also frequently obtained. For example, this same equivalent circuit refuses to fit data for the slightly different geometry of half-tooth width = 0.75 cm, slot width = 1.5 cm, slot depth = 0.7 cm, and cathode-anode gap = 1.7 cm.

TABLE 4.1
EXAMPLE EQUIVALENT CIRCUIT PHASE VELOCITY RESULTS

FREQUENCY GHZ	PREDICTED PHASE SHIFT, BASED ON $v_p = 0.98c$ IN DEGREES	EQUIVALENT CIRCUIT S_{21} PHASE (FIG. 4.7) IN DEGREES	% ERROR
1.8	-75.	-70.	6.5
2.7	-112.	-105.	6.3
3.6	-150.	-136.	9.3
4.5	-187.	-166.	11.2
5.4	-225.	-199.	11.6
6.3	-262.	-232.	11.5
7.2	-300.	-265.	11.7
8.1	-337.	-304.	9.8
9.0	-374.	-326.	12.8
9.9	-412.	-364.	14.1
10.8	-449.	-397.	11.6
AVERAGE ERROR			10.6

SUMMARY AND CONCLUSIONS

Various means for analysis of coaxial, corrugated outer conductor transitions between electromagnetic slow and fast wave regions have been investigated. The emphasis has been on identification of a reliable method for pre-production analysis of the matching effectiveness of transition designs.

Such structures may be viewed, in one sense, as a cascade connection of two ports. A common contemporary strategy for analyzing cascaded two-ports utilizes the ABCD matrix, as reported in Chapter 2. For this approach to give accurate results, the ABCD matrix characterization of each planar discontinuity in the coaxial slow to fast wave transition must be well known. A single-aperture Method of Moments numerical analysis would suffice for the discontinuity characterizations if the discontinuity planes were electrically isolated from each other. However, actual case studies indicate that the discontinuities in practical transition design electromagnetically interact with each other to the extent that a single-aperture MOM program does not yield acceptable results. Although the MOM analysis may be readily extended to a multiple-aperture capability, that is of no real benefit to the ABCD-matrix approach as, then, no procedure has been found for de-embedding the essential individual discontinuities from the "total" MOM solution.

The possibility of identifying a lumped-element equivalent circuit for slow wave cells is appealing, with results such as those presented in connection with the Chapter 4 example encouraging further work. In the course of this project, several dozen potential equivalent circuits have been examined in great detail through specific case studies. Although isolated cells have met with a high degree of success with regard to equivalent circuit modelling, a suitable circuit for general application has not been identified. While this goal has merit, and circuits akin to that of Figure 4.2(1) show promise, the success of the procedure in specific applications remains unreliable.

Experience to date indicates that the extended Moment Method analysis described in Chapter 3 is both accurate and reliable. The N-slot version of this program allows the analysis, in a single computer run, of an entire slow to fast wave transition. The only liability of this method is that the effect of individual discontinuities and the performance of individual cells is lost in the all-encompassing MOM solution. Overall, the extended MOM code affords an effective and valuable analysis tool.

ACKNOWLEDGEMENT

Special thanks are extended to Dr. Michael G. Harrison of the Weapons Laboratory (WL/NTCA) for his interest and support in this work. His permission to use the computer codes associated with reference [9] in this study and to include selected source code listings in this report are deeply appreciated. Furthermore, Dr. Harrison's active assistance with extending the original MOM codes and numerous technical consultations are gratefully acknowledged.

REFERENCES

- [1] S.Y. Liao, *Microwave Electron-Tube Devices*. Englewood Cliffs, NJ:Prentice-Hall, 1988, pp. 270-275.
- [2] R.B. Miller, *Intense Charged Particle Beams*. New York: Plenum Press, 1982.
- [3] R.G.E. Hutter, *Beam and Wave Electronics in Microwave Tubes*. Princeton, NJ:D. Van Nostrand, 1960, sec. 7-4.
- [4] R.E. Collin, *Foundations for Microwave Engineering*. New York:McGraw-Hill, 1966, pp. 381-383.
- [5] S.D. Conte and C. de Boor, *Elementary Numerical Analysis, an Algorithmic Approach, 3rd Ed.*. New York:McGraw-Hill, 1980, pp. 120-127.
- [6] W.J. Kleen, *Electronics of Microwave Tubes*. New York: Academic Press, 1959, p. 292.
- [7] Biggs, A.W., *Final Report, 1986 USAF Summer Faculty Research Program*, August 1986.
- [8] Ghose, R.N., *Microwave Circuit Theory and Analysis*. New York:McGraw-Hill, 1963, pp. 283-284.
- [9] Harrison, M.G., *An Analytical and Experimental Investigation of Planar Discontinuities in Coaxial Waveguides*, Air Force Weapons Laboratory Report No. AFWL-TR-79-187, March 1981.
- [10] Sussman-Fort, S.E., *TAME (Top Algorithms for Microwave Engineering), A Program for Analysis, Optimization, and Synthesis of Networks in the Frequency Domain*, Department of Electrical Engineering, State University of New York at Stony Brook, 1988.

**Appendices can be obtained from
Universal Energy Systems, Inc.**